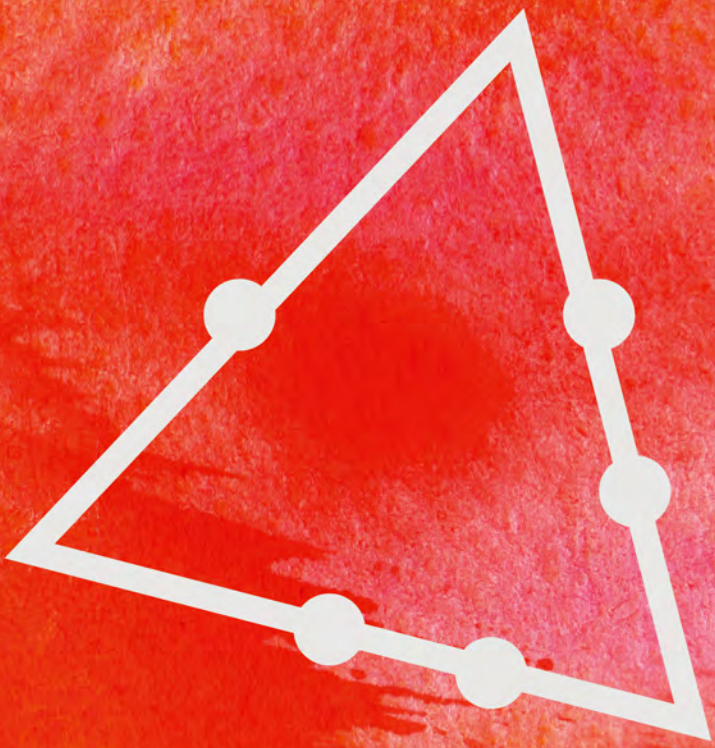
Merete Tangstad, Gabriella Tranell,
Halvard Tveit & Eli Ringdalen (Eds.)

Production of high silicon alloys

2. edition



FAGBOKFORLAGET

Production of high silicon alloys

Merete Tangstad, Gabriella Tranell, Halvard Tveit
and Eli Ringdalen (Eds.)

Production of high silicon alloys

2. EDITION

FAGBOKFORLAGET

First published 2026 by Vigmostad & Bjørke AS,
© 2026 copyright of the selection and editorial matter, Merete Tangstad, Gabriella Tranell, Hallvard Tveit & Eli Ringdalen.
© 2026 copyright of the individual chapters is held by the respective authors.

This work, available from https://oa.fagbokforlaget.no, is licensed under the Creative Commons Attribution 4.0 International (CC BY 4.0) license.

This license grants permission to copy and redistribute the material in any medium or format, and to remix, transform, and build upon the material for any purpose, even commercially. The exercise of these freedoms is granted on the following terms: You must give appropriate credit, provide a link to the license, and indicate if changes were made. You may do so in any reasonable manner, but not in any way that suggests the licensor endorses you or your use. You may not apply legal terms or technological measures that legally restrict others from doing anything the license permits.

The license text in full is available at https://creativecommons.org/licenses/by/4.0/

The license may not give you all the permissions necessary for your intended use. For example, other rights such as publicity, privacy, or moral rights may limit how you use the material.

This book is published with financial support from
FFF – The Norwegian Ferroalloy Industry Research Association Silicon for chemical and solar industry
FME ZeMe pr.no 350325 funded by the Norwegian Research Council
SiH2 pr.no 325464 funded by the Norwegian Research Council
Safeci pr.no 326802 funded by the Norwegian Research Council
Queen EU grant agreement 101178144

ISBN print edition: 978-82-450-6389-9
ISBN digital edition: 978-82-450-6341-7
DOI: https://doi.org/10.55669/oa8808

Enquiries about this book can be directed to:
fagbokforlaget@fagbokforlaget.no
www.fagbokforlaget.no

Cover design by Vigmostad & Bjørke AS
Typeset by Have a Book

Vigmostad & Bjørke AS is Eco-Lighthouse certified,
and the books are produced in environmentally certified printing houses.



Preface

Anders Schei, Johan Kr. Tuset and Halvard Tveit published the reference book 'Production of High Silicon Alloys' in 1998 with Tapir Forlag. It was groundbreaking work then and is still one of the most frequently read and referenced sources. The book described and explained thermodynamics, and the use of thermodynamics, in industrial silicon operations. Over the last 30 years, however, there has been extensive research and development on the various reactions occurring in the process, as well as on new raw materials and new processes. This revised book, *Production of High Silicon Alloys*, uses portions of the original book, as the thermodynamics and the description of industrial phenomena are still valid for today's operation. In addition, it includes the knowledge obtained over the last 30 years, both scientifically and industrially. This includes kinetics of fundamental reactions, behavior of raw materials, new industrial approaches, refining and quality of solidified materials, as well as environmental questions.

A saying states that 'It takes a village to raise a kid', but in this case it has also taken a large metallurgical community to write the book. The layout of the previous book has been kept, to a large extent, and the main authors who have contributed are:

- Chapter 1 Introduction has been written by Merete Tangstad and Harry Rong
- Chapter 2 Chemistry of the Si–O–C system is revised by Merete Tangstad
- Chapter 3 The carbothermic process of silicon is revised by Merete Tangstad
- Chapter 4 Additional elements in the silicon process is rewritten by Merete Tangstad, Gabriella Tranell and Kai Tang
- Chapter 5 The commercial silicon/ferrosilicon process is revised by Eli Ringdalen
- Chapter 6 Electric operation is written by Gudrun Sævarsdottir
- Chapter 7 Enthalpy balance and energy recovery is revised by Merete Tangstad
- Chapter 8 Operational problems is written by Merete Tangstad
- Chapter 9 Modified and alternative processes is written by Ida Kero, Eli Ringdalen and Gabriella Tranell

- Chapter 10 Silicon alloy refining is rewritten by Gabriella Tranell
- Chapter 11 Solidification is written by Andrea Broggi, Halvard Tveit and Javier Bullon
- Chapter 12 Environmental aspects is written by Ida Kero and Gabriella Tranell
- Chapter 13 Safety is written by Halvard Tveit

(The words 'written', 'rewritten' and 'revised' all mean the same here; that some parts have been kept from the original book, but the major part is new material.)

We also want to express our deep gratitude to Ingrid Gamst Page, who has handled the administrative work, carried out quality checks of pictures and references, and applied for permissions. This book would not have been possible without her participation. Lingyi Ren has re-drawn many figures to give the book a consistent look throughout, and Kai Tang, Yan Ma, Lynn Agnes Sarkol, Thor Sjursen, Isabel Farrell, Mengyi Zhu, Marit Buhaug Folstad and Erlend Lunnan Bjørnstad have contributed through discussions, improved figures and graphs, and additional thermodynamic diagrams. FactSage and HSC Chemistry are important tools for all metallurgists and are used extensively in this book to show thermodynamic values and trends. We also want to mention the people who take time out of their busy schedules to arrange conferences where new industrial knowledge is presented together with advances in research and development. As seen in the references, invaluable information for this book has come from 'Silicon for Chemical and Solar Industry' and 'International ferroalloy conference', which are organized every second and third year.

We appreciate the funding from:

- FFF – The Norwegian Ferroalloy Industry Research Association
- Silicon for chemical and solar industry
- FME ZeMe pr.no 350325 funded by the Norwegian Research Council
- SiH2 pr.no 325464 funded by the Norwegian Research Council
- Safeci pr.no 326802 funded by the Norwegian Research Council
- Queen EU grant agreement 101178144

Thank you to Gosia Adamczewska from Fagbokforlaget for making this journey easier.

Table of Contents

1
Introduction 15
Merete Tangstad and Harry Rong
1.1 Metallurgical production of high-silicon alloys 16
1.2 Silicon applications 21
Ferrosilicon alloys 21
Silicon as an alloying element 22
Silicon for chemical use 22
Silicon for electronic use. 23
Silicon for photovoltaics 24
1.3 Availability of raw materials. 25
1.4 Sustainability 26

2
Chemistry of the Si–O–C system 29
Merete Tangstad
2.1 Species in the system. 29
Silicon 30
Carbon 30
Oxygen 30
The Si–C system. 30
The Si–O system 32
The C–O system. 34
2.2 Equilibria in the system 34
2.3 Kinetics in the Si–O–C system 41
SiO + 2C = SiC + CO(g) 41
SiO_2 + SiC→3SiO(g) + CO(g) 46
SiO_2 + Si → 2SiO(g) 51
Condensation reactions 54
Metal producing reaction – SiO(g) + SiC = 2Si + CO(g), reaction 62
Reaction between SiO_2 and C 65
Reaction between Si and CO gas. 70

3
The carbothermic process of silicon 77
Merete Tangstad
3.1 The origin of the silicon furnace 77
3.2 Observation of the submerged arc furnace 79
The furnace system 79
Observation of the working furnace 81
3.3 The inner structure of the reacting furnace 91
3.4 Reactions in the furnace 95
Qualitative description 95
Stoichiometric analysis of the reactions in the furnace 97
3.5 Critical reactions in the carbothermic process of silicon 105

4
Additional elements in the silicon process 109
Merete Tangstad, Gabriella Tranell and Kai Tang
4.1 Liquid silicon as solvent for impurities and alloying metals 109
Phase diagrams and activities 109
Density 116
4.2 Silica as solvent for impurity oxides 117
Phase diagrams and activities 121
Viscosity 128
Density 130
Interfacial properties 130
4.3 Distribution of elements 137
General thermodynamic overview 139
Ca and Al distribution 144
Volatile impurities 152
4.4 Alloying elements 154
Ferrosilicon 155

5
The technical silicon process 167
Eli Ringdalen
5.1 The furnace and the plant 167
5.2 The processes taking place in the silicon furnace 168
5.3 Raw materials for silicon and ferrosilicon production 173
Silicon source – Quartz 176

Reduction materials 180
Wood chips 188
The iron source 189
5.4 The silicon and ferrosilicon plant 190
The furnace 191
The electrical supply and the electrodes 191
Raw materials handling and feeding to the furnace 192
Stoking and preparation of materials charge in the furnace 193
Tapping of liquid silicon or ferrosilicon 193
Gas treatment and energy recovery 194
5.5 Furnace operation and control 195
Process measurements 196
Control system 196
Metallurgical competence 197
5.6 Process models 197
Background and concept for Elkem process models 199
Comparison of the modelling concepts 222

6
Electric operation 229
Gudrun Sævarsdottir
6.1 The distribution of heat generation in the furnace 230
Heat production 231
The heat distribution 232
Andreae's rule 235
Westly's rule 236
6.2 Current paths 239
Distribution between paths 239
Current through the charge 244
Current through the electric arc 250
6.3 Electrical Furnace System 253
The reactance in the furnace 255
6.4 Energy control of the silicon furnace 258
Measurement systems 259
Electric operation 260
6.5 Electrode consumption 263

7
Electrical energy consumption, enthalpy balance and energy recovery 269
Merete Tangstad
7.1 Stoichiometric analysis of energy balance 269
The simplified Si furnace 269
Temperature in the off-gas 278
7.2 The industrial silicon process 279
Energy losses from the process 279
Carbon – volatile compounds 281
Carbon – surface burning and losses of fine sized material 283
Other minor deviations from an ideal process 283
7.3 Production of ferrosilicon 284
7.4 The material and energy balance for a ferrosilicon process with SiO loss 284
7.5 Real life – a silicon and a ferrosilicon furnace 287
7.6 Energy recovery from the process 289
Conceivable energy recovery 289
7.7 Exergy analyses 292

8
Operational problems 297
Merete Tangstad
8.1 Deposits in the furnace 297
Slag accumulations 298
Deposits of SiC 302
Formation of crusts in the upper parts of the charge 310
8.2 Tapping 311
Conceptual tapping model 312
Gassing through the taphole 320

9
Modified and alternative processes 325
Ida Kero, Eli Ringdalen and Gabriella Tranell
9.1 General 325
9.2 Modified carbothermic process 327
Closed furnace 327
Direct current 331
Split furnace body 332

Carbon Capture (CC) and Carbon capture and use (CCU) 334
Composite agglomerates. 340
Blast furnace. 347
Plasma reactor 347
Non-atmospheric pressure 351
9.3 Non-carbothermic processes and reductants 353
Hydrogen 355
Methane, CH_4. 360
Metallothermia 360
Electrolysis 364
9.4 Alternative silicon sources for new processes 367

10
Silicon alloy refining 375
Gabriella Tranell
10.1 Oxidation and slagging of impurities 376
Fundamental reactions and element distribution equilibria 378
Equilibrium reaction paths. 381
Mass and heat balance. 388
Oxygen and carbon in refined metal 392
10.2 Refining by Chlorination 394
10.3 Refining towards Solar Grade Material 397
Removal of carbon. 399
Removal of (metal) impurities by directional solidification 400
Removal of boron 404
Removal of phosphorus 411

11
Solidification of Si and Si-alloys. 429
Andrea Broggi, Halvard Tveit and Javier Bullon
11.1 Introduction 429
11.2 Thermodynamics and phase diagram. 429
11.3 Solidification processes. 433
Product Requirements 433
Traditional casting methods for FeSi and silicon 434
Alternative casting methods. 436
Copper casting 437

Water granulation 439
Cast to shape process 440
Atomization in inert gas or air 441
11.4 Solidification and product properties 441
Solidification processes 441
Solidification speed and grain growth in silicon rich-alloys 442
Transformation below the melting point of silicon 448

12
Environmental aspects 455
Ida Kero and Gabriella Tranell
12.1 General 455
12.2 Occupational health 456
12.3 Pollution control 457
Emissions to soil and water 458
Emissions to air 458
CO_2 and other greenhouse gas emissions 459
Sulphur dioxide, SO_2 460
Nitrogen oxides, NO_X 460
Particulate matter (dust) emissions 461
Particle-bound organic compounds including Polycyclic aromatic hydrocarbons 462
Particle-bound inorganic compounds: Trace elements and heavy metals . . . 463

13
Safety 469
Halvard Tveit
13.1 General about industrial safety 469
13.2 General hazards for the silicon industry 471
13.3 Process specific hazards for the silicon industry – energy out of control . . . 472
Eruption of water vapour and process gas from the charge 473
Explosion due to water encapsulated in molten or very hot metals and materials 480
Dust explosions – primary and secondary explosions or the formation of explosive gases or metal fines after a primary explosion 481
Burning of skin due to contact with warm gas or liquid or warm silicon . . . 483
13.4 Active and passive measures for increased safety 483
13.5 Conclusion 484

Appendix A
Equilibrium calculations **487**
Reactions in the submerged arc furnace 487
Brief description of the system 487
Calculation of equilibria 488
Equilibria with two condensed phases 490
Equilibria with three condensed phases 497
Equilibrium with four condensed phases 499
The data sources 499
Common errors in equilibrium calculations 501
Loss of accuracy by data treatment 502
Combination of species that cannot coexist 502
Ignoring important species 503
Inattention to the phase rule 503
Unsuitable interpretation of the reaction conditions 503
Erroneous use of 'The reaction goes to the right for $\Delta G° < 0$' 505

Appendix B
Pilot scale excavations **507**

Appendix C **514**

About the authors **527**

Index **529**

Tangstad, M. and Rong, H. (2026) 'Introduction', in M. Tangstad, G. Tranell, H. Tveit and E. Ringdalen (Eds.), *Production of high silicon alloys* (2. ed.) (pp. 15–28). Fagbokforlaget. https://doi.org/10.55669/oa880801

1

Introduction

Merete Tangstad and Harry Rong

Silicon is the second-most abundant element in the earth's crust after oxygen. In its natural form, it is almost exclusively combined with oxygen as fairly pure silicon dioxide and silicates. Silicon dioxide, in the form of flint, was a main tool for humans in the Stone Age and, later, silicates have been essential in materials such as ceramics and glass. Silicon was recognized as an element in the early nineteenth century and was produced industrially, as silicon or in alloys, from the end of that century. Around 1950, extremely pure silicon was produced and used in semiconductors, the key unit in computers and other electronic devices. Elementary silicon has a semi-metallic, shiny look; it is hard but rather fragile and not suited to the making of structural materials. Silicon is more commonly used to improve the properties of other materials, such as aluminium. Therefore, silicon and its alloys were relatively unknown to the general public before the computer industry made it famous and Silicon Valley became a symbol of the modern world.

This chapter gives a short survey of the production and use of high-silicon alloys. Finally, the availability of raw materials and the sustainability of the production process are discussed.

This work is licensed under the Creative Commons Attribution 4.0 International License.
To view a copy of this license, visit https://creativecommons.org/licenses/by/4.0/

1.1 Metallurgical production of high-silicon alloys

Silicon is produced industrially by reducing silicon dioxide with carbon in arc furnaces. In an idealized form, this can be written as a mass balance:

$$SiO_2 + 2C \rightarrow Si + 2CO \qquad [1.1]$$

We will see later that the real process is more complex. In industry, the available raw materials are not pure, and the product will contain other elements. With pure raw materials and electrodes, it is possible to obtain silicon with less than 1–2 per cent of other elements. This product is traditionally called 'silicon metal' even though solid silicon is not a metal but a semiconductor. The furnace behavior during the production of silicon has several features that are markedly different from the corresponding behavior during the production of most metals. These features will be discussed in detail later; here it suffices to state a few characteristic features of the silicon process:

1. The gas in the hottest zone of the furnace has a high content of a silicon-containing gas that must be recovered in the outer charge layers to obtain a high silicon recovery.
2. The silicon-recovering reactions in the outer charge layers heat the charge to a high temperature and create a sticky charge that does not flow easily into the high-temperature zone.
3. The gas from the furnace contains significant amounts of fine particles consisting of SiO_2, called microsilica or condensed silica fume.
4. The hot off-gas is suited for energy recovery, and microsilica and energy are important by-products in many plants.

This characteristic behavior of silicon furnaces will also be found if we add a limited amount of metals to the charge. The most common alloying element is iron. Silicon content is given by numbers. For example, FeSi75 means an iron-silicon alloy with 75 weight % silicon. In practice, there may be up to several per cent of other elements than silicon and iron. In this book,

the term high silicon alloys include all the silicon-containing alloys where the silicon dominates the behavior in the furnace. We also include alloys that can be produced by metallurgical refining of high silicon alloys from the arc furnace. Such metallurgical refining may be done by slag treatment, gas purging or crystallization. This definition includes the purest silicon that can be made by metallurgical means, but not semiconductor silicon made through distillation and decomposition of compounds containing silicon.

The production of high silicon alloys is presently based on the carbothermal reaction that is idealized in Reaction [1.1]. In practical operation, there is always some silicon loss in the gas. This is mainly due to a loss of SiO gas. The SiO combusts together with CO above the charge with the abundant air. This can be summarized in the following equations:

$$\text{x} \qquad SiO_2 + 2C \rightarrow Si + 2CO_g \qquad [1.2]$$

$$\text{1–x} \qquad SiO_2 + C \rightarrow SiO_g + CO_g \qquad [1.3]$$

$$\text{1–x} \qquad SiO_g + \frac{1}{2}O_2 \rightarrow SiO_2 \qquad [1.4]$$

$$\text{1 + x} \qquad CO_g + \frac{1}{2}O_2 \rightarrow CO_2 \qquad [1.5]$$

Equations [1.2] and [1.3] describe the process seen inside the furnace. Equations [1.4] and [1.5] include the reactions that take place above the charge layer. Here, x denotes the silicon yield.

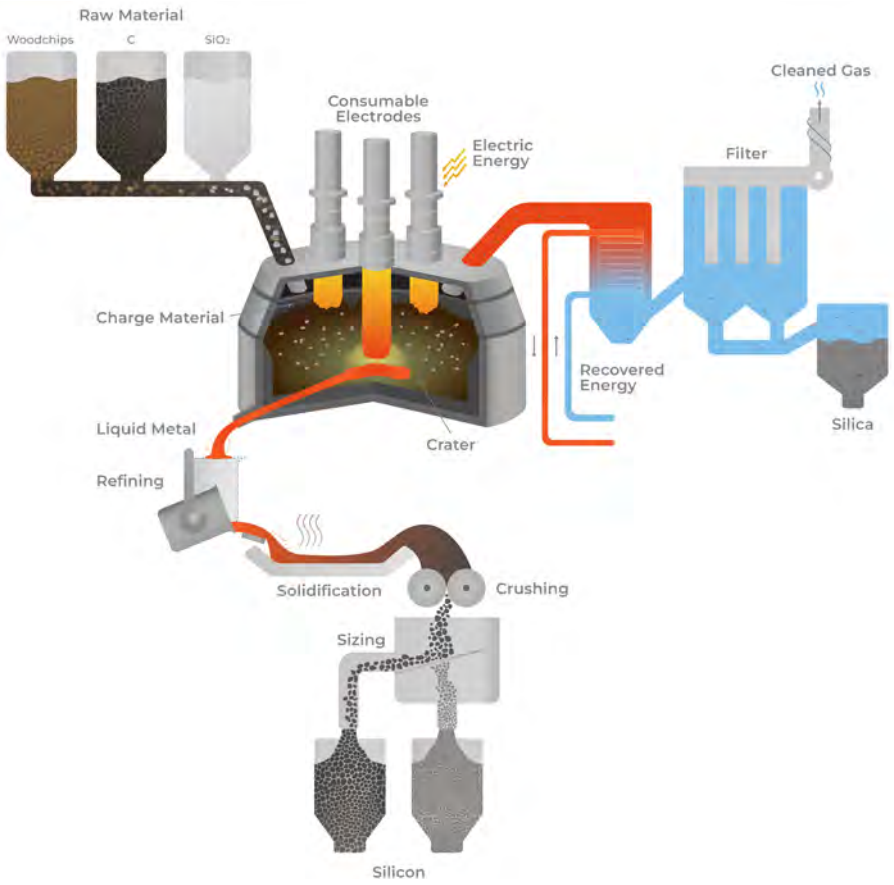


Figure 1.1 *A typical plant for the production of metallurgical grade silicon (after Tangstad, 2013).*

Figure 1.1 shows a typical silicon plant producing metallurgical grade silicon. The core of the plant is the arc furnace. A typical furnace has a pot with a diameter of around 10 meters, which is filled with charge materials. Three electrodes, submerged in the charge, supply a three-phase current that passes through the contents of the furnace. The current heats part of the charge to about 2000°C in the hottest region. At this high temperature, silicon dioxide is reduced to molten silicon. The silicon is tapped from the bottom of the furnace through a taphole and refined by slag treatment and/or gas purging. During refining, oxides and particles of carbide are removed, and the com-

position is adjusted to the specified value. After refining, the molten alloy is allowed to cool in a suitable mold and is then crushed to the specified size. The consumption of electric energy is 11–13 MWh per metric ton of silicon in most plants.

The gas from the furnace burns above the surface of the charge. Its heat content is of the same order of magnitude as the electric energy added to the furnace. This heat can be used in a heat recovery station for heating or to produce electricity in a power plant. About 30% of the electric energy can be recovered from the off-gas. If the energy is recovered as steam, about 60% of electric energy can be recovered. The filtered gas still has some impurities, mainly sulfur dioxide. The dust in the filter consists mainly of amorphous SiO_2 with a particle size around 0.1 μm and is sometimes named condensed silica fume or microsilica. The silica fume has a specific surface around 20 m^2 per gram. It can be used as an addition or filler to concrete, ceramics, refractory, rubber etc. A furnace produces 0.1–0.4 tons of silica per ton of silicon.

The products of the process are:

1. High silicon alloy.
2. Condensed silica fume.
3. Recoverable heat energy.

The most important high silicon alloys are silicon (higher than 96 per cent silicon) and ferrosilicon with 90, 75 or 65 per cent silicon. Any composition in the Fe–Si system can be produced, and small amounts of alloys of other compositions are produced. Special compositions are most common when small amounts of additional elements, such as magnesium, calcium and rare earth metals, are added. High silicon Al-Si alloy can be produced in the arc furnace, but it has not yet found a large market.

The world production in 2019 of the main high silicon alloys is shown in Figures 1.2 and 1.3. The total production is approximately 2.8 million tons of silicon and 6 million tons of silicon contained in ferrosilicon. Compared to the numbers of 1997, when the previous silicon book was published, global production of silicon and ferrosilicon increased by 3 and 2.3 times, respectively. China, in particular, increased its production from 24% and 31% of global production to 70% and 74%, respectively.

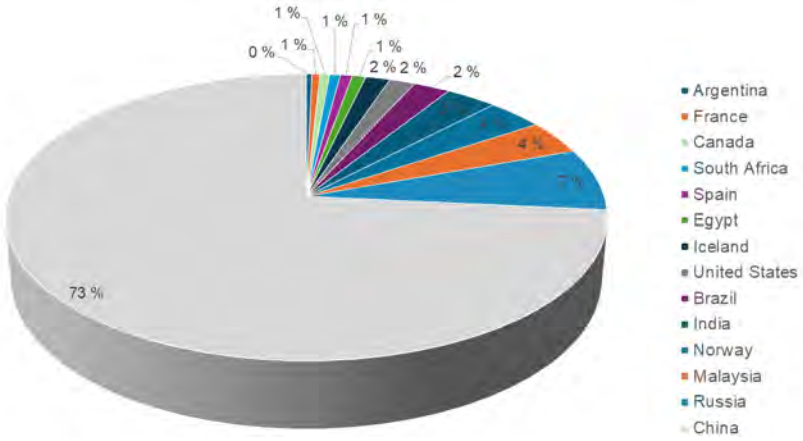


Figure 1.2 *The figure shows the global production of silicon by countries in 2019 which was in total about 2 810 000 tons. (Aurelien and Ayre, 2021) [With permission from The Norwegian Ferroalloy Producers' Research Association – FFF].*

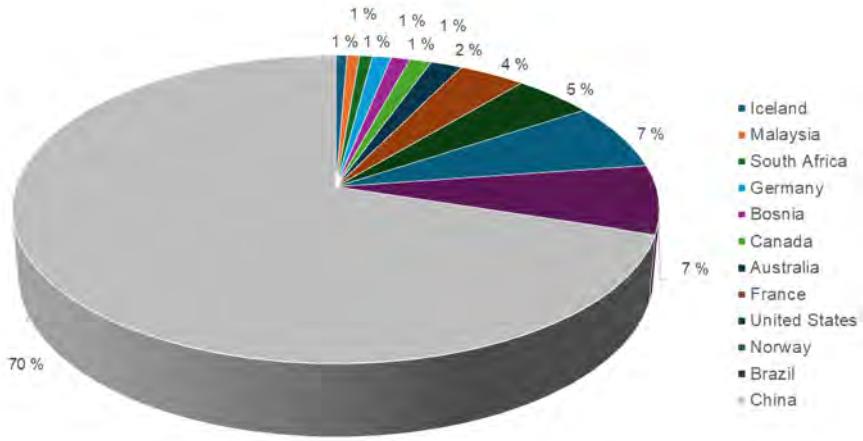


Figure 1.3 *The figure shows the global production of silicon in ferrosilicon by countries in 2019 which was in total about 6 million tons. (Aurelien and Ayre, 2021) [With permission from FFF].*

1.2 Silicon applications

The main applications for silicon, illustrated in Figure 1.4, are:

1. Deoxidation and alloying of steel and cast iron (mainly ferrosilicon)
2. Raw material for solar cells
3. Alloying of other metals, especially aluminium (mainly silicon)
4. Raw material in the chemical industry (mainly silicon)
5. Raw material for the semiconductor industry
6. Ceramic and refractory products

Ferrosilicon alloys

The largest application of ferrosilicon is steel and cast iron production. The deoxidation task is to bind and remove oxygen and oxides in steel. One example is stainless steel production: ferrosilicon reduces the Cr-rich slag, and consequently most of the valuable elements in the slag, such as chromium and manganese, are recovered.

As an alloying element, silicon is used to increase elasticity and tensile yield, as well as annealing resistance, for different steel qualities.

In cast iron applications, ferrosilicon is used as a base for inoculant materials. Inoculation of liquid iron is the practice of adding small quantities of alloys, which induce graphite nucleation and thereby realize the graphitization potential of the liquid. This use of silicon for the application mentioned above is not expected to grow rapidly, since the iron and steel industry grows slowly, and the consumption of silicon per ton of product decreases.



Figure 1.4 *Examples of usage of silicon and ferrosilicon alloys (Graphic: Lingyi Ren).*

Silicon as an alloying element

Alloying in other metals consumes about 30% of the production of silicon. The use of silicon as an alloying element for aluminium is parallel to ferrosilicon for steel. The main difference is that iron is normally a contaminant in aluminium. The need to achieve low iron content in silicon induces several process parameters, such as the choice of raw material and the use of special iron-free electrodes for silicon production.

Silicon for chemical use

The main products from the chemical industry are silicones, which are silico-organic polymers. They consist of long chains –O–Si–O– where the two other bonding positions are taken by organic groups, usually the methyl $-CH_3$ groups.

The first step in the production of silicones is to react silicon with methyl chloride in the presence of a copper catalyst and promoters, for instance zinc and tin, in a fluidized bed reactor. In the second step, dimethyldichlorosilane is hydrolysed to replace the chlorine atoms with hydroxyl groups (silanol). Finally, silicone (polysiloxane) is produced by condensation polymerisation

of the silanols, forming long polysiloxane chains with alternating silicon and oxygen atoms.

The impurities present in silicon can impact the selectivity for dimethyldichlorosilane, the reactivity between methyl chloride and silicon, and the yield in the process. It is therefore common to adjust the silicon production parameters (raw materials, refining process and casting process) to optimize performance.

The properties vary over a wide range of liquid oils, greases, rubbers and solid resins. Silicones are chemically inert, water-repellent and stable up to about 400°C. They are used as lubricants, hydraulic fluids, protective coatings, electric insulators and artificial body parts.

Fumed silica is used as filler in a series of products. Silicon is converted to $SiCl_4$ in reaction with HCl. The $SiCl_4$ is later burned to SiO_2 with an extremely high specific surface (fumed silica). The production process can be varied and gives a set of product types with a strong variation in price. Fumed silica can also be produced from by-products from the production of silicones (CH_3SiCl_3).

Silicon for electronic use

Another important application of silicon is its use in semiconductors in everyday electronic devices. This use is well known, even if it stands for a rather small percentage of the total silicon consumption (about 40 000 tons per year in 2025). Silicon for semiconductors must be extremely pure, with an overall content of other elements in the low ppb range (9–11N). This purity is obtained by a complex chemical purification of metallurgical grade silicon. Several processes are possible, but at present the so-called Siemens process is the most important. There, the silicon is transformed to a silicon-containing gas:

$$Si + 3HCl(g) \overset{300°C}{\rightarrow} HSiCl_3(g) + H_2(g) \qquad [1.6]$$

The gas is purified by distillation and reduced to silicon at high temperature (1100°C) in the presence of large amounts of hydrogen. A small amount (about 5%) of HCl is typically produced as a by-product, which can be reacted with silicon. The silicon produced in the chemical vapour deposition (CVD) process is typically called polysilicon.

$$4HSiCl_3(g) \overset{1100°C}{\rightarrow} Si + 3SiCl_4(g) + H_2(g) \quad [1.7]$$

$$4HSiCl_3(g) + H_2(g) \overset{1100°C}{\rightarrow} 3Si + SiCl_4(g) + 8HCl(g) \quad [1.8]$$

The real process is more complicated than shown here, and the yield of silicon is rather low for most producers. The product is deposited on silicon rods in bell jars with cooled steel walls. Deposition is a slow process, and much energy is used both to keep the interior of the bell jar cold and to heat the reaction gases. There has been a major improvement in the design of the bell jars (CVD reactors) to lower power consumption. Power consumption is today typically less than 50 MWh per metric ton.

Silicon for photovoltaics

Photovoltaic cells convert energy in light directly to electricity. The cells can be made from many materials, but silicon is the most dominant main material, since it is available in virtually unlimited quantities, is non-poisonous, and only moderately expensive. For many years, multi-crystalline solar cells were the dominant technology, and the specification for these types of solar cells was less strict (6N) than the specification for semiconductor silicon.

Recently (2020–2023), technology has changed from multi-crystalline solar cells to mono-crystalline solar cells that require a higher purity (9N). Therefore, polysilicon has become the preferred raw material for solar cells. By-products from polysilicon production that previously could be recycled into multi-crystalline solar cell production need new recycling processes.

Due to the high amount of $SiCl_4$ by-product from the Siemens process described above, the production of $HSiCl_3$ for solar applications has changed to mainly recycle the $SiCl_4$. This is done by reacting Si with $SiCl_4$ and H_2 at 500°C and high pressure (up to 30 bars). While the Siemens process needs about 4 kg of metallurgical silicon to produce 1 kg of polysilicon, the recycling process only needs about 1.2 kg metallurgical silicon.

Trichlorosilane ($HSiCl_3$) can also be converted to SiH_4. Several companies have developed technology for the decomposition of SiH_4 to granular polysilicon in a fluidized bed reactor. This technology typically had some contamination from the reactor wall, making it very difficult to use in the production of mono-crystalline solar cells. Therefore, coating of the reactor

walls is required to obtain high enough purity of the polysilicon. The advantage of the fluidized bed decomposition process is significantly lower energy consumption (less than 10 MWh per metric ton).

1.3 Availability of raw materials

The silicon process can only be operated with lumps of quartz or quartzite (10–150 mm), and due to losses in the refining process, quartz with low Al content is preferred. The silicon process needs quartz/quartzite that are thermally stable. Some quartz qualities disintegrate when exposed to heat, and they cannot be used in silicon production. In addition, there are strict requirements for impurities in quartz, such as iron and titanium, and therefore only a few quartz deposits are suitable for silicon production. As the total production of metallurgical grade silicon is increasing, the availability of high-quality quartz for this product segment is challenged. The earth's crust is, however, estimated to contain about 28 per cent silicon bound as SiO_2 and silicates. A large fraction of this exists as relatively pure SiO_2 in huge deposits. As long as pure SiO_2 is available, it will be the favored source of silicon. SiO_2 can be upgraded from quartz-containing rock species, and even extraction from silicates is possible, but with a higher environmental impact and higher cost.

The resources of reduction materials are more limited. An important source is coal, which can be used either directly or as a char after heating. The specification of the product composition limits the number of coal types that can be used. The process also requires a certain reactivity of the carbon material, which further reduces the number of available types of coal. Petroleum coke from the oil industry is normally very pure, but it can have lower reactivity. Renewable materials, such as charcoal and other biobased carbon materials, have partly replaced fossil carbon. Though charcoal has a lower mechanical strength compared to coal and char, it has a higher reactivity and may be beneficial for the process. Though charcoal is termed a renewable raw material, it still has an environmental impact through its Global Warming Potential and other factors. It is hence important to focus on sustainable growth and production processes. It is also expected that other biomass than lumpy charcoal will be used ahead, like e.g. agglomerated pyrolysed biomass.

It is also important for society to use more recycled materials. In the silicon production process, this could, in the future, be agglomerates of SiO_2 or carbon, or composite agglomerates containing both carbon- and SiO_2-fines, and, for the FeSi producers, iron sources.

Silicon production is dependent on electric energy. A change in global energy use or the energy price may affect silicon production. Production of silicon is mainly found in areas with availability of low-cost electric energy.

1.4 Sustainability

Environmental impacts of silicon and ferrosilicon are one of the drivers shaping the production processes, together with cost and product quality. Environmental impacts can be investigated by Life Cycle Assessments (LCA) to determine the quantitative impacts. One of the major impacts of the silicon process is the Global Warming Potential, given by the emissions of CO_2 equivalents from the process itself or from the energy used.

The major CO_2 emissions are from the fossil carbon in the production process, like coal and coke. As today's processes need lumpy, solid carbon, the only short-time mitigation is to replace the fossil carbon with bio-carbon. Most plants today already use woodchips for permeability and some lumpy charcoal as a reductant. The goal is hence to substitute more of the fossil carbon with charcoal, to decrease the total CO_2 emissions. Charcoal has better properties when it comes to permeability and reactivity; however, it typically has lower mechanical strength and will thus create more fines and dust. The reduction of the Global Warming Potential is, however, also dependent on the equivalent CO_2 emissions from the charcoal production itself. Today, some producers have significant methane (CH_4) emissions during the charcoal production process due to incomplete combustion and lack of treatment of the off-gas from the charcoal furnaces.

Though not yet used extensively industrially, it is also expected that biomass agglomerates will be an important part of the reductants in the years to come. As the need for charcoal is much higher than the production of charcoal, not all producers can expect to have access to lumpy charcoal. There is hence a drive towards using other biomass materials, like e.g. agricultural waste. Here, the trace elements will be of importance. One can also agglomerate

the biochar to design a more optimal product, with e.g. higher mechanical strength, and hence have less fines and dust formation.

For silicon plants that are relying on fossil electricity, energy produced by combustion of fossil fuels, energy production can emit more CO_2eq. than the silicon process itself (Sævarsdottir *et al.*, 2021). For plants consuming renewable energy, this will of course be minimal. Energy is hence a vital part of the environmental impact and cost, and it is important to use less energy per ton of silicon and to recover energy from the process. The energy can be recovered both through hot water and production of energy from high-temperature off gas.

Recycling silicon will reduce environmental impacts. Today, silicon is extensively recycled together with Al in Al–Si parts. The silicone industry is developing methods to recycle silicone products, but it will not be feasible to convert silicones back to silicon. The solar industry has grown from very small volumes 30 years ago to consuming about 30% of the silicon produced today. Recycling technology has been developed for sawing fines (Kerf), and there is now also considerable research on recycling solar cells. As growing numbers of solar cells are taken out of operation, the need for recycling will increase. Raw materials that today cannot be used in the production of silicon due to size can be agglomerated and reused.

References

Aurelien, H. and Ayre, W. (2021) Assessment of the global and regional carbon footprint from the production of ferroalloys. Internal report. Norway: FFF.

Sævarsdottir, G., Kvande, H. and Magnusson, T. (2021) 'Greenhouse gas emissions from silicon production – development of carbon footprint with changing energy systems', in *Proceedings of INFACON XVI, International Ferro-Alloys Congress*. Trondheim, Norway. Available at: https://doi.org/10.2139/ssrn.3926088.

Tangstad, M. (2013) *Metal production in Norway*. Oslo: Akademika Publishing.

Tangstad, M. (2026) 'Chemistry of the Si–O–C system', in M. Tangstad, G. Tranell, H. Tveit and E. Ringdalen (Eds.), *Production of high silicon alloys* (2. ed.) (pp. 29–75). Fagbokforlaget. https://doi.org/10.55669/oa880802

2

Chemistry of the Si–O–C system

Merete Tangstad

The only abundant natural sources of silicon are silicon dioxide or silicates, which can be derivatives of silicon dioxide. This chapter considers the reactions that are important in the reduction of silicon dioxide to silicon by carbon. The chemical compounds and the phase relations are first outlined, followed by a discussion of equilibria and the reaction kinetics of the main reactions.

2.1 Species in the system

Figure 2.1 provides a graphical survey of the species in the ternary Si–O–C system. There are no commonly accepted ternary compounds in the system.

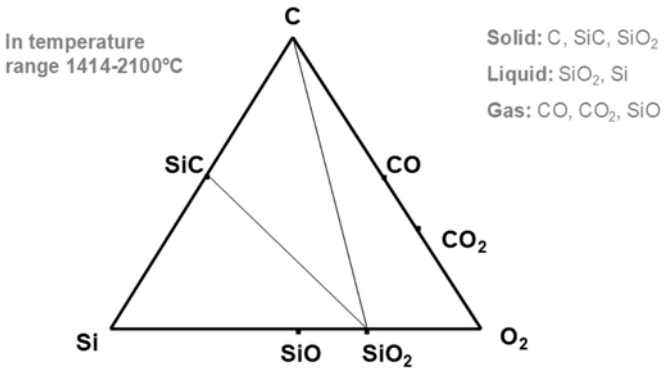


Figure 2.1 *Schematic diagram of the phase relations in the Si–O–C system.*

This work is licensed under the Creative Commons Attribution 4.0 International License. To view a copy of this license, visit https://creativecommons.org/licenses/by/4.0/

Silicon

The melting point of silicon is reported as 1412 ± 2°C (Yaws *et al.*, 1981), but several values in the range 1400–1420°C have been suggested in various papers. Silicon is a semiconductor in the solid state, but in the liquid state it has the same electrical conductivity as a metal.

The content of Si(g), Si_2(g), Si_3(g) and Si_4(g) above liquid silicon is low. The vapour pressures are $5 \cdot 10^{-4}$, $1 \cdot 10^{-5}$, $2 \cdot 10^{-6}$, $9 \cdot 10^{-12}$ bar at 2000°C, respectively. These species are important in the evaporation of Si and SiC, but their contents are very low.

Carbon

The stable modification is graphite. It does not melt at 1 bar pressure, but sublimates at about 3500°C. Carbon materials used in the production of high silicon alloys consist of carbon-containing compounds such as coal, coke, charcoal and petroleum coke. Further details are given in the description of raw materials in Chapter 5. It is usually assumed that the thermodynamic properties of the fixed C in these materials are close to the thermodynamic properties of graphite. However, when it comes to the kinetics, that is, the rate of the reactions, this will of course not be the case.

Oxygen

Oxygen is a bimolecular gas, O_2, that is partly dissociated into atoms at high temperatures. The vapour pressure of free oxygen is very low under the conditions required for SiO_2 reduction. Even so, this vapour pressure is sometimes convenient as a variable in equilibrium calculations.

The Si–C system

The Si–C phase diagram is shown in Figure 2.2. The only stable condensed compound in the Si–C system is SiC, which occurs in several hexagonal polytypes called α-SiC and one cubic modification called β-SiC. According to the JANAF Thermochemical Tables, the cubic β-SiC is more stable than the hexagonal α-SiC at all temperatures, but the difference is so small that it is unimportant in the equilibrium evaluation of the system (Chase *et al.*, 1985).

According to Scace and Slack (1959), SiC decomposes peritectically at 2830°C, giving a liquid with 19 at % C, as seen in the phase diagram in Figure 2.2a. They investigated the system up to about 3000°C with an overpressure of about 20 bar of argon to suppress the vaporisation of the sample. The solubility was extended tentatively to the melting point of C at a pressure of about 100 bar.

The eutectic temperature is very close to the melting point of pure silicon, as seen in Figure 2.2b. Measured values of the content of carbon in silicon in equilibrium with SiC are shown in Figure 2.3, and the results scatter considerably. Analyses of samples of industrial silicon metal give 100–200 ppmw C after ladle treatment around 1450–1500°C. The solubility at the melting point may be lower than this, but reported values in excess of 200 ppmw must be deemed incorrect due to solid SiC particles being present.

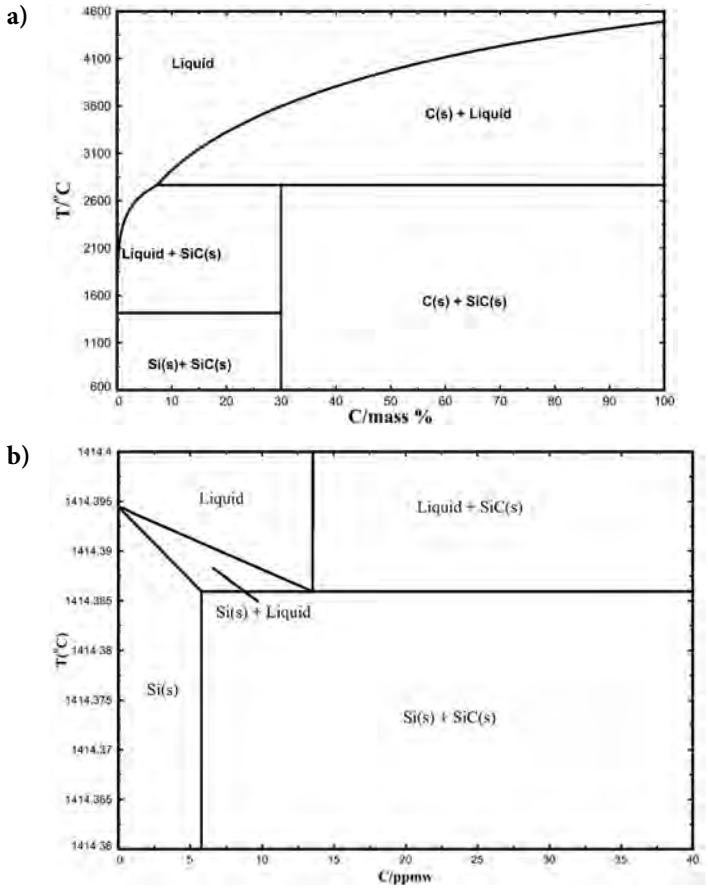


Figure 2.2 *a) The Si–C binary phase diagram calculated by the use of FactSage using the FTlite database where b) shows the magnified area at low C levels.*

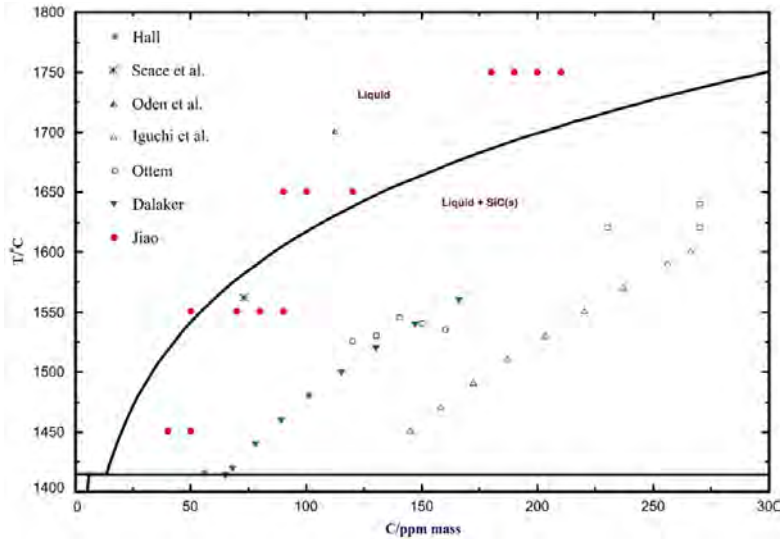


Figure 2.3 *The content of C in liquid silicon in equilibrium with SiC summarized by Jiao (Hall, 1958; Scace and Slack, 1959; Oden and McCune, 1987; Iguchi and Narushima, 1993; Ottem, 1993; Dalaker and Tangstad, 2009; Jiao, 2020) [With permission from J.M. Jiao].*

The gas species SiC_2 and Si_2C are the most stable binary gas species in this system, with a gas pressure of $2 \cdot 10^{-4}$ and $3 \cdot 10^{-4}$ bar, respectively, at 2000°C (HSC ver. 9.8.1.2).

The Si–O system

There are two stable compounds, SiO_2 and SiO, in the Si-O system. SiO_2 appears in the solid forms quartz, tridymite and cristobalite, all of which have high- and low-temperature modifications. High temperature cristobalite is said to melt at about 1725°C, but, as the heat of melting is low and the resulting melt is very viscous, it is easily undercooled to a glass. A tentative Si–SiO_2 phase diagram is shown in Figure 2.4a. It is correct in principle, but it should not be used quantitatively. It can also be mentioned that Stevens and Hand found that tridymite is not a stable phase in the pure Si-O system and is rarely found in SiO_2 samples excavated from industrial furnaces (Stevens and Hand, 1997). Figure 2.5 shows the oxygen solubility according to FactSage in the high silicon area. Since the ingoing data on oxygen solubility are rather uncertain, the result must be seen only as a tentative diagram (Tang , 2009, Mikkelsen, 1985).

SiO is a gas that is stable at high temperatures, and it is a very important participant in the reactions in the silicon process. It has been claimed that SiO also can exist as a thermodynamically stable solid, but no convincing evidence has been produced.

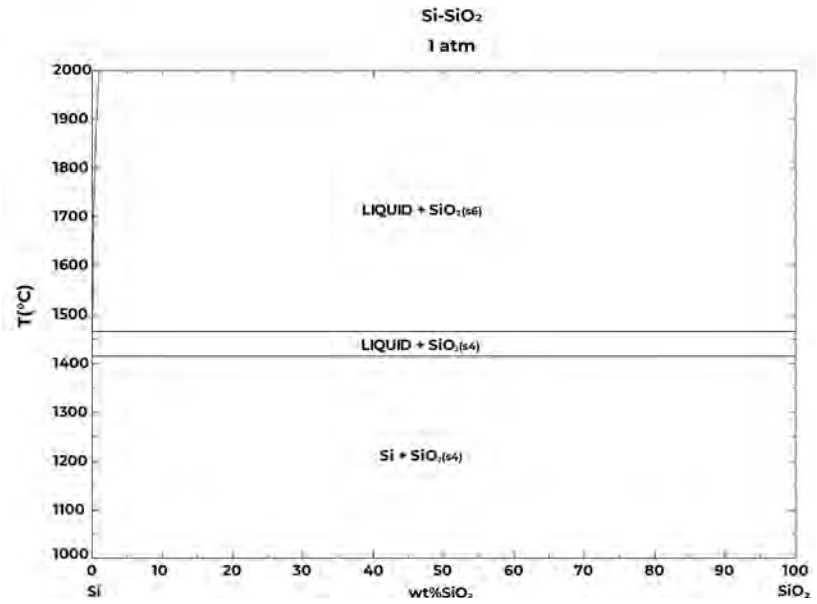


Figure 2.4 *The Si-O phase diagram calculated by FactSage.*

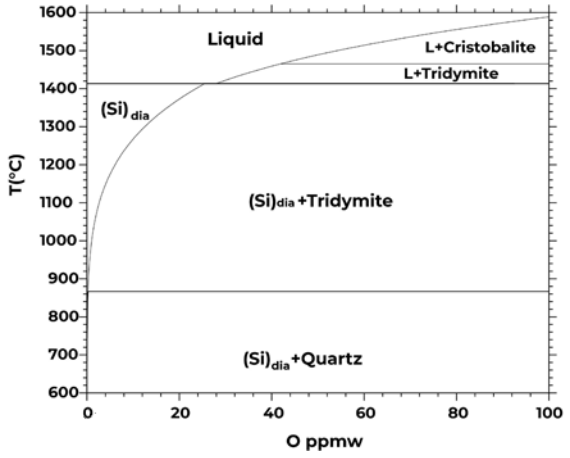


Figure 2.5 *The Si-O phase diagram at low oxygen contents calculated by FactSage.*

The C–O system

The two compounds CO and CO_2 in the system are both gases. In equilibrium with solid carbon, the CO pressure will be close to 1 bar, as shown in Figure 2.6 above 1000°C. In silicon production, one can hence assume a very low CO_2 pressure below the charge level. When FeSi is produced using iron oxides, CO_2 will, however, be produced.

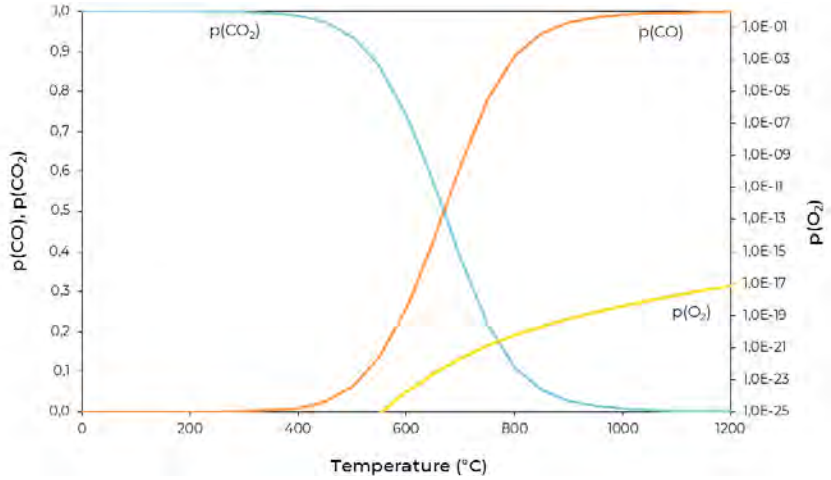


Figure 2.6 *CO and CO_2 gas pressures [bar] in equilibrium with solid carbon, versus temperature. The respective oxygen pressure is shown in the secondary axes. (Calculated with HSC ver. 9.8.1.2).*

2.2 Equilibria in the system

Equilibrium calculations give the final end-state of a reaction, but they do not indicate the time necessary to reach equilibrium. Some reactions are completed in less than a second, while others may take thousands of years. It is therefore not possible to predict the result of a reaction from equilibrium calculations with certainty. If the equilibrium calculations show that a reaction is possible at a given temperature, the rate may be increased by various means, and a process development may be justified. However,

if the calculation shows that the equilibrium is unfavorable, the reaction will not run even with very reactive reactants. Therefore, an estimation of the equilibria gives background understanding of the chemical behavior of the system.

In a reduction furnace there will always be several solid or liquid phases and one gas phase in a reaction zone. Rather than considering specific reactions in the zones, we may regard a zone as a chemical system consisting of a number of phases. The calculation of the equilibria for the interesting phase combinations is given in detail in Appendix A, and the main conclusions will be summarized here. The phase combinations will have a certain equilibrium gas pressure, and this pressure can be used to estimate the reactions of the reduction process. The phase rule for the system gives a relation between the number of phases *Ph* and the number of degrees of freedom *F*:

$$Ph + F = 5 \qquad [2.1]$$

The number of degrees of freedom gives the number of thermodynamic variables that have to be fixed to determine the system completely. The gas phase is always present in the reduction process, and, for convenience, we can count the number of condensed phases Ph_{cond}, which is one less than *Ph*. The system has four species SiO_2, C, SiC and Si that are condensed in the temperature range of the process. The combination SiO_2(s)–SiO_2(l) at the melting point of silicon is not of interest in the understanding of the process. The thermodynamic variables of this system are the temperature, the pressure and the composition of the phases. The number of condensed phases thus determines the variables that must be fixed to determine the system completely, as shown in Table 2.1. If we fix all the necessary properties except one, we have a system with one degree of freedom. In the system we can select one property as the free variable and draw graphs of any property as a function of this variable.

Table 2.1 *Thermodynamic variables necessary to determine the system Si–O–C completely.*

Phcond	F	Thermodynamic variables to be fixed to determine the system	
1	3	Temperature, total pressure, partial pressure of one gas species	
2	2	Temperature, total pressure	or
		Temperature, partial pressure of one gas species	or
		Pressure, partial pressure of one gas species	or
3	1	Temperature	or
		Total pressure	or
		Partial pressure of one gas species	
4	0		None

With the simultaneous presence of the four condensed phases SiO_2, C, SiC and Si, the system is completely determined. This means that the total pressure, the gas composition and the temperature are all given. Extrapolating the thermochemical calculation with the species present around 2000°C shows that the coexistence temperature must be higher than 2700°C, and the pressure more than 2000 bar. At this temperature, the solubility of C in Si is very high, and the species SiC dissociates peritectically. Therefore, there is no justification for extending the extrapolation to higher temperatures. In any case, the temperature and pressure are far outside the range that is interesting in the study of the silicon production furnace.

For three condensed phases, the system is completely determined when the temperature, the pressure, or the content of one gas component is determined. For our purposes, the temperature is selected as the free variable. The system has four possible combinations of the condensed phases SiO_2, C, SiC and Si, but two combinations are unstable because they contain C and Si, which will react to form SiC according to reaction [2.2].

$$Si(s,l) + C(s) = SiC(s) \qquad [2.2]$$

This reaction is displaced to the right for all temperatures up to the peritectic point of Figure 2.2. The gas pressures for the remaining stable combinations are given as functions of the temperature in Figure 2.7 and Figure 2.8. The gas species CO_2, Si, Si_2C and SiC_2 have been included in the calculation, but their partial pressures fall outside the graphs. The figures show fixed points where the total pressure of each combination is equal to an ambient atmosphere of 1 bar. These points are at about 1520°C and 1800°C for the C–SiO_2–SiC and Si–SiO_2-SiC systems, respectively, depending on the database used. These fixed points have also been determined experimentally.

System SiO_2–SiC–C	(Rein and Chipman, 1963)	1533°C
System SiO_2–SiC–Si	(Gjerstad, 1968)	1819°C

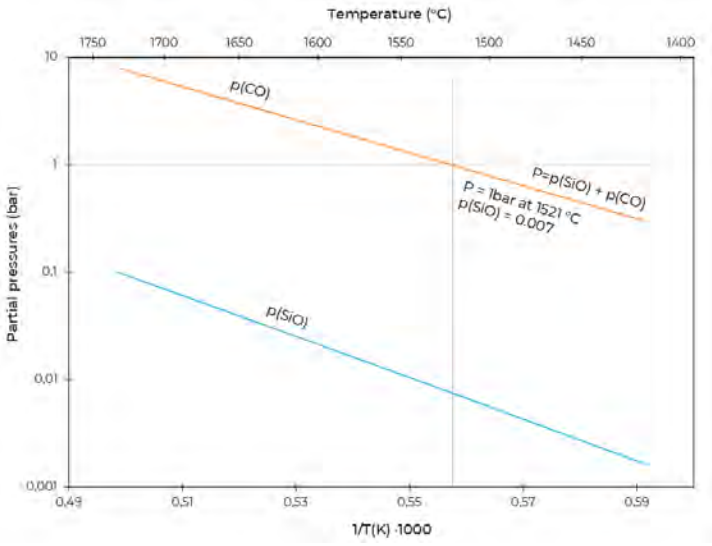


Figure 2.7 *Equilibrium pressure above the condensed phase combination SiO_2–C–SiC calculated in the temperature range 1400–1700°C from HCS ver.9.8.1.2. The graphs for p_{CO} and P are superimposed.*

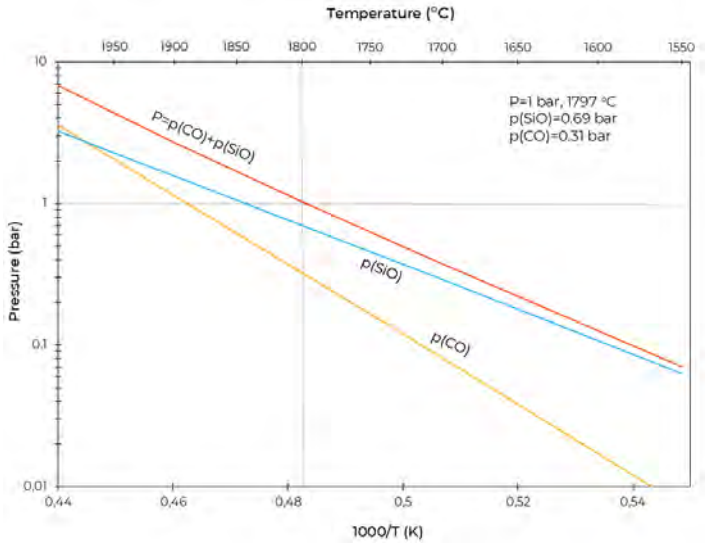


Figure 2.8 *Equilibrium pressure above the condensed phase combination SiO_2–SiC–Si calculated from HCS ver.9.8.1.2.*

In the silicon furnace process, there are of course not only two fixed temperatures, but a gradual increase from the charge top to the high temperature zone. As such, the case where two condensed phases are in equilibrium with a gas phase better explains the gas pressure and the phases present in an industrial furnace. For two condensed phases, the system has six combinations of the four condensed phases. The system is determined if we fix the temperature and the total pressure, and the SiO partial pressure can be shown in a graph as a function of the temperature. Figure 2.9 shows the SiO pressure as a function of temperature at 1 bar for the five combinations that are interesting for a discussion of the silicon process.

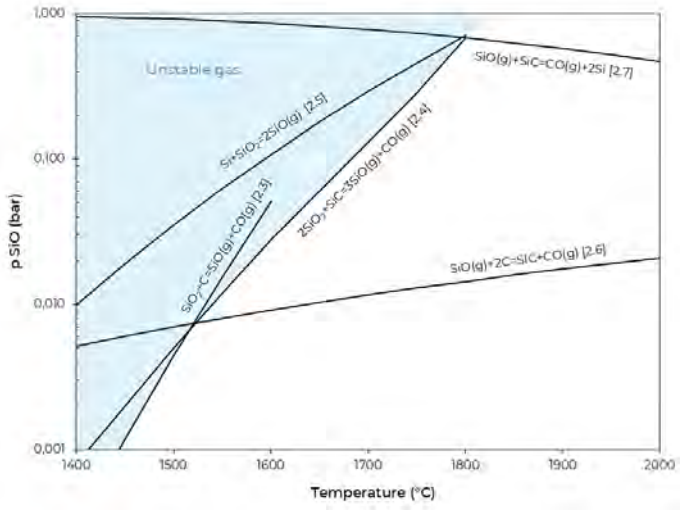


Figure 2.9 *Equilibrium SiO pressures above the condensed phase combinations C–SiC, SiO_2–C, SiO_2–SiC, SiC–Si and SiO_2–Si calculated from the HSC ver. 9.8.1.2. Total pressure, P, is 1 bar, and P = p(SiO) + p(CO).*

Three of the combinations have condensed species on the left-hand side and only gas on the right-hand side:

$$SiO_2(s,l) + C(s) = SiO(g) + CO(g) \quad [2.3]$$

$$2\ SiO_2(s,l) + SiC(s) = 3\ SiO(g) + CO(g) \quad [2.4]$$

$$SiO_2(s,l) + Si(s,l) = 2\ SiO(g) \quad [2.5]$$

Each of these reactions splits the area of Figure 2.9 in two. The gas is unstable for gas compositions corresponding to points to the left of them. If such gas compositions appear, the reaction is reversed and results in condensation of the gas. The fourth and the fifth combinations correspond to reactions that consume SiO(g):

$$SiO(g) + 2\ C(s) = SiC(s) + CO(g) \quad [2.6]$$

$$SiO(g) + SiC(s) = 2\ Si(s,l) + CO(g) \quad [2.7]$$

The sixth combination, reaction [2.8], is metastable, since Si and C will react to SiC according to Reaction [2.2]. This metastable equilibrium is not fulfilled in the reduction of SiO_2, and it will not be discussed further.

$$SiO(g) + C(s) = Si(s,l) + CO(g) \quad [2.8]$$

Figure 2.9 can be used to illustrate the SiO pressure in an industrial FeSi/Si furnace, under the assumptions of chemical equilibrium, as shown in Figure 2.10. In the high temperature zone (> 1800°C), the SiO pressure is given by equation [2.7]. It will hence range from 0.68 bar at 1800°C to 0.47 bar at 2000°C. When the gas rises in the furnace to lower temperatures, it will form condensed phases, either by reaction [2.4] and/or [2.5]. As [2.4] has the lowest SiO pressure, the gas would react until the SiO pressure was equal to that of reaction [2.4], illustrated by the red line. We can use Figure 2.10 to discuss the overall reactions in the industrial furnace. At less than 1400°C, the SiO leaving the charge should be less than 0.001 bar. With a typical industrial Si yield of 80–90%, the SiO pressure is closer to the area 0.01–0.1, showing that

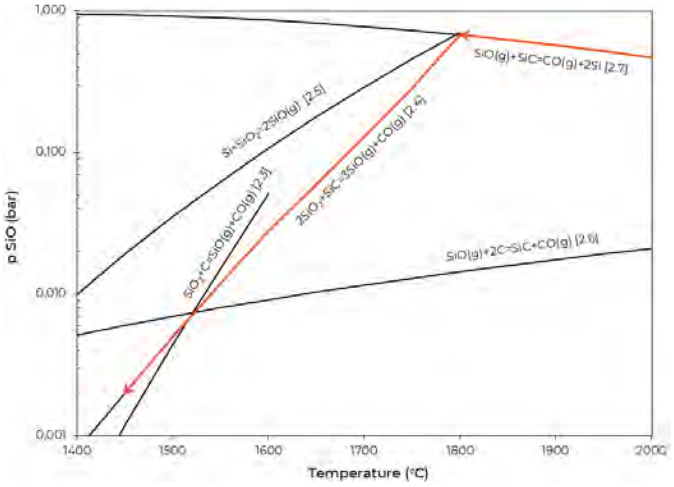


Figure 2.10 *Equilibrium SiO pressures above the condensed phase combinations C–SiC, SiO_2–C, SiO_2–SiC, SiC–Si and SiO_2–Si calculated from the HSC ver. 9.8.1.2. Red lines indicate the SiO pressure in an industrial furnace under the assumption of chemical equilibrium.*

the gas has not reacted to the equilibrium state with SiO_2 and SiC as it should have, according to reaction [2.4]. As the SiO gas pressure is higher in industrial furnaces than in reaction [2.4], it also means that the SiC formation from carbon material, reaction [2.6], will occur at all temperatures above 1400°C.

2.3 Kinetics in the Si–O–C system

The equilibrium determines the final state of a system, but the establishment of equilibrium may take a long time. Therefore, knowledge of the kinetics is important in predicting the behavior of a system.

SiO + 2C = SiC + CO(g) [2.6]

As shown by the equilibrium calculations in Chapter 2.2, the SiO pressure in the high temperature zone will vary from ⅔ to about ½ as the temperature varies from 1800 to 2000°C. As will be seen in Chapter 3, this will give a Si-yield between 33 and 50% if carbon is not capturing the ascending SiO gas according to reaction [2.6]. The capture of the SiO gas, reaction [2.6], will hence be one of the most important reactions in the high silicon furnace process. The reactivity of this reaction has been investigated in a number of studies. To mention just a few, the doctoral theses of Myrhaug, Myrvågnes, Ramos, and Jayakumari give a thorough summary of the literature, as well as new knowledge regarding this reaction (Jayakumari, 2020; Myrhaug, 2003; Myrvågnes, 2008; Ramos, 2018).

The topochemical model, also called the shrinking core model, can be used to explain the reaction mechanism. This model may be used if diffusion into the unreacted particle is slow, or if the chemical reaction is very fast. At the start of the reaction, the SiO gas will meet the surface of the carbon particle, and a SiC layer is formed. For the reaction to continue: a) the SiO gas must diffuse through the SiC layer; b) the chemical reaction must occur between C and SiO gas; and c) the CO gas must be able to diffuse through the SiC layer. This is illustrated in Figure 2.11. Charcoal particles are typically transformed according to a topochemical model, as seen in Figure 2.12 (Jayakumari, 2020; Myrhaug, 2003; Raaness and Gray, 1995; Videm, 2000, 1995). Although other carbon materials like coal and petroleum coke do not necessarily have the same

topochemical structure, as found by Jayakumari (2020), the topochemical model can still be used to model the rate of the reaction.

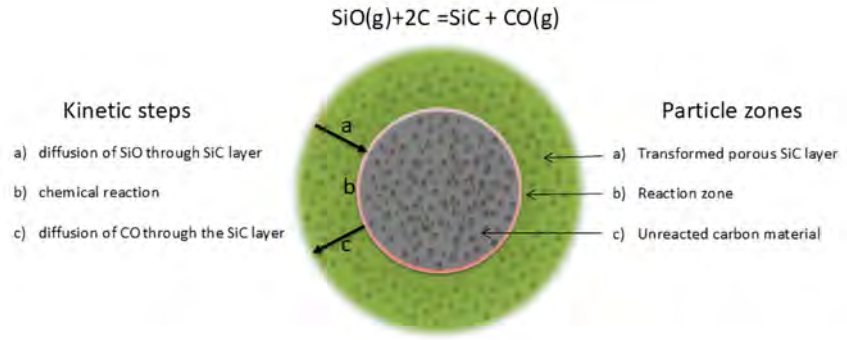


Figure 2.11 *Topochemical reaction of a carbon particle.*

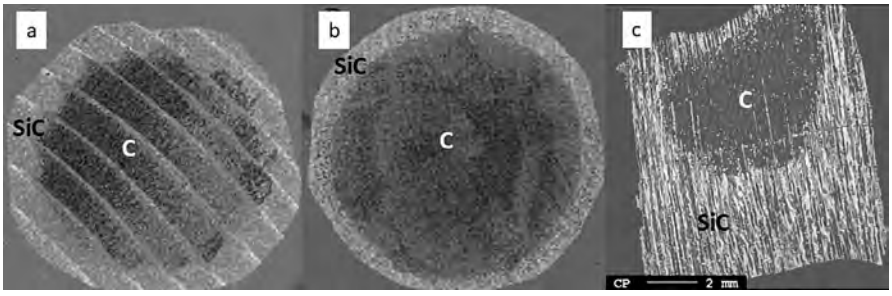


Figure 2.12 *Partly reacted charcoal particles (Myrhaug, 2003; Jayakumari, 2020) [With permission from L.V. Myrhaug].*

It has been found that diffusion of SiO gas into, and CO out from, the reaction zone affects the rate. When diffusion determines the rate, the rate can be expressed by

$$\frac{dX}{dt} = \frac{12 \cdot D_{SiO} \Delta C_{SiO} M_{SiO}}{\rho_{SiO} d_0^2 \left[\left(1 - X\right)^{-1/3} - 1 \right]} \qquad [2.9]$$

where X is the fraction reacted, t is the time (s), D_{SiO} is the diffusion coefficient of SiO gas in the SiC materials (cm^2/s), ΔC_{SiO} is the concentration gradient of

SiO gas, M_{SiO} is the molar weight (g/mol), ρ is the density (g/cm^3), and d_0 is the diameter (cm) of the original particle. The following equation therefore expresses the total time it takes to convert the particle:

$$t_{tot} = \frac{\rho_{SiO} d_0^2}{24 \cdot D_{SiO} \Delta C_{SiO} M_{SiO}} \quad [2.10]$$

In these equations, the diffusion of SiO gas has been used, however, the diffusion of CO gas may of course be expressed in the same manner. A higher SiO pressure in the bulk phase, or a lower CO pressure in the bulk phase, will therefore increase the rate, as the concentration gradient ΔC_{SiO}, or ΔC_{CO}, increases.

It can also be noted that the time is proportional to the square of the particles' original diameter, d_0. This means that if the particles double in size (i.e., in diameter), the rate will decrease by a factor of four, and the total time it takes to convert the particle will therefore increase by a factor of four. Small particles have a shorter diffusion path than larger particles.

The diffusion coefficient, D_{SiO} or D_{CO}, is determined by the structure of the transformed SiC materials, and especially by the porosity in the transformed SiC. When the porosity is higher, gas diffusion will increase. This is illustrated in Figure 2.13, which shows that, within a group of carbon materials (e.g. charcoal), the reactivity increases with porosity or, in other words, increases with lower density. However, the correlation between SiO reactivity and porosity within a carbon group can also be quite low. Jayakumari and Tuset stated that SiO reactivity correlated with the bulk weight, specific surface area and CO_2 reactivity (Jayakumari and Ringdalen, 2022; Tuset and Raaness, 1976). Such a correlation was, however, not found in the medium reactive carbons. It has also been discussed whether the main effect is not the porosity as such, but rather the cell wall thickness (Jayakumari, 2020), as the cell wall thickness is typically correlated with porosity and density. As SiC has a larger molar volume compared to carbon, it is expected that the porosity will decrease with the reaction, and the SiC layer may be denser. This means that it will be harder for SiO to diffuse into the cell wall, and the dependency on cell wall thickness may therefore be important.

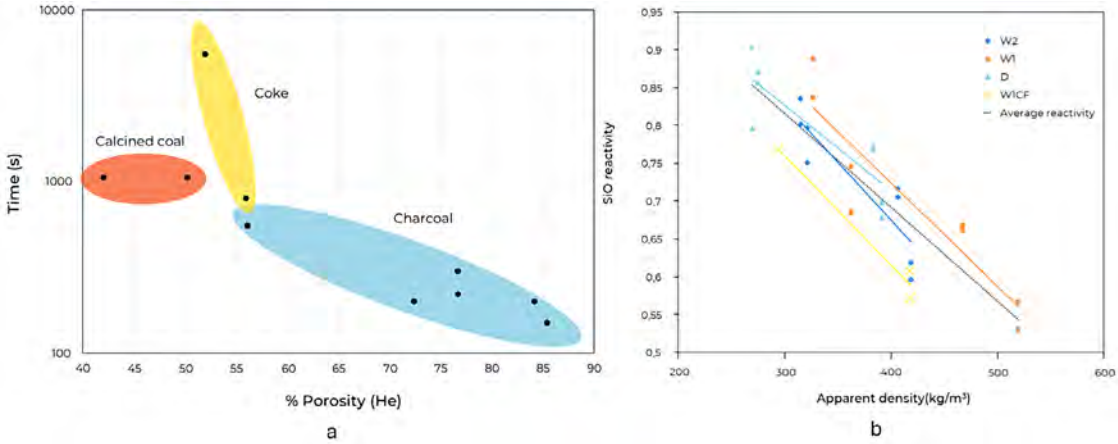


Figure 2.13 *Increasing porosity generally increases the SiO reactivity as shown in a) where the total time of reaction decreases with increasing porosity (Myrhaug, 2003) and b) SiO reactivity for eucalyptus charcoal from varying clones and production methods where the main effect on SiO reactivity was found to be the density (Ramos, 2018) [Used with permission from L.V. Myrhaug and D. Ramos].*

The SiO reactivity of coal has been investigated by a number of researchers, such as Raaness and Gray (1995), Narciso-Romero *et al.* (1999), Videm *et al.* (2000), and Myrvågnes (2008). In an effort to correlate the petrographic and anisotropic properties of the coals with SiO reactivity, it was seen that a higher rank will decrease the SiO reactivity, as shown in Figure 2.14. The figure shows the SiO reactivity of nine bituminous coals and their rank. Low-rank coals with low vitrinite reflectance are reported to show higher SiO reactivity (i.e., a lower amount of unreacted gas) than bituminous coals. The petrographic properties of the coal also influence the physical properties of the resultant coke and chars, such as porosity, pore size distribution and the type of porosity (Raaness and Gray, 1995).

Carbon reductants such as chars and coke derived from coal and petroleum exhibit a variety of microscopic textures that differ in the size and shape of their anisotropic units. Narciso-Romero *et al.* investigated several cokes derived from coal and petroleum (Narciso-Romero *et al.*, 1999). They found a high correlation between the size, shape and crystallographic order of the anisotropic carbon components (optical textures) and SiO reactivity. Other factors, such as porosity and the Fe, Ni and vanadium contents of the ashes,

also affect the formation of SiC. Videm *et al.* (2000) investigated cokes obtained from coals of different rank and type. The cokes consist of a binder carbon phase, produced from reactive macerals which soften during carbonisation (optical textural components), and a filler carbon phase, derived from inert macerals during carbonisation. They found that the SiO reactivity of metallurgical cokes was mainly determined by the content of the binder carbon phase within the cokes, as well as their volume weight and porosity.

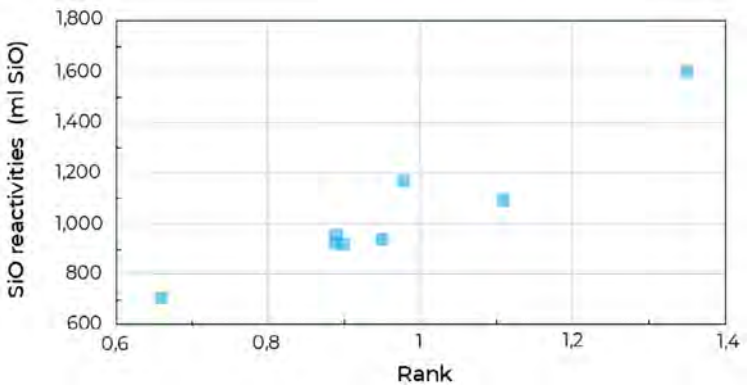


Figure 2.14 *SiO reactivity for coals, showing that a higher rank will decrease the SiO reactivity (Raaness and Gray, 1995) [With permission from M. Raaness].*

The most typical carbon materials used are coal, charcoal, char and petroleum coke, and, especially for FeSi, also metallurgical coke. Each material has quite a large SiO reactivity range, as also shown in Figure 2.15. The overall trend, however, is that charcoal and coal typically have a higher SiO reactivity compared to coke and petroleum coke. It can, however, be mentioned that SiO reactivity is usually measured at low SiO pressures, and one cannot rule out that the differences between the various carbons may be different at higher SiO pressures.

The formed SiC layer may spall off, or it may have very low strength and thus increase the amount of fines in the furnace. In some materials, the produced SiC layer will also be so dense that the reaction will stop before all carbon is transformed. These phenomena are not described thoroughly in the literature and will therefore not be discussed further here (Paull and See, 1978; Tuset and Raaness, 1976).

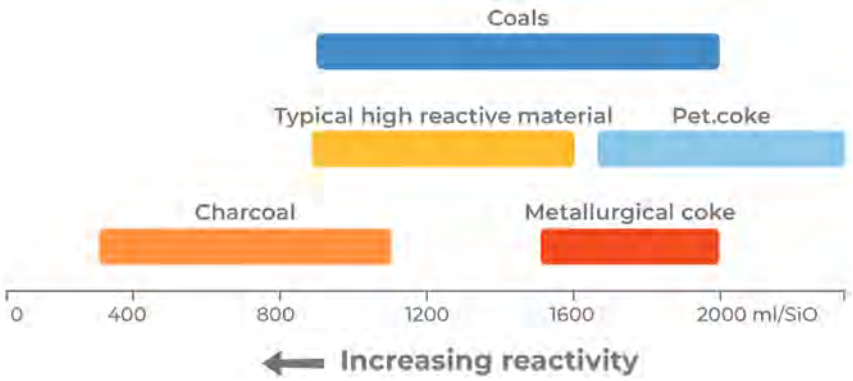


Figure 2.15 *SiO reactivity for various carbon materials, where a lower number of SiO gas not reacting signifies a high SiO reactivity (Raaness and Gray, 1995).[With permission from M. Raaness].*

$SiO_2 + SiC \rightarrow 3SiO(g) + CO(g)$ [2.4]

The reaction between SiO_2 and SiC is one of the two main reactions producing SiO gas in industrial furnaces and the other is the reaction between SiO_2 and Si. At temperatures lower than the melting temperature of SiO_2, both reactant species are solid. For the reaction to occur directly, the particles must be in contact. However, first, the contact surface will be small and, second, as the reaction starts to occur, the particles will no longer be in contact. It is therefore believed that the overall reaction happens through the gas phase. At the SiO_2 surface, CO-gas will react according to the following reaction:

$$SiO_2 + CO(g) = SiO(g) + CO_2(g) \quad [2.11]$$

Thermodynamically, the CO_2 pressure is very low above 1500°C ($< 10^{-4}$), and the CO_2 will therefore react with the SiC particles according to Reaction [2.12].

$$SiC + 2\ CO_2(g) = SiO(g) + 3CO(g) \quad [2.12]$$



Figure 2.16 *Illustration of the reaction $2SiO_2(s) + SiC(s) = 3SiO(g) + CO(g)$.*

The overall rate of a reaction can be expressed as the general equation for all kinetic reactions:

$$rate = \frac{driving\_force}{resistivity} \qquad [2.13]$$

In this context, the rate can be expressed as weight change per time unit, $\frac{dw}{dt}$, or as the fraction of reactant reacted per time unit, $\frac{d\alpha}{dt}$, where α is the fraction of reactant reacted. α will then go from 0, when no reaction has occurred, to 1, when all the reactant is consumed. Typically, α can be given in % instead of as a fraction. The correlation between the two parameters describing the reaction rate is:

$$\frac{d\alpha}{dt} = -\frac{1}{w_0}\frac{dw}{dt} \qquad [2.14]$$

The initial weight of the sample is w_o.

When the reaction rate is kinetically controlled by the chemical reaction, the driving force is the distance from equilibrium. Typically, the distance from equilibrium can be expressed as the difference between the equilibrium constant K and the ratio of the real gas pressures Q, when SiO_2 and SiC are pure species and hence their activities are 1:

$$K - Q = K - \frac{p_{SiO}^3 p_{CO}}{a_{SiO2} a_{SiC}} = K - p_{SiO}^3 p_{CO} \qquad [2.15]$$

p_{SiO} is the partial pressure of SiO gas, p_{CO} is the partial pressure of CO gas, a_{SiO2} is the activity of SiO_2 in quartz, and a_{SiC} is the activity of SiC. Based on this equation, it can be seen that when CO is added to the system, the reaction is expected to proceed more slowly. The resistivity is generally given as the inverse of the conductivity, where the conductivity is typically a function of temperature and of the geometrical relations between the reactants. This can mathematically be written:

$$Resistance = \frac{1}{A^{*}k} \qquad [2.16]$$

where A* is the geometrical factor and k is the rate constant.

- A* is dependent on the shape and form of the raw materials, how they are mixed (sizing, pellets, particles etc.), and the total size of the raw materials, that is, the extent of the reaction, α. It is also expected that A* will change dramatically when the quartz melts.
- k is a rate constant that depends on temperature according to the Arrhenius equation: $k = k^{0}\exp\left(\frac{-E}{RT}\right)$, where E is the activation energy, R is the gas constant, and T is the temperature in Kelvin. The microstructure and pollution elements in the SiO_2 and SiC may also affect the rate constant.

Based on the above discussion, the rate can be written as:

$$\frac{d\alpha}{dt} = A^{*}k\left(K - p_{SiO}^{3}p_{CO}\right) \qquad [2.17]$$

The real gas pressures of SiO and CO in the pellets are not known, and the rate equation can be simplified to reaction [2.18].

$$\frac{d\alpha}{dt} = f(\alpha)k(T) \qquad [2.18]$$

The simplification is a product of one function that accounts for the geometrical relations, $f(\alpha)$, and one that accounts for the temperature, k(T).

It must be emphasized that this temperature-dependent part also accounts for the temperature-dependent part of the equilibrium constant. This is also discussed previously by Filsinger and Bourrie (1990). Based on this, Tangstad derived the specific equation for SiO_2/SiC pellets, as shown in Reaction [2.20] (Tangstad *et al.*, 2019).

$$\frac{d\alpha}{dt} = k_0 A\left(1-\alpha\right)\cdot\exp\left(\frac{-Q}{RT}\right) \quad [2.19]$$

$$\frac{d\alpha}{dt} = 1.9\cdot10^8\left(1-\alpha\right)\cdot\exp\left(\frac{-460\cdot10^3}{RT}\right) \quad [2.20]$$

The term $1.9 \cdot 10^8$ represents the reaction area times the reaction constant: $1.9\cdot10^8 = 1.9\cdot10^5\cdot A^o_{SiO2}\left(\frac{cm^2}{g}SiO_2\right)$ if the area of SiO_2 determines the reaction rate, or $1.9\cdot10^8 = 3.24\cdot10^5\cdot A^o_{SiC}\left(\frac{cm^2}{g}SiC\right)$ if SiC determines the reaction area.

This equation was valid for the reaction between 1600 and 2000°C. In some of the experiments, the SiO_2:SiC ratio was measured after the experiment, and it was seen that some side reactions, such as elemental silicon formation, also took place.

Most of the published literature, except for Khrushchev (2000), reports the activation energy to be between 350 and 550 kJ/mol, as seen in Table 2.2. The reaction was studied from 1270 to 2033 °C, both below and above the melting temperature of SiO_2. Khrushchev measured a higher activation energy than the others, of about 800 kJ/mol above the melting temperature. This can possibly be attributed to the larger particle size used (0.16–0.20 mm). The high activation energy was attributed to carbon diffusion in SiC being the rate-determining step, as the temperature dependency of C diffusion in SiC is in the same area.

Table 2.2 *Published data for the activation energy for the reaction* $SiO_2 + SiC = 3SiO(g) + CO(g)$.

Author	Technique	Temperature (^{0}C)	Activation energy (kJ/mol)
(Pultz and Hertl, 1966)	Isothermal weight loss in reduced pressures	1270–1430	406–548
(Filsinger and Bourrie, 1990)	Thermogravimetery	1833–2033	348
(Khrushchev, 2000)	Isothermal weight loss	1800–1900	794–823
(Andersen, 2010)	Thermogravimetry, non-isothermal	1450–2000	T < 1750°C 370–420 (avg. = 402)
(Bao *et al.*, 2013)	Isothermal	1550–1820	351
(Ni, 2015)	Isothermal	1650–1750	Dip at 1730°C
(Tangstad *et al.*, 2019)	Non-isothermal	1650–2000	424–464 kJ/mole

As will be discussed in Chapter 5, natural quartzes go through various phase transformations with increasing temperature. At low temperatures, α-quartz is the stable phase. At atmospheric pressure, a second-order phase transformation to β-quartz occurs at 573 °C (Stølen, 2004). Before entering the high-temperature phase cristobalite, it transforms to an amorphous phase. The extent of the amorphous phase varies between different natural quartzes, as described by Ringdalen (Ringdalen, 2014; Ringdalen and Tangstad, 2016). Pure SiO_2 melts at 1996 K (1719 °C). However, it may start to soften at temperatures between 1873–2073 K (1600 to 1800 °C). This indicates that the reaction between SiO_2 and SiC may occur with various polymorphs and at different stages of solid, softened, and melted SiO_2. It should also be mentioned that the viscosity of liquid SiO_2 is very high. It is $2 \cdot 10^7$ Poise at the melting temperature and decreases to $5 \cdot 10^4$ Poise at 2000 °C. The reaction rate may therefore be affected by the polymorph, even in the solid state. Wiik suggested that cristobalite would give a higher reaction rate when SiO_2 reacted with carbon, compared to quartz (Wiik, 1990). This contradicts Tangstad, who observed the same reaction rate for quartz and cristobalite (Tangstad *et al.*, 2019). Hakamada suggested that amorphous silica would react faster than quartz, both with C and with SiC (Hakamada *et al.*, 2010).

Poch found that the reaction is rather slow in mixed powders [SiO_2 + x SiC] at 1 bar pressure in a stream of CO and Ar below 1550°C, but that the rate increases with rising temperature (Poch and Dietzel, 1962). Below about 1800°C, the stoichiometry of the reaction is close to Reaction [2.4], but at higher temperatures there is an additional weight loss that is thought to be due to evaporation of Si from Reaction [2.7]. In vacuum, the reaction rate is significant at lower temperatures (Wiik, 1990). According to Tuset (unpublished work quoted by Wiik, 1990), the reaction rate seems to be quite insensitive to the type of SiO_2 material. However, it increases strongly when crystalline industrial SiC is replaced by, for example, SiC made from charcoal.

$SiO_2 + Si \rightarrow 2SiO(g)$ [2.5]

There are a few published projects regarding SiO formation from silica and silicon (Andersen, 2010; Bao *et al.*, 2013; Sindland, 2020). Using particles, Sindland observed an exponential increase in the reaction rate with temperatures from 1650 to 1950°C (Sindland, 2020). Andersen and Bao, who used pressed mixed powder, experienced a reduction in the rate between about 1720°C, the melting point of silica, and about 1860°C (Andersen, 2010; Bao *et al.*, 2013). Because silica is quite viscous at low temperatures, the gas may be trapped in the pellets and hence reduce the reaction rate. When particles are used, the gas can escape more easily. Accordingly, Sindland did not observe this reduction in reaction rate when using particles from 1 to 8 mm. This was also verified by Kyaw, who found that a mix of particles gave a higher reduction rate than mixed powders or granules (Kyaw and Tangstad, 2024).

The wettability between molten silica and silicon is not very high, as shown in Figure 2.17. Interaction of silicon with 4 natural quartz sources shows a wettability of about 90°C (Sindland, 2020), and this does not vary significantly between different quartzes. This means that, when the quartz particles and the silicon particles melt, the silicon will agglomerate into larger droplets in the melted silica, as shown in Figure 2.18.

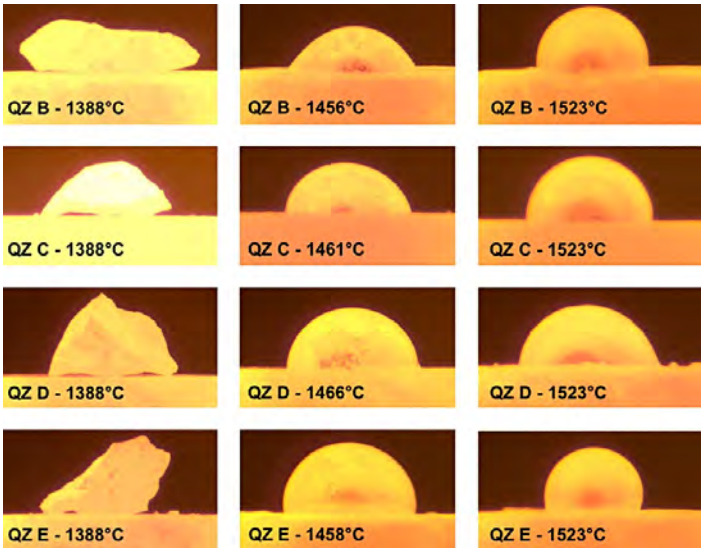


Figure 2.17 *Interaction of silicon with 4 natural quartz sources showing a wettability of about 90°C (Sindland, 2020) [With permission from C. Sindland].*

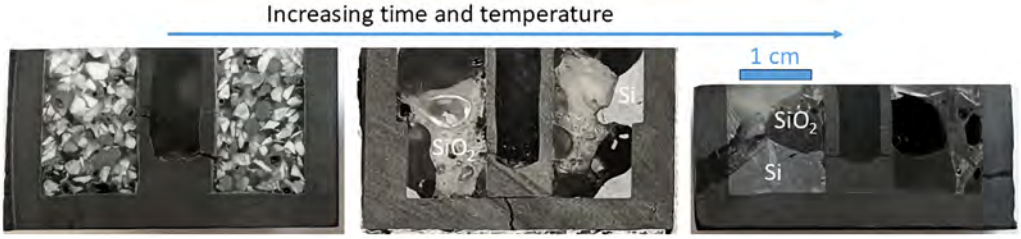


Figure 2.18 *The silica and silicon behavior with increasing reaction. This figure shows that the silica will agglomerate, and the silicon will agglomerate, into larger particles during melting, lowering the reaction area between the two phases (Sindland, 2020) [With permission from C. Sindland].*

The reaction rate between the silica and silicon particles can be expressed by the same simplified equation used for the SiO_2 + SiC reaction shown in [2.19].

$$\frac{d\alpha}{dt} = 6.28 \cdot 10^9 A_{0,Si} F(1-\alpha) \cdot \exp\left(\frac{-557 \cdot 10^3}{RT}\right) \qquad [2.21]$$

where $6.28 \cdot 10^9$ g·s^{-1}·m^{-2} is the frequency factor, $A_{0,Si}$ (cm^2·g^{-1}) is the original surface area of the Si particles, α is the degree of reaction varying from 0 to 1, and 557 kJ/mol is the apparent activation energy. This value is quite close to the activation energy found by Andersen (2010) below the melting point of quartz, which was between 438 kJ/mol and 528 kJ/mol for SiO_2/Si pellets. The factor F accounts for silica-particle agglomeration when both the silicon and silica are liquid. F equals 1 below the melting temperature of quartz and 0.5 above the melting temperature of quartz. This is a simplification of the true reaction area and how it changes with increasing temperature. However, it fits the experimental points quite well, as seen in Figure 2.19. In this figure, it can also be seen that the 5 different natural quartzes, with quite different properties in melting, pollution content and phase transformation degree, have quite similar reaction rates.

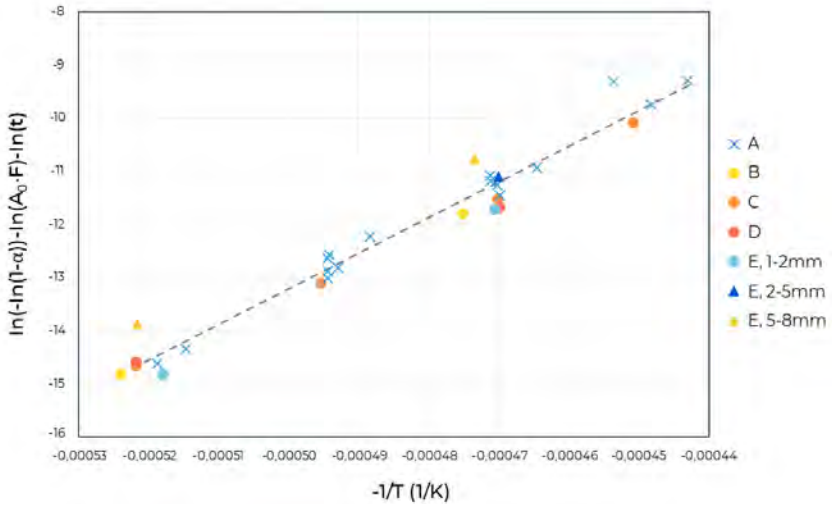


Figure 2.19 *An Arrhenius plot showing the comparison of the experimental results and the reaction rate given by equation [2.20]. The experiments were performed at various holding times, particle sizes in the range 1 to 8 mm and for 5 different commercial natural quartz sources.*

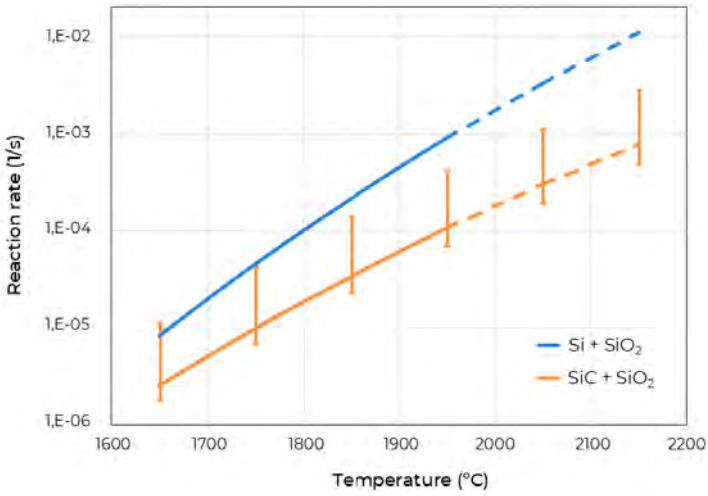


Figure 2.20 *Comparison of reaction rate of the two SiO producing reactions given by [2.19] and [2.21] using 1–2 mm silica particles for the Si + SiO reaction and 1–2 mm silica particles for the SiO_2 + SiC reaction. The dotted part of the lines are extrapolated outside the temperature range of the models (Sindland, 2020). [With permission from C. Sindland].*

In industrial furnaces, the SiO gas may be produced by both the SiO_2 + Si reaction [2.5] and the SiO_2 + SiC reaction [2.4]. A comparison of the rates given by the rate equations in [2.19] and [2.21] for particle sizes of 1–2 mm is shown in Figure 2.20. It shows that the rates of the two reactions are within a factor of 10. This means that the area between the reactants will be one of the main factors determining whether most of the SiO gas comes from reaction [2.4] or [2.5], because the area changes by a factor of 10 if the particle diameter is decreased by a factor of 3, assuming circular particles.

Condensation reactions

The 'condensation reactions' is an industrially common name for the reactions that occur from the gas phase to condensed phases, such as the reverse of reaction [2.4] and [2.5].

$$3SiO(g) + CO(g) = 2SiO_2 + SiC \qquad \text{reversed [2.4]}$$

$$2SiO(g) = SiO_2 + Si \qquad \text{reversed [2.5]}$$

The SiO_2 + Si condensate is typically recognized as a dense brown mass that glues the particles together, as shown in Figure 2.21. Microscopically, it consists of Si spheres in a matrix of SiO_2. This has been recognized and studied by several researchers, including Tangstad, Vangskåsen, Ksiazek, and Broggi, to mention a few (Broggi *et al.*, 2021; Ksiazek *et al.*, 2015; Tangstad *et al.*, 2010; Vangskåsen, 2012, 2011). The spherical particles may vary in size and can therefore give different shades of brown, as seen in Figure 2.23. Solid substrates, such as charge materials in a furnace, will hence be covered with layers of condensed materials in various shades.

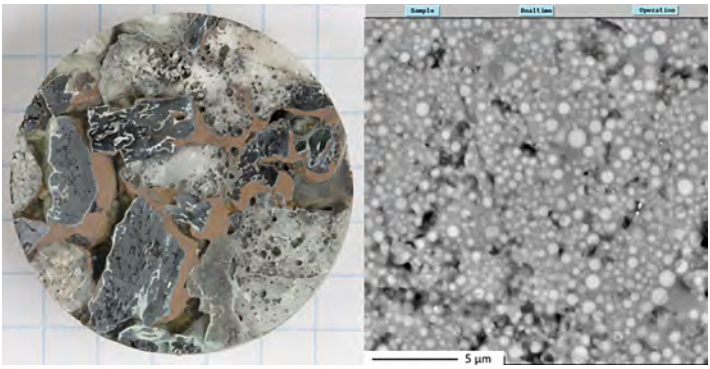


Figure 2.21 *Brown condensate, consisting of Si spheres in a SiO_2 matrix, condensed on quartz and SiC particles. (Tangstad et al., 2010).*

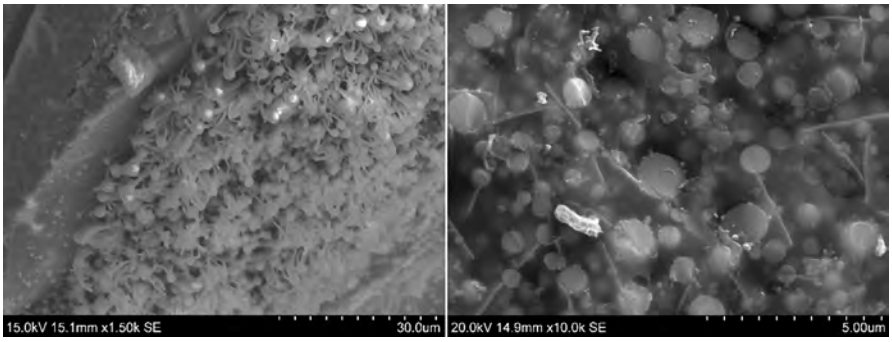


Figure 2.22 *Brown condensate shown with two different magnifications: spherical silicon particles in a SiO_2 matrix. (Broggi et al., 2021)[With permission from A. Broggi].*

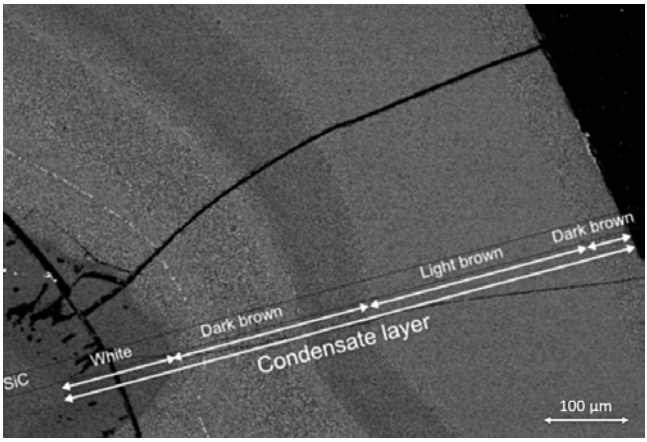


Figure 2.23 *Layers of brown Si and SiO_2 condensate with various silicon sphere sizes giving various brownish colours, condensed on a SiC particle. Adapted from. (Vangskåsen, 2012) [With permission from J. Vangskåsen].*

When investigating the SiO_2 + Si condensate more closely, additional features can be observed. First, there are cracks between the silicon spheres, as seen in Figure 2.24. Silicon can flow through these cracks in the silicon matrix and accumulate into larger silicon spheres, which may explain the variation in sphere size. As the condensate is heated while it descends with the charge materials in the furnace, the silicon spheres increase in size, as seen in Figure 2.25. It has also been observed that silicon separates from the condensate at temperatures above the melting point of silica, above 1720°C, as shown in Figure 2.26. The silicon produced as part of the condensates may therefore contribute to the silicon produced in the furnace, as the separation will be faster than the backreaction of Si + SiO_2 = 2SiO(g), reaction [2.5].

Although this condensate mainly consists of silicon and silica, microscopic investigations have also shown that some SiC forms on the surface of the silicon spheres, as shown in Figure 2.27. It is believed that SiC may form directly from the CO- and SiO-gas, as more SiC is present than could be precipitated from the dissolved carbon in the elemental silicon phase. This is of course due to the low carbon solubility, as shown in Figure 2.3.

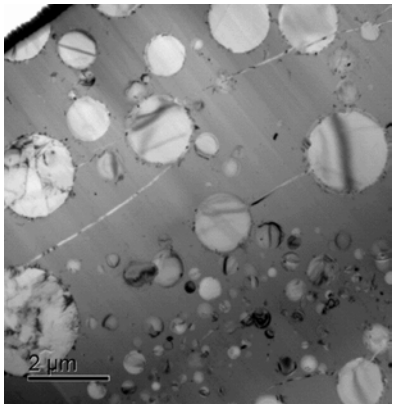


Figure 2.24 *Silicon spheres in a SiO_2 matrix where the large Si spheres are connected by cracks (Broggi, 2021). [With permission from A. Broggi].*

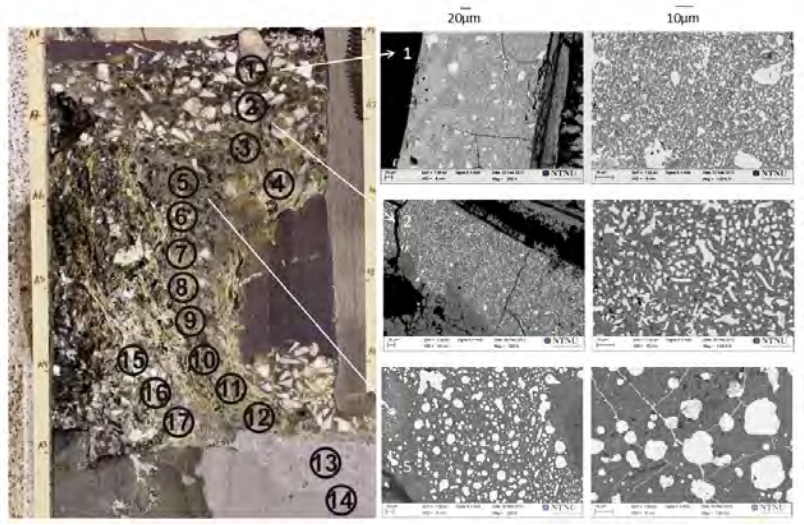


Figure 2.25 *Condensates investigated from a pilot scale furnace that show how the silicon particles grow in size over time and temperature (Vangskåsen, 2012). [Permission from J. Vangskåsen].*

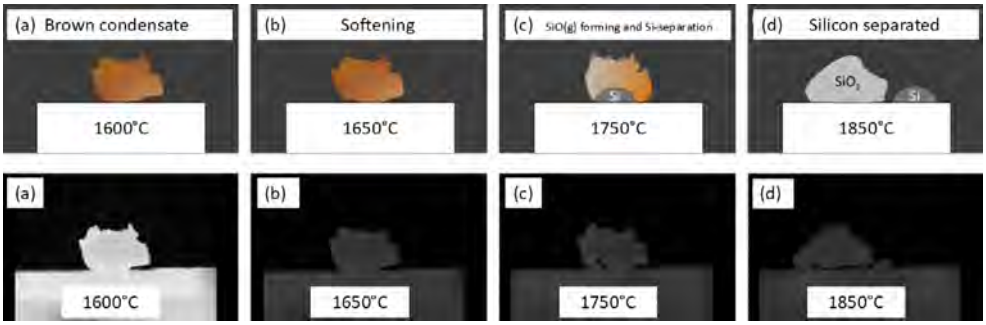


Figure 2.26 *Separation of silicon from the SiO_2 + Si condensate at high temperature (Broggi, 2021, Vangskåsen, 2012)[With permission A. Broggi and J. Vangskåsen].*

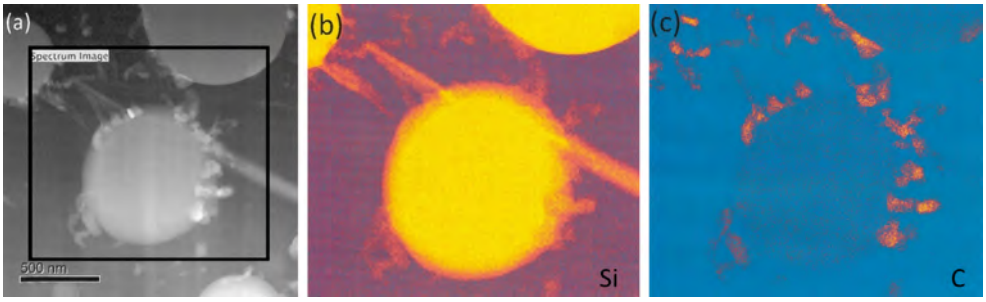


Figure 2.27 *Silicon and carbon mapping of a Si sphere, signifying that there are some SiC particles on the surface of the larger Si spheres (Broggi, 2021). [With permission A. Broggi].*

The SiO_2 + SiC condensate from the reversed reaction [2.4], $3SiO(g) + CO(g) = 2SiO_2 + SiC$, has been found to be a white, blue or orange cottonlike structure. The condensates consist of nanowires with and without nodules, as seen in Figure 2.28. The colour mainly depends on the size and amount of nodules (Broggi, 2021). The nanowires form with a SiC-core surrounded by a SiO_2 layer, as seen in Figure 2.29. Both due to the melting point depression of nano-sized materials and the exothermic energy released by the condensation reaction, the SiO_2 is liquid over a large temperature range. When liquid, the SiO_2 layer

will try to lower its surface energy by contracting into spherical particles and hence, SiO_2 nodules form. The SiO_2 is amorphous silica, and the SiC core has a high density of stacking faults (Broggi, 2021).

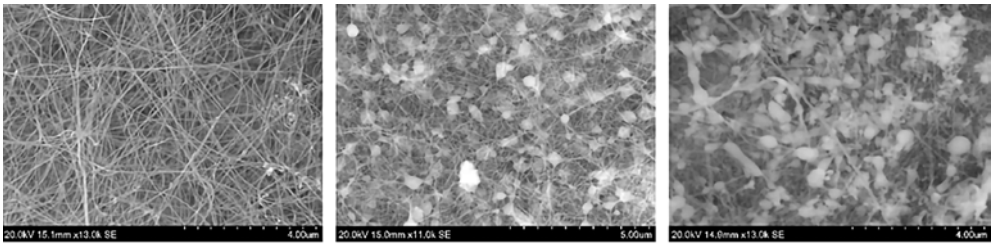


Figure 2.28 *SiO_2 + SiC condensates as wires, with and without nodules. The various colours are reflecting the size and amount of nodules (Broggi, 2021).[With permission A. Broggi].*

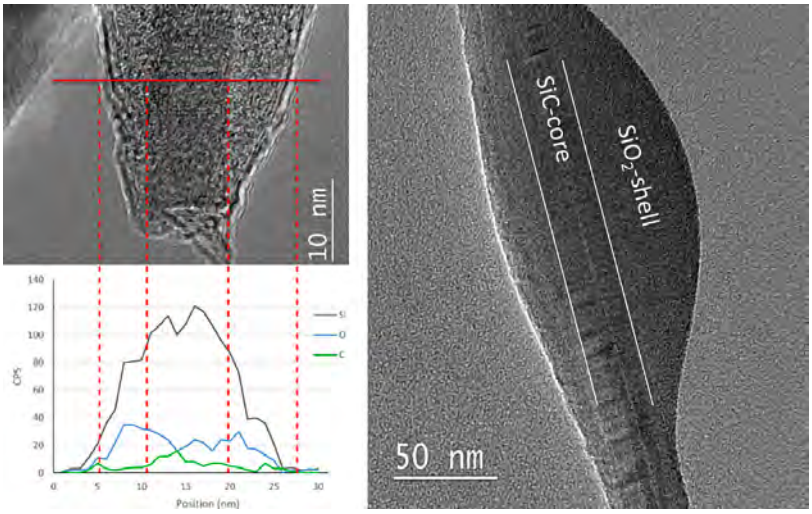


Figure 2.29 *Example of nanowires in the SiO_2 + SiC condensate, where the nanowires contain a SiC core surrounded by a SiO_2-shell. The right picture shows the SiO_2-layer starting to form a nodule (Broggi, 2021) [With permission A. Broggi].*

The condensate will typically form between 1000 and 1800°C. At higher temperatures, the driving force is low, and at lower temperatures the reaction rate is slow. It seems that the Si + SiO_2 condensate forms in a smaller temperature range between 1600–1750°C, while the SiO_2 + SiC can form at both higher and lower temperatures. The presence of a substrate increases condensate formation, and according to Broggi (2021) it seems that there will be more condensation with smaller particle sizes, which equals a larger condensation area.

In small scale experiments, where the temperature gradient between 1900 and 1000°C in industrial furnaces has been simulated, it is seen that typically 10–20% of the SiO gas formed will produce condensates, while the rest will go through the charge into the off gas system (Broggi, 2021). This shows that the condensation reactions according to the reversed reaction [2.4] and [2.5] are not in equilibrium. Broggi (2021) calculated the SiO-pressure based on the starting SiO pressure and the condensed material found in the experiments, as shown in Figure 2.30. The results show that the real SiO pressure in the gas is much higher than the equilibrium pressure for the condensation reactions. This agrees with industrial experience that the off-gas out of the furnace has a much higher SiO-content compared to the condensation equilibrium reactions.

The condensation reactions are exothermic, with a high absolute reaction enthalpy at 1500°C: –616.6 kJ/mol for $2SiO(g) = SiO_2 + Si$ and –1404 kJ/mol for $3SiO(g) + CO(g) = 2SiO_2 + SiC$. This means that both reactions have an adiabatic product temperature above 6000°C. This heat will of course be distributed to the surrounding gas and charge particles. However, this distribution takes time, and the condensation will therefore stop locally. If the high temperature zone is about 1950°C (the SiO-pressure in the high temperature zone is about 0.5), then 20% of the SiO gas is condensed. The condensation reaction will then have increased the bulk temperature in the low temperature zone by about 200°C and this may also stop condensation from occurring. It is therefore believed that a total condensation of about 10%–20% of the SiO in the gas is possible, as was also found in the experimental setup (Broggi, 2021).

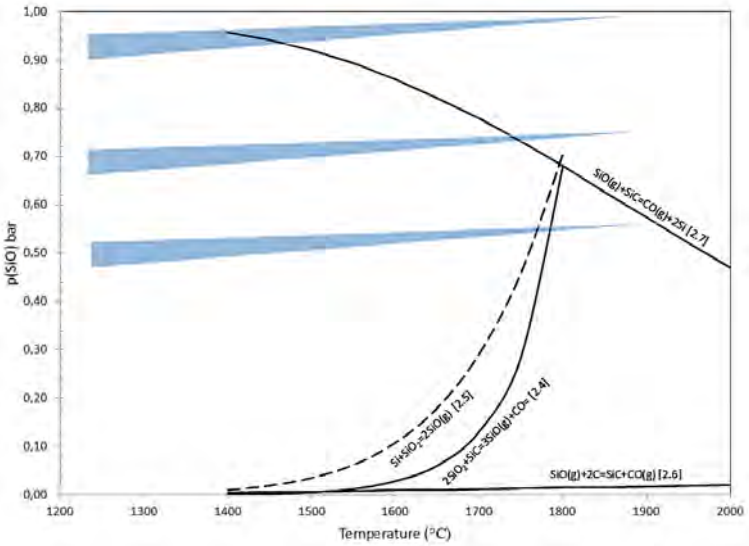


Figure 2.30 *Calculated SiO pressure during cooling of SiO- and CO-gas starting at 1 bar SiO pressure, 0.75 bar SiO pressure and 0.55 bar SiO pressure starting at 1900°C based on amount of SiO and CO condensed experimentally. Adapted from (Broggi, 2021).[Used with permission from A. Broggi].*

In industrial furnaces, the condensate can clog the charge materials and stop the raw materials descending in the furnace. The clogging will also prevent the gas from being distributed evenly in the charge. Clogging of the charge material is seen to occur mainly between 1500 and 1750°C (Broggi, 2021, Vangskåsen, 2011). At higher temperatures, the SiO_2 will be liquid, and the strength of the condensate will be low. At lower temperatures, the condensate will not be dense, but more a cottonlike structure. It is also in this temperature area that the brown Si + SiO_2 condensate forms, which seems to be tougher and more effective in gluing the charge together. The strength of the condensate was measured by Vangskåsen (2012), and it was found to be in the range 120–500 MPa when the condensate was excavated from the area below the 1670°C isotherm. For comparison, Portland cement is about 40 MPa and natural quartz in the area 130–370 MPa. When the condensate was extracted at higher temperatures, the strength decreased to 30–120 MPa, and this was believed to be due to the drainage of the Si particles and the softening of the silica.

Metal producing reaction – SiO(g) + SiC = 2Si + CO(g), reaction [2.7]

Traditionally, it is assumed that Si is produced in the metal pool area, where SiO_2 reacts with Si and SiC, producing SiO gas. This gas then reacts with SiC to produce silicon. This may still be the main reaction producing silicon, however, in the last years this view has been challenged. As mentioned in the previous subchapter, the silicon produced in the Si + SiO_2 condensate will separate from the condensate and end up in the tapped silicon. It was estimated that this can be as much as 10% of the total silicon produced (Vangskåsen, 2012). Next, as will be mentioned in Chapter 6 Electric operation, the arcs may go to the SiC-crusts surrounding the electrodes. When this happens, the energy will be developed in the SiC crusts. This means that when the SiO_2 meets the crust, SiO will be developed, and Si may be produced. This has been seen in the samples excavated from an industrial FeSi75 furnace, as shown in Figure 2.31.

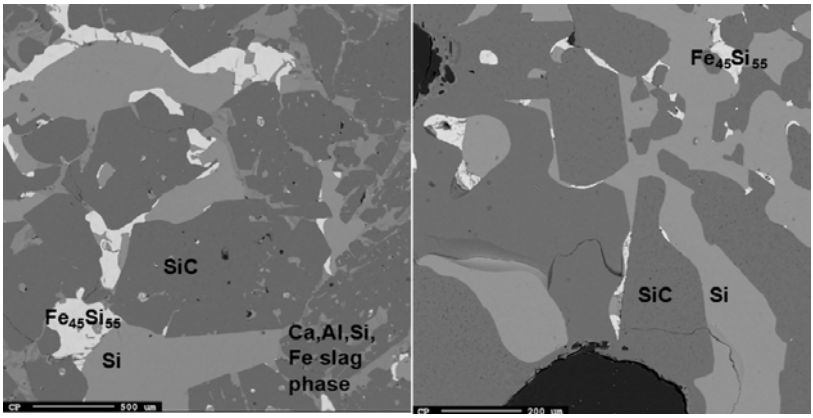


Figure 2.31 *FeSi produced in the SiC crust high up in an industrial FeSi75 furnace 400 mm from the charge top and 250 mm and 550 mm horizontally from the electrodes (Tranell et al., 2010).*

According to the equilibrium calculations shown in Figure 2.9, the SiO pressure is only high enough to produce elemental silicon above about 1800°C. Below this temperature, the condensation reactions give too low an equilibrium SiO pressure. As discussed in the last sub-chapter, the condensation

reactions may, however, be slow, and a higher SiO pressure may therefore be present. Si production in SiC at lower temperatures has also been observed. Tangstad *et al.* (2010) reported silicon produced as low as 1500°C in SiC particles. Tangstad *et al.* (2010) also reported elemental silicon at 1760°C, which is more in agreement with the findings of Jayakumari (2020), where Si was found in the SiC particles between 1600 and 1700°C. It was also found that SiC from charcoal produced more elemental silicon than SiC from coal and petroleum coke (Jayakumari, 2020; Jayakumari and Ringdalen, 2022). Both Tangstad *et al.* (2010) and Jayakumari (2020) used Si + SiO_2 mixtures to produce SiO gas, giving a high SiO pressure in the set-up. Sindland *et al.* found that β-SiC from charcoal reacted faster and produced more silicon than commercial α-SiC and α-SiC from crust material at temperatures above 2000°C (Sindland *et al.*, 2026).

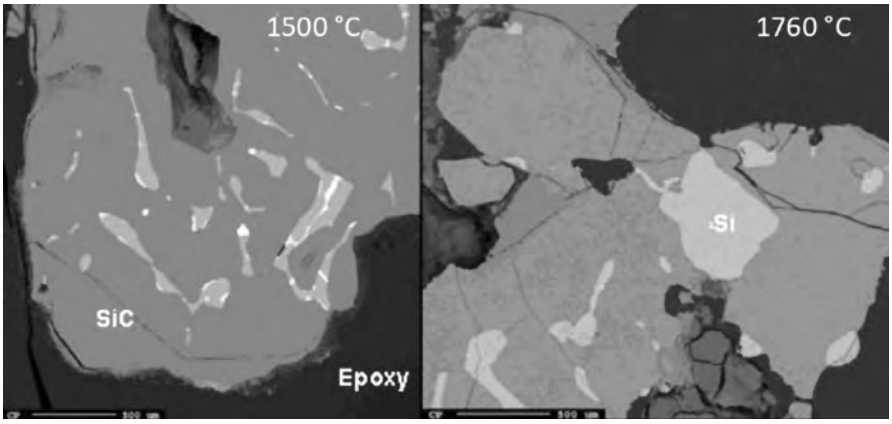


Figure 2.32 *SiC particles from a 75 kVA Si-simulator showing that elemental silicon can be found inside the SiC particles as low as 1500°C (Tangstad et al., 2010) (Light grey is silicon, mid-grey is SiC and black is epoxy-filled cavities).*

Silicon has, however, also been seen in the SiC pores in pilot scale experiments where the gas contains both SiO and CO (Vangskåsen, 2012), as shown in Figure 2.33. Sample 6, where silicon is formed in the SiC pores, was extracted high up in the charge material. The quartz is, however, melted, which means that the temperature was higher than 1700°C. As the particles descend in the furnace, the silicon content in the SiC particles gradually increases. Silicon

in the SiC particles was also seen in the low temperature area of a pilot scale experiment reported by Myrhaug (2003). It may be debated whether the metal in the SiC particles is from condensate reaction [2.5], where SiO gas produces silica and silicon. SiO_2 has, however, never been found together with the silicon in the SiC pores and it is therefore believed that this is not the case.

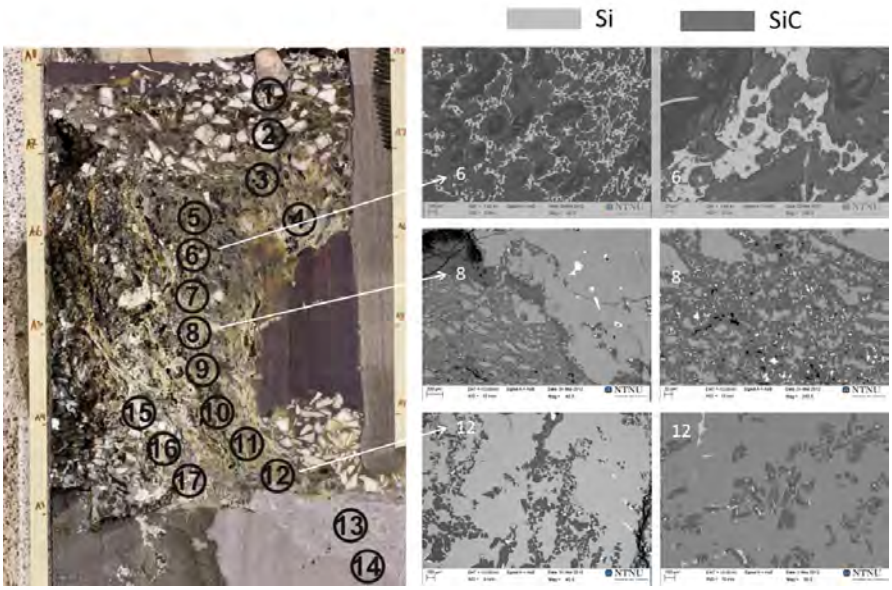


Figure 2.33 *SiC particles taken out at different positions in the partly transformed charge materials in a 150 kW pilot scale experiment with a top and bottom electrode. It is seen how the amount of silicon in the SiC particles increases as the materials are getting closer to the high temperature area (Vangskåsen, 2012) [Permission from J. Vangskåsen].*

As will be discussed in Chapter 4, there is also more slag in the furnace than was previously assumed. This may also mean that, when liquid SiO_2 comes down into the area below the electrode tips, it will dissolve in the slag. The dissolved SiO_2 may form SiO gas or silicon when it reacts with SiC. This has, however, not been experimentally investigated and is still a theory.

To sum up the areas where the metal producing reactions occur:

1. In the metal pool below the electrodes, where molten quartz produces SiO gas with Si or SiC, hence, the Si is produced from the SiO gas from reaction [2.7]. This will happen above 1800°C.
2. In the metal pool below the electrodes, where dissolved SiO_2 in slag produces SiO gas with Si or SiC and hence, the Si is produced from the SiO gas from reaction [2.7]. This will happen above 1800°C.
3. In the SiC crater wall next to the electrodes, where molten quartz produces SiO gas with SiC. Hence, the Si is produced from the SiO gas from reaction [2.7]. This will probably happen above 1800°C, as the crater wall may be quite warm. This can happen quite high up in the furnace when SiC crusts are produced.
4. In the SiC particles in most of the charge area, probably above 1600–1700°C. This will again probably occur according to reaction [2.7].
5. When the SiO gas is condensed to silicon and silica according to reaction [2.5], the silicon will perspire out of the condensate and may contribute up to 10% of the total silicon production. Reaction [2.5] will mainly be happening between 1500 and 1800°C.

Reaction between SiO_2 and C

Motzfeldt investigated the reaction between SiO_2 and C based on the hypothesis that it is a solid-state reaction (Motzfeldt and Steinmo, 1973). Particles of 1–2 mm of SiO_2 and C (graphite) were heated together in vacuum. A slow reaction started at 1450°C. The reaction pressure over SiO_2–C-SiC is then about 0.5 bar. After the reaction, the SiO_2 grains were apparently unchanged, but the C grains had a thin layer that was identified as β-SiC (cubic). SiC was also present outside the points of contact between SiO_2 and C and therefore, this cannot be a solid-state reaction. They also showed that the reaction could proceed without direct contact. Here, they heated a silica rod in vacuum while it hung at a predetermined distance from the walls in a graphite tube. The reaction started at about 1450°C, as with the particle mixture. The reaction

must hence be through the gas phase. The proposed reaction mechanism for the reaction between SiO_2 and C gives

$$SiO_2(s,l) + CO(g) = SiO(g) + CO_2(g) \quad [2.11]$$

$$CO_2(g) + C(s) = 2\ CO(g) \quad [2.22]$$

with the expected overall reaction

$$SiO_2(s,l) + C(s) = SiO(g) + CO(g) \quad [2.3]$$

Here, the SiO partial pressure increases and reaches a value where SiC becomes stable. Calculation shows that the content of CO_2 at equilibrium is very low at 1 bar:

$$\frac{p_{CO2}}{p_{CO}} \approx 10^{-4} \text{ (Nearly independent of the temperature)}$$

Wiik (1990) investigated the reaction thoroughly and showed beyond doubt that when solid SiO_2 is heated in an atmosphere containing CO, it reacts to form SiO and CO_2. He ran a systematic set of experiments to elucidate the mechanism of the reaction between SiO_2 and C, and his results seem to be reasonably well explained by a model that assumes a local equilibrium content of CO_2 close to the surface of the SiO_2 and the C particles.

Ozturk and Fruehan investigated the gasification of SiO_2 in a stream of CO, He–CO and Ar–CO at 1650°C (Ozturk and Fruehan, 1985). They treated spheres of diameter 0.60–0.95 cm made from 'commercially available fused quartz' with the gas in a thermobalance and monitored the weight loss by the reaction:

$$SiO_2(s) + CO(g) = SiO(g) + CO_2(g) \quad [2.11]$$

The active modification of SiO_2 is uncertain, since the fused SiO_2 may gradually change to cristobalite during the run. The SiO flux reported per unit surface was almost independent of the sphere diameter, gas velocity and gas composition. Therefore, Ozturk and Fruehan concluded that the rate was

not controlled by gas-phase mass transfer. They indicated that the formation of CO_2 on the silica surface may be rate-determining. The numerical value of the SiO flow was ~$6.5 \cdot 10^{-8}$ moles cm^{-2} s^{-1}. This is not a rate constant that applies to all conditions, but it can be taken as an indication of the largest rate that can be obtained from an available surface at a temperature below the melting point of SiO_2.

The SiO gas produced may also react with any available C present according to reaction [2.6]:

$$SiO\ (g) + 2C = SiC + CO(g) \qquad [2.6]$$

In pellets with intimate contact between the SiO_2 and the carbon, the SiO has time to react with the carbon and will therefore not leave the system. Weimer *et al.* (1993) proposed the reaction mechanism given by reactions [2.22] and [2.6], as illustrated by Figure 2.34. They also included an initial reaction at the contact point directly between the SiO_2 and the C particles, reaction [2.3].

$$SiO_2 + 2C = SiO(g) + CO(g) \qquad [2.3]$$

The total reaction in the pellets will hence be according to reaction [2.23].

$$SiO_2 + 3C = SiC + 2\ CO(g) \qquad [2.23]$$

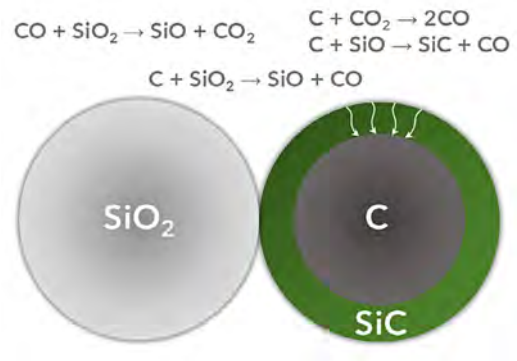


Figure 2.34 *Proposed mechanism forming SiC from SiO_2 and C materials.*

Li and Tangstad investigated the reaction mechanism between SiO_2 and carbon in SiO_2–C composite pellets for various carbon contents at 1650°C (Li and Tangstad, 2018, 2017). The reactions can be visualized by the weight loss, as shown in Figure 2.35. The weight loss is seen to be in two steps: first, a rapid step where the SiO_2 and C react to SiC according to the overall reaction [2.23]. It can be mentioned that very small amounts of SiO gas escape the system in this step, as the weight loss in the transition between the fast and slow step is very close to this reaction. This was also shown by chemical analyses at this point. When all the carbon is transformed to SiC, the SiO will be the main product according to reaction [2.4].

$$2\ SiO_2(s,l) + SiC(s) = 3\ SiO(g) + CO(g) \qquad [2.4]$$

Several authors have investigated the SiC formation from fine materials of SiO_2 and carbon, reviewed by Weimer *et al.* (1993) and Li (2017), to mention a few. The particle size is typically less than 1 μm; however, some investigate materials up to 40 μm. As seen in Figure 2.36, the temperature dependency (the activation energy) varies between the various works and the various carbon agents, and the literature reports activation energies in the area of 250 to 550 kJ/mol. Looking at the large picture, the temperature dependency can, however, be averaged according to the line marked as 3 in the figure, and gives an activation energy of 307 kJ/mol. It is also seen that when the SiO_2 melts, at about 1700°C, the rate will not continue to increase with temperature. As seen in the figure, carbon black fits quite good with the activation energy of 307 kJ/mol, while the charcoal seems to be higher and the coke seems to be lower. Whether this is a real difference or a result of experimental variation is unclear.

Within the same experimental investigation, investigating various carbon materials with the same sizing, Li *et al.* (2018) found that the charcoal reacted faster than coal and coke, which is in accordance with the SiO reactivity of the various carbon materials, as well as the CO_2 reactivity. Carbon black typically has a lower reactivity, however, as carbon black is typically of smaller size particles, the reactivity may still be in the same area. To obtain the highest amount of SiC, it is not only the reaction rate of the SiO gas with the SiC that is important, the SiO loss should also be minimized. It is hence important that the SiO production rate is in the same order of magnitude as the SiC production.

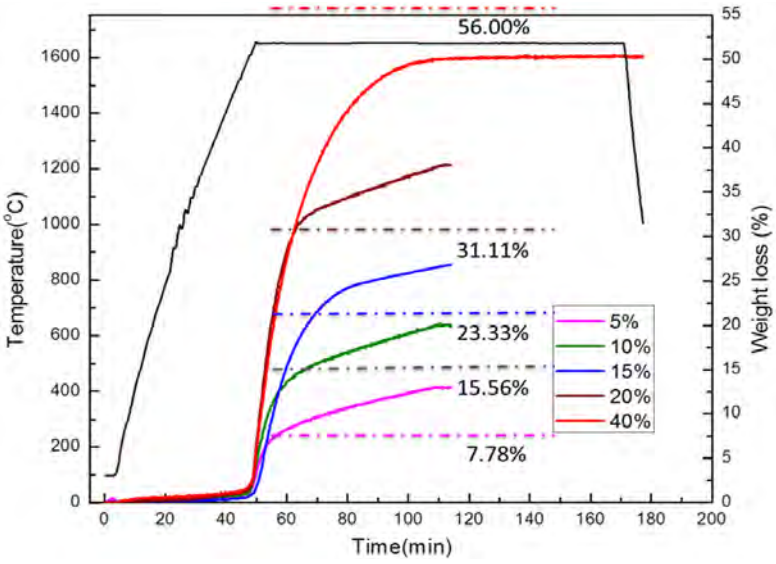


Figure 2.35 *Weight loss of SiO_2 pellets deposited with carbon with varying carbon contents ranging from 5 to 40% at 1650°C (Li and Tangstad, 2017). The weight loss is divided into two reaction steps where the first rapid stage is the SiC production with the total reaction $SiO_2 + 3C = SiC + 2\ CO(g)$ (as indicated by the horizontal lines) and the second slow reaction step is the SiO producing step where the total reaction is $2SiO_2 + SiC = 3SiO(g) + CO(g)$. Reproduced with permission from Springer Nature.*

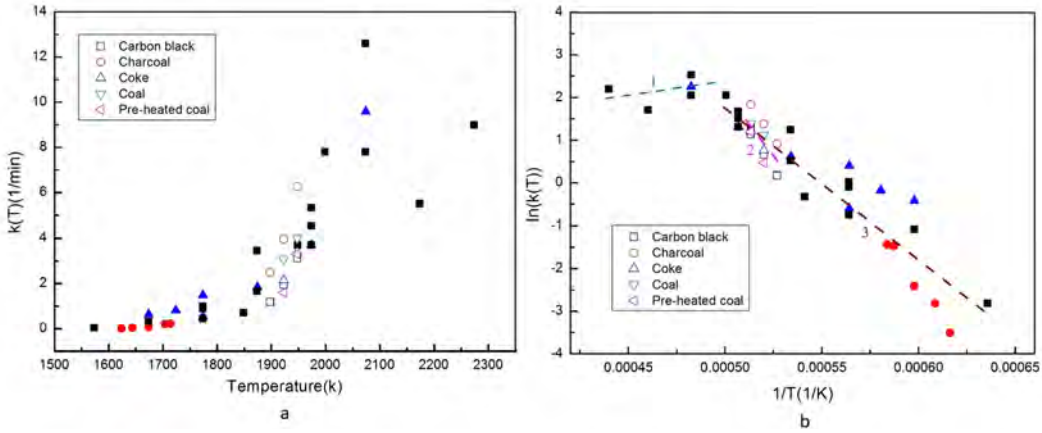


Figure 2.36 *Rate constant for reaction [2.23] $SiO_2 + 3C = SiC + 2\ CO(g)$ after the review of Weimer et al. (1993) and the work of Li (2017). (Solid icons – review of Weimer et al. (1993) and open icons – experimental work of Li (2017)).*

There has been an increasing interest in using natural gas as a carbon raw material. Methane (CH_4) will decompose when heated, and the investigations with carbon black and deposited carbon described above (Weimer *et al.* (1993) and Li and Tangstad (2017)) are a part of this. Methane may also be used directly as a gas and, as hydrogen is also present, this will change the reaction mechanism. This will further be discussed in Chapter 9 – Modified carbothermic processes.

The reaction between SiO_2 and C has been believed to be restricted in todays silicon production furnaces. However, as we are moving towards more use of waste materials, and hence the use of carbon and quartz composite agglomerates, this reaction will be of more interest. With a surplus of carbon, it is seen that the quartz in the agglomerates will react to SiC already at low temperatures and could be a valuable material in today's furnaces (Straum *et al.*, 2026).

Reaction between Si and CO gas

Produced Si and FeSi can also react back to SiC when CO-gas is present, as seen in lab-scale experiments (Ksiazek and Bao, 2024; Wintervoll, 2026). In CO-containing atmospheres, SiC may form through the reaction between liquid silicon and carbon monoxide (CO), as described in Equation [2.23]. In addition, the equilibrium between CO, CO_2 and solid carbon is governed by the Boudouard reaction, shown in Equation [2.22]:

$$Si(s,l) + 2\ CO(g) = SiC(g) + CO_2(g) \quad [2.23]$$

$$CO_2(g) + C(s) = 2\ CO(g) \quad [2.22]$$

with the expected overall reaction:

$$Si(s,l) + C(s) = SiC \quad [2.2]$$

Calculations show that the content of CO_2 at equilibrium is very low at 1 bar:

$$\frac{p_{CO2}}{p_{CO}} \approx 10^{-4}$$ (Nearly independent of the temperature)

The rate of SiC formation increased with increasing temperature. Even when the experiments were operated in Ar, a thin SiC layer (1–10 μm) formed on the silicon surface. This is believed to be due to trace elements of oxygen in the Ar gas reacting with the carbon parts in the furnace.

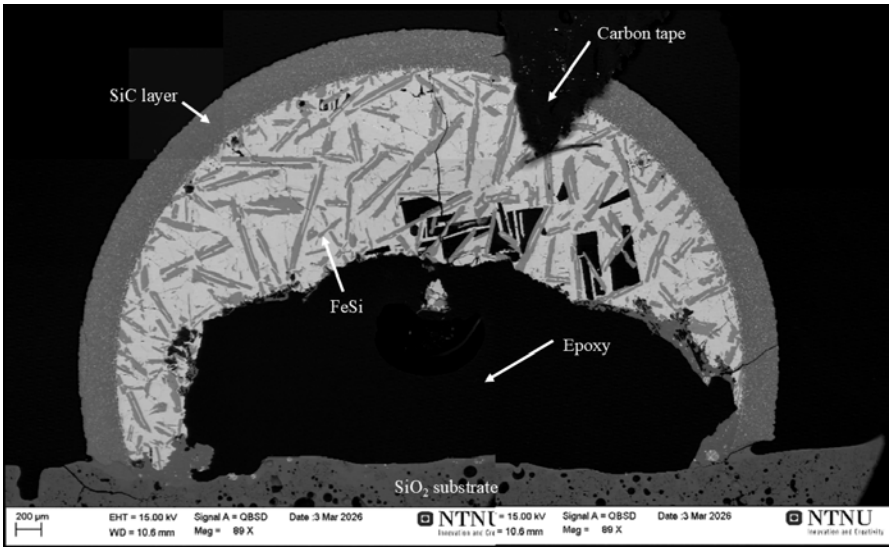


Figure 2.37 *SiC layer developed on a FeSi75 drop at 1650°C after 15 minutes in CO gas (Wintervoll, 2026).*

References

Andersen, V. (2010) *Reaction mechanism and kinetics of the high temperature reactions in the silicon process*. MSc thesis. Norwegian University of Science and Technology (NTNU), Trondheim, Norway.

Bao, S., Tangstad, M., Tang, K. and Ringdalen, E. (2013) 'Production of SiO gas in the silicon process', in *Proceedings of INFACON XIII*. Almaty, Kazakhstan, pp. 273–282. Available at: https://www.pyrometallurgy.co.za/InfaconXIII/0273-Bao.pdf

Broggi, A. (2021) *Condensation of SiO and CO in s*ilicon *and ferrosilicon production*. Doctoral thesis 2021:93. Norwegian University of Science and Technology (NTNU), Trondheim, Norway. Available at: https://hdl.handle.net/11250/2734899

Broggi, A., Ringdalen, E. and Tangstad, M. (2021) 'Characterization, thermodynamics and mechanism of formation of SiC–SiO_x core–shell nanowires', *Metallurgical and Materials Transactions B*, *52*, pp. 339–350. Available at: https://doi.org/10.1007/s11663-020-02014-4

Chase, M.V. Jr., Davies, C.A., Downey, J.R. Jr., Frurip, D.J., MacDonald, R.A. and Syverud, A. (1985) *NIST-JANAF* Thermochemical Tables. Available at: https://janaf.nist.gov/janbanr.html (Accessed: 22 May 2025).

Dalaker, H. and Tangstad, M. (2009) 'Time and temperature dependence of the solubility of carbon in liquid silicon equilibrated with silicon carbide and its dependence on boron levels', *Materials Transactions*, *50*, pp. 1152–1156. Available at: https://doi.org/10.2320/matertrans.M2009034

Filsinger, D.H. and Bourrie, D.B. (1990) 'Silica to silicon: Key carbothermic reactions and kinetics', *Journal of the American Ceramic Society*, *73*, pp. 1726–1732. Available at: https://doi.org/10.1111/j.1151-2916.1990.tb09820.x

Gjerstad, S. (1968) *Chemical metallurgical investigations concerning carbothermic reduction of alumina and silica*. Doctoral thesis. Norges Tekniske Høgskole (NTH), now Norwegian University of Science and Technology (NTNU).

Hakamada, M., Fukunaka, Y., Oishi, T., Nishiyama, T. and Kusuda, H. (2010) 'Carbothermic reduction of amorphous silica refined from diatomaceous earth', *Metallurgical and Materials Transactions B*, *41*, pp. 350–358. Available at: https://doi.org/10.1007/s11663-009-9332-1

Hall, R.N. (1958) 'Electrical contacts to silicon carbide', *J. Appl. Phys.*, *29*, pp. 914–917.

Iguchi, Y. and Narushima, T. (1993) 'Solubility of oxygen, nitrogen and carbon in liquid silicon', in *Proceedings of the 1st International Conference on Processing Materials for Properties*. Minerals, Metals & Materials Society (TMS), pp. 437–440.

Jayakumari, S. (2020) Formation and characterization of β- and α-*silicon carbide* produced during *silicon/ferrosilicon* process. Doctoral thesis 2020:252. Norwegian University of Science and Technology (NTNU), Trondheim, Norway. Available at: https://hdl.handle.net/11250/2678922

Jayakumari, S. and Ringdalen, E. (2022) 'Effect of varying SiO contents on Si and FeSi production', in *Proceedings of Silicon for the Chemical and Solar Industry XVI*. Online conference. Available at: https://doi.org/10.2139/ssrn.4118642

Jiao, J.M. (2020) Si-based phase change materials in thermal energy storage systems. Doctoral thesis, 220:137. Norwegian University of Science and Technology (NTNU).

Khrushchev, M.S. (2000) 'Kinetics and mechanism of reaction between silicon carbide and silica', *Inorganic Materials*, *36*, pp. 462–464. Available at: https://doi.org/10.1007/BF02758048

Ksiazek, M. and Bao, S. (2024) 'SiC forming reaction during the smelting of Si', in *Proceedings of Silicon for the Chemical and Solar Industry XVII*. Trondheim, Norway. Available at: https://doi.org/10.2139/ssrn.4942425

Ksiazek, M., Tangstad, M. and Ringdalen, E. (2015) 'Silicon production in laboratory scale induction furnace', in *Innovative Metallurgical Technologies and Processes: Ferroalloys*. Presented at the International Conference Advances in Metallurgical Process and Materials (AdMet), Kiev, Ukraine.

Kyaw, T.T. and Tangstad, M. (2024) 'Use of agglomerates in silicon production', in *Proceedings of Silicon for the Chemical and Solar Industry XVII*. Trondheim, Norway. Available at: https://doi.org/10.2139/ssrn.4945352

Li, F. (2017) *SiC production using SiO2 and Cagglomerates.* Doctoral thesis 2017:180. Norwegian University of Science and Technology (NTNU), Trondheim, Norway.

Li, F. and Tangstad, M. (2017) 'Carbothermal reduction of quartz with carbon from natural gas', *Metallurgical and Materials Transactions B*, 48, pp. 853–869. Available at: https://doi.org/10.1007/s11663-016-0887-3

Li, F. and Tangstad, M. (2018) 'Kinetic modeling of the reaction rate for quartz and carbon pellet', *Metallurgical and Materials Transactions B*, 49, pp. 839–845. Available at: https://doi.org/10.1007/s11663-017-1141-3

Li, F., Tangstad, M. and Ringdalen, E. (2018) 'Carbothermal reduction of quartz and carbon pellets at elevated temperatures', *Metallurgical and Materials Transactions B*, *49*, pp. 1078–1088. Available at: https://doi.org/10.1007/s11663-018-1195-x

Mikkelsen, J.C. (1985) 'The metallurgy of oxygen in silicon', *JOM*, *37*, pp. 51–54. Available at: https://doi.org/10.1007/BF03257741

Motzfeldt, K. and Steinmo, M. (1973) '*Kinetics of the reaction between carbon and refractory* oxides', paper presented at the Third Nordic High Temperature Symposium, pp. 91–109.

Myrhaug, E.H. (2003) Non-fossil reduction materials in the silicon process – properties and behaviour. Doctoral thesis 2003:67. Norwegian University of Science and Technology (NTNU), Trondheim, Norway.

Myrvågnes, V. (2008) *Analyses and c*haracterization *of fossil carbonaceous materials for silicon production*. *Doctoral thesis 2008:30*. Norwegian University of Science and Technology (NTNU), Trondheim, Norway.

Narciso-Romero, F.J., Rodríguez-Reinoso, F. and Díez, M.A. (1999) 'Influence of the carbon material on the synthesis of silicon carbide', *Carbon*, *37*, pp. 1771–1778. Available at: https://doi.org/10.1016/S0008-6223(99)00045-7

Ni, F. (2015) Kinetics of the reaction between quartz and silicon carbide in different gas atmospheres. MSc thesis. Norwegian University of Science and Technology (NTNU).

Oden, L.L. and McCune, R.A. (1987) 'Phase equilibria in the Al-Si–C system', *Metallurgical Transactions A*, *18*, pp. 2005–2014. Available at: https://doi.org/10.1007/BF02647073

Ottem, L. (1993) Solubility and thermochemical data of oxygen and carbon in liquid alloys of silicon and ferrosilicon. SINTEF Report No. STF34 F93027. Trondheim, Norway.

Ozturk, B. and Fruehan, R.J. (1985) 'The rate of formation of SiO by the reaction of CO or H_2 with silica and silicate slags', *Metallurgical Transactions B*, *16*, pp. 801–806. Available at: https://doi.org/10.1007/BF02667516

Paull, J.M. and See, J.B. (1978) 'The interaction of silicon monoxide gas with carbonaceous reducing agents', *Journal of the Southern African Institute of Mining and Metallurgy*, *7*, pp. 35–41.

Poch, W. and Dietzel, A. (1962) 'Formation of silicon carbide from silicon dioxide and carbon', *Ber. Dtsch. Keram. Ges.*, *39*, pp. 413–426.

Pultz, W.W. and Hertl, W. (1966) 'SiO_2 + SiC reaction at elevated temperatures. Part 1—Kinetics and mechanism', *Transactions of the Faraday Society*, *62*, pp. 2499–2504. Available at: https://doi.org/10.1039/TF9666202499

Ramos, D.C. (2018) *Quality of Eucalyptus charcoal for use in silicon production*. *Doctoral* thesis. Universidade Federal de Viçosa, Minas Gerais, Brazil.

Rein, R.H. and Chipman, J. (1963) 'The distribution of silicon between Fe–Si–C alloys and SiO_2–CaO–MgO–Al2O3 slags', *The Metallurgical Society of AIME*, *227*, pp. 1193–1203.

Ringdalen, E. (2014) 'Changes in quartz during heating and the effect on Si-production, initial studies', SINTEF, pp. 1–9.

Ringdalen, E. and Tangstad, M. (2016) 'Softening and melting of SiO_2, an important parameter for reactions with quartz in Si production', in Reddy, R.G., Chaubal, P., Pistorius, P.C. and Pal, U. (eds.) *Advances in Molten Slags, Fluxes, and Salts: Proceedings of the 10th International Conference on Molten Slags, Fluxes and Salts 2016*. Cham: Springer International Publishing.

Raaness, O. and Gray, R. (1995) 'Coal in the production of silicon rich alloys', in *Proceedings of INFACON* 7. Trondheim, Norway: FFF/SINTEF, pp. 201–220. Available at: https://www.pyrometallurgy.co.za/InfaconVII/201-Raaness.pdf

Scace, R.I. and Slack, G.A. (1959) 'Solubility of carbon in silicon and germanium', *The Journal of Chemical Physics*, *30*, pp. 1551–1555. Available at: https://doi.org/10.1063/1.1730236

Sindland, C. (2020) *Production rate of SiO gas from industrial quartz and silicon*. *MSc thesis*. Norwegian University of Science and Technology (NTNU).

Sindland, C., Andersen, V. and Tangstad, M. (2026) 'Silicon carbide reactivity: Reaction between silicon carbide polytypes and SiO gas', in *Proceedings of Silicon for the Chemical and Solar Industry XIII*. Kristiansand, Norway. Available at: https://www.ntnu.edu/si-conference

Stevens, S.J. and Hand, R.J. (1997) 'Polymorphism of silica', *Journal of Materials Science*, *32*, pp. 2929–2935.

Straum, I., Sindland, C., Andersen, V. and Myrvågnes, V. (2026) 'Behaviour of charcoal-quartz agglomerates under SiO-rich conditions', in *Proceedings of Silicon for the Chemical and Solar Industry XVIII*. Kristiansand, Norway. Available at: https://www.ntnu.edu/si-conference

Stølen, S. (2004) Chemical thermodynamics of materials: *M*acroscopic and microscopic aspects. Chichester: Wiley.

Tangstad, M., Ksiazek, M., Andersen, V. and Ringdalen, E. (2010) 'Small scale laboratory experiments simulating an industrial silicon furnace', in *Proceedings of INFACON XII*. Helsinki, Finland. Available at: https://www.pyrometallurgy.co.za/InfaconXII/661-Tangstad.pdf

Tangstad, M., Safarian, J., Bao, S., Ringdalen, E. and Valderhaug, A. (2019) 'Reaction rates of $2SiO_2 + SiC = 3SiO + CO$ in pellets at elevated temperatures', *AMMS*, *3*, pp. 1–11. Available at: https://doi.org/10.31031/AMMS.2019.03.000558

Tranell, G., Andersson, M., Ringdalen, E., Ostrovski, O. and Steinmo, J.J. (2010) 'Reaction zones in a FeSi75 furnace – results from an industrial excavation', in *Proceedings of INFACON XII*. Helsinki, Finland, pp. 709–716. Available at: https://www.pyrometallurgy.co.za/InfaconXII/709-Tranell.pdf

Tuset, J.K. and Raaness, O. (1976) 'Reactivity of reduction materials for the production of silicon', *Electric Furnace Proceedings*, pp. 101–107.

Vangskåsen, J. (2011) Investigation of the cavity formation *in the silicon process*. Student report. Norwegian University of Science and Technology (NTNU), Trondheim, Norway.

Vangskåsen, J. (2012) Metal-producing *m*echanisms *in the carbothermic silicon process*. MSc thesis. Norwegian University of Science and Technology (NTNU).

Videm, T. (1995) 'Reaction rate *of* reduction materials for the (ferro)silicon process', in *Proceedings of* INFACON VII. Trondheim, Norway: FFF/SINTEF. Available at: https://www.pyrometallurgy.co.za/InfaconVII/221-Videm.pdf

Videm, T. (2000) 'Reactivity and petrography', International Journal of Coal Geology, 43, pp. 243–256.

Weimer, A.W., Nilsen, K.J., Cochran, G.A. and Roach, R.P. (1993) '*Kinetics of* carbothermal reduction synthesis of beta silicon carbide', AIChE Journal, 39(3), pp. 493–503.

Wiik, K. (1990) *Kinetics of reactions between silica and carbon*. Doctoral *thesis 1990:60*. Norges Tekniske Høgskole (NTH), now Norwegian University of Science and Technology (NTNU), Trondheim, Norway. Available at: https://hdl.handle.net/11250/2396774

Wintervoll, H.E. (2026) *Formation of SiC from silicon and CO-gas*. *MSc thesis*. Norwegian University of Science and Technology (NTNU), Trondheim, Norway.

Yaws, C.L., Dickens, L.L., Lutwack, R. and Hsu, G. (1981) 'Semiconductor silicon: Physical and thermodynamic properties', *Solid State Technology*, pp. 87–92.

Tangstad, M. (2026) 'The carbothermic process of silicon', in M. Tangstad, G. Tranell, H. Tveit and E. Ringdalen (Eds.), *Production of high silicon alloys* (2. ed.) (pp. 77–108). Fagbokforlaget. https://doi.org/10.55669/oa880803

3

The carbothermic process of silicon

Merete Tangstad

This chapter starts with a brief history of the development of the electric furnace for high-silicon alloys. It then gives a detailed description of observations on the furnace and ends with an interpretation of these observations, in terms of the chemical reactions and material flows in the furnace.

3.1 The origin of the silicon furnace

Ferrosilicon alloys with up to about 20 per cent weight can be produced in a blast furnace by reduction of silica with carbon. Higher silicon contents were not possible in industrial furnaces before electric heating became available.

Edward Acheson did his first experiments with silicon carbide in 1891 (Acheson, 1911). He passed a strong current through a mixture of clay and coke by means of a rod of carbon. He obtained small amounts of a material that was so hard that it could cut glass, and found that it was the carbide of silicon. According to Acheson, the temperature of formation of silicon carbide was vastly higher than that required to fuse the walls of the furnace, but the walls were protected by the furnace charge. When the silicon carbide was overheated, the silicon evaporated and left pure graphite. Acheson developed these findings into a commercial production of silicon carbide and graphite. For silicon carbide the ideal overall reaction was

$$SiO_2 + 3\ C = SiC + 2\ CO \qquad [3.1]$$

This work is licensed under the Creative Commons Attribution 4.0 International License. To view a copy of this license, visit https://creativecommons.org/licenses/by/4.0/

The furnace was essentially heated by resistance in a core of conducting carbon and carbide. Occasionally the core became displaced, and hot spots appeared. In excavations after such runs, an apparently metallic product of bluish silver lustre was found. The product was identified as elemental crystalline silicon and called metallic silicon. Frank Tone (Tone, 1931) found that it probably was a product of the reactions

$$SiO_2 + 2\ C = Si + 2\ CO \qquad [3.2]$$

or

$$SiO_2 + 2\ SiC = 3\ Si + 2\ CO \qquad [3.3]$$

He decided to study the new product further and ran the first experiments to produce silicon in 1898, using a resistance furnace of the silicon carbide type. Both reactions gave silicon, but it was easier to operate with a charge of silica and silicon carbide. However, further experiments showed that an arc furnace gave better efficiency, and this furnace was finally adopted. It had just become available through the work of the French chemist Henry Moissan.

Moissan built his arc furnace in 1892, and temperatures of more than 2000°C became readily available for investigation. He treated several materials in it, including silica. Soon he could report that silica evaporated readily in a carbon-lined furnace run with 1000 ampere at 50 volts, and that it condensed to a very light product that remained stable in air for a long time (Moissan, 1895). Seen in the microscope, it consisted of small spheres of silica that were often bound together as fibres. The remains in the furnace contained crystals of silicon. When he treated a mixture of quartz and carbon, Moissan obtained silicon carbide crystals in a matrix of crystalline silicon.

This experience was soon developed into industrial production in a furnace where the electrodes were submerged in the charge. A few years later, a dissertation on ferrosilicon, with background in 'several years of practical experience in the electrometallurgical industry', could describe relatively large activity with several production plants and a wide patent literature (Pick, 1906).

Since this pioneering period, the process in the submerged arc furnace has undergone huge development in operational efficiency, size, electrodes, mechanical handling of raw materials, environmental protection, process control and quality management. Still, the fundamental principles – that is, the thermodynamics and the kinetics of the reactions – are very much the same.

3.2 Observation of the submerged arc furnace

Furnaces for silicon and high-silicon ferrosilicon behave similarly, and both will be described here.

The furnace system

Silicon and high-silicon ferrosilicon are produced in submerged arc furnaces. The most common type uses three-phase alternating current. A rough sketch is given in Figure 3.1. The electrodes in the corners of an equilateral triangle dip into a mixture of the charge materials. The inner structure of the furnace will be discussed later. The load can vary from less than 10 MW for small, old furnaces to more than 40 MW, and the geometrical dimensions vary roughly with the cubic root of the load. A typical small silicon metal furnace may be 20 MW, pot diameter 7 m, pot depth 2.7 m, electrode diameter 1.25 m and distance between the electrode centres 2.6 m. Many furnaces have pots that can rotate or oscillate at a speed corresponding to several days per rotation. This movement is believed to improve the tapping of the product and delay the formation of deposits at the bottom of the furnace. FeSi can also be produced in rectangular furnaces, with more than 3 electrodes, but that is not so common.

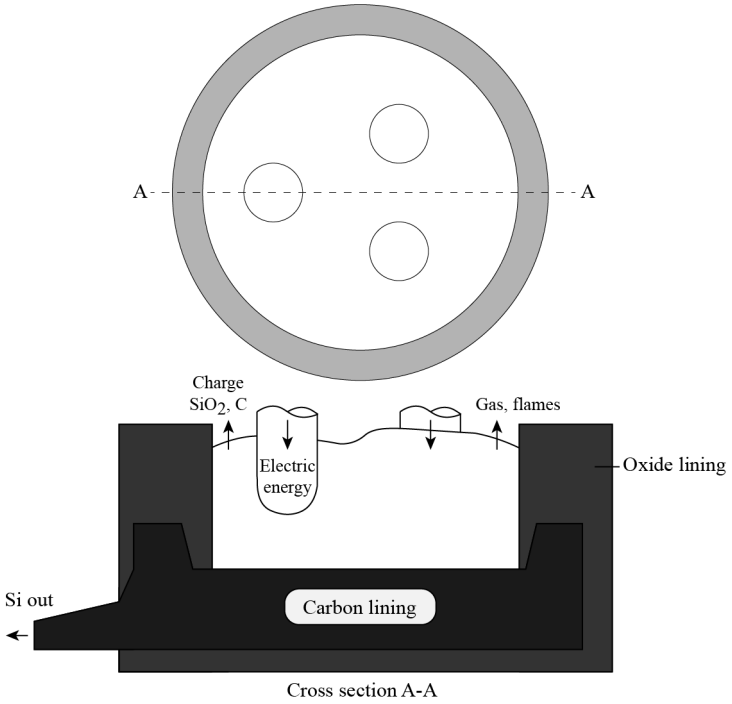


Figure 3.1 *The three phase submerged arc furnace for silicon.*

As shown in Chapter 2 (Chemistry of the Si–O–C system), the reaction between SiO_2 and C has SiO(g) and SiC(s) as intermediates. Some of the SiO leaves the furnace with the CO, and the overall chemical reaction in the furnace can be written as the following two equations, which produce silicon and SiO gas.

$$x \cdot (SiO_2 + 2C = Si + 2\,CO(g)) \qquad [3.2]$$

$$(1\text{-}x) \cdot (SiO_2 + C = SiO(g) + CO(g)) \qquad [3.4]$$

where x is the silicon recovery, or the silicon yield. The SiO and CO gases combust above the furnace, and SiO is oxidized to finely dispersed SiO_2, which forms the by-product 'silica fume'. Before gas cleaning plants were installed, this was seen as the well-known white smoke from silicon plants. Reactions [3.2] and [3.4] are strongly heat-consuming, and energy is taken from the

electric grid. The current passes between the electrodes (the path will be discussed later in Chapter 6 Electric operation), and heat is produced by the electric resistance of the furnace. The electric system has restrictions on load and current. Normally, the producer wants to run the furnace at maximum load, since it gives maximum production, and the operator must select the voltage and current that give the right heat production. The resistance is determined by the resistivity of the charge, the arc, and the electrode position. As the resistance of the furnace content is not stable, it is necessary to adjust the electric system by moving the electrode or changing the voltage when the current moves away from the chosen value. The control has two aims. The first is to avoid damage to the electric system by using too high a current and, if necessary, to break the current. This control is very rapid. The second aim is to adjust the resistance to give the furnace the chosen heat production at the right location in the furnace.

Observation of the working furnace

The inner operation of the working furnace is difficult to observe. The combination of high temperature and aggressive chemical surroundings allows very few materials for probes, and few measurements can be carried out inside the furnace. Therefore, understanding of the inner operation of the furnace is built primarily on indirect qualitative observations, industrial- and pilot-scale excavations, and general knowledge of the chemistry of the system.

The operator experience

The description of the behavior of the furnace can start with a description of what a furnace operator observes and does. The operational procedure changes from place to place, but a typical operation is a cyclic sequence:

- The furnace is stoked.
- The furnace is filled with charge according to the instructions. The charging can be continuous or discontinuous.
- The furnace is run until new stoking/charging is necessary.
- The operator decides the time for stoking according to the instructions and based upon observations, either personal or from camera or IR

camera systems: hot gas with white smoke from the furnace, smoke and temperature registration in the chimney, collapse of the charge cover on the furnace.
- The furnace is stoked.

The duration of a cycle depends upon the type of the charge, and it may vary from about 30 to about 75 minutes. For operation with the traditional batch charging, a typical sequence is that the furnace is filled during charging, and the top of the charge does not sink much during the period to the next stoking. Just after the charging, the flames are bluish-yellow, and the top layer is relatively cold. The top changes gradually during the cycle period. The charge becomes hotter until white-hot particles can be seen just below the top layer, and the flames change from yellow bluish to white, with a high white smoke content. The hottest areas appear in fairly regular rings around the electrodes. Sometimes part of the top collapses, and the resulting hole then looks like the opening of an intensely hot, large cavity. As a rule, it is necessary to stoke the furnace to get enough space around the electrode for the new charge, but the stoking may be light. First, a thin crust on the top of the cavity is broken, and a continuous deep depression some 30–50 cm wide is formed around the electrode. Remaining old charge is pushed towards the electrode and distributed evenly. The new charge is then placed on the top of the old one to a predetermined level. The amount of materials for a new filling depends on the density of the raw materials and the length of the cycle. With the more continuous charging systems, that is now becoming more common, smaller amounts of charge are fed each time and spread over a larger area of the charge top. There will then be less temperature variation at the charge top, and the phenomena seen during batch charging as described above will be less pronounced. A lighter and less frequent stoking can then be sufficient.

The product is tapped through a pre-prepared hole in the lining. The hole is opened by a graphite tapping electrode, or by burning with an oxygen lance or wood rods. With discontinuous tapping, the taphole is plugged with a special clay mixture when the flow of melt has stopped. Originally, the tapping was always discontinuous. The idea was that the silicon formed a pool at the bottom of the furnace, and by tapping this pool it should be emptied completely through a hole near the bottom of the furnace. According to this idea, the silicon should flow to the taphole until the bath was empty, and

then a jet of gas flames should erupt from the interior of the furnace through the open hole. At some plants, the tappers were instructed not to plug the taphole before the flame jet appeared. The aim was to secure that the production zone was kept close to the bottom, and to detect a build-up of a deposit early. However, often the jet flame did not appear even after burning of the taphole with the graphite electrode. The flow of silicon was less intense than in a newly opened hole, but the overall production was normal. In some plants, this taphole operation developed into continuous tapping, where the taphole was only plugged when it was necessary for repair or when rotation of the furnace made access to the tap hole difficult. In continuous tapping, the tap hole opening was refreshed by the graphite tapping electrode, or by blowing with an oxygen lance, when the flow became poor.

Probes in the furnace

The first thorough study of the inner structure of the furnace was published by Zherdev *et al.* who used simple mechanical and electrical probes to show that the electrodes were surrounded by large gas-filled cavities during operation (Zherdev *et al.*, 1968a; 1968b; 1965; 1962a; 1962b; 1960). A set of the results of the measurements is shown in Table 3.1. The size of the cavity increased with increasing content of silicon. It also depended on the rotation of the furnace (Zherdev *et al.*, 1968b). The cavity was largest on the side that moved towards the electrode. This was not an effect of the rotation of the field of the alternating current, since it changed when the rotation of the furnace changed. The cavity became smaller when the rate of rotation increased. A later study of the importance of furnace rotation showed that there was a critical rate of rotation (Zherdev *et al.*, 1968b). Slow rotation (135 h/rotation) had almost no influence, and the influence increased with increasing rate until the critical value of around 70 h/rotation. At a lower rotation rate, the cavity was largest on the side that moved towards the electrode, as in the earlier runs, but above the critical rate it was largest on the other side. Above the critical rate, the electrodes were forced out of the vertical position. It can, however, be noticed that furnaces with similar rotation speed showed very different size of cavity, ranging from almost non-existence to 2 m high during excavation; however, this will be discussed later in this chapter (Ksiazek *et al.*, 2016; Tangstad *et al.*, 2014; Tranell *et al.*, 2010).

Table 3.1 *Measured size of the cavity in a 9 MW ferrosilicon furnace (Zherdev et al., 1965).*

Alloy	Maximum distance electrode to crater wall	Distance electrode tip to bottom deposit	Maximum height of the cavity	Height of charge layer in contact with the electrode
FeSi45	0.50 m	0.20 m	1.20 m	0.50 m
FeSi75	0.60 m	0.30 m	1.40 m	0.32 m
FeSi90	1.20 m	0.16 m	1.70 m	0.06 m

The qualitative content of the work of Zherdev *et al.* had probably been recognized by many metallurgists before these publications. Tone indicated a cavity in a sketch of the process (Tone, 1909). However, the accepted theory around 1960 was that such cavities only appeared when the voltage was too low. Operators who knew from experience that they had a cavity chose to remain silent, to avoid criticism for erroneous operation. The observations of Zherdev *et al.* are now rather old, and furnace operation has improved a lot since they were published. The size of the cavity in present, well-run, large furnaces may be quite variable.

Otani *et al.* continued the work on the inner structure of the furnace (Otani *et al.*, 1968). They placed a visual probe into the cavity of furnaces sized 0.5 and 5 MW, and were able to see the surroundings of the electrode tip directly. This technique yielded several interesting observations. They confirmed that the electrode was surrounded by a cavity. The electrode tip usually stood 5 to 15 cm above a bottom deposit that consisted of a spongy aggregation of silicon carbide crystals, with molten silicon metal between the crystals. In discontinuously tapped furnaces, the molten silicon sometimes covered the silicon carbide completely. A viscous mass, which must have been molten quartz or molten quartz with carbon materials, frequently fell down close to the electrode tip, where it disappeared gradually. Formation of bubbles indicated reaction in this mass. When the furnace was tapped, a porous structure was left after the melt.

The temperature was read with an optical pyrometer. The electrode showed 2000–2400°C; the crater walls showed 100–200°C less (with some doubt about the accuracy); and the metal bath showed 1900–2100°C. Sometimes, light from a very hot source outside the field of view was apparent, and temperatures up to 3500°C were read. The lower part of the electrode was hottest, and Otani *et al.* concluded that the high temperature and high SiO content of the gas made SiC

unstable there. Therefore, the electrode was consumed from the sides and became tapered at the lower end. An electric arc was burning between the electrode and the bottom deposit. The end of the electrode was cut horizontally, which was thought to be caused by reaction with SiO_2 splattered onto the electrode. Otani *et al.* compared electrode consumption in the furnace with consumption in an arc chamber in an inert atmosphere, and concluded that chemical consumption of electrode was large compared with evaporation in the arc spots.

Otani *et al.* supplemented their observations with equilibrium calculations and summed up their understanding of the process in Figure 3.2. The materials in the roof of the cavity are glued together by condensate from the gas produced in the cavity, and the roof is consumed gradually from the bottom. When the inside of the roof is exposed to heat from the arc and energy-rich gas, the silica becomes fluid and sinks down with the carbon materials.

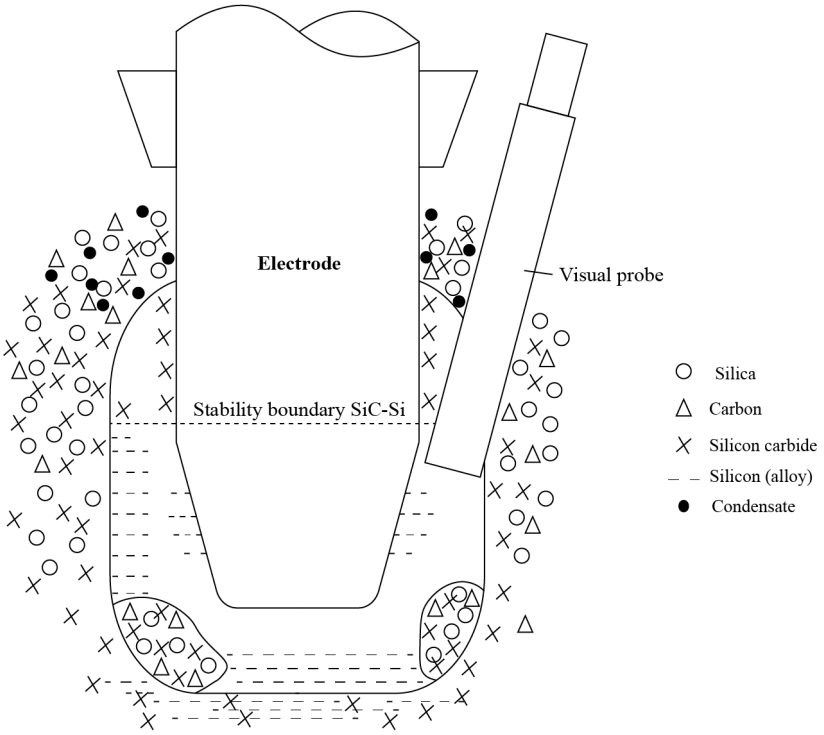


Figure 3.2 *The inner structure of a silicon furnace (after Otani et al., 1968). The visual probe is purged with inert gas during the observation to avoid deposits that can block the view.*

Otani's visual probe had a rather narrow field of view, and only a very small fraction of the cavity could be seen. At Elkem Research in Kristiansand (Norway), a probe was built into the side of a 50 kW furnace, and the results were later confirmed in a 500 kW furnace (Schei and Larsen, 1979; Schei and Larsen, 1982). In this arrangement, the field of view was much larger than in the furnace of Otani *et al.*

Normally, the view was fairly clear, but occasionally dark smoke covered some of the details, often simultaneously with smoke production from the top of the furnace. During stoking, materials from the upper layer were forced down into the space around the electrode tip. These materials collapsed within a few minutes, while large drops of silicon appeared on the surface. The silicon pool increased significantly during the collapse, in the first minutes after the stoking. The materials blocked the view at the beginning, but when they collapsed, the view into the cavity was normally very good until the next stoking.

An electric arc burned between the electrode and a pool of molten silicon. It moved around, but could stay in the same place for many seconds. Observation through a chopping disc showed that the arc was well developed, with a bright spot on the electrode when the electrode was the cathode, but rather unstable and difficult to see when the electrode was the anode. The arc moved around on the electrode. Often, it burnt from the horizontal end of the electrode, but sometimes it burnt from the sides. A thin, irregular layer of a liquid material flowed downwards on the surface of the electrode and left scars. Sometimes, this liquid apparently ignited and gave short-duration luminous spots.

Occasionally, a viscous melt came in at the top of the field of view and slid slowly towards the bottom. This material must be silica, and some solid particles in it probably consisted of silicon carbide and carbon. Clumps of the viscous melt floated around for a while on the silicon pool, and silicon drops appeared on its surface while it was gradually consumed. When melt particles came close to the SiC walls of the cavity, intense bubbling indicated reaction by mass transport through the melt. When the carbon content of the charge was kept too high for several hours, the bottom rose gradually and blocked the probe. However, when the carbon content was decreased, the deposit disappeared slowly. In later furnace excavations, accumulation of SiC is usually found as α-SiC walls around the electrode, and it may be this that blocked the view of the probe during the high carbon additions.

When a cold steel rod was set into the cavity of the furnace, it was immediately covered with a brown, dense substance that, in the microprobe, was found to consist of droplets of silicon in a matrix of silica, a typical Si and SiO_2 condensate. In one experiment, the intention was to take out a relatively large sample of the silica dust produced when the cavity gas burns. A graphite tube with an inner plug of the same length was placed with the tip well inside the cavity during stoking, and charge materials were filled in around it. The top of the tube protruded some ten centimetres above the charge. The furnace was operated until the cavity was well established and the charge with the graphite tube became quite hot. Then the plug was removed. A strong jet of gas from the tube burnt with intense white light, giving a dense white smoke, and the outside of the graphite tube became white-hot within a short time. However, the flames soon became weaker, and the gas flow through the hole disappeared in a few minutes. The inner wall of the tube had a several-millimetre-thick, dense layer of the brown substance, and inside was a brownish, woolly material. The experiment indicates that the condensation reaction of SiO to [SiO_2 + Si] is very rapid when cooled.

The temperature in the cavity in the small furnace was measured by two methods. The first was to place a graphite tube with a closed bottom into the cavity and read the temperature at the bottom of the tube using an optical pyrometer. When the tube was open at the top end, some species containing Si diffused through the graphite walls, filled the lower part of the tube with pure silicon, and blocked the sight. The tube could be kept open when the top was sealed and some inert gas was blown in. Most readings gave 2000 ± 100°C, but some readings were much higher. After such readings, the probe had scars indicating that an arc had burnt from the electrode to the pyrometer tube. In the second method, the crater content was photographed through the visual probe while the current through the furnace was shut off for a few seconds. The blacking density of the film was then measured and compared with a scale that was made by photography of objects of known temperature in a similar arrangement. These measurements also gave a result around 2000°C. Both methods give, in principle, the temperature of the condensed material where the reading was done, not the temperature of the gas.

Temperatures in the charge will vary both in horizontal and vertical directions. An average temperature in the charge, as a function of distance from charge-top, was calculated to increase almost linearly from 500°C to

1500°C in about 0.7 m. From 0.7 m and down to the cavity at 2.5 m, it further increased to 2000°C (Ringdalen *et al.*, 2020). This is not in accordance with industrial measurements in both FeSi and Si furnaces, where the temperature in the top layer of the charge is 1000–1200°C due to the exothermic combustion of CO and SiO as the gas meets the abundant air. Further down in the charge, between 0.5 and 1 m into the charge, the temperature was as low as 400–600°C (Ksiazek *et al.*, 2021). This was, however, between the electrodes and is dramatically lower than the calculated values. The temperature in the charge will vary with both the distance from the electrode and the charge-top, as well as with operational conditions.

Excavation of furnaces

Pilot- and industrial excavation has been done by Zherdev and Otani *et al.*, as discussed above, as well as pilot excavations (Müller, 1972; Schei, 1967; Schei and Sandberg, 1966). After 2010, a new period of pilot-scale excavations (Hoover *et al.*, 2022; Kamfjord, 2012; Myrhaug, 2003) and industrial excavations were carried out (Folstad, 2023; Jusnes, 2020; Ksiazek *et al.*, 2018, 2016; Tangstad *et al.*, 2014; Tranell *et al.*, 2010). Large-scale lab apparatus have also been used to simulate the industrial furnace, where a temperature gradient may be present from around 2000°C in the lower part of the crucible and 1200–1400°C on the charge top, and where up to 500 grams of silicon was produced in the lower part (Ksiazek *et al.*, 2015; Ringdalen and Tangstad, 2012; Saadieh *et al.*, 2018; Tangstad *et al.*, 2010). One can discuss if the shut-down furnace represents the conditions in the furnace during operation; however, when the furnace is shut down without melting it down and changing the electrodes, the zones and the materials found are believed to be close to the conditions during operation. Previously, the melt down of the furnace was believed to save time during the dig-out, however, the charge materials are typically very easy to dig-out, and there is a discussion if melting it down actually increases the amount of tough materials in the furnace like slag, metal and SiC crusts (Ksiazek *et al.*, 2018). If a furnace becomes available for careful excavation, it should be run normally until it is shut off in the middle of a stoking period. An experienced research metallurgist should be present all the time during the excavation and make a careful record of the observations, with description of the position and

surroundings of the samples taken out for further investigation. Samples gathered without a proper description of the furnace situation are almost worthless.

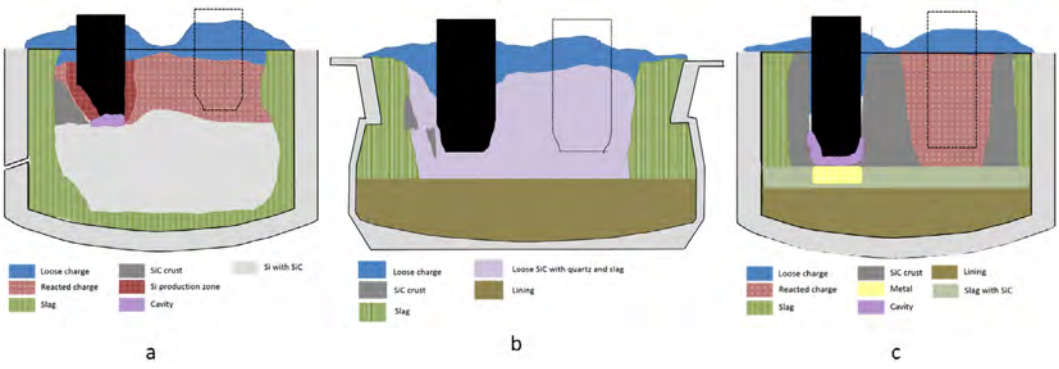


Figure 3.3 *Examples of industrial excavations of silicon furnaces: a) represents a small furnace, b) represents a large furnace with loose charge, and c) represents a large Si furnace with a high amount of SiC crust (Ksiazek et al., 2016) [Used with permission from M. Ksiazek].*

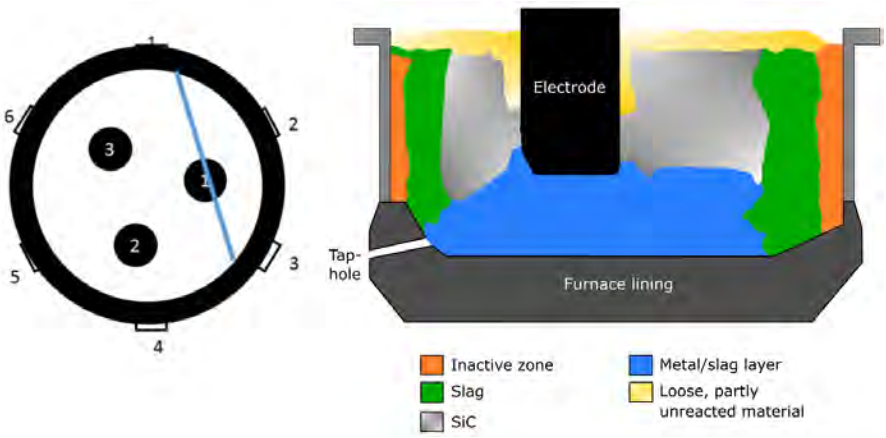


Figure 3.4 *Example of a FeSi75 furnace (Jusnes, 2020) [With permission from K. Jusnes].*

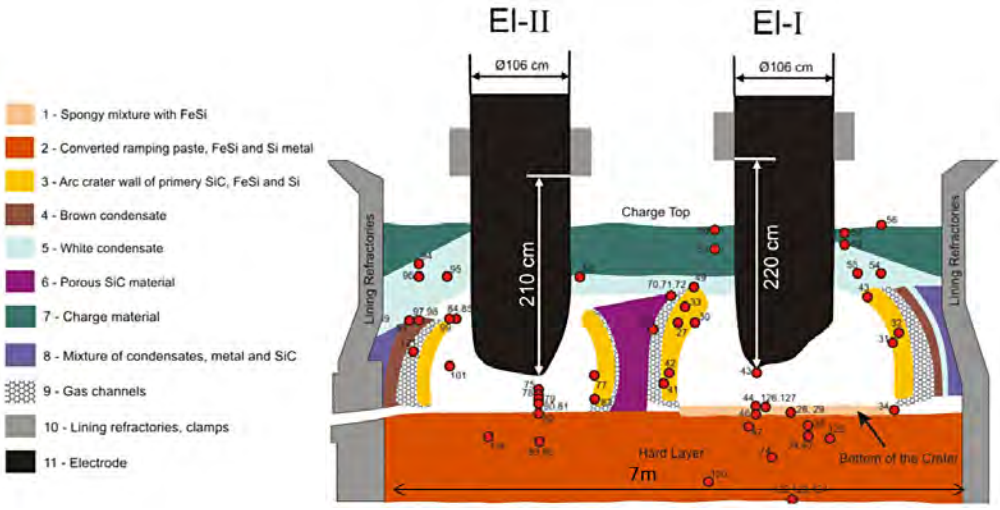


Figure 3.5 *Example of a FeSi75 furnace (same furnace, but different time, as in Figure 3.4) (Tranell et al., 2010).*

The zones found during excavations are illustrated in some examples in Figure 3.3 to Figure 3.5, where both silicon and FeSi furnaces are excavated. The zones present can differ considerably, despite the use of the same raw materials, the same product and similar furnaces. It is therefore believed that most of the zones present – and their extent and position – are due to operation over time, the raw materials, the carbon coverage, the energy density in the furnace, as well as furnace design and operational strategies. Differences between the furnaces include the position and extent of the cavity, the SiC crust and the slag present. The SiC crust and the slag will also be discussed in Chapter 8: Operational problems.

3.3 The inner structure of the reacting furnace

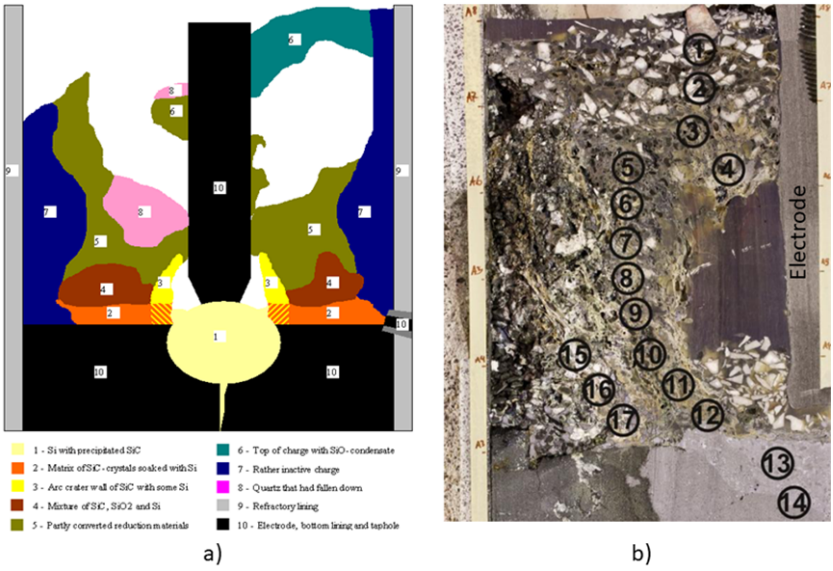


Figure 3.6 *Excavation of 150 kW pilot scale furnaces producing silicon a) (Myrhaug, 2003) b) (Vangskåsen, 2011) [With permission L.V. Myrhaug and J. Vangskåsen].*

The cavities in the furnaces can be found in two areas: around the electrode tip (also called the crater), and in the upper part of the charge, as seen in Figure 3.6a. These cavities can also be joined as one, as seen in Figure 3.6b. The top cavity has not been seen during industrial excavations, only in pilot-scale operation. As long as the industrial furnace is stoked regularly, it is believed that the higher cavities will be removed. The cavity around the electrode tip ranges from close to non-existent (Figure 3.3 and Figure 3.4) to relatively large (Figure 3.5). During excavation, materials in the lower part of the furnaces may be harder to spot and hence, a small cavity may be overlooked. Even in excavations where it was verified that no cavity was present, the materials could have descended after shutdown, or there could be no cavity during

operation (Ksiazek *et al.*, 2016). FeSi and silicon furnaces have a higher part of over-harmonics compared to coke bed processes like Mn-ferroalloy production (Barker *et al.*, 2007; Steenkamp *et al.*, 2017). This makes it probable that heating in Si/FeSi furnaces occurs with one or several arcs and hence, a cavity or cavities must be present. The point here is that the crater size can be large or very small. Another point is that the arc cannot be longer than around 10 cm with the voltages that are used in Si/FeSi furnaces. If the electrode is more than 10 cm from the silicon/FeSi layer, this means that the arcs will strike the sides of the electrode (Sævarsdottir and Bakken, 2010). As the electrode holders typically move more than 10 cm in a day, this shows that a significant part of the arcs strike horizontally from the electrode leg, as discussed in Chapter 6: Electrical operation. The cavity is formed because the charge does not descend, either due to condensates gluing the charge or due to the formation of a SiC crust.

The amount of SiC crust (α-SiC) varies. It may be totally absent (Figure 3.6b) or fill up a large part of the furnace volume (Figure 3.3c), but in most cases it will be somewhere in between. When the SiC crust is found, it is typically filled with silicon/ferrosilicon. If the arcs strike the SiC crust, which has a high electrical conductivity, the quartz meeting the SiC will be heated and react to liquid silicon. The silicon will then flow through the SiC crust and into the metal bath below the electrodes. When large SiC crusts are present, as in Figure 3.3c and Figure 3.5, gas channels are present in the crust; these may come from the SiO + SiC reaction to liquid silicon.

Slag is typically found in the inactive zones in the furnace towards the lining; however, it may also accumulate in the bottom of the furnace, forcing the electrodes up. The most reactive area is, however, around the electrodes, and the slag layers will not be discussed further here. More information about the slag in the furnace can, however, be found in Chapter 4: Additional elements in the silicon process and in Chapter 8: Operational problems.

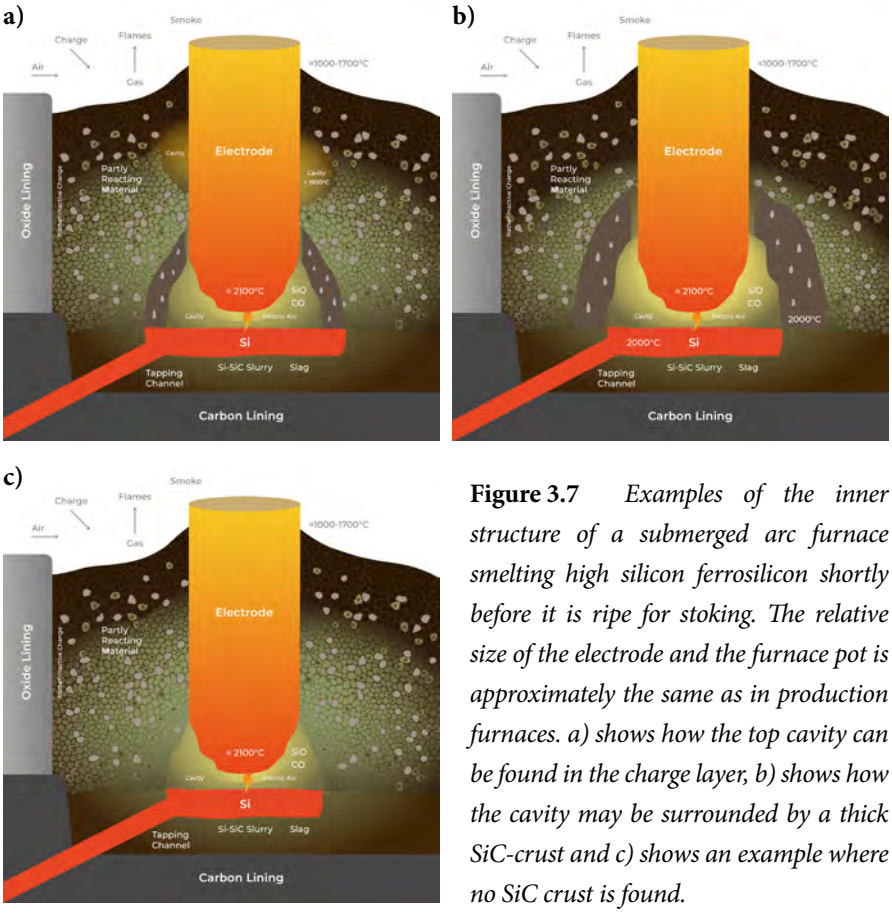


Figure 3.7 *Examples of the inner structure of a submerged arc furnace smelting high silicon ferrosilicon shortly before it is ripe for stoking. The relative size of the electrode and the furnace pot is approximately the same as in production furnaces. a) shows how the top cavity can be found in the charge layer, b) shows how the cavity may be surrounded by a thick SiC-crust and c) shows an example where no SiC crust is found.*

The experience and the observations described above provide examples of the overall picture of a working silicon furnace, as illustrated in Figure 3.7. It shows the furnace a short time before stoking. The electrode is surrounded by a gas-filled cavity. The cavity may however vary from very small to large, or it may form two separate cavities, as illustrated in Figure 3.7a. The cavities of the three electrodes are separated by charge materials in various states of conversion. The bottom of the cavity consists of a slurry of silicon and silicon carbide, possibly with an upper layer of relatively pure silicon. Higher up in the furnace, there are partly transformed charge materials: carbon particles partly converted to silicon carbide, softened or molten silica, and condensate.

The materials close to the inner area are heated enough to react, but the materials further away are rather inactive. The molten silica is highly viscous, and it may slowly flow down along the partly transformed charge (Dalaker, 2025).

The particles in the roof of the cavity are glued together so firmly that they do not descend. When the upper charge has lost the power to capture SiO from the gas, the operator breaks it down, fills in loose charge from the sides, and puts the necessary refill of new charge on the top. The transformed charge consists mainly of SiO_2 and SiC, with some Si from the condensate. These species react and produce SiO, which flows up through the new charge. The condensation reactions then heat the charge. The condensate glues the particles together to form a new thick deposit, which is consumed from below as the quartz melts and sinks down with other materials. It has been estimated that about 10% of the silicon produced may come from the condensate, as discussed in Chapter 2.

In operation with excess C in the charge, the carbon surplus will be deposited as SiC around the electrode. When the charge is corrected, the SiC can be consumed in the electrode path. At a distance away from the electrode, the SiC will be left as a wall, leaving a depression around the electrode. When the furnace is rotated, the depressions of the three electrodes will merge and result in a circular trench with walls of SiC, as seen in Figure 3.3c.

The temperature in the furnaces decreases towards the sides and below the high-temperature cavity. The tapped silicon is measured to be above 1900°C, though it loses temperature in the runner and in the ladle down to 1500–1600°C. The molten silicon is tapped through a tubular hole that reaches into the molten silicon slurry or slag from the outside. The tapping of the product can be carried out either continuously or discontinuously. Continuous tapping can go on for a long time with an even flow of silicon, without any gas jet out of the taphole. This observation shows that the taphole is not just an opening into a silicon bath, since a bath would soon be emptied down to the taphole, and then the crater pressure would send out a jet of gas. The tapping mechanism is probably that the molten silicon drains slowly through the slurry and/or the slag layer.

3.4 Reactions in the furnace

Qualitative description

This section will discuss the reactions in the furnace based on the information given above. This information is incomplete, and the reaction scheme must be treated with an open mind when more experimental material becomes available. Figure 3.7 shows the various zones of the furnace. In the hottest inner zone, the temperature of the condensed materials is around 2000°C, except for much hotter small volumes connected with the arc. The condensed species present are SiO_2, Si and SiC, with potentially some remaining free C. It is, however, rare that unreacted carbon is found in the high-temperature area at excavations. Any free C is unstable, and it will gradually change to SiC by reaction with SiO or Si.

The reaction between SiO_2 and SiC occurs in the hottest zone of the furnace, at the bottom and in the lower part of the crater. The reaction can formally be written as a combination of three reactions between condensed reactants, where Si and SiO-gas are produced:

$$2\ SiO_2(s,l) + SiC(s) = 3\ SiO(g) + CO(g) \qquad \Delta H >> 0 \qquad [3.5]$$

$$SiO_2(s,l) + Si(l) = 2\ SiO(g) \qquad \Delta H >> 0 \qquad [3.6]$$

$$SiC(s) + SiO(g) = 2\ Si(l) + CO(g) \qquad \Delta H > 0 \qquad [3.7]$$

The combined reaction can be written as

$$SiO_2(s) + x\ SiC = (2x - 1)\ Si + (2 - x)\ SiO + x\ CO \qquad [3.8]$$

The slowest part of this set of reactions is most likely the strongly endothermic production of SiO by Reactions [3.5] and [3.6]. If the reactions are too slow to consume all the heat added from the arc, the temperature will rise, and the reaction rate will rise until a balance is obtained. The silicon-producing Reaction [3.7] requires, as can be seen from Figure 2.9, a high SiO content in the gas to give silicon. The SiO needed for the reaction can be produced in the same area as the Si-producing reaction, or lower in the furnace.

The gas leaves the furnace mainly through the charge, and Si units in the gas should preferably be recovered by reactions in the charge, otherwise,

the Si units will leave the furnace. The conceivable recovering reactions are shown in Figure 2.9. When free carbon is available, the SiO can be bound by the reaction

$$SiO(g) + 2\ C(s) = SiC(s) + CO(g) \qquad [3.9]$$

which will give a resulting SiO content in the gas of less than 1 per cent at equilibrium. As the SiO loss of industrial furnaces is typically between 5–20%, the SiO pressure will be higher than 1% due to slow condensation reactions. These reactions are slow at temperatures below approximately 1500°C. When the gas passes through the cooler charge, the gas temperature drops, and the SiO becomes unstable. Observations show that the reaction

$$2\ SiO(g) = SiO_2(s,l) + Si(l) \qquad [3.10]$$

is preferred, even if the equilibrium graphs in Figure 2.9 show that the reactions

$$3\ SiO(g) + CO(g) = 2\ SiO_2(s,l) + SiC(s) \quad \text{Above 1512°C} \quad [\text{reversed } 3.5]$$

and

$$SiO(g) + CO(g) = SiO_2(s,l) + C(s) \quad \text{Below 1512°C} \quad [\text{reversed } 3.4]$$

are thermodynamically more favorable. All the Reactions [3.10], [reversed 3.4] and [reversed 3.5] are strongly heat-producing. The product of Reaction [3.10] is found in relatively thick layers of a brown condensate in places where it is easy to get rid of the heat of reaction.

Reaction [3.10] heats the fresh charge until the temperature is high enough for Reaction [3.9]. If the amount of free carbon is not sufficient to bind all the SiO, the remainder will condense according to Reaction [3.10] until the charge is heated to the condensation temperature. The remaining SiO will pass the charge and burn above it, giving the white smoke that is so characteristic of open silicon/ferrosilicon furnaces. The white smoke consists mainly of silica particles less than 0.1 μm. Though the condensation product SiO_2 + Si [3.10] is easier to find, the condensation product SiO_2 + SiC [reversed 3.5] is also found during excavations and during lab-scale experiments.

When the brown condensate of finely dispersed Si in SiO_2 is heated, the Si droplets unite into large drops that can fall from the SiO_2 in the roof above the cavity. A fraction of the condensation according to Reaction [3.3] occurs at temperatures where the silica is molten. At these temperatures, the unmixing may be almost instantaneous, and the condensation will consist of deposition of SiO_2 at the site of condensation, while the Si falls into the cavity at once. This reaction is expected to leave a deposit of silica with a minor amount of silicon.

An alternative interpretation of the role of the condensation is that the SiO_2 + Si brown mass evaporates as SiO when it flows back into the inner zone. This would give a sufficiently high content of SiO in the gas to allow production of Si. The two schemes, unmixing or evaporation, have the same overall effect on the furnace operation. However, as described in Chapter 2, it seems that most of the Si will unmix and not react with SiO_2.

The SiO-forming reactions, with consumption of Si, SiO_2 and SiC, take place mainly in the lower part of the cavity, or at the SiC crust crater walls, where the temperature is highest. The cavity increases at the top, where the materials react partially, then fall and react further closer to the bottom. Some silica can also flow along the wall of the cavity. With excess carbon, the reaction at the bottom will give an excess of silicon carbide, which over time will produce SiC crusts. With carbon deficiency, the reaction may result in complete vaporisation of all the silica.

Stoichiometric analysis of the reactions in the furnace

The qualitative description splits the furnace into two parts: an inner main reaction zone, where SiO_2 reacts with SiC and gives Si, SiO and CO, and an outer zone with low-temperature reactions. An overall understanding of the process can be obtained from a very simple model based on equilibria and mass balance restrictions on the flows into and out of the two zones. For simplicity, the energy needed to heat or cool the materials is neglected initially.

If we assume equilibrium between the phases SiO_2, SiC and Si at 1 bar in the inner zone of the furnace, we have, according to Figure 2.7 or 2.8, a ratio $p_{SiO}/p_{CO} \approx 2$. The overall reaction in the inner reaction zone is then:

$$3\ SiO_2 + 2\ SiC = Si + 4\ SiO + 2\ CO \qquad [3.11]$$

The inner reaction zone corresponds to the cavity and the inner layers of the charge in Figure 3.7.

First, we assume equilibrium also in the outer reaction zone, which corresponds to the low-temperature zone in Figure 3.7. The overall equilibrium reaction is:

$$SiO_2(s,l) + 3\ C(s) = SiC(s) + 2\ CO(g) \qquad [3.12]$$

We will balance a furnace process under these assumptions and give the result schematically in Figure 3.8. We need 3 SiO_2 and 2 SiC for the reaction in the inner zone. Addition of 2 SiO_2 + 6 C to the outer zone produces the 2 SiC. To consume the 2 SiC in the inner zone, we need 3 SiO_2, which can be added through the outer zone. The gas from the inner zone will normally pass through the outer zone, but since it could react with C, it is assumed to bypass the outer zone in the schematic representation. The process gives, as a product, 1 Si from 5 SiO_2, which means that the silicon recovery is only 20%.

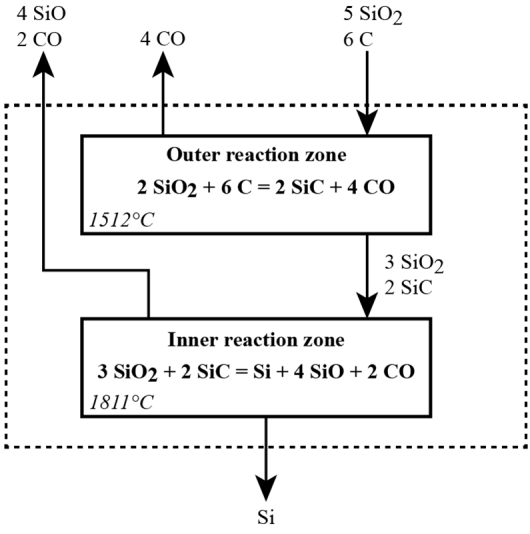


Figure 3.8 *Schematic presentation of the furnace reactions for full equilibrium in the inner and outer zones. The necessary heating or cooling of the mass flowing between the zones is ignored.*

Silicon recovery can be improved if SiO from the inner zone is captured by reaction with C in the upper part of the charge. This option is illustrated in Figure 3.9. In the scheme, SiO_2 is added directly to the inner zone to avoid the direct reaction between SiO_2 and C. In a real furnace, the low rate of the reaction between SiO_2 and C effectively blocks this reaction, as indicated in Chapter 2. As above, the inner zone needs 3 SiO_2 and 2 SiC. The 2 SiC are formed when SiO in the gas from the inner zone passes through the outer zone and consumes 4 C. Excess SiO is lost in the gas from the furnace. The process gives 1 Si from 3 SiO_2, that is, the silicon recovery has increased to 33 per cent.

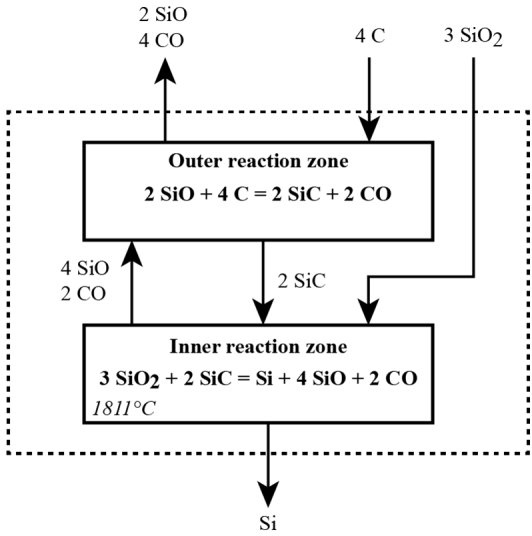


Figure 3.9 *Schematic presentation of the furnace reactions for equilibrium in the inner reaction zone while the reaction between SiO_2 and C is blocked in the outer zone. The temperature in the outer zone is assumed to be high enough to prevent any condensation of SiO in the gas. The necessary heating or cooling of the mass flowing between the zones is ignored.*

This silicon recovery is the highest that can be obtained if the reaction is carried out at equilibrium. In practical operation, 80–90 per cent silicon recovery is common, and close to 100 per cent can be obtained with favorable raw materials. The reason for this difference between experience and calculated results can be:

- Inaccurate thermochemical data
- The process is not running at equilibrium.

As discussed in Chapter 2, direct thermobalance measurements of the vapour pressure of the system SiO_2 + SiC + Si indicate that the calculated total pressure is fairly accurate. Therefore, the most probable reason for the difference is a deviation from equilibrium. Two non-equilibrium processes are likely to be important:

- A low reaction rate in the inner zone gives a favorable reaction temperature.
- The cavity gas is cooled as it passes through the outer reaction zone, and Si-containing species condense.

Heat is added to the furnace, and, if the combined rate of the strongly endothermic Reactions [3.6] and [3.7] is too low to consume the heat, the temperature will rise. As can be seen from the equilibrium diagram in Figure 2.8, the production of free silicon requires a lower SiO content in the gas the higher the temperature. This effect will be expressed by a parameter *s*, defined as

$$s = \frac{p_{SiO}}{p_{SiO} + p_{CO}} \qquad [3.13]$$

where the gas pressures apply to the inner reaction zone. The parameter *s* is assumed to be constant for given operating conditions. The value of *s* can be estimated from Figure 2.8, where, as an approximation, *s* can be set equal to the equilibrium gas ratio [3.11] for the Si-producing Reaction [3.5]. For complete equilibrium at 1811°C, it is 0.67. For *s* = 0.5, the temperature must be about 1980°C, and the inner-zone reaction becomes

$$SiO_2 + SiC = Si + SiO + CO \qquad [3.14]$$

For *s* = 0.5, the free C available in the charge is sufficient to bind all the SiO from the inner reaction zone, and a hundred per cent recovery is possible, as shown in Figure 3.10.

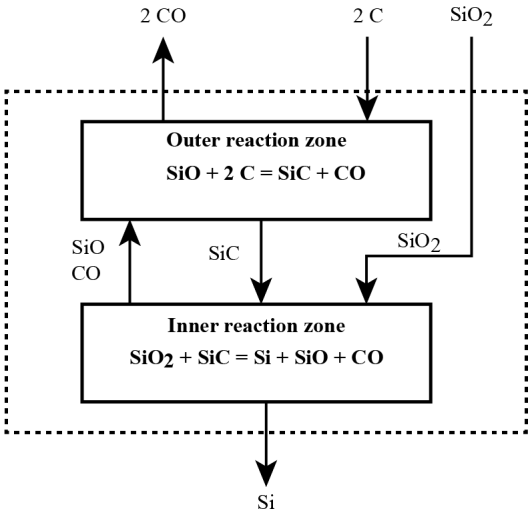


Figure 3.10 *Schematic presentation of the furnace for s = 0.50. This is the highest value of s that allows 100 per cent silicon recovery. The temperature in the outer zone is assumed to be high enough to prevent any condensation of SiO in the gas.*

In Figure 3.10 it was assumed that all the free C was converted to SiC by reaction with SiO in the outer reaction zone. However, it is known that this reaction often is incomplete. Lumps of carbon material react with the SiO in the gas and become covered with a layer of SiC. As this layer becomes thicker, the reaction slows down, and the lumps often retain a core of free carbon when they move into the inner zone. This transport of carbon into the inner reaction zone will influence the reaction. It can be characterized by a parameter *r*. We consider a quantity of charge with totally *c* moles of carbon, where c_r moles of carbon react with SiO according to Reaction [3.9].

$$r = \frac{C_r}{C} \qquad [3.15]$$

The parameter *r* can be considered a measure of the reactivity of the carbon material. The effect of low *r* is shown in Figure 3.11. Here the ratio *s* is 0.5, as in Figure 3.10 in the inner zone, but only two thirds of the free C react with SiO in the outer zone. Then *r* = 0.67, and the silicon recovery drops from 100 per cent in Figure 3.10 to 50 per cent in Figure 3.11. This example shows

that the recovery drops strongly if the reaction with C is incomplete in the outer reaction zone.

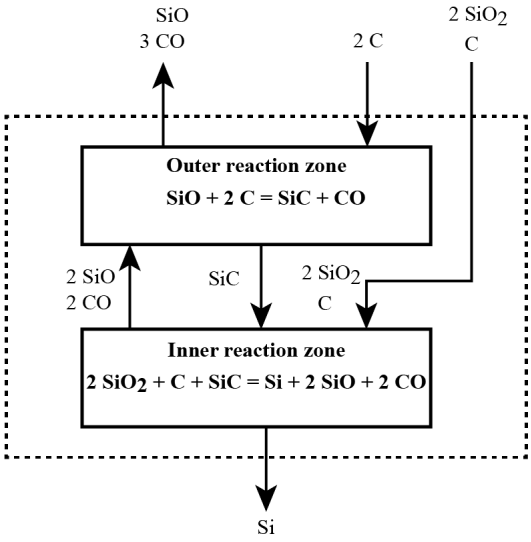


Figure 3.11 *Schematic presentation of the furnace reactions with s = 0.50 and r = 0.67. The temperature in the outer zone is assumed to be high enough to prevent any condensation of SiO in the gas.*

So far, the temperatures in the reaction zones have been assumed to be suitable for the expected reactions. In the furnace, however, heat is added mainly to the inner zone. In a furnace corresponding to the scheme of Figure 3.11, the raw materials are added cold to the outer reaction zone, where they are heated by the hot gas and by reactions. The heat capacity of the charge can absorb the heat of reaction for the SiO-catching condensation Reaction [reversed 3.6]. An estimation for a simplified situation, listed in Table 3.2, will indicate the order of magnitude of this effect. Here, the SiO_2 is added in the outer reaction zone, but the direct reaction between SiO_2 and C can be ignored, since the rate is low. It is seen that the energy in the SiO and CO gas from the high temperature zone, plus the exothermic reactions, is enough to heat the solid materials to close to 1700°C.

Table 3.2 *An example of estimation of the extent of condensation in a simplified version of the silicon process with data from HSC 9.0.*

Input species into the condensation zone				
	Temperature	**Amount**	**Heat content**	**Total H**
	°C	kmol	kJ	kJ
SiO(g)	1980	1.16	81	−39
CO(g)	1980	1	66	−45
SiO_2	25	1	0	−911
C	25	2	0	0
				−994
Output species out of the condensation zone				
	Temperature	**Amount**	**Heat content**	**Total H**
	°C	kmol	kJ	kJ
SiO_2	1700	1.08	127	−856
SiC	1700	1	78	6
CO(g)	1000	2	62	−159
Si	1700	0.08	8	8
				−1002

The estimate in Table 3.2 gives only an indication of the extent of condensation because the completeness of the reactions in the outer zone is uncertain. Heat loss during the operation is not included in the calculation. We include the calculated condensation in the overall reaction of Figure 3.11, which has the largest *s* value that can give 100 per cent silicon recovery without condensation. The results in Figure 3.12 show that *s* can be increased to about 0.54 while the silicon recovery is still 100 per cent when the condensation is included.

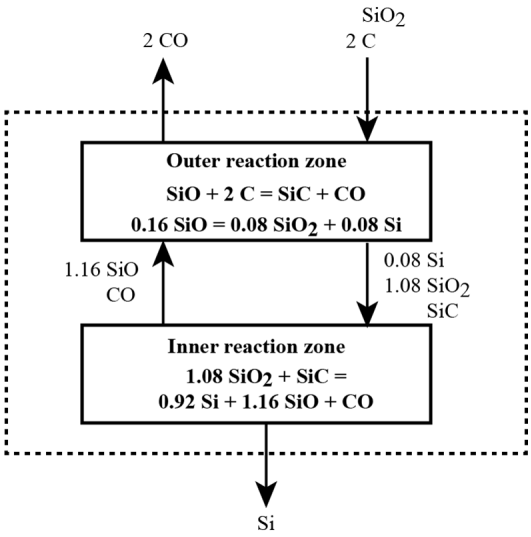


Figure 3.12 *Schematic presentation of the furnace reactions with s = 0.537 and r = 1.00. Condensation according to 2SiO = SiO_2 + Si runs to the extent estimated in Table 3.2.*

The condensation reaction

$$2\ SiO = SiO_2 + Si \qquad \text{[reversed 3.6]}$$

has been assumed in the discussion above. However, both condensation reactions [the reversed reactions 3.5 and 3.6] will occur in the furnaces as described in Chapter 2, and they will have the same effect in capturing SiO gas.

$$3\ SiO + CO = 2\ SiO_2 + SiC \qquad \text{Preferred above 1512°C} \qquad \text{[reversed 3.5]}$$

3.5 Critical reactions in the carbothermic process of silicon

The furnace observations and the discussion of the reaction models lead to the following conclusions:

- SiO_2 and SiC react in the inner hottest zone of the furnace and produce Si only if the SiO content of the gas is sufficiently high.
- CO from the inner zone must leave the furnace, and it necessarily carries a high content of SiO. This SiO must be recovered in the outer zone if the silicon recovery is to be high.
- The reaction between free C and SiO can capture the SiO in the outer zone and bring it back to the inner zone with the charge.
- The amount of SiO to capture depends on the content *s* of SiO in the inner zone.
- At equilibrium, the value of *s* in the inner zone is so high that the available free C is not enough to capture all the SiO.
- If *s* is decreased, for example by raising the temperature, the silicon recovery in the process increases.
- The silicon recovery decreases with an increasing C fraction that does not react in the outer zone.
- Condensation of SiO as [SiO_2 + Si] in the outer reaction zone can increase the silicon recovery.
- The amount of SiO that can be captured by condensation is limited, because the heat of condensation can raise the temperature of the outer zone to the temperature of condensation.

References

Acheson, E.G. (1911) 'Researches on electric furnace products', *Transactions of the Faraday Society*, 7, pp. 217–220.

Folstad, M.B. (2023) *Slag and its effect on Si and FeSi production*. Doctoral thesis 2023:317. Norwegian University of Science and Technology (NTNU), Trondheim, Norway. Available at: https://hdl.handle.net/11250/3096091

Hoover, H., Andersen, V., Sævarsdóttir, G. and Tangstad, M. (2022) 'Excavation of 160 kW pilot scale Si furnace', *AMMS*, 9. Available at: https://doi.org/10.31031/AMMS.2022.09.000707

Inside the ferrosilicon furnace (1979). Property of Elkem Research.

Jusnes, K.F. (2020) *Phase transformation and thermal degradation in industrial quartz*. Doctoral thesis 2020:205. Norwegian University of Science and Technology (NTNU), Trondheim, Norway. Available at: https://hdl.handle.net/11250/2675473

Kamfjord, N.E. (2012) *Mass and energy balances of the silicon process*. Doctoral thesis 2012:162. Norwegian University of Science and Technology (NTNU), Trondheim, Norway. Available at: https://hdl.handle.net/11250/249043

Ksiazek, M., Saadieh, R., Gærtner, H., Grådahl, S., Sægrov, B., Tangstad, M., Valderhaug, A. and Ringdalen, E. (2021) 'Industrial measurements of the gas and temperature in Si and FeSi production process', in *Proceedings of INFACON XVI*. Trondheim, Norway. Available at: https://doi.org/10.2139/ssrn.3922198

Ksiazek, M., Tangstad, M. and Ringdalen, E. (2018) 'The rapid Si-furnace excavation – an unique chance to investigate the interior of the furnace', in *Proceedings of INFACON XV*. Cape Town, South Africa.

Ksiazek, M., Tangstad, M. and Ringdalen, E. (2016) 'Five furnaces, five different stories', in *Proceedings of Silicon for the Chemical and Solar Industry XIII*. Kristiansand, Norway, pp. 33–42.

Ksiazek, M., Tangstad, M. and Ringdalen, E. (2015) 'Silicon production in laboratory scale induction furnace', in *Innovative Metallurgical Technologies and Processes: Ferroalloys*. Presented at the International Conference Advances in Metallurgical Process and Materials (AdMet), Kiev, Ukraine.

Moissan, H. (1895) 'Reduction of silica with carbon', *Soc. Chim. France*, 13, pp. 972–973.

Müller, M.B. (1972) 'Heat and mass balance for a FeSi furnace', *Scandinavian Journal of Metallurgy*, 1, pp. 145–155.

Myrhaug, E.H. (2003) *Non-fossil reduction materials in the silicon process – properties and behaviour*. Doctoral thesis 2003:67. Norwegian University of Science and Technology (NTNU), Trondheim, Norway.

Otani, Y., Saito, M., Usui, K. and Chino, N. (1968) 'The inner structure in submerged arc furnaces', in *VIth International Congress of Electroheat*. Brighton, pp. 1–7.

Pick, W. (1906) *Über Ferrosilicium*. Dissertation, Technischen Hochschule 'Fridericiana' zu Karlsruhe.

Ringdalen, E., Bao, S. and Tveit, H. (2020) 'Effect of melting properties of quartz in industrial Si and FeSi production', in *Proceedings of Silicon for the Chemical and Solar Industry XV*. Trondheim, Norway.

Ringdalen, E. and Tangstad, M. (2012) 'Reaction mechanisms in carbothermic production of silicon, study of selected reactions', in Downey, J.P., Battle, T.P. and White, J.F. (eds) *International Smelting Technology Symposium*. Hoboken, NJ, USA: John Wiley & Sons, Inc., pp. 195–203. Available at: https://doi.org/10.1002/9781118364765.ch24

Saadieh, R., Tangstad, M. and Wegge, H. (2018) 'Simulation of the ferrosilicon process using small-scale laboratory furnace', in *Proceedings of INFACON XV*. Cape Town, South Africa.

Schei, A. (1967) 'On the chemistry of ferrosilicon production', *Kjemi*, pp. 152–158.

Schei, A. and Larsen, K. (1982) 'A stochiometric model of the ferrosilicon process', *Electric Furnace Conference Proceedings*, 39, pp. 301–309.

Schei, A. and Sandberg, O. (1966) *Back reactions during production of silicon metal in a submerged arc electric furnace*. Scandinavian University Books. Oslo: Universitetsforlaget.

Tangstad, M., Ksiazek, M., Andersen, V. and Ringdalen, E. (2010) 'Small scale laboratory experiments simulating an industrial silicon furnace', in *Proceedings of INFACON XII*. Helsinki, Finland. Available at: https://www.pyrometallurgy.co.za/InfaconXII/661-Tangstad.pdf

Tangstad, M., Ksiazek, M. and Faaness, B. (2014) 'Zones and materials in the Si furnace', in *Proceedings of Silicon for the Chemical and Solar Industry XII*. Trondheim, Norway, pp. 24–27.

Tone, F.J. (1931) 'High-temperature products of silicon', *Industrial & Engineering Chemistry*, 23, pp. 1312–1316.

Tone, F.J. (1909) *Method of reducing metallic compounds*. US Patent 937,120.

Tranell, G., Andersson, M., Ringdalen, E., Ostrovski, O. and Steinmo, J.J. (2010) 'Reaction zones in a FeSi75 furnace – results from an industrial excavation', in *Proceedings of INFACON XII*. Helsinki, Finland, pp. 709–716. Available at: https://www.pyrometallurgy.co.za/InfaconXII/709-Tranell.pdf

Vangskåsen, J. (2011) *Investigation of the cavity formation in the silicon process*. Student report. Norwegian University of Science and Technology (NTNU), Trondheim, Norway.

Zherdev, I.T., Davats, V.N. and Polyakov, I.I. (1960) 'Investigation of the structure of the working space in ferrosilicon furnaces', *Izv. VUZ, Chern. Met.*, pp. 173–181.

Zherdev, I.T., Dekhanov, N.M., Volkhov, V.T., Davats, V.N. and Polyakov, I.I. (1962a) 'The structure of the bath in furnaces producing 45 per cent ferrosilicon', *Izv. VUZ, Chern. Met.*, pp. 77–87.

Zherdev, I.T., Moskovtsev, D.P. and Yaskov, E.S. (1965) 'The size of the gassfilled cavity in ferrosilisium furnaces', *Stal'*, 8, pp. 835–836.

Zherdev, I.T., Polyakov, I.I., Davats, V.N. and Moskovtsev, D.P. (1962b) 'Special properties of the structure of the bath in rotating ferrosilicon furnaces', *Izv. VUZ, Chern. Met.*, pp. 61–66.

Zherdev, I.T., Polyakov, I.I., Moskovtsev, D.P. and Yaskov, E.S. (1968a) 'Methods and results from investigations of the operation of ferrosilicon furnaces', Paper No. 113, in *Proceedings of the VIth International Congress of Electroheat*. Brighton, UK.

Zherdev, I.T., Polyakov, I.I., Semenov, V.E., Barashkin, I.I., Moskovtsev, D.P. and Yaskov, E.S. (1968b) 'Critical rate of rotation for ferrosilicon furnace bath', *Stal*, pp. 406–408.

Tangstad, M., Tranell, G. og Tang, K. (2026) 'Additional elements in the silicon process', in M. Tangstad, G. Tranell, H. Tveit and E. Ringdalen (Eds.), *Production of high silicon alloys* (2. ed.) (pp. 109–165). Fagbokforlaget. https://doi.org/10.55669/oa880804

4

Additional elements in the silicon process

Merete Tangstad, Gabriella Tranell and Kai Tang

Besides Si, O and C, which were already considered in Chapter 2, additional elements in small quantities will always enter the process as impurities originating from the raw materials and electrodes, as seen in Table 4.1. The main impurity elements by mass are Ti, Ca, Al, Mg, K and S. From an emission point of view, nitrogen in the atmosphere produces NO_x, however, this will be discussed in more detail in Chapter 12. Some elements may also be added deliberately to the charge mixture to make silicon-rich alloys of a desired composition. Of special importance is, of course, iron, added as scrap, mill scale and/or ore to produce ferrosilicon. This chapter focuses on the behavior of minor elements and their effect on the chemistry of the Si–O–C system. In this context, important properties include the relative stability of oxides and carbides of the elements involved, the volatility of these elements and their compounds, and their dissolution in the phases present.

4.1 Liquid silicon as solvent for impurities and alloying metals

Phase diagrams and activities

In its crystalline state, silicon has practically no solubility for metals. However, it forms stable silicides with most metals, except for its neighbours in the periodic table where Al, Ga and Ge are the most apparent examples. In its liquid state, by contrast, silicon forms continuous solutions with most metals.

This work is licensed under the Creative Commons Attribution 4.0 International License.
To view a copy of this license, visit https://creativecommons.org/licenses/by/4.0/

The occurrence of stable silicides in the solid state indicates strong attractions between solute and solvent atoms in the liquid state as well. Thus, an exothermic heat of mixing and a strong negative deviation from ideal behavior are expected for solutions of silicon and silicide-forming metals. Figure 4.1 shows the activity relations in the iron-silicon system and provides a typical example.

Table 4.1 *Elements in raw materials and electrode after Myrhaug (2003). Both % and ppm are given by weight.*

Parametr	Unit	Quartz	Coal	Coke	Charcoal	Wood chips	Petrolcoke	Electrode
Fixed carbon	%	—	39–62	81–95	75–85	20–26	88–93	85–99
Volatiles	%	—	34–58	2–5	10–25	70–75	7–12	1–10
Ash	%	—	1–5	1–10	0.5–10	1–10	0.05–1	0.1–5
Si	%	46.1–46.6	0.3–2	0.6–4	0.05–9	0.2–1	—[1]	—[1]
C	%	~0	71–81	84–96	81–91	45–50	94–97	91–97
O	%	53.1–53.6	10–16	1–7	2–15	40–45	2–3	2–8
H	%	~0	5–8	0.5–4	1–8	5–6	1–1.5	0.2–1.3
N	%	~0	1.5–2.5	0.1–0.2	0.3–1.0	0.1	0.2–0.5	0.05–0.5
Hg	ppbw	< 5–10	< 5–60	< 5–20	< 5	< 5	< 5	< 5–40
Ti	ppmw	20–200	50–600	60–4000	10–300	≈1	< 0.5–50	~100
Al	ppmw	300–3200	800–5700	1000–10000	100–6200	< 50–100	70–110	< 50–4000
As	ppmw	< 1–3	< 1–3	< 1–14	< 1	< 1–5	< 1–10	< 1–10
B	ppmw	< 10–45	< 10–110	< 10–100	< 10–16	< 10–23	< 10	< 10
Ba	ppmw	0.5–25	4–130	15–220	10–30	2–70	1–9	6–90
Be	ppmw	< 0.5–0.6	< 0.5–4	< 0.5–3	< 0.5	< 0.5	< 0.5	< 0.5
Bi	ppmw	< 0.5	< 0.5	< 0.5	< 0.5	< 0.5	< 0.5	< 0.5–2
Ca	ppmw	< 75–160	150–2400	600–3400	1000–4000	600–1000	< 75	200–1500
Cd	ppmw	< 0.1–1.5	< 0.1–1.1	< 0.1–1.1	< 0.1	< 0.1–0.3	< 0.1	0.6–1.2
Co	ppmw	< 1–200	1–16	6–120	< 1	< 1	< 1–13	< 1–13
Cr	ppmw	3–25	< 1–12	15–40	5–15	< 1–13	1.5–12	< 1–24
Cu	ppmw	1–3	1.5–22	4–40	2–7	1.8–4.3	< 1–6	< 1–20
Fe	ppmw	100–1500	700–5200	1400–9000	100–1700	< 100–1400	< 100–600	100–3500
K	ppmw	< 75–1700	< 75–1800	300–1800	100–1800	250–900	< 75	< 75–210
Mg	ppmw	20–140	80–1100	300–1400	200–1100	75–200	< 15–100	< 15–500
Mn	ppmw	3–600	4–110	< 1–270	80–120	10–50	1–6	50–3500

Para-metr	Unit	Quartz	Coal	Coke	Charcoal	Wood chips	Petrol-coke	Electrode
Mo	ppmw	< 2–8	< 2–4	< 2–7	< 2	< 2	< 2–12	< 2
Na	ppmw	50–170	< 320	230–2100	170–230	< 50–130	< 50–110	< 50–300
Ni	ppmw	< 1–9	2–33	3–240	~30	< 1–7	60–360	< 1–50
P	ppmw	< 5–50	< 5–143	16–160	80–300	20–110	< 5–13	< 5–170
Pb	ppmw	< 0.1–9	0.3–13	1–106	< 0.1–2.3	< 0.1–0.2	< 0.1–3.5	< 0.1–1.6
S	ppmw	< 5–1400	1200–8300	3300–11000	200–1500	100–1300	20000–50000	55–3400
Sb	ppmw	< 0.1–0.9	< 0.1–0.7	0.3–3.9	< 0.1	< 0.1	< 0.1	< 0.1–1.4
Se	ppmw	< 2–5.2	< 2–6.6	< 2–3.3	< 2	< 2	< 2	< 2
Sn	ppmw	< 0.5–2.2	< 0.5–2.7	< 0.5–3	< 0.5	< 0.5–4.5	1.1–2.4	< 0.5–2.4
Sr	ppmw	< 0.5–12	3–90	11–80	14–80	1.6–9	< 0.5–6.6	1.4–20
V	ppmw	< 1–4	2–60	4–30	< 1	< 1	400–1200	< 1–92
W	ppmw	< 0.5–640	< 0.5–3	< 0.5	< 0.5	< 0.5	< 0.5	< 0.5–0.8
Zn	ppmw	< 1–3	3–40	4–80	2–40	6–16	3–10	1–100
Zr	ppmw	< 0.5–3.3	0.8–3.3	< 0.5–1.5	< 0.5	< 0.5–1	< 0.5	< 0.5–1.7

The activity of element *i*, a_i, is expressed as a function of the mole fraction of *i*, X_i, in the liquid phase:

$$a_i = \gamma_i \cdot X_i \qquad [4.1]$$

An ideal solution is a solution in which the activities of the constituents are equal to their mole fractions:

$$a_i = X_i \text{ (Raoult's law)}$$

Real solutions deviate from ideal behavior. As expressed above, this deviation is described by introducing the activity coefficient, γ_i, which is a function of composition and temperature.

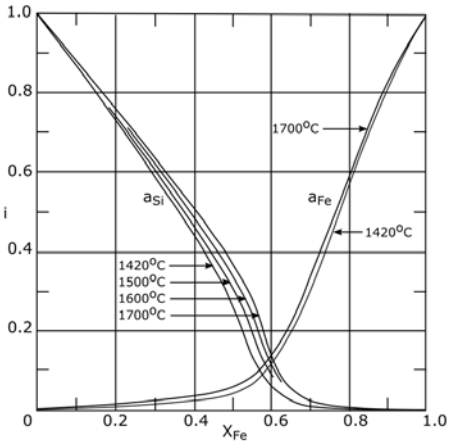


Figure 4.1 *Activities in the Fe–Si system after Elliot (Elliot et al., 1963; Saadieh, 2024).*

Negative deviation from ideal behavior as is the case for iron in silicon, implies that $\gamma_{Fe} < 1$. As seen from Figure 4.1, γ_{Fe} decreases with X_{Fe} and approaches a finite and non-zero value which takes a value equal to the slope of the activity curve at $X_{Fe} = 0$. Experiments have shown that this applies to metallic solutions in general and can be expressed as follows:

$$\gamma^0_{Me} = \left(\gamma_{Me}\right)_{X_{Me}=0} = \left(\frac{a_{Me}}{X_{Me}}\right)_{X_{Me}=0} = \left(\frac{da_{Me}}{dx_{Me}}\right)_{X_{Me}=0} \neq 0 \qquad [4.2]$$

The activity coefficient at infinite dilution is thus a property of the system. It varies with temperature, as determined by the relative partial heat of mixing for component Me at infinite dilution, by the relation:

$$\left(\frac{\partial ln\gamma^0_{Me}}{\partial\left(\frac{1}{T}\right)}\right)_P = \frac{\Delta\bar{H}^0_{Me}}{R} \qquad [4.3]$$

As $\ln \gamma^0_{Me}$ and $\Delta\bar{H}^0_{Me}$ are both negative for exothermic solutions, the γ^0_{Me}-value increases with rising temperature, which means that the system approaches ideality at high temperatures.

It follows from the definition of that the activity of a solute at infinite dilution can be expressed by

$$a_{Me} = \gamma^0_{Me} X_{Me} \quad [4.4]$$

It follows from the Gibbs-Duhem equation that, if Henry's law applies for the solute, Raoult's law applies for the solvent. It can further be shown that Raoult's law is obeyed more closely for the solvent than Henry's law is for the solute. This strengthens the statement already made: the presence of impurities has no significant effect on the activity of the solvent, irrespective of whether this happens to be silicon metal or a silicon-rich alloy.

The impurities in the silicon appear as members of a multicomponent system, where they interact not only with silicon but also with themselves and with each other. At low concentrations, however, the latter two effects are often neglected. Thus, the γ^0_{Me} remains as the main property to use in calculations based on the following equation

$$ln\gamma_i = ln\gamma_i^0 + \sum_{j=2}^{k} \varepsilon_i^j x_j \quad [4.5]$$

This property is provided for several elements in a compilation of thermochemical data on liquid silicon alloys by Engh *et al.* (2021). Thermochemical data for a smaller group of elements are shown in Table 4.2. γ_i^0 is the activity coefficient (at infinite dilution) if there is no interaction between the solute components. To determine how, for example, Al affects the activity of Ca in liquid silicon, one would need the interaction coefficient of Al on Ca, i.e. ε_{Ca}^{Al}. The interaction coefficients in liquid silicon for some elements are shown in Table 4.3 and Table 4.4. It can also be noted that $\varepsilon_j^i = \varepsilon_i^j$.

Often, it is more convenient to use the mass per cent, [%i], instead of the mole fraction, X_i, and the activity of an element can then be expressed as:

$$a_{i=} f_i \cdot [\%i] \quad [4.6]$$

In this case, the interaction coefficient ε_i^j is defined by the equation:

$$log_{10} f_i = \sum_{j=2}^{n} \varepsilon_i^j [\%j] \quad [4.7]$$

Note that in equation [4.5] and [4.7], component number 1 is the solvent.

Table 4.2 *Thermodynamics of binary silicon-based alloys.*

Solution Reaction	γ_i° (1700 K)	ΔG^o for *X* (J/mole)	ε_i^j	ΔG^o for wt. % (J/mole)	e_i^j	Data Source (Ref.)
Al (l) = Al	0.32	−9790 − 3.740T	2.3	−9790 − 41.694T	0.010	a (note 2)
B (s) = B	3.9	2400 + 9.894T	--	2400 − 20.456T	--	c, d, e
C (s) = C	99.4	63.785 + 0.715T	--	63.785 − 30.510T	--	f, g, h, i
Ca (l) = Ca	1.7×10^{-4}	−118.900 − 2.078T	9.9	−118.900 − 43.322T	0.045	d, j
Cr (l) = Cr	6.1×10^{-3}	−72.000	−3.2	−72.000 − 43.408T	−0.010	f
Cr (s) = Cr	8.2×10^{-3}	−51.500 − 9.623T	−3.2	−51.500 − 53.031T	−0.010	f
Fe (l) = Fe	0.024	−107.530 + 32.175T	−13.9	−107.530 − 11.827T	−0.056	f
Fe (s) = Fe	0.025	−92.340 + 23.765T	−13.9	−92.340 − 20.237T	−0.056	f
$1/2H_2(v) = H$	--	102.080 + 9.764T	--	102.080 − 0.86T	--	f
Mg (l) = Mg	0.272	−73.850 + 32.612T	2.6	−73.850 − 4.473T	0.011	a, k-l (note 2)
Mg (v) = Mg	2.3	−202.350 + 125.99T	2.6	−202.350 + 88.908T	0.011	a, k-l (note 2)
Mn (l) = Mn	0.022	−78.000 + 13.968T	8.1	−78.000 − 29.898T	0.039	f, g
$1/2\ N_2(v) = N$	--	−17.570 + 60.766T	--	−17.570 + 28.23T	--	m, n
$1/2\ O_2 = O$	--	−290.700 + 75.287T	--	−290.700 + 41.678T	--	f, o, p
$1/2P_2(v) = P$	--	−99.500 + 68.561T	3.0	−99.500 + 29.46T	0.013	d, q, r
Zn(l) = Zn	1.44	29.200 − 14.13T	--	29.200 − 59.442T	--	a

Notes: ***T*** **is in degrees Kelvin.**

1. **The liquid phase is metastable for the elements Cr, Fe, Mg at a temperature of 1700K. For example, iron is solid at this temperature.**
2. **Heat of solution and interaction coefficients were calculated from eq. [9] of a).**

Data source: a) (Safarian *et al.*, 2012) b) (Robinson and Tarby, 1971) c) (Mostafa and Medraj, 2017) d) (Sigworth, 2020) e) (Zaitsev and Kodentsov, 2001) f) (Bakke and Klevan, 1995) g) (Yoshikawa *et al.*, 2010) h) (Dalaker and Tangstad, 2009a) i) (Nozaki *et al.*, 1970) j) (Miki, 1999) k) (Eldridge *et al.*, 1967) l) (Rao and Belton, 1981) m) (Dalaker and Tangstad, 2009b) n) (Stull and Prophet, 1971) o) (O'Mara, 1990) p) (Carlberg, 1986) q) (Liang and Schmid-Fetzer, 2014) r) (A. I. Zaitsev *et al.*, 2001) s) (Miki *et al.*, 1997)

Table 4.3 *Interaction coefficients in liquid silicon.*

Mole ratio	Weight percent	Temperature (K)	Source
$\varepsilon_{Pb}^{Al} = 2.34$	$e_{Pb}^{Al} = 0.011$	1723	a
$\varepsilon_{Pb}^{Ca} = -9.0$	$e_{Pb}^{Ca} = -0.026$	1723	a
$\varepsilon_{Pb}^{Mg} = 10.2$	$e_{Pb}^{Mg} = 0.051$	1723	a
$\varepsilon_{Ca}^{Al} = 6.46$	$e_{Ca}^{Al} = 0.030$	1723	a
$\varepsilon_{Ti}^{Ca} = 25.3$	$e_{Ti}^{Ca} = 0.078$	1723	a
$\varepsilon_{Fe}^{Ca} = 2.25$	$e_{Fe}^{Ca} = 0.008$	1723	a
$\varepsilon_{Fe}^{Mn} = (99)$	$e_{Fe}^{Mn} = (0.22)$	1700	b
$\varepsilon_{Mn}^{Fe} = (99)$	$e_{Mn}^{Fe} = (0.22)$	1700	b
$\varepsilon_{P}^{Fe} = 7.43$	$e_{P}^{Fe} = 0.018$	1723	c
$\varepsilon_{P}^{Mn} = 12.0$	$e_{P}^{Mn} = 0.029$	1723	c

Data source: a) (Miki, 1999) b) (Bakke and Klevan, 1995) c) (Wagner, 1952)

Table 4.4 *Interaction coefficients in liquid Si–C–i[43], Si–O–i[22] and Si–H–i[22] alloys.*

At temperatures near the melting point of silicon						
element, i	ε_C^i	e_C^i	ε_O^i	e_O^i	ε_H^i	e_H^i
Al	−0.72	−0.004	−118	−0.56	--	--
B	−4.02	−0.052	−2.04	−0.03	--	--
C	--	--	0	−0.006	--	--
Ca	5.46	0.018	< 0	< 0.0013	--	--
Co	--	--	--	--	4.5	0.012
Cr	10.72	0.027	--	--	--	--
Fe	3.50	0.010	−6	−0.011	3.5	0.010
H	--	--	--	--	--	--
Mn	−1.58	−0.001	--	--	1.4	0.005
N	0.55	0.000	--	--	--	--
Ni	2.28	0.007	--	--	--	--
O	18.5	0.138	--	--	--	--
P	−5.67	−0.022	−45	−0.177	--	--
Zn	−3.39	−0.004	--	--	--	--

Phase diagrams, which are important for the solidification process, will be shown in Chapter 11.

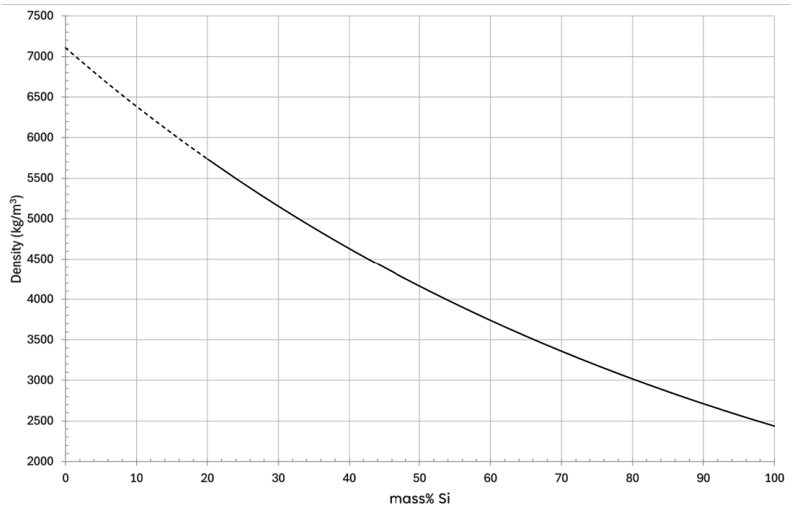


Figure 4.2 *Density of liquid Fe–Si-alloys at 1450°C, reproduced from Klevan (Dumay and Cramb, 1995; Klevan, 1997; Yaws et al., 1981), showing the correlation ρ(FeS, 1450°C) = 7106 · exp(−0.0107 · mass% Si) valid for mass% Si > 16.3%.*

Density

Density data were evaluated by Klevan (1997), who presented the diagram in Figure 4.2. This diagram is based on the work of Dumay and Cramb (1995) on Fe–Si alloys and Yaws *et al.* (1981) on liquid Si. The temperature dependence of the density of liquid silicon, as derived by Klevan, can be expressed by:

$$\rho\left(Si\right)_{liq} = 2533 - 0.45\left(T - T_m\right)\left[\text{kg/m}^3\right] \qquad [4.8]$$

Which gives

$$\rho\left(Si\right)_{liq} = 2510 \text{ kg/m}^3 \text{ at } 1450°\text{C and } 2470 \text{ kg/m}^3 \text{ at } 1550°\text{C}$$

The corresponding values for liquid FeSi75, calculated from Figure 4.2 and assuming the same temperature dependency as for silicon, are:

$$\rho\left(FeSi75\right)_{liq} = 3190 \text{ kg/m}^3 \text{ at } 1450°\text{C and } 3140 \text{ kg/m}^3 \text{ at } 1550°\text{C}$$

An interesting property to consider is the density of α-SiC. Klevan (1997) gives the following relation for this compound:

$$\rho\left(\alpha - SiC\right) = 3211 - 0.056\ T\ °\text{C}\left[\text{kg/m}^3\right] \qquad [4.9]$$

Which gives

$$\rho\left(\alpha - SiC\right) = 3125 \text{ kg/m}^3 \text{ at } 1550°\text{C}$$

It was previously believed that α-SiC was found in the refining slag, however, later investigations showed that this is β-SiC.

4.2 Silica as solvent for impurity oxides

The oxide phase is one of the main phases in silicon and ferrosilicon production because it is the main raw material. It is therefore important for process operation and will be present in all parts of the furnace. Although the carbothermic process for producing silicon and ferrosilicon is theoretically defined as a slag-free process, slag is still formed and regularly tapped along with the metal. During the excavation of industrial furnaces, slag has also been found accumulated in large amounts in the furnace. The amount of slag tapped depends on the total input of aluminium and calcium, their relative distribution in the feed, and the operational conditions of the furnace.

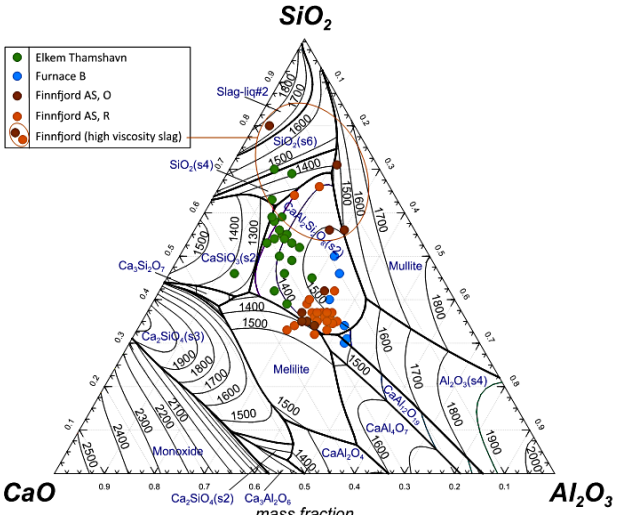


Figure 4.3 *Slag composition from 4 furnaces at 3 plants. Furnace R and O produce FeSi 75 and furnace B and Elkem Thamshavn produce silicon (Folstad and Tangstad, 2021; Jusnes et al., 2021b).*

Examples of tapped slags are given in Figure 4.3. The main part of the tapped slag composition varies from 30–60% SiO_2, with a CaO/Al_2O_3 ratio from 0.55 to 1.9, depending on the raw materials used (Folstad and Tangstad, 2021; Jusnes *et al.*, 2021b). The slag with the highest SiO_2 content was reported by the tappers to have a high viscosity, causing challenging tapping conditions. The normal samples from furnace O and R have a viscosity of around 7–30 poise at 1600°C, whereas the two challenging slags have a viscosity of 180 and 900 Poise at the same temperature. The slag will also contain small SiC particles, as shown in Figure 4.4 and hence, the viscosity will be even higher than the numbers represented by the pure slag composition. During excavations, as described in Chapter 3, slag layers are found inside the furnaces, typically surrounding the tapping channel (Folstad and Tangstad, 2021). The slag found inside the furnaces has a slag composition close to the tapped slag.

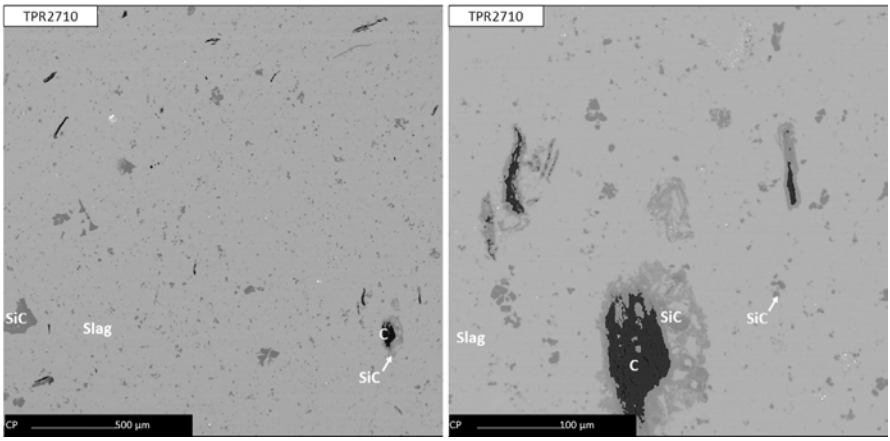


Figure 4.4 *Tapped slag with small SiC particles embedded in the slag matrix containing 25% SiO_2, 35% CaO and 39% Al_2O_3 at two magnifications (Jusnes et al., 2021a).*

Aluminium is present in coal as clay minerals, most commonly mica, which introduces some alkali metals [$(OH,F)_2(K, Na)Al_2(Si_3AlO_{10})$], and kaolinite [$(Al_4(OH)_8(Si_4O_{10})$]. Calcium quite often appears as calcite [$CaCO_3$]. Mica may also appear as an impurity in some quartzites, together with members of the feldspar group, anorthite [$Ca(Al_2Si_2)O_8$] is one such example. The clay minerals release their hydroxyl groups quite rapidly on heating, leaving the metal oxides behind in a concentrated form. These oxides are then exposed to carbon up to temperatures around 1600°C, and to silicon carbide at temperatures above this. Most of the alkali metal oxides will be reduced to metal vapours by carbon before silicon carbide is formed. Aluminosilicate and CaO are left behind in separated grains, where the silicate, on further heating, becomes selectively reduced to SiC or SiO, leaving the Al_2O_3 behind. Temperatures above 1800°C are needed for CaO and Al_2O_3 to be reduced to carbides, even with free carbon as a reductant. However, Al- and Ca-carbides have not been seen during industrial excavations. It is expected that most Ca and Al end up dissolved in the silicon and silica, rather than as individual phases, but some will also go to the gas phase, as seen later in this chapter.

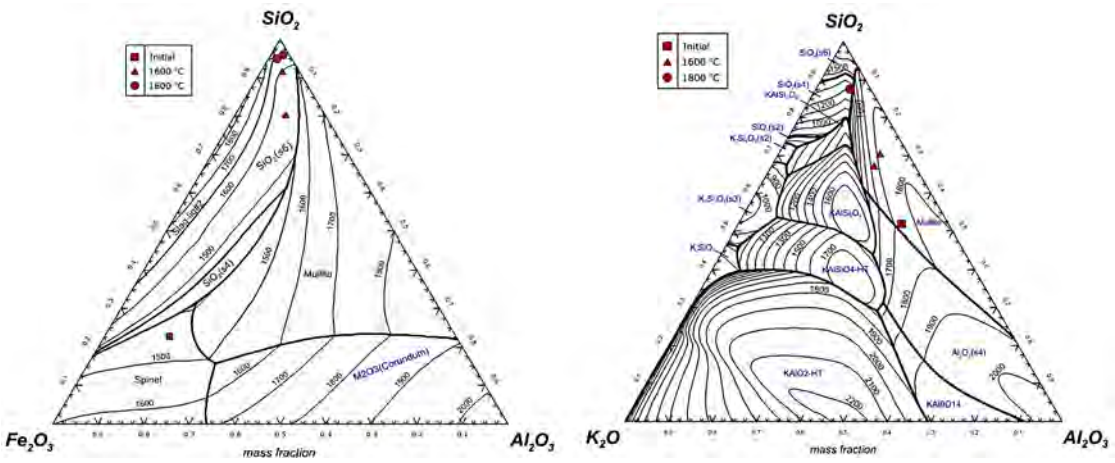


Figure 4.5 *The development of impurities in quartz with heating, showing how it will dissolve more SiO_2 at higher temperatures. Squares – initial composition of impurities, triangles – composition of impurities at 1600°C and circles – composition of impurities at 1800°C (Folstad, 2023). [Used with permission from M.B. Folstad].*

The impurities embedded in the quartzites are not accessible for reduction before the quartzite lumps decrepitate or melt. In the latter case, they dissolve into a phase that becomes increasingly enriched in SiO_2, as experimentally demonstrated in Figure 4.5. When the quartz meets SiC or carbon during heating, the SiO_2 will also react to form SiO gas. As a result, the stable oxides in the impurities will continuously increase in the oxide phase. Eventually, the consumption of silica slows down and stops, leaving some silica behind, tied up in a very viscous slag that is highly enriched in alumina. The slag tends to accumulate in the furnace unless it has the opportunity to dissolve CaO, which lowers the viscosity. This makes the slag sufficiently fluid to be tapped together with the metal. For this to occur in ferrosilicon smelting, Oterkjær (1976) suggests that the slag shall have a specific mass ratio between the CaO and Al_2O_3:

$$\frac{\%CaO}{\%Al_2O_3} > 0.6$$

Besides the three dominating oxides already highlighted, tapped slags from a ferrosilicon furnace also contain minor amounts of MgO (~1%), K_2O (~0.2%) and Na_2O (~0.05%). Transition metal oxides like FeO and TiO_2 are not found at detectable levels. Thus, if iron is analysed in ferrosilicon slags, it should be counted as a metal impurity.

Phase diagrams and activities

Most oxides are, in general, insoluble in solid crystalline silica. Most oxides are also insoluble in molten silica and produce two immiscible liquids in the high-silica end, as shown in Figure 4.6 a). Liquidus curves for the silica-rich part of the alkali and alkaline earth metal oxide-silica systems, and two divalent transition metal oxide-silica systems, are shown in Figure 4.7. The diagram shows that, except for BaO, small additions (beyond ~2%) of a divalent metal oxide lead to the separation of a second liquid phase. The alkaline metal oxides behave differently: they can give off their oxygen ions completely to the three-dimensional network of Si–O-bonds, which dominates the structure of molten silica, and place themselves interstitially within the network. In this way, a gradual breakdown of the silicate network takes place, giving the characteristics of glass melts. Examples of the two immiscible liquid phases are given in the SiO_2–CaO phase diagram shown in Figure 4.6 a). By contrast, examples of the SiO_2–K_2O phase diagram, where this is not the case, are shown in Figure 4.6 b). Figure 4.7 summarises the liquidus lines in the high SiO_2 area for several alkali and alkaline earth metals, and two transition metal oxides. It can be mentioned that the Cr_2O_3–SiO_2, Fe_2O_3–SiO_2 and TiO_2–SiO_2 phase diagrams also have the two-immiscible liquids area that the divalent Mn- and Fe-oxides show in Figure 4.7.

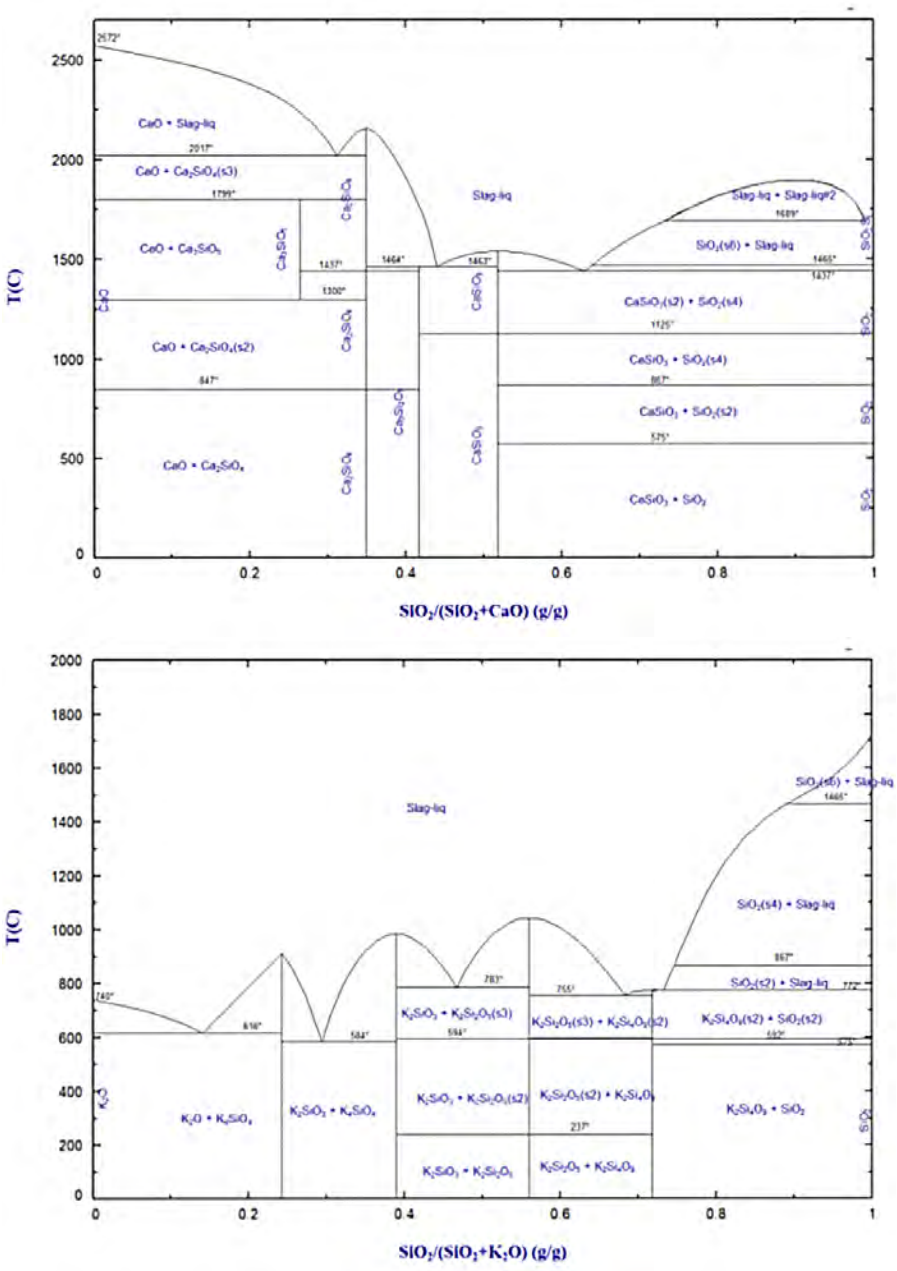


Figure 4.6 *Binary phase diagrams of the a) $CaO–SiO_2$ system and b) $K_2O–SiO_2$ system calculated by commercial FToxid database of FactSage software package.*

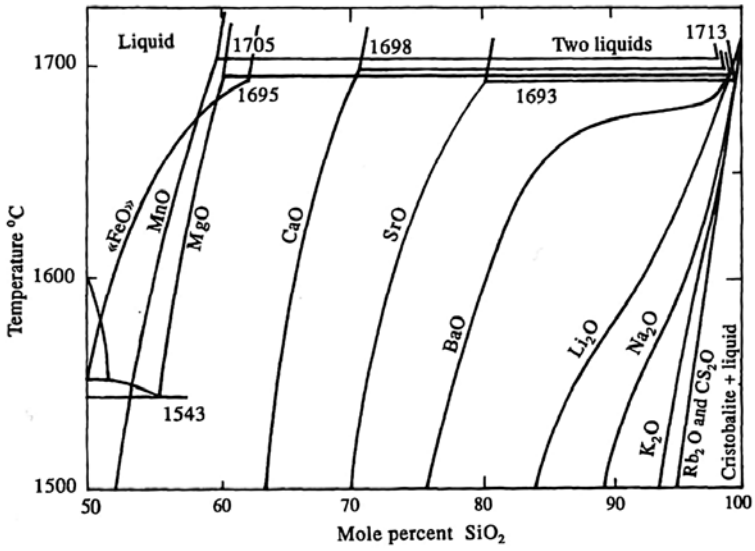


Figure 4.7 *Summary of high SiO_2 part of binary phase diagrams with alkaline-, earth-alkaline-, and transition metal-oxides where it is seen that most oxides have immiscible liquid area where two liquids coexist, while the alkali-oxides together with the heavy earth-alkali oxide like BaO will not have this immiscible liquid area.*

At the other end of the periodic system are B and Al, whose oxides are significant components in solar grade (SG) silicon production and in metallurgical grade (MG) silicon, respectively. These do not have a two-immiscible-liquids area, as exemplified by the Al_2O_3–SiO_2 phase diagram shown in Figure 4.8.

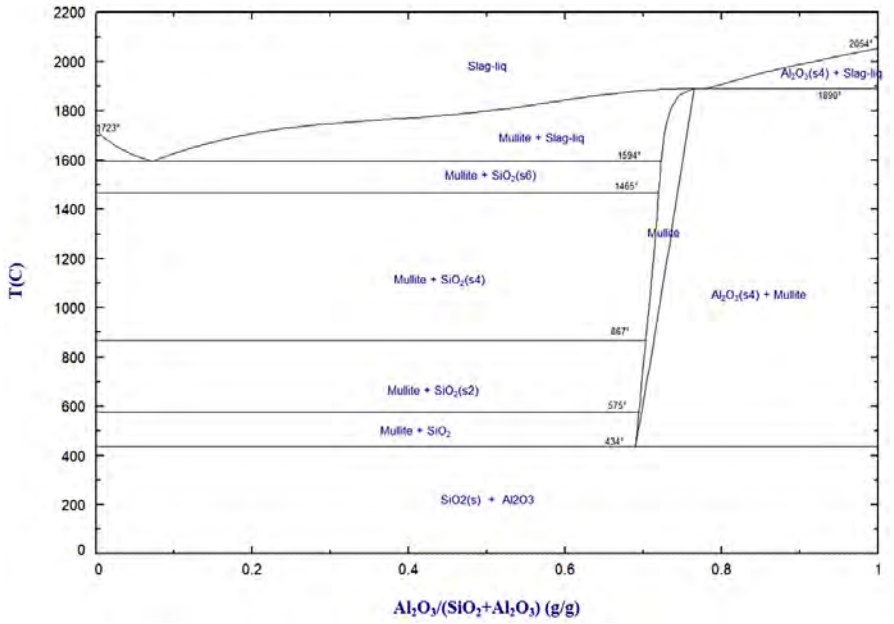


Figure 4.8 *The Al_2O_3–SiO_2 phase diagram calculated by commercial FToxid database in FactSage.*

The slags that form consist mainly of CaO, Al_2O_3 and SiO_2 inside the furnace, as well as during the refining step. It is therefore relevant to focus on the CaO–Al_2O_3–SiO_2-system, as described by the phase diagram in Figure 4.9. This diagram shows a projection of the liquidus surface: the boundaries between coexisting phases are shown by solid curves, and liquidus isotherms by lighter curves. The diagram also shows that a homogeneous liquid slag can form over a wide compositional range at temperatures above 1550°C. However, this area can shrink if the temperature is lowered to 1500°C owing to the precipitation of pseudowollastonite (CS), anorthite (CAS) and gehlenite (C_2AS).

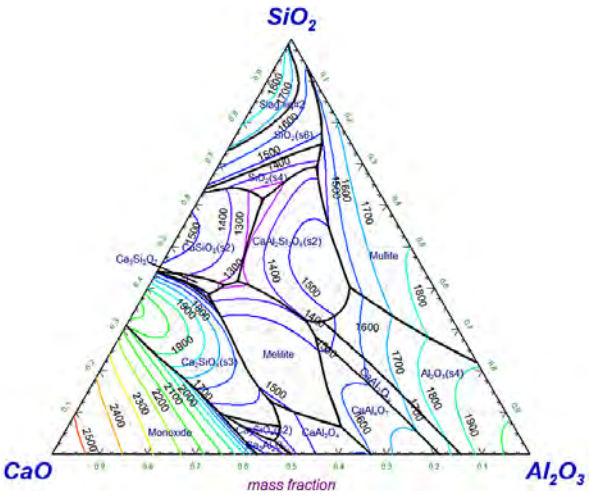


Figure 4.9 *Phase diagram of the Al_2O_3–CaO–SiO_2ternary system calculated by commercial FToxid database in FactSage.*

By adding small amounts of MgO to the SiO_2–CaO–Al_2O_3 system, the liquid region in the silica-rich part of the system expands in both temperature and composition. However, the four-component system can be described by a compositional tetrahedron at any particular MgO level. Figure 4.10 shows an example of such a diagram at 5wt% MgO.

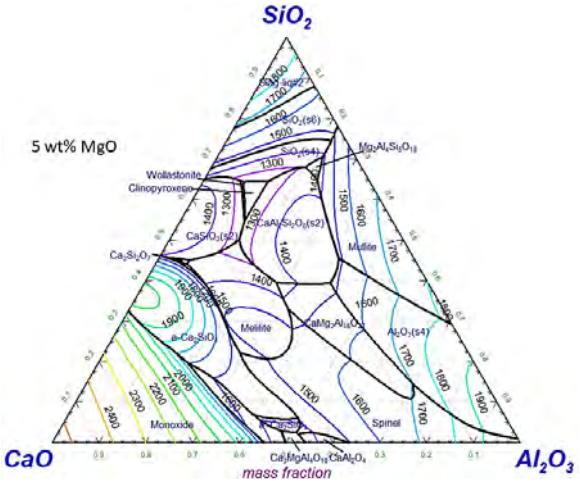


Figure 4.10 *Liquidus surface in the CaO–Al_2O_3–SiO_2–MgO-system with 5wt% MgO, Calculated by commercial FToxid database of FactSage software package.*

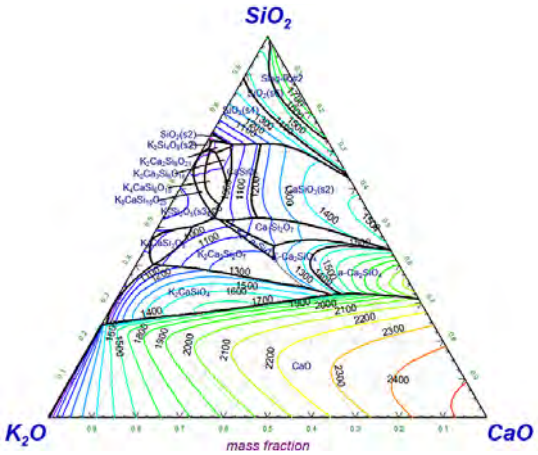


Figure 4.11 *The silica liquidus lines in alkali oxide–alkaline earth oxide–silica systems, calculated using the commercial FToxid database of the FactSage software package.*

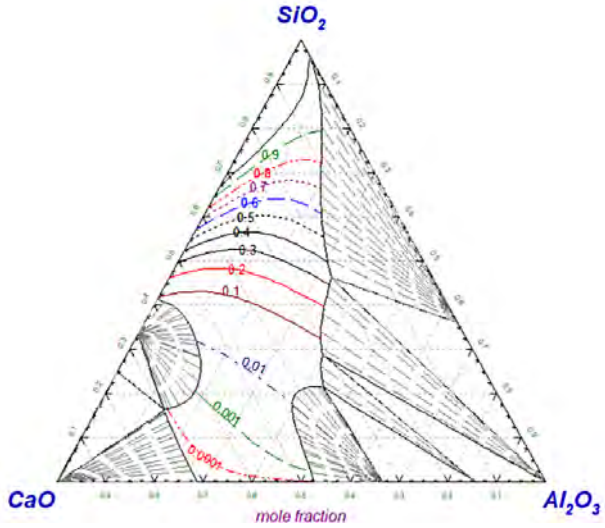


Figure 4.12 *SiO_2 activities in a $CaO–Al_2O_3–SiO_2$ slag at 1600°C by FactSage commercial software. Concentrations are given in mole fractions. Activity is referred to the pure solid oxide.*

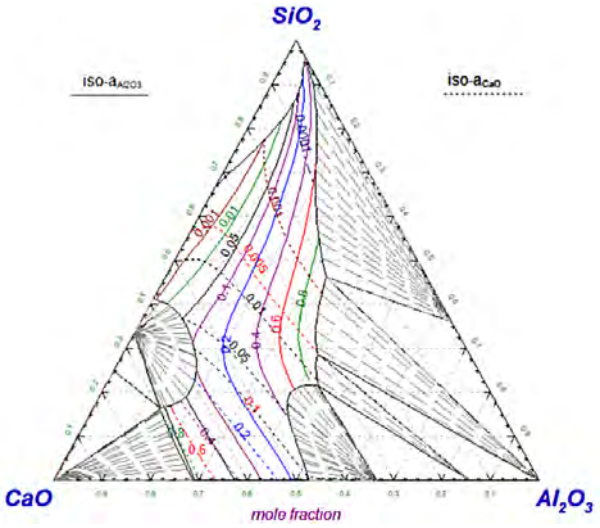


Figure 4.13 *Iso-activity lines of CaO and Al_2O_3 in the SiO_2–CaO–Al_2O_3 slag at 1600°C calculated by commercial software FactSage. Concentrations are given in mole fractions. Activity is referred to the pure solid oxide.*

Figure 4.12 and Figure 4.13 illustrate the isothermal Al_2O_3–CaO–SiO_2 diagram at 1600°C and depict the activities of SiO_2, CaO, and Al_2O_3 in the liquid region. In the two-phase areas, tie-lines indicate the composition of the liquid phase coexisting with a solid phase. In these areas, the activity is determined by the activity of the solid phase.

In the two-liquid immiscibility region near the SiO_2 corner, the SiO_2 activity approaches that of liquid SiO_2. This value is close to the solid SiO_2 activity and is approximately equal to one. Notably, the ratio of liquid SiO_2 activity to solid SiO_2 activity ranges from 0.94 to 1.02 between 1500 and 1800°C. Consequently, in both the two-liquid regions and the liquid + solid SiO_2 area, the SiO_2 activity remains close to 1. As observed in Figure 4.12, the SiO_2 activity decreases when moving downward in the liquid region. CaO is a basic oxide, Al_2O_3 is an amphoteric oxide, and SiO_2 is an acidic oxide. This means that, at constant SiO_2 content, the SiO_2 activity peaks at both the high CaO and high Al_2O_3 sides, but is slightly lower between these extremes.

Viscosity

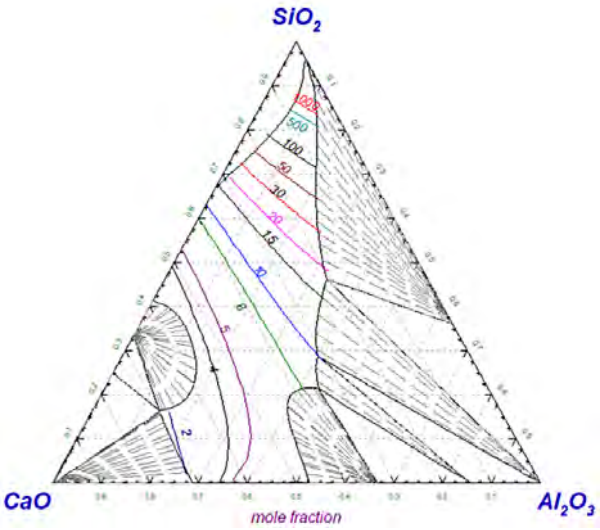


Figure 4.14 *Iso-viscosity (Pa·s) contours of $CaO–Al_2O_3–SiO_2$ melts at 1600°C (Tang et al., 2022) [Used with permission from K.Tang].*

Figure 4.14 shows the variation in viscosity within the liquid range of the system $CaO–Al_2O_3–SiO_2$ at 1600°C. From this diagram, it is worth noting that the iso-viscosity contours run nearly parallel to lines of constant $CaO/(SiO_2 + Al_2O_3)$ ratios, and that the rate of viscosity increase escalates dramatically at ratios < 0.20.

The presence of fluoride ions, added in the form of CaF_2, lowers the viscosity of aluminosilicate melts. This effect is quite considerable at low temperatures (1300°C), where a 60% decrease in viscosity has been recorded, but the lowering effect decreases with increasing temperature (Turkdogan, 1983). Replacement of CaO by an equal mass of MgO, on the other hand, seems to have a neutral, or even a slightly opposite, effect.

The viscosity decreases with increasing temperature. For liquid metals and simple ionic melts, the temperature dependency can be represented by an exponential equation of the Arrhenius type:

$$\eta = \eta_0 \exp\left(\frac{E_\eta}{RT}\right) \qquad [4.10]$$

This relation is usually not obeyed for polymeric melts because the degree of de-polymerization increases with rising temperature, resulting in a decrease in the activation energy for viscous flow. This effect is most apparent for acidic slags, which have the largest E_η-values. For the SiO_2–CaO–Al_2O_3 slag system, an increase in temperature from 1500 to 1600°C gives a drop in viscosity of about 50% in the CaO-rich region and 40% in the acidic region.

One should also be aware that the effective viscosity of a slag is strongly affected by the presence of solid particles in the melt. For the estimation of the effective viscosity η_e of a solid-melt suspension, Roscoe (1953) has given the following relation:

$$\eta_e = \eta\left(1-1.35\emptyset\right)^{-5/2} \qquad [4.11]$$

Where η is the viscosity of the liquid fraction of the suspension and Ø is the volume fraction of solid particles, assumed to be of uniform size and spherical shape. The types of solids that may occur in furnace slags are SiC particles and primary precipitates of mineral phases below liquidus temperature.

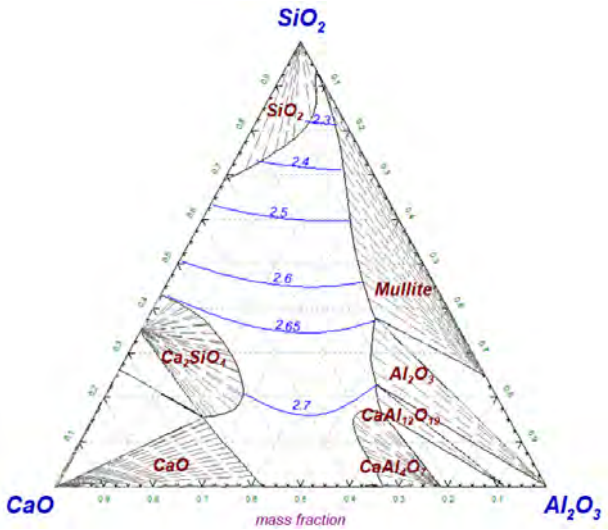


Figure 4.15 *Calculated liquid SiO_2-Al_2O_3–CaO density at 1600°C based on 652 experimental molar volume data available in the literature (Tang et al., 2022) [Used with permission from K. Tang].*

Density

Figure 4.15 shows the variation of density for $CaO–Al_2O_3–SiO_2$ melts at 1550°C. To see the implication of the data in Figure 4.15 in the furnace, as well as in refining, a comparison should be made with densities for the metal phase described previously in this chapter. It follows from the Figure that $CaO–Al_2O_3–SiO_2$ melts, in general, will have a lower density compared to liquid FeSi75. For liquid silicon, on the other hand, slags with a bulk density ≥ 2500 kg/m^3 (2.5 g/cm^3) have a higher density than the liquid silicon. The composition at which this occurs can be read from the diagram of Figure 4.15 for a pure ternary slag, but the presence of SiC may shift this limit towards higher contents of SiO_2 and Al_2O_3. Worth mentioning is that partial substitution of CaO by MgO has no noticeable effect on this limit.

Interfacial properties

The production of high-purity silicon requires the effective removal of metallic impurities like calcium and aluminium, as well as non-metallic inclusions such as SiO_2, Al_2O_3, and SiC. The efficiency of these removal processes is largely determined by the interfacial energies of the system. A fundamental understanding of these properties is therefore essential for process optimisation, leading to improved product quality and operational efficiency.

Interfacial properties are fundamentally thermodynamic in nature and play a crucial role in reaction kinetics, nucleation, and the formation of suspensions of solid particles or liquid droplets in molten slags. These properties are referred to as surface tension when the second phase is a gas and, unless otherwise specified, are measured under equilibrium conditions (Eustathopoulos *et al.*, 1999).

Surface energy is defined as the work required to increase the area of a surface by one unit. Since systems at constant temperature and pressure always tend towards minimizing free energy to reach equilibrium, the surface behaves as if it were in a state of tension. By definition, the surface tension, σ, expressed in mNm^{-1} is numerically equivalent to the surface energy in mJm^{-2} (Lu and Jiang, 2005).

In general, the surface tension of liquids decreases with increasing temperature, and the variation often follows a linear relation over a limited temperature range, i.e.:

$$\sigma = \sigma_0 + \left(\frac{d\sigma}{dT}\right)T \qquad [4.12]$$

Silicate melts which are rich in SiO_2 are highly polymerized and are exceptional, as they exhibit positive values for (dσ/dT). This is associated with structural changes in the melt caused by dissociation and formation of smaller anionic groups at higher temperatures. As the extent to which this happens varies with composition, a clear effect of temperature on the surface tension is not easily seen from the reported data for the SiO_2–CaO–Al_2O_3 melts. Figure 4.16 shows the surface tension of the liquid Al_2O_3–CaO–SiO_2 slag at 1600°C (Tang *et al.*, 2009). As seen, there is a decrease in surface tension with increasing SiO_2 concentrations. The surface tension increases slightly if CaO is substituted by MgO in these melts.

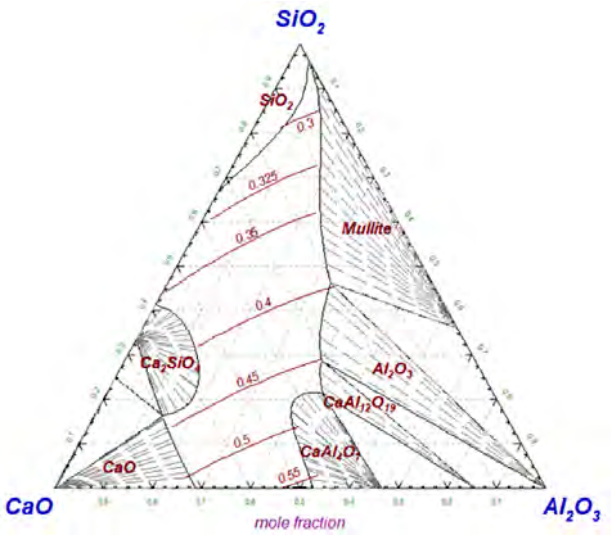


Figure 4.16 *Modelled iso-surface tension curves in SiO_2–Al_2O_3–CaO slag at 1600°C (Tang et al., 2013) [Used with permission from K.Tang].*

The surface tension of pure molten silicon has been the subject of extensive research, with reported values typically in the range 700–900 mN/m at its melting point (1414°C). Hardy derived the surface tension of liquid silicon from sessile drop measurements and arrived at the following expression, which is valid for the temperature range 1415–1600°C (Hardy, 1984):

$$\sigma = 885 - 0.28\left(T - T_m\right) \qquad [4.13]$$

With an uncertainty in the gradient of ± 0.004 mNK^{-1}, Hardy carried out his measurements with liquid silicon placed in a BN cup in a flowing argon atmosphere. He found that oxygen contamination lowered the surface tension of silicon. The surface tension increases when silicon is alloyed with iron. This is seen in Figure 4.17, where calculated and experimental data for the Fe–Si system at 1600°C are shown (Utigard, 1994). The diagram has been reproduced from the work of Klevan (1997), who included the results of Tang *et al.* (2009) and Hardy (1984) for pure silicon.

The presence of surface-active elements, particularly oxygen, can significantly alter the surface tension. Even minute amounts of oxygen can lower the surface tension of silicon, which has been a source of discrepancy in historical measurements (Mukai *et al.*, 2000). Modern experimental techniques, such as electromagnetic levitation, have allowed more accurate measurements under controlled atmospheres, leading to a better understanding of the intrinsic properties of molten silicon.

The interfacial tensions between Fe–Si alloys and $CaO–Al_2O_3–SiO_2$ slags are shown in Figure 4.18. This figure is reproduced from the work of Dumay and Cramb (1995), who employed the X-ray sessile drop method at 1450°C on two types of slag, composed as listed in Table 4.5. This method requires a certain density difference between the metal and the slag, and it loses accuracy at high silicon levels, as is also reflected in the results.

Table 4.5 *Slag compositions referred to in Figure 4.18. (Dumay and Cramb, 1995).*

Slag	wt% CaO	wt% Al_2O_3	wt% SiO_2
1	46	18	36
2	42	16	42

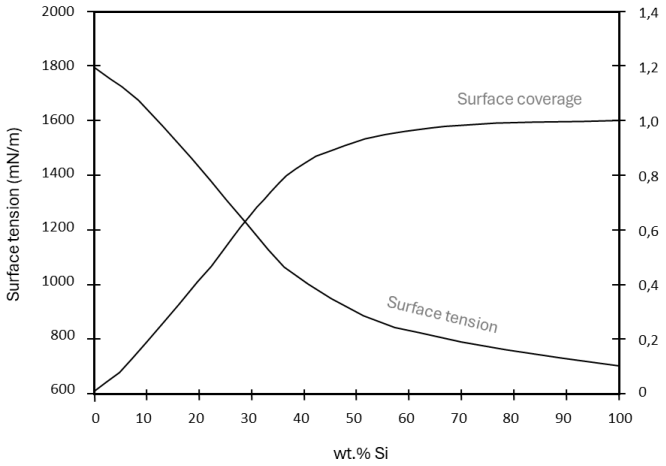


Figure 4.17 *Experimental and calculated surface tension and surface coverage of Fe–Si-alloys at 1600°C after Klevan (1997).*

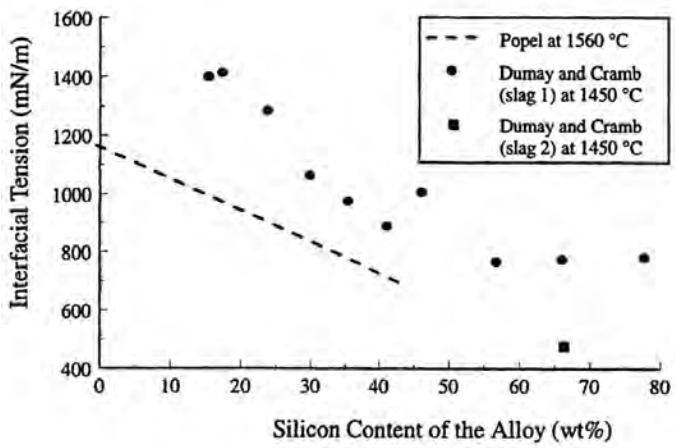


Figure 4.18 *Interfacial tension between Fe–Si-alloys and slags at 1450°C (Dumay and Cramb, 1995).*

The data from Dumay and Cramb reflect a situation in which the two phases are in chemical equilibrium. Experiments have shown that the transfer of reactants across the interface, due to chemical reactions between the two phases, lowers the interfacial tension. At high transfer rates, the interfacial tension

may drop to zero and even negative values have even been recorded. This creates interfacial turbulence and instabilities at the interface, and spontaneous emulsification may even occur as a result (Turkdogan, 1983).

By combining the surface properties quoted for the slag/metal system in question, we can derive an expression for the so-called spreading coefficient S, which measures the tendency for the slag to spread across the metal surface. For a situation as illustrated in Figure 4.19a, which shows a droplet of slag (s) in a gaseous environment resting at equilibrium on the surface of liquid metal (m), the spreading coefficient $S_{s/m}$ is defined as:

$$S_{s/m} = \sigma_{g/m} - \left(\sigma_{g/s} + \sigma_{s/m}\right) \qquad [4.14]$$

In this expression, g/m and g/s indicate the surface energies of the gas/metal and gas/slag surfaces, respectively, and s/m indicates the slag/metal interfacial energy. The angle between the tension vectors represented by the two terms in the parentheses in Equation 4.14 defines the contact angle θ, which becomes < 90° for positive values of S and > 90° for negative values. A more familiar definition of this angle, usually referred to as the wetting angle, is the one given in Figure 4.19b. This figure shows a sessile drop of liquid (l) at rest on a flat, horizontal solid surface (ss) in a gaseous environment (g). The contact angle can now be observed directly and is here defined by the respective tension forces by:

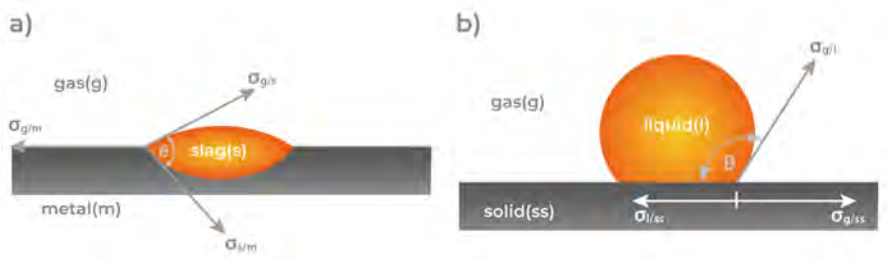


Figure 4.19 *Relations between the respective surface and interfacial tensions and the contact angle at equilibrium for (a) Slag on liquid metal for S > 0 (b) Liquid on solid for non-wetting conditions.*

$$\cos\theta = \frac{\sigma_{g/ss} - \sigma_{l/ss}}{\sigma_{g/l}} \qquad [4.15]$$

If we insert the approximate values into Equation 4.14, we may read from Figure 4.17 and Figure 4.18 that, for a metal with 70% Si, and neglecting a possible temperature dependency of the interfacial energy, we obtain the following for a slag with a surface energy of 500 mJm^{-2}:

$$S_{s/m} = 800 - \left(500 + 400\right) = -100\ mJm^{-2}$$

The negative value for S indicates favorable conditions for slag/metal separation. However, the spreading coefficient may easily become positive, and the conditions for phase separation less favorable, if exchange reactions between slag and metal across the interface are still running.

Tang *et al.* (2009) proposed the constricted Gibbs energy minimization algorithm to calculate the surface tensions of the liquid Si–Al–Ca metal and SiO_2–Al_2O_3–CaO slag phases. The basic assumption is that the monolayer-thick surface layer is in equilibrium with the bulk phase. Thermochemical properties of the molten slag and the surface properties of pure components are the only required input for the calculations. Interfacial tensions between metal and slag phases were then modelled by applying the modified Girifalco-Good equation. The proportional factor is expressed as a function of SiO_2 concentration. The spreading coefficient for liquid ferrosilicon alloy and molten SiO_2–CaO–Al_2O_3 slags can be expressed as:

$$S_{s/m} = \left(6.13 - 1.29 X_{SiO2}\right)\sqrt{\sigma_s \sigma_m} - 2\sigma_s$$

Tang *et al.* (2013) further developed the constricted Gibbs energy minimization algorithm to calculate the interfacial tensions between the liquid Si–Al–Ca metal and SiO_2–Al_2O_3–CaO slag. Figure 4.20 shows the model calculations with experimental data.

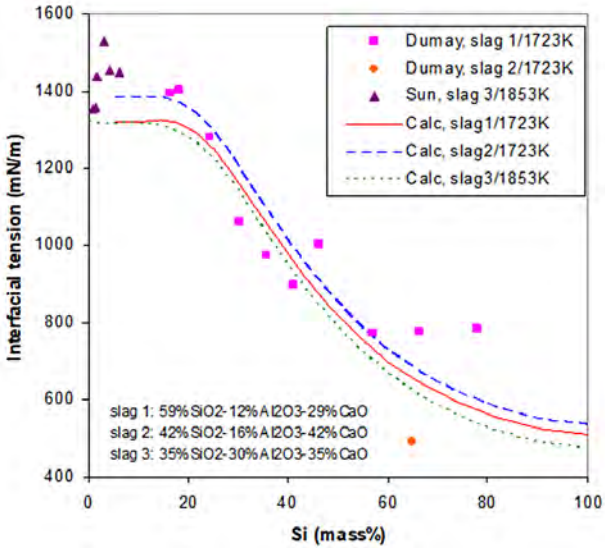


Figure 4.20 *Effect of Si content of Si–Fe alloys on the interfacial tension of ferrosilicon alloy and molten SiO_2–CaO–Al_2O_3 slags (Tang et al., 2013) [Used with permission from K. Tang].*

Silicon carbide will be present in all parts of the furnace, and it also enters the refining process as crystalline particles suspended in the metal phase. According to the literature surveyed by Klevan (1997), liquid silicon and Fe–Si alloys with > 33% Si wet SiC fairly well, almost independently of the crystalline form of SiC and the morphology of the specimens. Except for the work of Nogi and Ogino (1994), who claimed that silicon at 1550°C wets SiC completely, other investigators have recorded wetting angles that vary between −33–42° at temperatures ranging between 1430–1480°C, for both silicon and ferrosilicon.

The wetting behavior of silicate glasses on SiC was investigated by Yurkov and Polyak (1995). They found good or almost perfect wetting, with contact angles $\theta < 30°$, at 1400°C for glass containing 12–25% Al_2O_3, 5–17% CaO and 25–70% SiO_2 (Yurkov and Polyak, 1995). From these data, we are tempted to conclude that SiC is wetted better by silicate melts than by the metal phase. The system will therefore decrease its surface energy if the SiC particles migrate across the interface into the silicate melt. The surface energy decreases most if the SiC particles are small.

Our understanding of interfacial properties in high-temperature systems has been greatly advanced by the development of sophisticated experimental and computational methods. High-temperature X-ray radiography allows direct observation and measurement of contact angles and interfacial tension in sessile drop experiments. Electromagnetic and electrostatic levitation techniques enable the measurement of thermophysical properties of highly reactive melts, like silicon, without contamination from a crucible (Nogi and Ogino, 1994). In parallel, computational modelling has become an indispensable tool. Molecular dynamics (MD) and density functional theory (DFT) simulations provide insights into the atomic-scale structure and interactions at interfaces. Validated by experimental data, these models allow efficient exploration of the effects of composition and temperature on interfacial properties, guiding the design of new alloys and refining slags.

4.3 Distribution of elements

The elements added to the silicon furnaces will be distributed among various phases, such as gas, oxide, or metal, in varying amounts depending on the element content and temperature. Assuming thermodynamic equilibrium, every element will be present in all phases, and its amount in each phase is given by the chemical potential, which will be the same in all phases. If the same reference state is used, the activity of each element must be the same in all phases. For example, if three phases are present for Ca – liquid silicon, a slag, and a gas – then $a_{Ca(silicon)} = a_{Ca(slag)} = p_{Ca}$ = (gas), though one often uses a(CaO) instead of a(Ca) in slag. Another way to look at this is to state that the system will go to the phases and phase compositions that give the lowest Gibbs free energy.

Myrhaug and Kamfjord have both measured the element distribution in and out of the furnace, as seen in Figure 4.21 and Figure 4.22 (Kamfjord, 2012; Myrhaug, 2003). It must, however, be said that the accuracy of the chemical analyses of the material may vary, especially at very low element concentrations. The theory is that the distribution will be decided mainly by the boiling point of the element. Elements that have a boiling point above the temperature of the crater zone, that is 2000°C, will mainly go into the liquid silicon or ferrosilicon. Elements that have a lower boiling point will

condense in the silica fume above the charge, while the ones with the lowest boiling point will go in the off-gas. There are, of course, several exemptions from the rule:

- For some elements, the oxides have lower boiling points than the elements, like SO_3, SeO_2, As_2O_3, MoO_3 and WO_2, and may go to the gas phase in an oxidic form.
- It has been theorized that Pb will follow the gas to the charge top, where it can react with S and form PbS, which has a lower boiling point.
- In FeSi production, P may form the stable compound FeP, which is very stable, and this may explain why most of the P will go to the metal in FeSi production.

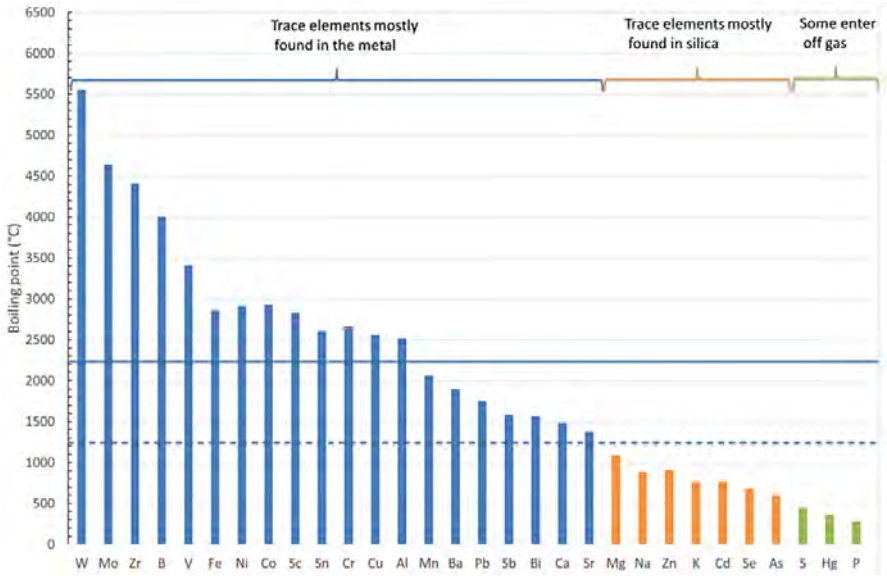


Figure 4.21 *Illustration of the boiling point model describing the element distribution in the output flows of a silicon furnace. Dotted line indicates the temperature in the hot zone and dotted line the temperature in the off gas (after Myrhaug, 2003). [Used with permission from L.V. Myrhaug].*

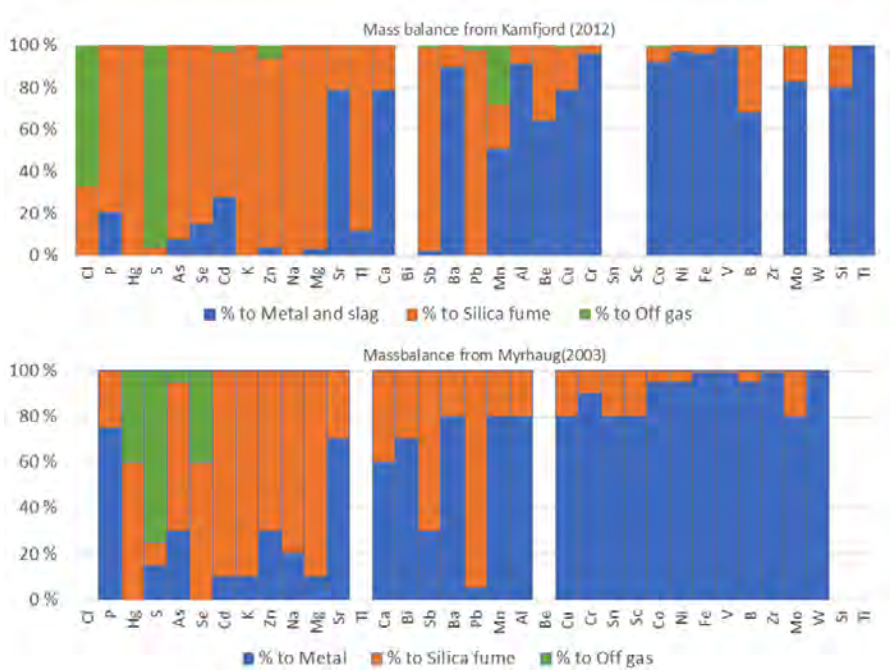


Figure 4.22 *The distribution of elements in the output flows of a Si furnace measured over 2 days from Kamfjord (2012) and from ferrosilicon production Myrhaug (2003). The elements are shown with increasing boiling point. [Used with permission from N.E. Kamfjord and L.V. Myrhaug].*

General thermodynamic overview

Most elements introduced into the furnace are in oxide form, with carbon being the notable exception. Silicon dioxide (SiO_2), added as quartz, is the primary oxide. Both quartz and carbon materials contain trace elements predominantly as oxides, such as CaO, Al_2O_3, FeOx, and TiO_2. In high-silicon ferrosilicon (FeSi) production, iron may be introduced as oxides (Fe_2O_3, Fe_3O_4, or FeO) or scrap metal. During the slag refining process, the oxide phase also plays a crucial role in determining the final metal composition.

This discussion will focus on the stability of oxides and their transition to elemental states, exemplified by the stability of SiO_2 and its conversion to elemental Si. Figure 4.23 presents an Ellingham diagram, which illustrates the standard Gibbs energies of oxide formation per mole of oxygen reacted. This

diagram provides a visual representation of the relative stability of selected metal oxides compared to those of silicon and carbon.

The diagram shows that the oxides of transition metals like Ni, Co and Fe are all less stable than SiO_2. This means that the oxides of transition metals are liable to be reduced to their pure metal state at a lower temperature than the reduction of SiO_2 to Si. It is also clearly seen that they become unstable in the presence of graphite and 1 bar CO pressure at low temperatures. For the lowest oxide of Fe, FeO, this happens at temperatures above the intersection point between the lines representing the reactions:

$$2Fe(s) + O_2(g\ of\ 1\ bar) = 2FeO_s$$

$$2C(s) + O_2(g\ of\ 1\ bar) = 2CO(g\ of\ 1\ bar)$$

Subtracting the first from the second reaction gives the reaction

$$2FeO + 2C = 2Fe + 2CO \qquad [4.16]$$

for which the change in standard Gibbs energy is zero at the temperature of intersection 720°C and is < 0 at higher temperatures. What is not seen so easily in the diagram is that the reduction of FeO to Fe may occur in CO/CO_2 mixtures, as CO is an effective reducing agent for FeO at temperatures below 1200°C.

If they appear as pure oxides in a charge mixture of SiO_2 and C, oxides like manganese should be completely reduced before the reduction of SiO_2. As the temperature needed for the manganese reduction to be completed is at a level where liquid slag formation may take place, a liquid MnO–SiO_2 slag will be formed.

The alkali metal oxides, which are represented by the compound K_2O and Na_2O in Figure 4.23, are also relatively stable at room temperature, but their stability decreases rather rapidly with increasing temperature due to the low melting and boiling points of the alkali metals. As shown, if present in their pure state, Na_2O and K_2O are reduced to metal vapour by reaction with carbon at around 1020°C and 830°C respectively.

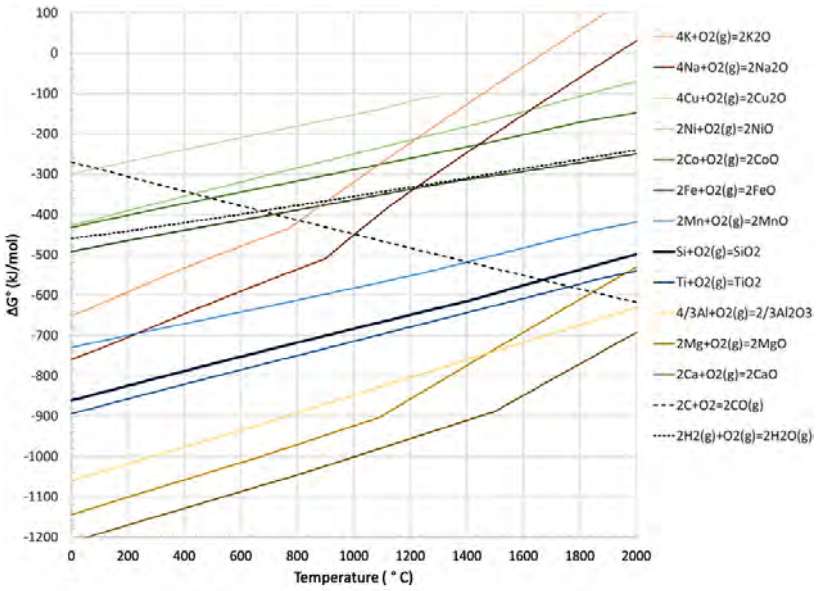


Figure 4.23 *The Ellingham diagram for the oxides of some relevant additional elements in silicon smelting (calculated by HSC v.9).*

The third group of metal oxides to consider are those that require a lower oxygen potential than SiO_2 to react and form metal in its standard state. This group comprises the alkaline earth metal oxides and alumina, which are among the most abundant of the impurities entering the furnace charge. Note that TiO_2, which is the least stable of the titanium oxides, also belongs to this group, as it is more stable than SiO_2 throughout the temperature range of interest.

The high stability of these refractory oxides, and the fact that they enter as impurities tied up in silicate minerals with oxide activities less than unity, make it reasonable to assume that they will survive as oxides up to the melting point of silica at around 1700°C, where they dissolve in a slag. As the temperature increases and liquid silicon starts to form around 1800°C, their destiny is then determined by partial distribution equilibria of the following type:

$$Si + \frac{2}{y}\left(Me_xO_y\right) = \frac{2x}{y}Me + \left(SiO_2\right) \qquad [4.17]$$

The equilibrium constant of the reaction[1]:

$$K_{4.17} = \frac{\left(a_{Me}\right)^{\frac{2x}{y}} \cdot a_{SiO_2}}{\left(a_{Me_xO_y}\right)^{\frac{2}{y}}} \cdot a_{Si} \ll 1 \; if \; the \; Me_xO_y \; is \; a \; refractory \; oxide \quad [4.18]$$

The same distribution reaction also applies at the final stage to the transition metals, as well as to the fraction of the alkali metals that may remain in the hot zone of the furnace at this stage. However, according to the examples, the K-values for these reactions are >> 1 as shown in Figure 4.24.

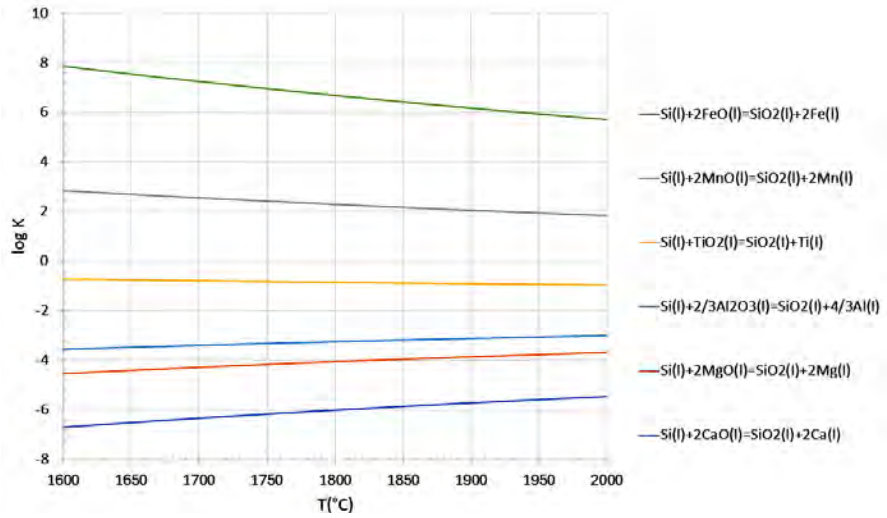


Figure 4.24 *Equilibrium constant based on HSC v.9 for various types of metal oxides participating in Reaction [4.18] with liquid slag and metal.*

1 Note that the reference state for the activities appearing in this generalised expression is defined by the data chosen to calculate the Gibbs energy change of the reaction. According to the formalism used above, the metal activities should be replaced by partial pressures for the volatile metals above their boiling point, i.e. at 897, 1093 and 1483°C, respectively, for Na, Mg and Ca.

The equilibrium constant is a function of temperature, as expressed in the van't Hoff equation:

$$\frac{dlnK}{d\left(\frac{l}{T}\right)} = -\frac{\Delta H^{\circ}}{R} \qquad [4.19]$$

It follows from this that, for the endothermic reactions with the refractory oxides, the equilibrium constant increases with temperature. This makes their reduction more favorable at high temperatures. For the reactions with the transition metal oxides, which are exothermic, the situation is the opposite.

In silicon smelting, as well as in the production of Si-rich alloys, liquid silica and silicon can both act as solvents for impurities, as previously discussed. Their activities in the expression for the equilibrium constant in Equation [4.18] are therefore expected to be close to unity if the metal phase contains > 98 wt%Si and the oxide phase is saturated in silica. This simplification gives the following for the activities of a dissolved element:

$$a_{Me} = \left(K_{[4.17]}\right)^{\frac{y}{2x}} \left(a_{Me_xO_y}\right)^{\frac{1}{x}} \qquad [4.20]$$

or for the partial pressure of a volatile element:

$$p_{Me} = \left(K_{[4.17]}\right)^{\frac{y}{2x}} \left(a_{Me_xO_y}\right)^{\frac{1}{x}} \qquad [4.21]$$

Expressing the activity in Equation [4.6] by an activity coefficient γ_{Me}:

$$a_{Me} = \gamma_{Me} \cdot X_{Me}$$

and transforming from mole fractions to weight% by inserting for, which applies for diluted solutions, we get the following for the concentration of an impurity element:

$$\left[\%Me\right] = \left(K_{[4.17]}\right)^{\frac{y}{2x}} \cdot \frac{100\ M_{Me}}{28.1} \cdot \frac{\left(a_{Me_xO_y}\right)^{\frac{1}{x}}}{\gamma_{Me}} \qquad [4.22]$$

or

$$\left[\%Me\right] = k_{eff} \frac{\left(a_{Me_xO_y}\right)^{\frac{1}{x}}}{\gamma_{Me}} \qquad [4.23]$$

There are, however, several cases where the activity of silicon and silica is not close to unity; that is, when % Si < 90 wt% and % SiO_2 < 90 wt%. The most obvious examples are FeSi alloys produced with, e.g., 52 wt% Si or 75wt% Si. The oxide phase in the lower part of the furnace, as well as the tapped slag, will also contain about equal amounts of SiO_2, Al_2O_3 and CaO. The amount of Me in the silicon phase will then be expressed by a_{Me}, as given by equation [4.18].

Ca and Al distribution

Over a period of 2 months, Oterkjær studied the operation of a ferrosilicon furnace producing standard Fe75Si and found that 60–70% of the total aluminium and 90–95% of the total calcium entered the furnace with the reduction materials. He also found that, on average, 70% of the total aluminium and 50% of the total calcium were recovered in the metal (Oterkjær, 1976). As slag weights were not recorded, his calculations of the losses are somewhat uncertain. However, he found that as much as 60% of the unrecovered aluminium and 30% of the unrecovered calcium were lost as fume in the off-gas, which is in agreement with Hauge's data (Hauge, 2022). The rest of the Al and Ca was tapped as a constituent of the slag, with an average composition of 31.5% SiO_2, 38.7% Al_2O_3, and 26.0% CaO, containing 3.8% SiC.

The concentrations of aluminium and calcium in the metal, which averaged around 1.5% and 0.4%, respectively, fluctuated from one day to the next, with the largest amplitudes for aluminium. These fluctuations are somewhat smoothed out in the plot in Figure 4.25, which shows the calculated recoveries in the metal phase on a weekly basis.

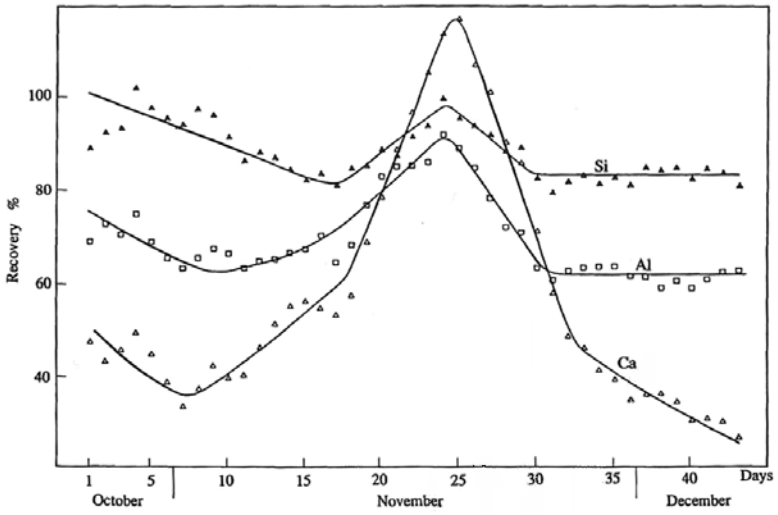


Figure 4.25 *Calculated recoveries of Ca, Al and Si in tapped metal for a period of ferrosilicon smelting after Oterkjær (1976).*

The peaks in the recoveries after 25 days are associated with a period of overcoking. The smaller fluctuations in the impurity recoveries were also found to be related to changes in the amount of carbon added. A decrease in furnace resistance was also found to increase the transfer of aluminium and calcium to the metal phase.

Comparing the work of Oterkjær (1976) with the industrial mass balance presented above from Myrhaug (2003) and Kamfjord (2012), 80–90% of the Al and 60–80% of the Ca entering the furnace will be distributed between the slag and the metal. As most of it will go to the metal, it goes without saying that the distribution of Al and Ca between the slag and metal phases will also be important in the refining process. In the furnace, the Al_2O_3 and CaO will be reduced, while in the refining step the Al and Ca will be oxidized. As the thermodynamics only discusses the end state, which governs both the reduction and the oxidation, this chapter will discuss the end-state distribution.

The equilibrium between the Al and Ca in the metal phase and the Al_2O_3 and CaO in the slag phase will be given by reaction [4.24] and [4.25]:

$$\underline{Al} + \frac{3}{4}\left(SiO_2\right) = \frac{3}{4}\underline{Si} + \frac{1}{2}\left(Al_2O_3\right) \quad [4.24]$$

$$\underline{Ca} + \frac{1}{2}\left(SiO_2\right) = \frac{1}{2}\underline{Si} + \left(CaO\right) \quad [4.25]$$

It follows from these equations that the reduction of a dissolved impurity is coupled with the distribution of silicon between the oxide and metal phases of silicon. Hence, it is also evident that the reduction of various dissolved elements is mutually coupled through similar reactions; i.e., as follows for the two elements considered:

$$\frac{2}{3}\underline{Al} + \left(CaO\right) = \underline{Ca} + \frac{1}{3}\left(Al_2O_3\right) \quad [4.26]$$

However, at low impurity levels, the transport of the impurity elements from the bulk of the slag to the slag-metal interface may very well take over as a rate-controlling step. The recorded bulk distribution will then deviate from the equilibrium values.

Typically, it is important to calculate the amount of Al and Ca in the metal. Based on reaction [4.24] and [4.25], the equilibrium constant can be described by the following reactions:

$$K_{Ca} = \frac{a_{CaO} \cdot a_{Si}^{1/2}}{a_{Ca} \cdot a_{SiO2}^{1/2}} \quad [4.27]$$

$$K_{Al} = \frac{a_{Al2O3}^{1/2} a_{Si}^{3/4}}{a_{Al} a_{SiO2}^{3/4}} \quad [4.28]$$

Reaction [4.27] and [4.28] can be rearranged to the following reaction, where the activities in the metal phase will be the focus:

$$a_{Ca} = \frac{a_{CaO} \cdot a_{Si}^{1/2}}{K_{Ca} \cdot a_{SiO2}^{1/2}}$$

$$a_{Al} = \frac{a_{Al2O3}^{1/2} a_{Si}^{3/4}}{K_{Al} a_{SiO2}^{3/4}}$$

With the activity of Ca and Al in the metal, the molar mass can be calculated as:

$$a_{Ca} = \gamma_{Ca} X_{Ca}$$

$$a_{Al} = \gamma_{Al} X_{Al}$$

The molar fraction will hence be given by the following equations:

$$X_{Ca} = \frac{a_{Si}^{1/2}}{\gamma_{Ca}} \cdot \frac{1}{K} \cdot \frac{a_{CaO}}{a_{SiO2}^{1/2}} \quad [4.29]$$

$$X_{Al} = \frac{a_{Si}^{3/4}}{\gamma_{Al}} \cdot \frac{1}{K_{Al}} \cdot \frac{a_{Al2O3}^{1/2}}{a_{SiO2}^{1/2}} \quad [4.30]$$

The amount of Ca in the metal is given by the metal composition, by a_{Si} and γ_{Ca}, the equilibrium constant K_{Ca}, and the slag composition, given by the activities of CaO and SiO_2. These numbers are all found previously in this chapter.

To calculate this in wt.%, the activity based on wt.%, $a_{Ca} = f_{Ca} \cdot$[wt.% Ca], can be used, or it can be calculated from the molar fraction. Assuming that the Ca level is less than 2%, the simplified equation 4.31 can be used:

$$\left[wt.\%\ Ca\right] = \frac{X_{Ca} \cdot M_{Ca}}{X_{Ca} \cdot M_{Ca} + X_{Si} \cdot M_{Si}} \cdot 100 \quad [4.31]$$

where M_{Ca} is the molar weight of Ca and M_{Si} is the molar weight of the solvent. For FeSi75, it would be the molar weight of FeSi75. By using this equation below 2% Ca, the inaccuracy would be less than 1%.

Programs like e.g. FactSage, using Gibbs free energy minimization algorithms, can calculate this directly. In Figure 4.26 to Figure 4.33 one can see the resulting wt.%Al and wt. % Ca in silicon, FeSi75 and FeSi50 in coexistence with an Al_2O_3, CaO, SiO_2 slag at 1550 and 1600°C.

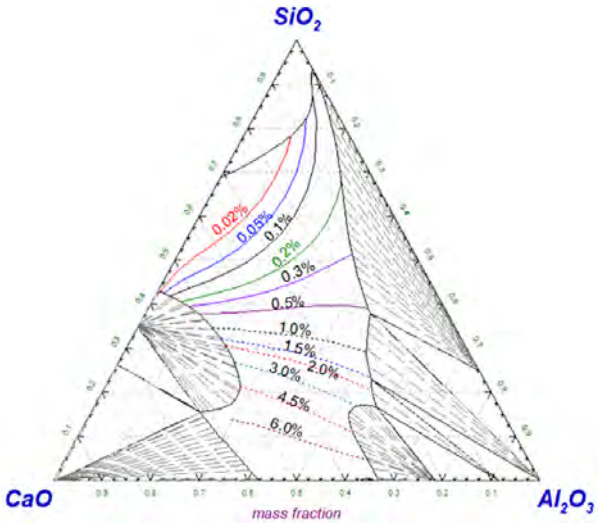


Figure 4.26 *Calculated iso-content contours for Al of metal/slag equilibria at 1600°C. The FactSage commercial software and its FToixd and FTlite databases have been used.*

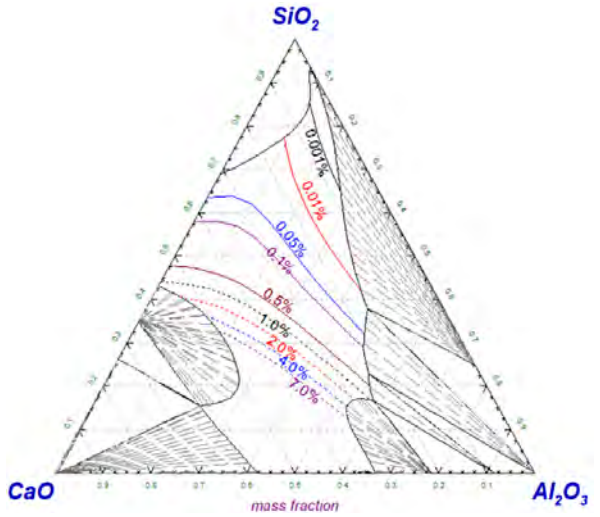


Figure 4.27 *Calculated iso-content contours for Ca of metal/slag equilibria at 1600°C. The FactSage commercial software and its FToixd and FTlite databases have been used together with the updated activity coefficient from (Jakobsson and Tangstad, 2015).*

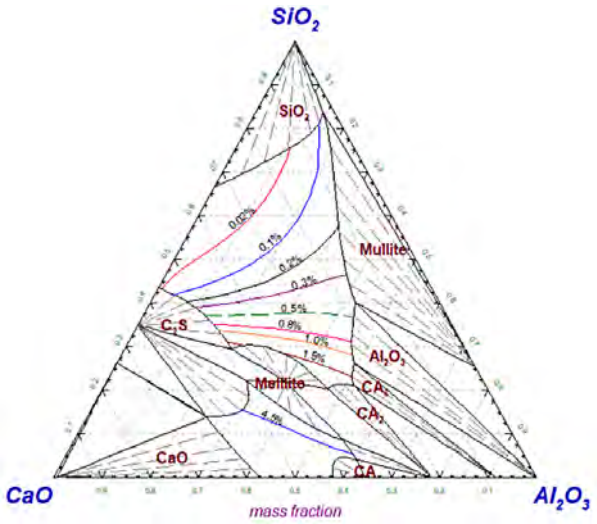


Figure 4.28 *Calculated iso-content contours for Al of metal/slag equilibria at 1550°C. The FactSage commercial software and its FToixd and FTlite databases have been used.*

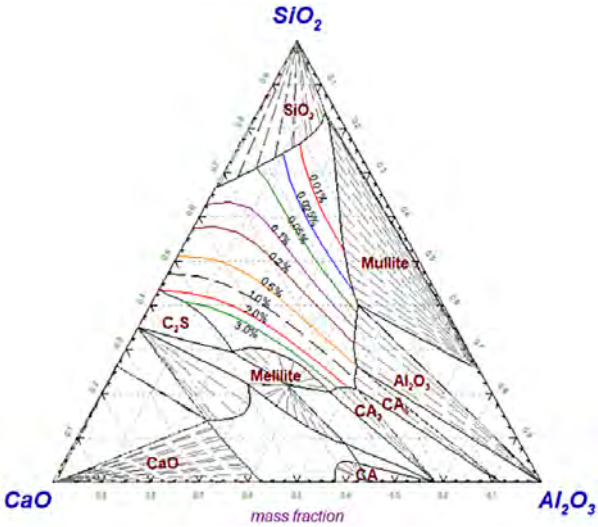


Figure 4.29 *Calculated iso-content contours for Ca of metal/slag equilibria at 1550°C. The FactSage commercial software and its FToixd and FTlite databases have been used together with the updated activity coefficient from Jacobsson and Tangstad (2015).*

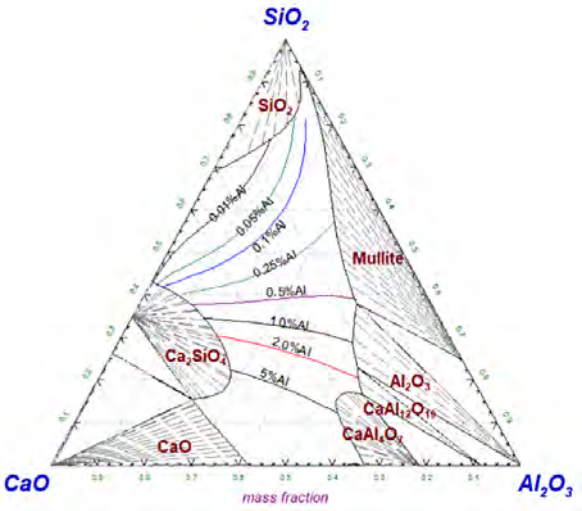


Figure 4.30 *Calculated iso-content contours for Al of FeSi75/slag equilibria at 1600°C. The FactSage commercial software and its FToixd and FTlite databases have been used.*

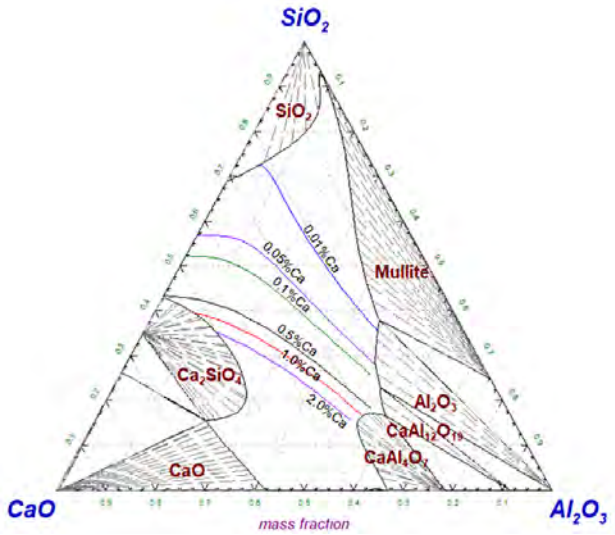


Figure 4.31 *Calculated iso-content contours for Ca of FeSi75/slag equilibria at 1600°C. The FactSage commercial software and its FToixd and FTlite databases have been used together with the updated activity coefficient from Jacobsson and Tangstad (2015).*

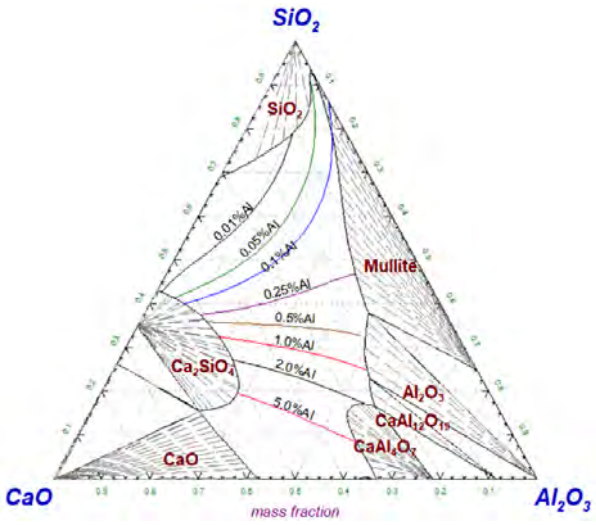


Figure 4.32 *Calculated iso-content contours for Al of FeSi50/slag equilibria at 1600°C. The FactSage commercial software and its FToixd and FTlite databases have been used.*

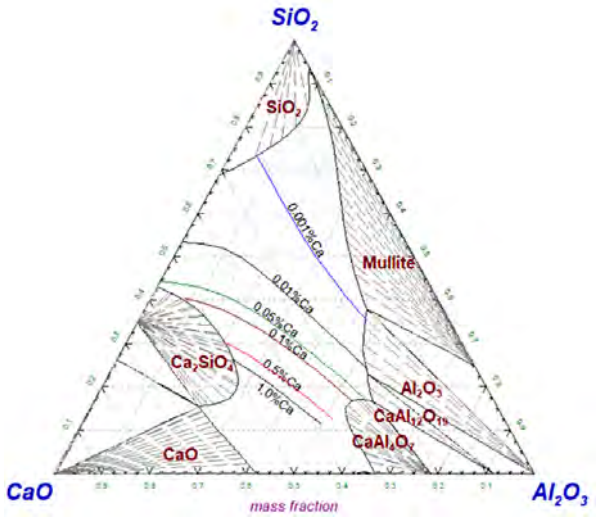


Figure 4.33 *Calculated iso-content contours for Ca of FeSi50/slag equilibria at 1600°C. The FactSage commercial software and its FToixd and FTlite databases have been used together with the updated activity coefficient from Jacobsson and Tangstad (2015).*

Volatile impurities

Moisture and chemically bound H_2O in the feed materials, together with volatile matter from coke, coal, char, and woodchips, are transported upwards through the charge by CO and SiO gases generated in the deeper, hotter regions of the furnace. During the initial heating stages, these volatiles are typically released as H_2O, H_2, CO, CO_2, and various hydrocarbons (C_xH_y).

Nitrogen enters as an organic constituent of the reductants. In the presence of alkali metal vapours at temperatures above 400°C, it forms alkali metal cyanides (KCN or NaCN). At temperatures above 1300°C, it forms HCN gas if hydrogen is also present at this stage. In the absence of these elements, the nitrogen is expelled as gaseous CN and C_2N at elevated temperatures (Jalkanen *et al.*, 1995). Possible cyanide emissions may cause an environmental problem in a closed furnace operation, but they will be effectively eliminated by combustion in an open or semi-closed furnace. Thermal NO_x is generated by direct oxidation of N_2 at temperatures above 1400°C, and reduced local temperatures on the charge top are therefore beneficial for reducing the NO_x emissions (Andersen, 2023; Kamfjord, 2012).

Sulfur, like nitrogen, is an inherent impurity in the reductant, but it is also present in sulfide minerals, e.g. pyrite. The fraction associated with the organic material is expected to be driven off as H_2S or COS at an early stage, together with sulfur liberated by the decomposition of pyrite. This decomposition takes place at about 700°C through the reaction:

$$FeS_2 = FeS + \frac{1}{2}S_2(g) \qquad [4.32]$$

The remaining sulfur, present as lower metal sulfides, is likely to survive up to the metal forming temperature, where an unknown fraction may be transferred to the gaseous state in the form of SiS(g).

From the mass balance and sulphur analyses for the various reduction materials used in ferrosilicon smelting given in we can calculate the weight-ratio between sulphur charged and silicon recovered as metal to be. This is about two orders of magnitude larger than recorded sulfur contents of tapped metal indicating that 98–99% of the charged sulfur leaves the process with the off-gases. This is in accordance with Kamfjord (2012) for a Si furnace, but higher than the reported values for a FeSi-furnace (Myrhaug, 2003).

Phosphorus, which is a critical impurity when metal quality is concerned, is also an inherent element in organic materials, but is in addition found as mineral particles, mainly in the form of apatite ($Ca_3(PO_4)_2$). Under oxidizing conditions, oxides of phosphorus volatilize at around 300°C as $P_5O_{10}(g)$, but in the presence of C/CO they form gaseous P_4O_6 at even lower temperatures, provided that the carbon reacts at such a low temperature. This component can survive in the presence of C/CO up to around 1250°C, where $P_2(g)$ becomes the dominating species. $P_2(g)$ is also the dominating species formed when elemental phosphorus evaporates at 907°C. The phosphorus tied up in the mineral apatite needs to be liberated by the reaction:

$$Ca_3\left(PO_4\right)_2 + 5C = 3CaO + P_2\left(g\right) + 5CO\left(g\right) \qquad [4.33]$$

This reaction proceeds to the right at t > 1430°C at a total pressure of 1 bar, but if the product gases are transported by flowing CO, it will proceed at reduced speed, also at lower temperatures.

The information above leads to the conclusion that phosphorus entering the process with the reductants should be efficiently transferred to the gas phase and flushed away. This may be true for a silicon process in which phosphorus is the only impurity, but it is not the case in a process where strong phosphide-forming metal impurities, like iron, manganese, magnesium and calcium, are present, as shown in the mass balances from Myrhaug (2003) and Kamfjord (2012) as shown previously in this chapter.

Iron, in particular, is expected to be in a metallized state, ready to react with gaseous P_2, at least in the area where the apatite decomposes, and thus contribute to the transport of phosphorus into the metal phase. From the thermodynamics of liquid steel, it is known that the presence of silicon in iron increases the activity coefficient of phosphorus. This implies that the efficiency of iron as a carrier for phosphorus decreases as the iron picks up silicon on its way towards the furnace hearth.

The amount of phosphorus that enters the pool of liquid metal is expected to remain there and appear in the tapped metal with typical concentrations of 25–50 ppmw and 130–300 ppmw P for Si-metal and Fe75Si, respectively. The argument behind this statement is based on data from the experimental work of Miki and Zaitsev, showing that the equilibrium pressure of mono- and diatomic phosphorus vapour over silicon with 50 ppmw P at 1600°C is

of the order of 10^{-8} bar (Miki *et al.*, 1996; A.I. Zaitsev *et al.*, 2001). Thus, the expected evaporation rate of phosphorus at an ambient pressure of one bar is extremely slow.

Potassium will be easily reduced from the oxide phase and produce potassium gas, which will leave the furnace and oxidize on the silica fume. According to Kamfjord (2012) and Myrhaug (2003), 90–100% of the potassium will leave the furnace, and 0–10% will enter the slag according to Figure 4.22. Usually, potassium is not found in the slag inside the furnace during excavations; however, exceptions are found with ~ 5% of K in the slag (Folstad, 2023; Hoover *et al.*, 2022). Potassium will be more stable in a slag than in K_2O or K_2CO_3. This can be illustrated by the temperature at which the partial pressure of potassium gas is about 1% i. e. 700°C in equilibrium with K_2O, 1050°C in equilibrium with K_2CO_3 and about 1500°C in equilibrium with the silicate ($K_2O \cdot SiO_2$).

4.4 Alloying elements

Various grades of ferrosilicon, with 45, 66, and 75% Si being the most common; silicomanganese with ~20 and 30% Si; silico-chromium; and calcium silicides containing up to 40 and 60% Si are all examples of commercial alloys with a high content of silicon.

These products are formed from multicomponent systems, as is also the case for silicon metal if impurities are included as part of the system. We recall from Chapter 2 that three condensed phases are needed to define our system of three components at a given temperature. As stated by Gibbs phase rule, the number of degrees of freedom increases by one for each new element added. If these additional elements are in fixed proportions to the main element, however, as is the case for a given charge mixture, an equal number of compositional restrictions is imposed on the system. Thus, the multicomponent system is still defined by the coexistence of three condensed phases at a given temperature.

The addition of the foreign oxides needed to produce the above-mentioned alloys, as well as the accompanying oxides present as constituents of ore minerals and those added deliberately as fluxing agents, may affect the silica reduction in various ways. A common characteristic is the effect caused by a lowering of the silicon activity in the metal phase, as already discussed in this

chapter. Another is slag formation, which is inevitable in processes for making silicomanganese, silico-chromium and calcium silicides, but not to the same extent in ferrosilicon and silicon smelting. Extensive slag formation changes the inner structure of the furnace and, thus, also the conditions for heat and mass transfer in the process, but it does not change the phase relations and the equilibrium that define the conditions for silica to be reduced. Thus, slag formation alone affects the thermodynamics of the system only by the effect it may have on the silica activity. The situation becomes different, however, if new phases appear in the high-temperature region of the system. This is the case in processes for making silico-chromium and calcium silicides, where phases like $Cr_5Si_3C_x$ and CaC_2, respectively, may form in the presence of the metal phase under given conditions. Phase constitutions that are different from those given in Chapter 2 will then determine the equilibrium conditions in the system. Consequently, these types of alloys are excluded from further discussion in this volume.

Ferrosilicon

Iron as an alloying element is added either in the form of scrap iron, mill scales, or iron ore, as lumpy material or as pellets. Independent of how it is added, however, iron is expected to enter the high-temperature region of the process (T > 1500°C) in a metallic state, as has been discussed previously in this chapter. An interesting question to discuss in this connection is how the reduction of the iron oxides proceeds, and how it may affect the fixed C balance of the process.

Let the symbol n_{Fe} (mol Fe per mol Si) define the amount of iron needed to produce a specific grade of ferrosilicon. If this iron enters as hematite pellets, which are reduced by CO in their solid state, it will occur in two consecutive steps:

$$FeO_{15} \rightarrow FeO \rightarrow Fe$$

As they are descending in a counter-current flow of gas produced from the idealized gross reaction:

$$SiO_2 + 2C = Si + 2CO$$

Table 4.6 shows the accumulated change in the gas composition for the completion of each reduction step for various grades of ferrosilicon, starting from 100% CO which enters from below.

Table 4.6 *Accumulated change in gas composition (%CO/(CO + CO_2)) caused by the stepwise reduction of hematite by CO during the production of various grades of ferrosilicon.*

Reduction steps (accumulated effect)	Direction of gas flow	FeSi75 n_{Fe} = 0.168	FeSi66 n_{Fe} = 0.259	FeSi45 n_{Fe} = 0.615
$FeO_{1.5}$ to FeO		87.4% CO	80.6% CO	53.9% CO
FeO to Fe		91.6% CO	87.0% CO	69.3% CO
Reducing gas	2 CO per Si	100% CO	100% CO	100% CO

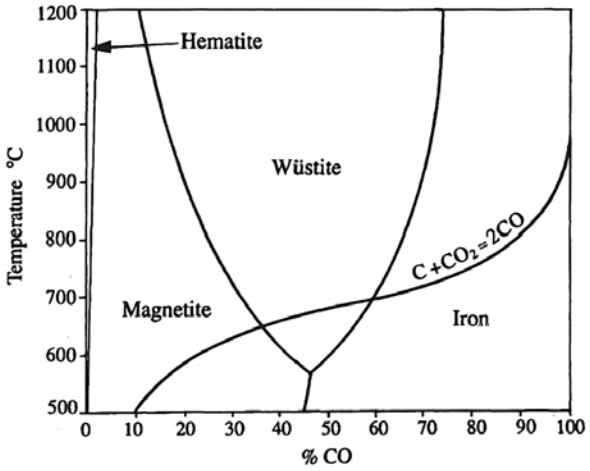


Figure 4.34 *Stability of iron oxides and solid C in CO–CO_2 mixtures of atmospheric pressure as function of temperature.*

If the values in Table 4.6 are compared with the stability of iron oxides in CO–CO_2 mixtures, as shown in Figure 4.34, it becomes evident that the quantity of CO produced by silica reduction in the heart of the smelting furnace can reduce the amount of hematite needed for the production of FeSi75 and FeSi66 at any temperature shown in the diagram. However, the amount of CO gas produced is not enough for complete FeOx reduction in the production of FeSi45 if

temperatures above 650–900°C are required. Figure 4.34 also shows that the product gas formed by the reduction of the iron oxides becomes unstable in the presence of solid C at temperatures above 700–830°C. Thus, if the last step of iron oxide reduction takes place at higher temperatures, thermodynamics of the system predict a net consumption of fixed C. The extent to which this happens, however, depends on the relative rates of the two reactions:

$$FeO + CO = Fe + CO_2 \quad [4.34]$$

$$CO_2 + C = 2CO \text{ (Boudouard reaction)} \quad [4.35]$$

In this connection, the reactivities of the iron ore pellets and the reductants used become key properties, along with residence time in the appropriate temperature range. Since the Boudouard reaction rate is the more temperature sensitive of the two, and is believed to initiate at around 900°C when reactive reductants are used, a slow increase in temperature up to this level is favorable. A simple heat balance indicates that, in smelting of FeSi75, this is achievable through an exchange of heat with the gas phase. Another factor that prevents fixed C from being consumed is that the char, produced in situ from coal and representing a reactive fraction of the reductants, is still giving off hydrocarbons; these are the first to react with CO_2. When charcoal is used, which is more reactive than coal, the extent of the Boudouard reaction will increase.

Although this may tempt us to conclude that, in the smelting of FeSi75, there is no need for extra additions of fixed C due to the use of iron ore pellets as the source for iron, these corrections are needed in the production of FeSi45 and probably also when smelting FeSi66. This statement is, however, disputed by experienced metallurgists, who have found it necessary to compensate for the reduction of FeO by the addition of fixed C also when smelting FeSi75. Their argument for this is the measured high temperatures of the gases leaving the furnace charge, which make the CO_2 unstable in the presence of C or volatiles.

When entering the high temperature region of the process, metallic iron dissolves carbon, and droplets of carbon-saturated iron may form at as low a temperature as 1153°C. If exposed to gas that contains SiO, these droplets can react and take silicon into solution, i.e. by the reaction:

$$SiO(g) + C = Si + CO \quad [4.36]$$

The capacity of the iron to take silicon into solution under the prevailing conditions is determined by the equilibria:

$$SiO_2(s) + C(s) = \underline{Si} + 2CO(g) \text{ at } t \leq 1500°C$$

$$SiO_2(s) + 2SiC(s) = 3\underline{Si} + 2CO(g) \text{ at } 1800°C \leq t \leq 1500°$$

as well as the silicon activity relations in C-saturated Fe–Si–C alloys. Results of equilibrium calculations on the iron-based system at P_{tot} = 1 bar, using data of (Rein, 1965), are shown by the dash-dotted curve in Figure 4.8, where the equivalent curve for the manganese-based system also is shown (Ding, 1993).

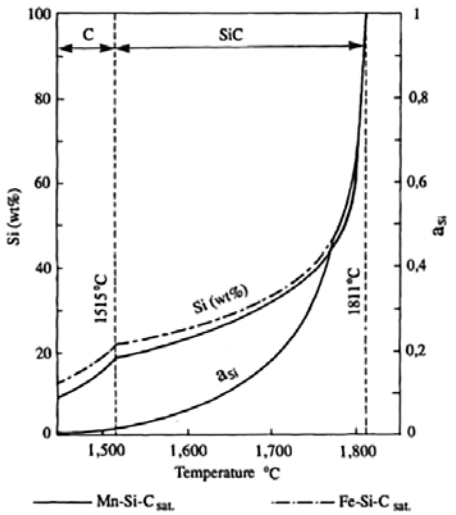


Figure 4.35 *Activity and concentration of Si as function of temperature for Fe–Si–C_{sat} and Mn-Si–C_{sat} alloys in equilibrium with SiO_2 at $P_{tot} = p_{CO} + p_{SiO} + p_{Mn}$ = 1 bar (Ding, 1993).*

The solubility of carbon in these systems varies with the concentration of silicon. In the iron-based system, at e.g. 1600°C, the carbon content drops from 5.4% C in the silicon-free alloy to 0.4% C at 22.4% Si, where the metal coexists with both graphite and SiC; it then decreases further to a minimum at around 50% Si within the stability range of SiC, as shown in Figure 4.36.

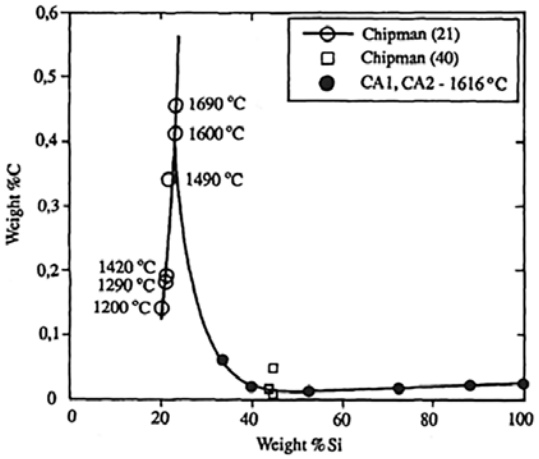


Figure 4.36 *Carbon in Fe–Si alloys in equilibrium with SiC at 1616°C and the graphite/SiC boundary for various temperatures (Ottem, 1993).*

The net heat effect of adding scrap iron to silicon is slightly exothermic. This results from the sum of two effects:

1. The heat required to raise the temperature of iron from room temperature to 1600°C
2. The exothermic heat of mixing of liquid iron and silicon at 1600°C.

The latter property can be taken from the integral relative enthalpy of mixing in the binary Fe–Si system at 1600°C. It is safe to say that these data also apply to carbon-saturated alloys, especially at high silicon concentrations, where the carbon solubility is extremely low, as Figure 4.36 shows.

Calculated heat effects for 1 mole of FeSi75 with $X_{Si} = 0.86$ are given in the first column of Table 4.7. The contributions from two alternative models for iron oxide reduction are also included in the next columns.

As shown, the specific energy consumption decreases slightly when the iron is added in oxidic form if the reduction proceeds indirectly with CO throughout. However, the energy requirement increases by about 200 kWh per tonne Si if the final step of the reduction leads to consumption of fixed C or volatile hydrocarbons. Independent of the net effect, the process benefits

from the fact that the endothermic terms of the heat balance in Table 4.7 are all located in a temperature region where the capacity of the charge to absorb heat is a critical factor.

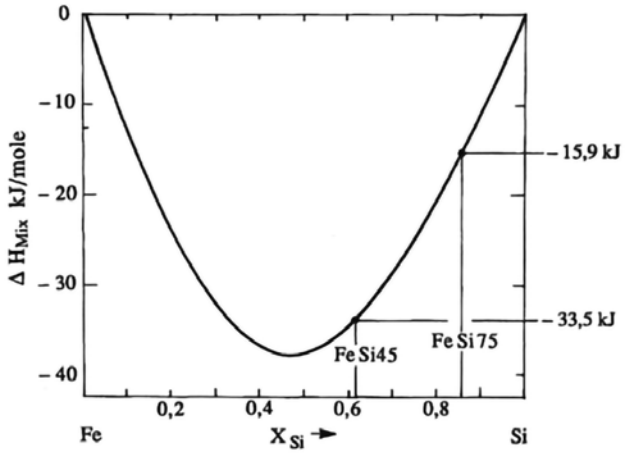


Figure 4.37 *Integral relative enthalpy of mixing in the Fe–Si system at 1600°C based on data from Kubaschewski (Kubaschewski et al., 1993).*

Table 4.7 *Calculated heat effects caused by alternative ways of adding and reducing the iron in the smelting of FeSi75 (X_{Si} = 0.86).*

Contribution to the enthalpy balance for n_{Fe} = 0.14	Addition as scrap iron	Addition as iron ore pellets and reduction of	
		$FeO_{1.5}$ →FeO by CO FeO→Fe by CO	$FeO_{1.5}$→FeO by CO FeO→Fe by C
	-	0.14 × 5 = 0.7	0.7
	-	0.14 × (−19) = −2.7	0.14 × 153.5 = 21.5
1.	0.14 × 77 = 10.8	10.8	10.8
2.	1 × (−15.9) = −15.9	−15.9	−15.9
Net heat effect (kJ)	−5.1	−7.1	17.1
Net energy (kWh/tonne Si)	−5.8	−82	197

In summary, adding Fe into the system will bring the following process changes:

1. For processes running at the same silicon yield, the addition of metallic iron slightly lowers (< 0.7%) the consumption of electric energy per unit of silicon produced. The specific energy consumption also decreases by ~1% if the iron is fed as oxide pellets, provided they are completely reduced indirectly by CO. However, it increases by 2–3% if the reduction proceeds directly by formation of CO. A slight increase in the specific consumption of fixed C may be associated with the latter mode of reduction.
2. The presence of iron improves the silicon yield of the process and, thereby, also the specific energy consumption. Effects contributing to this are:
    i. a lowering of the silicon activity, which makes the silica reduction possible at lower s-values. As a result, less SiO must be recovered in the upper shaft.
    ii. an increase in the capacity of the charge to adsorb heat released by condensation of SiO and to react chemically with SiO.

3. Iron increases the density of the metal phase. This increase in metal density improves the conditions for separating slag and metal in the furnace hearth, as well as in the tapping ladle.

References

Andersen, V. (2023) *Flue gas recirculation for the silicon process. Doctoral thesis 2023:135*. Norwegian University of Science and Technology (NTNU), Trondheim, Norway. Available at: https://hdl.handle.net/11250/3069034

Bakke, P. and Klevan, O.S. (1995) 'Thermodynamics of liquid silicon based alloys', in *14th PTD Conference Proceedings*. Presented at the 14th PTD Conference, Orlando, FL, USA, pp. 155–165.

Carlberg, T. (1986) 'Calculated solubilities of oxygen in liquid and solid silicon', *J. Electrochem. Soc.*, *133*, p. 1940. Available at: https://doi.org/10.1149/1.2109053

Dalaker, H. and Tangstad, M. (2009a) 'Time and temperature dependence of the solubility of carbon in liquid silicon equilibrated with silicon carbide and its dependence on boron levels', Materials Transactions, *50*, pp. 1152–1156. Available at: https://doi.org/10.2320/matertrans.M2009034

Dalaker, H. and Tangstad, M. (2009b) 'Temperature dependence of the solubility of nitrogen in liquid silicon equilibrated with silicon nitride', Mater. Trans., *50*, pp. 2541–2544. Available at: https://doi.org/10.2320/matertrans.M2009164

Ding, W. (1993) *Equilibrium r*elations *in the p*roduction *of manganese alloys*. Doctoral thesis. Norges Tekniske Høgskole (NTH), now Norwegian University of Science and Technology (NTNU), Trondheim, Norway.

Dumay, C. and Cramb, A.W. (1995) 'Density and interfacial tension of liquid Fe–Si alloys', *Metallurgical and Material Transactions B*, *26B*, pp. 173–176.

Eldridge, J.M., Miller, E. and Komarek, K.L. (1967) 'Thermodynamic properties of liquid magnesium-silicon alloys; discussion of the Mg-group IVB systems', *Trans. Met. Soc. AIMFE*, *239*, pp. 775–781.

Elliot, J.F., Gleiser, M. and Ramakrishna, V. (1963) *Thermochemistry for steelmaking*. Addition-Wesley, Pergamon Press.

Engh, T.A., Kvithyld, A. and Sigworth, G. (2021) *Principles of metal refining and r*ecycling. Oxford University Press.

Eustathopoulos, N., Nicholas, M.G. and Drevet, B. (1999) *Wettability at high temperatures*. Elsevier.

Folstad, M. and Tangstad, M. (2021) 'SiO_2–CaO–Al_2O_3 slags in Si/FeSi furnaces', in *Proceedings of* INFACON XVI. Trondheim, Norway. Available at: https://doi.org/10.2139/ssrn.3922187

Folstad, M.B. (2023) Slag and its effect on Si and FeSi production. Doctoral thesis 2023:317. Norwegian University of Science and Technology (NTNU), Trondheim, Norway. Available at: https://hdl.handle.net/11250/3096091

Hardy, S.C. (1984) 'The surface tension of liquid silicon', *Journal of Chrystal Growth*, *69*, pp. 456–460. Available at: https://doi.org/10.1016/0022-0248(84)90355-5

Hauge, E.G.R. (2022) *Scaling in the Si o*ff*-gas systems – the effect of alkali content*. MSc thesis. Norwegian University of Science and Technology (NTNU), Trondheim, Norway. Available at: https://hdl.handle.net/11250/3023783

Hoover, H., Andersen, V., Saevarsdottir, G. and Tangstad, M. (2022) 'Excavation of 160 kW pilot scale Si furnace', *AMMS*, *9*. Available at: https://doi.org/10.31031/AMMS.2022.09.000707

Jakobsson, L.K. and Tangstad, M. (2015) 'Thermodynamic activities and distributions of calcium and magnesium between silicon and CaO–MgO–SiO_2 slags at 1873 K (1600°C)', *Metallurgical and Materials Transactions B*, *46*, pp. 595–605. Available at: https://doi.org/10.1007/s11663-014-0268-8

Jalkanen, H., Kojo, M., Krogerus, H., Niemelä, P. and Oikarinen, P. (1995) 'Cyanides in FeCr submerged arc furnace production. Theoretical and practical considerations', in *Proceedings of INFACON VII*. Trondheim, Norway, pp. 179–190. Available at: https://www.pyrometallurgy.co.za/InfaconVII/179-Jalkanen.pdf

Jusnes, K.F., Hjelmseth, R., Folstad, M.B., Ditlefsen, N.S. and Tangstad, M. (2021a) 'Investigation of slag compositions and possible relation to furnace operation of a FeSi75 furnace', in *Proceedings of INFACON XVI*. Trondheim, Norway. Available at: https://doi.org/10.2139/ssrn.3930046

Jusnes, K.F., Ringdalen, E. and Tangstad, M. (2021b) 'The effects of cristobalite formation on disintegration of quartz', *Materials at High Temperature*.

Kamfjord, N.E. (2012) *Mass and energy balances of the silicon process*. *Doctoral thesis 2012:162*. Norwegian University of Science and Technology (NTNU), Trondheim, Norway. Available at: https://hdl.handle.net/11250/249043

Klevan, O.S. (1997) *Removal of C and SiC from Si and FeSi during ladle refining and solidification*. *Doctoral* thesis *1997:11*. Norwegian University of Science and Technology (NTNU), Trondheim, Norway. Available at: https://hdl.handle.net/11250/248844

Kubaschewski, O., Alcock, C.B. and Spencer, P.J. (1993) *Materials t*hermochemistry. *6th* edn. Pergamon Press.

Liang, S.-M. and Schmid-Fetzer, R. (2014) 'Modeling of thermodynamic properties and phase equilibria of the Si-P system', *J. Phase Equilib. Diffus.*, *35*, pp. 24–35. Available at: https://doi.org/10.1007/s11669-013-0269-3

Lu, H.M. and Jiang, Q. (2005) 'Surface tension and its temperature coefficient for liquid metals', *J. Phys. Chem. B*, *109*, pp. 15463–15468. Available at: https://doi.org/10.1021/jp0516341

Miki, T. (1999) 'Thermodynaic properties of Si–Al, –Ca, –Mg binary and Si–Ca–Al, –Ti, –Fe ternary alloys', *JIM*, *40*, pp. 1108–1116.

Miki, T., Morita, K. and Sano, N. (1997) 'Thermodynamic properties of titanium and iron in molten silicon', *Metall Mater Trans B*, 28, pp. 861–867. Available at: https://doi.org/10.1007/s11663-997-0014-6

Miki, T., Morita, K. and Sano, N. (1996) 'Thermodynamics of phosphorus in molten silicon', *Metall Mater Trans B*, 27, pp. 937–941. Available at: https://doi.org/10.1007/s11663-996-0007-x

Mostafa, A. and Medraj, M. (2017) 'Binary phase diagrams and thermodynamic properties of silicon and essential doping elements (Al, As, B, Bi, Ga, In, N, P, Sb and Tl)', *Materials*, *10*, p. 676. Available at: https://doi.org/10.3390/ma10060676

Mukai, K., Yuan, Z., Nogi, K. and Hibiya, T. (2000) 'Effect of the oxygen partial pressure on the surface tension of molten silicon and its temperature coefficient', *ISIJ International*, *40*, pp. S148–S152. Available at: https://doi.org/10.2355/isijinternational.40.Suppl_S148

Myrhaug, E.H. (2003) Non-fossil reduction materials in the silicon process – properties and behaviour. Doctoral thesis 2003:67. Norwegian University of Science and Technology (NTNU), Trondheim, Norway.

Nogi, K. and Ogino, K. (1994) 'The effect of oxygen on the surface tension of molten silicon', *Journal of the Japan Institute of Metals*, *58*, pp. 437–442.

Nozaki, T., Yatsurugi, Y. and Akiyama, N. (1970) 'Concentration and behavior of carbon in semiconductor silicon', *J. Electrochem. Soc.*, *117*, p. 1566. Available at: https://doi.org/10.1149/1.2407385

O'Mara, W.C. (1990) 'Oxygen, carbon and nitrogen in silicon', in *Handbook of Semiconductor Silicon Technology*. Elsevier S&T, pp. 451–549.

Oterkjær, H. (1976) *A study of the Al- and Ca-balance of industrial production of FeSi75*. *Doctoral thesis*. Norges Tekniske Høgskole (NTH), now Norwegian University of Science and Technology (NTNU), Trondheim, Norway.

Ottem, L. (1993) Solubility and thermochemical data of oxygen and carbon in liquid alloys of silicon and ferrosilicon. SINTEF Report No. STF34 F93027. Trondheim, Norway.

Rao, Y.K. and Belton, G.R. (1981) 'Thermodynamic properties of Mg–Si system', in *Chemical Metallurgy – A Tribute to Carl Wagner*. Presented at the Carl Wagner commemorative symposium on metallurgical thermodynamics and electrochemistry, TMS-AIME, pp. 75–96.

Rein, R. (1965) 'Activities in the liquid solution SiO_2–CaO–MgO–Al_2O_3 at 1600°C', *Transactions of the Metallurgical Society of AIME*, *223*, pp. 415–425.

Robinson, V.S. and Tarby, S.K. (1971) 'The thermodynamic properties of liquid Ag–Si alloys', *Metall Trans*, *2*, pp. 1347–1352. Available at: https://doi.org/10.1007/BF02913358

Roscoe, R. (1953) 'The viscosity of suspensions of rigid spheres', *Brit. J. Appl. Phys.*, *3*, pp. 267–269. Available at: https://doi.org/10.1088/0508-3443/3/8/306

Saadieh, R. (2024) *Process p*henomena *in furnaces producing ferrosilicon alloys*. Doctoral thesis 2024:199. Norwegian University of Science and Technology (NTNU), Trondheim, Norway. Available at: https://hdl.handle.net/11250/3132796

Safarian, J., Kolbeinsen, L. and Tangstad, M. (2012) 'Thermodynamic activities in silicon binary melts', *Journal of Materials Science*, *47*, pp. 5561–5580. Available at: https://doi.org/10.1007/s10853-012-6449-4

Sigworth, G.K. (2020) 'Thermodynamics of dilute liquid silicon alloys', *Canadian Metallurgical Quarterly*, *59*, pp. 251–261. Available at: https://doi.org/10.1080/00084433.2020.1771012

Stull, D.R. and Prophet, H. (1971) JANAF thermochemical tables. 2nd edn. NIST.

Tang, K., Chou, K.-C. and Lu, X. (2013) 'Modeling the interfacial tension of Fe–O–Si/SiO_2–CaO–Al_2O_3–FeO system using the modified Gibbs energy minimization technique', *Journal of M*etals *and M*etallurgy.

Tang, K., Olsen, J., Johansen, S. and Kolbeinsen, L. (2009) 'Modeling of the surface/interfacial tension for the ladle refining of silicon metal process', in *Proceedings of the VIII International Conference on Molten Slags, Fluxes and Salts*. Santiago, Chile.

Tang, K., van der Eijk, C., Gouttebroze, S., Du, Q., Safarian, J. and Tranell, G. (2022) 'Rheological properties of Al_2O_3–CaO–SiO_2 slags', *Calphad*, *77*, 102421. Available at: https://doi.org/10.1016/j.calphad.2022.102421

Turkdogan, E.T. (1983) *Physiochemical properties* of *of slags and glasses*. London: The Metal Society.

Utigard, T. (1994) 'Surface and interfacial tensions of iron based systems', *ISIJ International*, *34*, pp. 951–959.

Wagner, C. (1952) *Thermodynamics of alloys*. Cambridge, MA: Addison-Wesley Press.

Yaws, C.L., Li, K.-Y., Hopper, J.R., Fang, C.S. and Hansen, K.C. (1981) *Process feasibility study in support of silicon material* Task *1*. Final *report to Jet Propulsion Laboratory*. Californian Institute of Technology under NSA contract NA7100 for the U.S. Dept. of Energy, Division for Solar Energy.

Yoshikawa, T., Morita, K., Kawanishi, S. and Tanaka, T. (2010) 'Thermodynamics of impurity elements in solid silicon', *Journal of Alloys and Compounds*, *490*, pp. 31–41. Available at: https://doi.org/10.1016/j.jallcom.2009.09.190

Yurkov, A.L. and Polyak, B.J. (1995) 'Contact phenomena in interactionsin the system SiC–$SiO_{2-}R_xO_y$ in condensed matter', *J. Mat. Sci.*, *30*, pp. 4469–4478.

Zaitsev, A.I. and Kodentsov, A.A. (2001) 'Thermodynamic properties and phase equilibria in the Si-B system', *JPE*, *22*, pp. 126–135. Available at: https://doi.org/10.1361/105497101770338987

Zaitsev, A.I., Litvina, A.D. and Shelkova, N.E. (2001) 'Thermodynamic properties of Si–P melts', *High Temperature, 39*, pp. 227–232. Available at: https://doi.org/10.1023/A:1017570715796

Ringdalen, E. (2026) 'The technical silicon process', in M. Tangstad, G. Tranell, H. Tveit and E. Ringdalen (Eds.), *Production of high silicon alloys* (2. ed.) (pp. 167–228). Fagbokforlaget. https://doi.org/10.55669/oa880805

5

The technical silicon process

Eli Ringdalen

5.1 The furnace and the plant

Over more than 100 years of silicon production, silicon plants have developed towards bigger and more sophisticated equipment, greater automatization, and better control systems, as well as the implementation of technologies for energy recovery and reduced emissions. Nevertheless, the principal process is much the same. Industrial production of silicon and ferrosilicon is normally performed in low-shaft electrical reduction furnaces. The furnace is also named a submerged-arc furnace (SAF). Installed capacity, that is, the load of the furnace, is normally used as the 'size' of the furnace. Silicon and ferrosilicon furnaces may vary in size from approximately 1 MW up to 50 MW. The furnace requires infrastructure and supporting equipment for handling large streams of raw materials, liquid and solid metals, byproducts and gases, as well as for the supply and recovery of energy. As shown in Figure 5.1, a silicon plant thus consists of several production units (Tangstad, 2013). These can be divided into the following groups.

- The furnace where the silicon and ferrosilicon production takes place.
- Raw materials, their storage, handling and supply
- The electrical system supplying energy to the furnace.
- Off-gas handling and energy recovery system
- Units for processing and handling of produced silicon and ferrosilicon
- The control system

This work is licensed under the Creative Commons Attribution 4.0 International License.
To view a copy of this license, visit https://creativecommons.org/licenses/by/4.0/

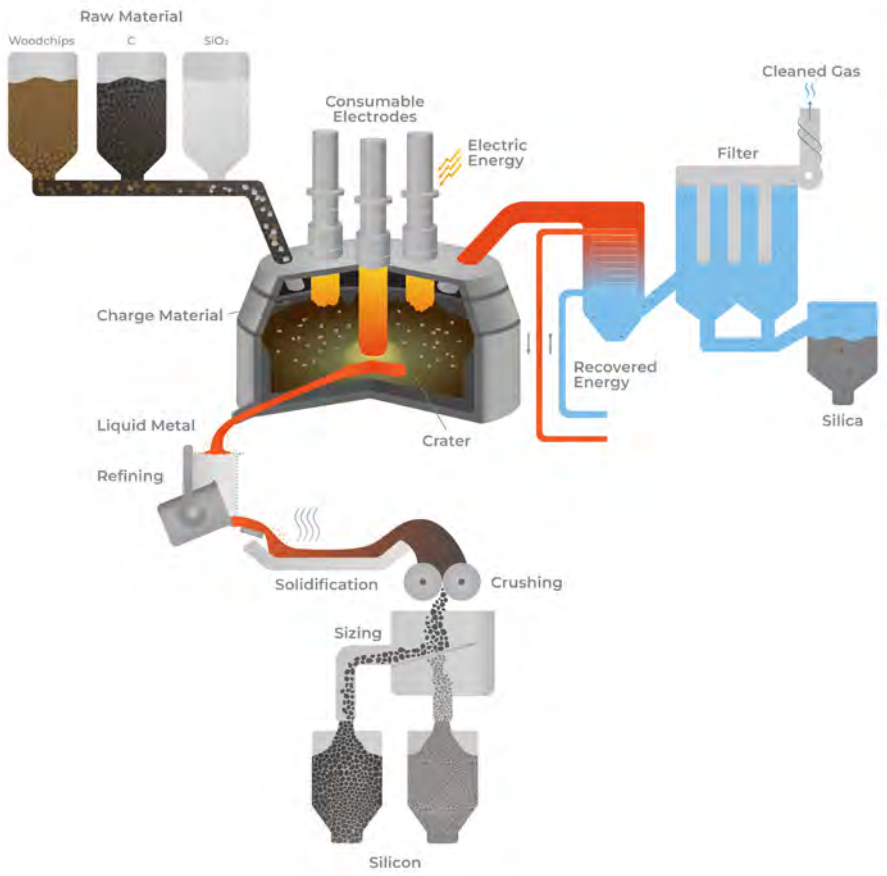


Figure 5.1 *A modern ferrosilicon plant with energy recovery and gas cleaning equipment. The furnace is semi-closed, with moveable ports marked with the horizontal lines in the upper part of the furnace. (Figure redrawn by Lingyi Ren). Based on Tangstad (2013).*

5.2 The processes taking place in the silicon furnace

The processes that take place in the silicon furnace form the basis for the requirements for the raw materials, the furnace, and the other parts of the silicon plant. The overall Si-producing mass balance is given by reaction [5.1]

$$SiO_2 + 2C = Si + 2\,CO \qquad \Delta H°_{2000°C} = 687\ kJ/mol \qquad [5.1]$$

The main raw materials are a silicon source, usually SiO_2 in the form of quartz, and a carbon reductant, most often a mixture of coal and biocarbon. Woodchips added to give a more porous charge will also contribute some carbon. In FeSi production, iron—either iron oxide or metallic iron—is another important raw material. Other raw materials, for instance limestone, may also be used, depending on the case.

Furnace excavations have established a schematic picture of the inner structure of Si and FeSi furnaces (Ksiazek *et al.*, 2016). As shown in Figure 5.2, they can be divided into four main reaction zones: the pre-reaction zone, the reacting materials, sometimes a SiC crust, and the cavity. In addition, there is the metal bath at the bottom of the cavity, and the inactive slag zone, consisting mainly of slag, along the furnace walls.

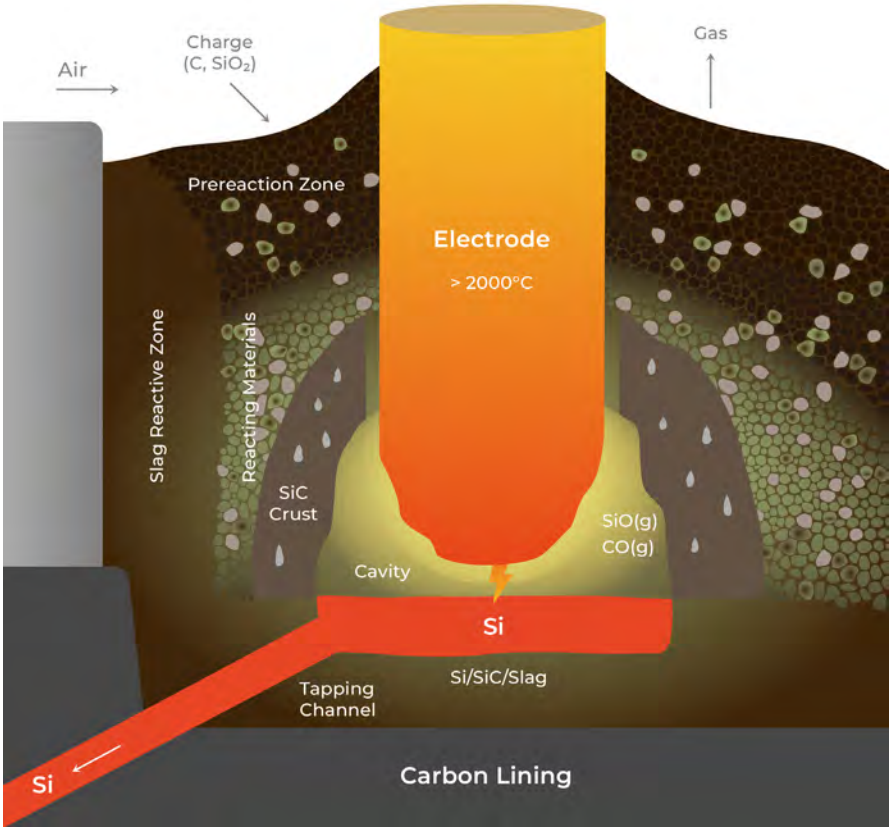


Figure 5.2 *Reactions and reaction zones in Si furnace. (Graphics: Lingyi Ren).*

The raw materials – the charge mixture with quartz and carbon source as the main constituents – are fed semi-continuously to the top of the pre-reaction zone (the charge top), where the temperature is around 700–1300°C (Johansen *et al.*, 1998). Liquid Si, at approximately 1900 °C (Ksiazek *et al.*, 2018), is tapped out at the bottom of the furnace. Off-gas, composed mainly of CO and SiO, leaves the pre-reaction zone at the charge top, where it burns with air to CO_2 and SiO_2. To obtain a high silicon yield, the off-gas must have a low SiO content. To obtain good furnace performance, there must be an even gas flow and good charge permeability in the furnace.

Quartz descends in the furnace and is reduced to SiO by reaction [5.5] and [5.6]. These reactions take place in the pre-reaction zone, the reacting materials zone, the SiC crust, and in the cavity at the top of the metal bath. The produced SiO will either react with carbon to β-SiC by reaction [5.4] in the pre-reaction zone or the reacting materials zone in the upper parts of the furnace. SiO will also react with SiC to Si by reaction [5.7] in the SiC crust or the cavity, where the temperature is higher. SiO gas that is not consumed by reaction [5.4] will either be captured in the charge by reaction [5.2] and [5.3] in the pre-reaction zone, or leave the charge mixture at the top of the furnace, followed by a decreased Si yield.

$$2SiO\,(g) = SiO_2(s, l) + Si(l) \qquad \Delta H^o_{1800°C} = -606\ kJ/mol \quad [5.2]$$

$$3SiO(g) + CO(g) = 2SiO_2(s, l) + SiC(s) \qquad \Delta H^o_{1800°C} = -1364\ kJ/mol \quad [5.3]$$

$$2C(s) + SiO(g) = SiC(s) + CO(g) \qquad \Delta H^o_{1800°C} = -78\ kJ/mol \quad [5.4]$$

$$SiO_2(s, l) + Si(l) = 2SiO\,(g) \qquad \Delta H^o_{2000°C} = 599\ kJ/mol \quad [5.5]$$

$$2SiO_2(s, l) + SiC\,(s) = 3SiO\,(g) + CO\,(g) \qquad \Delta H^o_{2000°C} = 1364\ kJ/mol \quad [5.6]$$

$$SiC\,(s) + SiO\,(g) = 2\,Si(l) + CO\,(g) \qquad \Delta H^o_{2000°C} = 167\ kJ/mol \quad [5.7]$$

Energy is supplied through the three electrodes, as described in Chapter 6. An electric arc is formed between the lower part of the electrode and either the metal bath or the SiC crust, forming a cavity around the electrode tip. Plasma in the cavity has a temperature higher than 3000 °C, which heats the

cavity walls (the SiC crust) by radiation. Electric current through the SiC crust generates additional energy for heating of the SiC crust and for endothermic reactions that take place in this zone. Here, the temperature is assumed to be more than 2000 °C. Tapped metal, both from Si and FeSi furnaces, has a temperature of around 1900 °C (Ksiazek *et al.*, 2018). The metal bath has at least this temperature inside the furnace.

Materials above the SiC crust are mainly heated by warm ascending gases generated in the lower zones in the furnace (the cavity and the SiC crust) and by exothermic reactions that take place higher up in the furnace. Back reactions with SiO – reactions [5.2] and [5.3], which are highly exothermic – are, together with reaction [5.4] (between SiO and C), the main contributors. Reactions in the material reaction zone with volatiles from carbon materials, and evaporation of water in woodchips and other raw materials, will also contribute to the temperature profile in the furnace. Burning of SiO and CO gas to SiO_2 and CO_2, above the charge top where oxygen is available, develops energy that gives a high off-gas temperature. The temperature can also be increased in a thin layer just below the top of the charge due to in-flow of oxygen in the materials at the top of the pre-reaction zone. Below the charge top, where oxygen is not present, the temperature decreases and is measured at around 600°C (Ksiazek *et al.*, 2021; Saadieh, 2024). Further down, the temperature will increase with depth. Modelled temperature profiles for selected Si and FeSi furnaces (Ringdalen *et al.*, 2019), though not valid for the upper, low temperature zones in the furnace, also indicate that the temperature does not increase linearly with increasing furnace depth. The raw materials are heated fast up to around 1600°C in the upper part of the furnace, in the pre-reaction zone and the upper part of the material reactions zone. In most of the furnace volume above the cavity, the temperature is between around 1600°C and 1800°C. An average heating rate of 5.5 °C/min and a material flow of around 0.3 m/hour has been estimated as normal for Si furnaces (Ringdalen *et al.*, 2019). In a 45 MW Si furnace, around 8000 Nm^3/h of gases is generated by the reaction in the furnace, giving a gas velocity in the material reaction zone of around 1 m/s (Nordhus, 2022). To have an even flow of gas, the material bed in these zones must have a high enough permeability. This limits the amounts of fines that can be present in the charge. The amount of fines in raw materials fed to the furnace, and generation of fines during their processing in the furnaces, are thus restricted as a part of raw material requirements.

SiO gas produced by the endothermic reaction [5.5] and [5.6] at high temperatures in the cavity and SiC crust will ascend to the reacting materials zone and pre-reaction zone, where the temperatures are lower. SiO will then react back to SiO_2 and SiC or Si by reactions [5.2] and [5.3], which are exothermic. Energy used in the cavity and SiC crust for reduction of SiO_2 to SiO by the endothermic reaction [5.5] and [5.6] will thereby be released in the material reaction zone and pre-reaction zone when SiO reacts back by reactions [5.2] and [5.3]. The extent depends on the amount of 'circulating' SiO. This transport of energy from the cavity and SiC crust to the reacting materials zone gives less energy available for final Si production in the SiC crust and cavity and is thus unwanted. This is discussed in more detail in Chapters 3 and 7.

To obtain a high silicon yield, reduction of SiO_2 to SiO by reaction [5.5] and [5.6] should take place at the higher temperatures in the cavity and SiC crust, where SiO gas is needed for the final production of Si by reaction [5.7]. A slow reaction rate for reaction [5.5] and [5.6] in the material reaction zone higher up in the furnace, where the temperature is lower, is thus preferred. SiO is produced at high temperatures in the cavity by reaction [5.5] when quartz pieces fall or molten quartz drips into molten Si in the crater, and by reaction [5.5] and [5.6] in the SiC crust and at the crater walls. SiO gas ascending from the crust will, in the material reaction zone, meet descending carbon and, at temperatures above around 1500 °C, and react with this to β-SiC according to reaction [5.4]. Complete conversion of carbon to SiC is crucial to achieve a high Si yield. Produced β-SiC will descend further down in the furnace and, in the SiC crust at temperatures above around 2000 °C, be transformed to α-SiC, which is the SiC polymorph found in the SiC crust. The final product, Si, is produced in the SiC crust and at the crater walls by reaction [5.7] between SiO and α-SiC. Produced silicon or ferrosilicon accumulates below the crater zone at the bottom of the furnace. It is tapped out through tap holes that are drilled through the lining.

When ascending SiO gas reacts back according to reaction [5.2] at lower temperatures in the material reaction zone, it will form a mixture of fine-grained SiO_2 and Si called brown condensate, while SiO gas that reacts with CO according to reaction [5.3] will form a fine-grained mixture of SiO_2 and SiC called white condensate. Condensates are abundant in the material reaction zone above the SiC crust, with brown condensates being most common. The condensates will glue the raw materials together, creating the so-called 'condensate layer'. To enhance gas flow from the lower to the upper part of the

furnace, and material flow downwards in the furnace, the condensate layer is regularly broken up with mechanical stoking from the top of charge.

Unreduced oxides in the raw materials, such as CaO and Al_2O_3 and others, will form a slag. Due to the relatively low amounts of these oxides in the raw materials, the amount of slag pr ton of alloy is relatively low. A small amount of slag is tapped out together with the alloy. Slag may also accumulate in the more inactive zones in the furnace and form a slag layer: a slag zone along the walls of the furnace and, in some cases, below the metal at the bottom of the cavity. Slag formation and its effect is discussed more in detail in Chapter 8.

5.3 Raw materials for silicon and ferrosilicon production

The main raw materials for current industrial Si and FeSi production are:

- Si-sources, normally one or several quartz sources.
- Reductants, various carbon sources.
- Iron sources for FeSi production, such as metallic iron or iron oxides.
- Wood chips to improve charge properties.

Smaller amounts are also used of:

- Additives for adjusting product quality and for refining.
- Recirculated internal and external waste materials.

The main raw materials are generally abundant. However, to be used in Si and FeSi production, the raw materials must meet specific criteria, which limits the available sources. Selecting suitable raw materials is therefore an important task in optimising Si and FeSi production. Raw material properties affect product quality, process performance and emissions.

Effects on product quality

The amount and type of contaminants that can be tolerated in the raw materials depend on the specific product. Silicon, and especially solar grade silicon,

requires pure raw materials, which limits raw material choice. The content of contaminants varies between different raw material sources. As illustrated in Figure 5.3, product quality is the result of the sum of each contaminant in all the raw materials and of the extent to which they end up in the product. The distribution of each contaminant between the different phases, and its content in the final product, can be calculated by a mass balance, where the distribution between the products is estimated or found using the boiling point model, as also discussed in Chapter 4 (Kero *et al.*, 2019; Myrhaug, 2003). In addition, electrodes contribute minor elements to the product. The relative importance of quartz, coal and electrodes to P, B and Fe content in solar grade silicon is illustrated in Figure 5.4 for a specific case (Myrhaug, 2003).

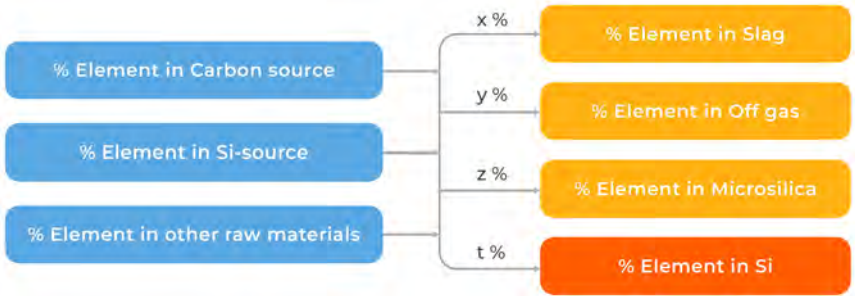


Figure 5.3 *Effect of raw materials on product quality.*

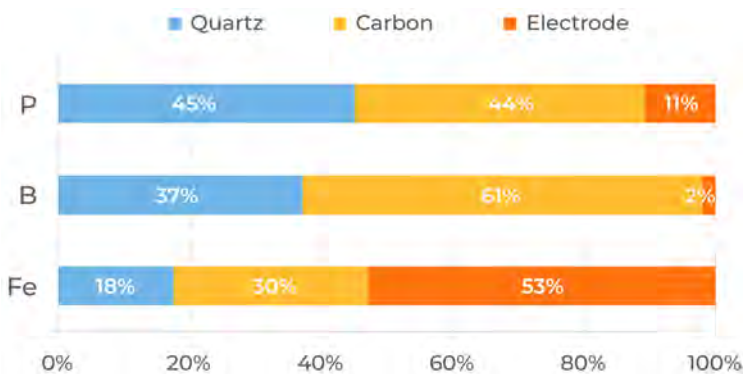


Figure 5.4 *Relative contribution of P, B and Fe from quartz, carbon and electrodes to solar grade silicon (Myrhaug, 2003) (Redrawn by: Lingyi Ren) [With permission L.V: Myrhaug].*

Raw material sizing

The required size and size distribution vary between raw materials, depending on their densities and required reactivities. The choice of size distribution also depends on the availability and cost of different fractions. Particles must be in a size that can be handled by the local material-handling and charging system. In addition, the minimum size must be limited to prevent raw materials being blown off from the charge top by the ascending off-gases. Loss of raw materials to the off-gas system increases raw material costs, but it may be more severe when it changes the carbon coverage. Wide size distributions, or large differences in sizing between different raw materials, may cause segregation and should therefore be avoided when this is not wanted. (Ringdalen *et al.*, 2022)

Reactions in a 20 MW Si furnace will develop around 1.3Nm^3/s of gas (Tveit *et al.*, 2020). Gas flow depends on the available area, but will be around 0.67 m/s at 1800 ^{o}C in the high-temperature zone in a 40 MW Si-furnace. The size distribution of raw materials must be within a range that ensures an even, well-distributed flow of gas through the material reaction and pre-reaction zone, up to the charge top. Build-up of high pressure and gas blows are mainly caused by the condensate layer (Tveit *et al.*, 2020) and by fine particles, less than around 2 mm (Ringdalen *et al.*, 2022).

The size distributions of raw materials in the furnace are normally different from the size distribution specified when they are purchased. As illustrated in Figure 5.5, raw materials disintegrate and generate fines during mining, transport to and handling at the plant, when they are fed to the warm charge top, and during heating in the furnace. The extent of fines generation at each step varies with raw material type and source.

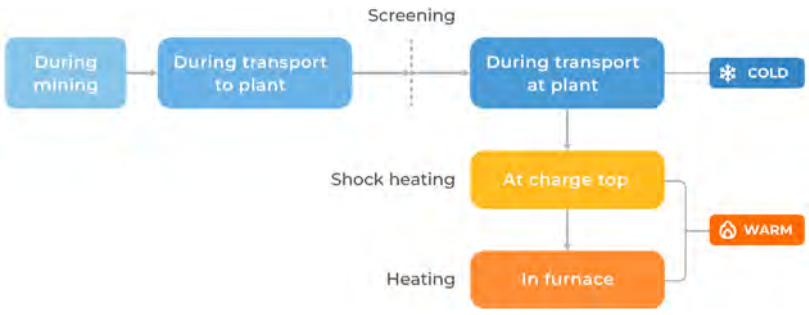


Figure 5.5 *Fines generation from raw materials in different steps during handling and processing.*

Silicon source – Quartz

Sources

The main silicon source is the mineral quartz, SiO_2. The main quartz sources are rocks such as quartzite, hydrothermal deposits, pegmatitic quartz and fluvial deposits. Normally, sources with a high content of SiO_2, above 98%, are used without any upgrading. At the mine, the quartz source is screened to the designated size, normally 10–150 mm, before it is shipped to the plant. Norwegian Si and FeSi producers use quartz both from national quartz sources and from quartz sources all over the world.

Role and effects in process

Silicon is produced from quartz by first reducing the quartz by reaction [5.5] and [5.6] to SiO, which is further reduced to Si by reaction [5.7].

$$2SiO_2 + SiC = 3SiO + CO \quad [5.5]$$

$$SiO_2 + Si = 2SiO \quad [5.6]$$

$$SiO + SiC = 2Si + CO \quad [5.7]$$

Final production of SiO takes place in the high temperature zone, around 1800°C. It is therefore preferred that most of the SiO is produced at high temperature, and that the reduction of quartz is slow at lower temperatures. The reaction mechanism is not well understood, but the reaction rate does not seem to depend on the quartz source itself (Folstad *et al.*, 2021; Sindland and Tangstad, 2021; Tangstad *et al.*, 2019). The reaction rate to SiO will, however, increase with decreasing particle size. Melting gives a higher contact area towards SiC and may increase the reaction rates. A large particle size and a long time to obtain final melting may thus be beneficial, as they promote reduction of quartz in the lower part of the furnace. At the same time, a large temperature interval between softening and melting may result in clogging in a large volume of the furnace, which is unwanted (Ringdalen *et al.*, 2019).

Properties

At 25 °C, the density of quartz is 2.65 g/cm^3. The melting point is approximately 1720 °C. In nature, SiO_2 is found in the form of the polymorph α-quartz. During heating, this is transformed to other polymorphs: β-quartz at 573°C and then, through an intermediate amorphous phase, to cristobalite (Jusnes, 2020; Ringdalen, 2015, 2014). The rate of transformation from β-quartz to amorphous SiO_2 and further to cristobalite varies considerably between different industrial quartz sources (He *et al.*, 2021; Jusnes, 2020; Ringdalen, 2014; Ringdalen and Tangstad, 2016). The transformation takes place through nucleation, which starts throughout the whole quartz particle. No correlation has been found between the content of different polymorphs and thermal strength (Jusnes, 2020), the reaction rate with SiC (Tangstad, 2019; Folstad, 2021), or the reaction rate with Si (Sindland, 2020). The change in structure is accompanied by a decrease in density, and the volume of SiO_2 increases by more than 20% during heating up to melting (Ringdalen, 2015).

Fines formation during handling and use of quartz varies between different sources, due to differences in both cold and warm strength (Jusnes *et al.*, 2018a). Warm or thermal strength includes both strength during heating for longer time, simulating heating in the charge mixture (TSI-Thermal Strength Index), and strength towards thermal shock when the materials are fed to the warm charge top. Fines generation will increase with increasing grain size, increasing number of cracks, and decreasing amount of muscovite in the quartz source (Jusnes, 2020). Both TSI and fines generation by thermal shock vary considerably between different quartz sources.

The melting temperature of quartz, around 1720°C, will be lowered by the content of minor elements such as alkalis (Dalaker, 2025). As an example, a silica source with 0.2% K_2O and no other contaminants will form the first molten phase at 770°C (solidus), while the temperature for complete melting (liquidus temperature) will only be lowered by around 5°C. Formation of the first melt will, at around 1600–1700 °C, make the particles start to soften (Ringdalen *et al.*, 2019). They will then become sticky and clog together, or with other solid materials. This will affect the downward material flow in the furnace. Quartz needs, in contrast to most materials, to be superheated before it is completely molten. The required time at the melting point, at the solidus temperature, or at higher temperature until complete melting is obtained varies, as illustrated in Figure 5.6, between quartz sources and can be several

hours (Ringdalen *et al.*, 2019). The mechanism behind the superheating and differences in melting properties is not completely clear, but the content of minor elements, as well as the high viscosity of molten silica, are indicated to play a role. In industrial Si and FeSi furnaces, quartz will thus be softened or partly molten in most of the charge volume that has a temperature between 1500°C and 1800°C.

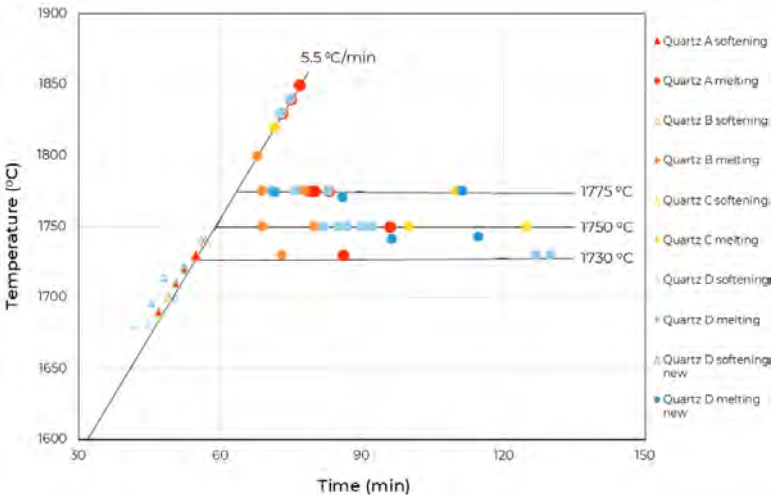


Figure 5.6 *Temperature and time needed for complete melting of different quartz sources (Adapted from Ringdalen et al., 2020).*

Liquid silica has a viscosity of around $2 \cdot 10^7$ Poise at the melting temperature, which is nearly the same as the softening point for glass and 10^9 times higher than the viscosity of liquid silicon. It will thus behave almost as a solid. The viscosity decreases rapidly with increasing temperature and is around $5 \cdot 10^4$ Poise at 2000°C. It is also affected by the content of other elements in the silica melt. Around 0.5–1% of contaminants, such as FeO, Al_2O_3 and CaO, will lower the viscosity by around 50–70%, with Al_2O_3 having the greatest effect.

Softening of quartz that clogs particles together is expected to have a negative effect on the flow of solid silica downwards in the furnace. The flow rate for molten silica is expected to increase as viscosity decreases. The rate of reactions involving silica will change during melting, as in reaction [5.6], where it decreased around the melting temperature and increased when the silica was completely

molten (Andersen, 2010; Andersen, 2009). Reaction rates are also expected to increase with decreasing viscosity. Differences between quartz sources in melting properties and in the content of minor elements that change viscosity are therefore expected to lead to differences in material flows and the rate of SiO production in the furnace. This may, in a transition period, give differences in furnace performance when the quartz source is changed, and may in some cases make it necessary to adapt operational parameters to the quartz source.

Quartz requirements

Requirements for the quartz depend on the specific product, the properties of the other raw materials, the operational strategy and the furnace design. The required maximum content of the various contaminants must be decided based on the product requirement and their content in the other raw materials. Low fines generation, i.e., high cold and warm strength and resistance towards thermal shock, is also important. A slow rate for SiO generating reactions [5.5] and [5.6] at temperatures below around 1800 °C will be beneficial. This ensures that most SiO is generated in the high temperature zone of the furnace, where it can be further reduced to Si. A relatively large particle size, around 10–50 mm, contributes to this. Melting properties may affect furnace operation, but their effect results from an interaction between several properties and is not yet quantified.

Test methods

There is no standard furnaceability test for quartz. However, some methods for measuring specific properties are used. Warm strength during longer heating is measured by the TSI (Thermal Strength Index) test (Aasly, 2008; Aasly and Dosaj, 2016; Ringdalen and Tangstad, 2016). This is a standard test in which the materials are heated for 30 minutes at 1300°C, and fines generation is then measured both after heating and after further tumbling. Several slightly different methods have been used. Resistance towards thermal shock is measured by dropping a 200-gram sample into a crucible preheated to either 1300°C or 1500°C, holding it there for 10 minutes, and measuring the resulting size distribution (Jusnes *et al.*, 2018b). Melting properties can be measured by a sessile drop apparatus (Nordnes, 2019; Ringdalen *et al.*, 2019).

Reduction materials

Sources

Traditionally, a mixture of different solid carbon reductants has been used in Si and FeSi production. Coal has been a main source, but petcoke and char, as well as metallurgical coke and several others, have also been used, as illustrated in Figure 5.7. Woodchips are added to obtain a more porous charge, but they also contribute to the carbon content in the charge mixture.

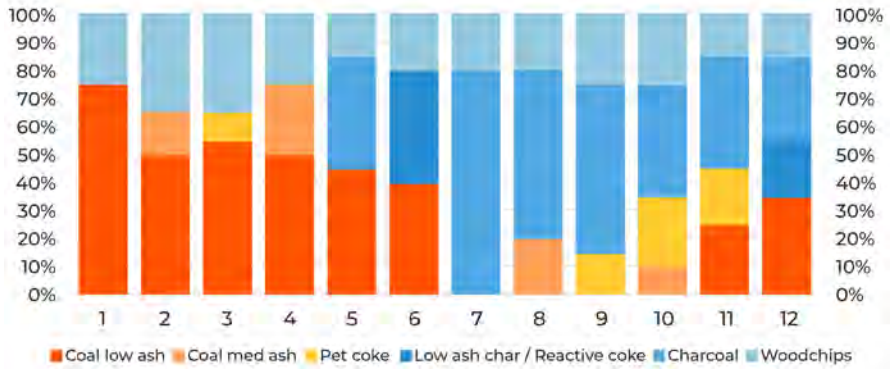


Figure 5.7 *Twelve carbon mixtures used in silicon production where numbers indicate various producers. (Myrvågnes, 2008) (Redrawn by Lingyi Ren) [Used with permission from V. Myrvågnes].*

Biobased reductants are increasingly substituting fossil carbon to reduce fossil CO_2 emissions. This forms part of the sustainability strategy for several producers[1] (Lindstad *et al.*, 2010). Both commercial biocarbon and designed biocarbon materials have been investigated and developed. South American Si and FeSi producers have traditionally used a large percentage of charcoal, often only charcoal in addition to woodchips (Sommerfeld *et al.*, 2021). Their charcoal is often made from eucalyptus grown on their own plantations. For coal to Si-production, Colombian coal is an important source for many producers.

1 https://www.prosess21.no/contentassets/d4c74305ab764cf2b24f3f61f0514f5d/prosess21_rapport_hovedrapport_web-1.pdf

Role and effects in process

Carbon is present in silicon at ppm levels, while ferrosilicon contains a higher level of carbon. The main part of the carbon will therefore generate CO_2 emissions, which is an environmental problem. Carbon is, however, necessary for production and has two crucial functions in the Si-process. Its main role is as a reductant, removing oxygen from SiO_2 and converting it to Si. As described above, in Section 5.1 and in Chapter 3, this is accomplished through a set of sub reactions. In addition, as a constituent in SiC, carbon is important for electrical conductivity and energy distribution in the furnace (Hoover, 2023). The properties of the carbon materials affect Si production and the operation of Si furnaces in different ways (Tangstad *et al.*, 2025):

- Generation of dust during transport and handling
  - Due to low cold strength
- Loss of fine particles of carbon to off gas
  - Due to low strength towards shock heating
- Off-gas composition and amount
  - Due to volatiles, moisture and contaminants that go to gas
- Rate for distribution of and variations in material and gas flow
  - Material flow is affected by volume of required carbon materials, which is determined by bulk density and % FixC of the carbon material
  - Gas flow is affected by the charge permeability, which depend on amount of fines in the charge and due to low thermal strength
- Furnace performance, energy consumption and yield
  - Important carbon properties are SiO reactivity and electrical conductivity
- Alloy quality

Carbon properties

Typical properties of some carbon reductants are given in Table 5.1.

Table 5.1 *Typical properties of some carbon reductants (Jayakumari et al., 2023).*

	Coal	Calcined coal (1200°C)	Charcoal	Pet-coke	Metallurgical coke
Fixed carbon (%)	58.36	91.9	90.32	89.8	86.10
Volatiles (%)	40.58		8.06	10	1.39
Ash (%)	1.06		1.62	0.2	12.51
Ash composition					
SiO_2 (%)					46.7
TiO_2 (%)		0.84	0.02	0.24	
Al_2O_3 (%)		25.9	0.4	7.0	34.45
Fe_2O_3 (%)		11.4	0.5	13.1	7.7
CaO (%)		2.7	47.0	17.1	4.6
MgO (%)		1.8	6.0	1.3	0.6
MnO (%)		0.09	3.20	0.75	0.11
Na_2O (%)		2.30	0.20	4.40	0.49
K_2O (%)		0.38	13.20	0.14	0.54
P_2O_5 (%)		0.27	5.50	0.52	
S (%)					0.80
P (%)					0.23
Bulk density (g/cm^3)		0.35–0.46	0.23–0.30		0.9–1.1
Porosity (%)		38–57	70–82	±20	44–55
CO_2 reactivity (%FixC/s)			$2.1–2.3\times10^{-2}$		$0.2–0.5\times10^{-2}$
Thermal abrasion strength: T.I.3 (%)		84	78–82		78–88

Chemical composition is, in most cases, the first property considered when choosing a carbon source. As illustrated in Figure 5.3, the required chemical composition for carbon materials depends on the requirements for the actual product and on the composition of the other raw materials. For Si, the B and

P content are often important constraints. The choice of carbon materials is also important for the environmental performance of the process. In addition to contributing to CO_2 emissions, carbon materials often contain sulfur and other unwanted tramp elements. If the carbon source contains mercury, this will evaporate in the process and be emitted into the environment with the off-gas. The accepted content of heavy metals and other emission elements depends on the installed gas treatment at the actual site.

The generation of fines during transport and handling, and due to heating inside the furnace, may lead to dust generation (Jahrsengene *et al.*, 2023) and to loss of carbon materials through the off-gas system. Uncontrolled carbon losses to the off-gas system will affect the carbon coverage of the furnace and have a negative impact on furnace performance. High cold and thermal strength is critical to avoid fines generation and is thus an important carbon property (Jayakumari *et al.*, 2023; Lindstad *et al.*, 2010; Monsen *et al.*, 2007). As seen in Figure 5.8, this will vary between carbon sources. Charcoal is more fragile than other carbon sources and therefore generates more fines. Increased fines and dust generation are among the challenges when biocarbon, which has lower strength, substitutes other carbon sources.

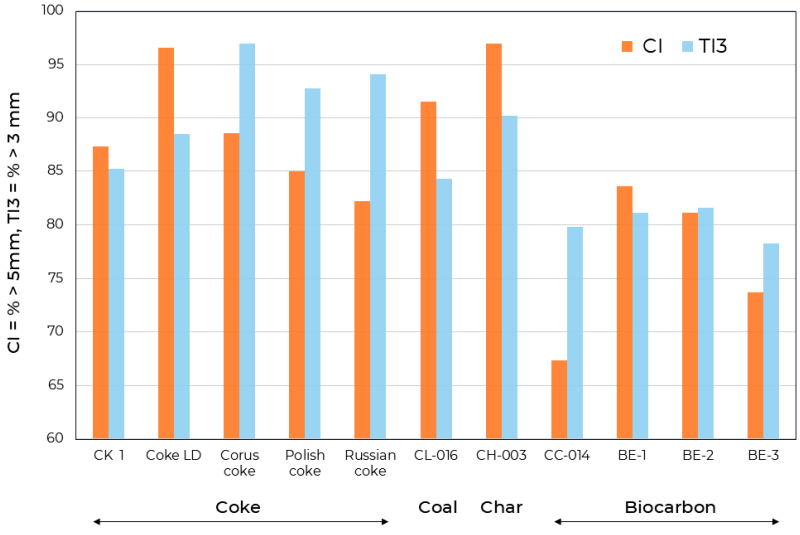


Figure 5.8 *Thermal strength of various carbon materials (CI is after CO_2 oxidation and TI are after subsequent tumbling). Adapted from values (Jayakumari et al., 2023).*

In the charge zone in the upper part of the furnace, the descending carbon materials are heated by the ascending gases, and volatiles and moisture are driven off. Below, in the reacted charge, carbon materials react with ascending SiO gas according to reaction [5.4], producing SiC needed both for SiO generation and for final Si production in the lower part of the furnace.

$$SiO\ (g) + 2C(s) = SiC(s) + CO(g) \qquad [5.4]$$

This reaction both captures SiO gas, reducing SiO loss, and converts carbon to SiC, which is required for final Si production. To capture as much SiO gas as possible and to have SiC available for final production, it is beneficial to use a carbon material that reacts easily with SiO gas. Carbon materials with a high rate of reaction with SiO, high SiO reactivity, and complete conversion of carbon to SiC are among the most important process parameters in the Si-process (Lindstad *et al.*, 2007; Suárez-Ruiz *et al.*, 2019). Both practical experience and laboratory measurements have shown that the ability of carbon to react according to reaction [5.4] is highly dependent on the carbon source and its properties. Charcoal normally has a higher SiO reactivity than coal, coke, and other carbon sources, and will therefore, with the same SiO content in the gas, capture more SiO gas than coal or coke during the same exposure time. Typical SiO reactivities are shown in Figure 5.9.

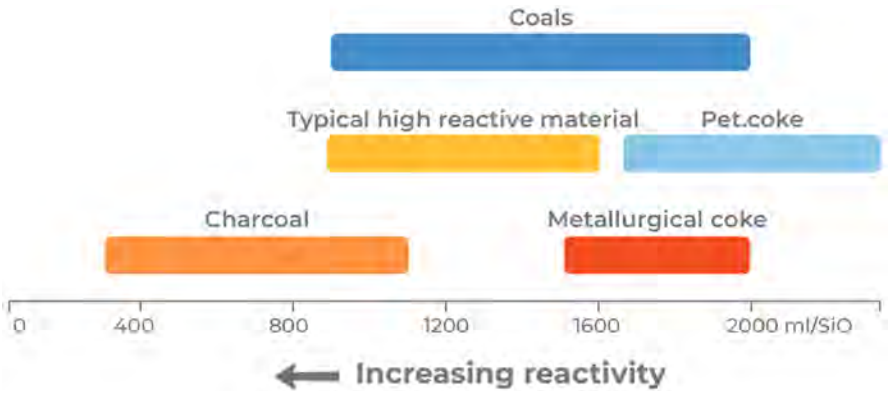


Figure 5.9 *SiO reactivity of different carbon materials where a lower number of SiO gas not reacting signifies a high SiO reactivity (adapted from Raaness and Gray, 1995) [Used with permission from M. Raaness].*

The reaction between carbon and CO_2, the CO_2 reactivity of the carbon materials (reaction [5.8]), can be measured by various methods. It is often given as the Carbon Reactivity Index (CRI) by carbon material suppliers ('ISO:18894:2006,' 2006). This test is based on fine-grained particles reacting with 100% CO_2, which is far from conditions in Si/FeSi furnaces. The conditions in the Sintef CO_2 reactivity test (Ksiazek *et al.*, 2022; Tangstad *et al.*, 2025), where larger particles are exposed to a gas with 50% CO + 50% CO_2, are closer to the conditions in industrial furnaces, although no SiO is present in the gas atmosphere. Further references to CO_2 reactivity are based on measurements using this method.

$$CO_2 + C = 2\ CO \qquad [5.8]$$

In Si and FeSi production, the temperature in the charge in most of the furnace is so high that very little CO_2 is expected to be present in the gas phase, and CO_2 reactivity is therefore probably of little importance. A correlation between SiO reactivity and CO_2 reactivity has been postulated, but, as seen in Figure 5.10 a), only a grouping into different values for the various sources can be found, and not a correlation within these groups. When carbon reacts with CO_2(reaction [5.8]), only gas is produced, while the reaction between carbon and SiO (reaction [5.4]) generates, as discussed in Chapter 2, a solid SiC layer in addition to gas. High porosity in carbon materials, such as in biocarbon, is therefore expected to have less effect on SiO reactivity than on CO_2 reactivity. This can be seen by comparing the correlation between SiO reactivity and porosity shown in Figure 5.10 b) with the correlation between CO_2 reactivity and porosity shown in Figure 5.10 c) (Jayakumari, 2020; Jayakumari and Ringdalen, 2022).

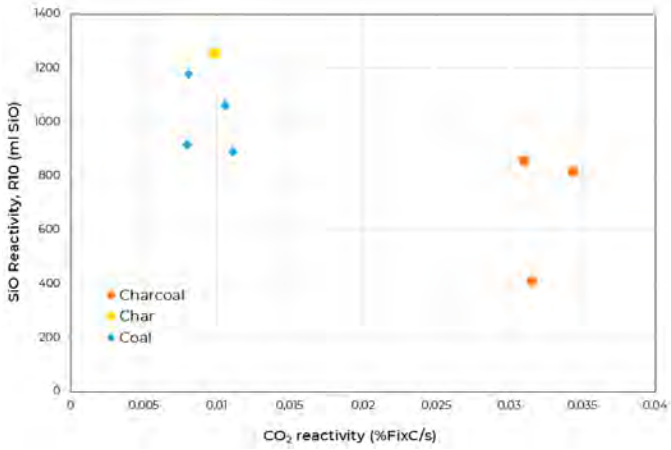
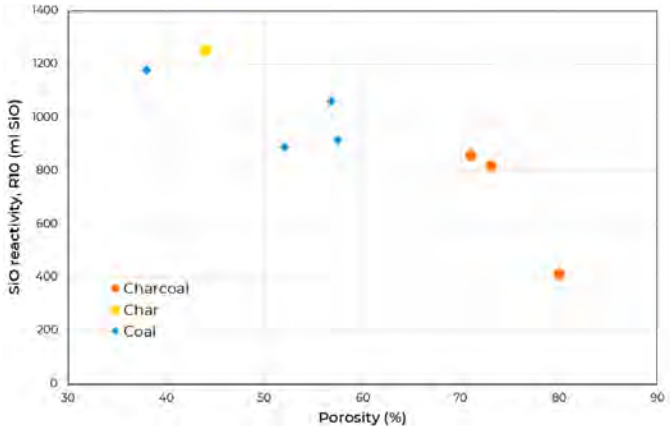


Figure 5.10a *Correlation between SiO reactivity, measured by SINTEF SiO. Reactivity test and CO_2 reactivity. Adapted from (Jayakumari and Ringdalen, 2022).*



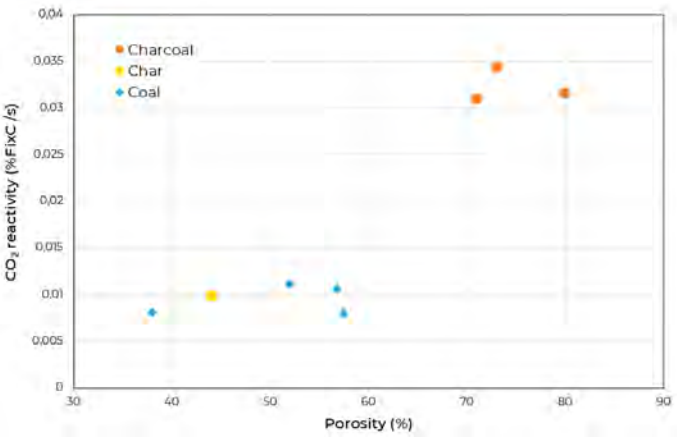


Figure 5.10b,c *Correlation between porosity and b) SiO reactivity measured by SINTEF SiO-reactivity tests and c) CO_2 reactivity. Adapted from (Jayakumari and Ringdalen, 2022).*

Reaction [5.4] between SiO-gas and carbon takes place at temperatures around 1500 °C to 1800 °C, producing β-SiC. This is converted to α-SiC as it descends into the high-temperature zone. SiC properties, and how fast it reacts with Si, are affected by the properties of the original carbon material. At the same temperature, more Si will be produced from SiC originating from charcoal than from SiC produced from coal (Jayakumari, 2020).

For good energy distribution in the furnace, it is beneficial that most of the currents go low down in the furnace. This requires high electrical conductivity and low electrical resistance in this zone. Electrical resistivity varies with the type of carbon materials in the charge mixture and the extent of their further transformation to SiC, as seen in Figure 5.11 (Hoover, 2023). Charcoal has a higher resistivity than coal and char. SiC has a higher resistivity than carbon, with partially transformed SiC having the highest resistivity but decreases slightly with content of Si. All carbon materials have higher resistivity than pure liquid Si. Since the total resistance is dominated by the contact resistance between particles, particle size has a major effect on overall resistance in the furnace.

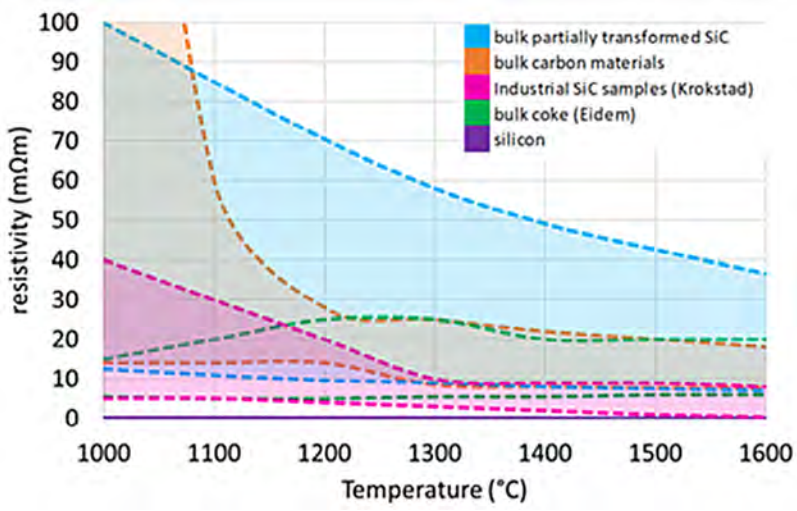


Figure 5.11 *Electrical resistivities of carbon materials, SiC and Si (Hoover, 2023). [Reprinted with permission from H. Hoover].*

Requirements to carbon materials

The main requirements for carbon materials for Si production can be summarized as

- Suitable chemical composition
  - low content of contaminants such as P, B, Fe, S and others
- High mechanical strength at cold and warm conditions
- High SiO reactivity
- Suitable (high) electrical conductivity
- High density

Test methods

Several methods are available to measure critical properties of carbon materials used in ferroalloy production (Smith-Hanssen *et al.*, 2023). For the Si process, the main dedicated measurement method is the SINTEF SiO-reactivity test (Lindstad *et al.*, 2007). In this test, the reaction rate between SiO and carbon is measured at 1650°C in an Ar–CO–SiO gas mixture with 13.5% SiO and 4.5% CO. Under these conditions, the reaction between SiO and C has a relatively slow rate. Differences between carbon materials are therefore more easily observed, but the measured SiO reactivities will not necessarily represent the reaction rate in industrial furnaces. Relative reactivities measured by the SINTEF SiO reactivity test for some common carbon sources are given in Figure 5.9 .

Wood chips

Woodchips are included in the charge mixture for silicon and ferrosilicon production by many producers, but at a low percentage, often lower than 10%. With a low Fix C content of around 10–20%, woodchips make only a minor contribution to the carbon content needed for reduction (Andersen *et al.*, 2023; Monsen *et al.*, 2001; Ringdalen and Gaertner, 2024). Woodchips are therefore mainly added not as a reductant, but to improve material and gas flow in the charge mixture (Saadieh, 2024). The low density and flat shape of wood chips contribute to high charge porosity, giving a more even gas flow.

Woodchips are also assumed to have a positive effect on furnace performance by decreasing the retention time of quartz, increasing energy content in the off-gas, and increasing charge resistivity.

Particle size and shape, and the content of contaminants, are the most important properties to consider when selecting a woodchips source. Typical sizes are in the range 7.5 cm^2 x 1.25 cm thick to 20 cm^2 x 2.5 cm thick (Saadieh, 2024), or match box size (Monsen *et al.*, 2001). Fines, such as sawdust, should be avoided since they burn at the charge surface. The amount of bark is often limited since it has a higher content of contaminants.

The iron source

To produce Ferrosilicon, FeSi, iron must be added to the charge mixture. The amount of iron source in the charge mix depends on % Fe in the iron source and the iron content in the designated product, such as FeSi55 with 45% iron or FeSi75 with 25% iron. The most used iron source is steel scrap, followed by iron ore pellets and mill scale (Saadieh, 2024). In addition to price and availability, chemistry and size are important properties to consider. The chemistry of all types of iron sources varies with the steel or iron ore they originate from and must be evaluated for each case. In steel scrap, the main tramp elements are Cu, Sn, Cr, Ni and Mo, which in the most used steel scrap quality, Q4, are around 0.25–0.35%.

Iron ore pellets are available in different qualities, with blast furnace (BF) or direct reduced (DR) pellets as the most common. In addition to iron oxide, they also contain up to around 5% SiO, 3% Al_2O_3 and CaO, and some MgO. With a particle size of around 9–16 mm and a strength high enough for processing in a blast furnace, the iron ore pellets are well suited to be handled in a ferrosilicon plant.

When iron oxides are used, they must be reduced to Fe in the furnace, either with an excess of CO gas or with carbon, which will then increase specific energy consumption. Iron scrap reduces the need for carbon and electrical energy in the process compared to iron oxide. However, iron oxide may be easier to control regarding chemical analysis. Iron oxide pellets are normally more suitable for automatic raw material handling equipment compared to non-uniform scrap pieces.

5.4 The silicon and ferrosilicon plant

The silicon process must meet the basic requirements for the process which are described in Chapters 2 and 3. The main challenges are the need for extremely high process temperatures, energy conversion, and the thermodynamic requirement that govern the processes involved. The main components of a silicon furnace are shown in Figure 5.1 and Figure 5.12. The furnace has some basic functions that must be included in the construction. Although the size and technological level vary between furnaces, all silicon furnaces must include:

1. The furnace shaft consisting of a shell and a lining that resist the temperature and chemical load
2. Electrical supply to the furnace consisting of electrical grid, transformers, bus bar and the electrodes.
3. Equipment for handling and feeding of raw materials to the furnace.
4. Equipment for stoking and preparation of the charge mixture in the upper part of the furnace
5. Equipment for tapping silicon or ferrosilicon from the lower part of the furnace
6. Gas cleaning and energy recovery systems

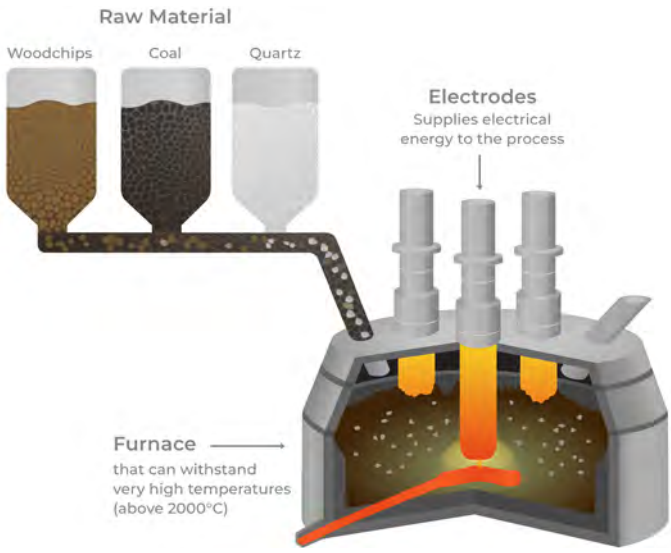


Figure 5.12 *Basic requirements for Si production.*

The furnace

The central part of the furnace comprises the furnace hood and the body. The furnace body consists of an outer steel shell and an inner lining that resists the temperature and chemical load required by the process. The silicon process is special because the raw materials partly perform the most demanding work on the lining. The lining is often made of oxide refractory near the outer steel shell. In the inner part of the furnace body, the lining is made of carbon material. The most severe challenge for the lining is below the electrodes and close to the tapping channels. There may be one or several tapping channels through the furnace body. The tapping channel may be made of carbon material or silicon carbide refractory.

The furnace hood is the upper part of the furnace. It has several functions: it collects the process gas; it shields the equipment from the process heat and the charging pipes; and the electrodes pass through the hood. The process gas is sucked out through pipes that pass through the hood and is transported further to the gas cleaning equipment and the chimneys. The hood may be open, but for modern, larger furnaces it is normally water-cooled and semi-closed. Semi-closed furnaces have furnace doors that open for inspection, stoking and charging. Both open and semi-closed furnaces allow abundant air to be available at the charge top. Semi-closed furnaces give a higher off-gas temperature, which is important if an energy recovery plant is connected to the furnace.

The electrical supply and the electrodes

Electrical energy is supplied to the furnace through electrodes, from the top of the furnace to the high temperature zone in the lower parts of the furnace. The energy supply system and the electrodes are a crucial part of silicon production. Good furnace performance requires good operation of the electrodes and energy supply. The electric operation is described in more detail in Chapter 6. There is a close interaction between furnace operation, energy supply and electrode operation.

Raw materials handling and feeding to the furnace

The system for handling raw materials includes transport, storage, weighing and mixing of the raw materials used in the process. Layout and technologies for the charging system are normally site dependent and vary from plant to plant and from furnace to furnace. The raw materials are transported from the supplier to the plant by railway, truck or boat. Most of the Norwegian silicon plants are located near the sea, where ships are the main transporters of the raw materials. Control of the supplier's chemical analysis is often carried out on arrival. Raw materials for up to several months of operation are stored temporarily at the plant, either outdoors, under a roof or indoors. Carbon materials can take up more moisture than quartz and are often prioritized for indoor storage in rainy areas. Many plants monitor the moisture in raw materials automatically, to better control the raw material mix.

From the storage area, the raw material is transported to the furnace. Often there are some smaller and more defined storage bins, called day bins. To obtain the right blend of raw material, predetermined tonnages of each raw material are weighed out from the silos before the raw materials are mixed and fed to the furnace. In modern furnaces, this is done by an automatic weighing system. The ratio between the different raw materials, called the material blend or charge mixture, is given to the weighing system through the control system of the furnace. To determine this ratio, the charge mixture that will give optimal furnace operation is chosen. This is adjusted based on realized furnace operation. The ratio between raw materials is one of the major challenges in furnace operation, and often the main task for the furnace metallurgist responsible for the furnace. From the weighing system, the raw material is transported to the furnace, usually on conveyor belts.

Adding new raw materials to the furnace, called charging, can be done in different ways (Andersen, 2023). In older, smaller furnaces, charging cars can be used. More often, however, the raw materials are added through charging tubes, which are connected to bins of mixed raw material and go down into the furnace through the furnace hood. The number and arrangement of charging tubes vary between furnaces. In many cases, there is a charging tube to the centre of the furnace, in addition to two or three charging tubes around each electrode, but other constellations are also seen. The raw materials are dropped from the charging tube to the charge top, giving the raw materials a thermal shock when they meet the warm charge top. Ideally, the raw materials should

be fed continuously to the furnace. The batch size and frequency of charging affect the fluctuations of moisture and volatiles in the off-gas (Andersen, 2023; Kamfjord, 2012). Different designs of charging systems have thus been developed (Myrhaug *et al.*, 2012).

Stoking and preparation of materials charge in the furnace

Condensates formed by reaction [5.2] and [5.3] are abundant in the charge above the SiC-crust, with brown condensates from reaction [5.2] being most common. They are sticky and glue the other charge materials together into a hard layer that hampers, or prevents, both the downwards flow of solid materials and the upwards flow of gases. To ensure an even flow of materials and gases, the condensate can be broken up by stoking. The most common method is to push materials at the top of the charge downwards and inwards in the furnace. This is done using an iron rod mounted on a truck (the stoking machine) that moves around the furnace on the floor outside the furnace shell. The material is stoked intermittently, normally either at fixed intervals or based on dust level in the off-gas. Alternative methods, such as a split body where the upper half of the furnace rotates, have been tried. In production of ferrosilicon, there is a lower SiO content in the gas and thus less condensate form. These furnaces, especially furnaces producing ferrosilicon with lower Si contents, are often operated without stoking.

Stoking requires access to the charge top from outside the furnace. This can be either via an open furnace or, as is most common today, through doors or ports in the furnace sides that are opened when stoking is required. Both alternatives allow an inflow of air that reacts with SiO to SiO_2 and with CO to CO_2, resulting in a high CO_2/CO ratio in the off gas.

Tapping of liquid silicon or ferrosilicon

Produced silicon or ferrosilicon is tapped out either intermittently, but in most cases it is tapped continuously through tap holes in the lower part of the furnace. The furnace has around 5–7 tapholes, constructed with a dedicated lining and front. The tapping channel is opened by a tapping tool. Several kinds of tapping tool are used, such as a steel rod for poking, oxygen lances, electrical graphite bars for burning, or other mechanized or manual equip-

ment. Fully automated tapping robots are being developed and are installed at many furnaces. Tapped metal has a temperature of around 1900 °C when it leaves the furnace. It might be accompanied by a jet of tapping gas (Andersen *et al.*, 2022; Ksiazek *et al.*, 2018). Each taphole is used for around 10 days, varying from furnace to furnace. It is then plugged with ramming paste, and a new taphole is opened. Silicon and ferrosilicon furnaces usually rotate, with a speed of around 25 days for one rotation, with a lot of variation from case to case. Some furnaces oscillate instead. The position for the tap hole will thus change, making it easier to use tap holes distributed around the furnace.

Good tapping, and thus good drainage of the metal, is vital for good furnace operation and to avoid operational problems. This is also described in Chapter 8. Metal produced in the cavity and below the electrodes has to be drained out through the tapping channels in the furnace and the lining to the tap hole (Tangstad *et al.*, 2021). Problems with drainage may lead to higher pressure in the cavity, loss of SiO-gas and lower Si-yield. It will also give a risk of gas jets from the taphole (Kadkhodabeigi, 2011). The taphole, tapping area and equipment are exposed to high temperatures and high mechanical and chemical stress. It is thus a part of the furnace that is difficult to automate and that requires much maintenance.

The liquid silicon or ferrosilicon is first tapped into ladles. Its composition can be adjusted by alloying or refining in the transport ladle as described in Chapter 10. Liquid Si or FeSi is then solidified by casting. Several ways of casting silicon and ferrosilicon, described in Chapter 11, are in use today.

Gas treatment and energy recovery

Silicon and ferrosilicon production are energy intensive processes. A large part, around 1/3 (Kamfjord, 2012), of the supplied energy will, as discussed in Chapter 7, go into the off-gas. The energy in the off-gas may, and is at many modern furnaces recovered as high temperature water or as steam, which can be further converted to electrical energy. SiO in the off-gas is burned with oxygen to silica fume, which consists of nano particles of SiO_2. The silica fume is normally removed from the off-gas in baghouse filters and is a valuable by-product. It can be used for different purposes, i.e. to improve concrete. Its value depends on the content of minor elements. Microsilica is one of the trade names used for silica fume.

The energy balance for the process presented in Chapter 7 assumes burning of the CO gas, the SiO gas and volatiles. The burning, and the temperature control with cooling air, results in a large amount of waste gas containing condensed silica fume. In theory, the furnaces could be closed, with no combustion of CO gas and volatiles. This presents several challenges and, so far, there have been only experimental trials of closed silicon furnaces and FeSi furnaces with high silicon content (Arnesen and Bjordal, 1980).

5.5 Furnace operation and control

Economy and sustainability in silicon production is dependent on the operation results. The main process parameters are furnace load (kW), silicon yield (%), specific energy consumption (kWh/ton) and CO_2 emissions (kg/ton alloy). Other parameters, such as product quality, emissions and operation time (%), are also important. Achieving and maintaining an economic and sustainable production process requires good process control. To achieve this, one must have a good combination of

- Process measurements
- Control system
- Metallurgical competence about the actual process

Metallurgical competence is the basis for good furnace operation and is the focus of the current book. Part of this competence can be systematized into various process models, as a help to the metallurgists and operators in making their decisions.

Process measurements provide data required to evaluate process performance and the effects of changes in the operational strategy, parameters or raw materials. They are used by the metallurgists and furnace operators and are also input into process models. Process measurements are also needed and are mostly used as input to the control system. Process measurements also include process surveillance by standard and infra-red camera.

Part of the furnace operation is automatic, and is done by the control system. The control is based on process measurements combined with set points given by those responsible for the furnace. This is especially useful for

electrode movements, since the electric parameters change very fast. It is also standard at most furnaces for several other operations, such as weighing and charging system and electrode slipping.

Process measurements

Process measurements are needed as input to the control system and to provide information for the metallurgist and furnace operators when deciding on operational and raw material parameters. The type of process measurements and the methodology is often plant or furnace specific. New methods are continuously developed. Details regarding process measurements will thus not be further described here.

Control system

Automatic operation requires a control system. To work well, this needs to be designed with control algorithms suited for the process it controls, to have input from reliable process measurements, and to use well-founded set-points chosen by the metallurgists. There is a development towards use of digital twins and artificial intelligence (AI) to support the control system and choice of set points.

The process parameters in silicon production have large variation in time delay. Electrical parameters have response within seconds, while some of the metallurgical parameters may need weeks or months to adjust. Build-up of carbon materials and distribution of reaction zones in the furnace are examples of these. The interaction between the electrical and metallurgical subsystem in the process is indicated on Figure 5.13. The electrical system may have a closed loop control due to the short time constants and the good signals from the process. Parameters in the electrical system, such as electrode position and slipping, voltage, current and load control, or transformer tap position, are in most furnaces computer controlled. The metallurgical system has longer time constants, more variation in time delay and less direct readings of main parameters from the process, and is normally partly computer controlled and partly operated by the metallurgist and the furnace operator.

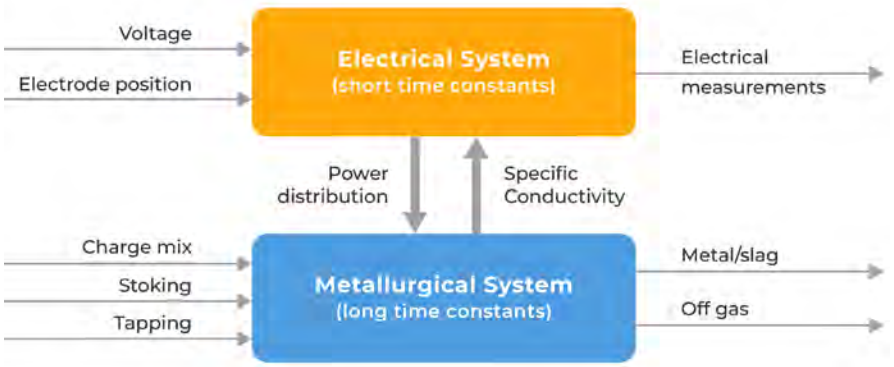


Figure 5.13 *The principal interaction between the metallurgical and the electrical system in the silicon process.*

Metallurgical competence

Metallurgical competence in the Si process is the key factor for good furnace operation. This is the focus of this book. Process competence is needed to optimize the raw material mixture, choose operational strategies, and select the set points for the various control systems. The development and implementation of new control systems require in-depth knowledge of the process.

Such competence can be systemized into process models as tools and aids for controlling and optimizing the process. Several process models have been developed and used over the years. Often, each plant or company uses its own in-house model. Fundamental theoretical and practical knowledge about the process is needed both to use and to develop models and control systems, and to know when the models should, or should not, be used.

5.6 Process models

Process models are decision-support tools in which metallurgical competence, and details about reactions and physical phenomena in the furnace, are systemized into an overall understanding of the process. The interdependent physical phenomena in a silicon furnace – including chemical reactions,

thermodynamics, kinetics, material and gas flow, electrical currents, and energy distribution, all relying on varying properties of different raw materials – can then be handled more easily. A model can cover a selected part of the Si/FeSi process, such as tapping, the electric arc, or the off-gas system. However, an overall model of the whole process is often the tool most needed by the furnace metallurgist, and this is what is described here. For a complex system such as the silicon furnace process, all models require a considerable number of assumptions and simplifications. The key is to capture the main effects of actual variables, within the variations expected in an industrial furnace, with reasonable requirements for the accuracy of input parameters and reasonable simulation time. A process model will therefore not simulate or explain all phenomena that take place in a silicon furnace, nor predict what is happening under completely new conditions; rather, it indicates what might happen when conditions or raw materials are changed. Process models are also a good tool for the metallurgist to investigate which choice of raw materials or conditions will give the best furnace performance when several alternatives are available.

The Si process was developed empirically. Modelling started, as described in Schei (1998), with various qualitative models in the 1970s, and continued with furnace models in the 1990s (Schei *et al.*, 1998). With the development of more advanced computer technology with higher capacity, and the development of AI tools, there has been a move towards more complex and more advanced models, such as transient models (Darmana *et al.*, 2012; Olsen *et al.*, 2022) and mathematical modelling (Sloman, 2018). The development of Digital Twins gives a closer connection between the models and operation (Linnestad *et al.*, 2022). Many producers develop their own process models, incorporating their own process competence and experience from their own operation. These are often confidential. Examples of producer models are the Elkem models, Si mod and FeSi mod (Sloman, 2018). These Elkem models are a further development of earlier published work. The concept and assumptions behind the models give insight into different approaches and challenges in the modelling of Si and FeSi furnaces.

Background and concept for Elkem process models

Elkem has developed two models of the silicon process:

- A stoichiometric model
  A very simple steady state model that combines equilibrium and kinetic considerations with material and energy balances. The model, which contains only arithmetic calculations, is implemented in Microsoft Excel, and a case can be calculated in a few seconds on a personal computer.
- A unidimensional dynamic model
  A model with simple rate laws for the chemical reactions. The material and heat balances are formulated as differential equations, which are integrated numerically by a suitable time stepping algorithm. Calculation of a case can take minutes to hours on a large personal computer.

The models are described in several publications. Schei and Larsen have given the metallurgical background for the stoichiometric model (Schei and Larsen, 1982). Schei and Halvorsen have developed the numerical calculation and discussed the silicon process based on calculated examples (Schei and Halvorsen, 1991). Halvorsen *et al.* (1993) have described the dynamic model from a metallurgical point of view, while Halvorsen *et al.* (1991) and Halvorsen (1994) have given a thorough discussion of the mathematical problems. Halvorsen has presented the use of both models in the education of process metallurgists in Elkem (Halvorsen, 1995).

The stoichiometric model

The model sees the silicon process as a combination of simple reactions between stoichiometric compounds of the main elements Si, O and C. It ignores the presence of foreign elements that always will be present in a real process. The simple model, also described in Chapter 3, is based on furnace observations and knowledge of the chemistry of the system. In this model, the gas from the inner zone of the furnace has a high content of SiO, and this SiO has to be recovered in the outer zone of the furnace if the silicon yield of the process is to be high. The recovery mechanism used was the reaction

$$SiO(g) + 2\,C(s) = SiC(s) + CO(g) \qquad [5.4]$$

In addition, it was indicated that the condensation mechanism

$$2\ SiO(g) = Si(l) + SiO_2(s,l) \qquad [5.2]$$

could be an important second main recovery mechanism. The other condensation reactions between SiO and CO seem to be so slow that they can be ignored in a rapid calculation. The recovery mechanisms are the core of the stoichiometric model, which is sketched schematically in Figure 5.14.

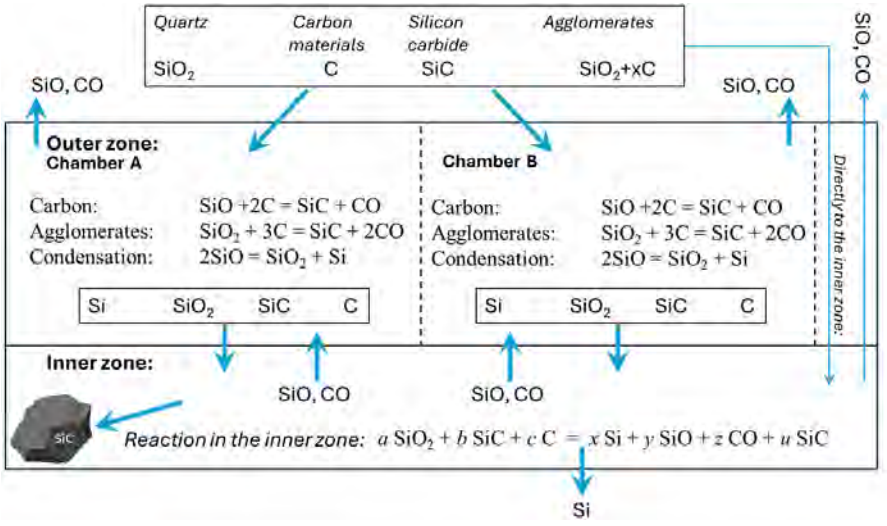


Figure 5.14 *Survey of the stoichiometric model with the material flows.*

The furnace is split into an inner zone, where SiO_2 and SiC react, and an outer zone, where the SiO in the gas from the inner zone is recovered. The raw materials are charged into the outer zone, where they interact with the outgoing gas in counter-current. The outer zone is split into two chambers to permit simulation of uneven gas distribution through the charge. The charge and gas can bypass the outer zone.

The inner zone

In the inner zone of the furnace, SiO_2, SiC and C disappear, while Si and gas SiO–CO are produced. Under some conditions, solid SiC is deposited in the lower part of the furnace. These observations are expressed by the inner zone reaction:

$$a\ SiO_2 + b\ SiC + c\ C = x\ Si + y\ SiO + z\ CO + u\ SiC \qquad [5.9]$$

This must be seen as a non-equilibrium overall reaction, since there are more phases than allowed by the phase rule for the given conditions. Equilibrium silicon production at fixed pressure is possible in the inner zone only for the condensed phases SiO_2, SiC and Si. The equilibrium gas is determined by the reaction:

$$SiO + SiC = 2\ Si + CO \qquad [5.7]$$

$$\frac{p_{CO}}{p_{SiO}} = K_{5.7} \qquad [5.10]$$

The equilibrium fraction of SiO in the gas is given by:

$$s = \frac{p_{SiO}}{p_{SiO} + p_{CO}} = \frac{p_{SiO}}{p_{SiO} + K_{5.7}} = \frac{1}{1 + K_{5.7}} \qquad [5.11]$$

Temperature and gas composition are completely determined with $s \approx 0.67$ at 1811°C. As shown in Chapter 3, this SiO content will give a silicon recovery of 33 per cent. However, the best obtained process recoveries are above 90 per cent, and the observed reaction temperature is about 2000°C. The real reaction therefore runs far from equilibrium.

Experience suggests that the slowest step is the heat-consuming break-up of SiO_2. When energy is added, the temperature rises and, consequently, the reaction rate increases until energy consumption and energy addition balance in a steady state. In this non-equilibrium reaction, the SiO content *s* of the gas in the inner zone is determined by the reaction kinetics. Thus, *s* is variable, however, in the stoichiometric model it is *assumed* to be constant for a certain combination of raw materials and operating conditions. As a first approximation, we assume that Reaction [5.7] is relatively rapid and that *s*

can be estimated from the temperature in Figure 5.15. The crater temperature 2000°C corresponds to an *s* value slightly below 0.50. This value can therefore be taken as a rough indication of the value of *s*.

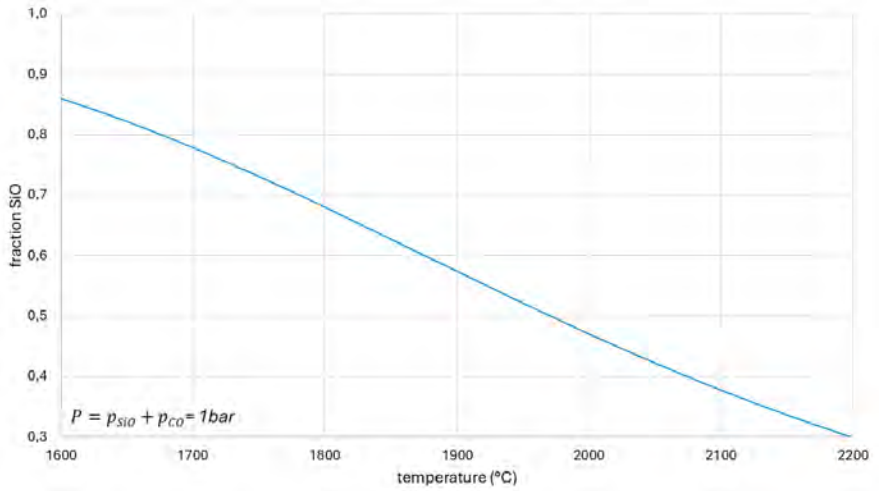


Figure 5.15 *The SiO content of the gas in equilibrium with the condensed phases Si and SiC calculated.*

The aim of the model is to describe steady-state operation, and it is assumed that Si is always present. Reaction [5.9] will then proceed as long as SiO_2 is present (x will be negative if Si is consumed). The flows a, b and c to the inner zone in Reaction [5.9] are assumed known, and the material balances for Si, C and O give three equations for the unknown coefficients x, y, z and u. Additional information can be taken from the general definition of s, and from the observation that the ratio between the gas pressures must be equal to the ratio between the gas flows. If SiC is present,

$$s = \frac{p_{SiO}}{p_{SiO} + p_{CO}} = \frac{y}{y + z} \qquad [5.12]$$

The element balances are

$$\text{Si:} \qquad a + b = x + y + u \qquad [5.13]$$

$$\text{C:} \qquad b + c = z + u \qquad [5.14]$$

$$\text{O:} \qquad 2\,a = y + z \qquad [5.15]$$

The solutions are

$$x = a\,(3 - 4\,s) - c \qquad [5.16]$$

$$y = 2\,a\,s \qquad [5.17]$$

$$z = 2\,a\,(1 - s) \qquad [5.18]$$

$$u = b + c - 2\,a\,(1 - s) \qquad [5.19]$$

These solutions apply when SiC is in excess, that is, for $u > 0$. In this case, the gas composition is controlled by the parameter s.

$$u = b + c - 2\,a\,(1 - s) > 0 \qquad [5.20]$$

$$\frac{b + c}{2a} > 1 - s \quad \text{Gas composition is controlled by } s \qquad [5.21]$$

When $u \leq 0$, this condition is not fulfilled, and the gas composition is instead controlled by the stoichiometry of the materials going into the inner zone. That is,

$$\frac{b + c}{2a} \leq 1 - s \quad \text{Gas composition is controlled by the stoichiometry} \qquad [5.22]$$

Reaction [5.9] then changes to

$$a\,SiO_2 + b\,SiC + c\,C = x\,Si + y\,SiO + z\,CO \qquad [5.23]$$

and the element balance gives the complete solution:

$$x = -a + 2\,b + c \qquad [5.24]$$

$$y = 2\,a - b - c \qquad [5.25]$$

$$z = b + c \qquad [5.26]$$

Therefore, to determine the coefficients of the reaction of the inner zone, one can use the inequalities [5.21] or [5.22] to decide which set of coefficients applies: [5.16]–[5.19] or [5.24]–[5.26].

The outer zone

The reaction in the outer chambers A and B recovers heat and SiO from the gas of the inner zone. The operation is assumed to run in a repeated cycle:

- The chamber is filled with cold charge materials
- The furnace is run until all the SiO_2 of the preceding filling is completely consumed in the inner zone
- The remaining materials in the chambers are stoked into the inner zone.

In Chapter 2 it was shown that the rate of the reaction between SiO_2 and C depends strongly on the particle size. In industrial furnace operation, the size is generally about one centimetre for carbon particles and several centimetres for quartz particles. For such particles, the reaction between SiO_2 and C will be very slow at the temperatures in the outer zone. However, if the materials are finely crushed and agglomerated, the rate will increase strongly. This option is included in the model, therefore, three reactions are assumed to be important in the outer zone:

The carbon reaction: $SiO + 2\,C = SiC + CO$ [5.4]

The agglomerate reaction: $SiO_2 + 3\,C = SiC + 2\,CO$ [5.27]

The condensation reaction: $2\,SiO = SiO_2 + Si$ [5.2]

The reactions in a chamber, and the flows into and from it, are sketched in Figure 5.16.

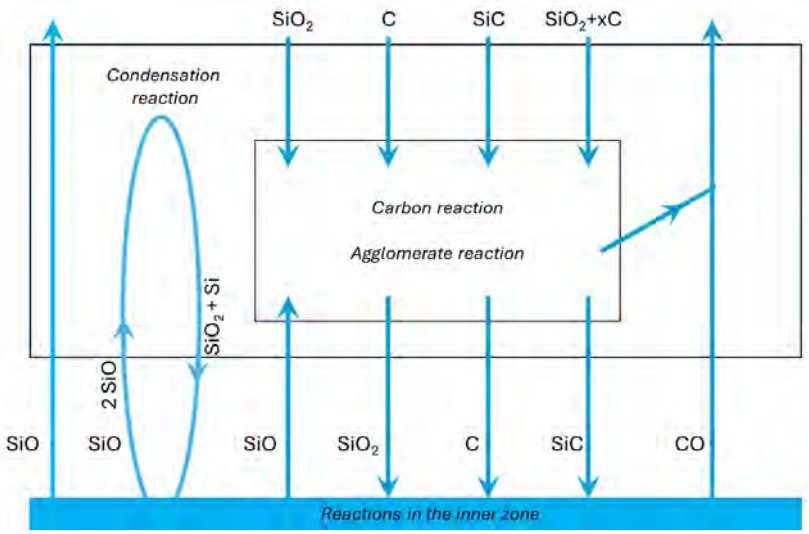


Figure 5.16 *The reaction in chamber A or B in the outer zone and material flows in and out of it.*

From practical experience, it is known that carbon materials often do not react completely. We therefore define a *reactivity number r*, which gives the fraction of the carbon that is available for reaction. Similarly, we define two reactivity numbers for the carbon in the agglomerates. First, there is a reactivity number for the direct reaction between SiO_2 and C in the agglomerate. Second, there is a reactivity number for any free carbon left after the SiO_2 has been completely consumed.

SiO from the inner zone is recovered either by reaction with carbon or by condensation. Condensation is strongly heat-producing, and the heat is absorbed either by raising the temperature of the ingoing raw materials or by heat-consuming reactions in the zone. The agglomerate reaction can absorb large quantities of heat. The amount of SiO that can be recovered is determined by the heat capacity (for heating and reaction) of the charge and by the carbon available.

When a sufficient amount of SiO is available, it is assumed that all the available C and the agglomerate react. SiO then condenses until the charge is heated to the condensation temperature. If the amount of SiO is insufficient, all the SiO reacts, and only a fraction of the charge is heated to the reaction temperature and reacts according to Reactions [5.4] and [5.27]. In that case, the reactivity numbers apply only to the heated fraction of the charge.

Calculation

The model has the following parameters that must have specified values:

- Amounts of SiO_2, C, SiC, agglomerate, content of SiO_2 and C in agglomerate.
- Distribution of the raw materials: Chamber A, Chamber B, directly into the inner zone.
- Distribution of the gas from the inner zone: Chamber A, Chamber B, directly out of the furnace.
- Reactivity number of the carbon in carbon materials.
- Reactivity number of the agglomerates.
- Thermal efficiency of the furnace.
- Temperature of the cold CO (CO leaving the furnace before the charge is heated to the condensation temperature).

As shown in the description of the inner zone, the reaction is easily calculated if the flow of materials entering the zone is known. The reaction in the outer zone is governed by a set of assumptions: the reaction between SiO and C runs until the available C is consumed; any remaining SiO is allowed to condense until the charge reaches the condensation temperature; and any excess free C goes into the inner zone. The reactions can be calculated from these assumptions and the heat balance when the material flows into the zone are known. The overall system is calculated by choosing arbitrary initial values for the flows into the inner zone and then iterating between the inner and outer zone until the reactions are consistent.

The model can be implemented on an Excel spreadsheet. The iteration typically converges within a few seconds. With known reactions, the energy consumption can be calculated.

Calculated examples

The use of the model will be demonstrated by some calculated examples. These examples show many properties of the silicon process, and together they provide a rough understanding of the process as background for the practical operation of a furnace. In the examples, the charge and the operational parameters are varied around a standard set that is shown in Table 5.2. The standard values are chosen to give reasonable results for all the steps in the calculation. However, it should be remembered that the calculations are examples based on the values of several parameters, and the conclusions should be interpreted with some scepticism concerning general applicability.

Table 5.2 *Standard values of the charge and the parameters used in the calculated examples from the stoichiometric model.*

Charge	**SiO_2**	**C**	**SiC**	**$SiO_2 + x$ C**
Composition in moles	1.00	1.85	0.00	0.00
Chamber A (fraction)	0.50	0.50		0.50
Chamber B (fraction)	0.50	0.50		0.50
Reactivity carbon				
Chamber A		0.72		0.90 (0.80)[1)]
Chamber B		0.72		0.90 (0.80)[1)]
Operation		Operation		
Gas distribution		Heat added in charge		
Chamber A (fraction)	0.5	Chamber A, kW		0.00
Chamber B (fraction)	0.5	Chamber B, kW		0.00
Cold CO		Aggl., x in $SiO_2 + x$ C		1.9
Chamber A (K)	298	s Minimum SiO inner zone		0.45
Chamber B (K)	298	Thermal efficiency		1.20

1) **The first value applies to the reaction between SiO_2 and C, while the value in the parentheses applies to the remaining free carbon after the direct reaction $SiO_2 + x$ C.**

Example 1 – Carbon content of the charge

The carbon content of the charge is one of the most important parameters of furnace operation, and the metallurgist can easily vary it. In industrial practice, the carbon content is chosen based on raw material analysis and former experience, and it is then corrected during operation according to furnace behavior. It can be described by the parameter x in $SiO_2 + x\,C$ (or by an analogous definition for SiC in the charge). The influence of the carbon content in the model is illustrated in Figure 5.17, where the success of the operation is characterized by the silicon recovery.

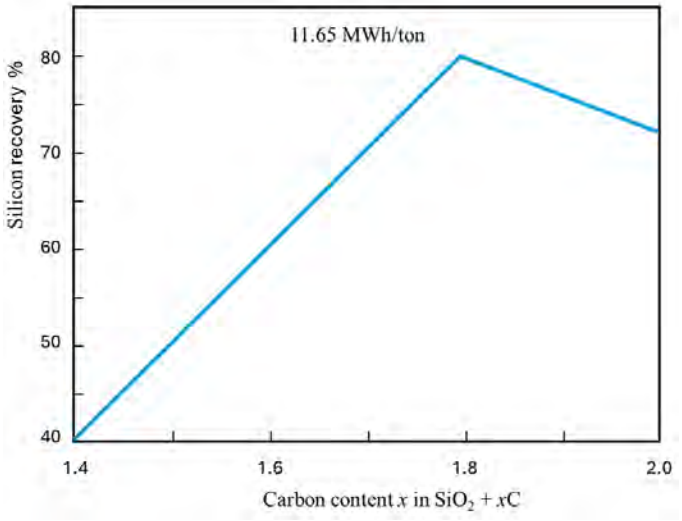


Figure 5.17 *The silicon recovery as a function of the carbon content of the charge calculated by the stoichiometric model.*

With the chosen parameters, the model gives a silicon recovery of about 80 per cent at an optimum value $x_{opt} \approx 1.8$. The recovery then drops strongly on either side of this maximum. A study of the details of the calculation shows that a carbon content lower than the optimum corresponds to an inner-zone reaction:

$$SiO_2 + x\,C = a\,Si + b\,SiO + c\,CO \qquad [5.28]$$

The SiO content of the gas will then be higher than the value corresponding to the parameter *s*. By contrast, a carbon content higher than x_{opt} gives a reaction of the type:

$$SiO_2 + x\,C = a\,Si + b\,SiO + c\,CO + d\,SiC \qquad [5.29]$$

The optimum carbon content depends on the values of the parameters in the calculation. The terms surplus or deficit of carbon should therefore refer to this optimum. If the furnace operates at the optimum carbon content, both an increase and a decrease will reduce the silicon recovery. Even with a surplus of carbon, there will be a silicon loss as SiO. However, if the operator tries to counteract this loss by adding more carbon, SiC will be deposited at the bottom of the furnace, and the overall silicon recovery will decrease.

Silicon lost as SiO reacts with O_2 above the charge and is captured as microsilica in the off-gas system. Silicon deposited as SiC at the furnace bottom will eventually block the operation, and large deposits must be avoided. Therefore, some metallurgists prefer to operate safely with a low carbon content, but at the price of reduced silicon recovery. The ability to run the furnace close to the optimum carbon content is a goal for furnace instrumentation and for the training of operators and metallurgists for silicon production.

Example 2 – Uneven gas distribution

In a unidimensional model, we assume that the flow of mass and the reactions are evenly distributed across the cross section of the furnace. This is evidently a rather crude assumption, as can be seen from the uneven distribution of the flames on the top of the furnace. The importance of this unevenness can be estimated from the model. An example is shown in Figure 5.18. The unevenness is characterized by a ratio:

$$Gas\ distribution\ ratio = \frac{Percentage\ of\ gas\ through\ chamber\ A}{Percentage\ of\ gas\ through\ chamber\ B} \qquad [5.30]$$

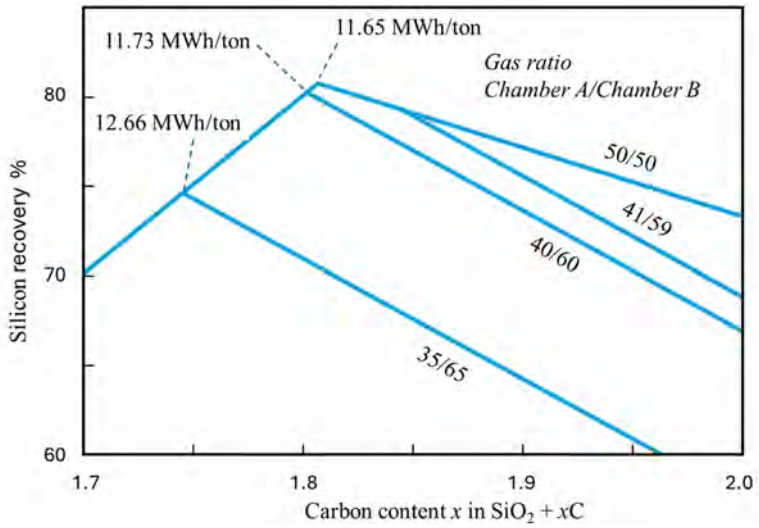


Figure 5.18 *The silicon recovery as a function of the carbon content of the charge calculated by the stoichiometric model for various gas distribution ratios. The silicon recovery has an optimum of 80.7% at x = 1.807.*

For the even gas distribution ratio 50/50, the silicon recovery as a function of the carbon content, goes through a maximum, as demonstrated above. With a moderately uneven distribution, the optimum silicon recovery is unchanged. However, on the right-hand side of the figure there is a range in which the Si recovery decreases more rapidly with increasing C content than it does for the even gas distribution. As the unevenness increases, this range of lowered silicon recovery covers an increasingly large part of the carbon distribution range, and at a certain value it reaches the optimum carbon content. With a further increase in unevenness, the obtainable silicon recovery decreases. In the model, the consequences of an uneven distribution are caused by incomplete counter-current flow between gas out and materials in. With excess gas through one chamber, the SiO-binding capacity of that chamber may be exceeded, while a lack of SiO in the other chamber may allow free C to enter the inner zone. The result is increased silicon loss, unless there is an excess of SiO-binding capacity in the system. Because of such an excess, the

lowering of the optimum silicon recovery does not start as soon as the gas distribution becomes uneven.

Uneven distribution of the raw materials will have a similar effect. Such uneven distribution may occur because of segregation in the charge. In the raw materials, the maximum lump size is about 100 mm for quartz and about 20 mm for carbon materials. This large variation in particle size may cause serious segregation in the charge materials during transport through the feeding system. The resulting unevenness in material distribution may also lead to uneven gas resistance and, consequently, uneven gas distribution. In special situations, uneven gas and charge distribution can counteract each other and give a fairly high silicon recovery.

Example 3 – Reactivity of carbon

The carbon materials will normally not react completely with SiO in the outer reaction zone, even when there is sufficient SiO available. They consist of particles up to 20 mm, where the reaction starts at the surface and forms a layer of porous SiC between the gas and the free carbon, as discussed in Chapter 2. The SiO has to diffuse through this layer to reach the carbon, and the reaction will slow down as the layer thickens. Normally, some free C will be left in the interior of the carbon particles when they are transferred to the inner zone. This behavior is simulated in the model by the reactivity number *r*, which is simply the fraction of the original carbon that will react in the outer zone if sufficient SiO is available. The influence of the reactivity number *r* is shown in Figure 5.19, where the silicon recovery is calculated as a function of *r* for two values of the parameter *s*. The reactivity number of the carbon can be controlled by the selection of raw materials. For a given carbon material, the reactivity number will increase with decreasing particle size.

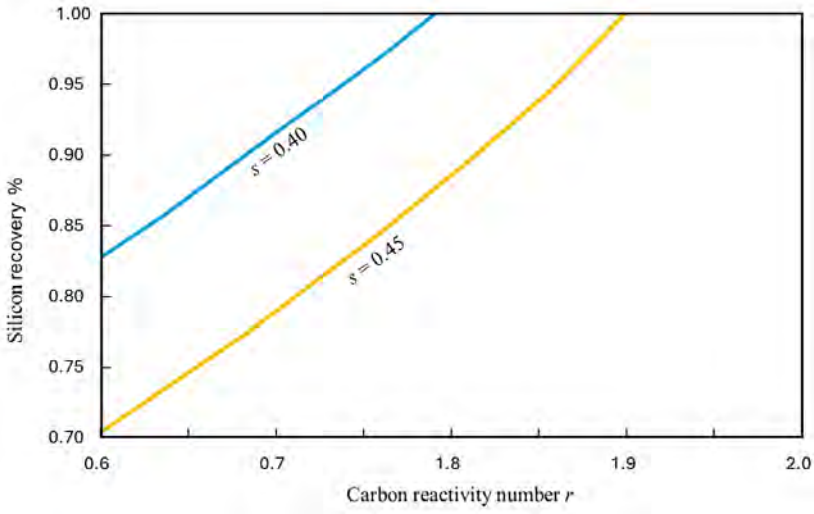


Figure 5.19 *The silicon recovery as a function of the carbon content of the charge calculated by the stoichiometric model for various values of the parameters r and s. At equilibrium in the inner zone s = 0.45 corresponds to 2036°C and s = 0.40 to 2091°C according to Figure 5.15.*

Figure 5.19 also shows the influence of the parameter *s*. As a first approximation, it has been identified with the equilibrium for Reaction [5.7] between SiO and SiC. Figure 5.15 shows that $s = 0.45$ corresponds to an inner zone temperature of about 2040°C, and $s = 0.40$ to about 2090°C. An increase in the inner zone temperature improves the silicon recovery strongly. However, the temperature cannot be regulated directly. Normally, the furnace is run with the maximum electric load, and the temperature is then determined by the rate of the heat-consuming reactions and by the addition of charge.

This example shows the advantages of a high temperature in the inner zone. There are, however, some drawbacks to a high temperature. The solubility of C will increase, and this C will precipitate as SiC when the alloy cools. Such precipitation may block the fissures through which the melt flows through the bottom to the taphole. A high temperature also increases the evaporation of silicon as Si(g). The Si(g) may react with C in a reversal of the reaction

$$SiO + SiC = 2\ Si + CO \qquad [5.7]$$

and deposit lumps of crystalline SiC in places where the heat of reaction can be given off.

Example 4 – Use of agglomerated charge

In a lump charge, there is negligible reaction between SiO_2 and C in the outer reaction zone, and the C can react mainly with the SiO from the inner reaction zone by Reaction [5.3]. The extent of this reaction is restricted by the amount of C available. In addition, some SiO is bound by the condensation Reaction [5.2]. However, this reaction is strongly heat-producing, and it will heat the charge to a temperature at which the SiO will pass through without condensing. The amount of SiO that can condense will increase if heat is removed. It has been suggested that the charge could be cooled by spraying water on the top of the charge. This cooling can, in principle, increase the condensation, but it will also decrease the thermal efficiency of the furnace, since it is difficult to find a useful application of the water vapour in the gas. The cooling will be more beneficial if the removed heat is used in the furnace process, for example by the reaction

$$SiO_2 + 3\ C = SiC + 2\ CO \qquad [5.27]$$

in the outer zone. This strongly heat-consuming reaction can run below the condensation temperature of SiO if finely ground SiO_2 and C are mixed and agglomerated in intimate contact. An example of calculated results is shown in Figure 5.20. For the parameters chosen, the silicon recovery can increase from about 80 per cent to 100 per cent. The stoichiometric model shows no theoretical limit to a 100 per cent silicon recovery. However, the price of the increased silicon recovery is a high load of condensate that may obstruct the gas flow and make stoking difficult and inefficient. No really successful industrial applications have been reported. Chapter 9 gives a further discussion of this option.

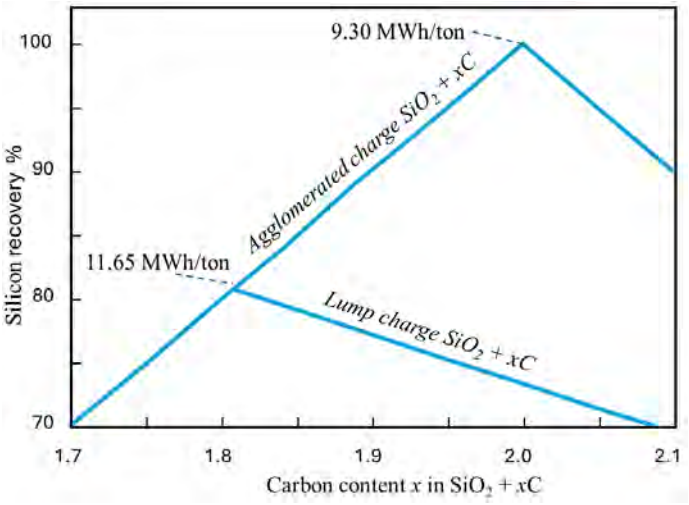


Figure 5.20 *The silicon recovery as a function of the carbon content of the charge calculated by the stoichiometric model for agglomerated and lump charge.*

The dynamic model

The stoichiometric model does not take into account the dynamic interaction between reaction kinetics, heat transfer, mass transfer, and electrical conduction. Therefore a more advanced model has been developed for the metallurgical behavior in the upper part of the furnace (Halvorsen *et al.*, 1993). The interaction between electric conductance and metallurgy is still neglected, and the electrode is treated only as a constant heat source. The furnace is split into two main parts (Figure 5.21): The shaft and the hearth. The shaft is split into an arbitrary number of segments, while the hearth is treated as a unity without any inner structure. Only the species SiO_2, C, SiC, Si, CO and SiO are considered. The model is one-dimensional and describes the height variations in the active part of the furnace for a 1 m^2 cross section area. The model calculates reaction rates, gas compositions and transport of material and energy between the segments. A brief discussion of the metallurgical content of the model will be given in the following. The mathematical formulation and solution are described by Halvorsen *et al.*, and Halvorsen (Halvorsen, 1994; Halvorsen *et al.*, 1993, 1991).

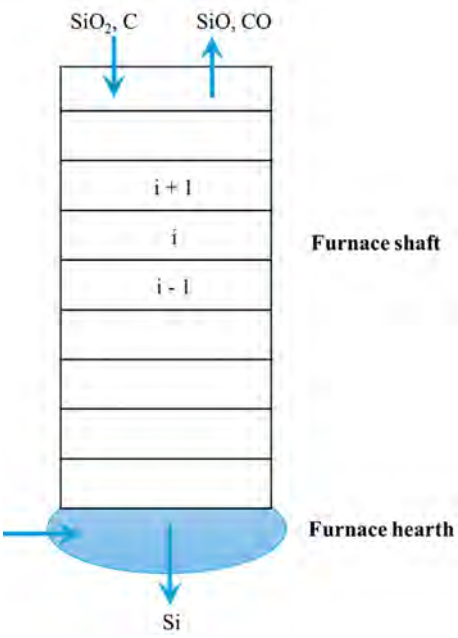


Figure 5.21 *Furnace hearth and shaft in the dynamic Elkem model of the silicon process. The shaft is partitioned into an arbitrary number of segments, while the hearth is treated as a unit.*

The reaction rate laws are based on deviation from equilibrium. For each reaction, a driving force is defined. As an example, the rate law for the reaction

$$SiO(g) + 2\,C = SiC + CO(g) \qquad [5.4]$$

is formulated as

$$R_{5.4} = a_{5.4} c_c \Delta p_{5.4} \exp\left(-\frac{e_{5.4}}{RT}\right) \qquad [5.31]$$

where

$R_{5.4}$ is the reaction rate (moles s^{-1} m^{-3}) of Reaction [5.4]
$A_{5.4}$ is the rate constant
c_C is the local concentration of carbon (moles m^{-3})
$\Delta p_{5.4}$ is the deviation from equilibrium pressure
E_{54} is the activation energy in the Arrhenius rate equation (kJ $mole^{-1}$ K^{-1})
R is the molar gas constant (kJ $mole^{-1}$)
T is the local temperature (K).

Reaction [5.4] causes a certain number of moles of SiO to be consumed, while the same number of moles of CO is produced. This property has been embedded in the model by defining the deviation from equilibrium as

$$\frac{p_{CO} + \Delta p_{5.4}}{p_{SiO} - \Delta p_{5.4}} = K_{5.4} \qquad [5.32]$$

where

p_{SiO} is the local SiO pressure
p_{CO} is the local CO pressure
$K_{5.4}$ is the equilibrium constant for Reaction [5.4] at the local temperature.

The reaction rates for the remaining reactions are defined analogously. In the hearth reactions, concentrations are replaced by the amount of material per m^2 cross-sectional area, since no height is defined for the hearth.

The reaction rates are proportional to the amount of the reactants only within certain limits. For instance, the reaction rate of the silicon-producing Reaction [5.7] is not likely to increase if more SiC is added to a hearth where there is already a large amount of SiC present. This is included in the model by specifying a maximum amount of hearth SiC that is available.

The kinetic parameters, such as $a_{5.4}$ and $E_{5.4}$ in Equation [5.31], should ideally be determined experimentally, and the form of the rate equation should apply to the critical step of the corresponding overall reaction. However, such data are not available. Therefore, the kinetic constants are defined for the overall reactions, and the values are determined by adjustment until the model predicts the furnace behavior reasonably well.

The dynamic model can be operated in two modes:

- The continuous feed mode
- The stoking cycles mode.

In the continuous feed mode, the height of the furnace is kept constant, and voids created by reactions are filled immediately from above. The shaft is refilled continuously with new charge to maintain the top level. In the stoking cycles mode, the top of the shaft is kept at a constant position. When voids

are created, the material content of the shaft shrinks, and the shaft–hearth interface moves towards the top. The furnace is stoked when predetermined conditions are fulfilled. During stoking, the content is pushed down until the shaft–hearth interface is in the original position, the upper part of the shaft is filled with new charge, and a new cycle starts.

Comparison with the stoichiometric model

Two computational series were compared. In one series, it was assumed that some of the SiC in the hearth was unavailable for reaction, while in the other series all the SiC was available. The silicon recovery from several runs in each series was plotted as a function of the molar ratio C/SiO_2 in Figure 5.22. The points in each series fell on two straight lines crossing at an optimum, as predicted by the stoichiometric model (Figure 5.17). For quantitative comparison, it is necessary to find parameters that are equivalent for the stoichiometric and dynamic models.

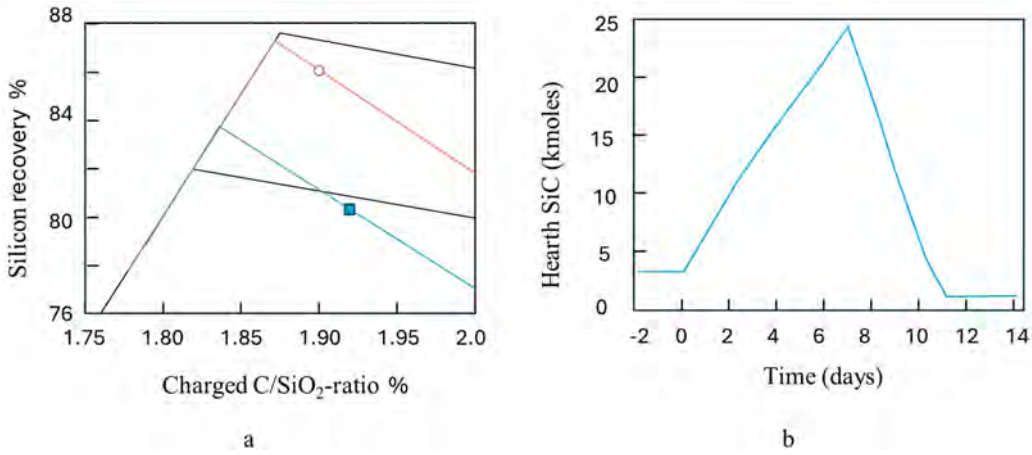


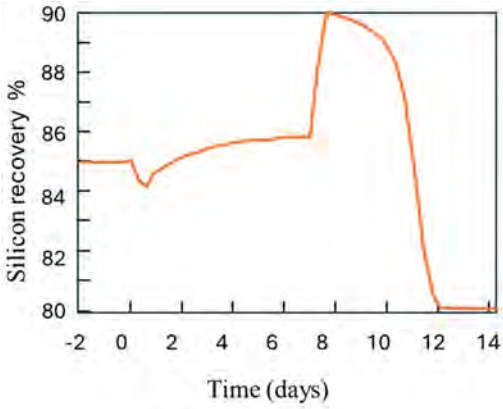
Figure 5.22 *Comparison of the dynamic and the stoichiometric models.*
Solid lines – the stoichiometric model.
Open circles – dynamic model without restricted availability of SiC in the hearth.
Filled squares – dynamic model with restricted availability of SiC in the hearth.

First, it was assumed that the hearth and shaft of the dynamic model correspond to the inner and the outer zone, respectively, of the stoichiometric model. The value of *s* was set equal to the SiO content calculated for the hearth in the dynamic model (s = 0.564 and 0.549, respectively, for runs with and without restrictions on the SiC availability in the hearth). The fraction *r* of the carbon reacting in the outer zone was then fitted so that the stoichiometric model gave the same Si recovery as the dynamic model with SiC restrictions in the hearth for the C/SiO_2 ratio 1.90. The result is shown in Figure 5.22a, but the two models deviate significantly. As an alternative comparison, both *s* and *r* were fitted to the series with restricted SiC availability (s = 0.445, r = 0.592). Then only the *s* value was changed (to 0.4339) to account for the difference between the two series. The results of the comparison are shown in Figure 5.22b. With these parameters, the dynamic and the stoichiometric models predict the same results.

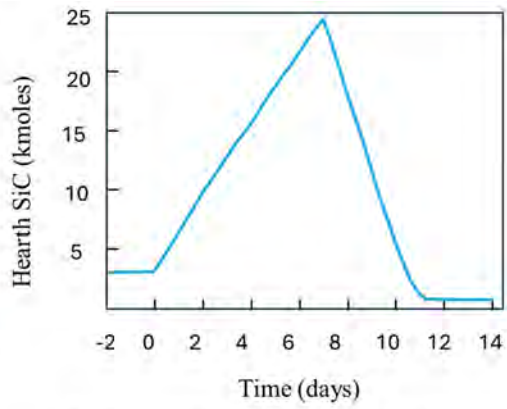
The fitted *s* values correspond to the SiO pressure between segments Nos. 4 and 5 in the dynamic model. Therefore, the inner zone of the stoichiometric model corresponds to the hearth and some of the lower segments in the dynamic model. The parameter *s* must be interpreted as the SiO content at the interface between the two zones. It describes the SiO content of the gas that leaves the SiO-producing zone, not the hottest part of the furnace.

Long-term dynamics

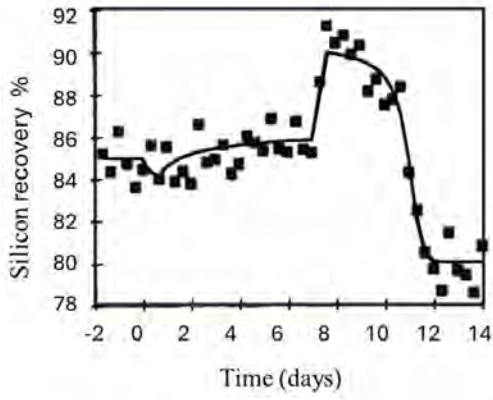
The long-term dynamics can be studied using the dynamic model in the continuous feed mode. An example of this application is given in Figure 5.23. The furnace is run close to the optimum carbon content, it is then run one week overcoked and one week undercoked. In practice, the optimum C/SiO_2 ratio will depend on raw material properties, furnace operation, and furnace construction.



a. Calculated results



b. Accumulation of SiC in the hearth



c. Calculated results with ±1.5% random noise added

Figure 5.23 *Dynamic behavior according to the dynamic model. A stable period (C/SiO_2 = 1.85, close to the optimum C content) is followed by one week with over-coking (C/SiO_2 = 1.90) and one week with undercoking (C/SiO_2 = 1.80).*

In the stable period, the furnace runs at 85 per cent Si recovery. When the C content is increased, the Si recovery drops for some hours. This is because the rate of SiC production increases with increasing C content of the charge, while consumption is proportional to the amount of SiC and therefore does not change initially. As the SiC deposits increase, the rate of SiC consumption and Si production also increases. The Si recovery then approaches asymptotically

a value slightly higher than the stable value before the increase in C content. This increase in silicon recovery means that the assumed optimum value was not correctly determined: the 85 per cent recovery really lies somewhat to the left of the optimum in a graph of the type in Figure 5.17. For a true optimum, an increased C content of the charge would give decreased silicon recovery.

When the C content is decreased after one week, the rate of SiC consumption is high because large SiC deposits are available, while the production of SiC drops. The deposits of SiC will therefore be converted to Si, and the Si recovery increases sharply. However, as the store of SiC is consumed, the rate of Si production decreases and approaches a stationary value corresponding to the new charge composition. The Si recovery therefore has to drop again after some time.

The furnace metallurgist can observe the silicon recovery, but not the accumulation of SiC. In addition, observations from a real furnace contain random noise. The furnace state may therefore easily be misinterpreted if the dynamic behavior is not properly understood. We assume that the metallurgist was uncertain about the carbon content of the charge during stable operation. Therefore, he or she added carbon to the charge at day zero and observed the results. At day 6 there was no clear change in the Si recovery (Figure 5.23c), and he or she decided to lower the C content. Shortly after the change, there was a significant improvement in the silicon recovery, and the operation became fairly stable for about three days. Then the recovery suddenly dropped drastically to a value lower than the value at day zero. The metallurgist might easily think, at this point, that some operational error had occurred.

In the model it is assumed that deposited SiC reacts readily with added SiO_2. However, experience shows that deposited SiC can be hard to remove, and excess SiO_2 to remove the deposits will often result mainly in increased electrode consumption. This effect is not included in the model.

Short-term dynamics

The stoking mode of the model is most suitable for studying the short-term dynamics. The temperature distribution in a furnace with a stoking cycle of 60 minutes is shown as an example in Figure 5.24. In this case, the height of the shaft is reduced from about 1 metre to 0.5 metre over the cycle period of 1 hour. At stoking, a 25 per cent fraction of the lower shaft materials

is transferred into the hearth zone, and the remaining fraction is pushed down until the interface hearth–shaft reaches the original start position. New charge is then added to the top of the charge to restore the normal shaft height. Immediately after stoking, the lower four segments are hot, while the others are filled with materials at room temperature. SiO_2 reacts with Si in the hearth, and the gas from the reaction passes through the shaft. When the SiO-rich gas meets the cold charge, the condensation Reaction [5.2] releases heat and the temperature rises. Thirty minutes after stoking, segments Nos. 5 and 6 are too hot for condensation, which now runs in segments Nos. 7, 8 and 9. In the hot segments, SiO can be captured in Reaction [6.4] as long as free C is available. Fifty minutes after stoking, the shaft is hot from bottom to top, and condensation runs only in the top segment, where the heat can be given off as radiation to the surroundings.

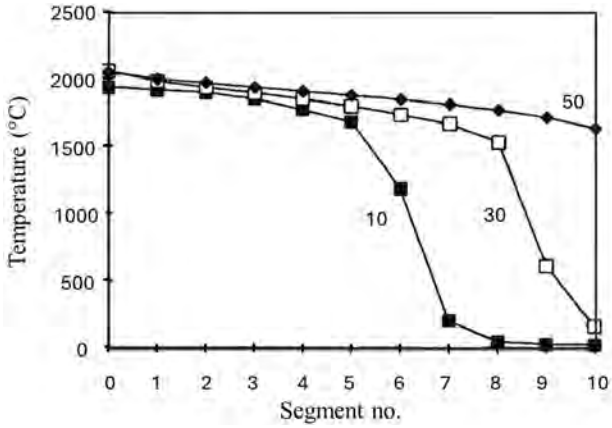


Figure 5.24 *The temperature distribution calculated after 10, 30 and 50 minutes in a 60-minute cycle by the dynamic model in the stoking mode.*

At the beginning of the cycle, SiO condenses almost completely in the upper layers. However, as the charge heats up to the top, SiO can pass through the charge without condensation and then leave the charge at the top. The amount of SiO lost is shown in Figure 5.25. The furnace blows for about 15 minutes before stoking. This observation indicates that more frequent stokings may reduce silicon loss, conversely, longer stoking periods should increase it. This last idea was tested by calculations. The increased stoking period, however,

changed the overall behavior of the furnace. The temperature of the hearth increased, and the SiO content of the gas became lower. The lowered SiO content more than compensated for the prolonged stoking period.

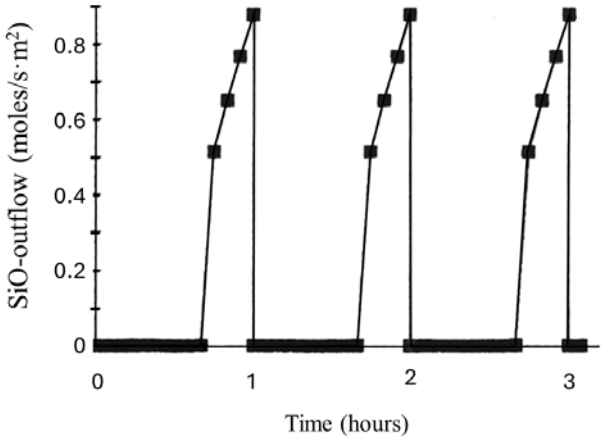


Figure 5.25 *The SiO loss from the furnace calculated for the 60 minute cycle by the stoking mode of the dynamic model.*

In any study of the stoking process, one must consider how stoking affects the process. The stoking period has to be long enough for the added materials to be completely consumed during the stoking period, otherwise, incompletely reacted raw materials will accumulate in the furnace. Model computations can provide insight that is of great value in such discussions.

Comparison of the modelling concepts

The mathematical models described provide means for different types of simulation. Each approach gives valuable understanding of the process and has applications where it is more suitable than the other models.

The Elkem stoichiometric model is very rapid and simple to use. It has been programmed as a spreadsheet document, and each computation takes only a few seconds. Nevertheless, it can show many of the characteristic properties of the silicon process, and it is suitable for training operators and metallurgists. However, it applies only to steady-state operation and does not show

the approach to steady state. The parameters of the model are lumped, which means that each parameter accounts for several physical effects. Therefore, they are not accessible for independent measurements.

In the Elkem unidimensional model, the shaft parameters have real physical meaning and can, at least in principle, be measured independently. The hearth parameters are lumped, but less so than the parameters of the stoichiometric model. When the model is run in the continuous feed mode, the parameters are averages over the stoking cycle. If corresponding values for the two modes are wanted, the parameters in the continuous feed mode should be adjusted until the two modes predict the same behavior.

The dynamic model is necessary when vertical variations in the shaft, or dynamic variations, are studied. In the continuous feed mode, it records the approach to steady state for a set of parameters. One computation takes several minutes on a powerful personal computer. This mode is suitable for studying the long-term development of the process. If variations within the stoking cycle are important, the model has to be run in the stoking mode. A case with a set of parameters has to be run until a fairly stable stoking cycle is obtained. In principle, the stoking mode can also be used to study the long-term dynamics, but the behavior is more easily seen when the properties are averaged over the stoking cycle.

Several models for various applications have been developed for the silicon process. A universal model will be very complex and most likely never be developed. Useful models require simplification, in which only the properties relevant to the purpose are included as different purposes require different models. Several models of specific zones in the Si-producing furnaces have been developed, such as for tapping, the off-gas system, and the crater and arc.

As a result of developments in computer and sensor technology and AI, more advanced and complex models covering many reaction zones have been possible. These are mainly developed and used by the separate Si and FeSi producers and, in most cases, not published or shared.

References

Aasly, K. (2008) *Properties and behavior of quartz for the silicon process*. Doctoral thesis 2008:236. Norwegian University of Science and Technology (NTNU), Trondheim, Norway. Available at: https://hdl.handle.net/11250/235844

Aasly, K. and Dosaj, V. (2016) 'Assessment of production performance of quartz in the Si-furnace', in *Proceedings of Silicon for the Chemical and Solar Industry XIII*. Kristiansand, Norway.

Andersen, V. (2009) *Investigation of thermal properties of quartz for the silicon industry under reducing atmosphere*. Specialization Project. Norwegian University of Science and Technology (NTNU), Trondheim, Norway.

Andersen, V. (2010) *Reaction mechanism and kinetics of the high temperature reactions in the silicon process*. MSc thesis. Norwegian University of Science and Technology (NTNU), Trondheim, Norway.

Andersen, V. (2023) *Flue gas recirculation for the silicon process*. Doctoral thesis 2023:135. Norwegian University of Science and Technology (NTNU), Trondheim, Norway. Available at: https://hdl.handle.net/11250/3069034

Andersen, V., Gaertner, H., Grådahl, S., Ksiazek, M., Einarsrud, K.E. and Tranell, G. (2022) 'Tapping gas from the silicon submerged arc furnace: An industrial measurement campaign', *JOM*, 74, pp. 3980–3989. Available at: https://doi.org/10.1007/s11837-022-05389-8

Andersen, V., Solheim, I., Gaertner, H., Sægrov-Sorte, B., Einarsrud, K.E. and Tranell, G. (2023) 'Pilot-scale test of flue gas recirculation for the silicon process', *Journal of Sustainable Metallurgy*, 9, pp. 81–92. Available at: https://doi.org/10.1007/s40831-022-00639-0

Arnesen, A.G. and Bjordal, J. (1980) 'Development and achievements with a closed 8,500 kW Elkem furnace producing 75% ferrosilicon', *Electric Furnace Conference Proceedings U.S.*

Dalaker, H. (2025) *FactSage calculations on the viscosities of silica melts*. SINTEF Report 2025:00140. Trondheim, Norway. Available at: https://hdl.handle.net/11250/3804988

Darmana, D., Olsen, J.E., Tang, K. and Ringdalen, E. (2012) 'Modelling concept for submerged arc furnaces', in *Proceedings of the 9th International Conference on CFD in the Minerals and Process Industries*. CSIRO, Melbourne, Australia.

Folstad, M.B., Ringdalen, E., Tveit, H. and Tangstad, M. (2021) 'Effect of different SiO2 polymorphs on the reaction between SiO2 and SiC in Si production', *Metallurgical and Materials Transactions B*. Available at: https://doi.org/10.1007/s11663-020-02053-x

Halvorsen, S.A. (1994) 'Mathematical models for the (ferro)silicon process', in *Proceedings of the 7th European Conference on Mathematics in Industry*. Stuttgart: P.G. Teubner, pp. 47–69.

Halvorsen, S.A. (1995) 'Mathematical modelling – an integrated part of Elkem's continued education for process metallurgists', in *Proceedings of INFACON 7*. Trondheim, Norway. Available at: https://www.pyrometallurgy.co.za/InfaconVII/729-Halvorsen.pdf

Halvorsen, S.A., Downing, J.H. and Schei, A. (1991) 'Developing a unidimensional simulation model for producing silicon in an electric furnace', in *Proceedings of the 4th European Conference on Mathematics in Industry*. Stuttgart: B.G. Teubner, pp. 293–298.

Halvorsen, S.A., Schei, A. and Downing, J.H. (1993) 'A unidimensional dynamic model for the (ferro)silicon process', in *Proceedings of the Electric Furnace Conference (1992)*, pp. 45–59.

He, J., Jusnes, K.F. and Tangstad, M. (2021) 'Phase transformation in quartz at elevated temperatures', *Asp. Min. Miner. Sci.*, 6, pp. 691–699.

Hoover, H. (2023) *Electrical resistivity of materials in the silicon furnace*. Doctoral thesis 2023:298. Norwegian University of Science and Technology (NTNU), Trondheim, Norway. Available at: https://hdl.handle.net/11250/3091823

International Organization for Standardization (2006) *ISO 18894:2006: Coke—Determination of Coke Reactivity Index (CRI) and Coke Strength After Reaction (CSR)*. Geneva, Switzerland: International Organization for Standardization.

Jahrsengene, G., Jayakumari, S., Kero, I.T. and Ringdalen, E. (2023) 'Sustainable metal production: Use of biocarbon and the concern of dusting', in *Proceedings of the 62nd Conference of Metallurgists, COM 2023*. Cham: Springer Nature Switzerland, pp. 1001–1007. Available at: https://doi.org/10.1007/978-3-031-38141-6_126

Jayakumari, S. (2020) *Formation and characterization of β- and α-silicon carbide produced during silicon/ferrosilicon process*. Doctoral thesis 2020:252. Norwegian University of Science and Technology (NTNU), Trondheim, Norway. Available at: https://hdl.handle.net/11250/2678922

Jayakumari, S., Jahrsengene, G., Ksiazek, M. and Ringdalen, E. (2023) 'Investigations on CO2 reactivity and thermal strength of carbon sources for ferroalloy and silicon production', in *Proceedings of the 62nd Conference of Metallurgists, COM 2023*. Cham: Springer Nature Switzerland, pp. 1009–1018. Available at: https://doi.org/10.1007/978-3-031-38141-6_127

Jayakumari, S. and Ringdalen, E. (2022) 'Effect of varying SiO contents on Si and FeSi production', in *Proceedings of Silicon for the Chemical and Solar Industry XVI*. Online conference. Available at: https://doi.org/10.2139/ssrn.4118642

Johansen, S.T., Tveit, H., Gradahl, S., Valderhaug, A. and Byberg, J.A. (1998) 'Environmental aspects of ferro-silicon furnace operations—an investigation of waste gas dynamics', in *Proceedings of INFACON VIII*. Beijing, China, pp. 59–63. Available at: https://www.pyrometallurgy.co.za/InfaconVIII/059-Johansen.pdf

Jusnes, K.F. (2020) *Phase transformation and thermal degradation in industrial quartz*. Doctoral thesis 2020:205. Norwegian University of Science and Technology (NTNU), Trondheim, Norway. Available at: https://hdl.handle.net/11250/2675473

Jusnes, K.F., Tangstad, M. and Ringdalen, E. (2018a) 'Cracks, disintegration and phase transformations in quartz', in *Proceedings of Silicon for the Chemical and Solar Industry XIV*. Svolvær, Norway, pp. 39–50.

Jusnes, K.F., Tangstad, M. and Ringdalen, E. (2018b) 'Shock heating of quartz used in silicon and ferrosilicon production', in *Proceedings of INFACON XV*. Cape Town, South Africa. Available at: https://www.pyrometallurgy.co.za/InfaconXV/

Kadkhodabeigi, M. (2011) *Modeling of tapping processes in submerged arc furnaces*. Doctoral thesis 2011:149. Norwegian University of Science and Technology (NTNU), Trondheim, Norway. Available at: https://hdl.handle.net/11250/248862

Kamfjord, N.E. (2012) *Mass and energy balances of the silicon process*. Doctoral thesis 2012:162. Norwegian University of Science and Technology (NTNU), Trondheim, Norway. Available at: https://hdl.handle.net/11250/249043

Kero, I.T., Eidem, P.A., Ma, Y., Indresand, H., Aarhaug, T.A. and Grådahl, S. (2019) 'Airborne emissions from Mn ferroalloy production', *JOM*, 71, pp. 349–365. Available at: https://doi.org/10.1007/s11837-018-3165-9

Ksiazek, M., Saadieh, R., Gærtner, H., Grådahl, S., Sægrov, B., Tangstad, M., Valderhaug, A. and Ringdalen, E. (2021) 'Industrial measurements of the gas and temperature in the Si and FeSi production process', in *Proceedings of INFACON XVI*. Trondheim, Norway. Available at: https://doi.org/10.2139/ssrn.3922198

Ksiazek, M., Smitch-Hansen, N., Rejdak, M., Baron, R., Larsen, S.Y. and Bao, S. (2022) 'Bio-coke for manganese alloy production', in *Proceedings of the Sustainable Industrial Processing Summit*. Flogen Star Outreach, pp. 171–188.

Ksiazek, M., Tangstad, M. and Ringdalen, E. (2016) 'Five furnaces, five different stories', in *Proceedings of Silicon for the Chemical and Solar Industry XIII*. Kristiansand, Norway, pp. 33–42.

Ksiazek, M., Tangstad, M., Ringdalen, E., Grådahl, S., Hustad, H.M., Holtan, J., Nymoen, A.B. and Kaukonen, S. (2018) 'Measurement of metal temperature during tapping of an industrial FeSi furnace', in *Proceedings of Furnace Tapping 2018*. Kruger National Park, South Africa.

Lindstad, T., Gaal, S., Hansen, S. and Prytz, S. (2007) 'Improved SINTEF SiO-reactivity test', in *Proceedings of INFACON XI*. New Delhi, India, pp. 414–423. Available at: https://www.pyrometallurgy.co.za/InfaconXI/414-Lindstad.pdf

Lindstad, T., Monsen, B. and Osen, K.S. (2010) 'How the ferroalloys industry can meet greenhouse gas regulations', in *Proceedings of INFACON XII*. Helsinki, Finland. Available at: https://www.pyrometallurgy.co.za/InfaconXII/063-Lindstad.pdf

Linnestad, K., Hildal, K., Jakobsson, L.K., Eidnes, S., Tjessem, V., Bjørnstad, E.L. and Wasbø, S. (2022) 'A hybrid digital twin for optimal Si-production', in *Proceedings of Silicon for the Chemical and Solar Industry XVI*. Trondheim, Norway. Available at: https://doi.org/10.2139/ssrn.4121131

Monsen, B., Grønli, M., Nygaard, L. and Tveit, H. (2001) 'The use of biocarbon in Norwegian ferroalloy production', in *Proceedings of INFACON IX*. Quebec City, Canada, pp. 268–276. Available at: https://www.pyrometallurgy.co.za/InfaconIX/268-Monsen.pdf

Monsen, B., Tangstad, M., Solheim, I., Syvertsen, M., Ishak, R. and Midtgaard, H. (2007) 'Charcoal for manganese alloy production', in *Proceedings of INFACON XI*. New Delhi, India, pp. 297–310. Available at: https://www.pyrometallurgy.co.za/InfaconXI/297-Monsen.pdf

Myrhaug, E., Tveit, H., Kamfjord, N., Andersen, J. and Grøvlen, Å. (2012) 'NOx emissions from silicon production', paper presented at *Silicon for Silicones*, Bergen–Ulvik, Norway.

Myrhaug, E.H. (2003) *Non-fossil reduction materials in the silicon process – properties and behaviour*. Doctoral thesis 2003:67. Norwegian University of Science and Technology (NTNU), Trondheim, Norway.

Myrvågnes, V. (2008) *Analyses and characterization of fossil carbonaceous materials for silicon production*. Doctoral thesis 2008:30. Norwegian University of Science and Technology (NTNU), Trondheim, Norway.

Nordhus, A. (2022) *Modelling gas flow in furnaces for Si production*. MSc thesis. Norwegian University of Science and Technology (NTNU), Trondheim, Norway. Available at: https://hdl.handle.net/11250/3026797

Nordnes, E. (2019) *Softening and melting properties of quartz*. MSc thesis. Norwegian University of Science and Technology (NTNU), Trondheim, Norway. Available at: https://hdl.handle.net/11250/3899522

Olsen, J.E., Darmana, D. and Tang, K. (2022) *Transient 3D modelling concept for submerged arc furnaces*. SINTEF Report No. 2022:00103. SINTEF Industry, Trondheim, Norway.

Raaness, O. and Gray, R. (1995) 'Coal in the production of silicon rich alloys', in *Proceedings of INFACON 7*. Trondheim, Norway: FFF/SINTEF, pp. 201–220. Available at: https://www.pyrometallurgy.co.za/InfaconVII/201-Raaness.pdf

Ringdalen, E. (2015) 'Changes in quartz during heating and the possible effects on Si production', *JOM*, 67, pp. 484–492. Available at: https://doi.org/10.1007/s11837-014-1149-y

Ringdalen, E. (2014) 'Quartz properties in the silicon production', in *Proceedings of Silicon for the Chemical and Solar Industry XII*. Trondheim, Norway, pp. 7–18.

Ringdalen, E., Bao, S. and Tveit, H. (2020) 'Effect of melting properties of quartz in industrial Si and FeSi production', in *Proceedings of Silicon for the Chemical and Solar Industry XV*. Trondheim, Norway.

Ringdalen, E., Bao, S., Tveit, H. and Nordnes, E. (2019) 'Melting properties of quartz and their effect on industrial Si and FeSi production', in *TRAVAUX 48: Proceedings of the 37th International ICSOBA Conference and XXV Conference "Aluminium of Siberia"*. Krasnoyarsk, Russia, 16–20 September 2019.

Ringdalen, E., Einarsrud, K.E. and Nordhus, A. (2022) 'Gas flow and pressure drop in charge material in silicon production', *JOM*, 74, pp. 3971–3979. Available at: https://doi.org/10.1007/s11837-022-05431-9

Ringdalen, E. and Gaertner, H. (2024) 'Effect of physical properties of biocarbon on Si and Mn-alloy production', in *Proceedings of INFACON XVII*. Beijing, China.

Ringdalen, E. and Tangstad, M. (2016) 'Phase transformations in quartz and its effect on furnace operation', in *Proceedings of Silicon for the Chemical and Solar Industry XIII*. Kristiansand, Norway, pp. 269–278.

Saadieh, R. (2024) *Process phenomena in furnaces producing ferrosilicon alloys*. Doctoral thesis 2024:199. Norwegian University of Science and Technology (NTNU), Trondheim, Norway. Available at: https://hdl.handle.net/11250/3132796

Schei, A. and Halvorsen, S.A. (1991) 'A stoichiometric model of the silicon process', in *Proceedings of the Ketil Motzfeldt Symposium*. Trondheim, Norway: Norwegian University of Science and Technology (NTNU), pp. 41–56.

Schei, A. and Larsen, K. (1982) 'A stoichiometric model of the ferrosilicon process', in *Proceedings of the Electric Furnace Conference*, pp. 301–309.

Schei, Tuset, J.K. and Tveit, H. (1998) *Production of high silicon alloys*. Trondheim, Norway: Tapir.

Sindland, C. (2020) *Production rate of SiO gas from industrial quartz and silicon*. MSc thesis. Norwegian University of Science and Technology (NTNU).

Sindland, C. and Tangstad, M. (2021) 'Production rate of SiO gas from industrial quartz and silicon', *Metallurgical and Materials Transactions B*, 52, pp. 1755–1771. Available at: https://doi.org/10.1007/s11663-021-02143-4

Sloman, B. (2018) *Mathematical modelling of silicon furnaces*. Doctoral thesis. University of Oxford, UK.

Smith-Hanssen, N., Jahrsengene, G. and Ringdalen, E. (2023) 'Biocarbon materials in metallurgical processes—investigation of critical properties', in Fleuriault, C., Steenkamp, J.D., Gregurek, D., White, J.F., Reynolds, Q.G., Mackey, P.J. and Hockaday, S.A.C. (eds) *Advances in Pyrometallurgy*. Cham: Springer Nature Switzerland, pp. 165–177. Available at: https://doi.org/10.1007/978-3-031-22634-2_16

Sommerfeld, M., Friedrich, B., Sommerfeld, M. and Friedrich, B. (2021) 'Replacing fossil carbon in the production of ferroalloys with a focus on bio-based carbon: A review', *Minerals*, 11. Available at: https://doi.org/10.3390/min11111286

Suárez-Ruiz, I., Diez, M.A. and Rubiera, F. (eds) (2019) *New trends in coal conversion*. Woodhead Publishing Series in Energy. Oxford, UK: Woodhead Publishing.

Tangstad, M. (2013) *Metal production in Norway*. Akademika Publishing.

Tangstad, M., Ringdalen, E., Olsen, J.E., Einarsrud, K.E., Myrhaug, E. and Reynolds, Q. (2021) 'Conceptual model of tapping mechanisms in FeSi/Si furnaces'. Available at: https://doi.org/10.2139/ssrn.3922189

Tangstad, M. and Ringdalen, E. (2025) 'Decarbonization ferroalloy production using biocarbon', *Minerals*, 15. Available at: https://doi.org/10.3390/min15030228

Tangstad, M., Safarian, J., Bao, S., Ringdalen, E. and Valderhaug, A. (2019) 'Reaction rates of 2SiO2 + SiC = 3SiO + CO in pellets at elevated temperatures', *Asp. Min. Miner. Sci.*, 3. Available at: https://doi.org/10.31031/AMMS.2019.03.000558

Tveit, H., Ringdalen, E. and Edfelt, H. (2020) 'Important parameters that control the crater pressure in a silicon furnace', in *Proceedings of Silicon for the Chemical and Solar Industry XV*. Trondheim, Norway, pp. 37–45.

Sævarsdottir, G. (2026) 'Electric operation', in M. Tangstad, G. Tranell, H. Tveit and E. Ringdalen (Eds.), *Production of high silicon alloys* (2. ed.) (pp. 229–268). Fagbokforlaget. https://doi.org/10.55669/oa880806

6

Electric operation

Gudrun Sævarsdottir

Metallurgical grade silicon and high silicon alloys are produced in Submerged Arc Furnaces (SAF), such as depicted in Figure 6.1. Here, electric current is passed through the raw material mix at various stages of conversion and releases the necessary heat to drive reactions by resistive heat dissipation. The overall reaction of the silicon process can be written as

$$SiO_2 + (1 + x)\,C + Q = x\,Si + (1\text{-}x)\,SiO + (1 + x)\,CO \qquad [6.1]$$

where Q is the heat that must be added to the strongly heat-consuming reaction. Equation 6.1 is an overall reaction that combines sub-reactions occurring at different locations in the furnace and at different temperatures. Since heat for the reactions in the furnace is released by resistive heat dissipation as electric current passes through the furnace, it is important that sufficient energy is released in the regions of the furnace where the reactions can occur. For example, the metal-producing reaction, which combines the reversed SiO condensation reaction [2.5] and the metal-producing reaction [2.7], requires temperatures above 1800°C to go to the right, at P_{tot} = 1 bar, and close to 2000°C for good silicon yield, as explained in Chapter 2. This high temperature is achieved and sustained by dissipation of electric energy in the furnace. This chapter describes some of the technical aspects of the systems supplying electric energy to the furnace, the conversion of electric energy to heat, the role and properties of electric arcs, and how heat production in the furnace can be controlled.

This work is licensed under the Creative Commons Attribution 4.0 International License.
To view a copy of this license, visit https://creativecommons.org/licenses/by/4.0/

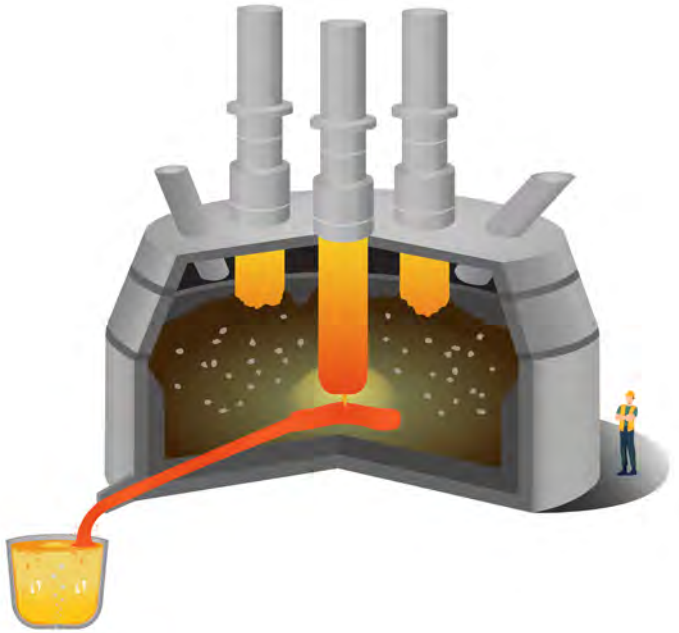


Figure 6.1 *A schematic drawing of a Submerged Arc Furnace.*

6.1 The distribution of heat generation in the furnace

A metallurgist seeking to maintain a well-operated furnace with a high Si-yield needs to pay attention to the selection and feeding of raw materials, ensure proper stoking and mixing, and tapping of the product. In addition, attention must be paid to the electric operation of the furnace, including selecting an appropriate set-point and control strategy for the raw-material mix in the furnace. Electric energy is fed into the furnace through the three electrodes, and a key aspect of the electric operation is to manage where in the furnace the heat is dissipated, and how much is released in the electric arcs as opposed to through Ohmic resistance in the charge.

Heat production

The basic law for resistive heating P as current I passes through a resistance R is:

$$P = I^2 \cdot R \qquad [6.2]$$

The main function of the Submerged Arc Furnace is to supply heat for the endothermic reactions contributing to the production of silicon, at the required temperature. Here, R is the combination of the resistances of the materials in the furnace and the arc resistances.

Most silicon furnaces are run with three-phase alternating current, and hereafter U and I refer to the RMS values of voltage and current. If the system is symmetric, the metal bath at the bottom represents the electrical zero point in the three-phase system. The electrode current I passes through a resistance R to the zero point, and real power $P = I^2 \cdot R$ is dissipated as heat. The furnace reactance, and the associated phase displacement φ between instantaneous current and voltage, leads to a relationship $P = U \cdot I cos\ \varphi$ between current, voltage, and the real load. This is further discussed in section 6.3. Here the furnace is modelled as a system in which the current passing directly between the electrodes is negligible.

The resistance R is as a rule called the *furnace resistance* or *phase resistance* and can vary slightly between the three electrodes, depending on the conditions around and below each electrode. In the ideal case of a symmetric load, the heat production is the same for all electrodes, and the total furnace heat production P from equation 6.2 becomes:

$$P = 3\ I^2 R = 3UI\cos\phi \qquad [6.3]$$

In the following discussion we will assume symmetrical load, even if furnaces are often run unsymmetrically. For unsymmetrical furnaces, the electrodes must be discussed separately.

As a rule, it is important to use the full production capacity, and the furnace will, as far as possible, be run at the fixed optimum load. An infinite number of combinations of voltage and current can give this load, but not all combinations are equally advantageous for the process. Several ideas have been used to establish the strategy for the electric operation of the furnace.

The heat distribution

According to the traditional understanding of the inner structure of the silicon furnace, we can hypothesize that the current is split into parallel branches: one through the arc and one through the charge. Although recent findings indicate a third type of path, through short arc discharges towards more conducting materials, we will combine that path with the charge current pathway in the following analysis. The current distribution is shown in an equivalent diagram for a single-phase furnace with bottom contact in Figure 6.2. This figure can also be interpreted as an illustration of one of the three phases in the furnace. Any current component passing between electrodes further up can be lumped in with the charge current.

It is not necessary, in this discussion, to separate a third type of likely current path: a short arc connecting the electrode and a conducting charge. However, it will be addressed later in the chapter.

As proposed by Westly, the current passing through the charge heats it up (Westly, 1974). This resistive heating, together with heat transfer from the crater zone (partly accomplished through SiO condensation and exothermic SiC formation), will melt silica (SiO_2) as it moves down in the furnace. In the crater zone, which is heated by electric arcs, the SiO_2 is consumed by the crater reaction. This reaction is strongly heat-consuming and requires a temperature of 1980°C to enable maximum yield. If the heat supply to the crater is insufficient, the reaction will not be complete, and molten SiO_2 will accumulate at the bottom. As molten SiO_2 is an oxide melt, it is called slag in other reduction processes. However, one should always remember that the slag in the silicon process is not a waste, but a valuable material that potentially can be utilized by improved operation (except for small amounts of Al_2O_3 and CaO). Westly continued his argumentation with a discussion of the conditions for complete consumption of the molten SiO_2.

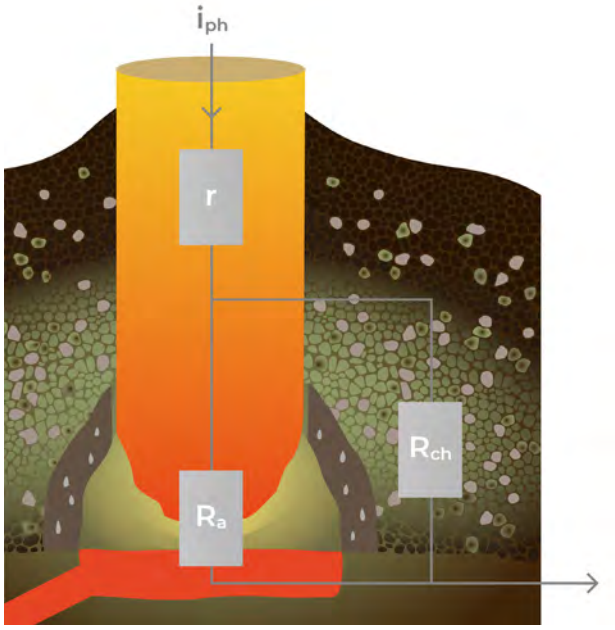


Figure 6.2 *Simplified equivalent diagram for the arc and charge resistance in a single-phase furnace.*

Westly defined a heat distribution coefficient, C:

$$C = \frac{Q_{ch}}{Q} = \frac{U^2 / R_{Ch}}{U^2 / R} = \frac{R}{R_{Ch}} \qquad [6.4]$$

where

U	is the voltage electrode – bottom
Q_{Ch}	is heat produced in the charge
Q	is total heat produced
R_{Ch}	is the resistance of the charge
R	is total resistance

The value of the coefficient C varies in the range $0 \leq C \leq 1$. The resistance of the charge varies fairly slowly during operation, while the resistance of the arc can vary rapidly. Its value will be influenced by the choice of electrode position. A too high value, with insufficient arc activity, gives typical symptoms:

- Large production of molten SiO_2 with some SiC
- The load varies only slightly, or only for a short time, when the electrode is raised or lowered
- The electrode consumption becomes low at the tip, but high further up on the side of the electrode, resulting in narrow electrodes.

According to the reasoning above, these symptoms will appear when the heat production in the charge melts more SiO_2 than the crater can consume. The coefficient C has then exceeded a maximum value, C_{max}, at which SiO_2 melting and crater consumption are balanced. The largest acceptable total resistance is therefore, for a given furnace, the charge resistance R_{Ch}.

If a furnace is operated at R_{max} and the arc resistance is increased while maintaining a constant charge resistance, the overall resistance of the furnace increases and the voltage must be raised to keep the load. The increased voltage will increase the charge current and therefore the heat release in the charge. Since the load is kept constant, the heat production in the arc will decrease. The increase in arc resistance has raised the ratio Q_{Ch}/Q above the acceptable value. It is therefore impossible to increase the total resistance unless the resistance of the charge is also increased.

The heat distribution theory states that a silicon furnace with a certain charge has a maximum resistance that is compatible with good operation. This maximum value is normally not known. The metallurgist selects an operating resistance and corrects it if the symptoms of too high resistance appear. For a chosen load, the current will be lower the higher the resistance. Since the heat losses in the conductors increase with increasing current, as do the stresses on the electrodes, the furnace metallurgist will operate with a resistance that is as high as possible. Therefore, R_{max} can be seen as an optimum resistance.

Andreae's rule

Andreae gave the first formulation of a relationship between electric operation and furnace behavior around 1930 (Andreae, 1933). He studied the available information from operating furnaces and found that furnaces with good operation results fulfilled a relation

$$\pi D R = k \qquad [6.5]$$

where D is the electrode diameter, R is the resistance of one electrode, and k is a constant for a given charge. The factor π was added because the electrode resistance was originally related to the electrode circumference, and k was often called the periphery resistance. The Andreae rule states that the optimum resistance depends on the electrode diameter but is independent of the load. The constant k has a value in the range 0.0030–0.0045 Ωm for silicon.

A simple derivation offers a physical interpretation of the k factor. If we consider the conducting part of the furnace as a cylindrical continuation of the electrode, and we insert the corresponding expression for R (with electric resistivity ρ and l as the length of the contact cylinder), Equation [6.5] changes to

$$k = \pi DR = \pi D \frac{\rho l}{\pi D^2 / 4} = 4 \frac{l}{D} \rho \qquad [6.6]$$

If the ratio l/D is constant, k is proportional to ρ, this statement can be expressed more generally: k is proportional to ρ if the conducting elements in the furnaces have the same proportions and differ only in size. Therefore, k expresses the specific resistivity of the charge. This charge resistivity should be interpreted as the resistivity of a certain volume within the furnace, which is difficult to reproduce for accurate measurement in a resistivity cell. In addition, if a significant part of the current passes through an arc, one should be cautious with models that assume conduction through regular geometric forms. However, Andreae's rule can also be useful for the silicon production process.

Westly's rule

Westly carried out a statistical analysis of almost one hundred silicon and ferrosilicon furnaces to establish the connection between load and current (Westly, 1979). He proposed a model to fit the data:

$$\ln I = A + B \cdot \ln P \qquad [6.7]$$

and fitted the constants to obtain an empirical relation for the furnaces:

FeSi 75: $\ln I = 2.453 + 0.641 \ln P$ 68 furnaces Correlation coefficient 0.986

Si metal: $\ln I = 2.381 + 0.660 \ln P$ 27 furnaces Correlation coefficient 0.974

Corresponding calculations for furnaces producing other commodities (calcium carbide, ferromanganese, silicomanganese, ferrochromium, silicochromium) gave B values in the range 0.655 to 0.731. Westly concluded that the variation in the B values was random and set it equal to 2/3. The relation between current and load is thus given by:

$$I = C_3 \cdot P^{2/3} \qquad [6.8]$$

where C_3 is a constant that varies to some extent because of the nature of the raw materials and the mode of operation. Westly calculated a mean value 10.662 for silicon metal and 10.865 for FeSi75 for the furnaces he had statistics from (with the units MW for P and kA for I).

The subscript 3 in the constant C_3 indicates that Equation [6.8] applies to a three-phase furnace, with P as the total load and I as the representative phase current. If the load for each electrode is used, individual constants C_1 can be calculated for the electrodes. The Westly rule has the same form whether it is given for one or three electrodes. In calculations, one must remember that P means the whole-furnace load in the C_3 formula, but only the load for one electrode in the C_1 formula. Therefore, the constants C_1 and C_3 are different.

$$I = C_1\left(\frac{P}{3}\right)^{2/3} = C_3 P^{2/3} \qquad [6.9]$$

$$\frac{C_1}{C_3} = 3^{2/3} = 2.08 \qquad [6.10]$$

As in the equations above, I is the phase current in one electrode, and P is the overall load of the furnace. Equation [6.10] is useful when comparing the electric operation of single- and three-electrode furnaces.

Westly also considered furnace operation with unreliable power availability. This involves operating the furnace at strongly reduced load for long periods (Westly, 1976; Westly, 1974). According to the Andreae rule, the resistance should then be constant, but Westly found that he had to change the resistance set point to achieve the best operation. However, when he made the value of the k factor dependent on the current density, the rule was still valid. The corrected k was determined as

$$k^2 i = k_1 \qquad [6.11]$$

where i is the current density in the electrode and k_1 is a new constant. Combined with the Andreae rule, this equation gives Equation [6.8], which is therefore useful both for dimensioning new furnaces and for changing the load on established furnaces.

The optimal electrical operation of a furnace must be determined during operation for each furnace and charge, but the experience embodied in the Westly rule provides a good estimate of a starting value. If, for some reason, it is necessary to run with a load lower than normal, the rule indicates how the load must be reduced to sustain optimum operation. Equation [6.8] can take several equivalent forms, and the most convenient form depends on the situation. The form in [6.8] is useful when a furnace is controlled for constant current, since it immediately gives the current setpoint when the load is known. If the furnace is controlled for resistance, an equivalent expression can be derived by combining Equation [6.8] with the equation for furnace load [6.3] which gives the following relationship:

$$P = 3I^2R = 3\ C_3^2 P^{4/3} R \Rightarrow\ P^{1/3} R = C_X \qquad [6.12]$$

The expressions for C_3 and C_X are not dimensionless, therefore, their numerical values vary with the choice of units. For C_3, the chosen units are normally kA and MW, giving C_3 a value of around 10. If we use the units MW and mΩ, C_X will be around 3. With this choice of units, the relationship between C_3 and C_X is:

$$C_X = \frac{1}{C_3^2} \cdot \frac{1000}{3} \qquad [6.13]$$

The Westly rule is an empirical rule based on experience with varying loads on the same furnace and on a statistical investigation of a large number of industrial furnaces. Its foundation is essentially the condensed experience of many metallurgists around the world. They tried to optimize operation by trial and error, and furnaces of many different sizes ultimately settled into a state described fairly accurately by the Westly rule. Thus, it seems safe to use it as an empirical rule, even though it lacks a theoretical foundation. It is equivalent to Andreae's rule for constant current density in the electrode, and it shows how Andreae's parameter *k* varies with the current density.

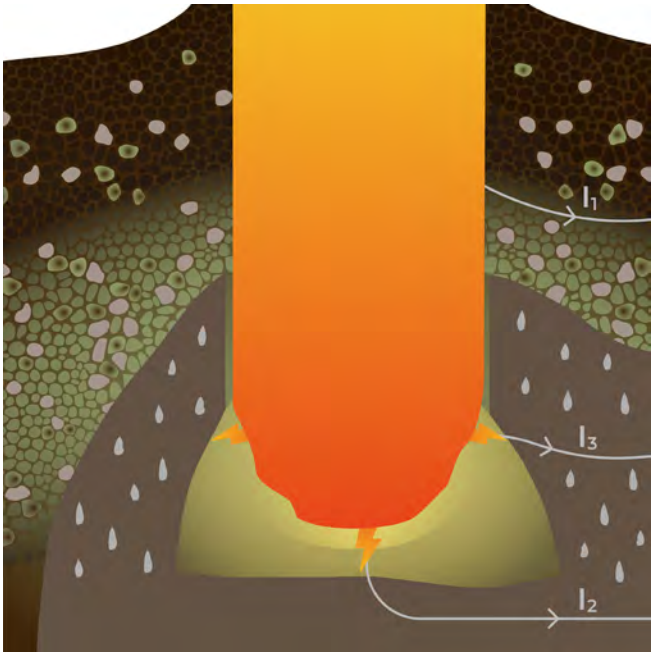


Figure 6.3 *A schematic of alternative current paths from the electrode through the furnace. The current paths correspond to the description in the text.*

6.2 Current paths

Furnace excavations have revealed large variability in the inner structure of furnaces. A schematic of one version of the current-conducting inner structure of the furnace is shown in Figure 6.3. Normally, the lower part of the electrode is surrounded by a cavity. The upper part of the cavity walls consists of a partly transformed charge of SiO_2, C, SiC and condensate with rather low conductivity. In some cases, it is partly converted to and mixed with Si, and is thus more conductive. The lower part mainly consists of reaction products, Si and SiC, mixed with molten silica, and has fairly high conductivity.

The material layers are volume conductors with a very large cross section, so the current is a distributed volume current. The figure indicates that there are principally three current paths from the electrode:

1. Electrode – charge – furnace interior
   Ohmic conduction through a bed of charge particles, denoted I_1 in Figure 6.3.
2. Electrode – gas space – high conductivity metal penetrated bottom – furnace interior
   Plasma arc in the gas-filled cavity towards metallic conduction, denoted I_2.
3. Electrode – narrow gas-filled gap to partly converted charge materials to furnace interior
   Combination of all conduction mechanisms listed above, denoted I_3.

Current passing from one electrode to the others is sometimes represented as a fourth current path, but it can be seen as a variant of the first one.

The current path from the furnace interior to the other electrodes is through any combination of the same mechanisms.

Distribution between paths

The distribution of the current between these paths is hard to measure, and the concept is mainly built upon indications and speculations. Estimates – based on methods such as estimating the slope of the Lissajous curve for the real voltage and current, as indicated in Figure 6.12.b – suggest that around

30–60% of the phase current passes without arcing, directly through charge materials (Haraldsson *et al.*, 2023; Sævarsdottir and Bakken, 2010).

The electric arc (or, more likely, arcs) is important for metal production, as arc temperatures above 10.000 K form a heat source that can supply heat to reactions that require very high temperatures to proceed in the right direction. In this lowest part of the furnace, the reactants SiO_2 and SiC are present. Along with the liquid Si and the gaseous products SiO and CO, they need a reaction temperature of around 1980°C to reach an equilibrium with equal partial pressures of SiO and CO, which enables a good Si yield (See eq. 2.7). There is likely more than one arc on each electrode. They are not in fixed positions, but move erratically around near the tip of the electrode or along the sides.

The resistance of the furnace is regulated by raising and lowering the electrode tip. When it is lifted above a certain position, the distance to conducting material at the side of the crater will be shorter than the distance to the bottom. Since the arcs will always try to find the path of lowest resistance, most of the current will go to path I_1 and I_3 at the upper part of the conducting hot furnace zone. If the sides of the cavity are steep, the resistance will then vary only slightly with the electrode position. The electrode will be consumed by the arc away from the tip, and it will develop an irregular form, but may remain long and narrow. The charge materials sink to the bottom of the cavity and, because of the distance from the arc, they receive a relatively low fraction of the heat. The result is that unreduced SiO_2, with some SiC, is collected at the bottom and is characterized by slag and problematic tapping. This state is what is normally interpreted as symptoms of the current path being too high in the furnace, or a 'short current path', which can be caused by a furnace resistance being above the allowed maximum (as previously discussed). A 'short current path' can be detected by a reduction in the furnace reactance, as displayed in the furnace control system, which increases the power factor cos(φ). This phenomenon is reported in (Tesfahunegn *et al.*, 2021).

The excess of the SiO_2-containing charge at the bottom has low conductivity, and it may make it difficult to re-establish the bottom arc even when the resistance is lowered. However, the largest resistance in the current path is still an arc, not a charge current. In a stationary furnace, the electrode will be in the centre of a hole into the high-conducting layer, and the arc may burn in any position around the electrode. In a rotating furnace, the electrode will be in a circular trench, and there are predominantly two directions – inwards

and outwards – that are open for the arc to the side. Upstream, the material will get closer to the electrode and arc, and electrode consumption will tend to be higher on that side. If a furnace is run for a long time on high resistance, the control system will place the electrode at the top of the high-conducting layer. If the two sides of the trench are not equally high, the electrode tip will be consumed preferentially on one side and develop a slanting tip.

A charge current I_1 passes a resistance that does not change significantly when the electrode is moved, except that the contact points connecting charge and electrode may be disrupted by the movement. The current through this path is not readily available for measurement, but the effect of the heating can give indications of its magnitude. The energy needed to heat the reactants to the reaction temperature is small compared with the heat of reaction. It has been argued that if a large fraction of the current flows along this path, the heat will melt the SiO_2, and the roof of the cavity will soon break down. Therefore, it can be concluded that the resistance along this path is much larger than the arc resistance, and that during normal operation only a relatively small fraction of the current flows through it. However, estimates from Lissajous curves with the reactance removed, as discussed above and shown in Figure 6.10.b, indicate a significant charge current component. If a furnace is operated at a resistance that is somewhat too high, the charge current will increase to some extent, but not enough to make the current insensitive to the electrode position.

The Westly rule is an empirical rule based on extensive practical experience. Westly showed that it could be derived theoretically by an extension of a study by Bøckman, where it is shown by dimensional analysis that (Bøckman, 1960; Westly, 1976)

$$\frac{R \cdot D}{\rho} = constant \qquad [6.14]$$

Here is the resistivity of the conducting space in the furnace, and D is a linear dimension. Bøckman's analysis assumes that furnaces of different sizes can be geometrically and electrically similar. Two furnaces are geometrically similar if all linear dimensions are scaled by the same factor. Linear dimensions include, for example, electrode diameter, electrode spacing, crucible diameter, and crucible depth. The furnaces are electrically similar if the current density

is the same at all corresponding points. When these similarity requirements are fulfilled, Equation [6.14] gives Andreae's rule.

We insert

$$R = \frac{P/3}{I^2} \text{ and } I = c_b D^2$$

into Andreae's rule, with constants c_b and c_c, and obtain

$$\pi RD = \pi \frac{P/3}{I^2} \sqrt{\frac{I}{c_b}} = c_c \frac{P/3}{I^{3/2}} = constant$$

$$\Rightarrow I = C_3 P^{3/2} \qquad [6.8]$$

Which is, again, Westly's rule, Equation [6.8].

However, there are difficulties with the assumptions behind this deduction. Bøckman's Equation [6.14] gives Andreae's rule only if the conductivity of the conducting volumes is the same at corresponding points in furnaces of various sizes. However, conductivity varies with temperature, which is in turn determined by the balance between heat production and heat loss.

Heat production is proportional to volume, while heat flow out of the volume depends on the product of surface area and temperature gradient. Most of the energy should be consumed by the heat-consuming reactions within the volume considered. As for heat loss, a larger furnace should lose proportionally less heat by conduction if the gradient is similar. However, significant heat and chemical energy are carried from the crater zone with the gases. So far, the argument has applied to a solid conductor. If the conductor is a fluid, as the plasma arc is, convection will contribute to heat transport and make the situation more complex. Therefore, it is not self-evident that the conducting volumes in two furnaces of different size will be electrically similar, which is a weakness in the assumptions on which the Westly equation is based. The simplifications made still enable a qualitative understanding of the important fundamentals.

In principle, the current distribution through the furnace can be calculated if the resistivity of the furnace content and its temperature dependence are known. Heiss set up a model of the electric smelting furnace based on

Maxwell's electromagnetic equations coupled with the temperature field (Heiss, 1982). However, the model produced rather complicated non-linear partial differential equations, and he had to apply strong simplifications. In recent years, Tesfahunegn and Herland have modelled the current distribution in Submerged Arc Furnaces for silicon and FeSi production. However, even with advances in computational power and access to sophisticated software platforms, the models require many simplifying assumptions to run (Herland *et al.*, 2019; Tesfahunegn *et al.*, 2021). Thus, different models yield different findings, depending on the simplifications made. Another difficulty is the continuing lack of reliable physical properties for the materials at the various reaction stages in the furnace, even though significant efforts have been made to measure these properties at elevated temperatures, as shown later in this chapter. Modelling the current distribution using the measured properties overestimates the furnace resistance. To obtain more realistic estimates, it would be necessary to measure at temperatures approaching 2000°C and to include the effects of molten slags. The effect of slags is even more important in FeSi furnaces, as iron oxide is reduced to metal by CO and increases the conductivity of both the charge and molten SiO_2 mixes.

Larsen *et al.* have simulated the alternating current electric arc in the silicon furnace, using data for SiO–CO gas compositions (Haraldsson *et al.*, 2024; Larsen, 1996; Sævarsdóttir, 2002). Nonetheless, much theoretical and experimental work remains to be done on the current through the charge and the gas cavity in order to obtain a full understanding. The empirical Westly rule is, therefore, still important and useful guidance for the practical metallurgist.

The Westly rule gives the optimum furnace resistance for a given load, based on empirical data. Heat distribution theory provides a physical interpretation, but it can only state that there is a maximum allowable furnace resistance. In the terminology of the Westly rule, it states that there is a minimum allowable value of C_3. The maximum allowable resistance can also be given an alternative interpretation. The furnace operator controls the resistance by raising or lowering the electrode, which means that a high resistance corresponds to longer, fewer arcs, or to a larger part of the current being forced through the resistive charge. This leads to more heating in the upper parts of the furnace and less in the lower part, where the metal is produced and tapped.

Sometimes the current through the furnace is analysed using a detailed equivalent circuit. An example is shown in Figure 6.4 (Sævarsdóttir, 2002).

In addition to the current paths shown, some current is conducted directly between the electrodes through the charge, but these paths are likely small. Moreover, when setting up an equivalent circuit, it is not possible to separate the resistive current paths higher up in the furnace from other ohmic parallel resistance.

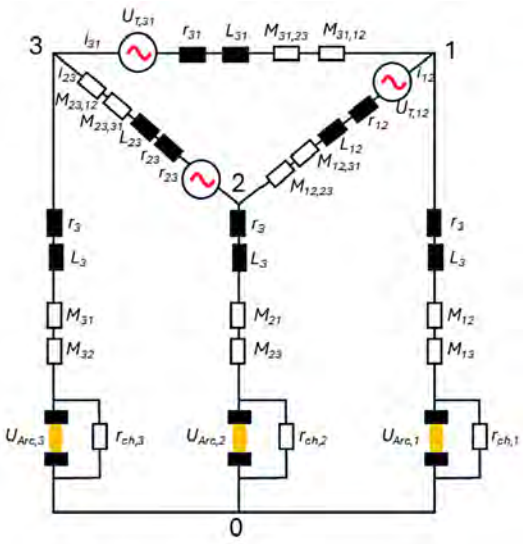


Figure 6.4 *Equivalent circuit for a three-phase submerged arc furnace. The figure shows the furnace part of a circuit with electrodes in Knapsack connection. [With permission from Sævarsdottir (2002)].*

Notation: I current, U voltage, L inductance and M mutual inductance; 1, 2, 3 the phase or electrode numbers.

Current through the charge

In this chapter we will explore the properties of the charge vs. the properties of the electric arcs.

How energy is dissipated in the furnace depends on the current paths within the furnace, which are determined by the electrical conductivities of the materials filling it. In the case of Si production, the charge materials fed into the furnace are a combination of quartz, coal, coke, charcoal and wood chips; in the case of ferrosilicon production, iron oxides are added. A number

of researchers have studied the physical properties of these charge materials, most importantly electrical conductivity. Krokstad measured the resistivity of several grades of industrial SiC crusts (Krokstad, 2014). These data, along with a summary of some available material property data as a function of temperature, are shown in Figure 6.5 (Eidem *et al.*, 2010). Hoover measured the resistivities of a range of compounds, as summarised in Figure 6.5 (Hoover, 2023; Hoover *et al.*, 2023, 2022). They also studied mixtures of charge materials, including quartz and iron oxide, with results for 1400°C as shown in Figure 6.6.

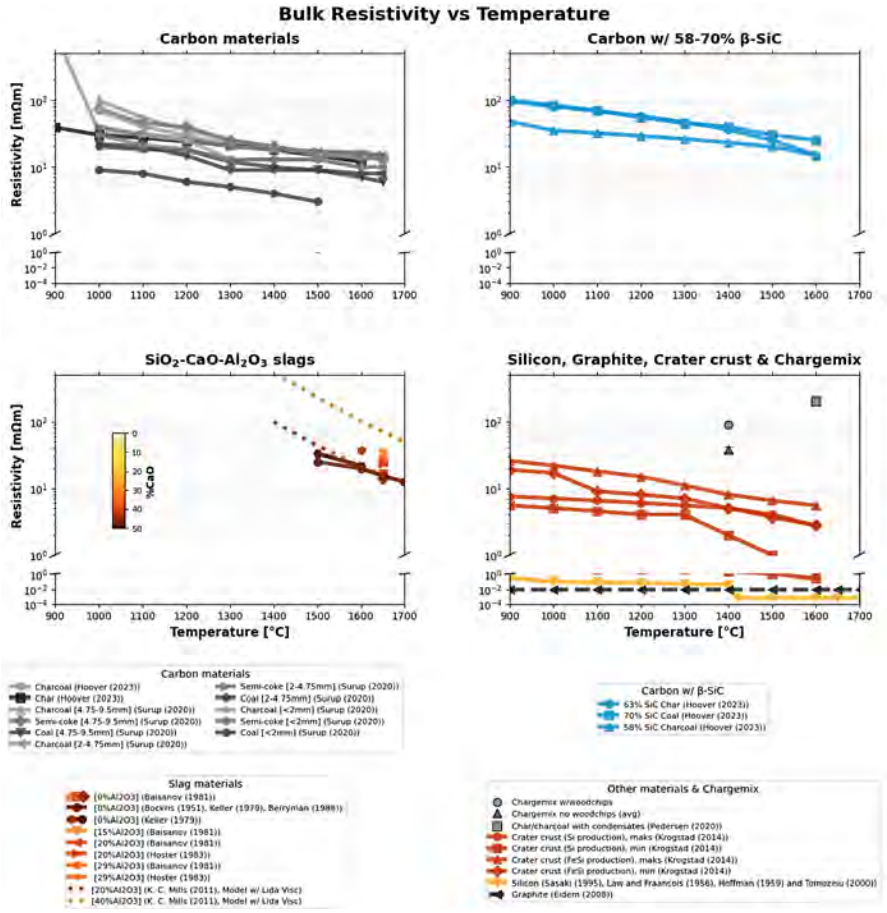


Figure 6.5 *The material resistivity of materials used in the silicon furnace compiled by Sindland (Sindland et al., 2027).*

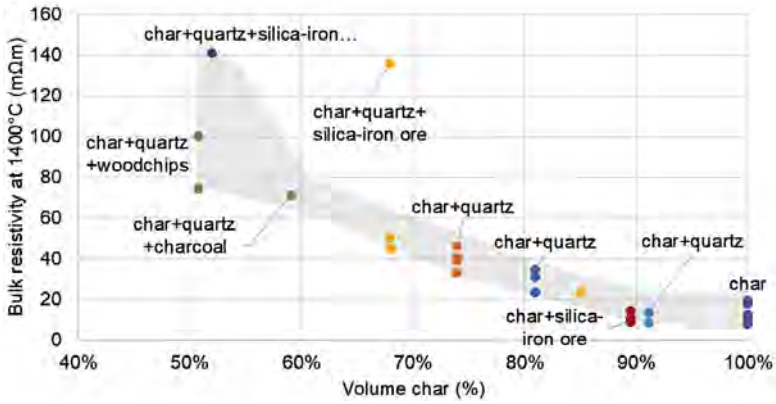


Figure 6.6 *Resistivity at 1400°C for all charge mixes as a function of the volume% char. Data points are labelled with their mixtures. [From (Hoover et al., 2023) used under Creative Commons CC BY licence].*

In general, the findings show a wide range of resistivities. Quartz is a relative insulator, whereas carbon materials show varying degrees of conductivity, depending on type and temperature. Coke is a relatively good conductor even at low temperature, while charcoal is the most resistive. Wood chips were not tested, but are assumed to be mostly insulating, however, they will turn to charcoal in the furnace. SiC, both intrinsic and from industrial crust, is less conductive than the carbon it is made from, even when Si metal is demonstrated within the SiC crust. However, as temperature rises towards and above 1600°C, the resistivity of all these materials converges towards values below 40 mΩm, and mostly below 20 mΩm. Much of the increase in conductivity in carbon materials occurs as volatiles are driven off, because carbon materials that are heat treated before the experiment have low resistivity even at lower temperatures. For the silica containing charge mixtures at 1400°C, resistivity ranges from 10 to 150 mWm, depending on parameters such as particle sizes, ratios and carbon type.

Older work by Vorob'ev and Mikulinski measured the resistivity of the charge mixture for Si, FeSi90 (ferrosilicon with 90% wtSi %), FeSi75, FeSi45 and FeSi20 (Vorob'ev and Mikulinski, 1969). At low temperatures, the silicon charge had the highest resistivity, and this resistivity dropped with increasing iron content. The iron was added as iron filings, which reduced the resistivity strongly. As temperature increased, however, the resistivity decreased for all charges, and at 1600°C all charges had the same resistivity, about 150 mΩm.

Rennie measured the resistivity of charges for FeSi75 with coke, char or coal as reductants (Rennie, 1975). Charges with coal had a high resistivity up to about 800°C, where the volatiles were driven off. The resistivity then became fairly constant with increasing temperature until 1400–1500°C, where it dropped rapidly. Rennie argued that this resistivity decrease occurred partly because softening of the quartz gave better contact between the particles. Resistivity was measured while the charge was heated to 1700°C over 6 hours. Measurement continued during cooling, and the resistivity remained low, which is consistent with the removal of volatiles improving conductivity.

It should also be emphasised that the type of carbon material influences charge conductivity: the higher the volatile content, the higher the resistivity. The porous structure of charcoal makes it slightly more resistive at high temperature than coal at high temperature, but at lower temperature the difference is much larger, presumably due to the volatile content. This can be seen from the data in Figure 6.7, where resistivities were measured for similar particle sizes. The coal was calcined at 1200°C before the resistivity measurements (Hoover *et al.*, 2023). In addition to Hoover's work, the figure includes data from (Pedersen, 2020).

Measurements also show that SiC has higher resistivity than the carbon it is made from, even when partly impregnated with Si. An example is shown in Figure 6.8. The data show that, in some cases, the SiC resistivity can be comparable to the heat treated coal, although the general rule is that SiC has higher resistivity.

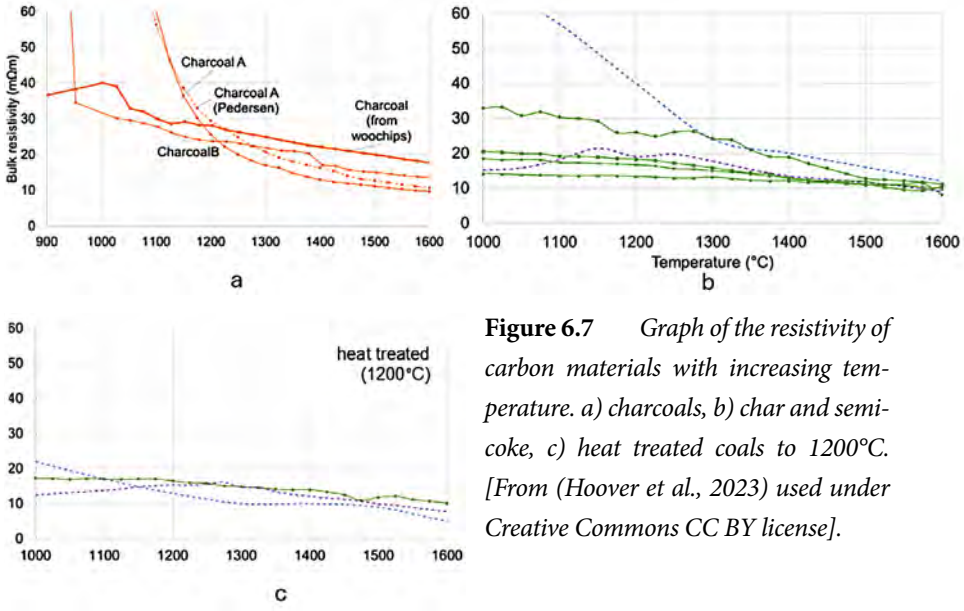


Figure 6.7 *Graph of the resistivity of carbon materials with increasing temperature. a) charcoals, b) char and semi-coke, c) heat treated coals to 1200°C. [From (Hoover et al., 2023) used under Creative Commons CC BY license].*

The relatively higher resistivity of SiC, compared with the unreacted carbon, partly goes against previous assumptions, for example in the earlier version of this book. For all these compounds, the resistivity decreases with increasing temperature, which reduces the difference between the different mixtures.

In general, it is not trivial to obtain reliable, repeatable measurement results from these systems. In addition to the intrinsic resistivity of the materials in the mix, the results depend on particle size, contact resistance and, more generally, the layout of materials and potential segregation in the case of mixed charges, as this affects the contact points and current paths. What can be said is that, although volatile-rich carbon materials will produce a more resistive furnace charge, the difference in resistivity decreases further down in the furnace as the temperature rises. Loose charge is also more resistive than a crusty charge with a more continuous structure. In general, the resistivity data presented here would give a much too high furnace resistance compared with the industrial furnace, so they should not be used uncritically. One factor is that the data are generally collected at temperatures below 1600°C, which should contribute to too high a resistance value, as the resistivity generally drops as temperature rises in these materials. In addition, the effect of molten slag is not included in the data. It is known that molten silica contributes to lowering the resistance, in particular in FeSi furnaces containing iron raw materials in the charge.

Excavations of furnaces show that the distribution of the different types of materials in the furnace is highly dependent on the operational conditions leading up to the furnace shutdown. A recreated cross section of two furnaces at Bjølvefossen FerroSilicon plant in Norway can be seen in Figure 6.8.

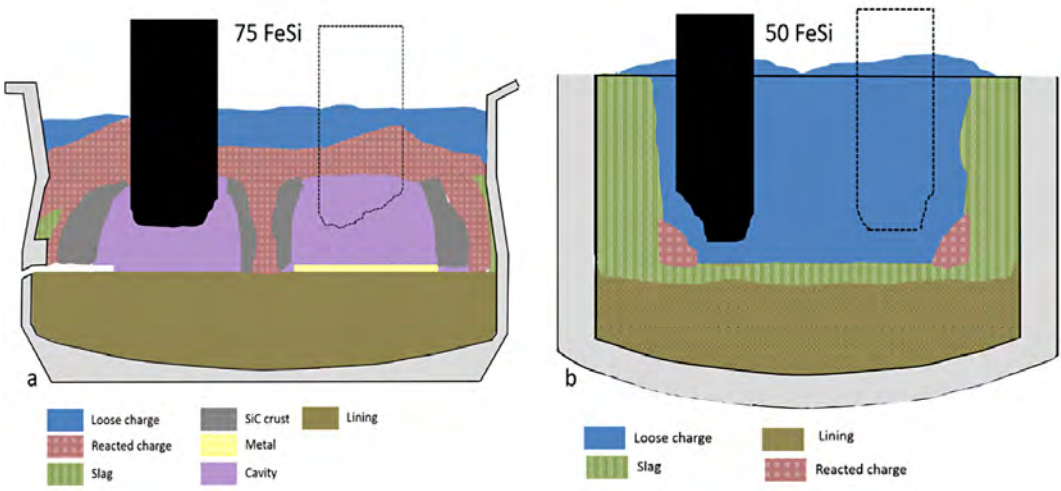


Figure 6.8 *Overview of zones in two FeSi furnaces: a) 75 FeSi in Finfjord, b) 50 FeSi in Elkem Bjølvefosen. [With permission from (Ksiazek et al., 2016)].*

Excavations have confirmed the existence of a gas-filled cavity, although its size varies, surrounding the electrode tip. This cavity is present in submerged arc furnaces used to produce high-silicon alloys, but not necessarily in other ferroalloy processes. Some excavations have revealed no cavity; however, it must be kept in mind that excavations are highly disruptive and are normally not carried out on well-operating furnaces. This cavity, also called a crater, is attributed to arcing, as a significant part of the phase current exits the electrode through one or more electric arcs. Arc formation requires a certain voltage drop, as it involves the electrical breakdown of gas molecules to form conductive plasma. The arc is described more thoroughly in the following section.

Table 6.1 *The order of magnitude of the resistivity of materials in the silicon process. (Based on Hoover et al., 2022; Krokstad, 2014; Schäfer, 1984; Valderhaug, 1992).*

Material	Temperature	Resistivity
Quartz	$T < 1800$ K 1800 K < T < 2000 K	$\rho > 10^4$ Ωm 10^2 Ωm < $\rho < 10^4$ Ωm
Carbon materials	$T < 1800$ K	500 mΩm > ρ > 10 mΩm ~0.1 Ωm for Graphite
Silicon carbide	$T \approx 2000$ K	1000 mΩm > ρ > 20 mΩm
Silicon	$T \approx 2000$ K	$\rho \approx 0.01$mΩm
Plasma	T > 15000 K	$\rho > 0.1$mΩm

Current through the electric arc

Gases have low electric conductivity and are generally seen as insulators, but if an electric field exceeds the dielectric strength of the gas, ionisation occurs, electric current can pass, and an arc is formed. The ionized gas, or plasma, has reasonably good conductivity, so a burning arc will pass current at a relatively low voltage. Plasma can occur in vacuum at room temperature, as electrons and ions can have different temperatures. At atmospheric pressure, temperatures above 10000–15000°C, depending on composition, are required to maintain the plasma. Atmospheric-pressure plasma is commonly referred to as thermal plasma and requires electrons and heavy particles to share a temperature, which is referred to as Local Thermodynamic Equilibrium. Electric arcs at atmospheric pressure are used for industrial applications such as welding, carbon-arc lamps and electric arc furnaces. To sustain the arc, the heat dissipation associated with the current must be sufficient to maintain plasma conditions. A high current generates a high degree of ionisation and low resistivity, while a lower current is associated with less ionisation and higher resistivity. In such cases, when the voltage drop decreases with increasing current, the characteristic is said to be *falling* or *negative*. For a given arc setup, this relationship is described by the Arc Characteristic, shown in Figure 6.9. This figure shows an example of a DC-arc characteristic and a circuit for determining it. The resistance R is regulated

until a predetermined current I flows through the arc, and the voltage drop V is measured. The resulting dependence is shown as the graph 'Arc' in the figure. This graph is the *characteristic* of the arc: it shows the voltage drop for a given current in the arc.

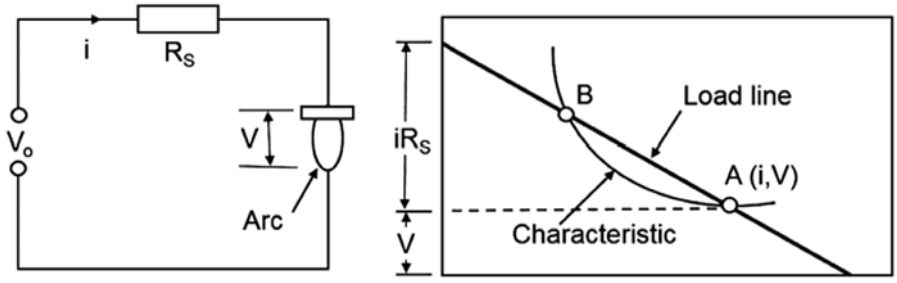


Figure 6.9 *The characteristics of a direct current electric arc (b) and the main elements of a circuit for its determination (a).*

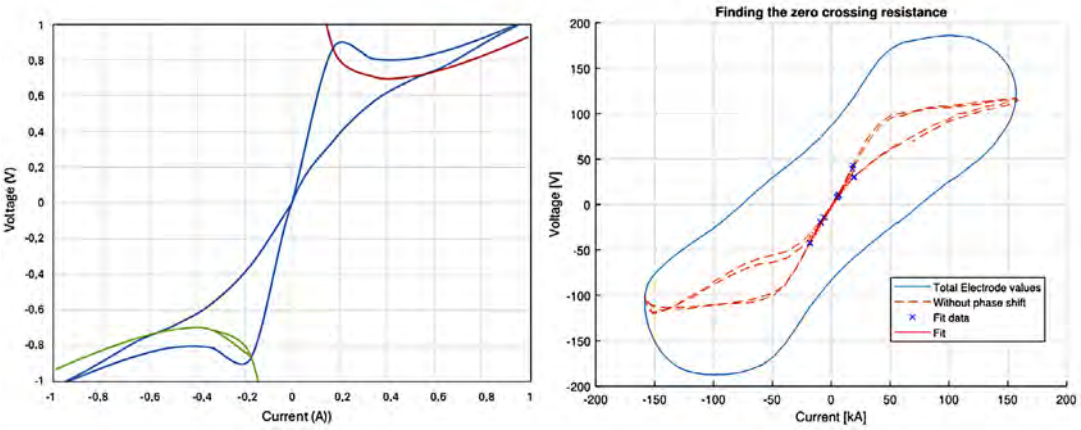


Figure 6.10 *Characteristics of an alternating current electric arc, excluding reactance, often referred to as Lissajous figures, showing the voltage drop versus the current, on the left. On the right it is shown how an upper limit for the charge resistance for one phase can be estimated, from (Haraldsson et al., 2023) [Reproduced with permission from Springer Nature].*

The relationship between the DC arc characteristic, which falls at lower current and rises at higher current, and the characteristics of an AC arc with the same properties is shown in Figure 6.10 (left) for normalized values. The right-hand plot shows real-time, high-resolution measurements of current and voltage at an electrode in a ferrosilicon furnace, processed to remove the phase shift due to the furnace reactance. The slope of the curve as it passes through zero can be read as a lower limit to the charge resistance for that phase, since at zero current the arc has a very high resistance.

For a normal ohmic resistance, the voltage drop increases linearly with increasing current, and the characteristic is said to be *rising* or *positive*. When the current becomes large enough, the characteristic of the arc may return to a rising characteristic; this is mostly the case at the current levels in industrial Si furnaces. In summary, for thermal electric arcs in industrial furnaces, the arc voltage does not change linearly with current because the resistance depends on current. This current dependence causes the non-linear current–voltage characteristics of arc furnaces, and the corresponding harmonics measured in the current and voltage waveforms. Figure 6.11 shows real-time, high-resolution measurements of current and voltage at an electrode in a ferrosilicon furnace, processed to remove the phase shift due to the furnace reactance (Haraldsson, 2025; Traustason, 2020). The shape of the red curves can be seen as an indicator of furnace operation, including the deviation from linearity, the area inside the curve, and the asymmetry between the positive and negative half-periods. On the left, the arc footprint for the three phases is shown, while the area enclosed by the arc in phase 2 is quantified.

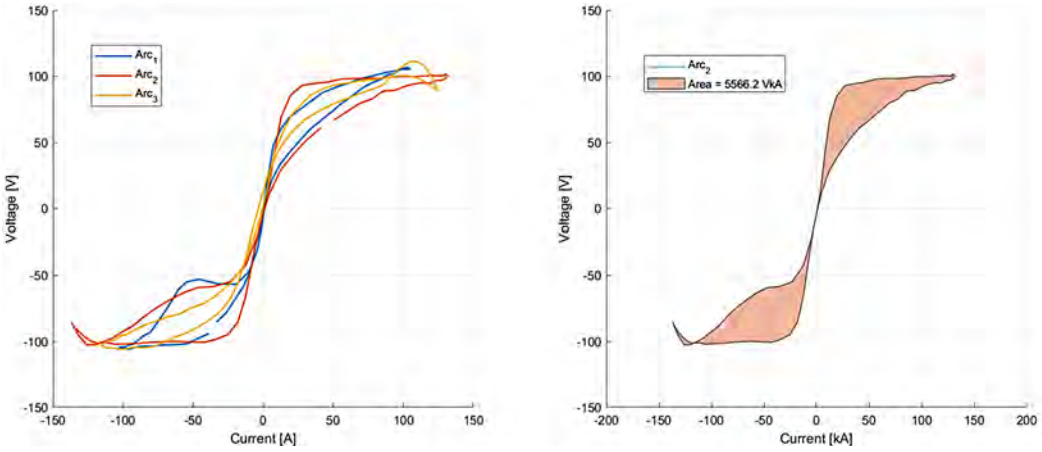


Figure 6.11 *Real-time high-resolution measurements of current and voltage on an electrode in a ferrosilicon furnace, processed to remove the phase shift due to the furnace reactance. Voltage is plotted as a function of current (Haraldsson, 2025) [Reproduced with permission from Springer Nature].*

Previously, it was assumed that the electric arc could be as long as half a metre, as the electrodes in a furnace often move by that amount, or more, to maintain the desired resistance. More recent data and simulation indicate that electric arcs burning in Si–O–C gas are unlikely to be much longer than 10 cm. If they are that long, there are probably more than one in parallel, based on the actual resistance level in the furnace (Sævarsdottir and Bakken, 2010).

6.3 Electrical Furnace System

In most cases, industrial Submerged Arc Furnaces used to produce silicon are three-phase, in the sense that three-phase current is passed into the furnace through three electrodes, and in exceptional cases through 6 electrodes. There are DC SAFs operated in other processes, for example ferrochromium production, but generally not for silicon production.

The high-voltage current supplied from the power transmission utility is stepped down, in two or more steps, to voltage and current levels appropriate for the furnaces. This is referred to as the 'secondary side' of the last transformer set, where the currents in each phase are typically in the order

of 100 kA. The circuit before the last transformation step is referred to as the 'primary side'. The high currents on the secondary side generate significant magnetic fields in the immediate area of the furnace, and this is taken into consideration for all equipment design. Ideally, the three transformers that step the voltage from the 'primary' side levels to the 'secondary' side are located symmetrically around the furnace. This practice is common because it minimizes any asymmetry in the electrical setup, which would be enhanced by the magnetic field and might have consequences for the electrical and metallurgical operations of the furnace. In some cases, for smaller furnaces with less magnetic interaction, there is one three-phase transformer that supplies current to all electrodes. The transformers are connected in a delta (D) connection to the 3 electrodes, which conduct electric power to the furnace through busbars and flexibles, and then to the contact clamps that are attached to the electrodes. This setup is called a knapsack configuration and is shown in Figure 6.12.

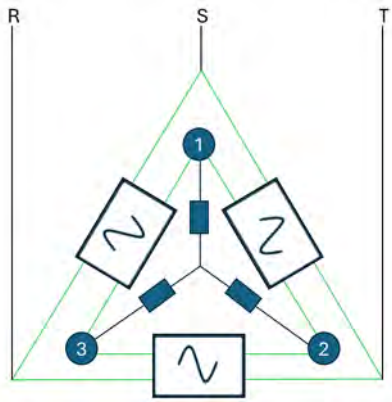


Figure 6.12 *Schematic showing the electrical arrangement for a three-phase furnace, the electrodes connected in a knapsack configuration to the transformers and connected in a star connection through the furnace interior.*

The three electrodes are then connected in a star connection (Y) through current paths inside the furnace. The transformers feeding current to the electrodes perform the last step-down in voltage to the operating D voltage U_D and current I_D on the secondary side of the transformer windings.

The D voltage translates to the phase voltage for the electrodes, $U_{Ph} = U_{\Delta} / \sqrt{3}$, and the phase currents relate to the D currents through $I_{Ph} = I_{\Delta} \cdot \sqrt{3}$. Under normal operation, phase voltages are typically of the order of magnitude of 100 V, and the currents of the order of 100 kA. The exact value depends on the size of the furnace and the raw materials. In general, larger furnaces have higher currents and lower resistances. This is associated with high magnetic field generation and inductance, which complicates furnace operation.

The furnace inductance leads to a phase shift φ between the current and voltage. This must be considered when calculating the real power generation in the furnace. The real power is then found by Equation [6.15]:

$$P = \sum P_{ph} = \sum U_{Ph} I_{Ph} \cos\left(\phi_{ph}\right) \qquad [6.15]$$

The factor cos(φ) is called the *Power Factor*, is always less than 1, and quantifies the extent to which real power generation is reduced due to reactance in the secondary circuit. For large furnaces, the Power Factor can be as small as 0.5.

The reactance in the furnace

For the sake of simplicity, let us consider a one-phase equivalent circuit representing the furnace, as shown in Figure 6.13.

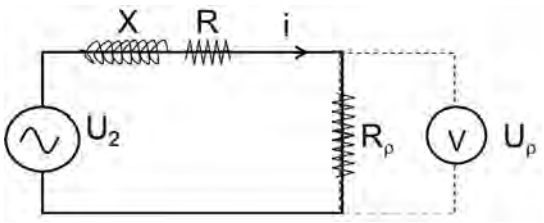


Figure 6.13 *Illustration of a one-phase equivalent circuit considered as a simplification of the three-phase AC submerged arc furnace circuit.*

Heat generation P due to resistive heating, as current I is passed through a resistance R, is:

$$P = I^2 R \qquad [6.2]$$

On the secondary side, inside industrial furnaces, three-phase AC currents of the order of 100 kA pass through the raw materials and arcs within the furnace. Together, these make up the load-bearing resistance. The high amperage involved leads to the creation of a strong magnetic field, which generates an inductive reactance in the system. This shows up as a time delay in the accessible instantaneous voltage, due to the energy needed to build up the magnetic field.

This delay is proportional to the change in current, with the proportionality constant *L*:

$$u(t)_L = -L\frac{di}{dt} \qquad [6.16]$$

L is called inductance and has units Henry [H]. In general, in RLC circuits, inductive reactance can be compensated by capacitive reactance, which is attributed to an accumulation of charge. In general, the contribution of capacitance to the instantaneous voltage manifests as a phase change in the opposite direction, as per equation [6.17].

$$u(t)_C = C\int idt \qquad [6.17]$$

Rather than working with instantaneous values for current and voltage, a more effective mathematical treatment uses complex numbers. Inductive reactance is defined as $X_L = \mathrm{w}L$ and capacitive reactance as $X_C = 1/\mathrm{w}C$, where $\mathrm{w} = 2{\cdot}p{\cdot}50$ Hz. *These form a combined reactance* $X = X_L - X_C$ *that contributes to the overall impedance Z* of a circuit, such that:

$$Z = \sqrt{X^2 + R^2} \qquad [6.18a]$$

Thus, a capacitance counteracts the contribution of inductance to the impedance. For the high amperage present on the secondary side of an AC industrial furnace, it is not practical to incorporate capacitance on the furnace's secondary side, and the secondary-side impedance becomes.

$$Z = \sqrt{X_L{}^2 + R^2} \qquad [6.18b]$$

Which, for large furnaces, can be significantly larger than R. The relationship between impedance, resistance, and reactance can be illustrated using vector plots called phasors, as shown in Figure 6.14.

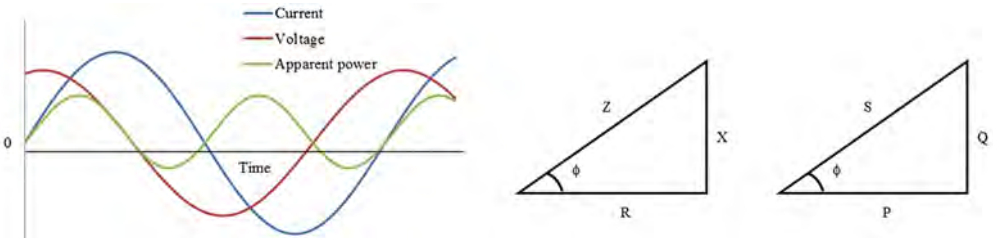


Figure 6.14 *shows the relationship between instantaneous current and voltage phase shifted by angle φ and their product, the apparent power (left) and the vector relationship between the impedance, reactance and resistance for a circuit and the apparent power, reactive power and real power (right).*

The total active power P[MW] that generates heat in the furnace is:

$$P = RI^2 = \frac{RU_2^2}{X^2 + R^2} \qquad [6.19]$$

The transfer of energy associated with creating and destroying the magnetic field is denoted by the so-called reactive power, Q_L[MVAr]:

$$Q_L = XI^2 = \frac{XU_2^2}{X^2 + R^2} \qquad [6.20]$$

The furnace's electrical equipment supplies the current and voltage required to provide the apparent power S[MVA], which combines active and reactive power:

$$S = \sqrt{P^2 + Q_L^2} \qquad [6.21]$$

The phase shift between instantaneous current and voltage is represented by the angle φ in Figure 6.14. Equation [6.19] can thus also be written in terms of φ, as $P = U \cdot V \cos \varphi$.

The *Power Factor*, *cos φ* indicates both the extent to which the furnace circuit must be over-dimensioned to accommodate the reactive power and the level of magnetic interaction between the three phases of the furnace. Large furnaces with high amperage can have a power factor below 0.57. Magnetic interactions refer to a phenomenon in which a change in conditions in one phase causes the phase current to change. The phase currents in the other two phases then also change significantly, even though the phase resistances for those phases are unchanged. This effect is much more significant in large furnaces with small *power factors* than in furnaces with a *power factor* close to unity. One way to mitigate this effect is to apply so-called *resistance control* rather than *current control*, as was addressed in the discussion of the electrical operation of the furnace.

The operator of the grid transmitting electric power to the silicon smelter sets an upper limit on the reactive power the smelter can pull from the grid. Therefore, the factory is equipped with capacitor banks that provide capacitive reactive power, counteracting the inductive reactive power contained in the magnetic field. These capacitors are normally installed between the initial voltage step-down from the transmission voltage level, on the primary side, and the furnace transformers stepping the voltage down to the delta on the secondary side.

6.4 Energy control of the silicon furnace

The purpose of the automatic energy control is twofold: to keep the furnace at the optimum electrical conditions and to protect the equipment from damage by excessive current. In addition, the furnace can have automatic electrode slip control and metallurgical control. The slip control moves the electrode relative to the hanger to compensate for electrode consumption. For Søderberg electrodes or composite electrodes, it must also secure acceptable baking conditions for the electrode. The main purpose of the automatic metallurgical control is to provide the correct amount of carbon to the charge.

The metallurgist has two independent variables to control the electric operation:

- The voltage, controlled by the tap position of transformers.
- The position of the electrode tip (which determines the resistance of the furnace).

The position of the electrode tip is continuous, while the voltage can normally be chosen in steps over a certain range. With two independent variables, it is possible to control only two parameters.

Measurement systems

For ease of access and manageable instrumentation, phase currents are measured on the primary side of the furnace transformers in Submerged Arc Furnaces. The phase currents are measured on an equivalent circuit, which mirrors the star connection on the secondary side.

To obtain the voltage for each electrode, some furnaces have a setup installed to measure voltage between the contact clamps feeding current into the electrode and an anticipated zero point at the bottom of the furnace. In this case, a loop is used to estimate the contribution to the voltage from the magnetic field generated by the furnace. This estimated contribution is then used to compensate for the effect of induction. This method of correcting for the magnetic effect is called Bøckman compensation (Bockman, 1960).

Other furnaces are controlled using voltage estimates based solely on measurements on the contact clamps. In this case, the zero-point measurement is missing. However, by assuming certain types of symmetry in the furnace, an estimate of the phase voltage is obtained. This type of instrumentation has proven relatively robust for furnace operation, although it can give erroneous results in the case of asymmetric furnace operation. Using a bottom contact provides an extra data point, which enables more accurate furnace control. This may, however, be complicated by the maintenance requirements of the Bøckman compensation and by the undeniable complication that the contact point underneath the furnace is not actually the zero-point, which is moving about somewhere within the furnace. Figure 6.15 is a simplified schematic of a measurement setup for a submerged arc furnace with a bottom contact. The Bøckman connection is not shown.

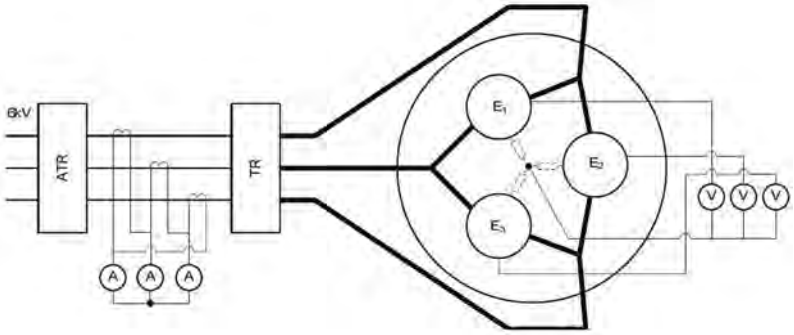


Figure 6.15 *Schematic of the measurement setup of a submerged arc furnace with a bottom contact for voltage measurement (after Baron et al., 2012).*

Electric operation

Since it is generally important to use the production capacity fully, the load is selected as one of the control parameters. When the load is known and the other electric parameters are determined, the optimum current can be calculated from the Westly rule, Equation [6.8]. The relation between the electric parameters can be expressed in a load nomograph, where the load is given as a function of the resistance for a set of voltage and current values. An example of a load nomograph is shown in Figure 6.16. The curves for the current have been calculated from the equation

$$P = 3\ I^2\ R \qquad [6.3]$$

The voltage curves can be obtained from the phase voltage V:

$$P = \frac{3\ V^2 \cos\varphi}{Z} = \frac{3\ V^2 R}{Z^2} \qquad [6.22]$$

Although the voltage listed in the nomograph is the potential between the transformers in the D, it is the phase voltage multiplied by a factor $\sqrt{3}$.

Here the impedance Z is given by.

$$Z = \sqrt{R^2 + X^2} \qquad [6.18]$$

In the actual furnace, the inductance X varies slightly as the electrode moves up and down, but, for the sake of simplicity, it has been assumed constant in the furnace when creating the nomograph in Figure 6.16.

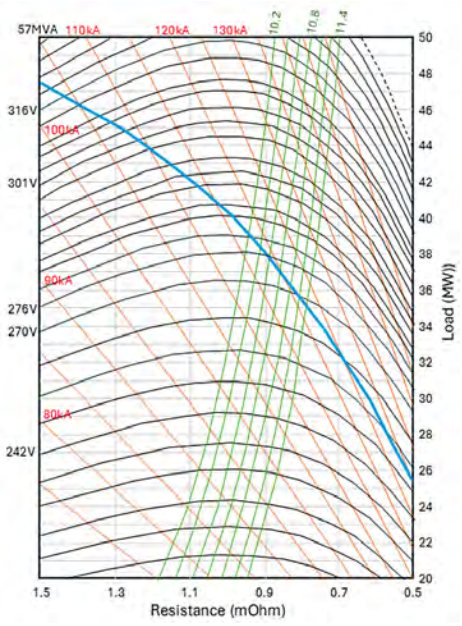


Figure 6.16 *Example of a load nomograph for a fictional submerged arc furnace with symmetric load. Definition of the variables: Inductive resistance 1.00 mΩ, load for the complete furnace, current and resistance for one electrode, voltage drop between two phases at the transformer.*

The use of the nomograph will be explained by an example. We want to run the furnace at a load of 37 MW, and we know from previous experience with the raw material mix that C_3 = 10.8 gives fairly good operation. The Westly rule Equation [6.8] then gives

$$I = 10.8 \cdot 37^{2/3} = 120 \text{ kA}$$

The nomograph gives a voltage ≈ 273 V for a current of 120 kA and a load of 37 MW. To achieve full load and optimum furnace operation, the furnace must be operated at 273 V between two phases in the secondary. If the transformers

have no step for 273 V, a nearby step must be chosen, and a middle course must be found between full load and optimum operation.

Once the transformer voltage has been set, the furnace can be controlled for either current or resistance, aiming at the optimal load.

If the furnace is controlled for current, a current setpoint is selected, and the energy controller keeps it at this value. To avoid too frequent movements of the electrodes the controller can have a dead-zone range and a defined time before action. Then the controller only acts when the current has exceeded the dead-zone bounds around the chosen setpoint for a certain time. The controller acts by raising or lowering the electrode. Then the resistance changes, and with a fixed voltage the current changes too. Figure 6.17 is a simple illustration for dead-band regulation.

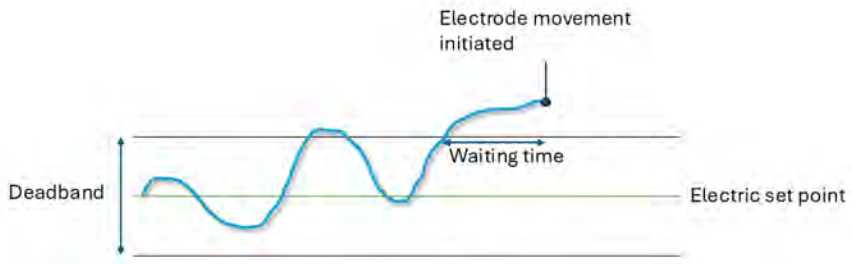


Figure 6.17 *An illustration of how a dead band regulation system works.*

In the example, the current is the control variable. Alternatively, one could control the C_3 factor, the resistance, or the impedance. Under idealized conditions these methods are equivalent, but in a real furnace they will normally differ.

Here, we have assumed that the load is symmetric, which is not always true for real furnaces. In that case, each electrode must be treated separately, and it becomes necessary to measure the voltage drop from the electrode to the bottom.

6.5 Electrode consumption

The electrodes in the furnace are consumed during operation. This must be compensated for by either adding electrode mass that continuously bakes in the furnace (Søderberg electrodes), adding prebaked blocks in the case of prebake electrodes, or using a combination of both for composite electrodes.

The electrode consumption is mostly due to two mechanisms:

- Heat load from the electric arcs, which sublimate the carbon material, in particular during the anode half-period (Sævarsdóttir *et al.*, 2007; Müller and Magnussen, 1972).
- Chemical erosion due to reaction with SiO gas that flows up from the crater zone, partly along the side of the electrode, as well as chemical load from SiO_2 slag at elevated temperatures.

Sævarsdóttir *et al.* (2007) modelled possible electrode erosion from an electric arc, based on the heat load on the electrode surface from both radiation and exchange of kinetic energy with particles in the arc, as well as electrons emitted from the surface. They concluded that the erosion increased approximately parabolically with the arc current, so the contribution to the total electrode erosion was highly dependent on the current distribution between arc and charge, and on the number of arcs on each electrode. If all current on an electrode carrying 120 kA were to pass through a single arc, the erosion from the arc would be similar to typical total electrode erosion for such a furnace. They found that the erosion was much greater when the electrode serves as anode than as cathode, mostly due to the cooling effect of electrode emission in the cathodic half-period.

Otani studied the electrode consumption in a simple arc chamber and concluded that the main consumption mechanism was chemical corrosion (Otani *et al.*, 1968).

Müller and Magnussen started with the hypothesis that the electrode consumption mainly is due to evaporation at the arc spot, and they set up a fairly elaborate arc chamber to test their hypothesis (Müller and Magnussen, 1972). They reasoned that the cathode and anode drop have a fixed voltage drop, and that the heat production at the electrode spot should therefore be proportional

to the current. The rate of evaporation should then also be proportional to the current, and the electrode consumption should be proportional to the number of ampere-hours. In the arc chamber, the evaporated carbon condensed on cooler parts of the electrode, and the weight loss indicated a low electrode consumption. In further experiments, the electrode was surrounded by a coke bed that should catch the carbon vapour. The evaporation loss then became approximately the same as for submerged arc furnaces when the electrode was anode, but lower when the electrode was cathode. Some typical data for electrode consumption in submerged arc furnaces are given in Table 6.2.

Table 6.2 *Typical electrode consumptions for smelting of FeSi 75 (after Müller and Magnussen, 1972).*

Load	Crater voltage	Energy consumption	Electrode consumption			Electrical
MWA	V	$\frac{\text{MWh}}{\text{ton}}$	$\frac{\text{kg}}{\text{h}}$	$\frac{\text{kg}}{\text{MWh}}$	$\frac{\text{kg}}{\text{kAh}}$	Connections
15.0	71	9.5	52	5.5	0.39	Three-phase AC
12.0	71	8.7	39	4.5	0.32	Three-phase AC
0.1	37	13.3	53	4.0	0.15	Single- phase AC
0.1	40	12.1	24	1.9	0.08	DC, electrode –
0.1	44	12.8	50	3.9	0.17	DC, electrode +

The electrode consumption reported as kg/MWh is almost the same for large and small furnaces, whereas it is lower in small furnaces when it is reported as kg/kAh. Müller and Magnussen argue that chemical consumption will be roughly proportional to production. Therefore, the observation that electrode consumption is independent of size indicates that chemical reaction is the main consumption mechanism (Müller and Magnussen, 1972). However, the strong dependence on the direction of direct current simultaneously corroborates the original hypothesis that evaporation at the electrode hot spots is important. Müller and Magnussen conclude that the question is incompletely answered, but they still think that vaporisation at the contact arc-electrode is important.

Vorob'ev and Zhuchkov pointed out that several factors influence electrode consumption, and that these can be arranged into two groups. Based on experiments in an arc chamber, Vorob'ev and Zhuchkov concluded that the arc accounted for about 10 per cent of the overall electrode consumption, and that chemical erosion accounted for the remaining about 90 per cent (Vorob'ev and Zhuchkov, 1974).

Westly stated that several parameters are important for electrode consumption, such as the quality of the electrode, the silicon content of the alloy, and the carbon content of the charge (Westly, 1985). The carbon content acts by influencing the corrosive character of crater gas.

References

Andreae, F.V. (1933) 'Communicated discussion to the paper "Electric arc and arc resistance furnaces and their power factor" by A. Wejnarth', *J. Electrochem. Soc.*, 63, pp. 344–348, paper pp. 309–343.

Baron, B., Świszcz, P. and Kraszewski, T. (2012) 'Some aspects of the analysis and the interpretation of electrical measurements of submerged arc-resistance furnace', *Przeglad Elektrotechniczny*, 88, pp. 211–213.

Bockman, O.C. (1960) 'Crater resistance of submerged arc smelting furnaces simulated by a simple model', *J. Electrochem. Soc.*, 107, p. 688. Available at: https://doi.org/10.1149/1.2427809

Eidem, P.A., Tangstad, M., Bakken, J.A. and Ishak, R. (2010) 'Influence of coke particle size on the electrical resistivity of cokebeds', in *Proceedings of INFACON XII*. Helsinki, Finland, pp. 349–358. Available at: https://www.pyrometallurgy.co.za/InfaconXII/349-Eidem.pdf

Haraldsson, H., Tesfahunegn, Y.A., Tangstad, M. and Sævarsdottir, G. (2024) 'Modelling of industrial electric arcs with changing plasma compositions and arc lengths', in *Proceedings of Silicon for the Chemical and Solar Industry VII*. Trondheim, Norway. Available at: https://doi.org/10.2139/ssrn.4942616

Haraldsson, H.V. (2025) *High current arc modeling for silicon submerged arc furnaces*. Doctoral thesis. Reykjavik University, Iceland.

Haraldsson, H.V., Traustason, H., Tesfahunegn, Y.A., Tangstad, M. and Sævarsdóttir, G. (2023) 'Measuring and processing of electrical parameters in a submerged arc furnace', in Wagstaff, S., Anderson, A. and Sabau, A.S. (eds) *Materials Processing Fundamentals 2023*. Presented at the TMS Annual Meeting. Cham: Springer Nature Switzerland, pp. 161–170. Available at: https://doi.org/10.1007/978-3-031-22657-1_14

Heiss, W.D. (1982) 'Modelling and simulation of electric smelting furnaces', *Ironmaking and Steelmaking*, 9, pp. 217–221.

Herland, E.V., Sparta, M. and Halvorsen, S.A. (2019) 'Skin and proximity effects in electrodes and furnace shells', *Metallurgical and Materials Transactions B*, 50, pp. 2884–2897. Available at: https://doi.org/10.1007/s11663-019-01651-8

Hoover, H. (2023) *Electrical resistivity of materials in the silicon furnace*. Doctoral thesis 2023:298. Norwegian University of Science and Technology (NTNU), Trondheim, Norway. Available at: https://hdl.handle.net/11250/3091823

Hoover, H., Fromreide, M., Sævarsdottir, G. and Tangstad, M. (2023) 'Bulk resistivity of materials in the Si/FeSi furnace', *Processes*, 11, 2115. Available at: https://doi.org/10.3390/pr11072115

Hoover, H., Sævarsdottir, G. and Tangstad, M. (2022) 'Electrical resistivity of charge materials in the Si/FeSi furnace', in *Proceedings of Silicon for the Chemical and Solar Industry XVI*. Trondheim, Norway. Available at: https://doi.org/10.2139/ssrn.4128047

Krokstad, M.A. (2014) *Elektrisk resistivitet i industrielle SiC-lag*. MSc thesis, in Norwegian. Norwegian University of Science and Technology (NTNU), Trondheim, Norway. Available at: https://hdl.handle.net/11250/249534

Ksiazek, M., Tangstad, M. and Ringdalen, E. (2016) 'Five furnaces five different stories', in *Proceedings of Silicon for the Chemical and Solar Industry XIII*. Kristiansand, Norway, pp. 33–42.

Larsen, H.L. (1996) *AC electric arc models for a laboratory set up and a silicon metal furnace*. Doctoral thesis. Norges Tekniske Høgskole (NTH), now Norwegian University of Science and Technology (NTNU), Trondheim, Norway.

Müller, M.B. and Magnussen, T.E. (1972) 'Electrode consumption and arc processes in submerged arc furnaces', paper presented at the *7th International Congress of Electroheat*, Warszawa, Poland.

Otani, Y., Saito, M., Usui, K. and Chino, N. (1968) 'The inner structure of the submerged arc furnace', paper presented at the *VIth International Congress of Electroheat*, Brighton, UK, pp. 1–7.

Pedersen, T.A. (2020) *Electrical resistivity in carbon materials converting to SiC*. Master thesis. Norwegian University of Science and Technology (NTNU), Trondheim, Norway. Available at: https://hdl.handle.net/11250/2785272

Rennie, M.S. (1975) *The electrical conductivity of the charge in a ferrosilicon furnace*. Report No. 1622. National Institute for Metallurgy, South Africa.

Sævarsdottir, G. and Bakken, J.A. (2010) 'Current distribution in submerged arc furnaces for silicon metal/ferrosilicon production', in *Proceedings of INFACON XII*. Helsinki, Finland, pp. 717–728. Available at: https://www.pyrometallurgy.co.za/InfaconXII/717-Saevarsdottir.pdf

Sævarsdóttir, G., Pálsson, H., Jónsson, M.P. and Bakken, J.A. (2007) 'Electrode erosion in submerged arc furnaces', in *Proceedings of INFACON XI*. New Dehli, India, pp. 752–761. Available at: https://www.pyrometallurgy.co.za/InfaconXI/752-Saevarsdottir.pdf

Sævarsdóttir, G.A. (2002) *High current arcs in silicon and ferrosilicon furnaces*. Doctoral thesis. Norwegian University of Science and Technology (NTNU), Trondheim, Norway.

Schäfer, J. (1984) *On the energy conversion in reduction furnaces producing silicon*. Dr. Ing. thesis. Universität Hannover, Hannover, Germany.

Sindland, C., Tangstad, M. and Andersen, V. (2027) 'Sindland *et al.* Phase distribution and electrical resistivity in silicon furnaces', paper presented at INFACON XVIII, Reykjavik, Iveland, 23–27 May 2027, in *Proceedings of INFACON XVIII*. Reykjavik, Iceland.

Tesfahunegn, Y.A., Magnusson, T., Tangstad, M. and Sævarsdottir, G. (2021) 'The effect of electrode movements on electrical characteristics of a submerged arc furnace', *JOM*, 73, pp. 2963–2972. Available at: https://doi.org/10.1007/s11837-021-04818-4

Traustason, H.G. (2020) Data acquisition of electrical parameters and interpretation of SAF data. MSc thesis. Reykjavik University, Iceland.

Valderhaug, A.M. (1992) *Modelling and control of submerged-arc ferrosilicon furnaces*. Doctoral thesis 1992:83. Norges Tekniske Høgskole (NTH), now Norwegian University of Science and Technology (NTNU), Trondheim, Norway. Available at: https://hdl.handle.net/11250/260770

Vorob'ev, V.P. and Mikulinski, A.S. (1969) 'The importance of the resistivity of the charge on the distribution of energy in the production of ferrosilicon alloys of various compositions', *Tr. Inst. Met.*, 19, pp. 107–110.

Vorob'ev, V.P. and Zhuchov, V.I. (1974) 'Consumption of electrodes in electric furnaces melting silicon ferroalloys', *Steel in USSR (Izv. VUZ Chern Met.)*, pp. 638–640, 39–42.

Westly, J. (1985) 'Electrode consumption in production of 75% and Si-met', paper presented at the *Electrical Furnace Conference (1984)*, Toronto, Canada, pp. 157–160.

Westly, J. (1979) 'Dimensions of reduction furnaces for Fe–Si and other ferroalloys', *J. de Four Electrique*, 1, pp. 14–19.

Westly, J. (1976) 'Critical parameters in design and operation of the submerged arc furnaces', *Proc. Am. Inst. Min. Metall. Pet. Eng. Electr. Furn. Conf.*, 33, pp. 47–53.

Westly, J. (1974) 'Resistance and heat distribution in a submerged-arc furnace', in *Proceedings of INFACON I*. Johannesburg, South Africa, pp. 121–127. Available at: https://www.pyrometallurgy.co.za/InfaconI/

Tangstad, M. (2026) 'Electrical energy consumption, enthalpy balance and energy recovery', in M. Tangstad, G. Tranell, H. Tveit and E. Ringdalen (Eds.), *Production of high silicon alloys* (2. ed.) (pp. 269–295). Fagbokforlaget. https://doi.org/10.55669/oa880807

7

Electrical energy consumption, enthalpy balance and energy recovery

Merete Tangstad

At first glance, the production of silicon should be easy. There is an abundant amount of silicon dioxide (SiO_2) in nature, which is a source of silicon. Silicon dioxide can be found as quartz or quartzite ores. The challenge in producing silicon or ferrosilicon is to separate silicon from oxygen while using as little energy and reduction material as possible. In current practical terms, the only way to produce silicon is to use solid carbon as a reduction agent. This chapter presents the energy balance for the use of carbon.

7.1 Stoichiometric analysis of energy balance

The simplified Si furnace

We will first discuss silicon production in the pure system Si–O–C, where we treat the process as a system of stoichiometric chemical reactions. The furnace reaction can formally be treated as a combination of two reactions, Equations [7.1] and [7.2]. Since, as a rule, it is convenient to refer the energy consumption to the silicon that is produced, we combine the reactions so that the coefficient for silicon is 1.

This work is licensed under the Creative Commons Attribution 4.0 International License.
To view a copy of this license, visit https://creativecommons.org/licenses/by/4.0/

$$SiO_2 + 2\,C = Si + CO \cdot 1 \quad [7.1]$$

$$SiO_2 + C = SiO + CO \cdot x \quad [7.2]$$

$$(x + 1)\,SiO_2 + (x + 2)\,C = Si + x\,SiO + (x + 2)\,CO \quad [7.3]$$

The reaction in the inner zone of the furnace occurs at a temperature of around 2000°C, and the measured temperature of the liquid silicon leaving the taphole is above 1800°C (Tangstad *et al.*, 2021). The liquid cools somewhat from the taphole to the ladle, and has a temperature of around 1600°C in the ladle. After casting, it cools to room temperature, which we set to 25°C. The gases leaving the top of the furnace have a measured temperature of around 1400°C, but can also be lower. Furnace gases are mixed with an excess of air and burned above the charge. This gives an overall process reaction:

$$(x + 1)\,SiO_2 + (x + 2)\,C + (x + 1)\,O_2 = Si + x\,SiO_2 + (x + 2)\,CO_2 \quad [7.4]$$

In addition, the excess oxygen and nitrogen in the air are heated to the temperature of the waste gas, which is here assumed to be around 150°C. Both the combustion reactions of SiO and CO, and the cooling of cast silicon, give off heat, while the sum of the furnace reactions consumes heat. The heat needed for the furnace reactions is added as electrical energy. All this information is summarised in Figure 7.1, where oxygen introduced as air is identified with the letter *m*. Table 7.1 lists the calculated changes in enthalpy for the various reactions involved when the actual temperatures in and out are included.

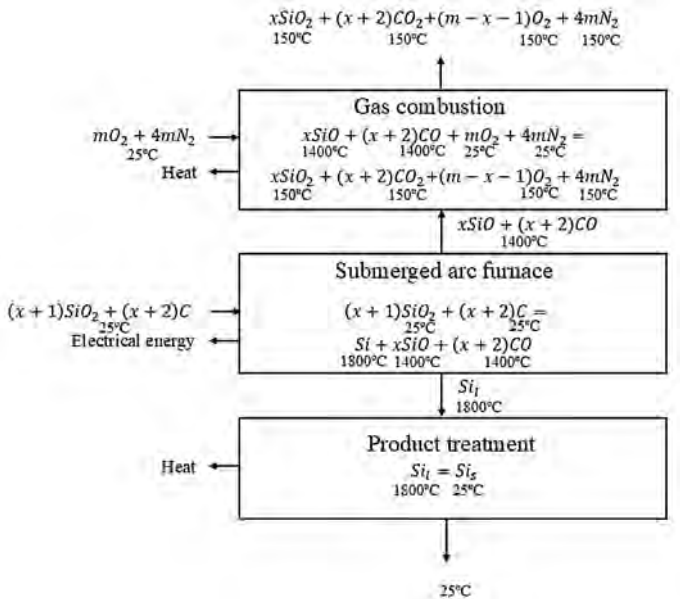


Figure 7.1 *Heat and mass flows in the silicon production process for the pure system Si–O–C. The numbers below the chemical symbols give the temperature in degrees Celsius. The temperature indications are based on observations in production furnaces. The total amount of oxygen to the process is m.*

Table 7.1 *The enthalpy change for some reactions needed to establish an energy balance for the complete silicon process (calculated by HSC Chemistry (Roine, 1997)). The numbers below the chemical species give the temperature in °C.*

Reaction	Change of H kJ		Reaction	Change of H kJ
SiO_2 + 2 C = Si + 2 CO 25 25 1800 1400	877		Si = Si 1800 25	−97.0
SiO_2 + C = SiO + CO 25 25 1400 1400	793		$SiO_2 = SiO_2$ 150 25	−6.3
Si + O_2 = SiO_2 25 25 25	−911		$CO_2 = CO_2$ 150 25	−5.1
C + O_2 = CO_2 25 25 25	−394		$N_2 = N_2$ 150 25	−3.6
SiO + 0.5 O_2 = SiO_2 1400 25 150	−852		$O_2 = O_2$ 150 25	−3.8
CO + 0.5 O_2 = CO_2 1400 25 150	−322			

By combining the data in Table 7.1, the enthalpy change for each of the three stages in Figure 7.1 can now be calculated as functions of the parameter x, which defines the silicon yield R through the reactions:

$$R = \frac{1}{1+x} \quad \text{or} \quad x = \frac{1-R}{R} \qquad [7.5]$$

Heat consumption of furnace reaction

$$= 877 + 793 \cdot x \frac{\text{kJ}}{\text{mol}}\text{Si} \qquad [7.6]$$

The solidification and cooling of the product Si will give off heat:

Heat given off in cooling of product

$$= 97 \frac{\text{kJ}}{\text{mol}}\text{Si} \qquad [7.7]$$

The gas from the charge of the furnace is mixed with excess air and burns. The heat given off from the combustion step is calculated from data in Table 7.1:

Heat from off-gas combustion

$$= 852 \cdot x + 322 \cdot (x+2) - 3.8 \cdot (m-x-1) - 3.6 \cdot 4m \frac{\text{kJ}}{\text{mol}}\text{Si} \qquad [7.8]$$

The waste gas with solid dust still has some energy left when it leaves the combustion zone at 150°C. According to data in Table 7.1, we have:

Heat in waste gas

$$= 6.3 \cdot x + 5.1 \cdot (x+2) + 3.8 \cdot (m-x-1) + 3.6 \cdot 4m \frac{\text{kJ}}{\text{mol}}\text{Si} \qquad [7.9]$$

If we look at the process as a chemical reaction, the items above give a complete description of the energy relations. However, if we look at the process from the point of view of energy economy, we must take into account the fact that the process consumes carbon that could have been used as a fuel. Until now, the reference state, where Gibbs energy is zero, has been defined as the

most stable elemental state at 25°C. When considering the energy economy, we set the reference state to the most oxidative state at 25°C. This means that both carbon and silicon will have a certain amount of energy, according to the reactions $C + O_2 = CO_2$ and $Si + O_2 = SiO_2$, respectively. According to data in Table 7.1, we have:

$$\textit{Heat value of silicon} = 911\,\frac{\text{kJ}}{\text{mol}}\text{Si} \qquad [7.10]$$

$$\textit{Heat value of carbon} = 394\cdot\left(x+2\right)\,\frac{\text{kJ}}{\text{mol}}\text{Si} \qquad [7.11]$$

The formulas in Figure 7.1 and the text above can be used in a spreadsheet to produce a table of the heat and mass balance for the complete silicon production process.

In this stoichiometric evaluation of the process, the energy values are reported as $\frac{\text{kJ}}{\text{mol}}\text{Si}$, which is the standard base for thermochemical calculations. For metallurgists, the unit $\frac{\text{MWh}}{\text{MT}}$ (MT = metric ton) is more familiar, and we can recalculate the result by the formula

$$\left[\textit{numerical value in}\,\frac{MWh}{MT\ Si}\right] = \frac{1000000}{M_{Si}\cdot 3600}\cdot\left[\textit{numerical value in}\,\frac{kJ}{mol\ Si}\right] \qquad [7.12]$$

where $M_{Si} = 28.09$ is the atomic weight of Si. The energy and material balance for the silicon process is given for several values of the recovery R in Table 7.2. The table reports values for the production of 1 MT of silicon, which is the most common basis for reporting consumption in the industry. However, sometimes we want to use another basis, e.g. a given electric load or a given consumption of quartz. Such a recalculation is simply a change of scale of the results in Table 7.2. If we want to calculate the silicon production for a 20 MW load at a silicon recovery of 0.90, for example, we can calculate this from the results in Table 7.2:

$$\textit{Production of Si} = \frac{1.0\cdot 20}{9.54} = 2.1\,\frac{MT}{hour}$$

The results are given in Table 7.3.

As a summary, the specific energy consumption will decrease with increasing silicon yield R, as there are large energy costs in making SiO gas in addition to liquid silicon. This has been shown in Table 7.2 and Table 7.3 and graphed in Figure 7.2, and is also summarised in equation [7.13]. With increasing silicon yield, R, the carbon consumption per tonne of silicon will also decrease, as less carbon will be used to produce SiO gas. However, the carbon consumption per tonne of SiO_2 will increase, as we will use less carbon per tonne of SiO_2 to produce SiO gas than liquid silicon, as seen in Figure 7.3. In the examples shown above, the liquid silicon leaves the furnace at 1800°C, and the CO and SiO gas at 1400°C. If the temperatures change, the energy consumption will also change; however, this effect is minor. Assuming the metal leaves the furnace at 1600°C instead of 1800°C, the energy consumption will decrease by 54 kWh/ton of Si, that is 0.45–0.62%, depending on the silicon yield. If the gas temperature changes from 1400 to 1300°C, the energy consumption is reduced by 0.8%, that is from 70 to 100 kWh depending on the Si yield.

$$\hat{E}_{Si}\left(theoretical\right) = 853 + \frac{7818}{R}\left[\frac{kWh}{tonne\ Si}\right] \qquad [7.13]$$

Where $\hat{E}_{Si}\left(theoretical\right)$ is the theoretical specific energy consumption and R is the Si yield, where $0 < R < 1$).

Table 7.2 *Material and energy balance for the silicon production process in the pure system Si–O–C. Data for the production of 1 MT Si.*

Silicon recovery R		1	0,9	0,8	0,7
Reaction parameter x		0,000	0,111	0,250	0,429
Air addition parameter m		2,000	2,223	2,500	2,858
Ratio air/gas production		5	5	5	5
Material balance					
In					
SiO_2	MT	2,139	2,377	2,674	3,056
C	MT	0,855	0,903	0,962	1,039
O_2	MT	2,279	2,532	2,848	3,255
N_2	MT	7,976	8,862	9,970	11,394
Out					
Si	MT	1,000	1,000	1,000	1,000
CO_2	MT	3,133	3,307	3,525	3,805
SiO_2	MT	0,000	0,242	0,544	0,932
O_2	MT	1,139	1,266	1,424	1,628
N_2	MT	7,976	8,862	9,970	11,394
Energy balance:					
In					
Chemical energy in C	MWh	7,79	8,22	8,76	9,46
Electrical energy	MWh	8,67	9,54	10,63	12,02
Sum in	*MWh*	*16,5*	*17,8*	*19,4*	*21,5*
Out					
Enthalpy in silicon (cooling and solidification)	MWh	0,96	0,96	0,96	0,96
Combustion and cooling of gas	MWh	6,06	7,33	8,92	10,95
Chemical energy in Si	MWh	9,01	9,01	9,01	9,01
Heat in waste gas	MWh	0,42	0,47	0,53	0,61
Sum out	*MWh*	*16,4*	*17,8*	*19,4*	*21,5*

Table 7.3 *Material and energy balance for the silicon process in the pure Si–O–C system – data for production in a 20 MW furnace.*

Silicon recovery		1	0,9	0,8	0,7
Reaction parameter x		0,000	0,111	0,250	0,429
Air addition parameter m		2,000	2,223	2,500	2,858
Ratio air/gas production		5	5	5	5
Material balance					
In					
SiO_2	MT/h	4,935	4,984	5,034	5,085
C	MT/h	1,973	1,893	1,811	1,728
O_2	MT/h	5,256	5,308	5,362	5,416
N_2	MT/h	18,397	18,579	18,766	18,956
Out					
Si	MT/h	2,307	2,097	1,882	1,664
CO_2	MT/h	7,227	6,934	6,635	6,330
SiO_2	MT/h	0,000	0,507	1,024	1,551
O_2	MT/h	2,628	2,654	2,681	2,708
N_2	MT/h	18,397	18,579	18,766	18,956
Energy balance					
In					
Chemical energy in C	MWh	17,970	17,241	16,498	15,739
Electrical energy	MWh	20,000	20,000	20,000	20,000
Sum In	*MWh*	*38,0*	*37,2*	*36,5*	*35,7*
Out					
Enthalpy in silicon (cooling and solidification)	MWh	2,212	2,011	1,805	1,596
Combustion and cooling of gas	MWh	13,980	15,368	16,781	18,221
Chemical energy in Si	MWh	20,780	18,888	16,958	14,989
Heat in waste gas	MWh	0,969	0,985	0,998	1,015
Sum out		*37,9*	*37,3*	*36,5*	*35,8*

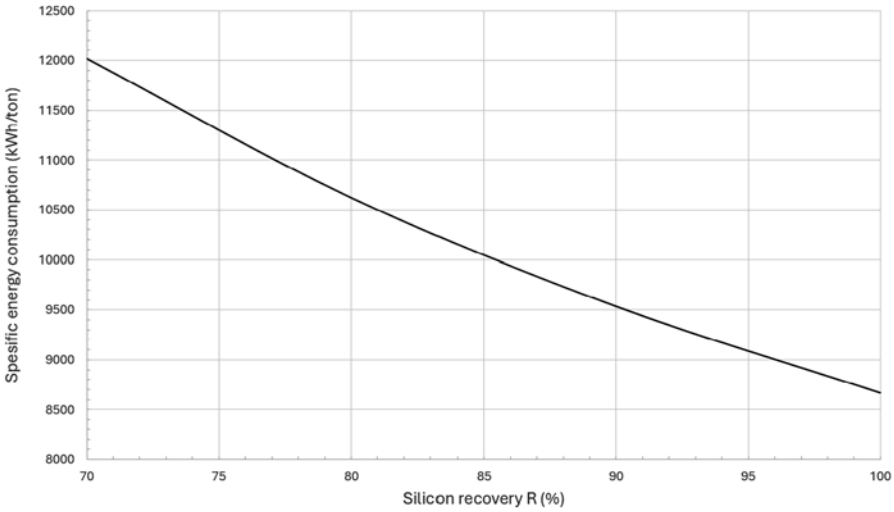


Figure 7.2 *Figure showing the specific energy consumption shown in Table 7.2.*

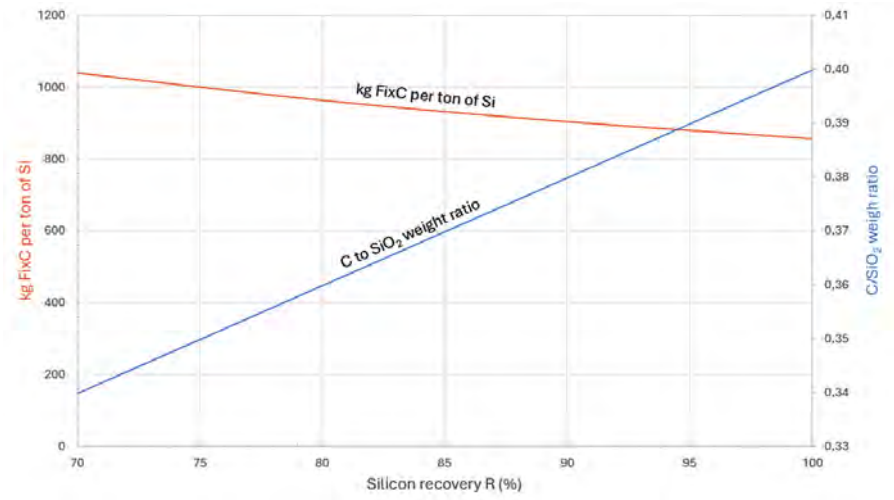


Figure 7.3 *Figure showing the theoretical consumption of carbon with increasing silicon recovery.*

Temperature in the off-gas

The temperature in the off-gas may be controlled by the amount of excess air. If the SiO and CO gas from the furnace is 1400°C on average, the off-gas temperature can be calculated as a function of the amount of air in the off-gas. This is done by balancing the enthalpy of combustion of the CO-gas and the SiO-gas with air against the specific heat content of the total off-gas. Figure 7.4 and Figure 7.5 show the off-gas temperature in a system with 80% silicon yield (calculated by HSC Chemistry (Roine, 1997)). Note the sharp increase in temperature during the burning of SiO-gas. The qualitative temperature for an industrial process will be commented on in Section 7.7.

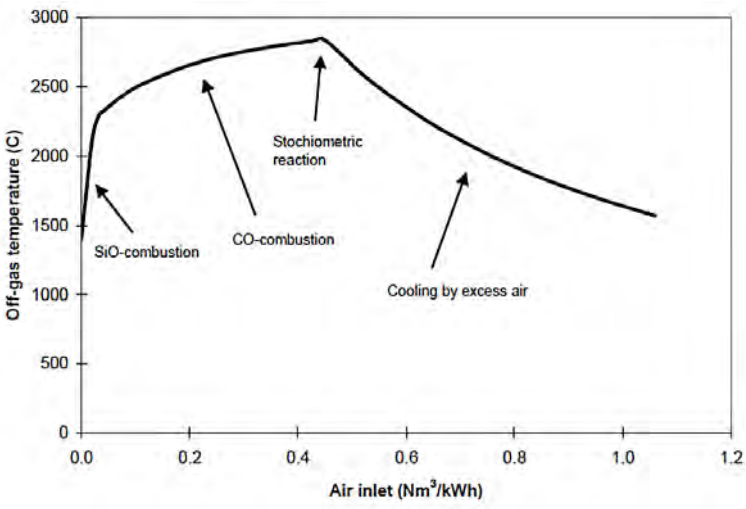


Figure 7.4 *The temperature in a theoretical silicon production process with 80% silicon yield. The sharp increase in the temperature during the SiO-combustion is due to the high enthalpy in the SiO-gas and the low total gas volume when a low amount of air is added.*

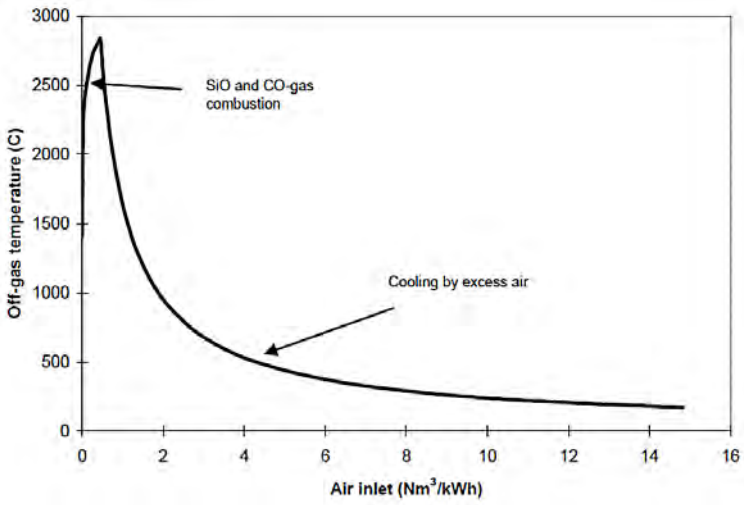


Figure 7.5 *The temperature in a theoretical silicon production process with 80% silicon yield. The figure shows the huge amount of excess air needed to control the off-gas temperature (Figure 7.5 is an extension of Figure 7.4).*

7.2 The industrial silicon process

The main difference between the theoretical process and an industrial process is related to the following: 1) energy losses from the process, 2) the use of non-pure carbon, 3) carbon losses to the off-gas system and 4) other minor deviations from an ideal process.

Energy losses from the process

To obtain a more realistic energy balance for a silicon process, it is necessary to take the different losses into account. There are several types of energy losses, which may vary from furnace to furnace. These include heat in cooling water equipment, in the off-gas, or as radiation heat from the furnace body. The loss of electric energy occurs because the large electricity supply to the process is delivered by a high current at low voltage from the transformers. Typical currents may be in the order of 100 000 A per electrode, which induces high losses in the electricity supply system. The losses are high in

the transformers, the electricity conductors, and the electrodes. The main energy loss is transferred to the cooling water in the transformers, busbars, and electrode support systems. From the electrodes, some of the loss will be in the form of radiation to the furnace hood or the surroundings.

The theoretical energy calculated above is plotted on the same graph as the results from some industrial furnaces (Figure 7.6) to estimate the effect of the energy loss. The graph shows a discrepancy of 2000–3000 kWh/tonne Si. This difference is mainly due to losses of electric energy that are normally measured at the transformers. To calculate the energy flow for a furnace, it is important to determine where the electric losses take place. For example, irrespective of whether the electric energy losses in the transformers are converted to cooling water losses or to heating the local surroundings of the transformers, this energy must be considered lost from the process. However, some of the electric energy loss is resistance heating of the electrodes, and some of this energy will be found as thermal energy in the off-gas from the process.

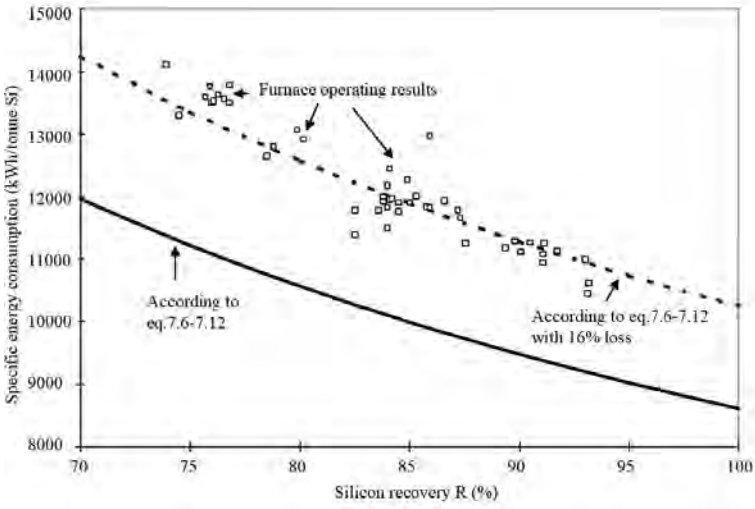


Figure 7.6 *Measured and calculated energy requirements for a silicon process as a function of silicon recovery to the metal. The dotted line represents the theoretical energy requirements with an energy efficiency = 0.84.*

An energy yield factor (e_y) may be introduced to describe the energy efficiency. This factor states how much electric energy the process receives compared to the total electric energy delivered to the process. The energy yield depends on the design of the furnace and the operational parameters. As seen in Figure 7.6, inserting an energy yield factor of 0.84 seems to provide a much better correlation between silicon recovery and specific energy consumption. The total specific energy consumption can then be calculated by expanding Equation [7.13] to Equation [7.14]:

$$\hat{E}_{Si} = \frac{1}{e_y}\left(853 + \frac{7818}{R}\right)\left[\frac{kWh}{tonne\ Si}\right] \qquad [7.14]$$

where $\hat{E}_{Si}$ is the theoretical specific energy consumption, R $(0 < R < 1)$ is Si yield, and $e_y\left(0 < e_y < 1\right)$ is the energy yield factor.

The reason for the variations in the industrial results may be that different furnaces have differing energy yield factors, or simply that there is inaccuracy in the figures.

Carbon – volatile compounds

In the theoretical calculations above, the reduction was assumed to be done with pure graphite. Normally, this is not the case in the production of silicon and silicon alloys. Coke, coal, charcoal and woodchips are the usual carbon sources. The amount of fixed carbon in the reduction agents is of interest to the process. In addition, coke and coal introduce other elements than carbon. The volatile hydrocarbons are of particular interest, as they add extra chemical energy to the input of the process. Coke normally has a low content of volatile hydrocarbons, often 0–10% weight. Charcoal typically contains 10–20% volatiles (Myrhaug, 2003; Smith-Hanssen, 2022). The volatile hydrocarbons will increase the amount of energy in the off-gas system, because they will burn together with the CO gas from the process. Table 7.4 gives examples of carbon materials used in the silicon production process.

The use of non-pure carbon will change the process in several ways:

- Accompanying volatile hydrocarbons add extra chemical energy
- Carbon materials contain ash with oxides such as aluminum oxide and calcium oxide which require energy to be reduced
- Water content must be driven off
- The accompanying extra mass may be beneficial to SiO-condensation

Table 7.4 *Examples of properties of carbon materials used (Andersen, 2023).*

Proximate		**Coal**	**Charcoal**	**Coke**	**Woodchips**
Moisture	%	8,17	1,4	6,31	6,68
FixC (d)	%DW	57,6	79	90,5	14,6
Volatiles (d)	%DW	40,4	17,7	6,64	84,2
Ash (d)	%DW	2,04	3,32	2,84	1,16
Ultimate					
C (d)	%DW	78	83	89,3	50,7
N (d)	%DW	1,58	0,39	1,78	0,2
O (d)	%DW	12	9,6	3,83	41,4
H (d)	%DW	5,79	3,71	1,83	6,48
S (d)	%DW	0,52	<0.1	0,42	0,11
Energy content					
NHV	kWh/kg	7,74	8,3	8,05	2,69
NHV/FixC	kWh/FixC	15,06	11,02	10,15	33,52

The large variation in the volatile content and the fixed carbon in the various carbon sources is seen in Table 7.4. This variation is important for the total energy in the combustion zone of the process. Exchanging coke for woodchips will increase the total weight of the reduction agent fed to the furnace for the same amount of fixed carbon, and it will dramatically increase the amount of volatile matter charged to the furnace. The volatiles from the woodchips are much lower in energy content than volatiles from coke and coal, due to the higher content of oxygen in the woodchips. The volatiles in the carbon

materials will go off at increasing temperatures. While CO_2 is emitted at, more or less, a constant rate between 200–700°C, CO and H_2 will leave the carbon materials between 200–800°C and 500–900°C, respectively. While the emissions of these gases from the carbon materials are quite similar for charcoal and coal, the amount of CH_4 will be much higher for coal, around 5 times higher. It will be emitted around 350–800°C for both materials (Smith-Hanssen, 2022). The various gas species were also measured inside the charge for a FeSi and Si furnace and, ignoring the SiO content, the gas, excluding the SiO gas, contained 80–90% CO, which is the product gas, but it also contained close to 10% H_2, around 5% N_2, and a couple of percentage of CO_2, O_2 and CH_4 (Ksiazek *et al.*, 2021).

Carbon – surface burning and losses of fine sized material

In an industrial silicon process, some losses in the carbon materials are observed. To ensure complete combustion of the furnace gas and control the temperature of the gas, it is necessary to allow a large amount of air into the furnace gas outlet. This cooling air may also contribute to some combustion of the reductants. The high gas velocity may result in 'wind sieving' or elutriation of carbon fines, especially for carbon materials below 1 mm, which are then burned in the off-gas system (Haugedal, 2025; Johansen *et al.*, 1991). The carbon loss may vary from furnace to furnace, but typical losses are in the order of 5% of the added carbon. The lost carbon will normally burn and add extra energy to the off-gas.

Other minor deviations from an ideal process

In the industrial silicon production process, minor elements of various kinds will normally be recovered in the product. These elements include aluminium, calcium and titanium, which may be reduced from oxides in the same way as silicon. This reduction will use some of the energy during reduction and, hence, appear to increase the specific energy for the silicon reduction. On the other hand, minor elements will also increase the total product-weight over that of pure silicon production.

7.3 Production of ferrosilicon

Iron-silicon alloys, called ferrosilicon, are mainly used for alloying steel and foundry iron. The most frequently used ferrosilicon grades are 75% ferrosilicon and around 50% ferrosilicon. The iron may be added as pure iron (scrap, iron bars etc.) or iron oxide.

Iron has a major effect on the reduction process as well as the energy balance, as described in Chapter 4. The specific electric energy consumption per ton of alloy is significantly reduced with increasing iron content. The addition of iron oxide will require somewhat more energy than would be true with a metallic iron source. Nevertheless, the specific electric energy consumption per silicon unit is normally lower for ferrosilicon compared to silicon. The principal impact of iron addition to the silicon production process is presented in Table 7.5.

Table 7.5 *The effects of iron addition to a silicon production process.*

No	Effect of iron addition	Comments
1	Higher mass flow per unit silicon.	Enhances the condensation of SiO gas in the upper part of the furnace. This may give higher Si recovery and accompanying lower electric energy consumption.
2	Iron decreases the activity of silicon in the melt.	Reduced silicon activity improves the silicon reduction at a given temperature.
3	Iron oxide reduction is an endothermic process.	The iron oxide reduction consumes energy; this results in higher energy consumption when using iron oxide as an iron source as compared to metallic iron.
4	Iron oxide reduction needs an additional reduction agent.	In ferrosilicon, the available reductants are silicon, CO gas, carbon and volatiles. The latter two are probably most important.

7.4 The material and energy balance for a ferrosilicon process with SiO loss

The chemical reaction for the formation of ferrosilicon with a SiO loss may be presented using metallic iron as an iron source:

$$a\ SiO_2 + b\ C + f\ Fe = c\ Si + d\ SiO + e\ CO + g\ Fe \qquad [7.15]$$

A simple mass balance gives the following equations:

Silicon balance: $a = c + d$ [7.16]

Oxygen balance: $2a = d + e$ [7.17]

Carbon balance: $b = e$ [7.18]

Iron balance: $f = g$ [7.19]

When iron oxide is used as an iron source, it is more difficult to calculate the amount of carbon required for the reduction of the iron oxide. In an industrial process, it seems that some of the reduction is performed by the volatiles from the carbon materials. In this calculation, only the last reduction step, from FeO to Fe, requires fixed carbon.

$$a\ SiO_2 + b\ C + f\ FeO = c\ Si + d\ SiO + e\ CO + g\ Fe \quad [7.20]$$

A simple mass balance gives the following equations:

Silicon balance: $a = c + d$ [7.21]

Oxygen balance: $2a + f = d + e$ [7.22]

Carbon balance: $b = e$ [7.23]

Iron balance: $f = g$ [7.24]

Note that no iron oxide loss is assumed.

The energy for the process will be calculated for ferrosilicon containing 75% and 50% silicon. First, a mole-based balance is constructed for these two cases. The molar weight of silicon is 28.09 g/mol, and iron is 55.85 g/mol. The iron balance is shown in Table 7.6.

Table 7.6 *Mass balance for 50% and 75% ferrosilicon*

Iron source	FeSi quality	a	b	c	d	e	f	g
Fe_2O_3	50%	1	1 + 1.701 c	c	1 – c	1 + 1.701 c	0.234 c	0.468 c
Fe_2O_3	75%	1	1 + 1.234 c	c	1 – c	1 + 1.234 c	0.078 c	0.156 c
Fe	50%	1	1 + c	c	1 – c	1 + c	0.468 c	0.468 c
Fe	75%	1	1 + c	c	1 – c	1 + c	0.156 c	0.156 c

For a specific case, a silicon recovery of 90% is chosen, and the result is presented in Table 7.7.

Table 7.7 *Mass balance for 50% and 75% ferrosilicon at 90% silicon yield*

Iron source	FeSi quality	a	b	c	d	e	f	g
Fe_2O_3	50%	1	2.53	0.9	0.1	2.53	0.211	0.42
Fe_2O_3	75%	1	2.11	0.9	0.1	2.11	0.070	0.14
Fe	50%	1	1.90	0.9	0.1	1.90	0.421	0.42
Fe	75%	1	1.90	0.9	0.1	1.90	0.140	0.14

Note the difference in the carbon requirement given by factor b in Table 7.7. The increase in carbon when using iron oxide is approximately 11% and 33% for 75% ferrosilicon and 50% ferrosilicon respectively, compared to the use of metallic iron. Such a difference is not normally observed, and the reason seems to be that both CO and the volatiles take part in the reduction of iron oxide. Carbon in the volatile material will not play the same role as the fixed carbon for silicon reduction, because only a minor part of this carbon participates in the silicon reduction. However, some of the volatiles may reduce the iron oxide. A rule of thumb for 75% ferrosilicon is that volatiles or CO reduce Fe_2O_3 to FeO, and it will only use reaction heat from the upper part of the process. The reduction from FeO to Fe is probably carried out by fixed carbon and will use electric energy from the process. For lower silicon grades, such as 50% ferrosilicon, almost the entire iron reduction process will require fixed carbon and will use electric energy. For FeSi52, it is shown that the difference in energy consumption will be about 16% higher if FeO is reduced with solid carbon, compared to CO gas (Saadieh, 2024). This discussion is very important for the process energy balance because volatile or CO-gases serving as reductants will not provide combustion energy in the off-gas.

7.5 Real life – a silicon and a ferrosilicon furnace

All the information above can be combined to calculate a mass and an energy balance for a real furnace. The calculation will be based on some simple characteristics of the furnace and the carbon materials discussed above. From the calculation a simple energy flow sheet can be drawn for the process.

The 'size' of a furnace is normally determined by the electric power. The power is often measured at the secondary transformers. From the transformer to the tip of the electrodes, electric losses occur due to resistance and inductance. In this calculation, it is important to divide the losses into various groups depending on where the energy will flow. An energy balance for the electric system from the transformers to the process is presented in Table 7.8

Table 7.8 *Electrical losses for a 10 MW silicon furnace*

Electric loss in:	Losses (kW)	Losses (% electric energy input)	Energy to be found as:
Transformers and busbars	400	4	Heat in the cooling water
Smoke hood, charging equipment, etc.	300	3	Heat in cooling water or as steam in a boiler
Electrode resistance	900	9	Partly radiation to the off-gas above the charge level, partly heating of raw materials
Total	1600	16	

The 'useful' electric energy from a 10 MW furnace, delivered to the process, is reduced by 16%. The electricity available for silicon production is hence 8.4 MW. Other losses should be considered. Heat losses from the furnace body are estimated at approximately 5% of the electricity input. The losses presented in Table 7.8 are indicative figures. Exact losses will vary from furnace to furnace due to different designs.

The material balance for the process may be calculated from Table 7.3 simply by multiplying the numbers by 8.4 MW/20 MW = 0.42. Once the fixed carbon requirement is established, the choice of carbon source will determine the energy in the process. The carbon reductants can be expressed as their percentage contribution to the total amount of fixed carbon fed to the process.

An example of a fixed carbon distribution could be a charge containing 10% from coke, 70% from coal and 20% from woodchips.

The following tables show the total energy flow in and out of the process. Note the importance of the volatiles in Table 7.9. The table shows that the electric energy is somewhat less than half of the energy into the process.

Table 7.9 *Energy delivered to a 10 MW silicon furnace.*

Energy type	Energy into the process (kW)	Part
Electric energy	10000	45%
Chemical energy fixed carbon	6353	29%
Chemical energy volatiles	5843	26%
Total	22196	100%

Table 7.10 shows the energy output from the process. Note that the energy in the off-gas output is 1.16 times the electric energy input to the process. The figures are indicative. To determine the exact energy distribution for a given design and operating strategy, calculations and/or measurements must be carried out.

Table 7.10 *The energy output from the 10 MW silicon furnace.*

Energy type:	Energy from the process (kW)	Part
Chemical energy product	7160	32%
Heat in product	730	3%
Energy in the off-gas	11353	51%
Cooling water	1822	8%
Radiation and convection	1131	5%
Total	22196	100%

The energy balance is also illustrated in Figure 7.8. These results may be considered typical for a silicon process, but the parameters used in the calculation may not apply to every furnace. To determine the energy balance for a specific furnace, calculations and/or measurements must be carried out, as e.g. Myrhaug (2003), Kamfjord (2010) and Takla (2013) did, to mention a few.

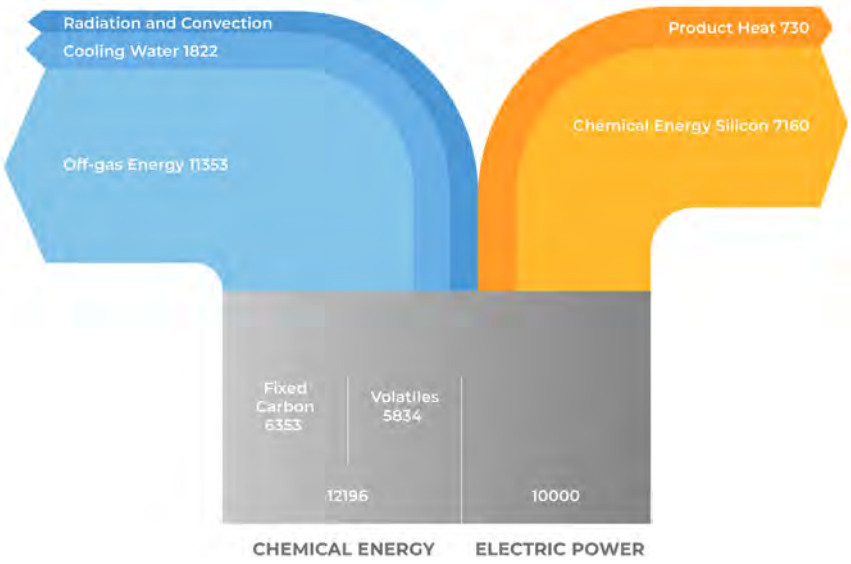


Figure 7.7 *showing the energy to and from a 10 MW silicon furnace.*

7.6 Energy recovery from the process

Conceivable energy recovery

A disadvantage of the current technology used to produce silicon alloys is the large amount of energy that is not used in the reduction step. As seen in Figure 7.8, only about 32% of the energy consumed is chemical energy in the product. In other words, approximately 68% of the energy is lost as waste heat. Some direct process improvements are conceivable, such as running the process with a high silicon yield, improving the furnace design to achieve lower electric energy loss, or reducing the amount of volatiles fed to the process. Another possibility is to install energy recovery systems. The most readily recoverable energy is in the cooling water. It could be used for various low-temperature purposes, such as fish farming or the heating of buildings.

The largest recoverable energy source is in the off-gas. In larger heat recovery systems, this energy can be used to produce warm water, saturated steam for heating, or superheated steam for electricity production. Today, most Si/FeSi plants in Norway do have energy recovery systems producing electrical energy. This could be done through boilers connected to the furnaces. In

the boilers, the off-gas is cooled down from 600–750°C to 170°C by passing it through a superheater, boiler and economiser heat exchangers. The boiler can produce superheated steam at approximately 460°C and 50 bar pressure. The steam can be fed to a multi-stage reaction turbine, which is linked to a generator. The electric energy produced is typically approximately 30% of the energy in the off-gas. Compared with the production of thermal energy as warm water or steam, the yield is lower when the energy is recovered as electricity.

The potential energy recovery increases with increasing off-gas temperature. It has already been mentioned that a high volume of cooling air is used to control the off-gas temperature. In industrial silicon production, the temperature is in the range from 200°C to 700°C after combustion and mixing with cool air. Normally, there is a limitation for the off-gas temperature to the filters that is around 150°C, to avoid the harmful generation of sulphurous acid.

The off-gas temperature for the theoretical silicon production process was calculated previously in this chapter. The industrial process will differ from this by having more gas components, such as volatiles and water vapour. This will make the temperature increase with increasing air inlet less than that shown in Figure 7.2. On the other hand, volatiles and carbon fines give extra energy when burned. The burning of volatiles and carbon fines will most likely take place after the SiO combustion, but before all the CO gas is burned.

The energy recovery system must be able to adjust to varying conditions at the furnace, both regarding carbon materials, Si-yield and load, to mention some. In Figure 7.9 and Figure 7.10, examples of daily variations can be seen, where the FixC may vary regarding over-coking and under-coking strategies, the amount of volatiles may change based on available raw materials, and the load may change. This will affect the flows out, and the energy in the off-gas changes about 20% from max to min. When the load also changes, the daily variations may be larger.

To increase energy recovery, the most important parameters are, according to Kamfjord (2010), a high furnace load, a larger furnace size and higher off-gas temperatures. As described above, volatiles will also affect the total energy content in the off-gas. Good access to cold cooling water will allow a lower condensator pressure, which also affects energy recovery.

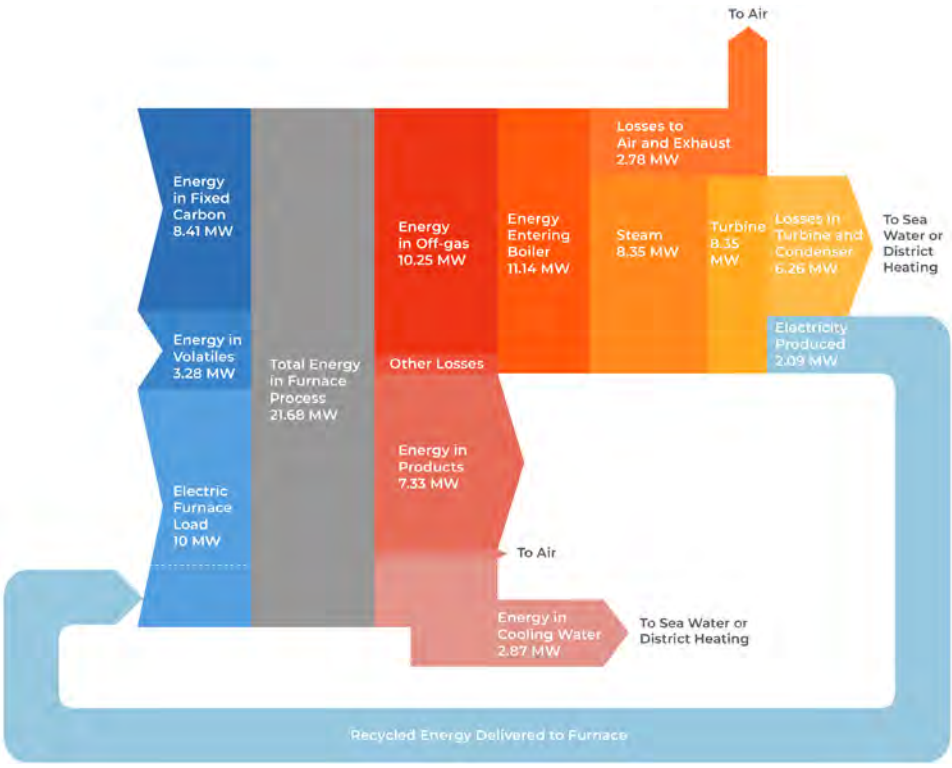


Figure 7.8 *shows a Sankey diagram where the energy recovery is shown (Kamfjord et al., 2010).*

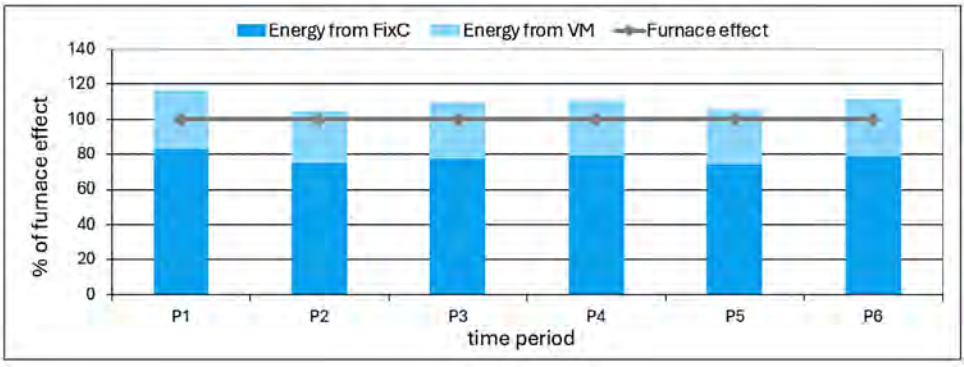


Figure 7.9 *Variation of energy into a FeSi furnace given as averages over 8 hours (Kamfjord et al., 2010).*

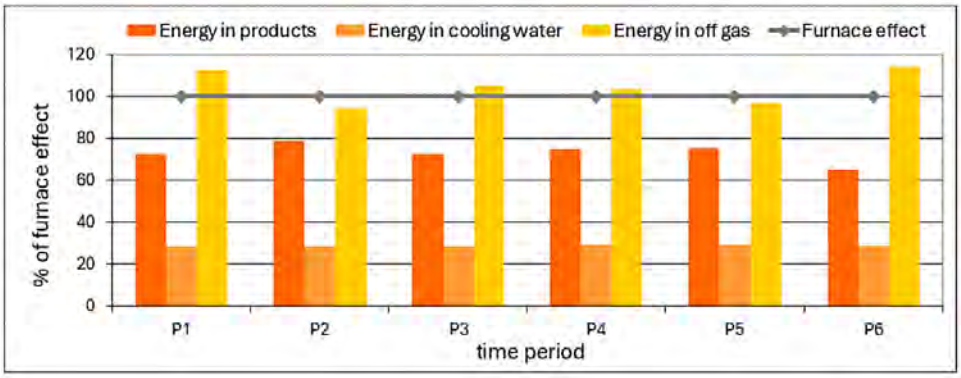


Figure 7.10 *Variation of energy from a FeSi furnace given as averages over 8 hours (Kamfjord et al., 2010).*

7.7 Exergy analyses

Exergy is the maximum amount of work obtainable when an energy carrier is brought from its initial state to a state of thermodynamic equilibrium with the common substances of the natural environment (by means of reversible processes) (HSC Chemistry). Exergy can also be used to quantify the 'quality of energy'. Hence, the exergy destruction during a process indicates how much the quality of the energy deteriorates. The quality of energy can be exemplified by 1 kWh of electrical energy having a higher exergy than 1 kWh of hot water. The exergy term also represents how easy it is to recycle energy, or to make electricity out of the energy, hence, the higher the temperature of a gas, solid or liquid, the higher the exergy.

The exergy content of a material flow contains chemical and physical energy, and here we will use the terminology described by HSC Chemistry.

$$E_{ch.} = \sum_k n_k b_k^{ref.} + \Delta G^0_{f(25°C,1bar)i}$$

where n_k is the stoichiometric amount of element k in the species, $b_k^{ref.}$ is the elemental exergy of element k and $\Delta G^0_{f(25°C,1bar)i}$ is the standard formation Gibbs free energy of the species.

$$E_{ph.} = \left(H_i - H_{i(25°C,1bar)}\right) - T_{25°C}\left(S_i - S_{i(25°C,1bar)}\right)$$

where H_i is the total enthalpy of the species at the temperature of T, $H_{i(25°C,1bar)}$ is the enthalpy of the species in the standard state, S_i is the total entropy of the species at the temperature of T, and $S_{i(25°C,1bar)}$ is the entropy of the species in the standard state. Today, one can use easy tools like e.g. HSC Chemistry to calculate the exergy and exergy destruction of processes in the same manner as enthalpy energy (=enthalpy) calculations.

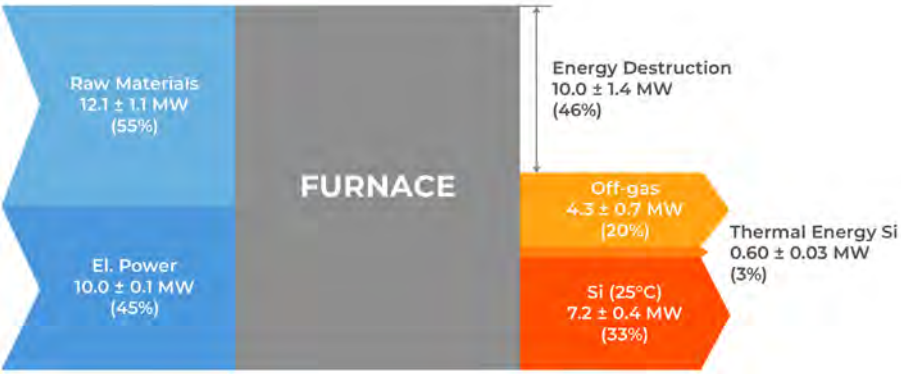


Figure 7.11 *A Grassman diagram illustrating the exergy flow for a 45 MW submerged arc furnace operating. The numbers are scaled to a 10 MW furnace. The off-gas temperature is 260°C. (Adapted from Takla et al., 2013).*

Takla *et al.* (2013) and Børset (2015) did calculations of the exergy destruction, or the exergy efficiency, for various Si process-cases. Figure 7.11 shows a case investigating the exergy flow in and out of the Si-process. The main exergy flows out of the process are the off-gas and the energy in the product, as also the enthalpy balances show (Figure 7.8, Figure 7.11). For this example, the exergy destruction is 46%, that is with an exergy efficiency of 54%. Both the electric energy and the carbon have high exergy contents, and we see that the ratios between the exergies in raw materials and electrical energy are about the same as the energy in the flows, as seen in Figure 7.11. As we are going from electrical energy and carbon to off-gas with low temperatures, the exergy destruction is quite high. Figure 7.12 shows a number of cases (Takla *et al.*, 2013; Tveit and Kolbeinsen, 2019), with varying degrees of exergy efficiency.

First, one can see that higher Si-yields give higher efficiency, as we are using less energy and fewer carbon materials per ton of silicon, and hence, the total input exergy will be lower. It can also be seen that if one recovers the energy in the off-gas, the exergy efficiency will increase about 20%. If we recover the energy in the off-gas, as well as using the thermal energy from the furnace and the heat in the product, the highest theoretical efficiency will be 75%, and the Best Available Technology (including recovery of energy in off-gas) is expected to be around 70%. Well driven Si-furnaces today, without energy recovery, are expected to be between 30–40% exergy efficiency.

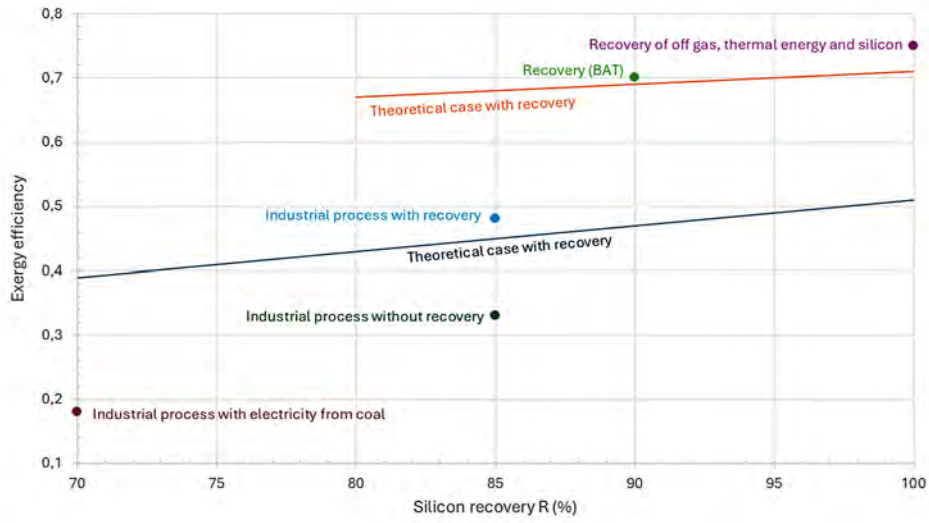


Figure 7.12 *Exergetic efficiencies for theoretical and industrial processes. Recovery means power production from thermal energy in the off-gas; for the theoretical process it means utilization of all the thermal exergy in the off-gas at 800°C. One case describing the industrial process also takes into account that the electric power is produced from coal. (Numbers are taken from Takla et al., 2013; Tveit and Kolbeinsen, 2019).*

References

Andersen, V. (2023) *Flue gas recirculation for the silicon process*. Doctoral thesis 2023:135. Norwegian University of Science and Technology (NTNU), Trondheim, Norway. Available at: https://hdl.handle.net/11250/3069034

Børset, M.T. (2015) *Energy dissipation and recovery in the context of silicon production*. Doctoral thesis. Norwegian University of Science and Technology (NTNU), Trondheim, Norway. Available at: https://hdl.handle.net/11250/4253628

Haugedal, H. (2025) *The effects of biocarbon on permeability and wind-sieving of charge for silicon production*. MSc thesis. Norwegian University of Science and Technology (NTNU), Trondheim, Norway. Available at: https://hdl.handle.net/11250/3220913

Johansen, S.T., Grådahl, S., Gammelsæter, R., Raanes, M., Arntsberg, A., Lindstad, T., Enstad, G. and Tveit, H. (1991) 'Clogging of ferro-silicon furnace off-gas channels at high temperatures'. The Minerals, Metals & Materials Society (TMS).

Kamfjord, N.E., Myrhaug, E.H., Tveit, H. and Wittgens, B. (2010) 'Energy balance of a 45 MW (ferro-) silicon submerged arc furnace', in *Proceedings of INFACON XII*. Helsinki, Finland. Available at: https://www.pyrometallurgy.co.za/InfaconXII/729-Kamfjord.pdf

Ksiazek, M., Saadieh, R., Gærtner, H., Grådahl, S., Sægrov, B., Tangstad, M., Valderhaug, A. and Ringdalen, E. (2021) 'Industrial measurements of the gas and temperature in Si and FeSi production process', in *Proceedings of INFACON XVI*. Trondheim, Norway. Available at: https://doi.org/10.2139/ssrn.3922198

Myrhaug, E.H. (2003) *Non-fossil reduction materials in the silicon process – properties and behaviour*. Doctoral thesis 2003:67. Norwegian University of Science and Technology (NTNU), Trondheim, Norway.

Roine, A. (1997) *HSC Chemistry for Windows v. 9*. Pori, Finland: Outotec Research.

Saadieh, R. (2024) *Process phenomena in furnaces producing ferrosilicon alloys*. Doctoral thesis 2024:199. Norwegian University of Science and Technology (NTNU), Trondheim, Norway. Available at: https://hdl.handle.net/11250/3132796

Smith-Hanssen, N. (2022) *Volatiles in carbon reductants*. Restricted SINTEF Report No. 2022:01242. Trondheim, Norway: SINTEF.

Takla, M., Kamfjord, N.E., Tveit, H. and Kjelstrup, S. (2013) 'Energy and exergy analysis of the silicon production process', *Energy*, 58, pp. 138–146. Available at: https://doi.org/10.1016/j.energy.2013.04.051

Tangstad, M., Ringdalen, E., Olsen, J.E., Einarsrud, K.E., Myrhaug, E., Reynolds, Q. (2021) 'Conceptual model of tapping mechanisms in FeSi/Si furnaces', in *Proceedings of INFACON XVI*. Trondheim, Norway. Available at: https://doi.org/10.2139/ssrn.3922189

Tveit, H. and Kolbeinsen, L. (2019) 'The (love & hate) role of entropy in process metallurgy', *Matériaux & Techniques*, 107, p. 506. Available at: https://doi.org/10.1051/mattech/2019028

Tangstad, M. (2026) 'Operational problems', in M. Tangstad, G. Tranell, H. Tveit and E. Ringdalen (Eds.), *Production of high silicon alloys* (2. ed.) (pp. 297–323). Fagbokforlaget. https://doi.org/10.55669/oa880808

8

Operational problems

Merete Tangstad

This chapter gives examples of operational problems where we can gain useful understanding from the inner structure of submerged arc furnaces. The selected examples are:

- Formation of deposits in the furnace
- Tapping

8.1 Deposits in the furnace

Formation of deposits is a well-known difficulty in the production of silicon and ferrosilicon. Three main types of deposits have been observed in excavations, as illustrated in Figure 8.1:

- Slag accumulation in the bottom of the furnace as well as on the periphery of the furnace
- α-SiC crusts surrounding the electrodes and as deposits in the lower part of the furnace
- Sintered charge materials in the upper layers of the furnace (also called top-crusts or condensate layer).

This work is licensed under the Creative Commons Attribution 4.0 International License.
To view a copy of this license, visit https://creativecommons.org/licenses/by/4.0/

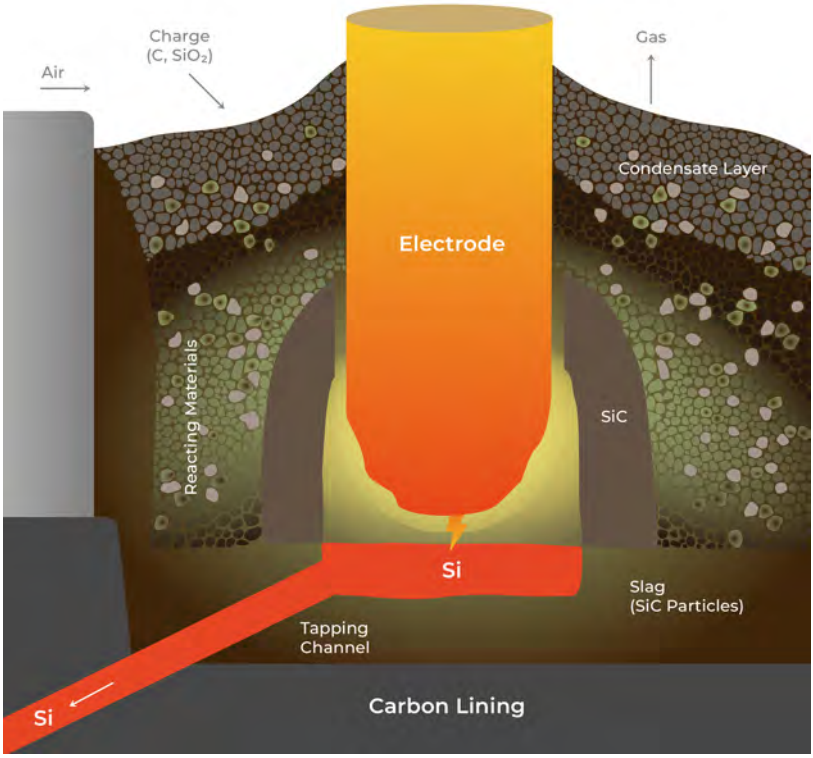


Figure 8.1 *Illustration of deposits in the furnace with 1) a top crust containing condensates gluing the charge, 2) SiC crust around the electrodes and 3) slag deposits in the bottom and on the side periphery of the furnace (Folstad et al., 2020) [With permission from Marit B. Folstad].*

The size of the deposits can range from filling large parts of the furnace volume to only small amounts. Deposits leave less room for the production process, hinder material and gas flows, and may affect the electrical current paths. Ideally, the process is run in such a way that deposits are not detrimental to operation. However, if large deposits occur, they must be removed.

Slag accumulations

The slag constituents in the silicon/ferrosilicon process are mainly SiO_2, CaO and Al_2O_3, as also discussed in Chapter 4. CaO and Al_2O_3 enter the furnace as impurity elements, and some SiO_2 from the quartz dissolves into the slag

phase. CaO can also be added separately, as e.g. lime, to adjust the properties of the slag. A major part of the added CaO and Al_2O_3 will be reduced to Ca and Al and enter the silicon/ferrosilicon. The distribution of Ca and Al between the slag and the silicon can be calculated by the following reactions:

$$2(CaO) + Si = 2Ca + (SiO_2) \quad [8.1]$$

$$2/3(Al_2O_3) + Si = 4/3Al + (SiO_2) \quad [8.2]$$

where the underlined elements signify the silicon/ferrosilicon phase and the parentheses denote the compounds in the slag phase. Some slag will thus be tapped together with the silicon/ferrosilicon. Although the amount of slag produced per ton of silicon/ferrosilicon may be low, slag may accumulate in the furnace and hence take up a large volume. The slag accumulated in the furnace is thus a SiO_2, CaO, Al_2O_3 slag. Its CaO/Al_2O_3 ratio is determined by the raw material composition, but the SiO_2 content will vary from 30wt% and up, as shown in Figure 8.2.

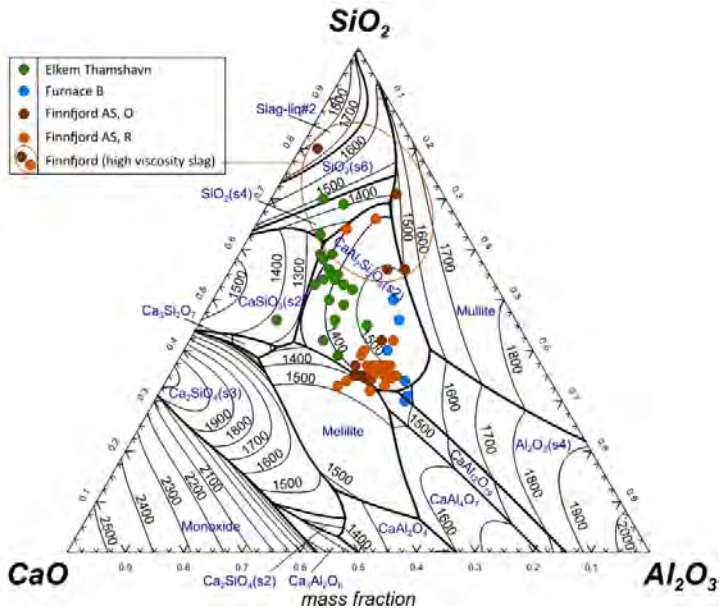


Figure 8.2 *Tap slag from industrial silicon and ferrosilicon furnaces. The same figure is shown in Chapter 4 as Figure 4.3 (Folstad, 2023). [With permission Marit B. Folstad].*

The viscosity of the slag is higher than the viscosity of silicon/ferrosilicon. Hence, slag flow out of the furnace is much more sensitive to temperature and composition variations than silicon/ferrosilicon flow. The viscosity is also affected by SiC particles in the slag. Slag wets SiC particles, so SiC particles will readily enter the slag phase from the silicon/ferrosilicon phase. The size and amount of SiC particles in the tapped slag will be lower than in the accumulated slag, as illustrated in Figure 8.3. As a result, slag flow will be slower than silicon/ferrosilicon flow in the furnace and will therefore accumulate in the lower part of the furnace. This will happen especially if the temperature in the lower part of the furnace is low, due to high electrical current paths in the furnace. A lower temperature affects the following three issues:

- As the slag viscosity is very temperature dependent, a low temperature will increase the viscosity of the slag phase.
- When the slag is heated to a high enough temperature, it will interact with the SiC and the SiO_2 will be reduced to elemental silicon. If the temperature in the high-temperature zone is too low, the SiO_2 will not be reduced and the slag will have a high SiO_2 content. The viscosity increases with increasing SiO_2 content in the slag (as discussed in Chapter 4), and hence the viscosity of the slag will be high.
- With the same argument as in the previous point, if the temperature in the high-temperature zone is low, the SiC particles in the slag will not react with the SiO_2, and hence there will be more SiC particles in the slag.

During excavations, slag has been found all the way at the top of the charge, at the periphery of the furnace. How the slag has formed or arrived in the upper part of the furnace is not known. There is not enough CaO and Al_2O_3 content in the raw materials to represent the slag composition, and hence it is believed to be coming from the bottom slag layer. There is overpressure in the high temperature zone of the furnace due to the high gas formation rate, and it has been calculated that this may press the silicon, and thus maybe also the slag, towards the furnace periphery (Kadkhodabeigi, 2011). If the pressure is high enough, slag may also be pressed upwards. The slag will freeze as it moves towards areas of lower temperatures, and the state of the slag is illustrated in Figure 8.4. At high temperatures, the slag will be liquid, and it will start to solidify at lower temperatures. In this figure, the slag composition is taken from excavations and the temperature is calculated (Folstad, 2023; Myrhaug, 2020).

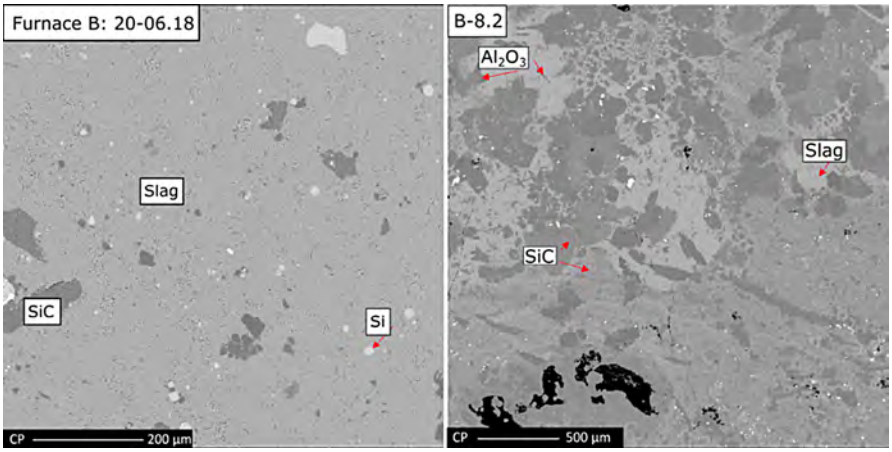


Figure 8.3 *EPMA image of a tapped slag sample to the left and an accumulated slag sample to the right collected during excavation. Both samples are from the same furnace (Folstad, 2023). [With permission Marit B. Folstad].*

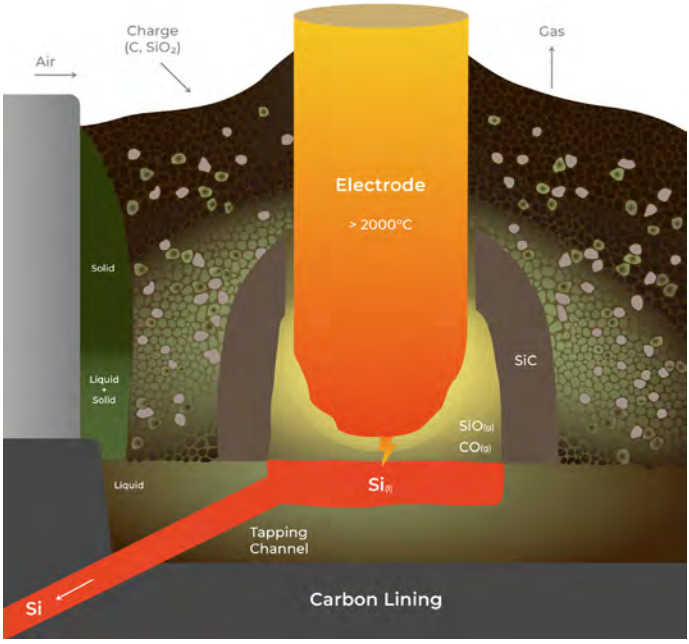


Figure 8.4 *Estimation on how the slag composition will be in the furnace; liquid, liquid + solid, or solid, based on calculated temperatures. (Folstad, 2020). [Used with permission from M.B. Folstad].*

Slag is also important for other silicon-containing production processes, such as silico-manganese, silico-aluminium and silico-calcium. In carbothermic production of silico-aluminium, the charge components react and give a mixture of aluminium oxide and aluminium oxy-carbides (Motzfeldt *et al.*, 1989). This mixture has some fluidity and sinks into a layer at the bottom of the furnace, but it is not fluid enough for tapping. The electrical conductivity is so high that resistance heating is impossible, so it must be heated by an electric arc above the melt. At the same time, this arc heats the charge higher up in the furnace, and a large fraction of the energy is used to melt new materials. As a result, the furnace is filled with incompletely converted raw materials unless it is possible to control the flow of materials into the inner zone. An illustrative example is a series of tests (unpublished Elkem work) to produce an alloy 60% Si and 40% Al from compound pellets [Al_2O_3 + 3 SiO_2 + 9 C (petroleum coke)]. The first tests were run in a 50 kW furnace with split furnace body. The resistance became very stable, and the charge sank down evenly without any stoking. The energy consumption in the very small furnace was 14 MWh/ton, which corresponds to an Al and Si recovery well above 90 per cent. When the process was transferred to a 500 kW furnace, the charge sank too rapidly and formed a highly conducting oxide melt. The furnace controller raised the electrode to a high position, and the heat produced more slag instead of completing the reaction.

Deposits of SiC

If more carbon is added in the raw materials than is consumed through the silicon- and SiO- formation, the carbon surplus will be transformed to SiC and accumulated in the furnace. The stoichiometric model (Figure 3.12 and Figure 9.6) demonstrates that an optimum C content gives a maximum silicon recovery at given operational conditions. If the C content is lower than the optimum, all the intermediate SiC is consumed, but the loss as SiO is higher than at the optimum. Some SiO is lost even at the optimum C content. If the metallurgist tries to increase the silicon recovery by increasing the content of C above the optimum, the loss as SiO will decrease as expected, but the silicon loss as accumulated SiC more than balances the gain. This SiC is deposited

in the lower part of the furnace, in the high temperature area, and when the deposit becomes large, it will obstruct operation severely. The optimum C content depends on the state of the furnace, and it is therefore not a fixed quantity that can be used permanently. The furnace metallurgist must observe the operation continuously and determine whether the C content is close to the optimum. Most plants today have models to calculate the carbon balance daily, i.e., the deviation between the carbon added and the carbon consumed. However, as no measurement is 100% correct (e.g. the analysed Fix C content in the raw materials and the raw materials weights at the plant, to mention a couple), one can never find the true optimal carbon content. By definition, one will always add more than is consumed, or less than is consumed, though the difference may be small in a well-operated plant.

One strategy is to run with a C content so low that there is always a safe C deficit relative to the optimum. A small excess silicon loss as SiO is acceptable during successful operation, but because the correct C content is not constant, it is easy to operate with too low an addition. Today, silicon recovery of 80–95 per cent is typical. Safe operation is complicated by effects omitted from the simple stoichiometric model, which assumes that excess SiO_2 always reacts with SiC in the inner zone. In real operation, however, the SiO_2 will also react with the electrode. As a result, safe operation can lead to unnecessarily high electrode consumption, which adds strongly to the cost of silicon.

The accumulated SiC may appear in at least three different states:

- Carbon particles (charcoal, coal, char, coke…) that have been transformed to SiC. This has not been seen during excavations, however, one would not be able to separate SiC particles that are in surplus from those that take part in the production process. A surplus of transformed carbon particles has, however, not been seen in the lower part of the furnace. It can also be mentioned that SiC particles have very low strength and may crumble over time or be transformed to other states (Hoover, 2023). The transformed carbon materials are β-SiC at temperatures below 2000°C. This will not be further discussed in this chapter, as the formation is already covered previously in this book, e.g. in Chapter 2.

- Small SiC particles that are mixed with the silicon and the slag. If the amount of this SiC is too high, it will, as described above, hinder silicon and slag flow and, in the end, lead to a crust-like material in the bottom of the furnace. This is due to the slag (as described above), the SiC particles, or a combination of these two factors. This SiC is found to be β-SiC, however, it has a much denser structure than the transformed raw materials and is believed to come either from precipitated SiC when the silicon experiences temperature changes, or from the reaction between Si and CO gas, $2Si + CO = SiO + SiC$, which is the reversed silicon producing reaction.
- α-SiC crust surrounding the electrodes. This crust has been nonexistent in some excavations, but in others it has been seen in large volumes (Ksiazek *et al.*, 2016; Tangstad *et al.*, 2014).

Formation of SiC in liquid silicon

When we add energy to a deposit of Si-containing SiC, the temperature rises. The phase diagram in Figure 8.5 and Figure 8.6 gives an indication of the behavior. As the temperature increases, the solubility of carbon in silicon becomes higher. Very close to the arc, where the temperature may be several thousand degrees, the carbon solubility may be at a percentage level, however, below 2000°C the solubility is at ppm level. When the silicon experiences temperature differences, it will dissolve SiC as the temperature increases and then precipitate SiC when it cools down again. If this was a closed system, the amount of SiC particles would be constant at a given temperature. However, it is seen in other systems, such as silicomanganese, that the metal dissolves other carbon materials available faster than the precipitated SiC, and in that case, the amount of precipitated SiC will increase over time (Davidsen, 2011). This may also happen in the silicon/ferrosilicon system.

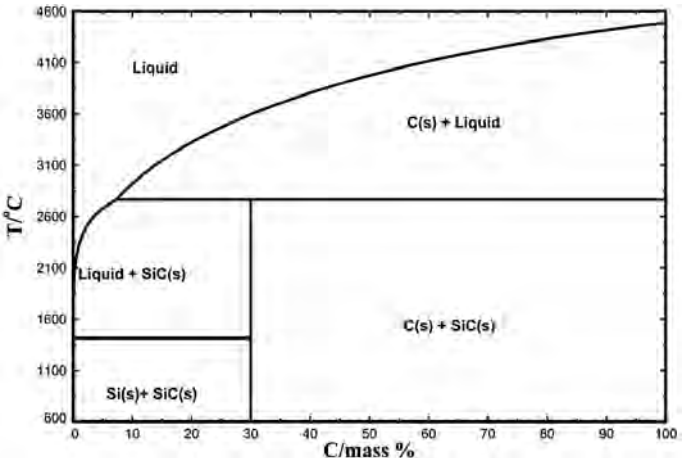


Figure 8.5 *(Figure 2.2 in Chapter 2) The Si–C binary phase diagram calculated by the use of FactSage using the FTlite database.*

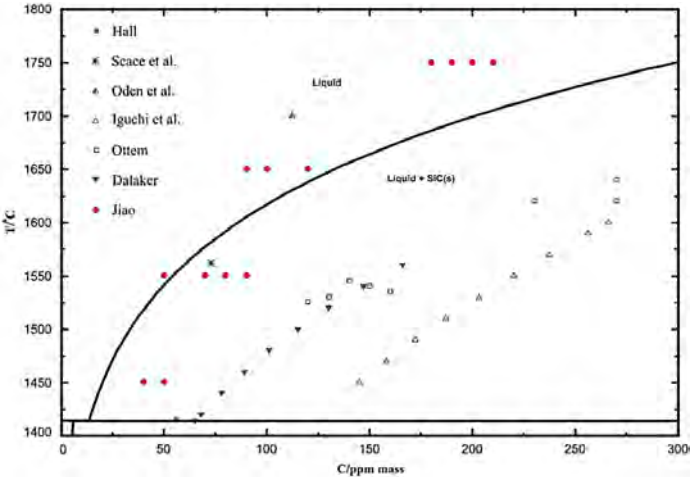


Figure 8.6 *(Figure 2.3 in Chapter 2) The content of C in silicon in equilibrium with SiC summarized by (Jiao, 2020) (Hall, 1958; Scace, 1959; Oden, 1987; Ottem, 1993; Iguchi, 1993; Dalaker, 2009). [With permission from J.M. Jiao].*

The formation of α-SiC crusts

Varying amounts of SiC crusts have been found in industrial furnaces during excavation. When there is a large amount of SiC crust, it may look as shown in Figure 8.7. Figure 8.8 shows that the crust is a dense material with gas channels, as also shown in Figure 8.9. Crystal formation can also be seen on the surface of the crust (Ksiazek *et al.*, 2016; Tangstad *et al.*, 2014; Tranell *et al.*, 2010).

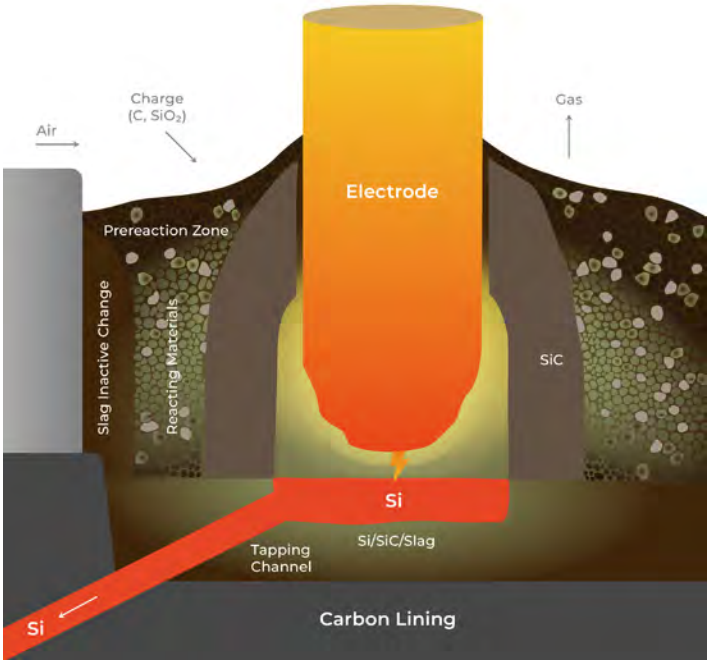


Figure 8.7 *a) General illustration of SiC crust and b) Schematic view of SiC crusts found during an industrial excavation (Folstad et al., 2020; Tangstad et al., 2014). [Used with permission from M. Folstad].*

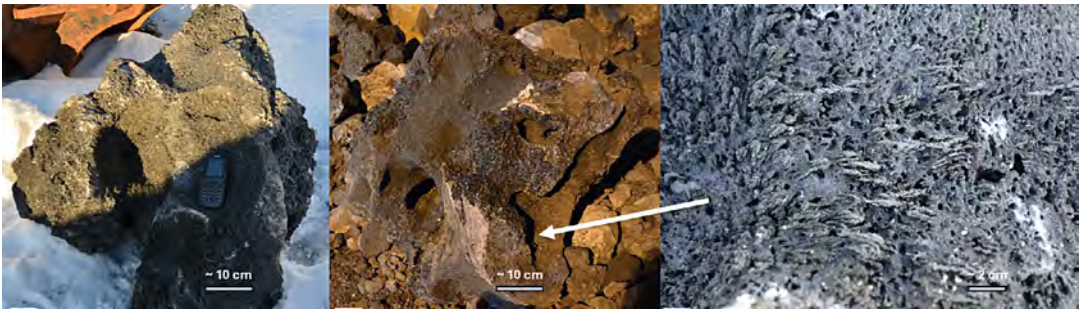


Figure 8.8 *Pictures of SiC crust excavated from an industrial furnace (Tangstad et al., 2014).*

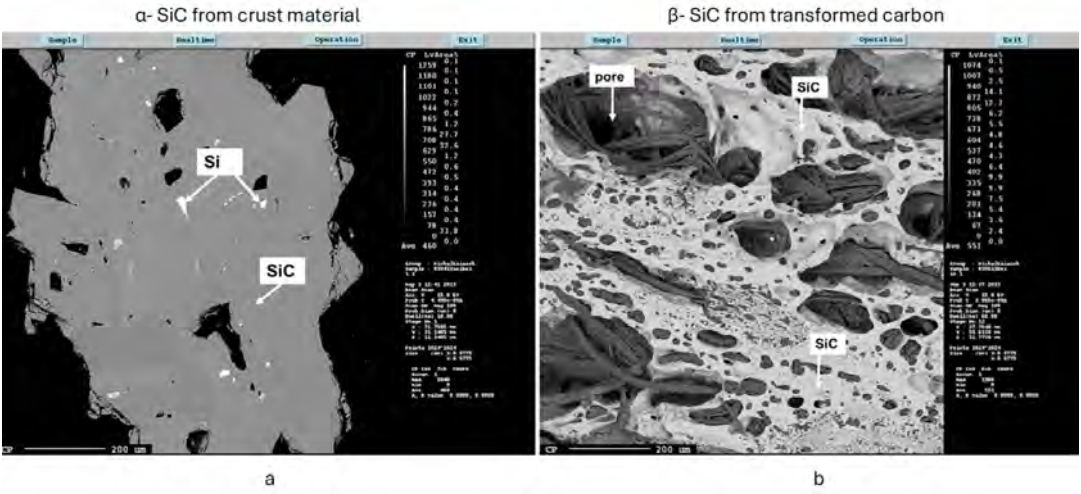


Figure 8.9 *Comparison of α-SiC structure (a) to β-SiC transformed charcoal (b) (Jayakumari, 2020) [Used with permission from S. Jayakumari].*

α-SiC is stable at high temperatures. Transformed charcoal, coal and petcoke have been observed to start transforming around 2100°C as shown in Figure 8.10. The transformation rate is also dependent on the original carbon material, as well as the amount of Si present. SiC from charcoal is seen to transform faster than SiC from coal and petcoke, and a higher amount of silicon in the structure will also increase the rate, as seen in the figure. In both laboratory samples (Jayakumari and Tangstad, 2020) and industrial samples (Figure 8.8 (Ksiazek *et al.*, 2016; Tangstad *et al.*, 2014)), crystals can be seen growing on the surface of the carbon particle. It has been proposed (Jayakumari and Tangstad, 2020) that the reaction proceeds via a gas reaction with activated atoms on the SiC surface and in the pores:

$$SiO(g) + 3CO(g) = SiC + 2\ CO_2(g) \qquad [8.3]$$

Because the surface and pores serve as nucleation sites, highly porous material, like charcoal, will react faster. The CO_2 formed will instantly react with SiC to produce SiO and CO gas, hence, the overall CO_2 pressure is very low at these temperatures.

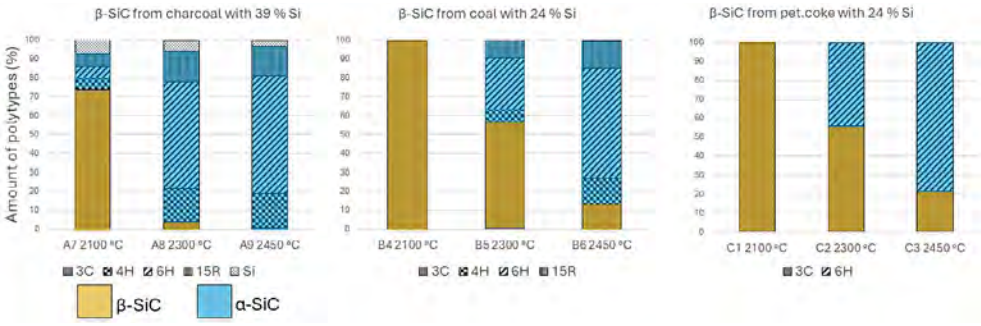


Figure 8.10 *Extent of transformation from β-SiC to α-SiC for charcoal, coal and petcoke at increasing temperatures (Jayakumari, 2020; Jayakumari and Tangstad, 2020) [Used with permission from S. Jayakumari].*

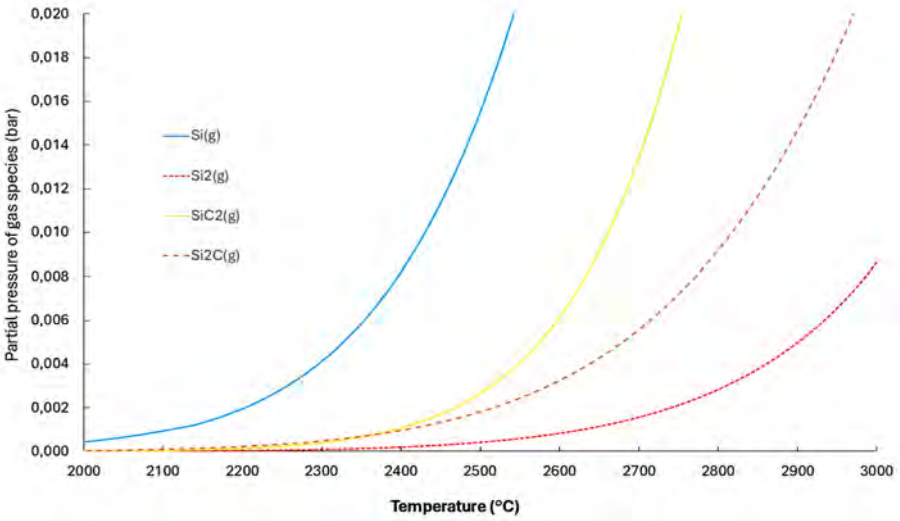


Figure 8.11 *Gas pressures of Si and SiC_x species from 2000–3000°C calculated at HSC Chemistry.*

It has also been discussed if the α-SiC is formed from gas species formed around the arc. Close to the arc, the temperature may be several thousand degrees, and if no oxygen is present in this area, there may be a high amount of gaseous Si and SiC_x species, as seen in Figure 8.11. As the gas species flows away from the arc, the temperature in the gas will drastically decrease down to around 2000°C, and the gas species will condense or react to form Si and SiC and an α-SiC crust.

Whether it is the temperature alone that transforms β-SiC to α-SiC, or whether it goes through the SiC_x gas species, is to date not known. However, both mechanisms require high temperatures and can thus only occur close to the electrodes. As the α-SiC crust has higher electrical conductivity than a bed of charge/bed of SiC particles, it is believed that much of the electrical energy is being produced in the SiC crust in addition to the arcs (Hoover, 2023). This means that when the charge meets the high-temperature SiC crust, the metal production may mainly form on the crust and not in the bottom of the furnace as previously described.

The removal of deposits

In principle, the Si–SiC deposits can be removed with excess SiO_2 in the charge. The Si loss will increase, since the charge now has a lower content of C than normal to react with SiO, but much of the energy and silicon in the deposit will still be recovered. However, SiO_2 tends to attack the electrode instead of the bottom deposit, and the electrode consumption increases strongly.

The concentrated heat of the arc can vaporize the SiC-Si deposit material that comes close to the arc. In a stationary furnace, the electrode tip can go close to the bottom by arcing, but it will dig a rather narrow hole. In a rotating furnace, it can dig a circular trench, but it cannot widen the trench to the sides. Perhaps the best removal of bottom deposit would be obtained if the electrode had a slow circular movement relative to the pot. The diameter of the circle could be perhaps some 20 centimetres.

Formation of crusts in the upper parts of the charge

Normally, the charge can be broken down around the electrode during the stoking operation, and a ring-shaped opening is formed around the electrode. When the furnace is open 30–40 cm from the electrode, stoking and charging is easy, and the gas distribution becomes uniform. The charge particles outside this opening are sintered together by silica and condensate, as discussed also in Chapter 2. Occasionally, the opening becomes very narrow. Then stoking becomes difficult, and the new charge does not give a layer that distributes the gas uniformly. The gas from the inner zone breaks out where the charge layer is thinnest. The result is a poor counter-current process, resulting in blowing and low silicon recovery.

The crust formation relates to the following condensation reactions, also described in Chapter 2:

$$2SiO = Si + SiO_2 \qquad [8.4]$$

$$3SiO + CO = 2SiO_2 + SiC \qquad [8.5]$$

When the operation starts from an empty furnace, the new charge is loose. In the high temperature part, around the electrode tips, SiO and CO gas is formed and flows into the colder part of the furnace, both the passive and

active part of the furnace. SiO and CO gas will diffuse into the colder materials and gradually fill the voids with SiC + SiO_2 and SiO_2 + Si, also called condensates. The term 'condensates' is not, strictly speaking, correct for these materials, however, due to the long industrial tradition of using it, it will also be used here. The mass in the condensation layer will be partly molten SiO_2, condensate and C materials partly converted to SiC. The condensation reactions are exothermic, and hence an increased amount of condensation will heat the top part of the charge. The condensates and the raw material mix forms a sintered mass that is difficult to break. When the active mass around the electrodes is stoked down, new, cold material will enter. This sequence is repeated in every stoking cycle. The high content of condensate and viscous silica makes the mass difficult to break.

The crusts may sometimes be weakened by heat from the electrode if the electrode is run in a high position, and then it may be possible to stoke them down. For very strong crusts, even blasting with explosives has been tried. When the remains of the crusts are brought down into the crater and heated, they react readily.

8.2 Tapping

The tapping efficiency is determined by the structure of the zones and the distribution of materials inside the furnace. The inner structure of the furnace is described in Chapter 3. The product is tapped from the furnace through a tubular hole that reaches into the zone where the silicon is molten at the bottom of the furnace. The tapping of the furnaces, that is, the drainage of the liquid silicon and some minor slag amounts, is an important sub-process, both economically and from an HES point of view. If the furnace is not drained properly, it will affect the Si-yield, as more SiO gas is produced and lost. The extent of drainage will also affect the electrode tip position and hence the electrical current paths. If the drainage has been too low for some time, liquid silicon will accumulate in the furnace. When the liquid metal is finally drained, the high amount of metal draining at high speed may cause both material and human damage. The discussion on the correlation between the furnace zones and the tapping is based on the paper describing the conceptual tapping of a silicon/ferrosilicon furnace (Tangstad *et al.*, 2021).

Conceptual tapping model

Tapping can be continuous or discontinuous. Ideally, the furnace is emptied rapidly when the tapping is discontinuous, but often the flow of alloy is rather slow, and the taphole is open most of the time. Then the real difference between continuous and discontinuous tapping is moderate.

Typically, one taphole is used at a time in the tapping of a silicon furnace. This means that the liquid silicon must flow through three different areas, as illustrated in Figure 8.12:

- Step 1: The liquid silicon must flow from the back electrodes to the tap-electrode area.
- Step 2: The liquid silicon must flow to the taphole, that is, through the material between the high temperature area, close to the tap electrode, and the taphole.
- Step 3: Through the taphole.

The tap rate can be determined by the sum of the resistance in these three steps. The tap-electrode is here defined as the electrode closest to the taphole. As the furnace pot is rotating, there will be two electrodes that have the same distance to the taphole at a fixed time. This is, however, only happening over a small time period.

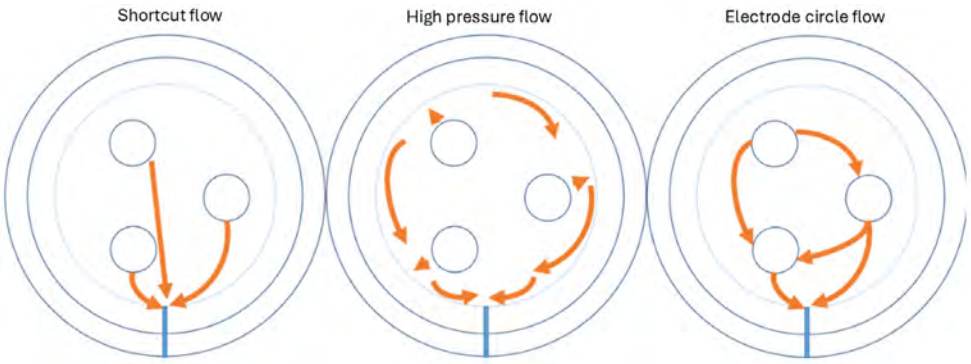


Figure 8.12 *Possible flow patterns from back electrodes to taphole area.*

In principle, one can visualize Step 1 in three conceptually different flow patterns, as illustrated in Figure 8.12. The simplest flow model for metal flow from the back-electrodes to the tapping hole is to visualize the furnace as a simple container holding a liquid, as also illustrated in Figure 8.13. The metal will then flow according to the shortcut flow model shown in Figure 8.12. This model assumes that the flow resistance and gas pressure are the same throughout the furnace, and the liquid will therefore take the shortest path from the electrode area, where it is produced, to the taphole. However, this is rarely the case in industrial furnaces, owing to pressure gradients and to materials that hinder flow.

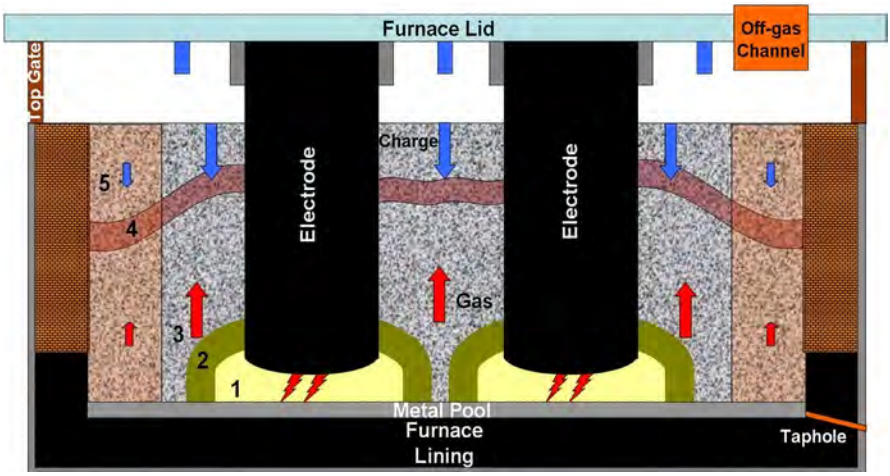


Figure 8.13 *A cut-through, graphical depiction of the submerged arc furnace used in high-silicon alloy production. Different zones have been formed in the charge, such as the crater zone (1), crater wall (2), softening and melting zone (3), crust formation zone (4), and stagnant charge zone (5) (Kadkhodabeigi, 2011). [Used with permission from M. Kadkhodabeigi].*

Kadkhodabeigi (2011) modelled the tapping flow from a Si and FeSi furnace based on the zones illustrated in Figure 8.13. In this model, Step 1 and Step 2 cannot be separated because there is a continuous metal bath in the lower part of the furnace. As seen in Figure 8.14, an overpressure of 3–4 kPa (30–40 mbar) has been measured in industrial furnaces due to gas production, and the pressure will therefore vary with the load, as seen in the figures. For a furnace with a horizontal, continuous metal pool, Kadkhodabeigi calculated that the metal would be pushed towards the side lining, as seen in Figure 8.15, using overpressures from 30–200 mbar in the calculation. This effect is also illustrated in the high-pressure flow model in Figure 8.12. The metal will therefore run along the lining wall to the taphole position. When the metal in front of the taphole no longer fills the taphole, the tapping rate will decrease, as illustrated after 350 seconds in Figure 8.15.

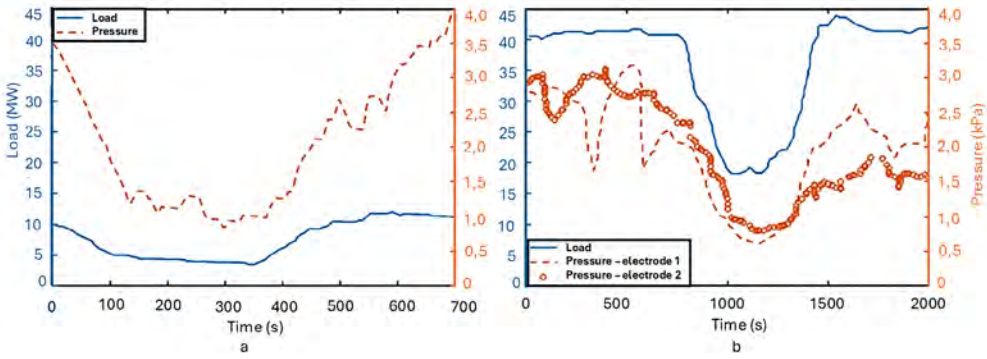


Figure 8.14 *Direct relation between crater pressure and furnace electric load, based on industrial measurements from different submerged arc furnaces used in silicon production (after Grådahl and Johansen, 1998; Tveit et al., 2002).*

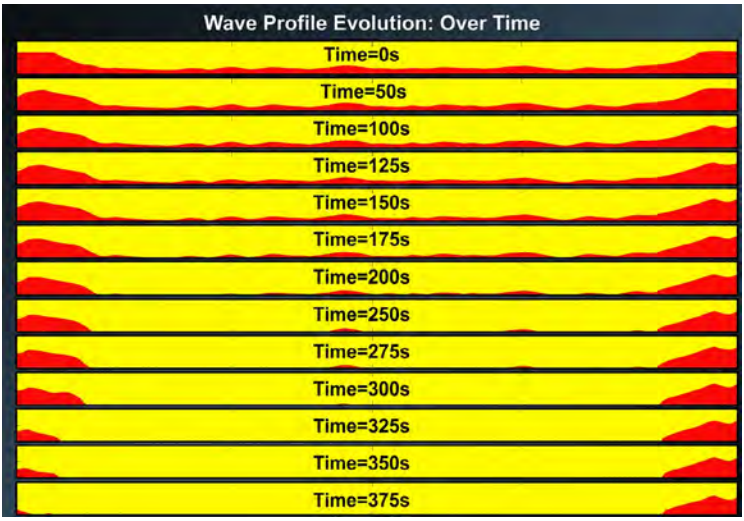


Figure 8.15 *Evolution of the metal pattern in the lower part of the central plane of the ferrosilicon furnace. This explains the reason for the sudden flow rate drop during furnace tapping when the metal level in front of the taphole decreases (Kadkhodabeigi, 2011). [Used with permission from M. Kadkhodabeigi].*

Though the higher pressure around the electrode tips is an important input to a model, other effects should also be included. First, as the metal is pressed into the cold, stagnant charge zone (also called the inactive zone), it will cool and may not have a warm, open space to flow into. Second, excavations have seldom shown an open metal pool in the bottom of industrial furnaces (Folstad and Tangstad, 2021; Folstad *et al.*, 2020; Ksiazek *et al.*, 2016; Tangstad *et al.*, 2014). (It must, however, be noted that when an excavation gets close to the furnace bottom lining, debris and materials from the rest of the furnace fall in, and the picture may not be so clear.) Figure 8.16 shows schematic pictures of various zones that have been found during excavation of industrial furnaces. It can also be noted here that the metal must be drained through a zone of slag with SiC particles, called the tapping channel, before it enters the taphole. The taphole is defined here as the channel through the hardware of the furnace, that is, the channel through the lining and the steel shell.

One pattern found under the electrode is a metal pool surrounded by a slag layer (Tangstad *et al.*, 2014), as illustrated in Figure 8.16 and Figure 8.17. The slag found in the lower part of the Si furnaces is believed to be liquid, as the liquidus temperature is around 1500°C (Folstad and Tangstad, 2021),

and the metal is tapped at 1800–1900°C (Ksiazek *et al.*, 2018; Werner, 2019). The temperature in the slag layer is, however, very dependent on the electrical current paths and the heat transfer in the furnace. Even though the slag is liquid, it is probably quite viscous, especially because it contains SiC particles. This also explains the accumulation of slag over time, as it is not being drained from the furnace. The metal pools below the electrodes may, however, form a ring of metal in the electrode motion path, as the furnace is rotating. This means that the metal will follow the electrode path during tapping, as shown in the electrode circle flow in Figure 8.12.

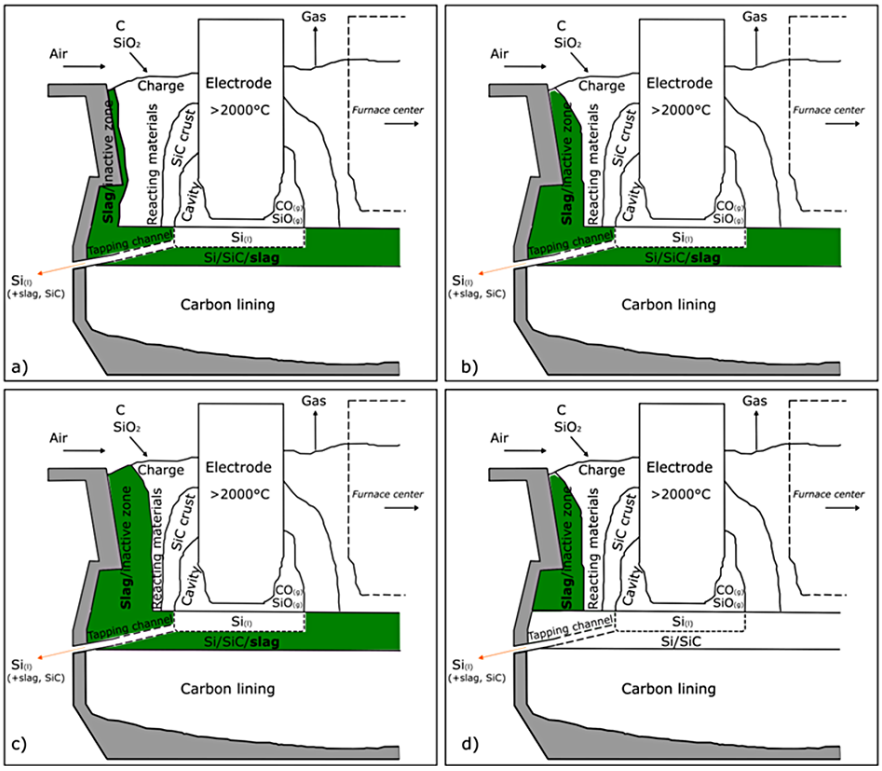


Figure 8.16 *Schematic figures illustrating the various zones in a Si furnace. The first case, a), shows an ideal situation with almost no slag along the furnace walls. The second case, b), shows an average situation, with a layer of slag/inactive zone that affects furnace operation. Case c) shows an accumulated furnace. The last case, d), shows the situation with no slag and SiC in the furnace bottom (Folstad and Tangstad, 2021). [Used with permission from Marit B. Folstad].*

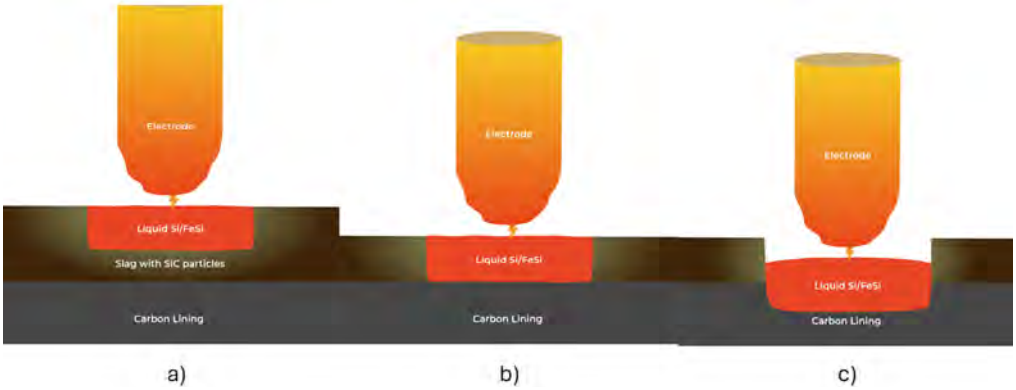


Figure 8.17 *Possible configurations of the metal pool under the electrode tip, surrounded by slag with SiC particles: a) high electrode positions due to a high amount of accumulated slag (Ksiazek et al., 2016) (Wacker 1); b) optimal electrode position; c) low electrode position due to lining wear (Tangstad et al., 2014).*

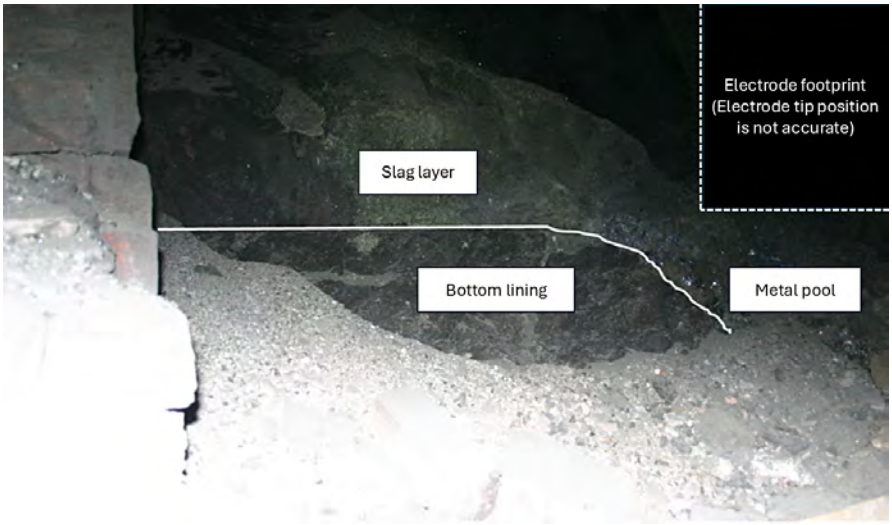


Figure 8.18 *Picture from excavation of Si furnace (Tangstad et al., 2021).*

So far, mainly Step 1 has been discussed, that is, the drainage from the back-electrodes to the tap-electrode. If this is modelled, by e.g. Computational Fluid Dynamics, any obstacles in the furnace will lower the tapping rate for some time, until the tapping rate again reaches the production rate. Obstacles include solidification of metal in cold areas, but in the models the effect on electrodes and furnace operation is typically not included. This may, of course, also reveal that the main problem is not Step 1, drainage from the back electrode to the taphole electrode, but actually Step 2: drainage from the tap-electrode, that is the hot area of the furnace, to the taphole, which is in the colder region (Folstad *et al.*, 2020).

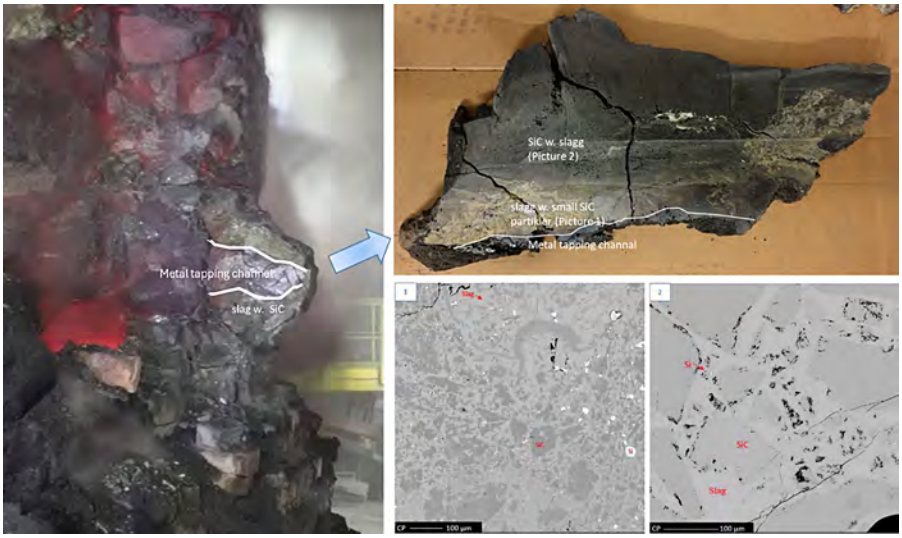


Figure 8.19 *Tapping channel from industrial excavation (Folstad et al., 2020). The left picture shows the tapping channel, the top-right picture shows the top of the same tapping channel, and the pictures below show the SiC particles in the slag matrix from two different areas (Folstad and Tangstad, 2021). [Used with permission from Marit B. Folstad].*



Figure 8.20 *Tapping channel from taphole through a slag layer (Tangstad et al., 2021).*

In a couple of industrial excavations, shown in Figure 8.18 to 8.20, where the excavation of the tapping area has been more focused, it is seen how the metal must flow through a more than 1 m thick slag zone before entering the taphole. The colour of the slag is often determined by the amount and size of SiC particles, as the darker area has more and larger SiC particles. It is therefore believed that the type and amount of slag in the proximity of the taphole will be important for the total drainage of the furnace (Folstad *et al.*, 2020).

Both large amounts of α-SiC crusts and smaller amounts have been observed in silicon furnaces. Though not verified, it seems that the SiC crusts are not present all the way down to the metal pools, hence, their influence on tapping is still an open question. It is, however, believed that the SiC crusts will distribute the electrical current paths a bit wider around the electrodes, and thus actually heat the area close to the electrode. This may affect the flow properties of both slag and metal.

Step 3, flow through the taphole, is dependent on the dimensions and maintenance of the taphole. There is not much information on this specifically for the silicon process, but more general information can be found in the extensive review by Nelson and Hundermark (2016).

High viscosity slag, that is, slag with a high SiO_2 content, low temperature, and SiC particles, can all lead to clogging of the taphole or tapping channel (Folstad, 2023). This is also discussed in Chapter 4. This slag will form balls or tubes as it exits the furnace. Partly transformed raw materials, like partly molten quartz or SiC particles, may also be tapped together with the silicon and slag. This is not seen during excavations in the high temperature area, and one may speculate whether materials from the inactive zones may come through uncontrolled tapping channels through the lining. Several methods are available to remove the obstacles, such as penetrating with powerful mechanical equipment, burning with a graphite electrode, or blowing with oxygen.

Gassing through the taphole

During normal tapping, silicon evaporates from the molten silicon and some smoke emerges. Occasionally, however, an intense, several metre long jet of burning gas emanates from the taphole. The taphole is said to be gassing or blowing. The gassing may disappear after a few hours, but sometimes it will go on for more than a week. If the gassing taphole is plugged and a new hole is opened, it will often start gassing shortly after. This observation indicates that the gassing often has a cause within the furnace and not in the outer part of the taphole. The gassing often starts without any warning. The production rate seems to be normal, but it drops significantly when the furnace gasses. Sometimes it has been observed that a lot of slag is tapped just before the gassing begins. Taphole blowing is a serious challenge in the (ferro)silicon process, as it means lower production, unpleasant working conditions in the tapping area, and generally smoke pollution of the internal environment of the plant.

To avoid taphole gassing, it is important to know the reason for it. General understanding of gas flow tells us that gassing through the taphole requires some overpressure in the inner zone of the furnace and an open channel from the overpressure through the taphole. Since the inner zone of an operating furnace produces gas, there will always be an overpressure that is large enough to push the gas out through the outer zone, as seen in Figure 8.14. Measurements of the crater pressure in production furnaces show that the overpressure varies strongly, but it is seldom larger than 0.1 bar (Grådahl *et al.*, 1997; Ingason, 1994; Johansen *et al.*, 1998; Tveit *et al.*, 2002). There is

a strong high-frequency variation, but generally the pressure is largest just after charging, and smallest when the furnace is ready for stoking. According to our comprehension of the inner structure of the furnace, the cavity is surrounded by a SiC wall. This SiC wall has, however, gas channels and will not be gas tight. The bottom consists of Si or slag containing SiC crystals. From calculations, it is seen that if the taphole is covered by slag or silicon, the gas will be forced from the crater through the charge (Kadkhodabeigi, 2011). If, on the other hand, the metal or slag is not covering the taphole, and additionally the charge has a low permeability due to too much condensate in the upper zone, the gas will exit the furnace through the taphole.

The metallurgist can, in principle, reduce the overpressure by establishing a porous outer zone with a low pressure drop. However, there will always be some overpressure in the furnace, and the main approach to the gassing problem must be to avoid leakage in the bottom gas sealing. Such leakages can be caused by damage to the taphole or a too-steep taphole that leads into the cavity or into cracks in the deposit. Often, however, it seems that the cause is inside the taphole. In that case, the gassing is often related to low electrodes. When the furnace is run with a long-term carbon deficit, the Si–SiC layer at the bottom will be consumed gradually, and the electrode will go deep and make the bottom very hot. The Si–SiC layer becomes thin, while slag and silicon become fluid and flow out with the tapping. Some solid slag and alloy close to the wall will melt, and gas passages through the crater wall may form. The result is that the gas-tight SiC–C layer at the bottom will leak. To stop the gassing, the metallurgist can use corrections that raise the electrodes. Practical means are higher voltage or increased carbon content of the charge. The low electrode position is an obvious suspect when the taphole gasses, since we can easily imagine the mechanism.

References

Davidsen, J.E. (2011) *Formation of* Silicon Carbide *in the* Silicomanganese Process (MSc thesis). Norwegian University of Science and Technology (NTNU), Trondheim, Norway,. https://doi.org/https://hdl.handle.net/11250/248911

Folstad, M., Tangstad, M. (2021) SiO_2–CaO–Al_2O_3 slags in Si/FeSi furnaces, in: Proc INFACON XVI. Trondheim, Norway. https://doi.org/10.2139/ssrn.3922187

Folstad, M.B. (2023) *Slag and its effect on Si and FeSi production* (Doctoral thesis 2023:317). Norwegian University of Science and Technology, (NTNU), Trondheim, Norway, https://hdl.handle.net/11250/3096091.

Folstad, M.B., Ksiazek, M., Tangstad, Merete, (2020) Slag in the Tapping Area in a Si Furnace., in: *Proc. Silicon for the Chemical and Solar Industry XV*. Trondheim, Norway, https://www.ntnu.edu/si-conference.

Grådahl, S., Johansen, S.T. (1998) Environment and furnace processes. Part 2. Norw. title: Miljø og ovnsprosesser. Del II.) (SINTEF report (in Norwegian) No. STF24 F98638).

Grådahl, S., Johansen, S.T., Hop, B.I., Tveit, H., Valderhaug, A. (1997) *Environment and furnace processes. Part 1.* SINTEF (Trondheim), Open report STF A97568. (SINTEF report No. STF A97568).

Hoover, H. (2023) *Electrical* Resistivity *of* Materials *in the* Silicon Furnace (Doctoral thesis 2023:298). Norwegian University of Science and Technology (NTNU), Trondheim, Norway, https://hdl.handle.net/11250/3091823.

Ingason, H.T. (1994) *Hollow electrodes in the production process of ferrosilicon* (Doctoral Thesis). Norges Tekniske Høgskole, NTH (Now Norwegian University of Science and Technology, (NTNU)), Trondheim, Norway.

Jayakumari, S. (2020) *Formation and characterization of β-and α-Silicon Carbide produced during Silicon/Ferrosilicon process* (Doctoral thesis 2020:252). Norwegian University of Science and Technology (NTNU), Trondheim, Norway. https://hdl.handle.net/11250/2678922.

Jayakumari, S., Tangstad, M. (2020) Transformation of β-SiC from Charcoal, Coal, and Petroleum Coke to α-SiC at Higher Temperatures. *Metall Mater Trans B 51*, 2673–2688. https://doi.org/10.1007/s11663-020-01970-1

Jiao, J.M. (2020) *Si-based phase change materials in thermal energy storage systems* (Doctoral thesis, 220:137). Norwegian University of Science and Technology (NTNU).

Johansen, S.T., Tveit, H., Gradahl, S., Valderhaug, A., Byberg, J.A. (1998) Environmental Aspects of Ferro-Silicon Furnace Operations-An Investigation of Waste Gas Dynamics, in: *Proc. of INFACON VIII*. Beijing, China, https://www.pyrometallurgy.co.za/InfaconVIII/059-Johansen.pdf, pp. 59–63.

Kadkhodabeigi, M. (2011) *Modeling of* Tapping Processes *in* Submerged Arc Furnaces *(Doctoral thesis 2011:149)*. Norwegian University of Science and Technology (NTNU), Trondheim, Norway. https://hdl.handle.net/11250/248862.

Ksiazek, M., Tangstad, M., Ringdalen, E. (2016) Five furnaces five different stories, in: *Proc. Silicon for the Chemical and Solar Industry XIII*. Kristiansand, Norway, pp. 33–42.

Ksiazek, M., Tangstad, M., Ringdalen, E., Grådahl, S., Hustad, H.M., Holtan, J., Nymoen, A.B., Kaukonen, S. (2018) *Measurement of metal temperature during tapping of an industrial FeSi furnace*. Presented at the Furnace Tapping 2018, Kruger National Park, South Africa.

Motzfeldt, K., Kvande, H., Schei, A., Grjotheim, K. (1989) *Carbothermal* Reduction *of* Aluminium. Aluminium-Verlag, Düsseldorf.

Myrhaug, E. (2020) KPN Controlled Tapping. Examples of conceptual models based on simplified comsol simulations, Industrial presentation from Elkem, KPN Controlled Tapping Meeting. NTNU, Trondheim, Norway.

Nelson, L.R., Hundermark, R.J. (2016) The tap-hole - key to furnace performance. *J. S. Afr. Inst. Min. Metall. 116*. https://doi.org/10.17159/2411-9717/2016/v116n5a12

Tangstad, M., Ksiazek, M., Faaness, B. (2014) Zones and materials in the Si furnace, in: *Proc. Silicon for the Chemical and Solar Industry XII*. Trondheim, Norway, pp. 24–27.

Tangstad, M., Ringdalen, E., Olsen, J.E., Einarsrud, K.E., Myrhaug, E., Reynolds, Q. (2021) Conceptual Model of Tapping Mechanisms in FeSi/Si Furnaces, in: *Proc INFACON XVI*. Trondheim, Norway. https://doi.org/10.2139/ssrn.3922189

Tranell, G., Andersson, M., Ringdalen, E., Ostrovski, O., Steinmo, J.J. (2010) Reaction Zones in a FeSi75 Furnace – Results From an Industrial Excavation, in: *Proc. INFACON XII,* Https://Www.Pyrometallurgy.Co.Za/InfaconXII/709-Tranell.Pdf. Helsinki, Finland, pp. 709–716.

Tveit, H., Halland, T., Landro, K.I., Johansen, S.T., Ravary, B. (2002) The tapping process in silicon production., in: *Proc. Silicon for the Chemical Industry VI*. Loen, Norway, pp. 39–46.

Werner, T. (2019) *As-tapped Liquid Silicon Temperature Measurements in an Industrial Furnace* (MSc thesis). Norwegian University of Science and Technology (NTNU), Trondheim, Norway, https://hdl.handle.net/11250/2623374.

Kero, I., Ringdalen, E. and Tranell, G. (2026) 'Modified and alternative processes', in M. Tangstad, G. Tranell, H. Tveit and E. Ringdalen (Eds.), *Production of high silicon alloys* (2. ed.) (pp. 325–374). Fagbokforlaget. https://doi.org/10.55669/oa880809

9

Modified and alternative processes

Ida Kero, Eli Ringdalen and Gabriella Tranell

9.1 General

The submerged arc process for silicon and high silicon alloys has now been in operation for about a century. During this time, efficiency has improved and the scale has, as seen in Figure 9.1, increased dramatically (Nelson, 2014). However, the fundamentals and main principles of the current process, as described in Chapters 2 and 3, are still very much the same.

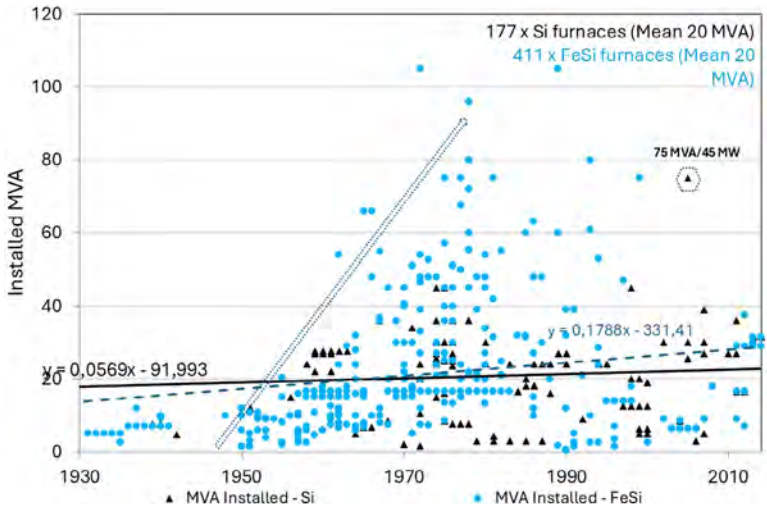


Figure 9.1 *Historical progression of installed MVA of silicon and ferroalloys furnaces (Based on Nelson, 2014).*

This work is licensed under the Creative Commons Attribution 4.0 International License. To view a copy of this license, visit https://creativecommons.org/licenses/by/4.0/

Silicon producers have continuously investigated methods to improve the existing carbothermic process and to develop and industrialize alternative process routes. The production of silicon metal and high silicon alloys is technically well established, and alloys with almost any specification can be produced using known technology. The initial drive behind process modification was mainly cost reduction. Subsequently, modifications and the development of new processes to improve the working environment and minimize emissions to the outer environment became increasingly important. In the wake of the climate crisis, the focus on developing new and improved carbon-lean processes has intensified. Decarbonization of the production process, including the energy supply system, is the first and most important step. Recirculation of by-products and the use of alternative raw material sources are other means of reducing the carbon footprint of the process.

With the scope of lowering or avoiding greenhouse gas emissions, some proposed modifications of the carbothermic process are described in the first part of this chapter. In the second part of the chapter, alternative process concepts are described.

The cost and risks of full-scale testing of modified and alternative processes are typically very high. As such, the path towards industrialization will often start with a combination of thorough mathematical modelling and small-scale experiments. If these are successful, they can be followed up with larger-scale and pilot experiments. The main performance indicators to consider during development of process modifications and alternative processes can be summarized as:

- Specific greenhouse gas (GHG) emissions (CO_2, CO, CH_4, NO_x, etc.)
- Other non-GHG emissions to outer and working environment (dust, SO_x, etc.)
- Economic feasibility
- Silicon yield
- Energy losses
- Flexibility in use of raw materials
- Operational and maintenance costs
- By-product quality and quantity (e.g. silica fume recovered from off-gas, slag)
- Process suitability for energy recovery and carbon capture
- Process adaptability for automation and control

Approaching a carbon neutral process, while continuing to rely on carbothermic reduction, can be done by using biocarbon reductants, as discussed in Chapter 5, and/or carbon capture, as described in Chapter 9.4 (Mathisen *et al.*, 2019; Surup, 2019). In a long-term perspective, there are many reasons to look for other technological solutions (Kero *et al.*, 2022). The presented methods for production of silicon without greenhouse gas emissions cover elimination of direct process emissions (Scope 1) in the reduction step, indirect emissions from electricity production (Scope 2), and transport or other activities/raw materials (Scope 3).

The diversity of silicon alloy products, both with respect to raw materials and reduction processes, must also be considered. The use of aluminothermic reduction may, for example, be a way to recirculate various industrial by-products into silicon alloys (Zhu *et al.*, 2024). There are many environmental aspects to consider beyond greenhouse gas emissions, for example, the generation of new types of wastes and emissions.

9.2 Modified carbothermic process

Closed furnace

Most silicon and ferrosilicon furnaces are open or semi-open, with an influx of air just above the charge level where the combustible gases (mainly CO and SiO) from the process oxidize. This is in contrast to most other ferroalloys produced in SAF, with only 26% of FeMn and none of FeNi production taking place in open/semi-open furnaces (Nelson, 2014).

The main advantages of closed furnaces are:

- Cooler charge top (less vapour/dust losses) and less oxidized materials will improve capture and control of emissions.
- Less dilution of the combustible gases (i.e., CO and H_2), making them suitable for later production of CO as a saleable by-product and for energy recovery and carbon capture.
- Less infiltration of air for combustion and cooling will give a smaller volume of off-gas and thus less amount of gas that needs to be cleaned. There will also be less direct energy losses through off-gas. The downstream off-gas handling systems can hence have a lower capacity.

The possibility of closing FeSi and Si furnaces has been investigated over the years by different companies, using different approaches. However, despite previous attempts at closing silicon furnaces, closed furnaces are not used for silicon production industrially today (Andersen, 2023; Monsen, 2009). Most modern and large furnaces are, however, semi-closed, with ports or doors that can be opened for inspection and stoking.

An obstacle for closing Si furnaces is the need for access to, and visual inspection of, the charge top for stoking, to obtain a sufficient downward flow of the materials and avoid clogging due to SiO condensation. Another obstacle, and the main challenge, is the handling of unburned gas with high amounts of SiO and tar, which might lead to scaling in the off-gas channels. The contamination of the valuable silica fume by-product will also be an issue.

With modern camera technologies, both standard and IR cameras, already installed at several furnaces, visual inspection is possible. The remaining obstacles – contamination of fumed silica and scaling in the off-gas handling system – need further research and development (Li *et al.*, 2024).

Closing of Si-furnaces has been investigated in pilot scale and by industrial campaigns, mainly by Dow Corning and Elkem (Monsen, 2009). It is also reported that a Japanese company operated a commercial furnace for FeSi75 successfully for a long time around 1970, with stoking carried out by 17 stoking machines that were operated through holes in the lid (Schei *et al.*, 1998). Dow Corning ran several pilot campaigns in the period 1987–1991, producing Si in closed furnaces (Dosaj *et al.*, 1991, 1994; Dosaj, 1995), which resulted in a patent (Arvidson *et al.*, 1991). The first experiments were run at 90 kW in a 0.1 MW AC furnace. Further work focused on DC technology, and pilot campaigns were run in a 2 MW DC furnace and then in a 6 MW DC furnace, operated in 12 campaigns for 3–6 weeks at up to 2.5 MW. The furnace was not rotating and was stoked by rods through holes in the lid. Charcoal (30–100%) was used as reductant to reduce the amount of volatiles and tar. The off-gas contained 70–75 vol % CO. The fume was not pure SiO_2 but contained both some Si and 2–14% SiC, with the highest levels with coal and the lowest with charcoal as reductant. There was no blockage of the pipes by silica fume when charcoal was used as reductant, but an incident occurred when a high percentage of coal was in the charge mixture. Dow considered the pilot campaigns to run well. Reported benefits included reduced oxidation of, and loss of, carbon at the charge top and fewer contaminants in the produced Si.

Material flow was one of the main challenges. The main reported challenges that stopped further upscaling and industrialization were downward material flow and energy distribution.

Elkem ran pilot and industrial campaigns from 1973 to around 1978 to produce FeSi in closed furnaces (Arnesen and Bjørdal, 1981; Lundberg, 1978; Schei *et al.*, 1998). Introductory experiments were first run in a 0.5 MW furnace and carried further in a 2 MW furnace. Then FeSi75 was produced in an 8.5 MW furnace at Elkem Bremanger in test campaigns for more than 3 years. Instead of stoking, the charge movement was controlled by the split furnace body, as described in a separate section, where a furnace ring rotated with a speed of 3–5 hours per revolution. The furnace was equipped with a complex system for feeding the raw materials. In the beginning, many practical difficulties resulted in a low operating time. In spite of this, the metallurgical operation was surprisingly easy and the silicon recovery high.

The gas from the furnace had to be cleaned because it contained silica dust, tar, and other unacceptable environmental pollutants. Wet scrubbing is an established technology for removing pollutants from the gas, but cleaning the water is expensive. Therefore, a dry gas-cleaning system was selected and after some development work, it operated satisfactorily. The dust had a volume weight of about one third of the volume weight from open furnaces, and its specific surface was slightly higher than the 20 m^2/g typical for open furnaces. The primary particles were equal to or smaller than those from open furnaces, but in filters and cyclones the dust behaved as if it consisted of larger particles.

An analysis of the dust is shown in Table 9.1 and of the gas in Table 9.2. The main difference is the very high carbon content. In the small-scale experiments, the dust also contained considerable amounts of free Si from the condensation reaction:

$$2\ SiO = SiO_2 + Si \qquad [9.1]$$

However, the dust from the industrial furnace had a very low content of Si. This was most likely caused by oxidation by water from the raw materials:

$$SiO + H_2O = 2\ SiO_2 + H_2 \qquad [9.2]$$

Thus, the chemical energy of the SiO is recovered as chemical energy in the gas, rather than as heat. A few samples were analysed for critical environmental contaminants, and the results showed that the dust contained about 0.4 wt% of PAH (polyaromatic hydrocarbons), as well as small amounts of phenols and cyanides. The gas contained tar, so it was necessary to run the dry filter at a temperature above the dew point of tar to avoid clogging. Such contaminants are destroyed effectively in the flames of open furnaces.

Table 9.1 *Average composition of the filter dust from open and closed furnaces producing FeSi75 (Arnesen, 1981).*

	Analysis wt%			
	SiO_2	**Si (met)**	**C (tot)**	**Ignition loss**
Open furnace	86–90	0	0.8–2.3	2–4
Closed furnace	80.3	0.25	9.3	8.3

Table 9.2 *Average composition of the gas from a closed furnace producing FeSi75 (Arnesen, 1981).*

Volume%								
CO	H_2	CO_2	O_2	N_2	CH_4	C_mH_n	H_2O	H_2S
70	20	3	< −0.5	4	2	0.3	8	0.1

While the closed furnace at Elkem Bremanger was being developed, a market for silica fume from open furnaces was successfully established, and the value of the fume subsequently became important to the overall economy of the process. Since the silica fume from the closed furnace contains too much carbon and toxic substances to be used without expensive treatment, it is uncertain whether the purified dust has the same sales value as dust from open furnaces.

Since small industrial closed furnaces have operated for long periods with fair metallurgical results and acceptable dry cleaning of the gas, there are no indications that operating a large furnace will be impossible. However, compared with an open furnace, the silica fume from the furnace is less valuable,

and the furnace produces more environmental contaminants that must be treated. With the upcoming CCS discussions and upgrading of the off-gas, this process will again be of interest.

Direct current

Direct current does not introduce any principal changes in the mechanism of the process, but it may reduce some costs and open the way to automation of stoking and charging.

Power plants sell alternating current, which needs to be transformed on site to direct current. Rectification has a direct cost and an energy loss, but these costs can be compensated by advantages in the process. The main expected benefits of direct current are:

- Strongly decreased electrode consumption (if the electrode is the negative pole).
- Decreased induction losses to the surroundings give higher thermal efficiency and avoids the need for expensive non-magnetic construction materials in the vicinity of the current conductors.
- The possibility of using a single-electrode furnace with bottom contact can give simpler furnace operation. With alternating current, the induction will be prohibitively large. With single-electrode furnaces, the reactor will be symmetrical, and the stoking and charging operation will be simpler and can be automated. It will be necessary to develop a reliable bottom contact, but it should be possible to solve this problem since the furnaces for high-silicon alloys use conducting carbon as the bottom lining.

Experiments in small direct current furnaces have confirmed reduced electrode consumption (Müller and Magnussen, 1972), but long-term experience is necessary to quantify the gain. The behavior of the furnace is similar for direct and alternating current, and the chemical reactions are essentially the same. However, one can expect a change in the gas flow in the crater (Andresen, 1995; Larsen, 1996). The arc acts as a pump that sets up a circulation of gas in the crater, and the resulting flow may be different if the flow is continuous rather than changing direction many times per second.

The internal heating of the electrodes will be different for direct and alternating current. In a cold electrode, heat production is uniformly distributed over the cross section with direct current, whereas it is highest near the surface with alternating current. This heating raises the temperature, and the direct current electrode will be hotter in the centre, since heat flow towards the surface requires a temperature gradient. Heating of the centre is self-amplifying, since the conductivity of the electrode material increases with temperature and the centre then draws more current. The excess temperature of the centre will be higher with larger electrode diameters. This internal heating may therefore set lower limits for the allowable load of DC electrodes compared with AC, especially for large diameters. If a single-electrode direct current furnace is to have the same productivity as the present three-electrode furnaces with alternating current, the electrode load will be three times as large. The craters around the electrode tip must then treat much more material than the craters in present-day furnaces. The metallurgical effects of such large craters are not known.

In summary, there is some doubt about the behavior of large direct current furnaces. The problems will appear mainly with large electrode diameters, and they cannot be investigated with small-scale experiments. Some understanding can, however, be obtained from mathematical modelling.

Split furnace body

The purpose of the split furnace body is to make the top of the charge sink continuously. This operation is expected to give constant production conditions and savings in investment and labour. The split furnace body changes the furnace process from semi-continuous to continuous.

As described in Chapters 3 and 5, silicon furnaces have cavities around the electrode tips and further up in the charge. The cavities occur because condensate from SiO in the gas glues the charge particles together, forming a bridge in the charge. This bridge is gradually consumed from below during operation, and the cavity expands, while the upper part of the charge stays in place until the bridge becomes thin and breaks down. Normally, it breaks down irregularly, and it is necessary to stoke down remains of the bridge to achieve a uniform distribution of the new charge and avoid bridges of sintered

charge around the electrodes. Before the bridge breaks down, the available free C in the charge materials has been transformed to SiC, and condensation has heated the charge to the condensation temperature. The materials then lose their ability to capture SiO, and the SiO content of the outgoing gas increases. The operator will normally stoke down the charge layer when the SiO loss increases sharply. The stoking can be mild, since the purpose is not to stir the content of the furnace, but only to remove obstructions to an even distribution of the new materials.

This discontinuous operation requires expensive stoking machines, large space around the furnace, and much labour. It leads to periodic variations in the charge content of the furnace, and there will be periods with high silica loss before and during stoking. Compared with standard operation, continuous operation with uniform sinking of the charge is expected to give higher Si recovery and constant conditions, without strong blows on the top of the furnace. The heat strain on the furnace hood and other equipment will be lower.

For a closed furnace, it is particularly important to achieve smooth operation with even sinking of the charge, since access to the surface is difficult. Krogsrud *et al.* worked on the development of an automatic stoking system for a closed furnace, and one of their ideas was to improve the material flow in the furnace through a reconstruction of the furnace (Krogsrud *et al.*, 1978). The upper part of the furnace wall was replaced by a separate rotating part called the *ring*. This ring, which rotated once every few hours, had a lining formed as a regular polygon, preferentially a nonagon. The rotation and the inner form should transfer force to the charge and improve sinking.

Some experience with the split furnace is recorded by Arnesen and Bjørdal (1981) for FeSi75 and by Tveit and Gard (1982) for silicon metal. The ring was operated with one rotation every few hours. The rotation could be in one direction, or with controlled changes in direction. The furnace ran with good results without stoking. On the furnace top, one could see that a thin charge layer close to the lining rotated with the ring, while the inner part of the charge was motionless or lagged behind. This relative movement created shearing forces in the charge, and a shearing circle was visible on the furnace top. The gas from the reactions came up, and the charge sank down smoothly within this circle. Compared with the standard furnace, the charge sank over a much wider area. The operators had to add charge where it was needed on

the top of the charge. The split body furnace needs a better distribution of the charge than the standard furnace, since there is no horizontal movement of the charge after addition. A 30 MW split body furnace was operated for about sixteen years with FeSi75 in Norway, with good operation without stoking.

The split body furnace has been run for years without stoking for FeSi75, and for long periods with silicon metal. This can make the operation continuous, with a strongly reduced tendency to blowing.[1]

Carbon Capture (CC) and Carbon capture and use (CCU)

Carbon Capture

With carbothermic Si production currently being the only commercial technology for Si/FeSi production, Carbon capture and storage (CCS) or CCU is hence a possible carbon abatement strategy for this industry, although a costly one (IPCC, 2022). For silicon production, the low CO_2 concentration in the off-gas is a challenge that both limits the technology available for CC and increases the cost of employing any available technology.

The reason for the low CO_2 content in the gas, as described in previous chapters, is that a large amount of air is introduced to the furnace hood to combust CO and SiO. This limits the temperature from the combustion and ensures strong enough under-pressure to contain the process in the hood. Operation of the baghouse filter capturing the silica fume sets limitations on the temperature of the off-gas (Fereday *et al.*, 2013). Higher furnace off-gas temperatures allow for less process gas dilution, as less ambient air is needed for temperature control, this also leads to higher CO_2 concentration in the off-gas. However, at a certain point, two other factors besides filter operation would start to limit the maximum off-gas temperature from the furnace. One is the need for under-pressure inside the hood to contain the process, which requires some suction of ambient air into the process. The other is the increased potential for scaling in the off-gas system, under the wrong hood conditions, due to the combustion of SiO gas into particulate silica fume (Hauge, 2022; Schei *et al.*, 1998). While the maximum operation temperature often is set by

1 Personal communication from Nygaard in 1998.

the filter bags, the minimum operation temperature is usually given by the acid dew point temperature, which is dependent on sulfur and moisture content in the off-gas (Belo *et al.*, 2014). Condensation of acids, specifically H_2SO_4, causes excessive corrosion issues; the off-gas temperature must therefore be kept sufficiently high. The most common and mature CC approach considered for the silicon industry is the use of chemical solvents such as amines to separate CO_2 from the reduction gas. Amines are water-soluble organic chemicals that contain reactive nitrogen atoms and can rapidly, selectively, and reversibly react with CO_2. For this technology, SO_2 in the flue gas causes free amine loss, which may lead to a rise in CO_2 capture energy consumption. SO_2 in the flue gas has also been shown to result in amine degradation, with heat stable salts produced (Gao *et al.*, 2015). Hence, the silicon furnace off-gas may require pre-capture SO_2 gas cleaning. An industrial pilot of amine-based CC from FeSi production in Mo i Rana, Norway, was carried out during 2022 and 2023 in a collaboration between Elkem and Aker Solutions, claiming above 95% CO_2 capture efficiency.

Carbon Capture and Use (CCU)

There are a number of well-known methods to convert CO_2 into useful industrial chemicals. Examples of these include:

- **Methanol synthesis:** CO_2 can be catalytically converted with hydrogen to produce methanol, which is a basic chemical building block for many other products.
- **Urea production:** This is a well-established process where CO_2 reacts with ammonia to produce urea, a key component in fertilizers.
- **Polymers:** CO_2 can be used in the production of polymers, plastics, and other materials, such as polycarbonates and polyurethane.
- **Synthetic fuels:** Using the Fischer-Tropsch process, captured CO_2 can be converted into synthetic fuels and other valuable products, such as building materials.
- **Other chemicals:** CO_2 can also be used to produce formic acid and synthesis gas.

While CO_2 separated from an industrial off-gas has different industrial applications, one innovative *direct* use of the FeSi furnace off-gas at the Norwegian Finnfjord plant is cultivation of photoautotrophic microalgae (diatoms) by utilizing the CO_2 in the gas as a carbon source in the photosynthetic production process. Additionally, the NO_x in the gas may be used by the diatoms as an inorganic nitrogen source. The diatom species is adapted to low temperatures and irradiance levels found in northern Scandinavia. Further, the cultivated species handle low pH levels, which is necessary since addition of Si production fumes with high (7–8%) CO_2 content lowers the pH in the photobioreactors.

Flue-gas recycling (FGR) for CCS or CCU

As an alternative to a closed furnace, and with a purpose of increasing the CO_2 content of the off-gas (allowing for a more cost-effective carbon capture), Andersen and co-workers did extensive modelling and pilot studies on flue gas recirculation (FGR) for MG–Si production (Andersen *et al.*, 2023b, 2023a, 2021). The basic principle of FGR is to replace some of the ambient air added to the process with cooled and cleaned recirculated flue gas, to avoid dilution of the CO_2 in the off-gas with additional air. FGR is also a known method for NO_X reduction in combustion processes (Qian *et al.*, 2013), a potential added bonus for the Si process (Houshfar *et al.*, 2012; Sidorkin *et al.*, 2016).

Andersen *et al.* (2021) developed a mass- and energy balance, based on available literature, for a 100 MW silicon operation with a flue gas de-sulfurization (FGD) unit and a conventional chemical absorption carbon capture plant. Results illustrate the change in off-gas compositions (Figure 9.2). With five different scenarios for extent of flue gas recycling, economic modelling illustrated potentially large savings by the introduction of FGR, given other factors such as charge composition, yield etc. being constant (Figure 9.3).

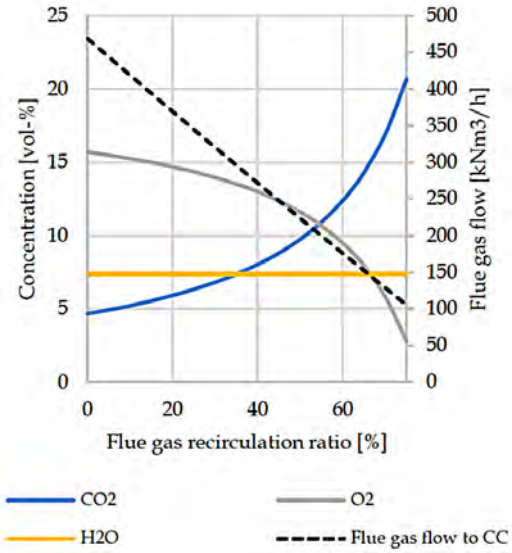


Figure 9.2 *HSC chemistry simulations of off-gas composition and flow to the carbon capture unit with different degrees of FGR (Andersen et al., 2021).*

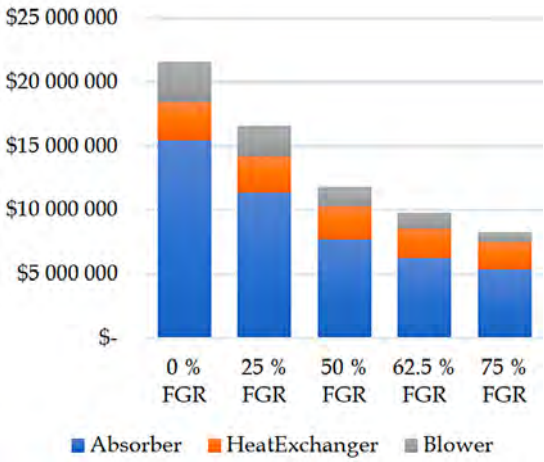


Figure 9.3 *Calculated cost for implementation of carbon capture for a 100 MW Si operation with different degrees of off-gas recirculation including absorbers, heat exchangers and blowers (Andersen et al., 2021).*

In their FGR piloting work, Andersen *et al.* used a rebuilt off-gas system on a 150 kW single electrode SAF, fitted with extensive measurements of gas composition of in-going and out-going gas to/from the furnace, as well as sampling of silica fume (Andersen *et al.*, 2023b). The composition of raw material used in the campaign is listed in Table 9.3.

Table 9.3 *Details of the raw material mix used for the pilot scale experiment (Andersen et al., 2023b).*

		Coal	Charcoal	Coke	Woodchips
Share of C-coverage	% of FixC	40	15	30	15
Compound					
Moisture	%	10.8	4.7	11.7	4.8
FixC	% DW	57.6	79	90.5	14.6
Volatiles	% DW	40.4	17.7	6.64	84.2
Ash	% DW	2.04	3.32	2.84	1.16
Elements					
Carbon	% DW	78	83	89.3	50.7
Nitrogen	% DW	1.58	0.39	1.78	0.2
Oxygen	% DW	12	9.6	3.83	41.4
Hydrogen	% DW	5.79	3.71	1.83	6.48
Sulfur	% DW	0.52	<0.1	0.42	0.11

Results obtained from the campaigns show that it is possible to reach above 20 vol% CO_2 in the off-gas by controlling the gas flow and the degree of gas recirculation (Figure 9.4). The measurements are well aligned with the modelled/calculated CO_2 contents. Figure 9.5 illustrates that, while the NO_x concentration in the off-gas increases with a higher degree of FGR, the total amount of NO_x generated is lower with FGR and also lower than the modelled content. While there was a concern that the quality of the silica fume product, as measured by its specific surface area (SSA), would be adversely affected by the lower oxygen content in the off-gas, it appeared that SSA was not significantly lowered through either lower gas flow or higher FGR (Andersen *et al.*, 2023).

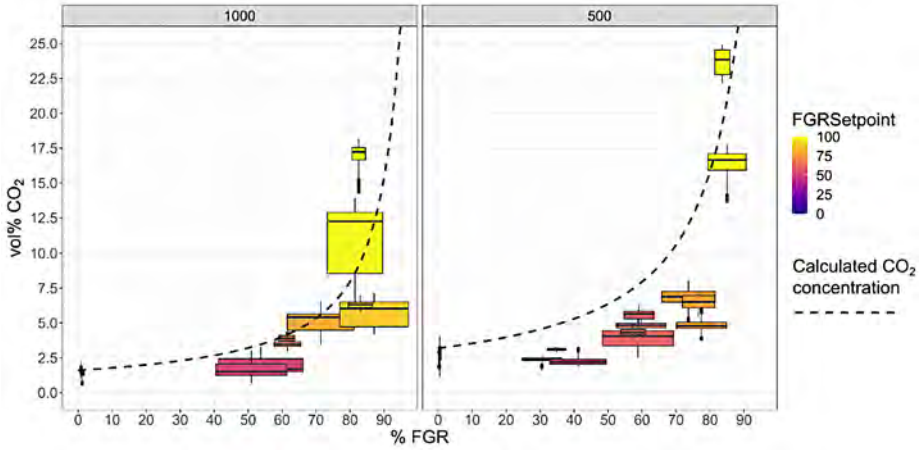


Figure 9.4 *CO_2 content in the off-gas measured and modelled for different FGR settings at total gas flows of 1000 Nm³/h and 500 Nm³/h respectively (Andersen, 2023).*

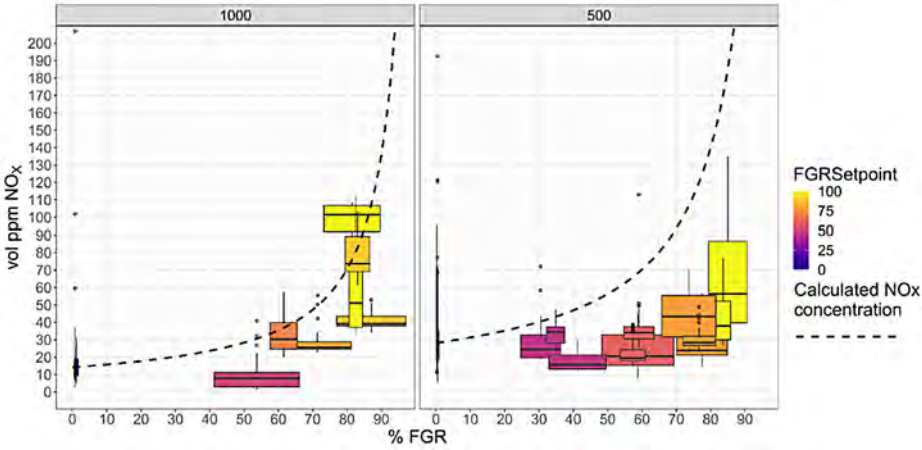


Figure 9.5 *NO_x content in the off-gas measured and modelled for different FGR settings at total gas flows of 1000 Nm³/h and 500 Nm³/h respectively (Andersen, 2023).*

Composite agglomerates

With composite agglomerates, the reaction scheme changes thoroughly, and the materials in the outer reaction zone increase their ability to recover SiO. In this section, the idea will be described first, then the available practical experience will be summarized, and the possibilities will be discussed.

The principle

In the standard process, SiO from the inner zone is recovered from the gas leaving through the outer zone, mainly by reaction with free C. When the raw materials SiO_2 and C are added as lumps, the direct reaction between them in the outer zone is so slow that it can be disregarded. If the materials are powdered and mixed, the reaction will be much faster. For use in a furnace, the mixed materials must be agglomerated to make the charge sufficiently porous to let the process gas out. Hot SiO-rich gas from the inner zone passes through the charge mix in the outer zone. Then the gas is cooled, and the strongly heat-producing condensation reaction:

$$2\ SiO(g) = SiO_2(s,l) + Si(l) \qquad [9.3]$$

will run. As explained in Chapter 2, this reaction is the main condensation reaction in a submerged arc furnace. The SiO pressure of this reaction is very low at, say, 1300°C, and the SiO content of the gas leaving the furnace may be low. However, the produced heat will raise the temperature of the charge to the condensation temperature, and then the SiO will be lost from the furnace. If the strongly heat-consuming reaction:

$$SiO_2(s,l) + 3\ C(s) = SiC(s) + 2\ CO(g) \qquad [9.4]$$

runs in the outer zone, it will consume the heat, and the temperature cannot rise at equilibrium above the co-existence point 1512°C for SiO_2–C-SiC. Therefore, when SiO-containing gas is conducted through a charge originally consisting of SiO_2 and C, the lowest layer will reach a temperature of 1512°C if the reactions are fast. The gas leaving this layer will contain about 4 per cent SiO, according to Figure 2.9 under equilibrium conditions. This gas will pass through the cool charge above, and SiO will condense to an extremely

low content. Stoichiometry of a reaction based on recovery of SiO by the condensation Reaction [9.3] is shown in Figure 9.6. The inner zone reaction corresponds to equilibrium between SiO_2, SiC and Si.

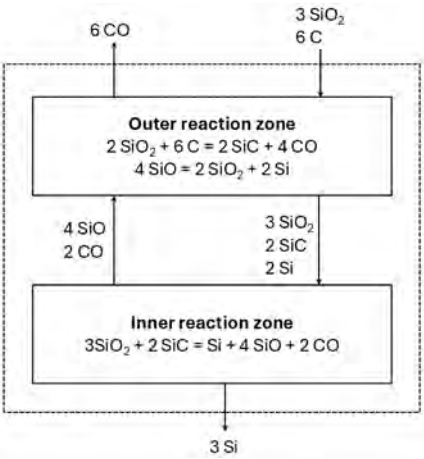


Figure 9.6 *Stoichiometry of a reaction based on recovery of SiO by the condensation Reaction [9.3]. The inner zone reaction corresponds to equilibrium between SiO_2, SiC and Si.*

The reaction in the inner zone is characterized in Chapter 3 by the content *s* of SiO in the gas leaving the zone.

$$s = \frac{p_{SiO}}{p_{SiO} + p_{CO}} \qquad [9.5]$$

The value $s = 0.67$ corresponds to equilibrium in the inner reaction zone. The discussion in Chapter 3 showed that the Si recovery will be only 33 per cent when SiO is recovered by reaction with C. A 100 per cent Si recovery requires a reduction of *s* to 0.50, and to ≈ 0.54 if condensation is allowed to heat the charge to reaction temperature. In Figure 9.6, the process is balanced stoichiometrically with rapid reaction between SiO_2 and C in the outer zone. The crucial point is now whether the charge in the outer zone can accept all the heat that this condensation produces. The heat balance for the outer reaction zone is calculated in Table 9.4. It is assumed that the reactions run at

a temperature slightly above equilibrium, that is, at 1800 K for the SiC-forming reaction and at 2100 K for the Si-forming reaction. The result shows a small net heat consumption in the outer zone. Therefore, the furnace top will be cool and the SiO loss low if the reaction between SiO_2 and C is fast.

Table 9.4 *Heat balance for the outer reaction zone of Figure 9.6 (Chase et al., 1985).*

Reaction	Heat consumption kJ
2 SiO_2 + 6 C = 2 SiC + 4 CO at 1800 K	1163.34
4 SiO = 2 SiO_2 + 2 Si at 1800 K	−1227.62
Heating of [3 SiO_2 + 6 C] from 298 to 1800 K	520.44
Cooling of [2 CO + 4 SiO] from 2100 to 298 K	−376.40
Sum	79.76

A gas containing 6 moles of CO and 4 per cent of SiO leaves the 1512°C zone at the bottom of the outer zone if the reaction between SiO_2 and C is infinitely fast. According to Figure 2.10, the equilibrium gas contains about 4 per cent of silicon. The 6 moles of CO in Figure 9.6 will contain $6 \cdot 4/96 = 0.25$ moles of SiO, which will give off about $1227.62/4 \cdot 0.25 \approx 77$ kJ when it condenses. This amount is low compared with the heat necessary to raise the temperature of the charge, and the SiO will condense in the upper layers of the outer zone. The heat is already included in the balance of Table 9.4. The charge can thus capture all the SiO given off from the equilibrium inner zone if the reactions proceed close to equilibrium. Although the accuracy of the assumptions and data behind this calculation are limited, the calculation demonstrates that the direct SiC-forming reaction is potentially more efficient than the reaction with C in capturing the SiO in the outer zone. The effect of agglomerated charge is also demonstrated in Example 4 in the Process model section in chapter 5.

However, the efficiency of the process is based on the assumption of rapid reaction. The condensation reaction is rapid if it can get rid of the heat, but the reaction between SiO_2 and C may be slow and the rate depends upon several factors, such as the reactivity and the particle size of the materials. The temperature will be higher than the value of the coexistence point for SiO_2–C–SiC, and the reaction between SiO_2 and C may therefore be incomplete. As a result,

the gas leaving the furnace will contain more SiO than expected from complete reaction. The situation is complex, and the reaction rates are known only qualitatively. In addition, in the industrial situation the raw materials are not pure elements, but natural raw materials with impurities. The conclusion of the examination is therefore only that rapid direct reaction in the outer zone may give a very high silicon recovery if the reaction between SiO_2 and C is rapid. It has been shown that composite reactions of quartz and charcoal are very fast and should hence be an asset in the silicon furnace (Straum *et al.*, 2026).

The kinetics of the reaction between SiO_2 and C are discussed in Chapter 2. The reaction is slow between lump materials, but faster when the materials are crushed finely and mixed. A practical application of the idea will thus include crushing or milling, mixing, and agglomeration. The overall reaction will then change, depositing large amounts of condensate in the upper layers of the charge, and it is expected that stoking the furnace will be more difficult. The furnace behavior using agglomerated materials has to be tested experimentally.

Pilot and industrial testing

The composite concept has been demonstrated in a 50 kW single electrode furnace with bottom contact (unpublished Elkem work). The raw materials quartz sand, carbon black, and ground petroleum coke were pelletised with sugar as a binder and dried. Three raw material combinations were tested as indicated in Table 9.5. The furnace was operated with visual observation into the crater. A fairly stable arc burned against a silicon bath. A viscous material moved slowly downwards from the roof and floated around on the silicon bath, where it was consumed while it sweated out silicon. The operation was fairly smooth for all charge combinations, and when the runs stopped after 1 to 2 days, the furnace was in a good state for further operation. The stoking was apparently no more difficult than for lump charges. A SiC bottom deposit began to build up at the start, but it could be removed by a period with carbon deficit. It seems that it is necessary to use a lower carbon content than for lump charge during the period where steady state conditions are established in the furnace. Later in the test, the furnace recovered easily from periods with excess of carbon when the charge was corrected. An initial increase in the SiC deposit was detected early by the visual observation, and the charge composition was corrected.

Table 9.5 *Results of reduction tests with composite pellets [SiO_2 + ≈2 C] in a 50 kW single electrode submerged arc furnace (unpublished Elkem work). Each energy consumption is a mean of more than one run.*

Raw materials	Energy consumption MWh/tonne	Comments
Ground quartz sand Carbon black[1)]	16	Smooth operation. Very low silica loss as smoke.
Ground quartz sand Ground petroleum coke	20	Smooth operation. Some silica loss as smoke.
Quartz sand Ground petroleum coke	24	Smooth operation. Considerable silica loss as smoke.

[1)] **Carbon black made by thermal decomposition of hydrocarbon gas, specific surface 7 m^2/g.**

The small furnace has a much higher heat loss than a production furnace, and the energy consumption is therefore always high. The 16 MWh/tonne consumption corresponds to a high silicon recovery, most likely more than 90 per cent (the material balance is not reliable for short tests). Petroleum coke is normally expected to give very poor operation when it is used as the only reductant. The fairly good result with this material therefore shows that the nature of the process has been changed. The results of Table 9.5 also indicate that finely ground materials are necessary to achieve sufficient Si recovery, at least on the small scale. The need to grind the quartz may be a serious difficulty because of the health hazard connected to quartz dust. It will be very difficult to avoid some dust during operation with agglomerates, especially if the agglomerates are dried.

The agglomerated charge has also been tested in industrial furnaces. An addition of a fraction of the charge as high-carbon briquettes [SiO_2 + ≈6 C] has improved the silicon recovery (Lask and Ruuth, 1989). Short-term runs with agglomerates [SiO_2 + ≈2 C] as the main raw material source have indicated that the process may run, but there are difficulties (unpublished Elkem work). The raw materials petroleum coke and silica sand were pelletized with sugar as a binder and dried. Even though the pellets became fairly strong, some were crushed during transport and weighing, and the dry materials produced dust. The pellets were charged to a furnace that operated fairly well on standard charge. They sank so easily that it was impossible to get a stable lid above the inner zone,

and the furnace was blowing almost constantly. The operators tried to stop the blowing by adding more charge, and as a result, the furnace was gradually filled with charge that had reacted incompletely. Almost no silicon was tapped. After a few hours, the operation was changed to standard charge, and the furnace recovered easily. In the next test, the pellets were mixed with some wood chips to impede the sinking. Then a stable lid formed above the reaction zone, and operation was possible. However, the inner zone of the furnace became very hot, and the reaction sometimes became violent during stoking or when the lid collapsed. The flames damaged the electric equipment under the hood and, in extreme cases, charge materials were thrown out of the furnace. Pure charcoal agglomerates were tested at one of the industrial FeSi furnaces at OFZ, and it was seen that the operation did not change dramatically compared to lumpy raw materials (Gryshan *et al.*, 2026). This has also been seen in other industrial SAF processes like FeCr[2], and hence the use of briquettes is a matter of quality.

Discussion

The production of agglomerates will have a cost that is permanently added to the raw material cost if the process is changed to composite agglomerates. Earlier, when the silicon recovery was often below 80 per cent, the potential for improved recovery could justify a change of process. Presently, however, the silicon recovery of well-run furnaces is about 90 per cent for silicon metal and higher for ferrosilicon, and the value of the recovery increase cannot pay the cost of ordinary agglomeration. Other advantages are therefore necessary to justify an agglomerated charge. Such advantages may be the availability of cheap waste material or the possibility of a smooth operation that is easy to control. In the future, the need for sufficiently pure raw materials may require an upgrading that gives powdery materials, and then agglomeration is necessary.

The experience in the 50 kW furnace indicates that the chemistry of the process works. However, the introductory tests on an industrial scale can give some challenges. Some of the problems could probably have been solved with more test work. In the runs with pellets [SiO_2 + ≈2 C] no stable roof on the inner zone was formed. The reason may be that the carbon content was too high in the starting period. The beginning reaction in the inner zone:

2 Presented by Ludvig Ånnhagen from Vargön Alloys at Pyro 26–28 May 2026, South Africa.

$$3\ SiO_2 + 6\ C = 2\ SiC + SiO_2 + 4\ CO \qquad [9.6]$$

gave a gas with a low SiO content, and the condensate formed in the upper layers was not enough to glue the pellets together and give a stable roof in the large furnace. After this, more pellets fell down, reacted, and consumed heat. Therefore, the temperature never became high enough for an extensive reaction in the next step:

$$2\ SiO_2 + SiC = 3\ SiO + CO \qquad [9.7]$$

With a larger excess of SiO_2 at the beginning of the pellet charging, the gas would contain more SiO, and a stable roof may have been formed with normal operation.

A main problem in the introductory large-scale tests was the violent reaction during stoking or spontaneous charge collapse. A tentative explanation for this behavior is suggested here. The temperature in the inner zone is determined by the balance between heat production and heat consumption. With low availability of silica, the energy consumption of the reaction will be low and the temperature will rise. The silica-containing agglomerate will need a higher temperature to become sufficiently fluid to sink down than would be the case with silica lumps in the standard charge. With agglomerated charge, the inner zone will have a higher temperature and more accumulated heat. When fresh materials enter the inner zone, the reaction may therefore be violent. It is hence important to have a controlled movement of the charge.

The split furnace body described earlier may be a means to obtain this control of charge movement. It induces the charge to sink smoothly, and the new agglomerates can be distributed continuously on the top of the charge. Then wet agglomerates can possibly be added without drying. The agglomeration can be put in as an operation in the transport chain to the furnace, and the weighing of the charge can be done on the powder side of the agglomeration. This set-up may reduce the cost of agglomeration significantly, and at the same time give a smooth operation.

The SiO loss will depend on the condensation temperature, as can be seen from Figure 2.10. The condensation is heat-producing, and the resulting temperature is determined by the temperature of the heat sink. The heat sink is the heat-consuming reaction:

$$SiO_2 + 3\ C = SiC + 2\ CO \qquad [9.8]$$

which, according to the equilibrium in Figure 2.10, can run at temperatures above the coexistence point for SiO_2–C–SiC at 1512°C. It is important to have a high reactivity of the materials, since high reactivity will make the reaction run at a temperature closer to the coexistence point, and therefore give a lower temperature and, consequently, a low SiO content. The results from the 50 kW furnace indicate that fine crushing of the quartz is necessary. The relation between agglomerate properties and reactivity has to be studied experimentally. Full-scale experiments will be very expensive, but the cost may be reduced by a pre-study that elucidates the situation by means of laboratory experiments, small-scale physical simulation and mathematical modelling.

In the discussion of the split charge, it was shown that the carbon charge would be hot at the top and therefore have a heat loss. This loss can be reduced by the addition of a suitable amount of compound agglomerate.

Blast furnace

While production of MG–Si in a blast furnace would be challenging, FeSi alloys have been produced industrially. One example is from the Chelyabinsk plant in west-central Russia, producing FeSi alloys containing up to 12.3% Si from limonite, siderite ores and quartzite (Lukin *et al.*, 1963). The production was carried out periodically, switching between iron and FeSi, with a coke consumption between 1.0–1.5 tonnes/tonne. The furnace was operated with a pre-heated (up towards 1000°C), oxygen-enriched air blast to increase the temperature and hence facilitate enhanced SiO_2 reduction. The periods of FeSi smelting lasted between 50–55 days, after which problems with tuyer burn-out were experienced due to clogging of the furnace hearth.

Plasma reactor

The submerged arc furnace can be characterized as a plasma furnace, since most of the heat is produced in an arc that is a plasma if we define a plasma as a gas with an ionization high enough to make it electrically conductive. However, in arc furnace technology the term plasma has commonly been reserved for arcs that are stabilized by an externally controlled gas jet.

A simple plasma furnace is obtained if a hole is drilled along the centre line of the carbon electrode and a gas is blown through the hole. The resulting gas jet tends to keep the arc in a stable position, as an elongation of the centre line of the electrode. This electrode will be consumed, like an ordinary carbon electrode. The most common plasma burners, however, have non-consumable electrodes made of temperature-resistant metals such as tungsten. A principle of a plasma burner installed in a silicon reactor is indicated in Figure 9.7. It consists of two non-consumable electrodes with a gas flow between them. Such a burner can run in two modes. In the *non-transferred arc mode,* the arc burns between the two electrodes, and the heat produced is transported away with the gas. In the *transferred arc mode,* the arc burns between the main electrode in the burner and the outside conductor. The heat is then produced in the cavity of the furnace. The silicon process has a very high consumption of electric energy, and it would need very large amounts of gas to transport all this energy as heat in a gas. Therefore, it is expected that the burner must work in the transferred arc mode in a silicon reactor.

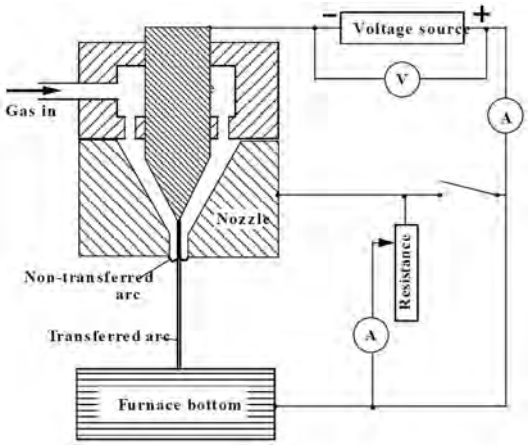


Figure 9.7 *Principles of a plasma burner in a silicon reactor. The operation starts with a non-transferred arc between the cathode and the nozzle, and after a short heating period the switch is broken and the main current goes through a non-transferred arc in the crater arc. A small arc between the nozzle and the cathode may be maintained to stabilise the arc.*

An alternative to the plasma burner is *inductive plasma heating*. The gas is then kept in the plasma state by induction, and the reactants can be added to the plasma.

The main expected advantages of a plasma reactor in the silicon reactor are:

1. The heat production is independent of the resistivity of the charge.
2. The electrode costs are reduced strongly.
3. The reaction volume will be smaller.
4. The process can use powder raw materials without agglomeration.
5. When Si condenses out of a very high temperature plasma, it may be separated from impurities that would stay in the product in the standard process.

The literature contains some references to plasma processes for silicon, and a few central contributions will be reviewed here. Dosaj and Rauchholz proposed a plasma reactor for the production of silicon (Dosaj and Rauchholz, 1987). They stressed that the burner should be the transferred arc type because it uses much less gas than the non-transferred arc burner. They gave few details of the reactor design, temperatures, and chemical reactions in the plasma reactor. Santén and Edström, and Eriksson and Santén, proposed a plasma furnace where the shaft was filled with carbon lumps while SiO_2 powder was blown into the reactor at the bottom (Eriksson and Santén, 1985; Santén and Edström, 1984). Some carbon powder could be mixed with the SiO_2 powder. A main advantage of the process is that it can use powdered SiO_2.

In the applications above, it seems that the plasma burner essentially replaces the carbon electrode as a heat source in a process where the main reactions appear to run at a temperature around 2000°C, as in the submerged arc furnace. In the thermodynamic discussion of the process, it has been shown in Chapter 2 that the SiO content of the gas from the final reaction between SiO_2 and SiC is high. Therefore, the standard process has to be run as a two-step process, in which SiO from the SiO_2–SiC reaction is captured in counter-current with the charge going in. However, if the process is run at a much higher temperature, the SiO content of the gas decreases, and a one-step process may be possible. Coldwell carried out an equilibrium calculation for the temperature range 500–6000 K (Coldwell, 1976). He considered only the

three base elements Si, C, O and the compounds SiO, SiO_2, SiC, CO, CO_2 and O_2, and concluded that Si would be formed at a temperature above a threshold value of about 2225°C. A computer simulation of the condensation as a function of the quench rate indicated that there exists a maximum in the amount of silicon produced (Coldwell, 1977). Coldwell and Roques tested the idea experimentally (Coldwell and Roques, 1977). The reactants SiO_2 and C were introduced into a radio frequency induction plasma where they reacted and vaporized. The product collected in a cooled tube was amorphous. It consisted of 25 to 250 μm globules that had to be sintered to give reproducible analyses. The yield was less than 15 per cent of the theoretical. The authors concluded that a high yield is unlikely by quenching of an Si-rich gas.

Hutchison *et al.* extended the equilibrium calculation by including all the chemical species and discussed the result when Si was allowed to condense from the gas by cooling (Chase *et al.*, 1985; Hutchison *et al.*, 1988). In the range of reactant mixture [SiO_2 + 1.1 C] to [SiO_2 + 2.35 C], the first condensed material to precipitate from the gas is Si(l), and then, at a lower temperature, SiC. With further cooling, all the Si(l) is transformed to SiC. Hutchison *et al.* assume that the molten silicon must be separated from the system at a suitable temperature. The best yield is found for a charge of composition [SiO_2 + 1.75 C], where the Si precipitation starts at 2807°C and the SiC precipitation at 2540°C. The maximum amount of silicon can be taken out just above the precipitation temperature of SiC. The amount of Si(l) is then 57 per cent of the total amount of silicon in the system. Therefore, the optimum condensation temperature is thought to be 2540°C.

According to the description of the Si–C system in Chapter 2, the Si that condenses from the C-containing gas at a high temperature will contain a lot of C in solution. At the optimum condensation temperature, the silicon is saturated with SiC, and the solubility of C can then be estimated from the phase diagram (Chapter 2) to be of the order of magnitude 20 at%. This C content corresponds to an alloy [4 Si + C], which after cooling will give 3 Si and SiC, or more than 30 per cent by weight of SiC in the silicon. The result is uncertain because the measurements behind the phase diagram scatter strongly. Hutchison *et al.* (1988) did not discuss the solubility of C in molten Si, and it is not clear how it is included in the calculation.

The advantages of plasma application have not been demonstrated. The most promising idea in the short run is to develop an inert electrode. Since the arc most likely must operate in the transferred mode and produce

the heat in the gas of the reactor, the resistance will depend on the properties of the charge. The operation problems will therefore be similar to the problems of the submerged arc furnace. This application is more a question of furnace design than of metallurgy.

The use of plasma technology is one of the processes where one can theoretically use H_2 as a reductant and thus cut the CO_2 emissions. This is further discussed in sub-chapter about hydrogen plasma.

Non-atmospheric pressure

Normally one assumes that the furnace will run at atmospheric pressure. Operation at non-atmospheric pressures causes obvious difficulties. The charging and the tapping must occur through a lock gate system, and the electrode connection must be airtight. The stoking must be carried out by machines without any visual observation of the furnace top. However, modern blast furnaces are run at a pressure of a few bar. Therefore, the problems with feeding or tapping through a non-atmospheric pressure lock gate can be solved. The carbon electrodes are penetrable for gas, but possibly the entire electrode system can be placed within the non-atmospheric hood, with immovable conductors through the shell. We conclude that non-atmospheric operation is not impossible, and it is justified to discuss the potential even if a process is not obviously attractive. The possibility has been discussed in the literature (Downing, 1965).

The influence on the equilibrium of a lower ambient pressure can be seen from Figure 2.7. The reaction temperature becomes lower, and the ratio p_{SiO}/p_{CO} increases. Silicon production has a lower recovery the higher this ratio is. For a limiting pressure ratio of 3, the silicon recovery is zero, which corresponds to the inner zone reaction:

$$2\ SiO_2(s,l) + SiC(s) = 3\ SiO(g) + CO(g) \qquad [9.9]$$

The temperature and pressure of this limiting reaction can be read approximately from Figure 2.7. The pressures p_{SiO} and p_{CO} are related by the stoichiometry:

$$\ln p_{CO} = \ln p_{SiO} - \ln 3 \qquad [9.10]$$

A graph is drawn parallel to p_{SiO}, at a vertical distance ln 3 below it. This graph crosses the p_{CO} graph at about 1740°C, with $p_{CO} \approx 0.12$ bar and $p_{SiO} \approx 0.36$ bar. At a lower pressure, it is impossible to establish equilibrium SiO_2–SiC–Si from a reaction between SiO_2 and SiC. Therefore, production of Si is impossible in an *isothermal* reaction at a pressure below about 0.5 bar. However, SiO_2 and SiC can react in vacuum and give a SiO-containing gas that produces Si by condensing to [SiO_2 + Si] at lower temperatures.

The equilibrium in Figure 2.8 shows how the equilibrium pressure of the coexistence point for SiO_2–SiC–Si varies with temperature. With increasing temperature, the total pressure of the reaction increases, while the molar fraction of SiO decreases. According to the discussion in Chapter 3, the amount of SiO to recover becomes less when this molar fraction decreases. Figure 3.12 indicates that the reaction with C can capture all the SiO if the gas of the inner zone contains less than 50 per cent of SiO. From Figure 2.8 we can read that this gas content corresponds to a temperature of about 1980°C and a total pressure of about 6 bar. Therefore, the inner zone reaction that gave only 33 per cent Si recovery at 1 bar can give 100 per cent recovery if the pressure is increased to 6 bar.

However, this favorable result seems to be related to temperature and not to pressure. The SiO content of the inner zone gas can be calculated from the reaction:

$$SiO(g) + SiC(s) = 2\ Si(l) + CO(g) \qquad [9.11]$$

The law of mass action gives:

$$\frac{p_{CO}}{p_{SiO}} = K_{9.11} \qquad [9.12]$$

An equilibrium constant K varies with temperature and not with pressure. This means that the equilibrium SiO content of the inner zone will be determined exclusively by temperature. The real process does not run at equilibrium, and observations indicate that the inner zone temperature is about 2000°C. The equilibrium benefit for a pressure of about 6 bar is therefore already used up, and the resulting operation is determined by the kinetics. By application

of the split charge method, it is possible to reach even higher temperatures for the Si-producing step.

The flow of charge into the inner zone is important for the reaction, and this flow increases as the viscosity of the molten SiO_2 in the charge decreases. The viscosity decreases when the temperature increases, therefore, we can expect the flow to increase. The coexistence points for SiO_2–C–SiC and SiO_2–SiC–Si move to higher temperatures when the pressure increases. Therefore, both the minimum temperature for reaction in the inner zone and the condensation temperature will be higher. The SiO_2 in the charge will become less viscous, and the flow into the inner zone will increase. This resulting flow of SiO_2 and other materials into the inner zone may require more energy for reaction than is added, and thus give melting of the charge and not reduction. This is the behavior that metallurgists describe as 'melting before smelting'.

Low pressure operation is a disadvantage for the submerged arc process for silicon, and silicon production is impossible by an isothermal reaction for pressures below about 0.5 bar. Low pressure can, however, be used for production of SiO that is later cooled and condensed to [SiO_2 + Si].

High pressure increases the temperature of the equilibrium reduction of SiO_2, and the increased temperature gives a more favorable equilibrium ratio p_{SiO}/p_{CO}. However, the same temperature obtained by other means will give the same ratio. The influence of high pressure upon the operation is not clear, but consideration of the material flow indicates that it may lead to incomplete reduction of the SiO_2 in the inner reaction zone. The situation is complex, and an overall advantage of increased pressure cannot be ruled out without experiments. The understanding of the flow processes, including the material properties, is not sufficient for reliable mathematical modelling, and experimental testing in a physical model of a submerged arc furnace is necessary.

9.3 Non-carbothermic processes and reductants

To avoid CO_2 emissions, other reductants not containing carbon must be found, or carbon must be reused in the process. Materials that have a thermodynamic potential to reduce SiO_2 to Si can be identified by an Ellingham diagram, as shown in Figure 9.8, which shows a selection of relevant reac-

tions for oxide reduction into metals. The difference in Gibbs free energy (on the y-axis) is the driving force for the reactions to go forward. From this diagram, elements like Ca, Al, Mg and Ba are strong reductants for most oxides and can be used to reduce quartz (SiO_2).

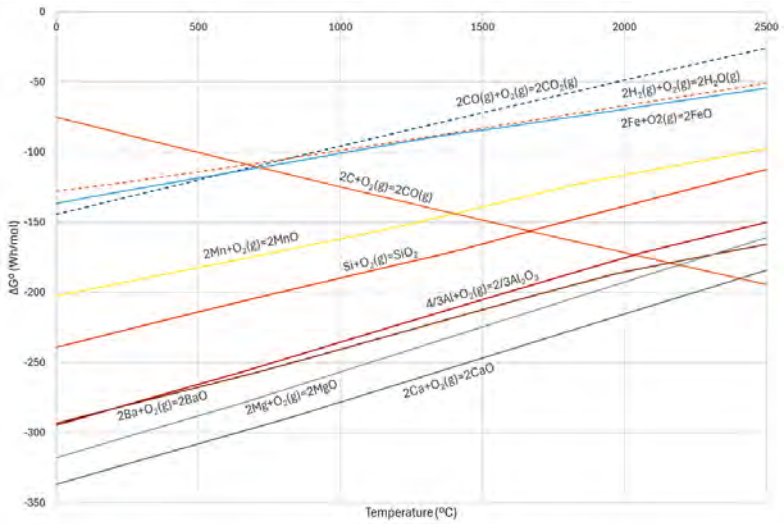


Figure 9.8 *Ellingham diagram for oxides (Calculated in HSC v.9).*

Reduction with gases is another alternative to reduction with solid carbon. Possible gaseous reductants include hydrogen (H_2) or methane (CH_4) and, in addition, processes involving these, such as hydrogen plasma or use of carbon from methane decomposition. Equilibrium considerations show that they have a lower thermodynamic potential than solid carbon. However, new gas-based processes may offer good alternatives to the gradually scarcer resources of suitable types of coal and give a potential for CO_2-lean production of silicon. To contribute to decarbonization of silicon production, the gaseous reductants must be produced from renewable sources. Hydrogen produced by traditional methods from coal or natural gas is energy-demanding and CO_2-emitting. Instead, so-called 'green' H_2 produced from water electrolysis using renewable electricity and so-called 'blue' H_2 produced from natural gas with carbon capture and storage (CCS) are alternative gas sources. Methane must be produced from biological sources, so-called bio-methane.

Hydrogen

Equilibrium discussion

We assume that we can establish equilibrium in the Si–O–H system without any speculation about how the reaction must be carried out in a process. The calculations will be based on a certain assumed reaction mechanism, but it is not necessary that this mechanism really occurs, since all consistent mechanisms for the same overall reaction will give the same result in equilibrium calculations. The mechanism used consists of several chemical reactions with equilibrium constants (Chase *et al.*, 1985).

The SiO_2–H_2 system has three components, and the phase rule then states:

$$Ph + F = 3 + 2 = 5 \qquad [9.13]$$

The important species in the system are SiO_2(s,l), Si(l), SiO(g), H_2(g), H_2O(g) and H(g). Other species, such as O_2(g), O(g), Si(g) and gaseous compounds (Si–O_x–Hy), are disregarded. Compared with carbon reduction, there is one important difference: carbon has the solid compound SiC with silicon, while hydrogen has only gaseous compounds, and they are not present in significant amounts at the temperatures of interest. In an isothermal production process, both the raw material SiO_2 and the product Si must be present as condensed phases in the hot main reaction zone, together with a gas phase. Therefore, the system has two degrees of freedom, and we must specify two properties to determine its state completely. We choose temperature and total pressure, and this enables the composition of the gas to be calculated.

When SiO_2(s,l) and Si(l) coexist with a gas phase, there will always be some SiO(g) present:

$$SiO_2(s,l) + Si(l) = 2\ SiO(g) \qquad [9.14]$$

Free silicon can be made by the reduction of SiO(g) by H2:

$$SiO(g) + H_2(g) = Si(l) + H_2O(g) \qquad [9.15]$$

At high temperatures, the H_2 molecules may dissociate:

$$H_2(g) = 2\ H(g) \qquad [9.16]$$

There are no inert gases present, and the other gas species in the system occur at such low partial pressures that they can be ignored in the calculation of the total pressure *P*. Therefore,

$$p_{SiO} + p_{H2} + p_{H2O} + p_H = P \qquad [9.17]$$

The SiO pressure is determined by Reaction [9.14]. The relation between p_{H2} and p_{H2O} is given by Reaction [9.15], and the relation between p_{H2} and p_H by Reaction [9.16]. By combining these, the partial pressure of H_2 can be found from the total pressure and the equilibrium constants for the reactions. Once the partial pressure of H_2 is known, the partial pressures of SiO, H_2O and H can be calculated from the equilibrium constants of Reactions [9.14], [9.15] and [9.16]. The overall equilibrium reaction can be written as

$$x\ SiO_2(s,l) + y\ H_2(g) = \quad z\ Si(l) + a\ SiO(g) + b\ H_2O(g) + c\ H(g) + d\ H_2(g) \qquad [9.18]$$

We consider that the reaction produces the equilibrium mixture for a total of *P* moles in the gas mixture. The partial pressures can then be interpreted as the number of moles of each species in the reaction, and the coefficients *a*, *b*, *c* and *d* of Equation [9.18] are known from the equilibrium calculation. The unknowns *x*, *y* and *z* represent the consumption of raw materials and the production of silicon. The element balance gives:

O: $\quad 2x = a + b$

H: $\quad 2y = 2b + c + d$

Si: $\quad x = z + a$

The efficiency of the reaction as a silicon producer can be evaluated by two criteria: high silicon recovery and low hydrogen consumption.

$$\text{The Si recovery } s = \frac{z}{x} = \frac{mol\ Si(l)\ produced}{mol\ SiO_2\ comsumed} \qquad [9.19]$$

The remaining silicon is lost as SiO(g), with energy and material costs. The resulting Si recovery as a function of pressure and temperature is shown in Figure 9.9. A negative Si recovery means that the Si has to be placed on the left-hand side of Reaction [9.19], and it is necessary to consume Si to establish the equilibrium. The results show that a very high pressure is necessary to produce Si with a high silicon recovery, and the hydrogen consumption is excessive. The pressures and temperatures used here require a very strong extrapolation of the thermochemical data compared with the original measurements, and the results should therefore be seen only as indications. The equilibrium relations at 1 atm, calculated by HSC and shown in Figure 9.10, show similar unfavorable thermodynamics (Ringdalen *et al.*, 2024).

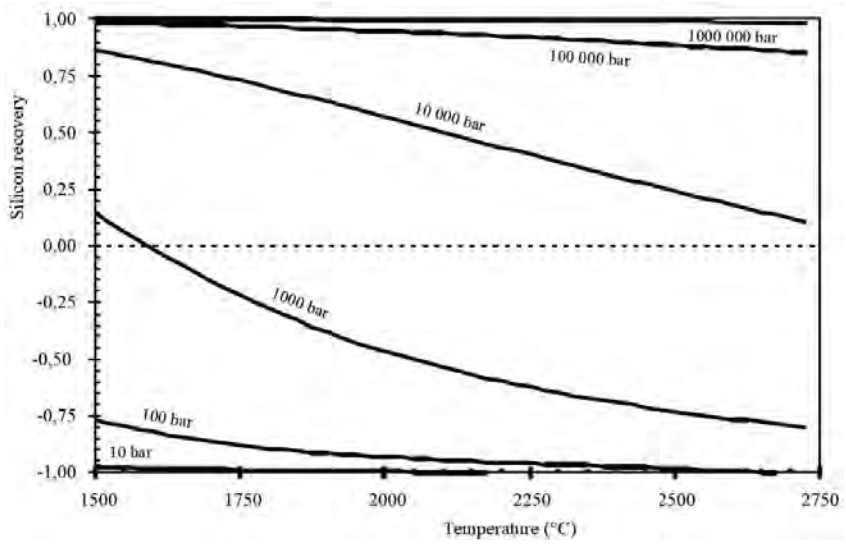


Figure 9.9 *Silicon recovery as a function of temperature for various pressures. A negative value means that the equilibrium reaction between SiO_2, Si and H_2 will consume Si and produce SiO.*

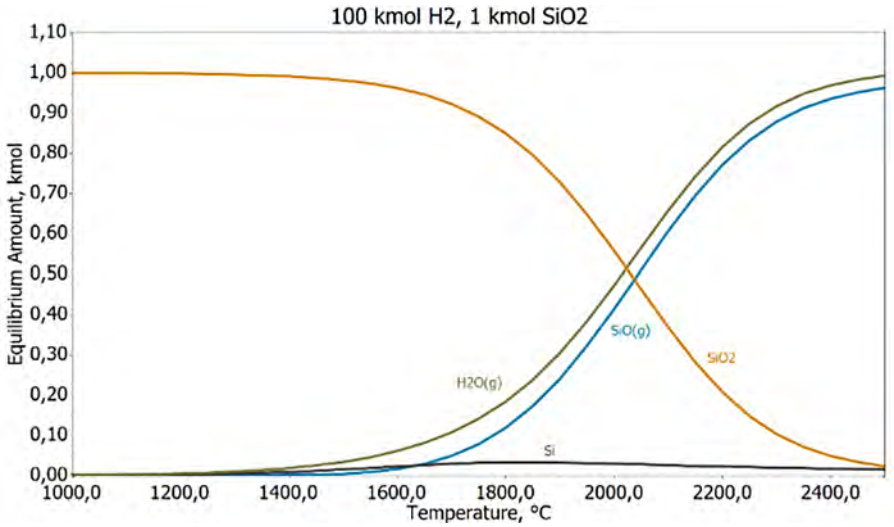


Figure 9.10 *Amount of SiO_2 that can be reduced with different temperatures at 1 atm. Equilibrium conditions calculated by HSC.*

The required high pressures are completely unrealistic in an industrial process. Therefore, it can be concluded that free Si cannot be produced by the reduction of SiO_2 by H_2 at equilibrium.

Development of new processes for production of Si with hydrogen will thus require alternative approaches to reduction of SiO_2 with H_2. Since today's industrial carbothermic Si production does not take place at complete equilibrium, this also makes it a natural way forward. The intermediate product, SiO gas, contributes to the unfavorable thermodynamics for Si production with H_2. An alternative could therefore be to produce SiO gas by other methods and then further reduce it to Si or Si-H compounds. Other alternatives include taking advantage of differences in kinetics for the involved reactions, using hydrogen plasma, or using alternative energy sources such as microwave. Examples of alternative processes based on these thoughts are presented below. They are on low TRL level, and fundamental investigations are needed to clarify whether they can be used in industrial Si-production.

SiH_2 process

In the proposed SiH_2 process, illustrated in Figure 9.11, SiO is produced from SiO_2 and Si in a separate reactor by reaction [9.20], and the produced SiO is reduced with hydrogen to Si according to reaction [9.21] in another reactor (Ringdalen *et al.*, 2024). At 1 atm, reaction 9.20 requires temperatures above around 1700°C, and reaction 9.21 temperatures below around 800°C, to give reasonable respectively SiO and Si production. Realization of a process based on this principle will thus require either conditions where Si can be produced from SiO at higher temperatures, or conditions where SiO will not react back to SiO_2 and Si when cooled down to temperatures where it can be reduced with H_2. Based on the well-known slow kinetics of SiO-dissociation, the last scenario seems most probable (Broggi, 2021).

$$SiO_2 + Si = 2SiO \quad [9.20]$$

$$SiO + H_2 = Si + H_2O \quad [9.21]$$



Figure 9.11 *Concept for SiH_2 process.*

Hydrogen plasma

Another alternative for hydrogen reduction of a stable oxide like SiO_2 is to excite the gas into a plasma. In the plasma state, hydrogen is present as ionic or radical species like H, H^+, H^{2+}, etc., which are far more reactive than the gas. The reduction could then take place according to reaction 9.22:

$$SiO_2 + 4H \rightarrow Si + 2H_2O \quad [9.22]$$

The reaction is thermodynamically favorable below 2589°C. However, hydrogen plasma studies on silicon dioxide reduction are limited in the literature. To date, only small-scale studies with scattered outcomes with respect to Si/SiH_4 production have been reported (Altmannshofer *et al.*, 2016; Gupta *et al.*, 2013; Sabat *et al.*, 2014; Watanabe *et al.*, 1999). In terms of industrialization of plasma production of silicon, Swedish company Green14 has announced their plans for technology exploitation, but no technical information has been published.

An alternative and even more energetic approach is to dissociate the SiO_2 itself to the plasma state: $SiO_2 > Si + 2O$. Silicon granules of 100–200 μm have been obtained with this technique (Grishin *et al.*, 2012).

Methane, CH_4

Methane gas (CH_4) used as a reducing agent is quite well-known. Traditionally, the methane has been provided by fossil natural gas, but it is equally possible to use biologically generated methane from biogas. Biogas is created from the biological digestion of organic material, and its main component is methane, CH_4, which can be a biological alternative to methane from fossil natural gas. CH_4 has a high reduction potential at temperatures above its equilibrium decomposition temperature (548°C), and metastable CH_4 has been shown to reduce oxides of manganese, chromium, and titanium faster than solid carbon. A major challenge is the spontaneous decomposition of the methane into hydrogen and carbon at the high temperatures necessary for SiO_2 reduction (Ostrovski and Zhang, 2006).

The carbon obtained from the cracking of the methane from biogas may, however, be used as an indirect source of biocarbon. Methane decomposition may be used to deposit carbon onto the ore itself (Li, 2017; Lindgård, 2015). Additionally, SiC can be quite readily produced by this method (Ksiazek *et al.*, 2014; Monsen *et al.*, 2013). Since SiC is an intermediate phase in a regular SAF, a part of the solid carbon might be replaced by methane.

Metallothermia

Metallothermia is thermally induced metal displacement reactions of the kind:

$$AX + B \rightarrow A + BX \qquad [9.23]$$

where A and B are metals while X most commonly is either oxygen or a halide.

Metallothermic reactions may be endo- or exothermic. Exothermic reactions continue spontaneously after ignition and are often referred to as 'thermite' or 'bomb' reactions (Habashi, 2018). Industrially, metallothermic reduction has been outcompeted for most metals except for some rare earth elements and other high-value metals (Xing *et al.*, 2018). More commonplace examples in modern industry include the Kroll process for titanium and the Pidgeon process for magnesium.

For a metallothermic reduction process to be considered climate neutral, a number of criteria must be fulfilled. Firstly, the reductant metal must be produced without greenhouse gas emissions. The thermodynamics are challenging because, for a metal to be a candidate for reducing another metal, it must have a strong affinity for the X-element in the compound to be reduced. This strong affinity makes the reductant very stable, so producing the reducing metal typically demands more energy than producing the actual product. Higher energy requirements also typically mean higher costs, which constitute an important commercial barrier.

Secondly, the reducing metal should have a high boiling point and a low vapour pressure, and it must be practically possible to handle it in safe and environmentally acceptable ways. Thirdly, if the reducing metal forms intermetallic compounds with the metal produced, this typically reduces the productivity of the process and may contaminate the product. A couple of exceptions exist, though, for example in magnesiothermia, and in those cases when the product alloy itself is valuable.

Finally, the reductant must be recyclable, cost-effective, and available in large enough quantities. Recycling would typically imply looping the reductant which, due to the inherent thermodynamic constraints, is an energy-intensive process.

Considering these criteria, most candidate metals from Figure 9.8 are disqualified. Calcium may be an interesting option because it is a fairly well-known and potent reducing agent for silicon, but the reaction can be explosive (Mishra *et al.*, 1985). Barium is less available, toxic, and highly unstable in the presence of oxygen.

Magnesiothermic reduction

While most Mg is currently produced via the carbon-intensive Pidgeon process, electrolytic production of magnesium metal (Mg) from $MgCl_2$ without significant CO_2 emissions is an alternative reductant in a magnesiothermic reduction of silica. Depending on the stoichiometry of the Mg:SiO_2 ratio in the reduction, different reaction products are formed, as described by equations 9.24–9.26. The structure of these reaction products, when Mg is reacted with natural quartz, was described by Rasouli *et al.* (2022), and illustrated in Figure 9.12.

$$SiO_2 + Mg = \frac{1}{2}Mg_2SiO_4 + \frac{1}{2}Si \ \Delta G^0_{1373} = -146.4 \ kJ \quad [9.24]$$

$$SiO_2 + 2Mg = 2MgO + Si \cdot G^0_{1373} = -243.4 \ kJ \quad [9.25]$$

$$SiO_2 + 4Mg = 2MgO + Mg_2Si \ \Delta G^0_{1373} = -272.1 \ kJ \quad [9.26]$$

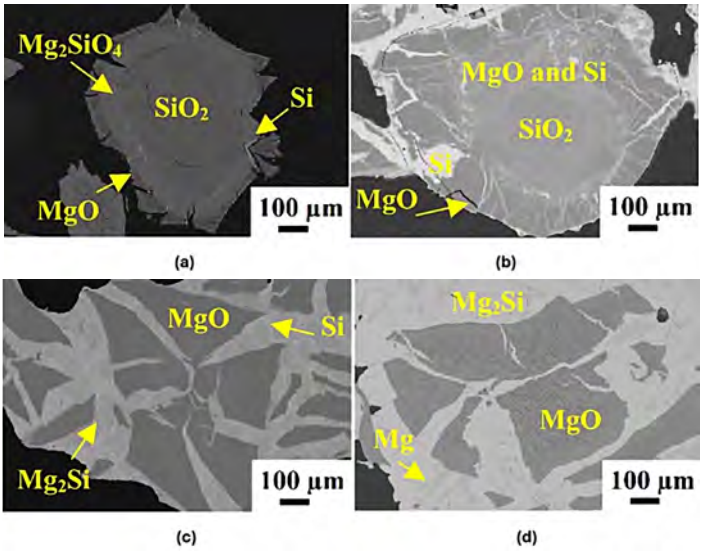


Figure 9.12 *(a) Backscattered electron image of magnesiothermically reduced natural quartz sample with a Mg:SiO_2 mole ratio of 1 and 120 min reaction time, (b) backscattered electron image of sample with a Mg:SiO_2 mole ratio of 2 and 120 min reaction time, (c) backscattered electron image of sample with a Mg:SiO_2 mole ratio of 3 and 120 min reaction time, (d) backscattered electron image of sample with a Mg:SiO_2 mole ratio of 4 and 10 min reaction time. Initial quartz particle size is 704 um for all samples. Adapted from Rasouli, 2022. [Used under Creative Commons Attribution 4.0 International License].*

After reduction, acid leaching (and/or other purification steps) may be needed to remove impurities and unwanted intermetallic phases (e.g. MgO, Mg_2Si, Mg_2SiO_4) from the Si product if it is used directly.

An interesting magnesiothermic approach makes use of intermetallic phases like Mg_2Si instead of avoiding them (as is usual in metallothermic practices). The idea is to use the intermetallic as the raw material for production of silane (SiH_4) through hydrolysis in e.g. HCl, which in turn constitutes the feed material for the Siemens or fluidized bed reactor processes (Tang *et al.*, 2023). However, SiH_4 will not be the only hydrolysis reaction product and other silanes such as Si_2H_6 and Si_3H_8 are co-products of the reaction. When the Mg_2Si/MgO reaction product is hydrolysed with HCl, the MgO will be converted to $MgCl_2$, which may be used as input in Mg electrolysis (Rasouli *et al.*, 2022).

Aluminothermic reduction

Aluminothermic reduction is a relatively well-known method for production of silicon and silicon alloys. Inefficiencies in solid-state reduction are caused by back-reactions and the formation of intermetallic phases, most notably mullite ($Al_6Si_2O_{13}$), which can be challenging to separate (Dietl *et al.*, 1982; Dietl and Holm, 1987; Sadique, 2011). These barriers are overcome in the liquid-state reduction of SiO_2 in SiO_2–CaO slags, forming liquid Si alloy (which is simply slag refined to MG–Si) and liquid CaO–Al_2O_3 slag, as demonstrated by the SisAl technology (Philipson *et al.*, 2021; Safarian and Tranell, 2024; Toli *et al.*, 2021; Zhu *et al.*, 2024). The CaO–Al_2O_3 slag may be hydrometallurgically processed to CaO (e.g. for input to new CaO–SiO_2 slag raw material) and Al_2O_3 (for Al electrolysis), or used directly as a product. The process was piloted at large scale (100´s of kg) using primary aluminium, aluminium scrap, and aluminium dross as reductants. Under the stoichiometric Al:SiO_2 conditions given by reaction 9.27, and using a 50/50 wt% SiO_2/CaO slag as raw material, an alloy with the approximate composition 75wt%Si15wt% Ca10wt% Al was formed, along with a slag containing 50–60% Al_2O_3, 40–45% CaO and small residual amounts of SiO_2/Si (< 5 wt%). Using slags with initially higher silica content, or applying a lower Al:SiO_2 ratio, formed alloys with higher silicon content. The results agreed largely with thermodynamic simulations as illustrated in Figure 9.13.

$$SiO_2 + \frac{4}{3}Al = Si + \frac{2}{3}Al_2O_3 \qquad [9.27]$$

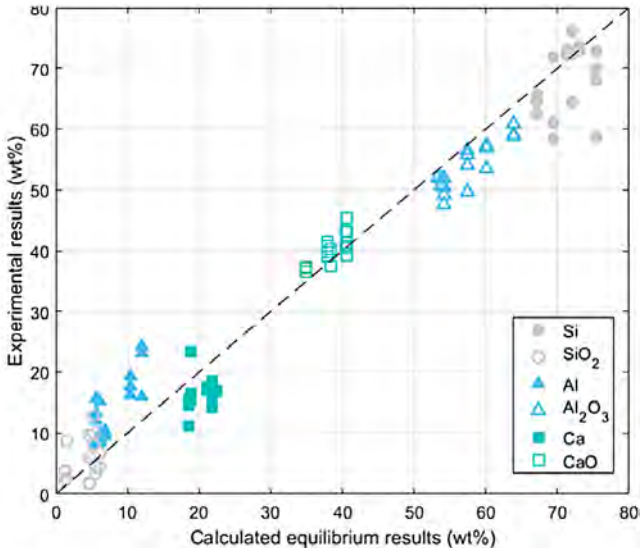


Figure 9.13 *Compositions of SiCaAl alloy and slag resulting from aluminothermic reduction of CaO–SiO_2 slag (Zhu et al., 2024) [Used under licence CC-BY 4.0].*

The resulting alloy, high in Ca and Al, was subsequently refined using different slags, obtaining an alloy with up to 99% Si.

A barrier to climate neutrality for aluminothermia is the production and regeneration of the Al. Today, Al is produced by electrolysis in the Hall-Heroult process. This process is not climate neutral. It emits large amounts of CO_2 through the consumption of the carbon electrode. In theory, however, Al electrolysis could be decarbonized (e.g. by the use of inert anodes or other measures). Climate neutral aluminium production could hence enable the climate neutral production of many other metals, including Si, by aluminothermic reduction.

Electrolysis

A climate neutral electrolysis process for direct production of silicon may short-cut some important process steps in the total value chain in a future scenario where the energy grids are decarbonized. The main technological

obstacle that must be overcome is to find a durable inert anode that either does not contribute to pollution of the product or gives the 'right' impurities for the product to still meet the specifications. For solar and electronic Si applications, for example, the focus is often to avoid dopants such as B and P in the product.

Utilizing electrolytes like the Hall-Heroult process (i.e. cryolite or other fluoride melts) with an inert anode might enable the production of CO_2-free silicon by electrolysis. Si electrolysis from SiO_2 with oxygen evolving anodes has a theoretical energy consumption of 12.0 kWh/kg Si (temperature range 1000°C, calculated for 80% current efficiency with HSC v.9). For comparison, carbothermal reduction has a theoretical energy requirement of 9.6 kWh/kg Si, which is substantially lower. Then again, direct comparison may be misleading because the two product grades are quite different. Electrolytic reduction processes have been reported to produce rather pure Si (99.99–99.999%). Hence, some refining steps might be avoided downstream in the value chain, which in turn would save energy.

Silicon is less noble than most metals, as well as hydrogen, and additionally has a high melting point. These constraints make electrolytic reduction of SiO_2 very challenging. It is not possible to use aqueous electrolytes, for example, since the high voltage necessary for splitting SiO_2 is higher than the decomposition voltage of water. So, even if SiO_2 were soluble in water, H_2 gas would be produced before Si and would thus consume the aqueous electrolyte.

Silicon must therefore be electrolysed either in a molten salt or in a molten oxide. Molten salt electrolytes can be used at temperatures in the range of 700–1000°C, which means that the Si must be deposited in the solid state. This, in turn, makes the processes relatively slow. To substantially increase the rate of production, the temperature must be above the melting point of Si (> 1410°C). This means that the only electrolyte types available are molten oxides.

In the following, some of the literature on Si electrolysis in various electrolytes will be discussed. It is important to note that most processes for reduction of SiO_2 have, so far, been investigated with consumable carbon anodes, which means that they emit CO_2. To become climate neutral, inert oxygen-evolving anodes suitable for the specific electrolytes must be developed. At the same time, replacing the carbon anode with an O_2-evolving anode would also result in an energy increase, since the thermodynamics are less favorable without the help of carbon.

Molten salt electrolysis

The most common molten salt electrolytes used for metal production from oxide feed are chloride and fluoride melts. The Hall-Heroult process for aluminium production has been, and still is, the major industrial electrolytic method. The process takes place in liquid cryolite (Na_3AlF_6). Fluoride melts, and especially cryolite, are used because of their high metal oxide solubility. Unfortunately, these salts are also very corrosive, and suitable inert anode materials are correspondingly hard to find.

Patented EW processes to produce Si from quartz in molten fluoride salts exist. These are often multistep electrolytic and electrorefining processes, claiming to produce Si of semiconductor quality after some additional refining (like zone refining, leaching and/or directional solidification). The temperatures are well below the melting point of silicon (1410°C). Hence, production occurs by solid-state deposition and is therefore slow. Si, being a poor conductor, limits the production rate even further. The low production rate is probably the main reason why no process of this type has been commercialized. Another important challenge is that fluoride salts are difficult to separate from the produced silicon (Elwell, 1982; Monnier and Barakat, 1965; Rao *et al.*, 1980).

Chloride salts do not readily dissolve oxides like quartz, but they are easier to remove from a solid Si cathode product than fluorides. The FFC Cambridge process (named after Fray, Farthing and Chen) circumvents the problem of low SiO_2 solubility by allowing a SiO_2 pellet to be directly reduced in a $CaCl_2$ melt. This was first suggested for reduction of titanium from TiO_2 (Chen *et al.*, 2000) but has also been proven at laboratory scale for silicon and other elements. In the FFC process, a pellet of the oxide raw material is polarized so that it constitutes the cathode of the system. The electrolyte consists mainly of liquid $CaCl_2$ with small amounts of CaO. As the reduction progresses, oxygen ions from the oxide are released into the melt and discharged at the anode, as CO/CO_2 if a consumable carbon anode is used, or as O_2 on an inert anode.

Other suggested processes include dissolving SiO_2 in a CaO-rich liquid electrolyte (Olsen, 2004). The temperature of this type of process would typically be 800–950°C, which is well below the melting point of Si. Consequently, the production occurs in the solid state and is slow. As for fluoride melts, the low production rate is seen as a commercial disadvantage (Nohira *et al.*, 2003; Yasuda *et al.*, 2007).

Molten oxide electrolysis (MOE)

Several electrolysis processes for producing liquid silicon by molten oxide electrolysis (MOE) have been suggested over the years. Such processes use SiO_2 as raw material and silicate electrolytes (De Mattei *et al.*, 1981). The greatest advantage of MOE is that it enables production at very high temperatures. Liquid deposition and favorable kinetics enhance the productivity rate. Metals produced in the molten state are also easier to harvest, as the separation between electrolyte and metal can be continuous. Generally, this is done by tapping (e.g. aluminium). In the case of silicon, however, the product alloy typically floats on top of the heavier electrolyte, and continuous separation would require siphoning.

Crucially, the high temperatures necessary to keep the silicon liquid imply very severe material challenges. For MOE, this is not only true for the (inert) anode but also for the cathode and container materials. Nevertheless, this type of process may offer reasonably good prospects for commercialization. Various electrolyte mixtures like $BaO–BaF_2–SiO_2$ have already been investigated, and multistep processes have been suggested to improve product purity (Elwell and Rao, 1988; Sadoway, 2001).

9.4 Alternative silicon sources for new processes

The most common raw material for bulk silicon and high-silicon alloy production is quartz. Sometimes ultrapure quartz is required, and in some cases the quartz goes through an acid washing process to remove certain impurities. Nonetheless, the overall purity of typical mineral quartz is quite high compared to many ores and other mineral raw materials used in metallurgical industries.

Silicon oxides can also be found in other materials like diatoms, rice husks, kerf, dust, and other by-products from various industries. Some non-oxidic by-products, like hydrofluorosilicic acid (H_2SiF_6), also exist. The use of by-products as silicon sources is attractive with respect to increased circularity and industrial symbiosis, but the volumes of silicon alloys required to ensure a global green transition will most likely mean that mined quartz minerals will continue to be a primary raw material for high-silicon alloy production for some time yet.

Silicon halides (i.e. chlorides, fluorides, bromides & iodides) are often less stable than the oxides and therefore easier to reduce. This makes them

attractive as feed to new reduction processes, particularly electrolytic and metallothermic ones. Among the halides, the chlorides are by far the most widely studied.

From the perspective of climate gas reduction, however, the use of halides is not necessarily a good idea. While the reduction step itself may not produce any CO_2, the quartz must always be halogenated first. This typically requires carbon and emits CO, as illustrated in the following example. First, the quartz is carbo-chlorinated:

$$SiO_2 + 2C + 2Cl_2 \rightarrow SiCl_4 + 2\ CO \quad [9.28]$$

Then, the tetrachloride can be reduced to Si, e.g. by sodium metal (Na):

$$SiCl_4 + 4\ Na \rightarrow Si + 4\ NaCl \quad [9.29]$$

But the sum net reaction is identical to the overall reaction of a submerged arc furnace:

$$SiO_2 + 2C \rightarrow Si + CO \quad [9.30]$$

A reduction process based on halide feed may therefore be less efficient, yet equally carbon intensive as carbothermic reduction.

If this obstacle could be overcome, though, a great many new possibilities open up. Many more metals/elements are able to reduce the halides than the oxide, including zinc, aluminium, sodium, potassium, and magnesium (Yasuda and Okabe, 2010). Using biocarbon in a carbochlorination would not require the same type of biocarbon as the SAF. Most notably, mechanical strength would not be crucial. Therefore, carbochlorination might be a cost-effective and circular way to use biocarbon fines and by-products from e.g. agri- or aquaculture to produce feed materials for new reduction routes.

Climate-friendly halide feed materials could, for example, be used in low-temperature electrolysis. If the gas evolved on the anode is a halide like chlorine, it is possible to use a carbon anode and still have a CO_2-free electrowinning process. Contrarily, if the gas evolved on the anode is fluorine, CF_4 gas may form. CF_4 is a climate gas with a global warming potential 6500 times higher than CO_2 (Maeda *et al.*, 2014; Platek *et al.*, 2017; Yasuda *et al.*, 2017).

References

Altmannshofer, S., Eisele, I. and Gschwandtner, A. (2016) 'Hydrogen microwave plasma treatment of Si and SiO2', *Surface and Coatings Technology*, 304, pp. 359–363. Available at: https://doi.org/10.1016/j.surfcoat.2016.07.038

Andersen, V. (2023) *Flue gas recirculation for the silicon process*. Doctoral thesis 2023:135. Norwegian University of Science and Technology (NTNU), Trondheim, Norway. Available at: https://hdl.handle.net/11250/3069034

Andersen, V., Einarsrud, K.E., Rasouli, A. and Tranell, G. (2023a) 'Silica fume formation in different gas atmospheres', *Industrial & Engineering Chemistry Research*, 62, pp. 4246–4259. Available at: https://doi.org/10.1021/acs.iecr.2c03987

Andersen, V., Knuutila, H.K., Braakhuis, L., Myrhaug, E., Einarsrud, K.E. and Tranell, G. (2021) 'CO2 capture for the silicon process – effects of flue gas recirculation', in *Proceedings of INFACON XVI*. Trondheim, Norway. Available at: https://doi.org/10.2139/ssrn.3926089

Andersen, V., Solheim, I., Gaertner, H., Sægrov-Sorte, B., Einarsrud, K.E. and Tranell, G. (2023b) 'Pilot-scale test of flue gas recirculation for the silicon process', *Journal of Sustainable Metallurgy*, 9, pp. 81–92. Available at: https://doi.org/10.1007/s40831-022-00639-0

Andresen, B. (1995) *Process model for carbothermic production of silicon metal*. Doctoral thesis 1995:35. Norges Tekniske Høgskole (NTH), now Norwegian University of Science and Technology (NTNU), Trondheim, Norway.

Arnesen, A.G. and Bjørdal, J. (1981) 'Development and achievements with a closed 8,500 kW Elkem furnace producing 75% ferrosilicon', paper presented at the *38th Electric Furnace Conference*, Pittsburgh, PA, USA.

Arvidson, A.N., Dosaj, V. and May, J.B. (1991) *Silicon smelting process in direct current furnace*. US Patent 5009703-A.

Belo, L.P., Elliott, L.K., Stanger, R.J., Spörl, R., Shah, K.V., Maier, J. and Wall, T.F. (2014) 'High-temperature conversion of SO2 to SO3: Homogeneous experiments and catalytic effect of fly ash from air and oxy-fuel firing', *Energy & Fuels*, 28, p. 7243. Available at: https://doi.org/10.1021/EF5020346

Broggi, A. (2021) *Condensation of SiO and CO in silicon and ferrosilicon production*. Doctoral thesis 2021:93. Norwegian University of Science and Technology (NTNU), Trondheim, Norway. Available at: https://hdl.handle.net/11250/2734899

Chase, M.V. Jr., Davies, C.A., Downey, J.R. Jr., Frurip, D.J., MacDonald, R.A. and Syverud, A. (1985) *NIST-JANAF Thermochemical Tables*. Available at: https://janaf.nist.gov/janbanr.html (Accessed: 22 May 2025).

Chen, G.Z., Fray, D.J. and Farthing, T.W. (2000) 'Direct electrochemical reduction of titanium dioxide to titanium in molten calcium chloride', *Nature*, 407, pp. 361–364. Available at: https://doi.org/10.1038/35030069

Coldwell, D.M. (1976) 'A thermodynamic analysis of the reduction of silicon oxides using a plasma', *High Temperature Science*, 8, pp. 309–316.

Coldwell, D.M. (1977) 'The molecular dynamics of product quenching in the silicon-carbon-oxygen system', *High Temperature Science*, 9, pp. 209–214.

Coldwell, D.M. and Roques, R.A. (1977) 'Reduction of SiO2 with carbon in a plasma', *J. Electrochem. Soc.*, 124(11). Available at: https://doi.org/10.1149/1.2133137

De Mattei, R.C., Elwell, D. and Feigelson, R.S. (1981) 'Electrodeposition of silicon at temperatures above its melting point', *J. Electrochem. Soc.*, 128, pp. 1712–1714. Available at: https://doi.org/10.1149/1.2127716

Dietl, J. and Holm, C. (1987) 'New aspects in aluminothermic reduction of SiO2', in Goetzberger, A., Palz, W. and Willeke, G. (eds) *Seventh E.C. Photovoltaic Solar Energy Conference*. Dordrecht: Springer Netherlands, pp. 726–730. Available at: https://doi.org/10.1007/978-94-009-3817-5_129

Dietl, J., Holm, C. and Sirtl, E. (1982) 'Aluminothermic reduction of quartz sand', in Bloss, W.H. and Grassi, G. (eds) *Fourth E.C. Photovoltaic Solar Energy Conference*. Dordrecht: Springer Netherlands, pp. 941–945. Available at: https://doi.org/10.1007/978-94-009-7898-0_154

Dosaj, V., Brumels, M.D., Haines, C.M. and May, J.B. (1991) *Silicon smelting in a closed furnace*. Report No. EGG-M--91551; CONF-9111206--1. EG and G Idaho, Inc., Idaho Falls, ID, USA.

Dosaj, V.D. (1995) *Collection and conversion of silicon furnace waste gas into higher value products: Phase 3, 6 MW pilot plant DC closed furnace technology*. Final report No. DOE/ID/12624--3. Dow Corning Corp., Midland, MI, USA. Available at: https://doi.org/10.2172/83036

Dosaj, V.D., May, J.B. and Arvidson, A.N. (1994) *Direct current, closed furnace silicon technology*. Report No. CONF-9406164--1. Dow Corning Corp., Midland, MI, USA.

Dosaj, V.D. and Rauchholz, A.W. (1987) *Plasma smelting process for silicon*. US Patent 4,680,096.

Downing, J.H. (1965) 'Fundmental reactions in submerged arc furnaces', *Proceedings of the Electric Furnace Conference 1963*, pp. 288–295, discussion pp. 295–296.

Elwell, D. (1982) 'Electrodeposition of solar silicon', in *Solar Energy Materials*, 6. North-Holland Publishing Company, pp. 123–145.

Elwell, D. and Rao, G.M. (1988) 'Electrolytic production of silicon', *Journal of Applied Electrochemistry*, 18, pp. 15–22. Available at: https://doi.org/10.1007/BF01016199

Eriksson, S. and Santén, S. (1985) *Method of manufacturing ferrosilicon*. US Patent 4,526,612.

Fereday, F.D., Raath, L. and de Montard, B. (2013) 'Guidelines for sizing baghouse filters used for ferroalloy and silicon metal furnace applications', in *Proceedings of INFACON XIII*. Almaty, Kazakhstan. Available at: https://www.pyrometallurgy.co.za/InfaconXIII/1015-Fereday.pdf

Gao, J., Wang, S., Wang, J., Cao, L., Tang, S. and Xia, Y. (2015) 'Effect of SO2 on the amine-based CO2 capture solvent and improvement using ion exchange resins', *International Journal of Greenhouse Gas Control*, 37, pp. 38–45. Available at: https://doi.org/10.1016/j.ijggc.2015.03.001

Grishin, Yu.M., Kozlov, N.P. and Skryabin, A.S. (2012) 'Experimental study of the plasmochemical method for the direct production of silicon from quartz', *High Temperature*, 50, pp. 459–463. Available at: https://doi.org/10.1134/S0018151X12040086

Gryshan, D., Wallin, M., Yermolov, M., Legemza, J., Korol, N. and Tranell, G. (2026) 'Industrial experience of using biocarbon briquettes in FeSi production process', in *Proceedings of Silicon for the Chemical and Solar Industry XVIII*. Kristiansand, Norway. Available at: https://www.ntnu.edu/si-conference

Gupta, V., Madaan, N., Jensen, D.S., Kunzler, S.C. and Linford, M.R. (2013) 'Hydrogen plasma treatment of silicon dioxide for improved silane deposition', *Langmuir*, 29, pp. 3604–3609. Available at: https://doi.org/10.1021/la304491x

Habashi, F. (2018) 'Metallothermic reactions – past, present and future', *Research and Reports on Metals*, 2.

Hauge, E.G.R. (2022) *Scaling in the Si off-gas systems – the effect of alkali content*. MSc thesis. Norwegian University of Science and Technology (NTNU), Trondheim, Norway. Available at: https://hdl.handle.net/11250/3023783

Houshfar, E., Khalil, R.A., Løvås, T. and Skreiberg, Ø. (2012) 'Enhanced NOx reduction by combined staged air and flue gas recirculation in biomass grate combustion', *Energy & Fuels*, 26, pp. 3003–3011. Available at: https://doi.org/10.1021/ef300199g

Hutchison, S.G., Richardson, L.S. and Wai, C.M. (1988) 'Carbothermic reduction of silicon dioxide—a thermodynamic investigation', *Metallurgical Transactions B*, 19, pp. 249–253. Available at: https://doi.org/10.1007/BF02654209

Kero, I.T., Sende Osen, K. and Dalaker, H. (2022) 'Technologies with potential for climate neutral silicon production', in *Proceedings of Silicon for the Chemical and Solar Industry XVI*. Trondheim, Norway. Available at: https://doi.org/10.2139/ssrn.4121151

Krogsrud, H., Bugg, N.E. and Piene, K. (1978) 'Recent advances in the development of the modern ferrosilicon furnace – the Elkem split furnace body', in *Proceedings of the 35th Electric Furnace Conference*, pp. 15–18.

Ksiazek, M., Tangstad, M., Dalaker, H. and Ringdalen, E. (2014) 'Reduction of SiO2 to SiC using natural gas', *Metallurgical and Materials Transactions E*, 1, pp. 272–279. Available at: https://doi.org/10.1007/s40553-014-0027-4

Larsen, H.L. (1996) *AC electric arc models for a laboratory set up and a silicon metal furnace*. Doctoral thesis. Norges Tekniske Høgskole (NTH), now Norwegian University of Science and Technology (NTNU), Trondheim, Norway.

Lask, G.W. and Ruuth, N. (1989) 'Development and use of Silgro carbon-silica briquettes in silicon metal furnaces', in *Proceedings of INFACON V*. New Orleans, USA. Available at: https://www.pyrometallurgy.co.za/InfaconV/251-Lask.pdf

Li, B., Yu, Y., Li, M., Tang, X. and Wang, S. (2024) 'New technology and development of submerged arc furnace for ferroalloy production', in *Proceedings of INFACON XVII*. Beijing, China, pp. 90–100.

Li, F. (2017) *SiC production using SiO2 and Cagglomerates*. Doctoral thesis 2017:180. Norwegian University of Science and Technology (NTNU), Trondheim, Norway.

Lindgård, H. (2015) *High temperature decomposition of methane on quartz pellets*. MSc thesis. Norwegian University of Science and Technology (NTNU), Trondheim, Norway.

Lukin, P.G., Popov, Yu.A. and Shaposhnikov, A.K. (1963) 'Production of blast-furnace ferrosilicon', *Metallurgist*, 7, pp. 157–160. Available at: https://doi.org/10.1007/BF00751390

Lundberg, N.H. (1978) 'A closed silicon furnace with a split furnace body', *Tidsskrift for Kjemi, Bergvesen og Metallurgi*, 38, pp. 6–8.

Maeda, K., Yasuda, K., Nohira, T., Hagiwara, R. and Homma, T. (2014) 'A new electrodeposition process of crystalline silicon utilizing water-soluble KF–KCl molten salt', *ECS Transactions*, 64, pp. 285–291. Available at: https://doi.org/10.1149/06404.0285ecst

Mathisen, A., Normann, F., Biermann, M., Skagestad, R. and Haug, A.T. (2019) 'CO2 capture opportunities in the Norwegian silicon industry', in *Proceedings of the 10th Trondheim Conference on CO2 Capture, Transport and Storage*. Presented at TCCS-10. Trondheim, Norway: SINTEF Academic Press.

Mishra, P., Chakraverty, A. and Banerjee, H.D. (1985) 'Production and purification of silicon by calcium reduction of rice-husk white ash', *Journal of Materials Science*, 20, pp. 4387–4391. Available at: https://doi.org/10.1007/BF00559326

Monnier, R. and Barakat, D. (1965) *Dual cell refining of silicon and germanium*. US Patent 3219561A.

Monsen, B. (2009) *Closed submerged arc furnace for silicon and ferrosilicon production – possibilites and challenges*. Confidential SINTEF Report No. F13819. SINTEF, Trondheim, Norway.

Monsen, B., Kolbeinsen, L., Prytz, S., Myrvagnes, V. and Tang, K. (2013) 'Possible use of natural gas for silicon or ferrosilicon production', in *Proceedings of INFACON XIII*. Almaty, Kazakhstan. Available at: https://www.pyrometallurgy.co.za/InfaconXIII/0467-Monsen.pdf

Müller, M.B. and Magnussen, T. (1972) 'Electrode consumption and arc processes in submerged arc furnaces', in *Paper No. 404 with Discussion*. Presented at the 7th International Congress of Electroheat, Warzawa, Poland.

Nelson, L.R. (2014) 'Evolution of the mega-scale in ferro-alloy electric furnace smelting', in Mackey, P.J., Grimsey, E.J., Jones, R.T. and Brooks, G.A. (eds) *Celebrating the Mega-scale*. Cham: Springer International Publishing, pp. 39–68. Available at: https://doi.org/10.1007/978-3-319-48234-7_3

Nohira, T., Yasuda, K. and Ito, Y. (2003) 'Pinpoint and bulk electrochemical reduction of insulating silicon dioxide to silicon', *Nature Materials*, 2, pp. 397–401. Available at: https://doi.org/10.1038/nmat900

Olsen, E. (2004) *Electrolyte and process for the manufacture or refining of silicon*. Patent NO317073B1.

Ostrovski, O. and Zhang, G. (2006) 'Reduction and carburization of metal oxides by methane-containing gas', *AIChE Journal*, 52, pp. 300–310. Available at: https://doi.org/10.1002/aic.10628

Philipson, H., Wallin, M., Einarsrud, K.E. and Tranell, G. (2021) 'Kinetics of silicon production by aluminothermic reduction of silica using aluminum and aluminum dross as reductants', in *Proceedings of INFACON XVI*. Trondheim, Norway. Available at: https://doi.org/10.2139/ssrn.3922132

Platek, A., Piwek, J., Fic, K., Schubert, T., Gentile, P., Bidan, G. and Frackowiak, E. (2017) 'Electrochemical performance of silicon nanostructures in low-temperature ionic liquids for microelectronic applications', *Journal of Materials Chemistry A*, 5, pp. 22708–22716. Available at: https://doi.org/10.1039/C7TA08175H

Qian, F., Chyang, C.-S., Yeh, C. and Tso, J. (2013) 'Effect of operating conditions on NOx and CO emissions in a pilot-scale vortexing fluidised-bed combustor with flue gas recirculation', *Chemical Engineering & Technology*, 36, pp. 268–276. Available at: https://doi.org/10.1002/ceat.201200146

Rao, G.M., Elwell, D. and Feigelson, R.S. (1980) 'Electrowinning of silicon from K2SiF6–molten fluoride systems', *J. Electrochem. Soc.*, 127, pp. 1940–1944. Available at: https://doi.org/10.1149/1.2130041

Rasouli, A., Herstad, K.E., Safarian, J. and Tranell, G. (2022) 'Magnesiothermic reduction of natural quartz', *Metallurgical and Materials Transactions B*, 53, pp. 2132–2142. Available at: https://doi.org/10.1007/s11663-022-02513-6

Ringdalen, E., Svenum, I.-H. and Aarnæs, T. (2024) 'SiH2 – a new process for Si-production based on hydrogen', in *Proceedings of Silicon for the Chemical and Solar Industry XVII*. Trondheim, Norway. Available at: https://doi.org/10.2139/ssrn.4942625

Sabat, K.C., Rajput, P., Paramguru, R.K., Bhoi, B. and Mishra, B.K. (2014) 'Reduction of oxide minerals by hydrogen plasma: An overview', *Plasma Chemistry and Plasma Processing*, 34, pp. 1–23. Available at: https://doi.org/10.1007/s11090-013-9484-2

Sadique, S. (2011) *Production and purification of silicon by magnesiothermic reduction of silica fume*. MSc thesis. University of Toronto, Ontario, Canada. Available at: https://tspace.library.utoronto.ca/handle/1807/25788

Sadoway, D. (2001) 'From oxygen generation to metals production: In situ resource utilization by molten oxide electrolysis', 1, p. 525.

Safarian, J. and Tranell, G.M. (2024) *Process for the production of commercial grade silicon*. Patent EP4279453A3.

Santén, S. and Edström, J.O. (1984) *Method of manufacturing silicon from powdered material containing silica*. US Patent 4,439,410.

Schei, A., Tuset, J.K. and Tveit, H. (1998) *Production of high silicon alloys*. Trondheim, Norway: Tapir.

Sidorkin, V.T., Tugov, A.N., Moshnikov, A.N., Vereshchetin, V.A. and Bersenev, K.G. (2016) 'Effect of flue gas recirculation on the technical and environmental performance of a boiler', *Power Technology and Engineering*, 49, pp. 354–358. Available at: https://doi.org/10.1007/s10749-016-0627-5

Straum, I., Sindland, C., Andersen, V. and Myrvågnes, V. (2026) 'Behaviour of charcoal-quartz agglomerates under SiO-rich conditions', in *Proceedings of Silicon for the Chemical and Solar Industry XVIII*. Kristiansand, Norway. Available at: https://www.ntnu.edu/si-conference

Surup, G.R. (2019) *Renewable reducing agents for the use in ferroalloy industries*. Doctoral thesis. University of Agder, Kristiansand, Norway.

Tang, K., Rasouli, A., Safarian, J., Ma, X. and Tranell, G. (2023) 'Magnesiothermic reduction of silica: A machine learning study', *Materials*, 16, 4098. Available at: https://doi.org/10.3390/ma16114098

Toli, A., Tsaousi, G.M., Balomenos, E., Panias, D., Heuer, M., Philipson, H. and Tranell, G. (2021) 'Sustainable silicon and high purity alumina production from secondary silicon and aluminium raw materials through the innovative SisAl technology', in *International Conference on Raw Materials and Circular Economy*. Presented at RawMat 2021. MDPI, p. 85. Available at: https://doi.org/10.3390/materproc2021005085

Tveit, H. and Gard, E. (1982) 'Experience in operating a 9 MVA furnace with split body concept producing silicon metal', in *Proceedings of the Electric Furnace Conference*. Kansas City, USA, pp. 327–331.

Watanabe, T., Soyama, M., Kanzawa, A., Takeuchi, A. and Koike, M. (1999) 'Reduction and separation of silica-alumina mixture with argon–hydrogen thermal plasmas', *Thin Solid Films*, 345, pp. 161–166. Available at: https://doi.org/10.1016/S0040-6090(99)00071-1

Xing, Z., Lu, J. and Ji, X. (2018) 'A brief review of metallothermic reduction reactions for materials preparation', *Small Methods*, 2, 1800062. Available at: https://doi.org/10.1002/smtd.201800062

Yasuda, K., Maeda, K., Hagiwara, R., Homma, T. and Nohira, T. (2017) 'Editors' choice—silicon electrodeposition in a water-soluble KF–KCl molten salt: Utilization of SiCl4 as Si source', *J. Electrochem. Soc.*, 164, pp. D67–D71. Available at: https://doi.org/10.1149/2.0641702jes

Yasuda, K., Nohira, T., Hagiwara, R. and Ogata, Y.H. (2007) 'Direct electrolytic reduction of solid SiO2 in molten CaCl2 for the production of solar grade silicon', *Electrochimica Acta*, 53, pp. 106–110. Available at: https://doi.org/10.1016/j.electacta.2007.01.024

Yasuda, K. and Okabe, T.H. (2010) 'Solar-grade silicon production by metallothermic reduction', *JOM*, 62, pp. 94–101. Available at: https://doi.org/10.1007/s11837-010-0190-8

Zhu, M., Philipson, H., Blandhol, K., Djupvik, V., Engvoll, K., Safarian, J., Tang, K., Görnerup, M., Pastor-Vallés, E., Wallin, M. and Tranell, G. (2024) 'Pilot-scale aluminothermic production of silicon alloy and alumina-rich slag', *ACS Sustainable Chemistry & Engineering*, 12, pp. 14795–14809. Available at: https://doi.org/10.1021/acssuschemeng.4c05326

Tranell, G. (2026) 'Silicon alloy refining', in M. Tangstad, G. Tranell, H. Tveit and E. Ringdalen (Eds.), *Production of high silicon alloys* (2. ed.) (pp. 375–428). Fagbokforlaget. https://doi.org/10.55669/oa880810

10

Silicon alloy refining

Gabriella Tranell

Si and FeSi alloys are typically refined in their liquid state, where the furnace alloy is processed into an alloy that satisfies product specification. Generally, this occurs during/after the alloy is tapped from the SAF into a ladle. Of the several impurity elements present in Si and FeSi alloys, Ca and Al are considered especially important by the industry, due to their abundance in the raw materials, ease of refining, and impact on customer use. Two routes are available for refining these:

- Those based on oxidation and slagging of impurities
- Those based on chlorination and removal of impurities as volatile chlorides

Oxidation and slagging of impurities is the method used in the industry today, with the chlorination process seeing minor industrial interest, owing to the environmental, handling, and waste problems associated with the use of chlorine and the formation of corrosive metal chlorides.

To produce high purity silicon, e.g., with the intention to use as solar- or electronic-grade silicon, supplemental refining processes are required. Typically, solar grade silicon (SOG–Si > 99.9999% purity) is produced by HCl gas chlorination of MG–Si (> 96% Si) to trichlorosilane ($SiHCl_3$), which is purified by distillation and thermally decomposed in H_2 to pure silicon in a Siemens reactor. This chemical refining process has been extensively described in literature, for example by Hesse and Pätzold (2006) and Yang (2019).

This work is licensed under the Creative Commons Attribution 4.0 International License.
To view a copy of this license, visit https://creativecommons.org/licenses/by/4.0/

With the exponential growth in the silicon-based solar cell industry since the turn of the century, research into cost-effective and environmentally advantageous methods of producing solar grade silicon entered a new era in the early 2000s. Since then, the research and development of metallurgical processes designed for the removal of harmful impurities like carbon, boron, phosphorus and metals (Fe, Al, Cr, Ti etc.) has resulted in a large body of publications.

In this chapter, Section 10.1 covers the fundamental and industrial aspects of oxidation and slagging of impurities, with a special focus on Ca and Al, while Section 10.2 provides a short summary of Si refining by chlorination. Finally, Section 10.3 gives an overview of relevant pyro- and hydrometallurgical refining techniques to further purify MG–Si into high purity silicon, such as slag-, solvent-, gas/plasma-, vacuum-, crystallization and acid-treatments.

10.1 Oxidation and slagging of impurities

Impurity elements with greater oxygen affinity than Si can be refined from the liquid alloy by oxidation and associated formation of an immiscible slag phase. Oxygen can be introduced by:

- A gas, either as pure oxygen gas or part of a gas mixture, like synthetic air (oxygen/nitrogen mixture) or atmospheric air. Oxygen may also be introduced passively, as the alloy is exposed to air, which is the case during most post-furnace liquid handling processes.
- Addition of solid oxidizing agents, such as Fe_2O_3, SiO_2, and oxides containing alloying elements.
- Addition of a suitable slag from a different process.

Development of the 'Inject plug' in the early 1980s revolutionized Si and FeSi refining, allowing ladles to tolerate high specific flowrates from a bottom mounted plug (Skei, 1991). The bubble column formed by purging gas through such a configuration creates a high contact area between the alloy, gas and produced slag, while also providing a high degree of mixing and intermixing, to ensure refining occurs throughout the whole vessel. This development made bottom mounted gas purging the most common refining

practice employed by industry today (Holta, 1995), even though top mounted lances are also available.

Typically, gas purging occurs in the ladle, either throughout the SAF tapping cycle and continuing for some time after, if necessary, or at a designated refining station, depending on the desired composition and other practical considerations, like equipment availability and logistics. Alloy temperatures are typically around 2000°C when tapped from the SAF, however, when the alloy reaches the ladle, it typically ranges between 1500 and 1700°C. The tapping process and ladle are illustrated in Figure 10.1.

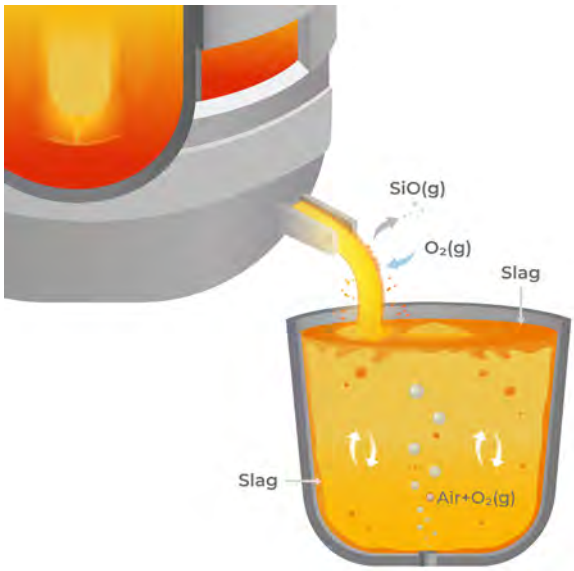


Figure 10.1 *Schematic of furnace tapping and oxidative bottom blowing in a refining ladle.*

Gas purging may be combined with the addition of slag-forming compounds such as limestone/burnt lime ($CaCO_3$/CaO) and silica sand. These may also act as oxidizing agents, and will be further discussed in Section 10.1.2. This addition is usually carried out by injection when a top mounted lance is used for gas purging, or by direct charging if a bottom mounted porous plug is used. The way the 'oxygen' is introduced affects the heat balance and the kinetics

of the refining process, as discussed in Sections 10.1.2 and 10.1.3. The oxidation reactions are exothermic, providing a way to increase/maintain the alloy temperature without the need for external heating of the ladle. However, to control the alloy temperature and maintain SiO_2 formation preferentially over SiO fuming (see reactions [10.1] to [10.3]), the alloy can be cooled by adding cooling metal. This cooling metal may consist of alloy fines, lower value alloys, etc., and allows the plant to recycle or upgrade production side streams.

The slag needs to be separated from the alloy during/before casting to avoid slag contamination of the alloy product. Density and viscosity differences between the two phases are therefore critical, as these determine the slag flowability and whether it sinks or floats on the alloy. In Chapter 4, it was shown that $CaO–Al_2O_3–SiO_2$ melts in general will float on liquid FeSi75, while for liquid Si, this varies for different slag compositions (Figure 4.15).

Fundamental reactions and element distribution equilibria

With the introduction of an oxidizing gas, typically oxygen-enriched air, Ca, Al and other impurities less noble than silicon are predominantly transferred to a slag phase created through reactions between the gas and melt. A small fraction of Ca and Al in the metal, along with other elements with high vapor pressures, such as Mg, K and Na, also report to the tapping/refining gas as oxide particulate matter (Næss *et al.*, 2013).

Bjørnstad described the initial nucleation and growth of slag droplets on gas bubbles from a bottom mounted plug (Bjørnstad and Tranell, 2021). Initially, as the gas bubbles ascend, the most abundant element, Si in the alloy, reacts with oxygen in the gas phase to form SiO_2 (liquid or solid) nuclei on the gas/metal interface, and SiO gas in the gas bubble, through equilibrium reactions 10.1 and 10.2. These nuclei serve as a starting point for further slag formation, thereby defining the oxygen potential at the slag/alloy interface. This allows the driving force for nucleation to be expressed as a local oversaturation of dissolved oxygen in the alloy. As the SiO_2 nuclei grow, Ca and Al will react, shifting the slag composition towards equilibrium with the alloy. Bjørnstad and Tranell (2021) also showed that the interfacial tension for a liquid slag on a gas substrate surrounded by a liquid Si alloy gives rise to individual slag nuclei, instead of a film, as illustrated in Figure 10.2.

The Gibbs energy functions for the reactions between the Si-alloy and gas [10.1–10.3] are valid from 1773 to 2273K (FACTSage 8.3):

$$2Si_{(l)} + O_{2(g)} = 2SiO_{(g)}\ \Delta G^{o}(J) = -326194 - 91.986T\ (K) \quad [10.1]$$

$$2Si_{(l)} + O_{2(g)} = 2SiO_{2((s,l)}\ \Delta G^{O}(J) = -938047 + 193.25T\ (K) \quad [10.2]$$

The formation of SiO_2 as a precursor to slag formation is sensitive to melt temperature and the oxygen partial pressure of the refining gas. Above a certain temperature, *Tcrit*, the SiO_2 product becomes unstable, and the only oxidized product becomes SiO gas (reaction 10.3). This does not facilitate refining, it only causes loss of silicon product to gas. Hence, cooling metal is used to control the metal temperature. *Tcrit* is dependent on, and increases with, the oxygen content of the gas, as illustrated by Figure 10.3.

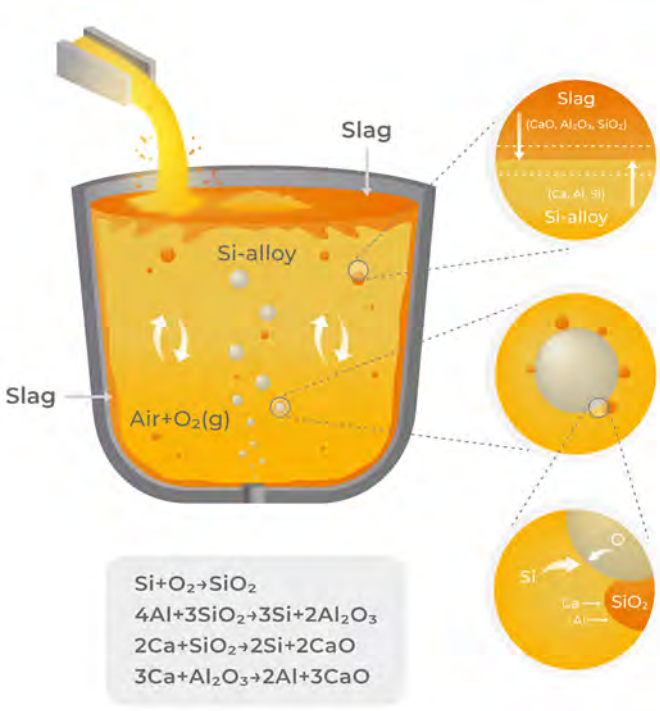


Figure 10.2 *Schematic representation of the metal/slag/gas interface.*

$$SiO_2(s,l) + Si(l) = 2\ SiO(g)\ \Delta G^{O}(J) = 611801 - 285.22T\ (K) \qquad [10.3]$$

The critical temperature, in degrees Celsius, can be expressed as a function of oxygen mole fraction in the gas mixture per mole of silicon, x, as shown below:

$$T_{crit} = \frac{71229}{33.2531 + 2ln(1+x) - 2ln(2x)} \qquad [10.4]$$

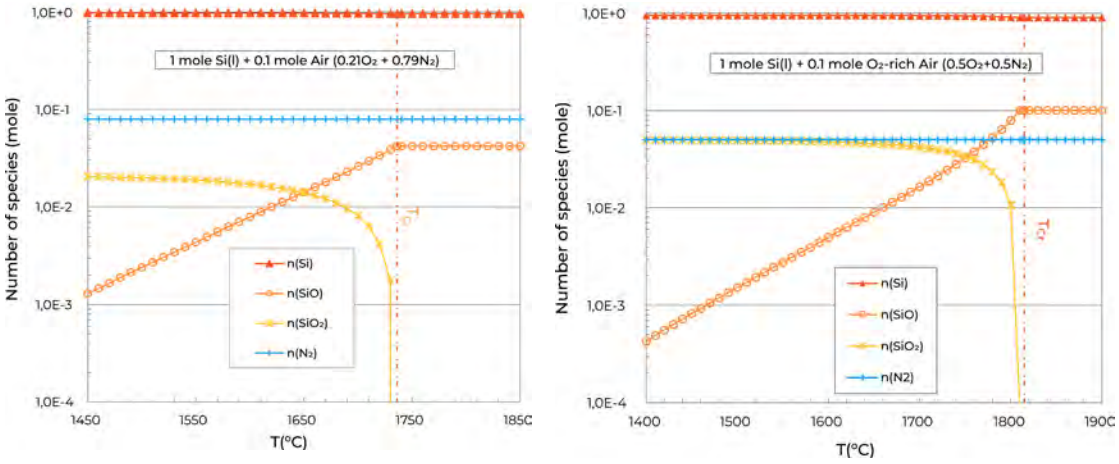


Figure 10.3 *The moles of SiO_2 and SiO respectively formed at different temperatures, calculated from reaction 10.4 for two examples of different gas compositions, assuming the activities of Si and SiO_2 are close to unity at the gas/metal interface.*

As the SiO_2 nucleus grows, it reacts with dissolved Ca, Al, and other impurities less noble than Si, according to reactions 10.5–10.7. This results in a SiO_2–CaO–Al_2O_3 slag droplet on the metal/gas interface. SiO_2 will continue to determine the slag's surface properties until the concentration of CaO and Al_2O_3 reaches a critical limit, because SiO_2 has greater surface activity than CaO and Al_2O_3. After reaching this critical limit, the slag droplet's surface properties become highly dependent on composition and determine whether it detaches or stays on the bubble surface.

$$\underline{Al}+\frac{3}{4}\left(SiO_2\right)=\frac{3}{4}\underline{Si}+\frac{1}{2}\left(Al_2O_3\right)\ \Delta G^O\left(J\right)=-81204-7.1097T\left(K\right) \quad [10.5]$$

$$\underline{Ca}+\frac{1}{2}\left(SiO_2\right)=\frac{1}{2}\underline{Si}+\left(CaO\right)\ \Delta G^O\left(J\right)=-95595-12.262T\left(K\right) \quad [10.6]$$

$$\underline{El}+\frac{y}{2x}\left(SiO_2\right)=\frac{y}{2x}\underline{Si}+\frac{1}{x}\left(El_xO_y\right) \quad [10.7]$$

For global slag-alloy equilibrium, the oxidation of various dissolved elements is mutually coupled through exchange reactions such as [10.8] for Ca and Al:

$$\underline{Al}+\frac{3}{2}\left(CaO\right)=\frac{3}{2}\underline{Ca}+\frac{1}{2}\left(Al_2O_3\right)\ \Delta G^O\left(J\right)=62189+11.283T\left(K\right) \quad [10.8]$$

Based on thermodynamic data, the calculated iso-concentration contours for calcium and aluminium in liquid Si and FeSi, in equilibrium with SiO_2–CaO–Al_2O_3 slags at 1550°C and 1600°C respectively, are illustrated in Figures 4.26–4.33. Deviations from the expected equilibrium may occur, in some cases resulting from slow reaction kinetics between solid inclusions and high viscosity slags, as discussed in Section 10.1.2. At low impurity levels, transport of impurity elements from the bulk alloy to the slag/alloy interface may be a rate-limiting step.

Equilibrium reaction paths

Earlier in this chapter we discussed the primary reactions taking place during refining processes, where impurities are oxidized and removed as part of a separate slag phase. This section expands on that discussion by considering how the liquid alloy composition changes to equilibrate with a slag, and how an equilibrium can be modified to reach a target composition. Figure 10.4 illustrates the isothermal map of the SiO_2–CaO–Al_2O_3 slag system. From this map, it becomes evident that relatively small changes in the ladle temperature may quickly affect the liquid slag composition through precipitation of solids, thereby also affecting the equilibrium alloy composition.

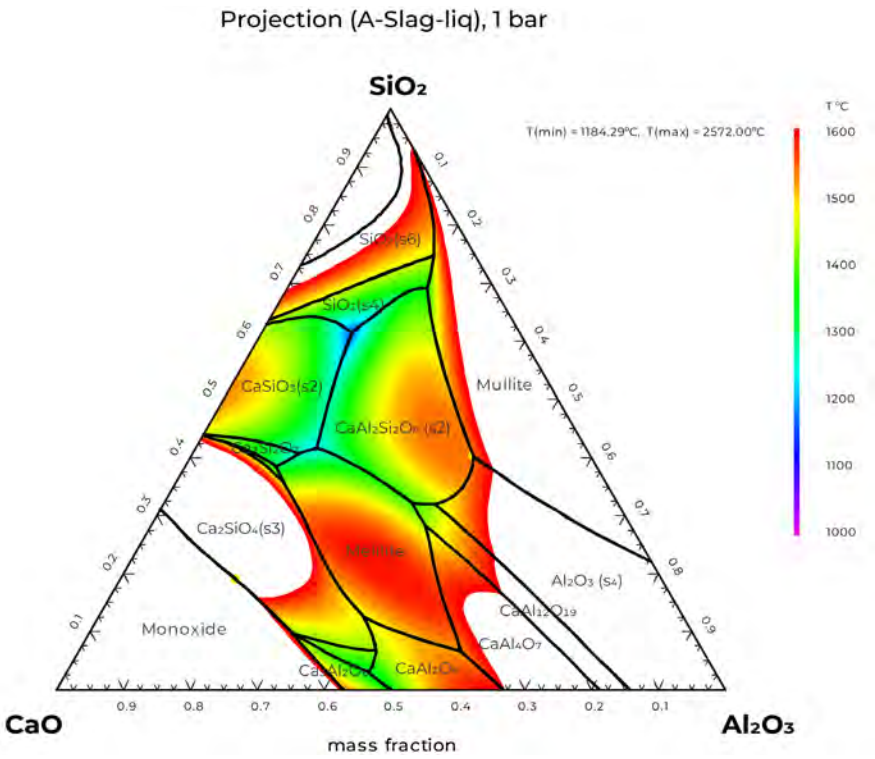


Figure 10.4 *SiO_2–CaO–Al_2O_3 slag liquidus projection drawn with FACTSage 8.3.*

Based on step-wise isothermal equilibrium calculations (Figure 10.5) and laboratory experiments by Bjørnstad *et al.*, we can first discuss what happens when a FeSi75 or MG–Si alloy is blown (isothermally) with an oxygen-bearing gas, without any initial tapped slag present or slag additives (CaO or SiO_2) (Bjørnstad *et al.*, 2022).

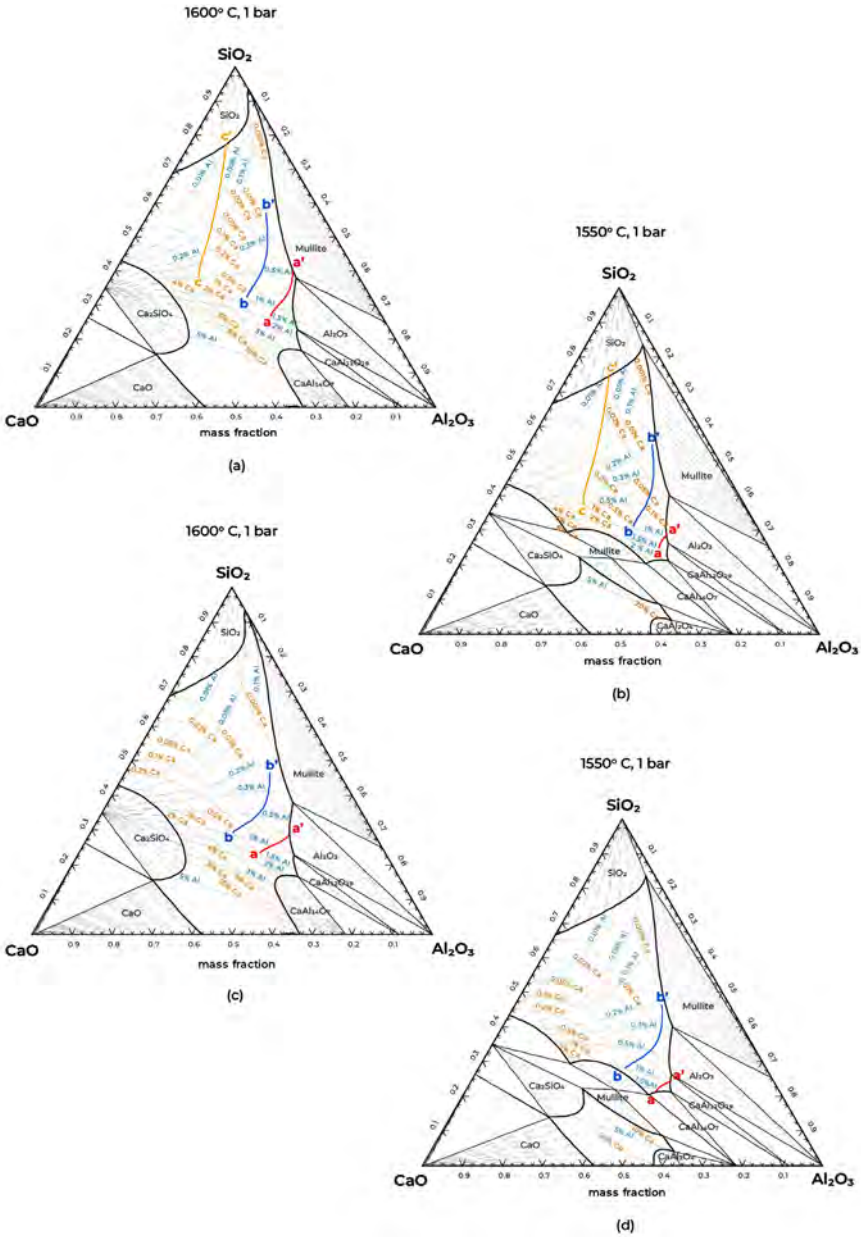


Figure 10.5 *Theoretically calculated alloy compositional paths (a-a´, b-b´, c-c´) for a) MG–Si alloy with different initial Ca and Al compositions at 1600°C, b) MG–Si alloy with different initial Ca and Al compositions at 1550°C, c) FeSi75 alloy with different initial Ca and Al compositions at 1600°C, d) FeSi alloy with different initial Ca and Al compositions at 1550°C.*

In Figure 10.5, iso-Al and iso–Ca contours were calculated using the FactSage software, with the commercial database FTOxid for the liquid slag phase and a private database for liquid Si–Al–Ca–Fe alloys, taking into account more accurate Ca-activity data at 1600°C and 1550°C respectively (Jakobsson and Tangstad, 2015). The figure illustrates oxidative refining of MG–Si, initially containing 1.5wt% Al and 0.5wt% Ca at point ***a***, 1wt% Al and 0.5wt% Ca at point ***b***, and 0.5wt% Al and 1wt% Ca at point ***c***, for both 1600°C and 1550°C. By introducing oxygen into the refining vessel, the compositions change along the curves ***a–a´***, ***b–b´,*** and ***c–c´*** respectively. For the FeSi75 case, the refining paths for the two starting compositions, 1.5wt% Al and 0.5wt% Ca at point ***a,*** and 1wt% Al and 0.5wt% Ca at point ***b***, are marked.

Due to the higher oxygen affinity/oxidation rate of Ca compared to Al, alloys with high initial Al:Ca ratios produce slag that becomes saturated with Al_2O_3 or mullite. This forms viscous alumina-rich slag and/or solid alumina-rich inclusions. Without additional quartz and lime in the refining vessel, this represents the practical refining limit[1]. This occurs more rapidly at lower temperatures, because the liquid slag region is smaller. Thus, if the initial calcium content is low and no fluxes are added, two different types of slag may form: a free-flowing, sinking type (due to its higher density) in the initial stage of the process, which tends to accumulate at the bottom of the reaction vessel, and a highly viscous and partly solidified type at the end, floating on top of the metal. The results align well with the laboratory measurement results by Bjørnstad *et al.* and illustrate that, regardless of the tapped alloy composition and temperature, the oxidation initially results in a CaO-rich slag and an increasingly Ca-depleted alloy (Bjørnstad *et al.*, 2022). For Ca:Al ratios ≥ 1, subsequent gas bubbles entering the bath form slags richer in SiO_2, with decreasing calcium-to-aluminium ratios. From the point where the alloy reaches a composition corresponding to the formation of solid slag/oxide, refining slows down, and the refining path transitions from refining by slag formation to refining by global slag equilibrium. This transition is critical for industrial production, because further gas purging alone to lower the aluminium concentration will result in product losses (i.e., excess oxidation

1 Thermodynamic calculations indicate further refining following the Al_2O_3/mullite–liquid phase boundary. While this is theoretically viable, the physico-chemical properties of the slag will not make this path practically possible.

of the Si-alloy). The problem is that the more slag is present in the ladle, the more slag must be generated to change its composition. Producing this slag and changing the refining path requires silica, resulting in an exponentially cumulative loss of silicon to silica formation if extra silica is not added to the ladle. This also agrees with observations made during unpublished industrial trials (described by Tuset, 1992).

Industrially, there are methods to modify the equilibrium and reaction route to alter the final alloy composition:

- making new/more slag or solid precipitates,
- changing global slag or alloy composition,
- changing the temperature.

Making new/more slag or solid precipitates

- If slag is physically removed, a new slag will form. With a lower availability of slag-forming impurities, the alloy will move towards a different equilibrium composition.
- Adding a slag will influence the equilibrium pull from the start, which, depending on alloy/slag composition, may differ from the equilibrium attained during initial oxidation of the alloy alone. This may unintentionally be the case when slag from the SAF is tapped together with the alloy into the ladle, as described by Folstad *et al.* (2023).

Figure 10.6 illustrates two simulated cases in which an Si alloy with the composition 1wt% Al and 0.5wt% Ca, or 0.5wt% Al and 1wt% Ca, is refined by air, or in which an initial amount of furnace slag is tapped together with the alloy. In the latter case, this initial slag is either 5wt% of the alloy weight (with composition 60wt% SiO_2, 25wt% CaO and 15wt% Al_2O_3) or 5wt% of the alloy weight (with composition 30wt% SiO_2, 35wt% CaO, 35wt% Al_2O_3). As illustrated by the graph, for the alloy tapped with a higher Al content, the tapped slag in both cases contributes to a refining path that reaches a more aluminium-lean alloy composition. In a case with a more calcium-rich tapped alloy, the tapped slag composition plays a more important role in determining the refining path.

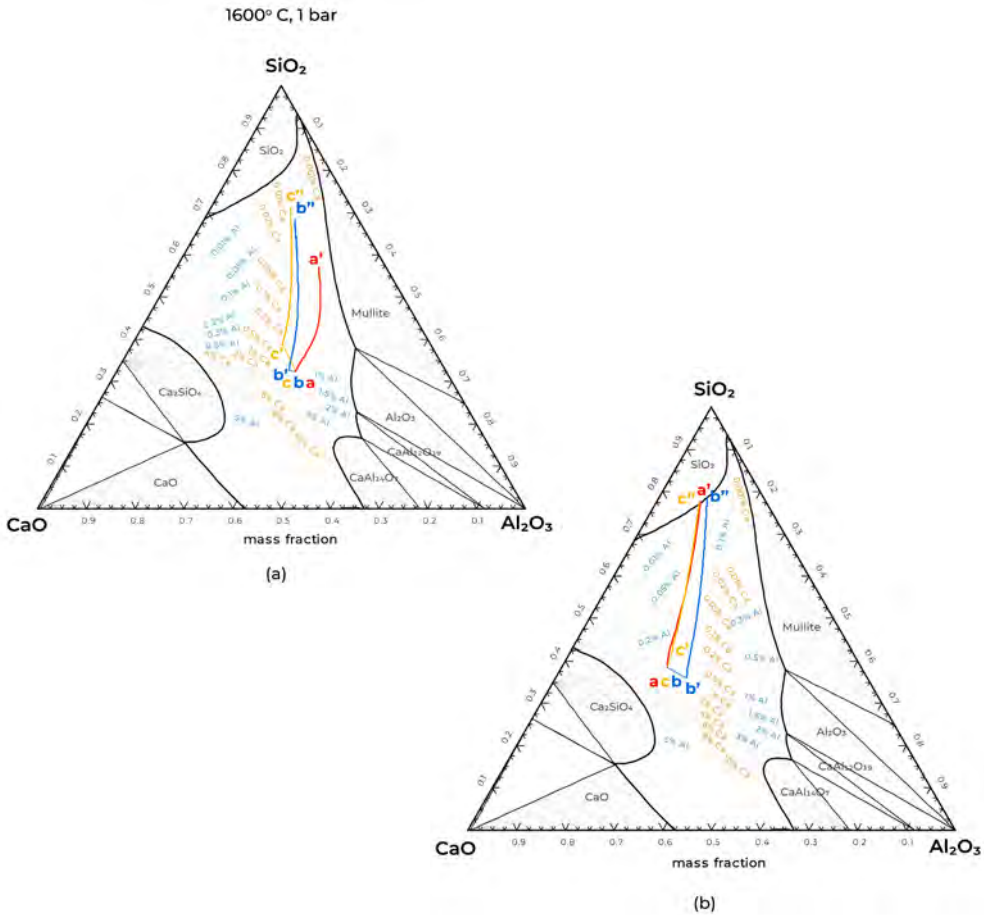


Figure 10.6 *(a) Simulated refining paths for a tapped Si alloy containing 1wt% Al and 0.5wt% Ca without furnace slag (a–a´), 5wt% furnace slag of initial alloy weight with composition 30wt% SiO_2, 35wt% CaO, 35wt% Al_2O_3 (b–b´–b"), or 5wt% furnace slag (c–c´–c") of initial alloy weight with composition 60wt% SiO_2, 25wt% CaO, 15wt% Al_2O_3. (b) Simulated refining paths for a tapped Si alloy containing 0.5wt% Al and 1wt% Ca without furnace slag (a–a´), 5wt% furnace slag of initial alloy weight with composition 30wt% SiO_2, 35wt% CaO, 35wt% Al_2O_3 (b–b´–b"), or 5wt% furnace slag (c–c´–c") of initial alloy weight with composition 60wt% SiO_2, 25wt% CaO, 15wt% Al_2O_3.*

Changing global slag or alloy composition

By strategically changing the availability of specific species at given times, one may shift to a more desirable reaction path or force a target equilibrium. One strategy for maintaining refining without excessive losses of silicon product is therefore to add both slag formers, such as limestone or burned lime, and silica in some form, to adjust the global slag composition. Recycled glass, containing around 70–75wt% SiO_2, 10–11wt% CaO and 13–14wt% Na_2O, has also been proposed as a low-cost material, but it brings some sodium into the metal (60–80 ppmw Na) and, if the glass contains lead oxide, may contaminate the metal with traces of lead (Haaland *et al.*, 1994). An example of an intended change in the alloy refining path is illustrated in Figure 10.7, which describes the difference between isothermal (1550°C) air-blowing and air-blowing + slag additives to FeSi75. The ***a-a'*** refining path is defined by air-purging (identical to Figure 10.4). The final metal phase consists of 0.9wt% Al and 0.1wt% Ca, whereas the slag consists of 24.5wt% SiO_2, 49.5wt% Al_2O_3 and 26wt% CaO. To further remove Al from the metal phase, slag additives (SiO_2 and CaO) are added. Assuming the final Al wt % to be 0.02wt% and Ca wt% to be 0.005wt%, addition of SiO_2 and CaO is required at the b" point of the above figure. The refining path is now represented by the ***b–b'–b"***. The final contents of metal are 0.02wt% Al and 0.005wt% Ca, and the slag consists of 66wt% SiO_2–16wt % Al_2O_3–18wt % CaO.

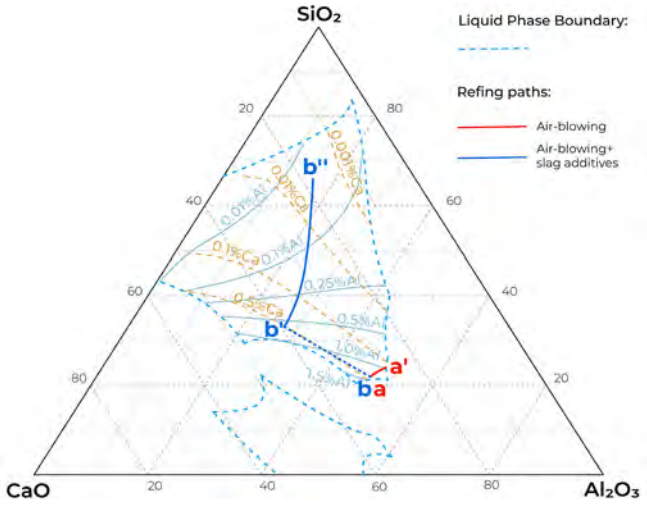


Figure 10.7 *Refining path for FeSi75 at 1550°C with air-blowing, with and without slag additives.*

While the global slag composition affects the final alloy composition, the interaction between slag and alloy may also be inhibited. This can affect the reaction path and kinetics by limiting the slag's equilibrium pull. This may be due to both limited slag/alloy contact area and other mass transport barriers, such as high viscosity or solid slag phases.

Changing the temperature

The alloy temperature will decrease if left alone, but insulation, external heating, and exothermic/endothermic reactions/phase changes will all affect the temperature in their own way. Temperature affects reaction kinetics, the phase of reaction constituents, reaction priority, and much more. Some aspects of the total heat balance will be further described in Section 10.1.3.

Mass and heat balance

We now look at the mass and energy balance for the FeSi case described in Section 10.1.2, following the refining line b–b'–b". Assuming the final Al% to be 0.02wt% at the b" point of the above figure, addition of SiO_2 and CaO is required, as outlined in the prior section. The refining path is now represented by the b–b'–b". The final contents of metal are 0.02wt% Al and 0.0005wt% Ca, and the slag consists of 66wt% SiO_2–16wt% Al_2O_3–18wt% CaO. A mass and energy balance model, using HSC Chemistry (illustrated in Figure 10.8), can be used to explain details about the refining process.

For the aluminium to be lowered from 1.5wt% to 0.02wt%, i.e. by Δ[% Al] = 1.48

A quantity of 14.8 kg Al per tonne of alloy corresponding to:

$$14.8 \cdot \frac{M_{Al_2O_3}}{2M_{Al}} = 14.8 \cdot 1.89 = 28 kg Al_2O_3 \qquad [10.9]$$

has to be transferred to a slag with ≤ 16wt% Al_2O_3.

This defines the minimum quantity of refining slag (Wr) required:

$$\frac{\Delta\left[\%Al\right] \cdot 1.89}{\left(\%Al_2O_3\right)_R} \cdot 1000 = 175 \frac{kg}{tonne} alloy \qquad [10.10]$$

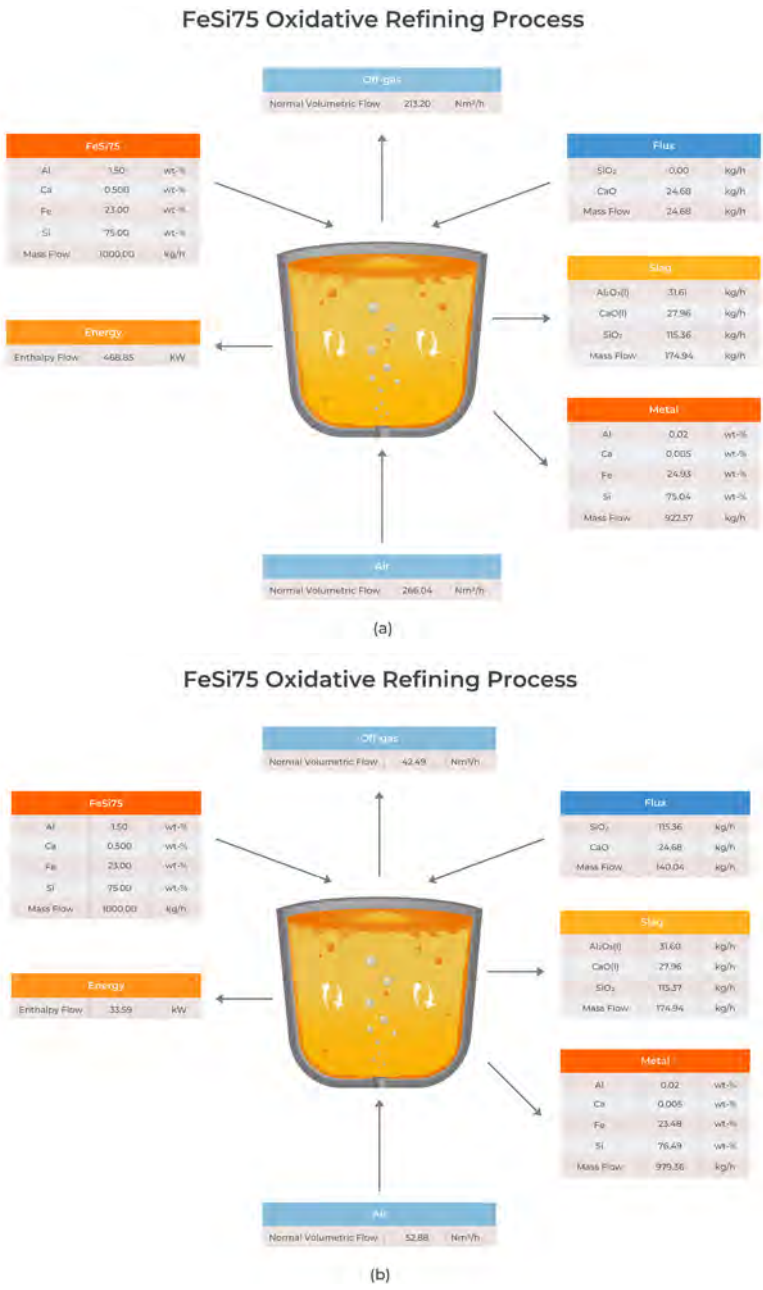


Figure 10.8 *HSC model parameters for FeSi refining model: (a) silica required for the formation of the final slag is produced 100% by oxidation of silicon; (b) silica required for the formation of the final slag is added totally as SiO_2 in the form of silica sand. The input T for the FeSi75 is 1550°C and the air and flux 25°C.*

If W_F kg of furnace slag with an alumina content of (wt% $Al_2O_3)_F$ enters the refining vessel, the total slag quantity needed increases by:

$$W_t = W_r + W_F \cdot \frac{(\%Al_2O_3)_F}{(\%Al_2O_3)_R} \qquad [10.11]$$

For $W_5 = O$, the material balance for our case will then be as given in Table 10.1.

Table 10.1 *Material balance for refining of FeSi75 as described in the text and given in kg/tonne alloy.*

Zero addition of silica (oxidation of Si, Al and Ca)											
Initial metal		**Flux**		**Air**		**Final metal**		**Final slag**		**Off-gas**	
Al	15	CaO	24.68	O_2	78.72	Al	0.20	Al_2O_3	27.96	N_2	259.24
Ca	5					Ca	0.05	CaO	31.61		
Fe	230			N_2	259.24	Fe	230	SiO_2	115.36	SiO	5.89
Si	750					Si	692.33				
Sum	1000		24.68		337.95		922.57		174.94		265.12
All the SiO_2 in slag added as silica (no oxidation of Si, only oxidation of Al and Ca)											
Initial metal		**Flux**		**Air**		**Final metal**		**Final slag**		**Off-gas**	
Al	15	CaO	24.68	O_2	15.65	Al	0.20	Al_2O_3	27.96	N_2	51.53
Ca	5					Ca	0.05	CaO	31.60		
Fe	230	SiO_2	115.36	N_2	51.53	Fe	230	SiO_2	115.37	SiO	1.39
Si	750					Si	749.11				
Sum	1000		140.04		67.17		979.36		174.94		52.92

As indicated in the table, the silica required for the formation of the final slag in Table 10.1 can be produced 100% by oxidation of silicon, or it can be added totally or partly as SiO_2 in the form of silica sand. The calculated heat effects associated with the two most extreme ways of supplying the silica are given in Table 10.2.

Table 10.2 *Energy balance for refining of FeSi75 as described in the text and given in kWh per tonne alloy.*

Species	Zero addition of silica		All the SiO_2 in slag added as silica	
	Input total enthalpy	Output total enthalpy	Input total enthalpy	Output total enthalpy
Al	8.82	0.12	8.82	0.12
Ca	2.12	0.02	2.12	0.02
Fe	83.60	83.60	83.60	83.60
Si	669.05	617.60	669.05	668.26
CaO	−77.62	−80.06	−77.60	−80.05
SiO_2		−424.58	−485.80	−424.59
O_2	0		0	
N_2	0	128.02	0	25.45
Al_2O_3		−105.78		−105.78
SiO		−1.83		−0.43
Surplus heat	468.85		33.59	

The calculations show that the oxidation of dissolved calcium and aluminium generates sufficient heat to keep the temperature theoretically constant at 1550°C, even if all the silica is added as SiO_2. In this case, however, there is almost no surplus heat available to cover the heat losses. There will also be a heat deficit if air is used instead of oxygen for blowing. This is seen from Figure 10.9, which shows the effect of a mixed supply of silica and SiO_2 produced by oxidation of Si, using oxygen or air.

$$Ca(l) \rightarrow Ca_{(1\%\ in\ Si(l))} \Delta\bar{H}^{O}_{Ca} = -191.3 \frac{kj}{mole} \quad [10.12]$$

$$Al(l) \rightarrow Al_{(1\%\ in\ Si(l))} \Delta\bar{H}^{O}_{Al} = -116.8 \frac{kj}{mole} \quad [10.13]$$

$$Si(l) \rightarrow \underline{Si}_{(in\ FeSi75(l))} \Delta\bar{H}^{O}_{Si} = -308 \frac{kj}{mole} \quad [10.14]$$

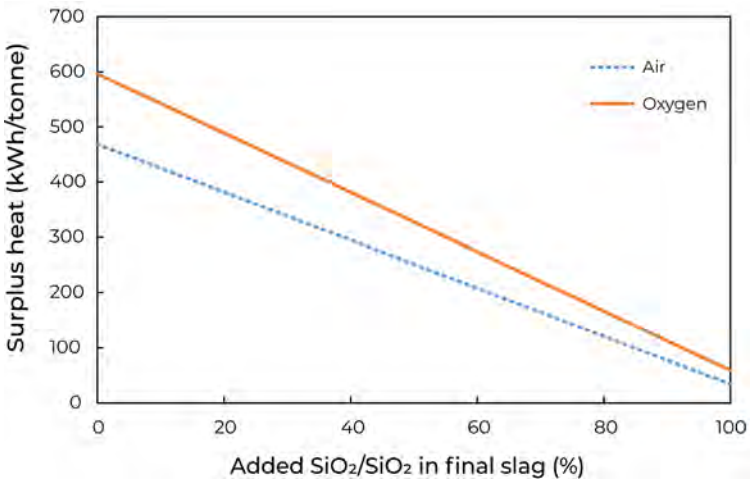


Figure 10.9 *Calculated heat effect vs the relative amount of SiO_2 in the final slag added as silica during ferrosilicon refining at 1550°C.*

Table 10.3 summarizes the heat losses related to oxidative ladle refining of silicon and ferrosilicon.

Table 10.3 *Summary of data on heat losses related to oxidative ladle refining at 1550°C from a ladle lined with ordinary fireclay bricks according to Christensen (1988).*

Heat loss source	kW/m^2
Ladle walls and bottom (275°C)	7
Ladle cover (230°C)	4.5
Radiation losses from a partly slag-covered ferrosilicon surface during tapping	115–180
Radiation losses from empty ladle after pouring	130

Oxygen and carbon in refined metal

Oxygen and carbon in refined liquid metal are present both as dissolved elements and as suspended phases: slag droplets, crusty aluminium silicates, or silica films in the case of oxygen, and silicon carbide particles in the case of

carbon. As the solubility of oxygen and carbon decreases to a few ppm when the metal solidifies, these elements appear in solidified metal almost entirely as oxide and carbide inclusions, respectively, as discussed in Chapter 4. Thus, the lowest concentrations that can be reached for oxygen and carbon in bulk metal refining are determined by their solubility in the liquid metal at the casting temperature.

Studies show that the actual oxygen and carbon content in refined metal is much higher than their reported solubilities. This is particularly true for oxygen in silicon, where the conditions for phase separation are extremely unfavorable. Laroze investigated representative samples of silicon that had been refined and cast in various ways and found that the oxygen content varied between 0.04 and 0.70 wt% O (Laroze, 1994). The same absolute level and variation in oxygen has also been reported by others (Forwald *et al.*, 1994). This is an issue when producing alloys for methyl-chlorosilane production, as the reactivity and selectivity of the feed is highly dependent on the type and distribution of intermetallic phases. These phases form during the solidification process and rely on a given balance between metallic constituents such as Ca, Al and Fe. If oxygen is present in the metal, unknown fractions of Ca and Al are tied up in oxide inclusions that behave as inert constituents in the direct process (Forwald *et al.*, 1994). Analytical methods such as atomic absorption or x-ray fluorescence spectroscopy do not distinguish between elements that are present as oxides and those present as intermetallics, with Eie *et al.* suggesting that the amount of active intermetallics in silicon can be derived on the basis of results from leaching tests (Eie *et al.*, 1998).

In order to minimize the oxygen content, the refining process should be carried out in a way that prevents crusty silica- or alumina-rich films from forming initially by:

- Maintaining a reservoir of calcium in the system by the addition of CaO or CaO-containing silicates
- Activating the fluid bottom layer of slag throughout the entire purging process
- Avoiding 'over-oxidation' at the termination of the refining process
- Preventing gas bubbles from collapsing by adding an inert component to the oxygen, i.e., by using air especially at the end of the blow.

Specifications of carbon in refined products have up to now been stricter for producers of ferrosilicon than for metallurgical grade silicon, due to requirements from demanding customers within certain sectors of the steel industry, e.g., producers of silicon-alloyed steel sheets for electrotechnical applications, and some stainless steel producers which specify <200 ppmw C in FeSi75. Thus, the carbon problem has been more actively addressed by producers of ferrosilicon than by those of silicon. The extensive studies of Klevan are a reflection of this (Klevan, 1997). According to Klevan's work, when the metal is tapped from the furnace it contains 700–1100 ppmw C, which corresponds closely to the solubility at the metal forming temperature in the hearth of the furnace. When this metal is delivered as standard lumpy FeSi75 after casting, crushing and screening, a statistical treatment of the analyses of 779 shipments from one plant over a three-year period shows that the carbon content has dropped to an average of 300 ppmw C (Klevan, 1997). The average figures for ferrosilicon delivered as water granulated or refined qualities during the same period were 210 and 120 ppmw C, respectively. This implies that the carbon, which precipitates as SiC particles as the temperature drops during tapping and handling, is physically removed as particles to a fairly large extent. While there is a large variation between reported solubilities of carbon in silicon, the work by Dalaker and Tangstad determined the carbon content as a function of temperature as: $C_C = 839.4 \cdot \exp(-19856/T)$, giving a solubility of 65 ppmw at the silicon melting point of 1414°C (Dalaker and Tangstad, 2009).

10.2 Refining by Chlorination

The use of various types of halides for purification of metallurgical grade silicon in its liquid state has been studied because of their potential use in solar grade silicon production (Hunt *et al.*, 1976). This text focuses on the use of chlorine only, as this is the only type of halide that is used commercially and is, in addition, the one that has been found most effective on elements like calcium and aluminium. For other impurities that are present, the average percentage removal obtained from 20 experiments has been summarized by Hunt *et al.* (1976) as follows:

0%	for Fe, Ni, Ti, and V
20–50%	for Cr, Cu, and Mn
10%	for P
40%	for B (not reproduced in more recent experiments)

When Cl_2 is introduced as bubbles rising through pure liquid Si, it reacts to form gaseous silicon chlorides. $SiCl_4$, $SiCl_3$ and $SiCl_2$ are the main components formed at a total pressure of 1 bar. SiCl forms in minor amounts and, together with Cl_2, can be neglected as a constituent of the gas phase. If calcium is present at low concentrations, gaseous $CaCl_2$ and negligible amounts of CaCl(g) are formed, as seen from a reaction of the following type:

$$SiCl_4(g) + 2\,\underline{Ca} = Si(l) + 2\,CaCl_2(g) \qquad [10.15]$$

Here, $SiCl_4(g)$ enters with the partial pressure as given by the equilibria between Si(l) and Cl_2 at P_{total} = 1 bar. $CaCl_2$ melts at 771.85°C, boils at 1934.77°C, and has a vapour pressure of 0.018 bar at 1423°C. The partial pressure of $CaCl_2$, as calculated for reaction [10.15], will reach this value for $a_{Ca} = 1.14 \cdot 10^{-10}$ at 1423°C. The concentration of calcium corresponding to this activity is 2 ppmw Ca if $\gamma_{Ca} = 1 \cdot 10^{-4}$ is used as an appropriate activity coefficient for calcium in silicon at 1423°C. The same calculations carried out for 1523°C give 10 ppmw Ca as the equilibrium concentration of calcium in the presence of liquid $CaCl_2$.

The Al removal by chlorinating reactions is shown in Figure 10.10. The chlorination refining process is more efficient than the oxidation refining process for Al and Ca removal, and for the recovery rate of the metal (Figure 10.11).

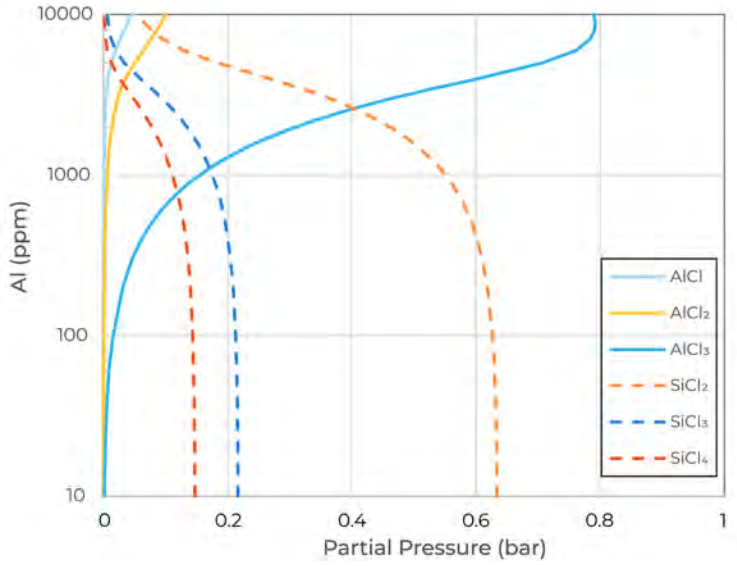


Figure 10.10 *Calculated equilibrium gas compositions over liquid silicon containing various concentrations of Al in the presence of Cl_2 at 1423°C and $P_{Total} \approx \Sigma p_{MeCl2} = 1$ bar.*

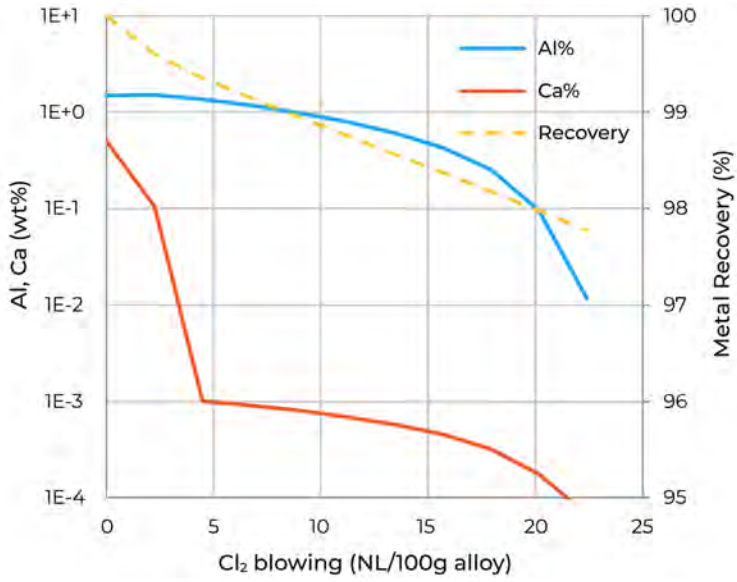


Figure 10.11 *Calculated metal recovery and resulting Al and Ca concentrations in a Cl_2 refined Si at 1423°C.*

Aluminium forms a variety of chlorides, all of which are in the gaseous state above 180°C. Of these, $AlCl_3$ and $AlCl_2$ appear to be the most stable at temperatures around 1400°C. Both components are more stable than the chlorides of silicon. Thus, when liquid Si containing Al is treated with Cl_2, the chlorine is converted almost selectively into gaseous $AlCl_3$ and $AlCl_2$ at high concentrations of Al. At low contents of Al, the chlorides of Si become the dominating gas components. This is also seen from Figure 10.10, which shows how the calculated equilibrium composition of the gas phase varies with the Al concentration at 1423°C and a total pressure of 1 bar. In these calculations $\gamma_{Al}^{O} = 0.1$ has been used. Liquid silicon will be refined for Al as long as the Al/Si ratio in the gas phase is greater than the Al/Si ratio of the metal phase. According to the data used in these calculations, these two ratios become equal at 2.3 ppmw Al. This concentration represents the theoretical purification limit if the chlorination is conducted at 1423°C and $P_{total} = 1$ bar, provided that pure Cl_2 is used as the chlorinating agent.

If a mixture of Cl_2 and Ar is used, the purification limit will be even lower, and the calculations will predict a lower limit if a larger and more realistic γ_{Al}^{O} value is used. In the initial stage, when silicon containing both calcium and aluminium is treated with Cl_2, nearly all supplied Cl_2 will be consumed by Ca to form liquid $CaCl_2$. As the Ca concentration decreases, a gas phase of atmospheric pressure forms, and Al starts to react together with some silicon. The composition of the gas phase will then change with the decreasing Al concentration, as indicated in Figure 10.11. In addition to the components given, the gas will also be saturated by $CaCl_2(g)$ as long as $CaCl_2(l)$ is present. In this period, the Ca concentration in the metal levels off at the limits given, but it will continue to decrease as soon as the liquid chloride phase disappears due to evaporation. The advantage of using an Ar/Cl_2 mixture with a low content of chlorine during the evaporation stage is hence clear.

10.3 Refining towards Solar Grade Material

While MG–Si specifications vary according to its application, the purity demand on solar grade silicon (SoG-Si) is substantially stricter and is generally obtained through chemical purification. Table 10.4, adopted from the review paper of Hosseinpour and Tafaghodi Khajavi, summarizes literature

data of elemental specifications for different silicon grades (Hosseinpour and Tafaghodi Khajavi, 2018a). With the development towards high-efficiency cells based on single-crystal silicon materials, purity is often even more stringent than those described below.

Table 10.4 *Impurity specifications for different silicon grades. (Adapted from Hosseinpour and Tafaghodi Khajavi, 2018a).*

Impurity content (ppm)			
Impurity	Solar grade silicon (Baba *et al.*, 2000; Dietl and Wohlschlager, 1981; Hunt, 1984; Parisi *et al.*, 1980)	Metallurgical grade silicon (98–99%) (Bathey and Cretella, 1982; Chu *et al.*, 1978; Dietl, 1983)	99.5% (Baba *et al.*, 2000; Hunt, 1984; Kapur and Choudary, 1983)
Al	< 0.1	1000–4000	50–600
Fe	< 0.1	1500–6000	100–1200
Ca	< 1	250–2200	100–300
Mg	< 1	100–400	50–70
Mn	<< 1	100–400	50–100
Cr	<< 1	30–300	20–50
Ti	<< 1	30–300	10–50
V	<< 1	50–250	< 10
Zr	<< 1	20–40	< 10
Cu	< 1	20–40	< 10
B	0.1–1.5	10–50	10–15
P	0.1–1	20–40	10–20
C	0.5–5	1000–3000	50–100

With the rapidly growing Si-based photovoltaic market, great efforts have been made – particularly during the past two decades – to establish alternative metallurgical methods to the Siemens-based chemical route for removing critical elements to these low levels (Chigondo, 2018; Safarian *et al.*, 2012). While effective removal of metallic impurities, and to some extent carbon/nitrogen as solid SiC/Si_3N_4 particles, may be obtained via, for example, directional solidification, the solid–liquid segregation of neither boron nor phosphorus makes this a viable direct method for removing such impurities.

In the following sections, metallurgical techniques for the removal of carbon, metallic impurities, boron and phosphorus are described.

Removal of carbon

Several investigators have contributed to carbon removal, and the methods employed have been: settling combined with directional crystallization (Aulich *et al.*, 1986; Mühlbauer *et al.*, 1991), filtration combined with oxidation (Sakaguchi and Maeda, 1992), decarburization by inert gas purging or under vacuum (Klevan, 1997; Sakaguchi and Maeda, 1992) and the use of plasma (Thomas *et al.*, 1992) or electron beam melting techniques (Ikeda and Maeda, 1992). In contrast to ferrosilicon, the removal of suspended SiC particles in silicon by settling is found to be effective. The settling rate in a quiet bath of silicon is given by Stokes's equation:

$$v = \frac{d^2 g}{18\eta}\left(\rho_1 - \rho_2\right) \qquad [10.16]$$

where g is the acceleration of gravity; d is the diameter of a SiC particle; η is the viscosity of silicon ($0.8 \cdot 10^{-3}$ Ns/m^2 at 1450°C); and ρ_1 and ρ_2 are the densities of SiC (3200) and Si (2517 kg/m^3 at 1450°C), respectively. This can be exemplified by calculating that SiC particles larger than 10 μm in diameter will settle to the bottom of a 10 cm deep layer of silicon in 30 minutes. This has been utilized in the purification methods employed by Aulich *et al.* on silicon produced by carbothermic reduction from high purity raw materials (Aulich *et al.*, 1986). The metal was tapped at 1750°C into high purity molds and allowed to cool slowly to 1450°C, where it was kept for a certain period of time before the mold was cooled from the bottom in order to achieve unidirectional solidification. The remaining SiC particles were then pushed ahead of the solidification front and became concentrated in the top layer of the ingot. After cutting away the top and bottom layers, the metal was found to contain 5 ppmw C.

An alternative treatment of high purity silicon produced by carbothermic reduction was presented by Ciftja (2009) and Sakaguchi and Maeda (1992). They claim that suspended SiC particles are effectively removed by filtration through a packed bed of spherical particles of silica. A further decrease in

carbon is achieved in a subsequent treatment, where the metal is decarburized by flushing and stirring with argon in the presence of silica. Under optimal conditions, the decarburization rate will then be controlled by the reaction pressure of CO, as defined by the equilibrium:

$$\underline{C} + \frac{1}{2}SiO_2(s) = \frac{1}{2}Si(l) + CO(g) \qquad [10.17]$$

With

$$K_{10.17} = \left(\frac{a_{Si}}{a_{SiO_2}}\right)^{\frac{1}{2}} \frac{P_{CO}}{a_C^1} = exp\left(-\frac{36558}{T} + 19.5\right) \qquad [10.18]$$

where the activities of Si and SiO_2 can both be assumed as unity, and the activity of C, which refers to a 1% solution as the standard state, can be replaced by [% C]. Inserting T = 1773 K (1500°C) and [% C] = 0.005 (50 ppmw C) in the expression for K, we arrive at: $P_{CO} = 0.32 \cdot 0.005 = 1.5$ mbar as a maximum value for the reaction pressure of CO. The decarburization process is therefore expected to be slow, and dependent on the specific flow rate of argon, as also experienced by (Sakaguchi and Maeda, 1992). In their experiments, they used between 4–6 hours to reach 10 ppmw C from the initial 50 ppmw. Klevan developed a mathematical model that describes the kinetics of the decarburization process in detail when using inert gas purging (Klevan, 1997). When this model was tested on experimental data in which metallurgical-grade silicon was purged with a mixture of argon and oxygen, it became clear that the overall decarburization rate was controlled by the mass transfer coefficient of carbon at the metal/gas interface. The obvious reason for this was the formation of a dense silica/slag layer at the interface, which slows down the diffusion rate of CO.

Removal of (metal) impurities by directional solidification

The crystal structure of silicon means that the solid solubility of most elements is very limited compared to their liquid solubility in silicon. Table 10.5 lists the solid solubility of selected elements in Si.

Table 10.5 *Solid solubilities of selected elements in silicon, reproduced from (Møll, 2014).*

Atom	Maximum Solid Solubility (at/cm^{-3})	Reference	Atom	Maximum Solid Solubility (at/cm^{-3})	Reference
Al	$2.0 \cdot 10^{19}$	(Trumbore, 1960)	N	$4.5 \cdot 10^{15}$	(Hull, 1999)
B	$6.0 \cdot 10^{20}$	(Trumbore, 1960)	Ni	$8.0 \cdot 10^{17}$	(Hull, 1999)
C	$3.0 \cdot 10^{17}$	(Hull, 1999)	O	$3.0 \cdot 10^{18}$	(Hull, 1999)
Cu	$1.5 \cdot 10^{18}$	(Trumbore, 1960)	P	$1.3 \cdot 10^{21}$	(Hull, 1999)
Fe	$3.0 \cdot 10^{16}$	(Trumbore, 1960)	Sn	$5.0 \cdot 10^{19}$	(Trumbore, 1960)
Mn	$3.0 \cdot 10^{16}$	(Trumbore, 1960)	Zn	$6.0 \cdot 10^{16}$	(Trumbore, 1960)

Hence, as liquid silicon containing impurities starts to solidify, an almost pure silicon phase will form first, enriching the liquid in impurities. This mechanism is purposefully used to refine silicon in controlled crystallization processes such as Bridgman directional solidification, illustrated in Figure 10.12. In such a process, heat is slowly extracted from molten silicon from the bottom of the crucible, maintaining an equilibrium surface between the solidified and molten solvent (Si). Assuming that the bulk concentration of the solute in the liquid is homogeneous and that there is no back-diffusion from the solid to the liquid, the distribution of the solute between solid and liquid Si can be expressed by the equilibrium distribution coefficient k, defined as:

$$k = \frac{C_S}{C_L} \qquad [10.19]$$

where C_S and C_L are the solid and liquid concentrations of the solute at the solid–liquid interface. k values for selected elements are listed in Table 10.6. As seen from the table, the segregation coefficient for most metals is very low, while those for B and P are relatively high.

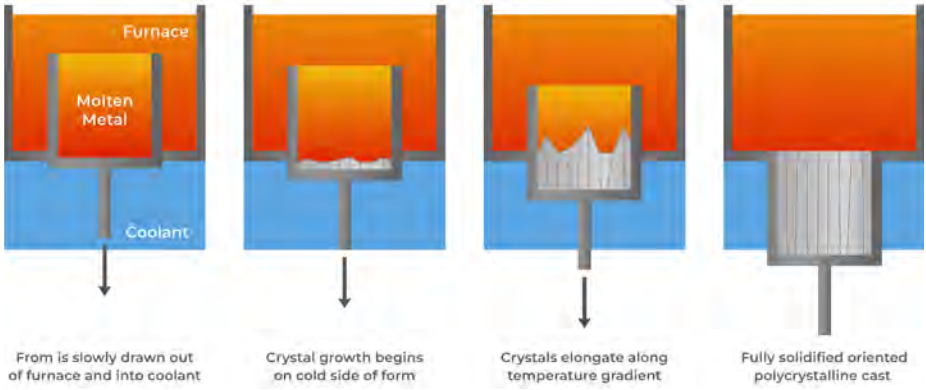


Figure 10.12 *Illustration of the directional solidification process.*

Table 10.6 *Equilibrium solid–liquid distribution coefficients for selected solutes in silicon.*

Impurity	Segregation coefficient	Impurity	Segregation coefficient
B	0.80	Fe	$6.4 \cdot 10^{-6}$
P	0.35	Ti	$2.0 \cdot 10^{-6}$
C	$5.0 \cdot 10^{-2}$	Cu	$8.0 \cdot 10^{-4}$
Al	$2.8 \cdot 10^{-3}$	Mg	$3.2 \cdot 10^{-6}$
Li	$1.0 \cdot 10^{-2}$	S	$1.0 \cdot 10^{-5}$
Ag	$1.0 \cdot 10^{-6}$	As	$3.0 \cdot 10^{-1}$
Au	$2.5 \cdot 10^{-5}$	Sb	$2.3 \cdot 10^{-2}$
Ni	$1.0 \cdot 10^{-4}$	Zn	$1.0 \cdot 10^{-5}$
Ca	$8.0 \cdot 10^{-3}$	Bi	$7.0 \cdot 10^{-4}$
Mn	$4.5 \cdot 10^{-3}$	Cr	$1.1 \cdot 10^{-5}$

For a starting concentration C_0 of the solute, the mass balance of the system can be expressed as:

$$C_S f_S + C_L f_L = C_0 \qquad [10.20]$$

Where f_S and f_L are the fractions solid and liquid, respectively.

By rearranging equations 10.19 and 10.20 into the so-called Gulliver-Scheil equation, we can describe the concentration of solute in a given fraction of solid material:

$$C_S = kC_0(1 - f_S)^{k-1} \quad [10.21]$$

Because of the exponential increase in solute concentration in the last solidifying part of the material, this part (typically around 10% of the weight) can be removed from the solidified ingot if this technique is used for refining purposes.

While the assumption of negligible back-diffusion from the solid to the liquid during solidification is valid for most elements, there are exceptions, such as Fe and Cu. Several authors have experimentally documented significant (back) diffusion of iron from intrinsic and extrinsic (e.g. from the crucible) sources during solidification of both multicrystalline and single-crystal silicon (Kvande *et al.*, 2008; Wen *et al.*, 2024). The degree of iron diffusion during different cooling rates has been modelled by Boulfrad (2012), as shown in Figure 10.13.

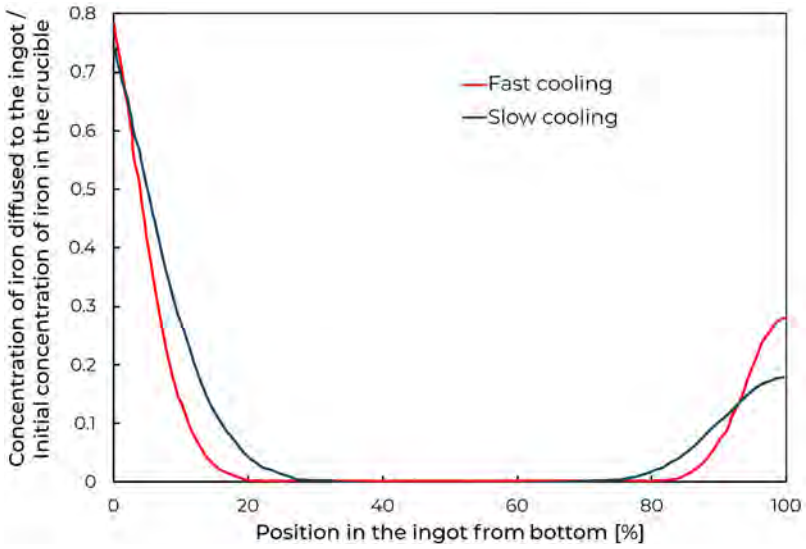


Figure 10.13 *Modelled content/diffusion of iron contained in feedstock and crucible as a function of ingot height during directional solidification. (Updated from figure in (Boulfrad, 2012)).*

Removal of boron

Boron has nearly the same affinity towards oxygen as silicon and forms gaseous suboxides such as BO, an analogue to SiO. Its condensed stable oxide (B_2O_3) behaves, like SiO_2, as an acid in the presence of alkali and alkaline earth metal oxides at slag-forming temperatures. From this starting point, oxidative refining of boron may seem challenging. However, considerable industrial and scientific efforts have been placed on developing methods to remove boron, either as a constituent of a slag or in the form of a gaseous suboxide at elevated temperatures.

Slag refining

The transfer of boron to the slag phase can be described as a two-step reaction: oxidation at the metal-slag interface, followed by dissolution of the oxide into the ionic slag liquid, according to:

$$B + \frac{3}{4}O_2 = \frac{1}{2}B_2O_3 \qquad [10.22]$$

$$\frac{1}{2}B_2O_3 + \frac{3}{2}O^{2-} = \left(BO_3^{3-}\right) \qquad [10.23]$$

The overall boron equilibria / transfer can hence be expressed by:

$$B + \frac{3}{4}O_2 + \frac{3}{2}O^{2-} = \left(BO_3^{3-}\right) \qquad [10.24]$$

However, because the distribution between boron in metal and slag is coupled to the Si/SiO_2 equilibrium, the generic reaction is often expressed as:

$$\underline{B} + \frac{3}{4}\left(SiO_2\right) = \left(BO_{1.5}\right) + \frac{3}{4}\underline{Si} \qquad [10.25]$$

The equilibrium constant K for [10.25] will hence be described by:

$$K = \frac{\left(a_{Si}^{Si\ alloy}\right)^{3/4}}{a_B^{Si\ alloy}} \cdot \frac{a_{BO_{1.5}}^{slag}}{\left(a_{SiO_2}^{slag}\right)^{\frac{3}{4}}} = \frac{\left(a_{Si}^{Si\ alloy}\right)^{3/4}}{\left(a_{SiO_2}^{slag}\right)^{\frac{3}{4}}} \cdot \frac{\left(x_{BO_{1.5}}^{Slag}\right)}{x_B^{Si\ alloy}} \cdot \frac{\gamma_{BO_{1.5}}^{slag}}{\gamma_B^{Si\ alloy}} \qquad [10.26]$$

Data for the Henrian activity coefficient for boron in pure silicon are illustrated as a function of temperature in Figure 10.14.

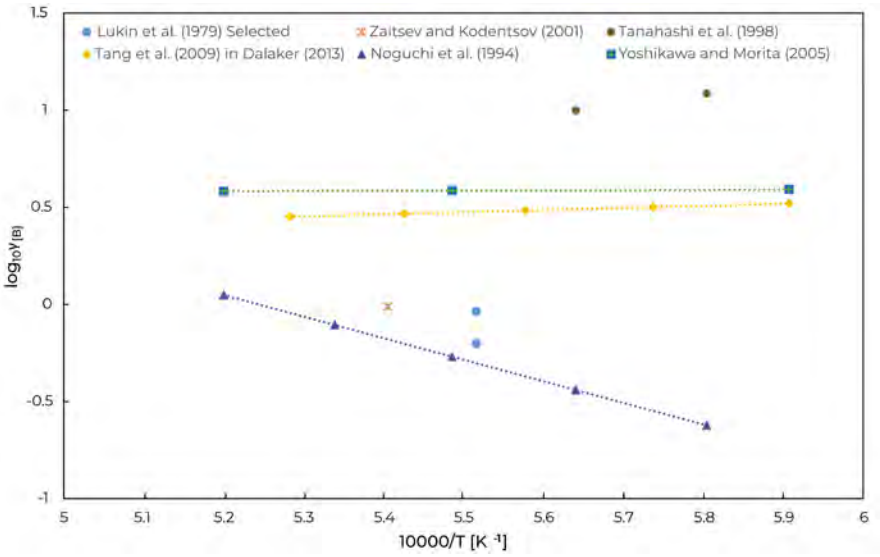


Figure 10.14 *The Henrian activity coefficient of dissolved boron in silicon (Dalaker, 2013; Lukin et al., 1979; Morita, 2005; Noguchi, 1994; Tanahashi et al., 1998; Tang et al., 2009; Zaitsev and Kodentsov, 2001).*

While the positive deviation from ideality, found by most researchers, works in favor of slag refining of B, more complex thermodynamic data are often sparse. Hence, an experimentally determined metal slag distribution coefficient, L_B, as expressed by [10.27], is often used to evaluate the refining efficiency of the system:

$$L_B = \frac{\left(wt\%B\right)\ in\ slag}{\left[wt\%B\right]\ in\ silicon} \qquad [10.27]$$

A large number of researchers, as summarized in Table C-1 in Appendix C, have investigated the boron distribution between slag and silicon for a number of slag systems. Selected experimental data are illustrated in Figure 10.15.

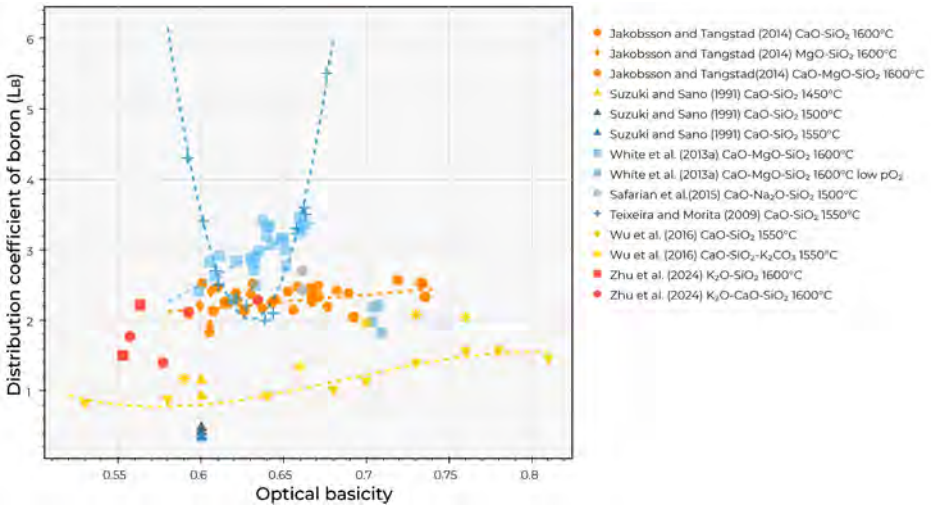


Figure 10.15 *LB values for selected slag systems in equilibrium with silicon (Jakobsson and Tangstad, 2014; Safarian et al., 2015; Suzuki and Sano, 1991; Teixeira and Morita, 2009; White et al., 2013a; Wu et al., 2016; Zhu et al., 2024).*

As seen by the figure, typical L_B values are concentrated around 2 for CaO–SiO_2-based slag systems. As such, the reported distribution coefficients render slag refining rather weak for boron unless very large volumes of slag are used in a batch process, or it is implemented in a process where metal and slag are equilibrated in a stepwise counter-current flow pattern. Nevertheless, slag refining was successfully implemented industrially by Elkem Solar, resulting in silicon with boron concentrations as low as 0.23 ppmw (Søiland *et al.*, 2014). In systems where one of the slag compounds is volatile, such as Na_2O in the Na_2O–CaO–SiO_2 system, additional boron removal via volatilization may also be involved. Such systems are, however, not very practical for industrial implementation.

Solvent refining and combinatory slag/solvent refining

Similarly to the acid leaching method described in Section 10.3.5, the basic principle of solvent refining is to adjust the impurity segregation behavior during Si solidification via alloying. The solvent element is cho-

sen to retain impurities to a higher degree than silicon and to create a low temperature melting point system with silicon. During cooling, primary Si is first precipitated, and the impurities continuously enrich the remaining liquid phase until it is fully solid. The Si crystals may subsequently be purified by acid washing, and the remaining binary alloy can be used for other applications.

The Si–Al melt is the most studied solvent refining system, first reported by Obinata and Komatsu, 1957. The segregation behavior of both P and B in the Si–Al melt was later investigated by Yoshikawa and Morita, 2003, 2005. It was found that both segregation coefficients decrease with decreasing temperature, as illustrated for B in Figure 10.16. With Ti addition into the Si–Al melt, B can be effectively removed due to the formation of TiB_2 precipitates. In addition to the Si–Al system, a number of other solvent refining systems have been developed with good purification performance, such as Si–Sn (Hu *et al.*, 2013), Si–Fe (Hosseinpour and Tafaghodi Khajavi, 2018, 2019) and Si–Cu (Huang *et al.*, 2016).

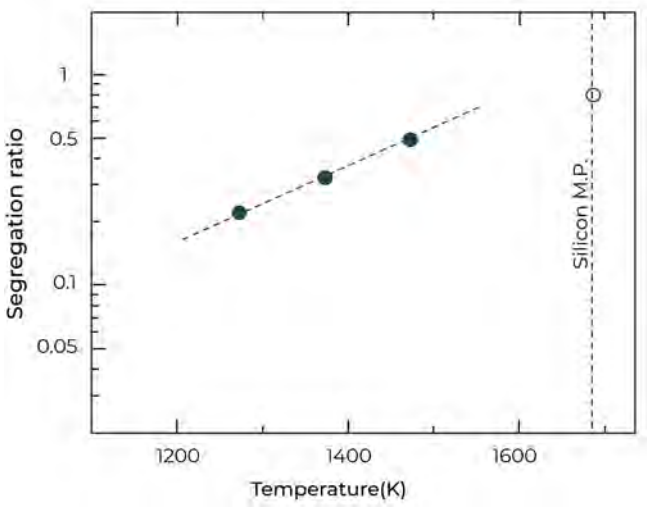


Figure 10.16 *Temperature dependence of segregation ratios of boron between solid silicon and Si–Al solvent. Data from Yoshikawa and Morita, 2012.*

A combined slag/solvent refining approach to increase the refining efficiency is to alloy the silicon melt (e.g., with Sn, Cu etc.) and combine it with a suitable slag system, thereby increasing the L_B value. This is summarized in Figure 10.17, adapted from (Thomas *et al.*, 2021), where D_B values, which are normalized L_B values by oxygen partial pressure, are presented as a function of slag optical basicity for various Si-alloy systems.

$$D_B = \frac{L_B}{\left(p_{O_2}\right)^{\frac{3}{4}}} \qquad [10.28]$$

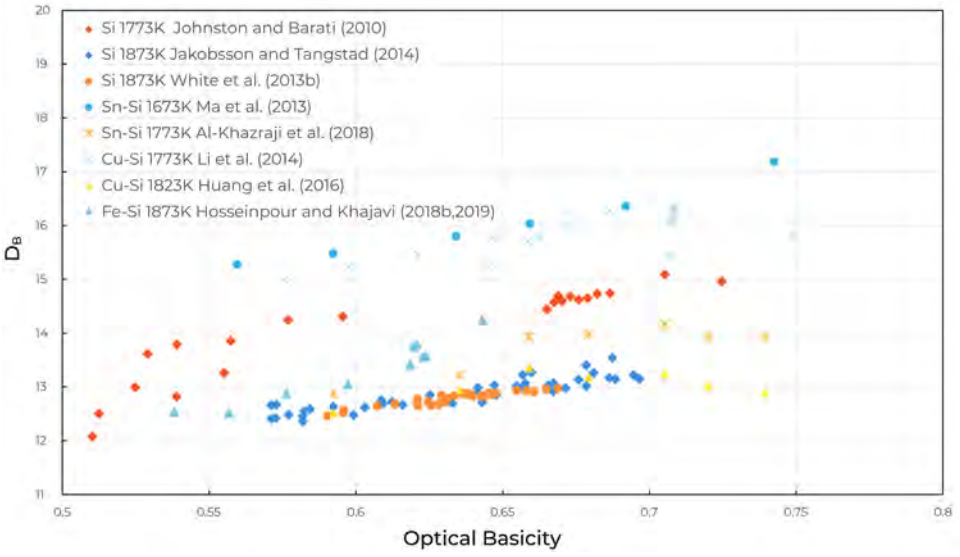


Figure 10.17 *Calculated DB values from slag refining of different silicon alloys (adapted from (Thomas et al., 2021)) (Al-khazraji et al., 2018; Hosseinpour and Tafaghodi Khajavi, 2019, 2018b; Huang et al., 2016; Jakobsson and Tangstad, 2014; Johnston and Barati, 2010; Li et al., 2014; Ma et al., 2013; White et al., 2013b) [Reproduced with permission from SNCSC].*

The relationship between L_B value in alloyed Si system (L_B^*) and in unalloyed Si melt system (L_B^0), with the same slag composition, can be estimated using the following equation (Zhu *et al.*, 2021):

$$\frac{L_B^*}{L_B^0} = \left(\gamma_{Si}^{*Si-Me\ melt}\right)^{\frac{1}{4}} \left(\frac{1}{1-x_A^{*Si-Me\ melt}}\right)^{\frac{3}{4}} exp\left(\varepsilon_{Me}^B x_{Me}^{*Si-Me\ melt}\right) \cdot \left(1 + \frac{M_{Me} - M_{Si}}{M_{Si}} x_{Me}^{*Si-Me\ melt}\right) \quad [10.29]$$

where $x_{Me}^{*Si-Me\ melt}$ represents the concentration of the alloying element Me in the Si-Me melt, $\gamma_{Si}^{*Si-Me\ melt}$ denotes the activity coefficient of silicon in the Si-Me melt, ε_{Me}^B indicates the interaction coefficient between the alloying element and the boron impurity, and M_{Me} is the molar mass of the alloying element.

Given these variables, to improve the L_B value it is preferable to choose an alloying element with a positive interaction coefficient ε_{Me}^B and a high alloying element concentration $x_{Me}^{*Si-Me\ melt}$, as these significantly affect the exponential term and power term in the formula. Moreover, an alloying system with a positive activity coefficient of silicon $\gamma_{Si}^{*Si-Me\ melt}$ also promotes boron removal. In addition, if the alloying metal has a higher molar mass, i.e. $M_{Me} > M_{Si}$, the alloying process can magnify the L_B value by physically diluting the boron mass fraction in the metal phase.

Gas refining

Since the early plasma work of Theuerer, the potential of purifying silicon from boron as volatile B species has been known (Theuerer, 1956). More intense efforts in the area started in the late 1980´s (Amouroux *et al.*, 1987) and early 1990´s (Suzuki *et al.*, 1992, 1990), when this method of removing boron was demonstrated using a plasma torch with Ar-H_2O as the plasma gas.

Plasma-enhanced refining of P was also used by Khattak to refine silicon using combinations of reactive gas, slag and vacuum (Khattak *et al.*, 2002). Nordstrand and Tangstad (followed by Safarian *et al.*, Sortland, Altenberend *et al.* and Vadon *et al.*) first introduced the use of a gas lance delivering H_2-H_2O-containing gases with no active heating, demonstrating that such refining is also possible without the aid of plasma (Altenberend *et al.*, 2017; Nordstrand and Tangstad, 2012; Safarian *et al.*, 2014; Sortland, 2015; Vadon

et al., 2018). Using plasma leads to ionization of the reactive gases (O_2, H_2O, H_2, etc.), forming O, H, OH, O + , OH + species in the plasma flame and hence enhancing their chemical reactivity. These gas species react with the silicon melt containing B, forming, for example, HBO, HBO_2, BO, B_2O, BO_2 species. Thermodynamic data for the system have been assessed by (Tang *et al.*, 2012). The oxidation/volatilization of boron takes place simultaneously with oxidation of Si, also leading to formation of SiO and associated Si losses. While the exact boron volatilization reaction may vary depending on the type of gas/conditions used, a simplified description of the reactions between dissolved boron and water vapour, forming HBO in equilibrium with its silicon counterpart SiO[2], may be written:

$$B + H_2O = HBO + \frac{1}{2}H_2 \qquad [10.30]$$

$$Si + H_2O = SiO + H_2 \qquad [10.31]$$

$$B + SiO + \frac{1}{2}H_2 = HBO + Si \qquad [10.32]$$

The equilibrium partial pressure, p_{HBO}, for a given boron concentration in the melt can hence be calculated using the expression:

$$\frac{p_{HBO}}{x_B} = \gamma_B \cdot \frac{K_{Eq.10.32}}{p_{O_2}^{1/2}} \cdot p_{SiO} \cdot p_{H_2}^{1/2} \qquad [10.33]$$

The purification rate/efficiency is, however, affected by the gas type, flow rate and refining temperature, as illustrated by Figure 10.18.

Table C–2 in Appendix C summarizes research in the area to date.

2 Silicon may, however, also form Si–O–H species. (Jacobson *et al.*, 2005; Opila *et al.*, 1997).

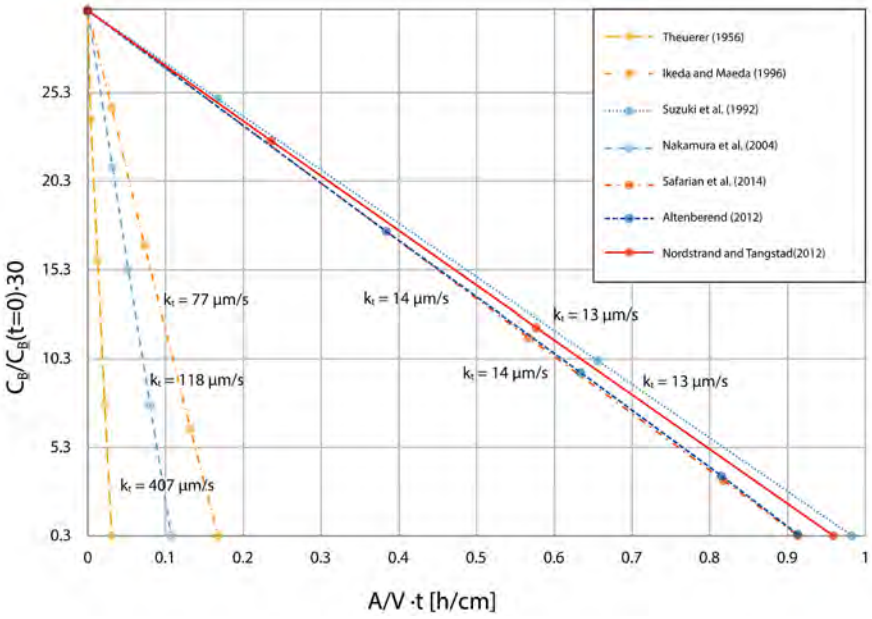


Figure 10.18 *The rate of boron refining by gas blowing with the aid of plasma (Ikeda and Maeda, 1996; Suzuki et al., 1992; Theuerer, 1956), or without the aid of plasma (Altenberend, 2012; Nakamura et al., 2004; Nordstrand and Tangstad, 2012; Safarian et al., 2014) (after Sortland, 2015). [Used with permission from Ø.S. Sortland].*

Removal of phosphorus

Two main metallurgical methods are interesting for removal of phosphorus from silicon: vacuum refining and alloying-aided acid leaching.

Vacuum refining

Unlike boron, phosphorus displays a high standard vapour pressure at elevated temperatures and is hence potentially a candidate for refining via vacuum evaporation treatment, as illustrated by Figure 10.19. This is summarized by Safarian and Tangstad from available thermodynamic data (Safarian and Tangstad, 2012a).

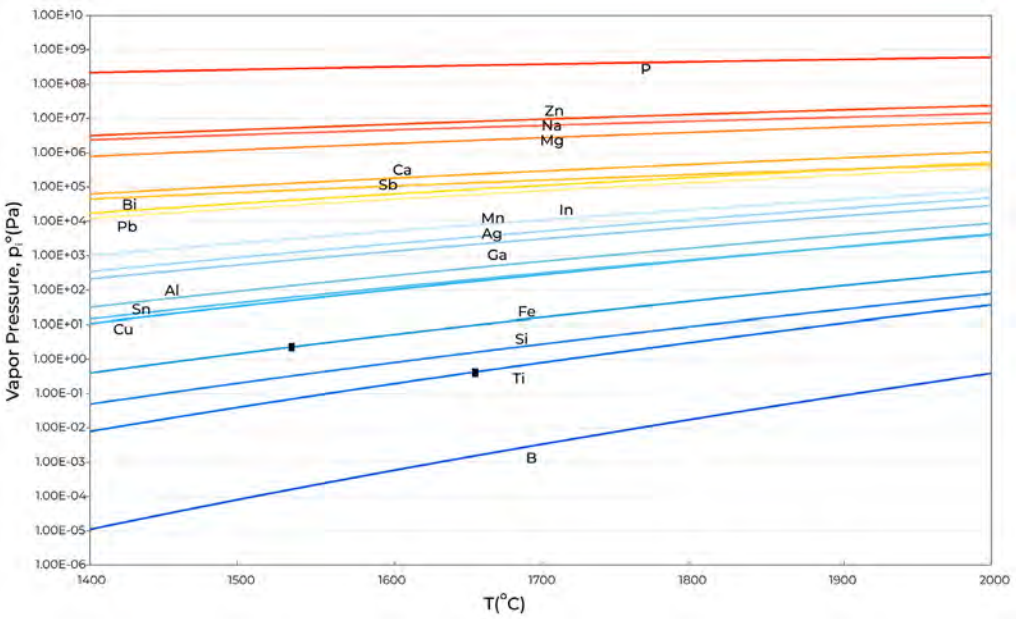


Figure 10.19 *The changes in standard vapour pressure over pure substances with temperature (Safarian and Tangstad, 2012a). Creative Commons CC BY license.*

The viability of P-refining of silicon via evaporation/vacuum treatment is, however, dependent on both thermodynamic and kinetic factors. Miki *et al.*, Zaitsev *et al.*, Schlesinger, Safarian and Tangstad, Liang and Schmid-Fetzer, Hoseinpur and Safarian, and Hoseinpur *et al.* have all contributed to the thermodynamic understanding of the behavior of phosphorus in liquid silicon at different temperatures and pressures through measurements and modelling (Hoseinpur *et al.*, 2022; Hoseinpur *et al.*, 2021; Hoseinpur and Safarian, 2021; Liang and Schmid-Fetzer, 2014; Miki *et al.*, 1996; Safarian and Tangstad, 2011; Schlesinger, 2002; Zaitsev and Kodentsov, 2001). While early work took into account only the desorption/evaporation of monoatomic (P) and, primarily, diatomic (P_2) gas species, Hoseinpur showed that phosphorus may occur concurrently as several different gaseous species (P, P_2, P_3, P_4, SiP, Si_2P, Si_3P and SiP_2) over Si, where their relative prevalence depends on temperature and the concentration of P in the liquid. He introduced three main groups

of reactions leading to phosphorus evaporation from the melt surface, as depicted in Figure 10.20:

1. Molecular evaporation: formation and desorption of phosphorus species (P, P_2, and P_4) at the melt surface.
2. Decomposition of transient silicon phosphides: in this mechanism, the transient silicon phosphides are decomposed to phosphorus species (P, P_2, and P_4) and other lower phosphides (Si_xP_y).
3. Evaporation of lower silicon phosphides (formed in mechanism 2) formed at the melt surface: in this mechanism, the transient silicon phosphides could directly desorb at the melt surface.

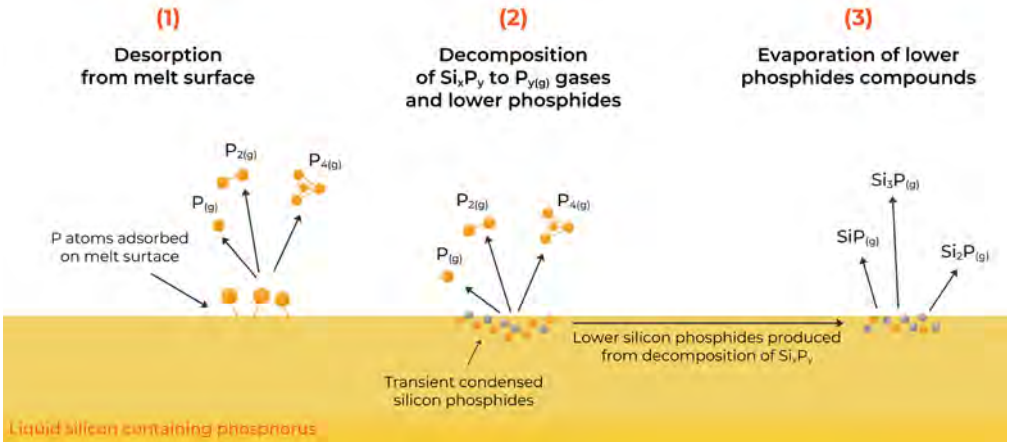


Figure 10.20 *Schematic of different mechanisms for P evaporation from liquid Si (Hoseinpur et al., 2022). Creative Commons Attribution 4.0 International License.*

The partial pressures of different gas species as a function of melt composition were measured by Hoseinpur *et al.* through a Knudsen effusion cell at 1442°C, and are summarized in Figure 10.21 (Hoseinpur *et al.*, 2022). As seen from the figure, at a temperature close to the Si melting point the gas is dominated by the monoatomic P and P_2 species at higher P concentrations, while the phosphide species are more prevalent than P_2 at low-P concentrations.

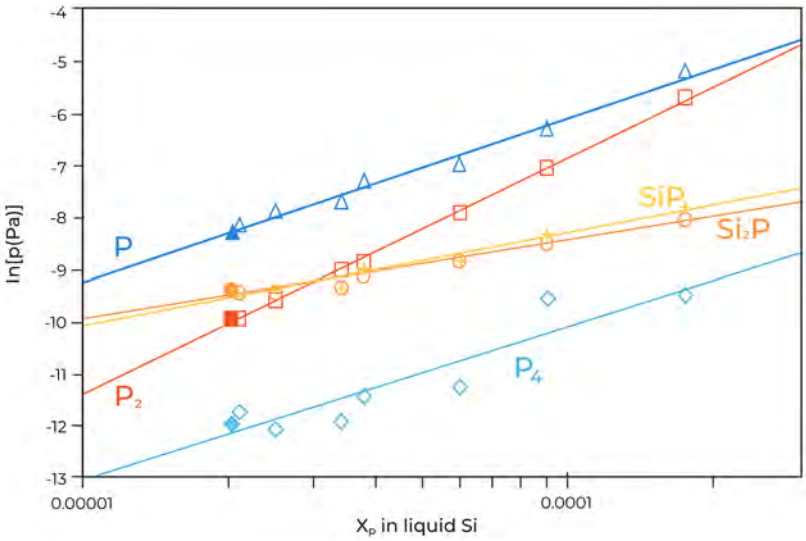


Figure 10.21 *Partial pressures of different gaseous P species as a function of P concentrations at 1442°C from (Hoseinpur et al., 2022). Creative Commons Attribution 4.0 International License.*

The relative partial pressures of species are also temperature dependent, and experimental evidence suggests that at ultra-high temperatures (> 1750°C) the P_4 species is a major contributor to the gas composition. The thermodynamic feasibility of removing phosphorous from silicon, i.e. whether the evaporation rate of phosphorous dominates over that of Si, may be evaluated through the 'volatility coefficient' for phosphorous, *a*, expressed through:

$$\alpha = \left[\frac{\gamma_p \cdot p_p^{\circ} \cdot \sqrt{M_{Si}}}{\gamma_{Si} \cdot p_{Si}^{\circ} \sqrt{M_p}} \right] \qquad [10.34]$$

where γ_{Si} and γ_P denote the activity coefficients of Si and P respectively, P°_{Si} and P°_{p} the saturated vapour pressures of Si and P, and M_{Si} and M_P the molar masses of Si and P. For selective evaporation, *a* has to be > 1. The Henrian activity coefficient for P in dilute solution of Si (γ°_{P}) as a function of T can be calculated according to reaction [10.36], using the Gibbs energy change for

the diatomic evaporation of phosphorous [10.35] determined by Zaitsev *et al.* with pure phosphorous as reference state (Zaitsev *et al.*, 2001):

$$\frac{1}{2}P_2(g) = P(l)\ \Delta G^0 = -99500 + 29.46T\ J/mol \quad [10.35]$$

$$ln\left(\gamma_P^o\right) = 2.08 - \frac{4766}{T} \quad [10.36]$$

Safarian and Tangstad calculated α values for a number of elements in dilute solution with Si, including P, using data from Figure 10.19 together with known activity coefficients. They found the volatility coefficient for P to be in the range 22–15 in the temperature range 1400–2000°C (Safarian and Tangstad, 2012b).

The rate of P evaporation at different temperatures and vacuum conditions has been investigated since the first reported studies by Suzuki *et al.* (Suzuki *et al.*, 1990). Subsequent studies were carried out by Yuge *et al.*, Hanazawa *et al.*, Zheng *et al.*, Safarian and Tangstad, Hoseinpur and Safarian, and Hoseinpur *et al.* (Hanazawa *et al.*, 2004; Hoseinpur *et al.*, 2022; Hoseinpur and Safarian, 2021; Safarian and Tangstad, 2012b, 2011; Yuge *et al.*, 2001, 1997; Zheng *et al.*, 2011, 2010). Most published data show that the rate fits a first order kinetic model according to:

$$ln\left(\frac{[P\%]_0}{[P\%]_t}\right) = k_p\left(\frac{A}{V}\right)t \quad [10.37]$$

where $[P\%]_0$ and $[P\%]_t$ denote the initial and instant concentrations of phosphorus in the melt, respectively. The A/V ratio describes the geometry of the melt, where A and V are the surface area and volume of the melt, and k_p the total mass transfer coefficient. From experimental data on the P reduction rate at different temperatures, the relationship between k_p and T was obtained. Figure 10.22, adapted from Hoseinpur and Safarian, summarizes the data from various studies (Hoseinpur and Safarian, 2021). It is clearly seen that the evaporation mass transfer is significantly increased at high temperatures (> 1800°C).

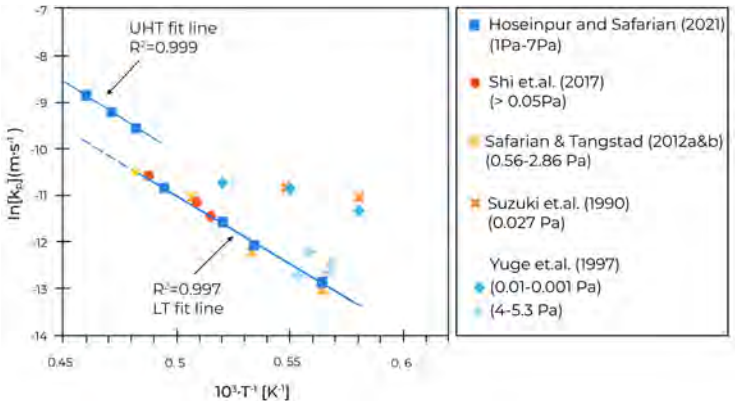


Figure 10.22 *P evaporation mass transfer coefficient as a function of temperature (Adapted from (Hoseinpur and Safarian, 2021)). (Hoseinpur and Safarian, 2021; Safarian and Tangstad, 2012a, 2012b; Shi et al., 2017; Suzuki et al., 1990; Yuge et al., 1997) Creative Commons CC-BY-NC-ND license.*

Acid leaching

Due to the low solid solubility of most elements in silicon, as discussed above, metal impurities largely segregate during solidification and precipitate as silicides at the silicon grain boundaries, as illustrated in Figure 10.23, taken from the PhD work of Zhu (Zhu, 2021).

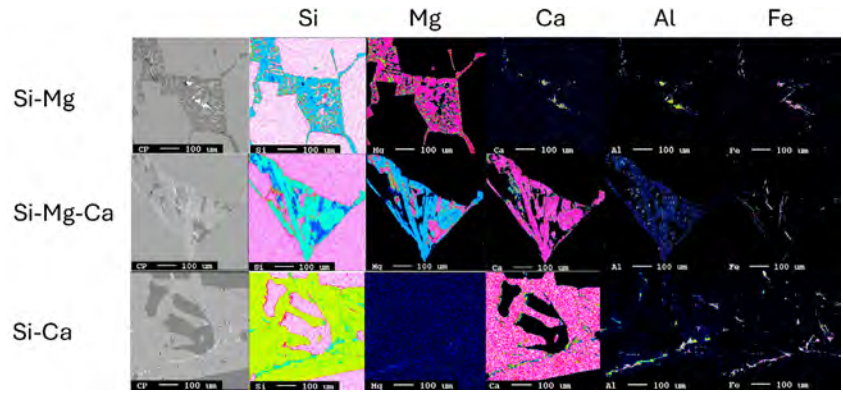


Figure 10.23 *Segregation of impurities to complex silicides in a primary silicon matrix in solidified Si–4.7 wt% Mg, Si–2.5 wt% Mg–2.1 wt% Ca, and Si–3.6 wt% Ca alloy system (Zhu, 2021). Printed with permission from M. Zhu.*

As was illustrated by Table 10.6, P has a high segregation coefficient compared to most metals. This makes it challenging to separate directly via segregation in Si alone, and difficult to remove via subsequent acid leaching. However, by adding certain alloying elements with a high affinity for P, such as Ca and Mg, the segregation of P can be significantly enhanced. In a binary alloying system (Si–Me), the P segregation coefficient can be estimated by the following equation:

$$k_P^{Si-Me} = k_P^{Si} exp\left(\frac{\varepsilon_{Me}^P x_{Me}}{1-f_s}\right) \quad [10.38]$$

where k_P^{Si} is the P segregation coefficient in pure silicon, which is 0.35, and x_{Me} denotes the concentration of alloying elements Me in alloy liquid. ε_{Me}^P represents the interaction coefficient between Me and P, and f_S represents the solid fraction of primary Si. It is seen that a negative ε_{Me}^P and high alloying concentration x_{Me} promote the P segregation.

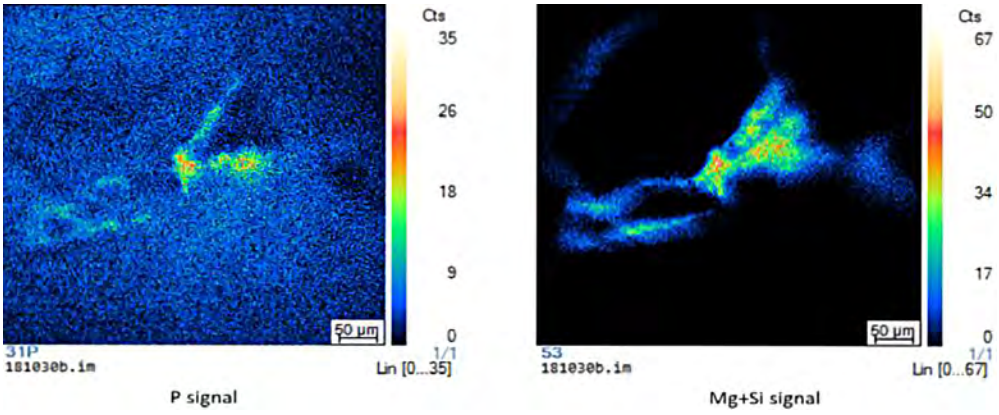


Figure 10.24 *P segregation in Mg-doped Si alloy observed by SIMS elemental mapping (Zhu et al., 2020a). Open access article under the CC BY license.*

As shown in Figure 10.24, P impurity can segregate together with the alloying elements and remain in the dissolvable silicide phase. This allows its removal, along with other metallic impurities, through acid treatment that preferentially attacks the silicides at the grain boundaries rather than the primary silicon grains.

Considerable research, as summarized in Table C–3 in Appendix C, has been performed to study impurity extraction from Si by acid leaching. It has been found that most metallic impurities can be effectively extracted by optimizing two perspectives: improving segregation through the selection of alloying elements, concentration, and cooling rate; and enhancing leaching separation efficiency by adjusting acid type, pH, leaching temperature, time, and particle size of the leaching materials. A typical acid leaching procedure and important factors are illustrated in Figure 10.25.

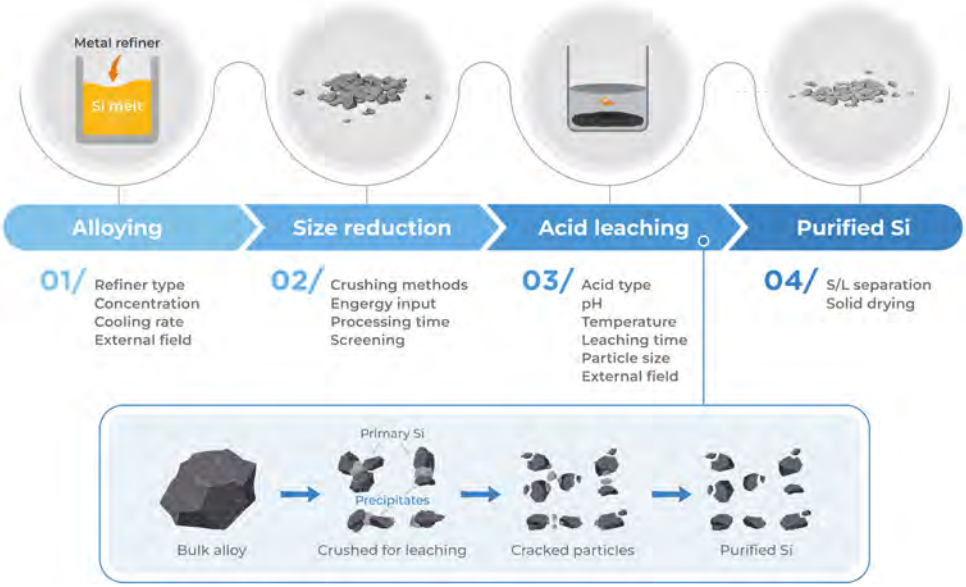


Figure 10.25 *A typical acid leaching procedure with the main factors governing purification performance, including an illustration of particle size evolution and the removal of dissolvable precipitates enriched with impurities.*

Figure 10.26 illustrates the concentration/degree of removal of Ca, Al, P, and other impurities as a function of leaching time in 10% HCl solution at a temperature of 60°C, for a starting Si–Ca–Al alloy that primarily consists of 75.18wt% Si, 14.94wt% Ca, and 9.07wt% Al. The alloy has a P content of 12.4 ppmw and other minor metallic impurities such as Mg, Fe, Mn, Ti, V, and Ga. It is evident that P segregated into the leachable precipitate phase is removed along with these phases.

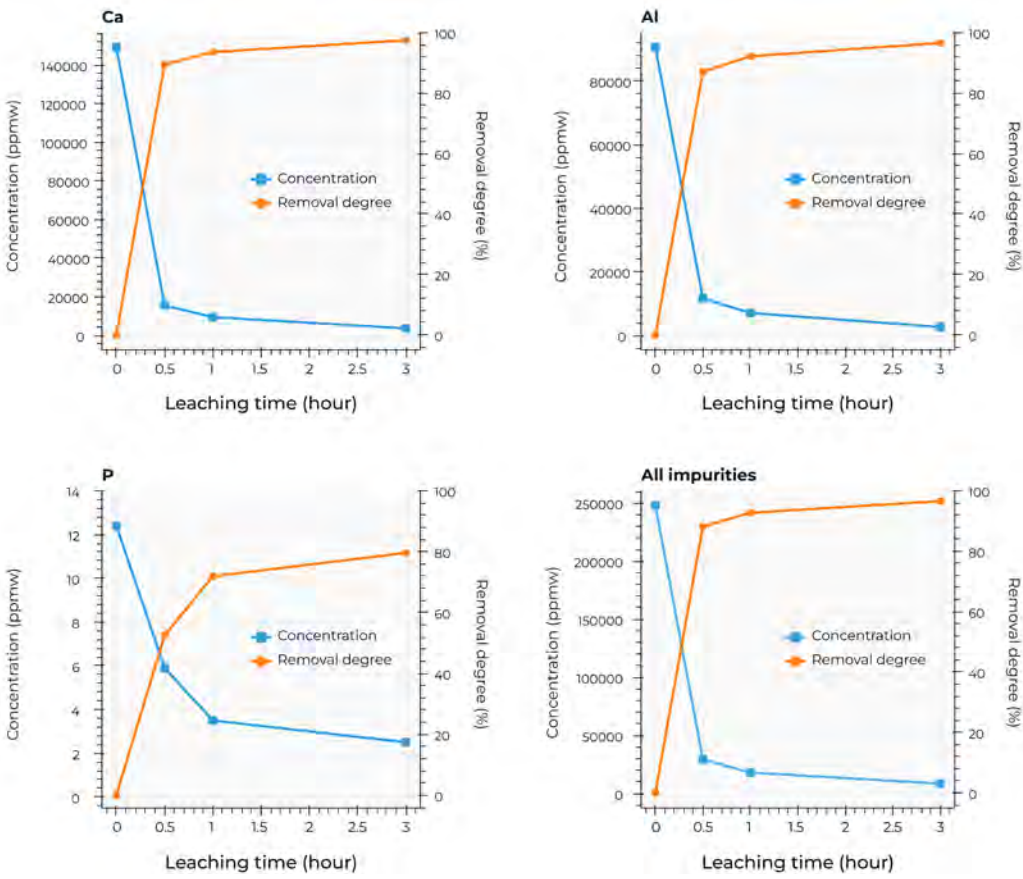


Figure 10.26 *The effect of leaching time on the removal of Ca, Al, P and other impurities from a Si-14.94 wt% Ca-9.07 wt% Al alloy containing 12.4 ppmw P, leached in 10% HCl at 60°C (Zhu et al., 2022) Printed with permission from M. Zhu.*

Using the Scheil equation to describe P segregation behavior in a Si-Me binary alloy system, and assuming that all precipitates formed during the eutectic transformation are removed, the following formula can be derived to describe the P removal degree (η) after acid leaching (Zhu *et al.*, 2020a):

$$\eta = \left\{ 1 - \frac{1 - \dfrac{exp\left(k_P^{Si} E_i \left(\dfrac{\varepsilon_{Me}^{P} X_{Me\ in\ Si(l)}^{initial}}{1 - f_s^{Eu}} \right) \right)}{exp\left(k_P^{Si} E_i \left(\varepsilon_{Me}^{P} X_{Me\ in\ Si(l)}^{initial} \right) \right)}}{f_S^{Eu}} \right\} x100\% \qquad [10.39]$$

where the $E_i(x)$ function is defined as the integral $E_i(x) = \int_{-\infty}^{x} \frac{e^t dt}{t}$, $X_{Me\ in\ Si(l)}^{initial}$ represents the initial doping concentration of alloying element Me in Si melt, and f_s^{EU} denotes the primary Si solid fraction at the eutectic point.

The selection criteria for the alloying system include high affinity for impurities, limited solubility in Si, and formation of a dissolvable phase; it should also be cost-effective, ensuring high Si recovery and an environmentally friendly leaching process. While Mg has been proven to be an effective getter for P, reaching high Si recovery, Ca additions are more efficient. They require a lower concentration in the solidifying metal for the same P removal effect and offer faster leaching kinetics. Mixing Ca and Mg is considered to capture the advantages of both elements. A comparison of the impurity removal degree of P, Al, Fe and Ti in the Mg–Si, Ca-Si and Ca–Mg–Si alloying systems after 3 h acid leaching by 10% HCl at 60°C under magnetic stirring is illustrated in Figure 10.27.

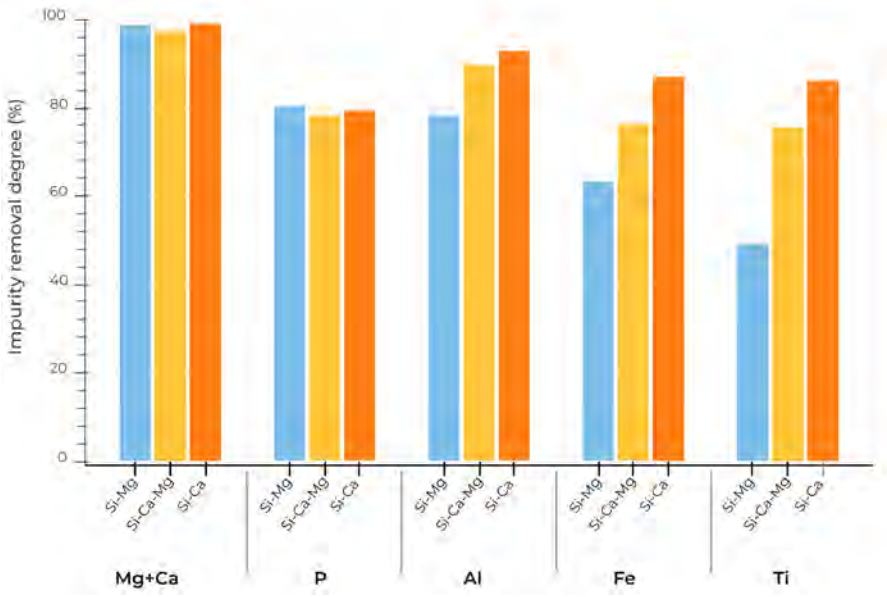


Figure 10.27 *Comparison of impurity removal degree of P, Al, Fe and Ti in Si-4.7wt% Mg, Si-2.5wt% Mg–2.1wt% Ca, and Si-3.6wt% Ca alloy systems after 3 h acid leaching in 10% HCl at 60°C (Zhu et al., 2020b). Open access licensed under CC-BY.*

References

Al-khazraji, R., Li, Y. and Zhang, L. (2018) 'Comparison between slag refining processes for B removal with metallurgical grade silicon and Si–Sn alloy', *Metallurgical Research & Technology*, 115, 312. Available at: https://doi.org/10.1051/metal/2018047

Altenberend, J. (2012) *Kinetics of the plasma refining process of silicon for solar cells*. Doctoral thesis. Université de Grenoble, France.

Altenberend, J., Chichignoud, G. and Delannoy, Y. (2017) 'Study of mass transfer in gas blowing processes for silicon purification', *Metallurgical and Materials Transactions E*, 4, pp. 41–50. Available at: https://doi.org/10.1007/s40553-016-0105-x

Amouroux, J., Morvan, D., Apostolidou, H., Slootman, F., Rouchaud, J.C. and Fedoroff, M. (1987) 'Photovoltaic silicon production by plasma process', in Goetzberger, A., Palz, W. and Willeke, G. (eds) *Seventh E.C. Photovoltaic Solar Energy Conference*. Dordrecht: Springer Netherlands, pp. 719–725. Available at: https://doi.org/10.1007/978-94-009-3817-5_128

Aulich, H.A., Schulze, F.W., Urbach, H.P. and Lerchenberger, A. (1986) 'Solar-grade silicon prepared by carbothermic reduction of silica', in *Proceedings of the Flat-Plate Solar Array Project Workshop on Low-Cost Polysilicon for Terrestrial Photovoltaic Solar-Cell Applications*. Las Vegas, USA.

Baba, H., Hanazaka, K., Yuge, N., Kato, Y., Hiwasa, S. and Aratani, F. (2000) 'Development of NEDO melt-purification process for solar grade silicon by pilot plant', *Photovoltaic Solar Energy Conference 16th*, pp. 1675–1678.

Bathey, B.R. and Cretella, M.C. (1982) 'Solar-grade silicon', *Journal of Materials Science*, 17, pp. 3077–3096. Available at: https://doi.org/10.1007/BF01203469

Bjørnstad, E.L., Jung, I.-H., Van Ende, M.-A. and Tranell, G. (2022) 'Oxidative refining of metallurgical grade silicon: Lab-scale measurements on the overarching refining behavior of Ca and Al', *Metallurgical and Materials Transactions B*, 53, pp. 1103–1111. Available at: https://doi.org/10.1007/s11663-022-02425-5

Bjørnstad, E.L. and Tranell, G. (2021) 'Nucleation of SiO2–CaO–Al2O3 slag in oxidative ladle refining of metallurgical grade silicon', *Metallurgical and Materials Transactions B*, 52, pp. 1392–1412. Available at: https://doi.org/10.1007/s11663-021-02132-7

Boulfrad, Y. (2012) *Investigation of the red zone of multicrystalline silicon ingots for solar cells*. Doctoral thesis 2012:184. Norwegian University of Science and Technology (NTNU), Trondheim, Norway.

Chigondo, F. (2018) 'From metallurgical-grade to solar-grade silicon: An overview', *Silicon*, 10, pp. 789–798. Available at: https://doi.org/10.1007/s12633-016-9532-7

Chu, T.L., van der Leeden, G.A. and Yoo, H.I. (1978) 'Purification and characterization of metallurgical silicon', *J. Electrochem. Soc.*, 125, p. 661. Available at: https://doi.org/10.1149/1.2131520

Ciftja, A. (2009) *Solar silicon refining; inclusions, settling, filtration, wetting*. Doctoral thesis 2009:103. Norwegian University of Science and Technology (NTNU), Trondheim, Norway.

Dalaker, H. (2013) 'Thermodynamic computations of the interaction coefficients between boron and phosphorus and common impurity elements in liquid silicon', *Computer Methods in Materials Science*, 13, pp. 407–411. Available at: https://doi.org/10.7494/cmms.2013.3.0459

Dalaker, H. and Tangstad, M. (2009) 'Time and temperature dependence of the solubility of carbon in liquid silicon equilibrated with silicon carbide and its dependence on boron levels', *Materials Transactions*, 50, pp. 1152–1156. Available at: https://doi.org/10.2320/matertrans.M2009034

Dietl, J. (1983) 'Hydrometallurgical purification of metallurgical-grade silicon', *Solar Cells*, 10, pp. 145–154. Available at: https://doi.org/10.1016/0379-6787(83)90015-7

Dietl, J. and Wohlschlager, M. (1981) *Process for purifying metallurgical-grade silicon*. US Patent 4304763.

Eie, M., Gangstad, A., Rong, H.M., Semb, H. and Sørheim, H. (1998) 'Method for determination of active aluminium in silicon', in *Proceedings of Silicon for the Chemical Industry IV*. Geiranger, Norway.

Forwald, A.G., Rong, H.M. and Vogelaar, G.T. (1994) 'Oxygen in silicon; occurrence and influence on the direct process to methylchlorosilanes', in *Proceedings of Silicon for the Chemical Industry II*. Loen, Norway.

Hanazawa, K., Yuge, N. and Kato, Y. (2004) 'Evaporation of phosphorus in molten silicon by an electron beam irradiation method', *Materials Transactions*, 45, pp. 844–849. Available at: https://doi.org/10.2320/matertrans.45.844

Hesse, K. and Pätzold, U. (2006) 'Survey over the TCS process', in *Proceedings of Silicon for the Chemical Industry VIII*. Trondheim, Norway, pp. 157–166.

Holta, H. (1995) 'Tinject refining during 15 years', in *Proceedings of INFACON VII*. Trondheim, Norway: FFF/SINTEF, pp. 463–472. Available at: https://www.pyrometallurgy.co.za/InfaconVII/463-Holta.pdf

Hoseinpur, A., Andersson, S., Tang, K. and Safarian, J. (2021) 'Selective vacuum evaporation by the control of the chemistry of gas phase in vacuum refining of Si', *Langmuir*, 37, pp. 7473–7485. Available at: https://doi.org/10.1021/acs.langmuir.1c00876

Hoseinpur, A. and Safarian, J. (2021) 'Vacuum refining of silicon at ultra-high temperatures', *Vacuum*, 184, 109924. Available at: https://doi.org/10.1016/j.vacuum.2020.109924

Hoseinpur, A., Sergeev, D., Müller, M. and Safarian, J. (2022) 'On the phosphorus evaporation from liquid silicon by Knudsen effusion mass spectrometry', *Metallurgical and Materials Transactions B*, 53, pp. 1066–1081. Available at: https://doi.org/10.1007/s11663-022-02445-1

Hosseinpour, A. and Tafaghodi Khajavi, L. (2018a) 'Slag refining of silicon and silicon alloys: A review', *Mineral Processing and Extractive Metallurgy Review*, 39, pp. 308–318. Available at: https://doi.org/10.1080/08827508.2018.1459616

Hosseinpour, A. and Tafaghodi Khajavi, L. (2018b) 'Thermodynamics of boron removal in slag refining of Fe–Si alloy', *Journal of Alloys and Compounds*, 768, pp. 545–552. Available at: https://doi.org/10.1016/j.jallcom.2018.07.246

Hosseinpour, A. and Tafaghodi Khajavi, L. (2019) 'Phosphorus removal from Si–Fe alloy using SiO2-Al2O3–CaO slag', *Metallurgical and Materials Transactions B*, 50, pp. 1773–1781. Available at: https://doi.org/10.1007/s11663-019-01586-0

Huang, L., Lai, H., Gan, C., Xiong, H., Xing, P. and Luo, X. (2016) 'Separation of boron and phosphorus from Cu-alloyed metallurgical grade silicon by CaO–SiO2–CaCl2 slag treatment', *Separation and Purification Technology*, 170, pp. 408–416. Available at: https://doi.org/10.1016/j.seppur.2016.07.004

Hull, R. (ed.) (1999) *Properties of crystalline silicon*. EMIS Datareviews Series. London: INSPEC, The Institution of Electrical Engineers.

Hunt, L.P. (1984) 'Compositional analysis of silicon for solar cells', *J. Electrochem. Soc.*, 131(8). Available at: https://doi.org/10.1149/1.2115985

Hunt, L.P., Dosaj, V., McCormick, J. and Crossman, L.D. (1976) 'Production of solar-grade silicon from purified metallurgical silicon', in *Proceedings of the Photovoltaic Specialists Conference*. Louisiana, USA.

Haaland, D., Lindstad, L.H. and Tuset, J.K. (1994) 'Use of alkali oxide slags in silicon refining', in *Proceedings of Silicon for the Chemical Industry II*. Loen, Norway, pp. 271–281.

Ikeda, T. and Maeda, M. (1992) 'Purification of metallurgical silicon for solar-grade silicon by electron beam button melting', *ISIJ International*, 32, pp. 635–642. Available at: https://doi.org/10.2355/isijinternational.32.635

Ikeda, T. and Maeda, M. (1996) 'Elimination of boron in molten silicon by reactive rotating plasma arc melting', *Materials Transactions, JIM*, 37, pp. 983–987. Available at: https://doi.org/10.2320/matertrans1989.37.983

Jacobson, N.S., Opila, E.J., Myers, D.L. and Copland, E.H. (2005) 'Thermodynamics of gas phase species in the Si–O–H system', *The Journal of Chemical Thermodynamics*, 37, pp. 1130–1137. Available at: https://doi.org/10.1016/j.jct.2005.02.001

Jakobsson, L.K. and Tangstad, M. (2014) 'Distribution of boron between silicon and CaO–MgO–Al2O3–SiO2 slags', *Metallurgical and Materials Transactions B*, 45, pp. 1644–1655. Available at: https://doi.org/10.1007/s11663-014-0088-x

Jakobsson, L.K. and Tangstad, M. (2015) 'Thermodynamic activities and distributions of calcium and magnesium between silicon and CaO–MgO–SiO2 slags at 1873 K (1600°C)', *Metallurgical and Materials Transactions B*, 46, pp. 595–605. Available at: https://doi.org/10.1007/s11663-014-0268-8

Johnston, M.D. and Barati, M. (2010) 'Distribution of impurity elements in slag–silicon equilibria for oxidative refining of metallurgical silicon for solar cell applications', *Solar Energy Materials and Solar Cells*, 94, pp. 2085–2090. Available at: https://doi.org/10.1016/j.solmat.2010.06.025

Kapur, V.K. and Choudary, U.V. (1983) *Silicon purification*. US Patent 4388286A.

Khattak, C.P., Joyce, D.B. and Schmid, F. (2002) 'A simple process to remove boron from metallurgical grade silicon', *Solar Energy Materials and Solar Cells*, 74, pp. 77–89. Available at: https://doi.org/10.1016/S0927-0248(02)00051-X

Klevan, O.S. (1997) *Removal of C and SiC from Si and FeSi during ladle refining and solidification*. Doctoral thesis 1997:11. Norwegian University of Science and Technology (NTNU), Trondheim, Norway. Available at: https://hdl.handle.net/11250/248844

Kvande, R., Geerligs, L.J., Coletti, G., Arnberg, L., Di Sabatino, M., Øvrelid, E.J. and Swanson, C.C. (2008) 'Distribution of iron in multicrystalline silicon ingots', *J. Appl. Phys.*, 104, 064905. Available at: https://doi.org/10.1063/1.2956697

Laroze, G. (1994) 'Influence of oxygen pollution of silicon metal in the Rochow synthesis', in *Proceedings of Silicon for the Chemical Industry II*. Loen, Norway, pp. 121–127.

Li, M., Utigard, T. and Barati, M. (2014) 'Removal of boron and phosphorus from silicon using CaO–SiO2–Na2O–Al2O3 flux', *Metallurgical and Materials Transactions B*, 45, pp. 221–228. Available at: https://doi.org/10.1007/s11663-013-0011-x

Liang, S.-M. and Schmid-Fetzer, R. (2014) 'Modeling of thermodynamic properties and phase equilibria of the Si-P system', *J. Phase Equilib. Diffus.*, 35, pp. 24–35. Available at: https://doi.org/10.1007/s11669-013-0269-3

Lukin, S.V., Zhuchkov, V.I., Vatolin, N.A. and Kozlov, Y.S. (1979) 'The physicochemical properties of Si-B alloys', *Journal of the Less Common Metals*, 67. Available at: https://doi.org/10.1016/0022-5088(79)90019-5

Ma, X., Yoshikawa, T. and Morita, K. (2013) 'Removal of boron from silicon-tin solvent by slag treatment', *Metallurgical and Materials Transactions B*, 44, pp. 528–533. Available at: https://doi.org/10.1007/s11663-013-9812-1

Miki, T., Morita, K. and Sano, N. (1996) 'Thermodynamics of phosphorus in molten silicon', *Metallurgical and Materials Transactions B*, 27, pp. 937–941. Available at: https://doi.org/10.1007/s11663-996-0007-x

Morita, K. (2005) 'Thermodynamic property of B in molten Si and phase relations in the Si–Al–B system', *Material Transactions*, 46, pp. 1335–1340. Available at: https://doi.org/10.2320/MATERTRANS.46.1335

Mühlbauer, A., Diers, V., Walther, A. and Grabmaier, J.G. (1991) 'Removal of C/SiC from liquid silicon by directional solidification', *Journal of Crystal Growth*, 108, pp. 41–52. Available at: https://doi.org/10.1016/0022-0248(91)90352-6

Møll, M.F. (2014) *Solidification of silicon: Macro- and microstructure as functions of thermal history and composition*. Doctoral thesis 2014:21. Norwegian University of Science and Technology (NTNU), Trondheim, Norway.

Nakamura, N., Baba, H., Sakaguchi, Y. and Kato, Y. (2004) 'Boron removal in molten silicon by a steam-added plasma melting method', *Materials Transactions*, 45, pp. 858–864. Available at: https://doi.org/10.2320/matertrans.45.858

Noguchi, R. (1994) 'Thermodynamics of boron in silicon melts', *Metallurgical and Material Transactions B*, 25B, pp. 903–907. Available at: https://doi.org/10.1007/BF02662772

Nordstrand, E.F. and Tangstad, M. (2012) 'Removal of boron from silicon by moist hydrogen gas', *Metallurgical and Materials Transactions B*, 43, pp. 814–822. Available at: https://doi.org/10.1007/s11663-012-9671-1

Næss, M.K., Kero, I. and Tranell, G. (2013) 'A new method for estimation of emissions and sources of measurements error in the silicon refining process', *JOM*, 65, pp. 997–1006. Available at: https://doi.org/10.1007/s11837-013-0661-9

Opila, E.J., Fox, D.S. and Jacobson, N.S. (1997) 'Mass spectrometric identification of Si–O–H(g) species from the reaction of silica with water vapor at atmospheric pressure', *Journal of the American Ceramic Society*, 80, pp. 1009–1012. Available at: https://doi.org/10.1111/j.1151-2916.1997.tb02935.x

Parisi, A., Pelosini, L. and Pizzini, S. (1980) *Process for purifying silicon*. US Patent 4241037.

Safarian, J., Tang, K., Hildal, K. and Tranell, G. (2014) 'Boron removal from silicon by humidified gases', *Metallurgical and Materials Transactions E*, 1, pp. 41–47. Available at: https://doi.org/10.1007/s40553-014-0007-8

Safarian, J. and Tangstad, M. (2011) 'Phase diagram study of the Si–P system in Si-rich region', *Journal of Materials Research*, 26, pp. 1494–1503. Available at: https://doi.org/10.1557/jmr.2011.130

Safarian, J. and Tangstad, M. (2012a) 'Vacuum refining of molten silicon', *Metallurgical and Materials Transactions B*, 43, pp. 1427–1445. Available at: https://doi.org/10.1007/s11663-012-9728-1

Safarian, J. and Tangstad, M. (2012b) 'Kinetics and mechanism of phosphorus removal from silicon in vacuum induction refining', *High Temperature Materials and Processes*, 31. Available at: https://doi.org/10.1515/htmp.2011.143

Safarian, J., Tranell, G. and Tangstad, M. (2012) 'Processes for upgrading metallurgical grade silicon to solar grade silicon', *Energy Procedia*, 20, pp. 88–97. Available at: https://doi.org/10.1016/j.egypro.2012.03.011

Safarian, J., Tranell, G. and Tangstad, M. (2015) 'Boron removal from silicon by CaO–Na2O–SiO2 ternary slag', *Metallurgical and Materials Transactions E*, 2, pp. 109–118. Available at: https://doi.org/10.1007/s40553-015-0048-7

Sakaguchi, K. and Maeda, M. (1992) 'Decarburlzation of silicon melt for solar cells by filtration and oxidation', *Metallurgical Transactions B*, 23, pp. 423–427. Available at: https://doi.org/10.1007/BF02649660

Schlesinger, M.E. (2002) 'The thermodynamic properties of phosphorus and solid binary phosphides', *Chemical Reviews*, 102, pp. 4267–4302. Available at: https://doi.org/10.1021/cr000039m

Shi, S., Li, P., Meng, J., Jiang, D., Tan, Y. and Asghar, H.M.N. ul H.K. (2017) 'Kinetics of volatile impurity removal from silicon by electron beam melting for photovoltaic applications', *Physical Chemistry Chemical Physics*, 19, pp. 28424–28433. Available at: https://doi.org/10.1039/C7CP05080A

Skei, B. (1991) 'Refining of silicon alloys by the Tinject process', *Proceedings. Electric Furnace Conference*, 48, pp. 225–232.

Sortland, Ø.S. (2015) *Boron removal from silicon by steam and hydrogen*. Doctoral thesis 2015:268. Norwegian University of Science and Technology (NTNU), Trondheim, Norway. Available at: https://hdl.handle.net/11250/2364812

Suzuki, K., Kumagai, T. and Sano, N. (1992) 'Removal of boron from metallurgical-grade silicon by applying the plasma treatment', *ISIJ International*, 32, pp. 630–634. Available at: https://doi.org/10.2355/isijinternational.32.630

Suzuki, K., Sakaguchi, K., Nakagiri, T. and Sano, N. (1990) 'Gaseous removal of phosphorus and boron from molten silicon', *Nippon Kinzoku Gakkai-si*, 54, pp. 161–167. Available at: https://doi.org/10.2320/jinstmet1952.54.2_161

Suzuki, K. and Sano, N. (1991) 'Thermodynamics for removal of boron from metallurgical silicon by flux treatment', in Luque, A., Sala, G., Palz, W., Santos, G. and Helm, P. (eds) *Tenth E.C. Photovoltaic Solar Energy Conference*. Dordrecht: Springer Netherlands, pp. 273–275. Available at: https://doi.org/10.1007/978-94-011-3622-8_68

Søiland, A.-K., Dolmen, M.G., Heide, J., Thisted, U., Halvorsen, G., Ausland, G., Friestad, K., Preis, P., Peter, K., Graf, O., Bartel, T. and Tronstad, R. (2014) 'First results from a simplified Elkem Solar route—input to tolerance limits', *Solar Energy Materials and Solar Cells*, 130, pp. 661–667. Available at: https://doi.org/10.1016/j.solmat.2014.04.012

Tanahashi, M., Fujisawa, T. and Yamauchi, C. (1998) 'Activity of boron in molten silicon', *Shigen To Sozai*, 114, pp. 807–811.

Tang, K., Andersson, S., Nordstrand, E. and Tangstad, M. (2012) 'Removal of boron in silicon by H2-H2O gas mixtures', *JOM*, 64, pp. 952–956. Available at: https://doi.org/10.1007/s11837-012-0368-3

Tang, K., Øvrelid, E.J., Tranell, G. and Tangstad, M. (2009) 'A thermochemical database for the solar cell silicon materials', *Materials Transactions*, 50, pp. 1978–1984. Available at: https://doi.org/10.2320/matertrans.M2009110

Teixeira, L.A.V. and Morita, K. (2009) 'Removal of boron from molten silicon using CaO–SiO2 based slags', *ISIJ International*, 49, pp. 783–787. Available at: https://doi.org/10.2355/isijinternational.49.783

Theuerer, H.C. (1956) 'Removal of boron from silicon by hydrogen water vapor treatment', *JOM*, 8, pp. 1316–1319. Available at: https://doi.org/10.1007/BF03377873

Thomas, R.E., Mantini, M.J., Rudder, R.A., Malta, D.P., Hattangady, S.V. and Markunas, R.J. (1992) 'Carbon and oxygen removal from silicon (100) surfaces by remote plasma cleaning techniques', *J. Vac. Sci. Technol. A*, 10, pp. 817–822. Available at: https://doi.org/10.1116/1.577678

Thomas, S., Barati, M. and Morita, K. (2021) 'A review of slag refining of silicon alloys', *JOM*, 73, pp. 282–292. Available at: https://doi.org/10.1007/s11837-020-04474-0

Trumbore, F.A. (1960) 'Solid solubilities of impurity elements in germanium and silicon', *Bell System Technical Journal*, 39, pp. 205–233.

Tuset, J.K. (1992) 'The refining of silicon and ferrosilicon', in *Proceedings of INFACON VI*. Cape Town, South Africa, pp. 193–199. Available at: https://www.pyrometallurgy.co.za/InfaconVI/1193-Tuset.pdf

Vadon, M., Sortland, Ø., Tangstad, M., Chichignoud, G. and Delannoy, Y. (2018) 'Passivation threshold for the oxidation of liquid silicon and thermodynamic non-equilibrium in the gas phase', *Metallurgical and Materials Transactions B*, 49, pp. 3330–3342. Available at: https://doi.org/10.1007/s11663-018-1381-x

Wen, S., Hu, J., Dai, H., Li, Y., Li, H., Xu, X. and Zhao, F. (2024) 'High efficiency solar-grade silicon producing by directional solidification through controlling diffusion of impurity', *Separation and Purification Technology*, 351, 128129. Available at: https://doi.org/10.1016/j.seppur.2024.128129

White, J.F., Allertz, C. and Sichen, D. (2013a) 'Boron partitioning between SiO2–CaO–MgO slags and liquid silicon at controlled nitrogen potential', *International Journal of Materials Research*, 104, pp. 650–656. Available at: https://doi.org/10.3139/146.110913

White, J.F., Allertz, C. and Sichen, D. (2013b) 'The thermodynamics of boron extraction from liquid silicon using SiO2–CaO–MgO slag treatment', *International Journal of Materials Research*, 104, pp. 229–234. Available at: https://doi.org/10.3139/146.110867

Wu, J., Wang, F., Ma, W., Lei, Y. and Yang, B. (2016) 'Thermodynamics and kinetics of boron removal from metallurgical grade silicon by addition of high basic potassium carbonate to calcium silicate slag', *Metallurgical and Materials Transactions B*, 47, pp. 1796–1803. Available at: https://doi.org/10.1007/s11663-016-0615-z

Yang, D. (ed.) (2019) 'Part 1. Polycrystalline silicon', in *Handbook of Photovoltaic Silicon*. Springer.

Yuge, N., Abe, M., Hanazawa, K., Baba, H., Nakamura, N., Kato, Y., Sakaguchi, Y., Hiwasa, S. and Aratani, F. (2001) 'Purification of metallurgical-grade silicon up to solar grade', *Progress in Photovoltaics: Research and Applications*, 9, pp. 203–209. Available at: https://doi.org/10.1002/pip.372

Yuge, N., Hanazawa, K., Nishikawa, K. and Terashima, H. (1997) 'Removal of phosphorus, aluminum and calcium by evaporation in molten silicon', *J. Japan Inst. Metals*, 61, pp. 1086–1093. Available at: https://doi.org/10.2320/jinstmet1952.61.10_1086

Zaitsev, A.I. and Kodentsov, A.A. (2001) 'Thermodynamic properties and phase equilibria in the Si-B system', *JPE*, 22, pp. 126–135. Available at: https://doi.org/10.1361/105497101770338987

Zaitsev, A.I., Litvina, A.D. and Shelkova, N.E. (2001) 'Thermodynamic properties of Si–P melts', *High Temperature*, 39, pp. 227–232. Available at: https://doi.org/10.1023/A:1017570715796

Zheng, S., Chen, W.-H., Cai, J., Li, J.-T., Chen, C. and Luo, X.-T. (2010) 'Mass transfer of phosphorus in silicon melts under vacuum induction refining', *Metallurgical and Materials Transactions B*, 41, pp. 1268–1273. Available at: https://doi.org/10.1007/s11663-010-9422-0

Zheng, S., Engh, T.A., Tangstad, M. and Luo, X.-T. (2011) 'Numerical simulation of phosphorus removal from silicon by induction vacuum refining', *Metallurgical and Materials Transactions A*, 42, pp. 2214–2225. Available at: https://doi.org/10.1007/s11661-011-0621-3

Zhu, M. (2021) *Silicon purification by acid leaching and slag refining techniques*. Doctoral thesis 2021:117. Norwegian University of Science and Technology (NTNU), Trondheim, Norway. Available at: https://hdl.handle.net/11250/2738488

Zhu, M., Arntsen, A.S. and Safarian, J. (2022) 'Silicon recovery via the acid leaching of a Si–Ca-Al alloy produced by the SisAl process', in *Proceedings of Silicon for the Chemical Industry XVI*. Trondheim, Norway. Available at: https://doi.org/10.2139/ssrn.4123122

Zhu, M., Azarov, A., Monakhov, E., Tang, K. and Safarian, J. (2020a) 'Phosphorus separation from metallurgical-grade silicon by magnesium alloying and acid leaching', *Separation and Purification Technology*, 240, 116614. Available at: https://doi.org/10.1016/j.seppur.2020.116614

Zhu, M., Wu, G., Azarov, A., Monakhov, E., Tang, K., Müller, M. and Safarian, J. (2021) 'Effects of La2O3 addition into CaO–SiO2 slag: Structural evolution and impurity separation from Si–Sn alloy', *Metallurgical and Materials Transactions B*, 52, pp. 3045–3063. Available at: https://doi.org/10.1007/s11663-021-02232-4

Zhu, M., Wu, G., Tang, K., Müller, M. and Safarian, J. (2024) 'Combined silicon refining for boron removal and Si-Kerf recycling using K2O–CaO–SiO2 slags', *Chemical Engineering Journal*, 488, 150788. Available at: https://doi.org/10.1016/j.cej.2024.150788

Zhu, M., Yue, S.Y., Tang, K. and Safarian, J. (2020b) 'New insights into silicon purification by alloying–leaching refining: A comparative study of Mg–Si, Ca–Si, and Ca–Mg–Si systems', *ACS Sustainable Chemistry & Engineering*, 8, pp. 15953–15966. Available at: https://doi.org/10.1021/acssuschemeng.0c05564

Broggi, A., Tveit, H. og Bullon, J. (2026) 'Solidification of Si and Si-alloys', in M. Tangstad, G. Tranell, H. Tveit and E. Ringdalen (Eds.), *Production of high silicon alloys* (2. ed.) (pp. 429–454). Fagbokforlaget. https://doi.org/10.55669/oa880811

11

Solidification of Si and Si-alloys

Andrea Broggi, Halvard Tveit and Javier Bullon

11.1 Introduction

Casting process parameters influence the mechanical properties and the product's homogeneity, which in turn affect product quality and cost. This chapter presents fundamental background knowledge on casting processes for MG–Si and iron-silicon alloys with more than 30 wt% Si. The first part covers the thermodynamics of solidification for different ferrosilicon alloys. The second part covers solidification processes, from traditional casting to new methods. The final part presents relevant industrial and academic results on the relationship between the solidification of silicon alloys and product properties.

11.2 Thermodynamics and phase diagram

The phase diagram of the Fe–Si system is shown in Figure 11.1. The temperatures and compositional ranges in this diagram cover the typical values found during tapping of liquid silicon ferroalloys. Recent measurement campaigns at silicon and ferrosilicon plants show that the temperature of silicon is between 1800–2000°C as it leaves the tap hole (Tangstad *et al.*, 2021). The alloy then cools rapidly, due to radiation losses and the low heat capacity of the liquid, reaching a temperature between 1500–1700°C in the ladle.

This work is licensed under the Creative Commons Attribution 4.0 International License.
To view a copy of this license, visit https://creativecommons.org/licenses/by/4.0/

There are 4 solid phases in the range 30–100 wt.% Si:

FeSi: Often referred to as e-phase, FeSi melts at 1410°C.

Fe_3Si_7: This phase, also known as High Temperature Fe_3Si_7 (HT–Fe_3Si_7) or ζ_α-phase in older literature, is characterized by vacancies left by approximately one out of six Fe atoms at elevated temperatures. It is stable between 948–1214°C.

$FeSi_2$: Stable below 996°C, $FeSi_2$ is referred to as the Low Temperature $FeSi_2$ (LT–$FeSi_2$) phase or ζ_b-phase in older literature. It can form, together with solid silicon, from the eutectoid reaction at 948°C from Fe_3Si_7. Alternatively, it can form from Fe_3Si_7 together with FeSi in a peritectoid reaction.

Solid silicon phase: Solid silicon forms above 50 wt.% Si in the alloy, with pure Si being the nominal composition. Silicon dissolves less than 1 ppm Fe in the solid state (Nakajima and Usami, 2009).

The invariant points in the phase diagrams above 33 wt%Si are the following:

T: 1410°C;	FeSi phase melts congruently	$FeSi_{(s)} = FeSi_{(l)}$
T: 1211°C;	At 50%Si	$L \leftrightarrow Fe_3Si_7 + FeSi$ (eutectic)
T: 1214°C;	At 57%Si	$L_2 \leftrightarrow Fe_3Si_7 + Si$ (eutectic)
T: 1215°C;	Fe_3Si_7 melts congruently	$Fe_3Si_{7(s)} = Fe_3Si_{7(l)}$
T: 996°C;	wt% Si between 33–50%	$Fe_3Si_7 + FeSi \leftrightarrow FeSi_2$(peritectoid)
T: 948°C;	wt% Si above 57%	$Fe_3Si_7 \leftrightarrow FeSi_2 + Si$ (eutectoid)

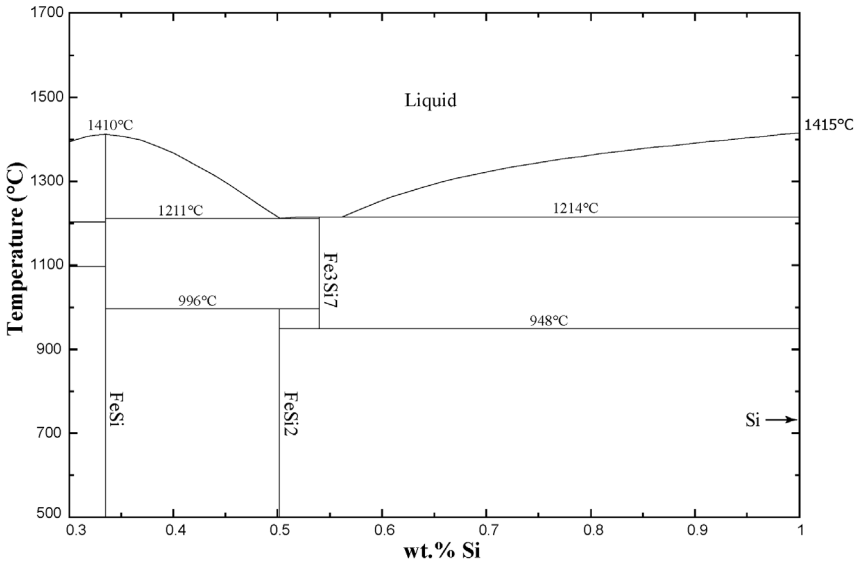


Figure 11.1 *Phase diagram of the Fe–Si system (calculated in FactSage).*

A solidification path is a diagram that shows the progressive change in the relative fraction of phases present over a temperature interval, as a liquid of known composition is cooled. In this section, the solidification paths for FeSi45, FeSi75 and FeSi92 are shown in Figure 11.2 and described. Other solidification paths may be illustrated using the lever rule in the Fe–Si phase diagram. Figure 11.2 a) shows the solidification path for the FeSi45 alloy, which at low temperatures ends up in the FeSi–$FeSi_2$ area. At 1295°C, FeSi begins to precipitate from the liquid, and the liquid gradually becomes richer in Si. At 1250°C, the liquid and FeSi are present in a ratio of 4:1. At 1211°C, the liquid is completely converted to Fe_3Si_7 and FeSi in a ratio of 56% to 44%. This situation remains constant until 996°C, where Fe_3Si_7 and FeSi transform into $FeSi_2$ through the peritectoid reaction.

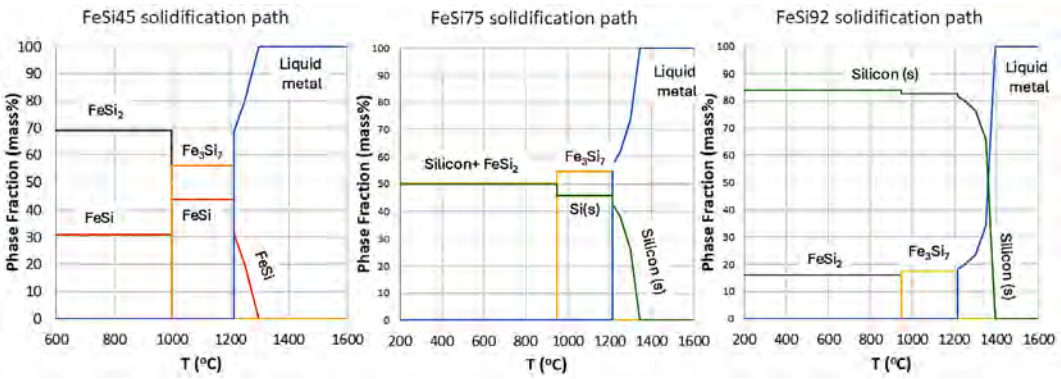


Figure 11.2 *Solidification path for FeSi45, FeSi75 and FeSi92 (calculated by FactSage).*

FeSi75 and FeSi92 both end up in the silicon and $FeSi_2$ area at low temperatures, as seen in Figure 11.2 b) and c). FeSi75 starts to precipitate solid silicon at 1344°C, whereas FeSi92 starts to precipitate silicon at 1395°C. Almost pure silicon precipitates due to the low solubility of iron in solid silicon. The liquid gradually becomes richer in Fe until it reaches the Fe_3Si_7 composition at 1214°C. Below this temperature, the liquid phase converts into solid Fe_3Si_7, with the remainder being the Si phase. The eutectoid reaction from Fe_3Si_7 to $FeSi_2$ and silicon increases the amount of the Si phase.

Figure 11.3 shows the enthalpy of pure silicon and other FeSi alloys as a function of temperature. For 100% pure silicon, a large amount of thermal energy is released at 1414°C during the phase change from liquid to solid silicon. Normally, small amounts of trace elements like Al, Ca, Fe etc. create a small temperature range for solidification rather than a single point of solidification. The latent heat of silicon is about 7 times higher per ton compared to Fe, and hence, the latent heat of the alloy decreases dramatically when Fe is added to the alloy, as seen in Figure 11.3.

The enthalpy of pure Si at the melting point (1414°C) is 86 kJ/mol, with the latent heat being approximately 50 kJ/mol. Therefore, more than half of the energy is released during solidification, while the rest (approximately 36 kJ/mol) is released during cooling of the solid phase. The amount of thermal energy released during silicon solidification is about 9% of the electrical energy used in the process; hence, there are large possibilities for energy recovery in the industry.

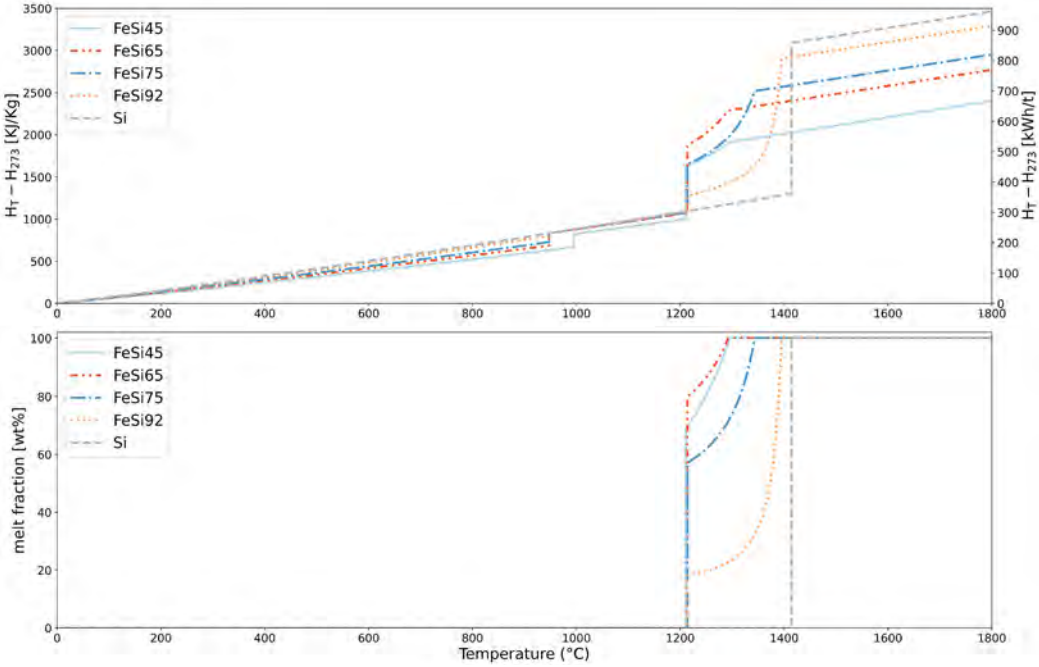


Figure 11.3 *Enthalpy of silicon and silicon alloys and the melt fraction as a function of temperature (calculated in FactSage).*

11.3 Solidification processes

Product Requirements

The main requirements for silicon alloys are high homogeneity, high strength, high purity and a tailored grain size distribution. Generally, a fast solidification process improves homogeneity and strength due to a smaller grain size and less segregation. Conversely, a slowly cooled cast results in more trace elements being concentrated in the centre of the ingot than at the edges, necessitating additional grinding and sieving steps (Andresen, 2006).

Ideally, shock freezing of the liquid would conserve the distribution of all the elements. However, the significant heat generated during solidification, recrystallization at the liquidus, and diffusion at temperatures above 400°C prevent the ideal distribution from being achieved in any industrial process

(Leblanc *et al.*, 2004). Smaller crystals are more abundant at grain boundaries, allowing a more even distribution of the intermetallic phases in rapid cooling technologies (Margaria, 1994; Baud and Margaria, 1995).

Traditional casting methods for FeSi and silicon

The two traditional casting methods for silicon and ferrosilicon currently in use are casting in iron molds and casting on a bed of Si/FeSi fines (or pieces, as practised in some plants in the USA). In both methods, the main cooling mechanisms are thermal conductivity to the mold and radiation from the top of the cast silicon.

Figures 11.4 and 11.5 show casting in an iron mold. A runner is sometimes used between the transport ladle and the iron mold to reduce the kinetic energy of the liquid metal stream. Casting molds can be either static or placed on belt machinery, with both circular and linear moving casters in use today. The size of the mold (also called beds) typically ranges from 0.5 to 2 meters, with a casting thickness of 5 to 30 mm. A cast iron mold is usually about 100 mm thick. Despite precautions such as using a runner, iron molds undergo significant thermal shock and wear. Additionally, the iron in the mold can dissolve into the Si/FeSi alloy, causing extra contamination.

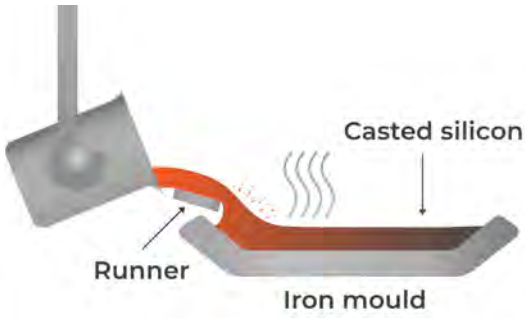


Figure 11.4 *Traditional casting in iron mold.*

Thin casting in beds filled with fines is the most commonly used casting method today. The fines range in size from 0–2 mm and come from the crushing steps of earlier casts (Møll, 2014). This method involves simply pouring

silicon from a ladle into a fines bed and allowing it to cool into a cake. The cake is removed from the mold as soon as possible, ready to be crushed and sieved, typically using a crane or forklift. Cooling of the cake to room temperature takes about 12 hours, according to Leblanc *et al.* (2004).

The lifespan of the mold increases when fines are placed in the bed. The fines protect the mold from wear and protect the alloy from Fe dissolution from the mold walls. However, as stated by Bullon and More, there are both advantages and disadvantages associated with using fines in the process (Bullòn and More, 2002). Fines from earlier grinding steps are reused, minimizing waste as much as possible. The fines are recycled in the process because their market value is about 20% lower than that of sized silicon. Each cast can produce up to about 10% of fines. The use of fines, however, increases product inhomogeneity, as they typically contain a higher concentration of impurities. This is a concern for customers who seek the highest purity in their raw materials and want to minimize the fraction of fines. It has been observed that fines introduce more oxygen and impurities into the final product compared to copper casting techniques (Nygaard, 2006). Due to the low thermal conductivity of the fines, a large concentration difference within the ingot may arise. The casting is mainly cooled from the top by radiation and convection, which can induce segregation at the centre of the cast (Tveit, 1988).



Figure 11.5 *Traditional thin casting in mold with silicon fines (Møll, 2014).*

Other common features of traditional casting processes include:

- *Simplicity and Acceptable Quality*: The processes are simple, and the product quality is acceptable. Traditional casting strikes a good balance between product quality and cost. Among the currently available techniques, it requires the lowest initial capital investment in equipment and infrastructure.
- *Long Production Time*: The production time is quite long. It takes approximately 30 minutes to cast and cool the metal in a mold, and several hours before it is taken to the pre-crushing area. This is followed by two crushing processes and at least two sizing processes.
- *High Costs:* Although the initial investment is relatively low, the operating costs are high. It requires a lot of personnel, equipment, material movements, and results in losses (such as fines). This solidification technique is therefore most suitable for smaller, non-automated production where minimizing upfront investment is a priority.
- *Cooling Attempts*: There have been attempts to use water to cool down the cast iron mold. However, this method has proven to be neither practical nor safe for casting silicon (Nygaard, 2006).

Alternative casting methods

Copper casting technologies and water granulation are interesting processes because they offer a good balance between properties and costs. They provide higher homogeneity and cleanliness than traditional cast iron casting methods and require fewer grinding steps. These techniques rely on strong thermal shock during solidification. This can trigger a 'self-grinding' process in the product, influence grain size, and reduce the impurity level. However, it is difficult to find the right balance between the number of grain boundaries and the amount of intermetallic phases (Nygaard, 2006). When it is not possible to tune the particle size through the intrinsic properties of the alloy, a grinding step must be introduced into the process.

Advanced cast-to-shape methods such as atomization or air-granulation technologies are believed to provide higher quality than copper casting. However, they are difficult to implement at industrial scale, due to high maintenance and production costs.

Copper casting

Copper casting consists of casting silicon alloys onto a cooled copper plate. This technique gained attention at the beginning of the 2000s, as described by Bullòn *et al.* (2007). It is defined as 'the adaptation of the continuous casting technology in steel to the silicon industry'. The ladle is connected to a tilting device, which allows the melt to fall continuously onto the plates. A runner distributes the metal across the full width of the plate. The molten metal meets water-cooled copper and starts to solidify. Vibration of the copper plate causes the metal to move forward. At this point, the metal is already solid (about 1100°C at the bottom surface). When it falls from the copper plate to the first iron plate, the metal starts to break up. Vibrations are then adjusted to transport the alloy along the iron plate while breaking it into pieces. When the silicon leaves the machine, its temperature drops to 500°C. The copper and iron plates remain perfectly clean, and no fines are incorporated into the product. Figure 11.6 shows how the copper casting machine looked in 2002 at the Ferroatlantica plant in Sabon, Spain.



Figure 11.6 *Schematic of the copper casting machine at Ferroatlàntica's Sabon plant (Bullòn et al., 2007).*

The copper casting process has several advantages:

- *The solidification time is very short*. The whole process takes about 15 minutes, from the ladle to sizing and storage. Solidification on the copper plate takes 30 seconds, the metal then moves from the copper plate less than 5 minutes later, and the remaining time is spent along the remaining two iron plates. By comparison, complete solidification of a single thin cast on fines takes approximately 30 minutes.

- *Copper casting does not have challenging crushing and sieving steps.* Vibration of the copper plates and the strong thermal gradient trigger a 'self-grinding' process. As a result, the expensive and time-consuming grinding steps are not carried out.
- *Copper casting gives a comparable solidification rate to the water granulation* (Andresen, 2006). This implies that copper-cooled silicon does not allow impurities sufficient time to segregate, thereby improving uniformity. In the copper casting machine, grains follow the cooling direction, whereas traditional fines casting results in disorganized crystals with random orientation.
- *No fines are used, and less fines are produced*. A direct consequence of not adding fines is a lower oxygen content in the material, resulting in reduced oxidation caused by fines. In addition, the amount of fines produced by self-crushing is lower. Bullòn and More (2002) report the formation of 3% fines below 5 mm and 1% fines below 1 mm with the copper casting machine, which is significantly lower than the 10% and 4% respectively for < 5 mm and < 1 mm fractions estimated in their study for conventional casting.
- *Improved slag segregation thanks to a slower ladle tilting process*. Thanks to the higher slag viscosity and density, slag remains in the ladle or on the runner instead of falling onto the copper plate, giving a slag content of about 1.22% in the silicon. The percentage of slag fragments in the material larger than 5 mm is lower.
- *The life span of the copper plates is higher compared to the traditional casting technique.* Bullòn and More reported that the machine did not experience significant mechanical erosion after more than 1,000 casts (approximately 40,000 tons of silicon). Primary maintenance involves replacing or turning the copper plate. Due to its symmetry, flipping the plate once it is worn out is sufficient. It was estimated that copper plate replacements add about €15 per ton to the cost of silicon.
- *The installation is easy to automate and optimize*. This implies reduced costs related to personnel, equipment, material movements, and losses in fines. A grinder could be added at the end to achieve finer granulometries. In addition, a load cell was applied under the ladle to tune the flow rate of silicon being cast onto the copper plate. These improvements are described in Bullòn *et al.* (2007).

Water granulation

Water granulation can be used both for silicon and ferrosilicon casting. The process is based on controlled teeming of metal into water. The metal stream from the ladle is split into droplets before reaching the water. The granules are continuously removed from the bottom of the granulation tank for dewatering and drying, before they are screened, stored, and shipped (Leblanc *et al.*, 2004). Plants have operated with either flowing water or still water. Figure 11.7 shows the principal process for water granulation.

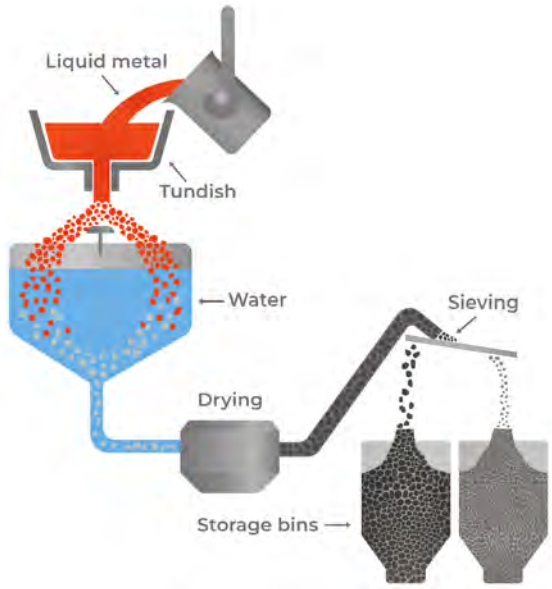


Figure 11.7 *Water granulation principle.*

The main features of the process can be listed as:

- *Water granulation gives fast solidification compared to other techniques* (Andresen, 2006), resulting in higher product homogeneity and shorter production times. The high heat-transfer rate, combined with the small size of the metal droplets, provides quick solidification and a strong alloy.
- *Water granulation avoids both fines and lumps formation.*

- *There have been problems related to hydrogen formation* since the 1970s, which created uncontrollable explosions (Nygaard, 2006). Studies on the drop formation energy and its effect on the product size distribution were carried out (Nygaard and Brekken, 1994). The intensity of the explosion and the degree of fragmentation during water granulation depend on the Al/Ca content in the molten drop (Hildal *et al.*, 2000). Alloyed specimens release more hydrogen than pure silicon drops, as a higher amount of Al or Ca in the Si-metal enhances the oxidation reaction. The increased level of impurities will, however, prevent steam explosions. Molten silicon drops with small content of Ca and Al descend in the water tank twice as fast as pure silicon drops. The reason for these events is not yet explained; however, this is why many water granulation installations have been shut down.

Cast to shape process

Elkem developed the first cast to shape process in 1995 at Fiskaa Silicon, Norway. Liquid silicon was poured into several rod-shaped molds, machined into the surface of a rotating copper roller. The small rods broke into pieces when they fell out of the molds.

The cast to shape technology was also 'blended' with copper casting to further increase the cooling rate. This technique was presented in 2004 by Leblanc *et al.* Sixteen identical copper segments form a huge horizontal rotating wheel. The copper is water cooled through internal channels. Just before one complete rotation, silicon is pushed off the wheel and down into a bin. When the product falls into the bin, it will break 'as a china plate falling on a hard floor, and very little small splinters or powder will occur' (Leblanc *et al.*, 2004).

These two casting methods aimed to avoid crushing and screening, and thereby to improve product yield and quality compared to traditional fines casting. The processes looked promising, but high costs were the main reason why cast to shape technology was not brought to industrial scale (Nygaard, 2006). Another issue is the continuous exposure of the casting equipment to immense heat. These casting methods may require stricter temperature and mass flow control, leading to higher levels of automation, more advanced technologies, and greater initial investments.

Atomization in inert gas or air

The atomization process consists of spraying silicon from an atomizer. The droplets freeze very quickly, and a high proportion of intermetallic phases forms at the grain boundaries rather than in primary silicon. A small-scale test for atomization, or 'granulation in air', was carried out at Wacker-Chemie in 1992. An air-blowing pipe was directed horizontally towards the liquid silicon, which was falling between the tapping spout and the ladle. As the velocity of the air was increased, the liquid silicon stream began to granulate. Most of the liquid silicon was converted into small drops, which froze to an average size of around 1 mm.

Some features of the atomization process are listed as:

- *It is difficult to tune the silicon particle size with high precision*. Nygaard (2006) quotes, as an example, a plant in Brazil producing about 40% of its particles with a size between 50–200 μm. The rest was coarser than 200 μm and therefore needed a subsequent milling step.
- *The potential properties could not defend the costs*, despite large savings from avoiding casting, crushing and milling. In fact, the technology was implemented at industrial scale without success.
- *Finally, water, air and oxygen must be eliminated* when using inert gas atomization. If they are not removed correctly, drops will be covered in a thick layer of oxide. Oxidation of the final product decreases product quality and brings extra maintenance and machinery costs to the solidification unit.

11.4 Solidification and product properties

Solidification processes

Structure index number (QF) and cooling rate

The chosen solidification process is directly related to the cooling rate. Since the cooling rate cannot be measured in absolute terms, Pachaly (1994) introduced the concept of the Structure Index Number (QF). The higher the QF, the faster the solidification rate and the higher the homogeneity of the material. QF is defined as the ratio between the area portion of the intermetallic phases at the grain boundaries and the area portion of intermetallic phases

in primary silicon. The value is computed after analyzing the structure of silicon samples by image analysis. QF therefore reflects variations in average grain size as the solidification technique changes. Table 11.1 lists some of the QF values estimated by Pachaly for most of the silicon solidification processes described in this book.

Table 11.1 *Structure index number as a function of solidification procedure describing the ratio between the area portion of the intermetallic phases at the grain boundaries and the area portion of intermetallic phases in primary silicon (Pachaly, 1994).*

Solidification process	QF
Mold cast 50 cm on thick fines layer in isolated mold	0.10
Mold cast 50 cm on thin fines layer in isolated mold	0.25
Mold cast 40 cm on thick fines layer	0.26
Mold cast 40 cm on thin fines layer	1.58
Mold cast 30 cm on thin fines layer	2.34
Mold cast 10 cm on thin fines layer	6.02
Continuous cast 10 mm on copper	10.09
Water granulated 10–15 mm	23.21
Water granulated 5–10 mm	29.55
Air granulated 2–3 mm	42.60
Atomized	63.92

Solidification speed and grain growth in silicon rich-alloys

A model for grain growth has been reported by Kattamis *et al.* (1967). A smaller grain radius has a greater impact on surface tension than a larger grain radius. As shown in Figure 11.8, the dendrite arms are considered to consist of one arm with radius a and a thinner arm with radius r_o. This model appears to accurately represent grain growth in silicon-rich ferro-alloys.

It was found that grain coarsening occurs between 1412.8°C and 1396°C for MG–Si (Kinoshita and Champier, 1981), which is close to the melting point.



Figure 11.8 *Model for coarsening of a dendrite grain structure (adapted from Kattamis et al., 1967).*

As grain radius increases, a composition gradient develops in the liquid phase: it is steeper outside a smaller grain than outside a larger grain, which makes the larger grain more stable. In 75% ferrosilicon, the silicon content is higher near the surface of a smaller grain than near the surface of a larger grain. Consequently, silicon diffuses from the smaller grain to the larger grain, stimulating silicon precipitation at the larger grain. Conversely, the reduced silicon content at the surface of the smaller grain may induce some melting of the smaller grain. This process is crucial to the formation of the alloy structure. Kattamis *et al.* (1967) calculated the correlation between the solidification time t_c and the dendrite or grain size d. The effect of the equation on microstructure is illustrated in Figure 11.9.

$$t_c = kd^3 \qquad [11.1]$$

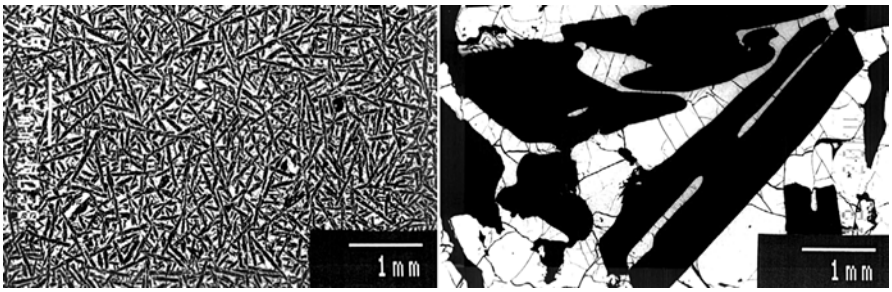


Figure 11.9 *Left: Grain size of rapidly solidified ferrosilicon (1170°C/min). Ref. the 1 mm length line. Equivalent grain size is measured to be 59 μm. Right: Grain size of very slowly solidified ferrosilicon (0.21°C/min). Ref. the 1 mm length line. Equivalent grain size is measured to be 784 μm.*

By increasing the cooling rate by a factor of 10^4, the morphological spacing for silicon-rich alloys decreases by an order of magnitude. The relationship is shown in Figure 11.10, which gathers results from Tveit (1988) and Forwald (1997). The cooling rate varied over a long range, either by looking into industrial production or by varying the efficiency of the insulation of the ferrosilicon cast.

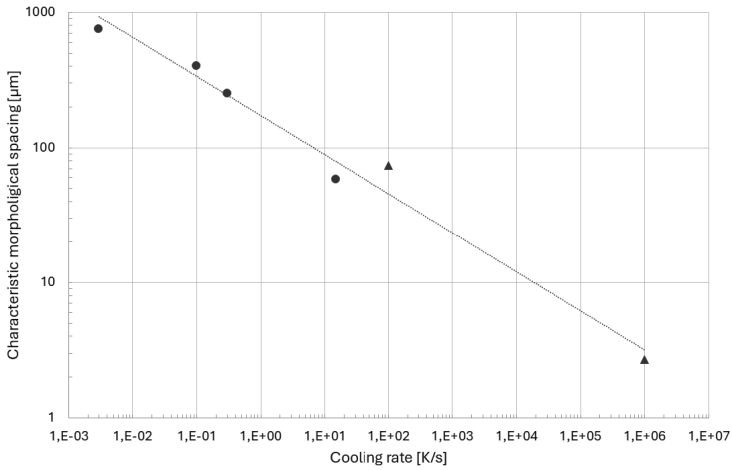


Figure 11.10 *Morphological spacing vs. cooling rate for some Si-rich alloys (Forwald, 1997). Legend: 'spheres' = results from (Tveit, 1988); 'triangles' = results by (Forwald, 1997).*

The final effect of the cooling rate on the grain size distribution is seen in Figure 11.11. The graph shows the grain size distribution of iron mold cast, water granulated and thin cast silicon metal. The curves for iron mold casting and thin casting are wide compared to water granulation, which has a very steep particle size distribution curve. A steep curve corresponds to more uniform particle size distributions and to a lower fines percentage. Most of the fraction for water granulation is below 3 mm, while the majority for iron mold and fines casting is between 10–100 mm or 7–10 mm, according to the product chosen.

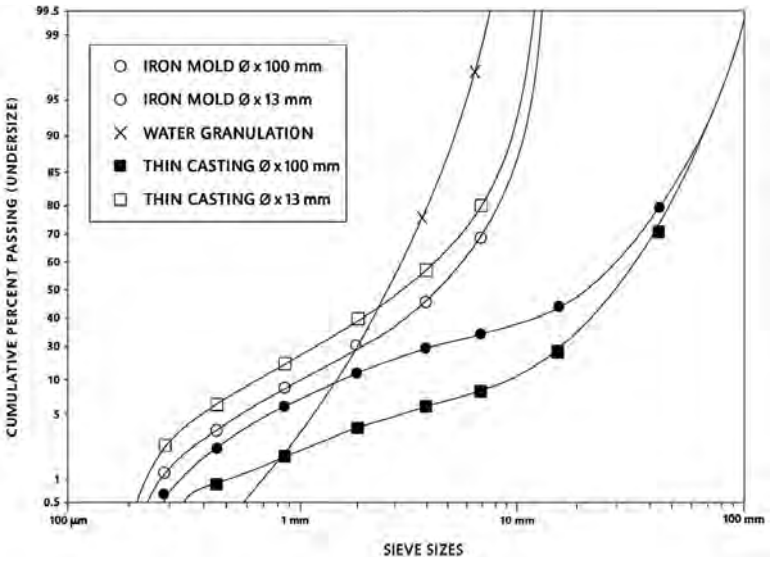


Figure 11.11 *Size distribution of conventional casting, water granulation and thin casting (Leblanc et al., 2004).*

Casting MG–Si in fines

Most of the impurities in a 10 cm thick cast are found close to the centre, between 5.0–7.5 cm from the top of the cast. It was found that this zone corresponds to the area where the temperature is still high after about 20 minutes of solidification, as shown in Figure 11.12. The position of the impurities is related to the cooling rate at different positions. Møll modelled the temperature at different positions in a 10 cm thick cast during solidification

(Figure 11.13). The positions close to the top and the bottom surface cool fast initially (10 cm, 9 cm, 7.5 cm, 0.5 cm and 1 cm), while the central portion of the cast (3 cm, 4 cm, 5 cm) keeps a higher temperature for longer. The results were also confirmed by characterization of silicon casts at different positions. Figure 11.14 shows the microstructure at the top, the centre and the bottom of the cast. The liquid silicon at the bottom is found together with the impurities, which increase the liquid density (Møll, 2014). Material coming from the top and the bottom zones in the cast has higher purity compared to the central part, where segregation and lower cooling rates are favored.

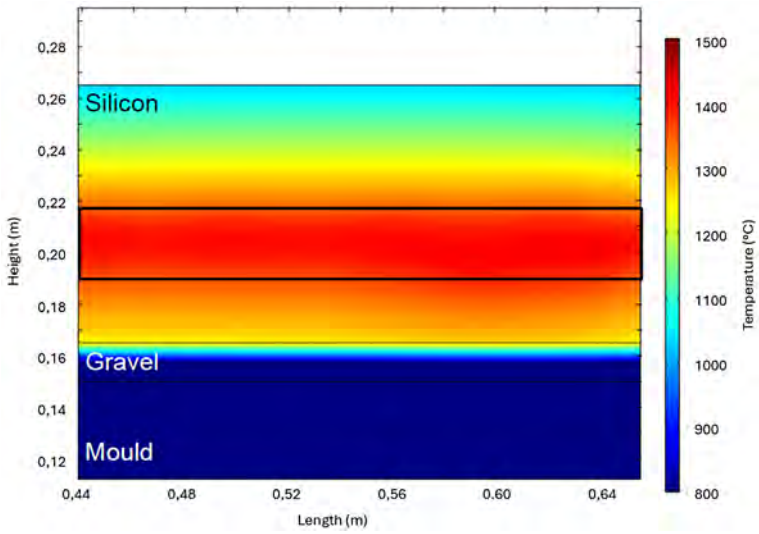


Figure 11.12 *Surface plot, 1250 seconds (about 20 minutes) after the start of solidification obtained by the COMSOL model. Regions with temperatures below 800°C are illustrated in dark blue. The area inside the rectangle corresponds to the sample extracted 5.0–7.5 cm from the top of the cast. The microstructure in the black rectangle zone is comparable to Figure 11.14b (Møll, 2014). [Used with permission from Maria F. Møll].*

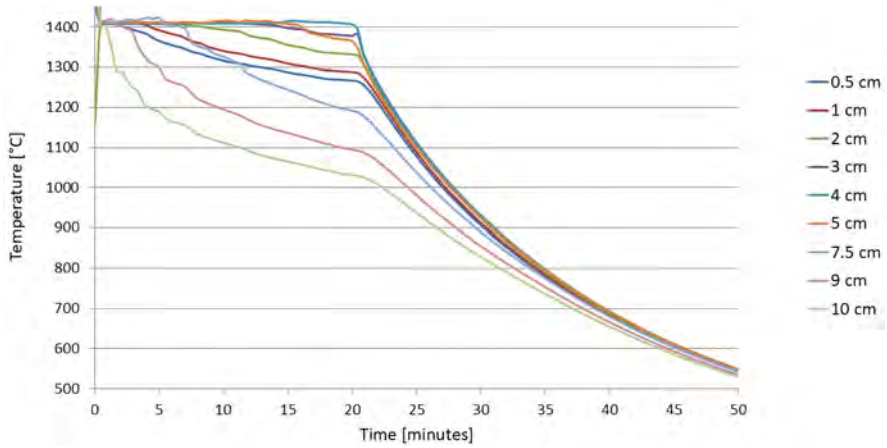


Figure 11.13 *Temperature in different positions from the bottom of the 10 cm modelled cast. It is seen that when the position was close to the top or bottom surface, the temperature decrease is fast initially, but slow subsequently due to the heat from other areas that must be transported through the surfaces (Møll, 2014). [Used with permission from Maria F. Møll].*

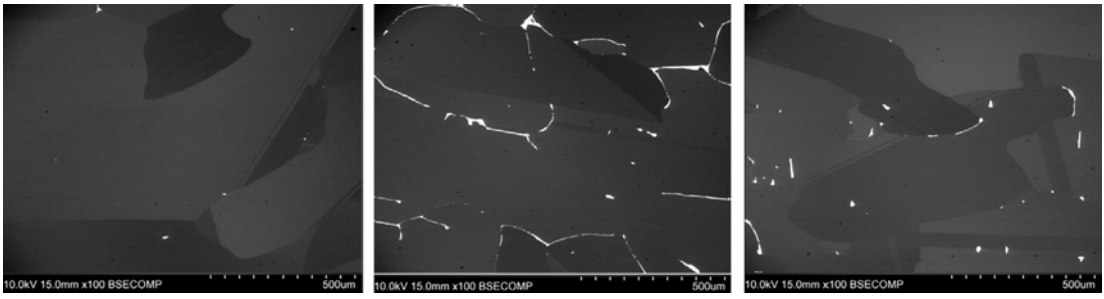


Figure 11.14 *Microstructure of thin cast samples at top (a), centre (b) and bottom (c) of the cast. The concentration of intermetallic phases is highest at the centre of the cast (Broggi, 2015) [Used with permission from A. Broggi].*

The amount of heat to be removed increases with the height of the cast (Møll, 2014). Figure 11.15 shows the temperature–time profile of casts of different heights, modelled at 1 cm above the fines. For thicker casts (> 5 cm), the cooling rate is quite similar in the temperature range where the silicon grain size is affected (1414–1396°C), highlighted by the blue rectangle. However,

for thinner casts, the cooling rate is faster, and the coarsening temperature interval is crossed very quickly, resulting in a smaller average grain size.

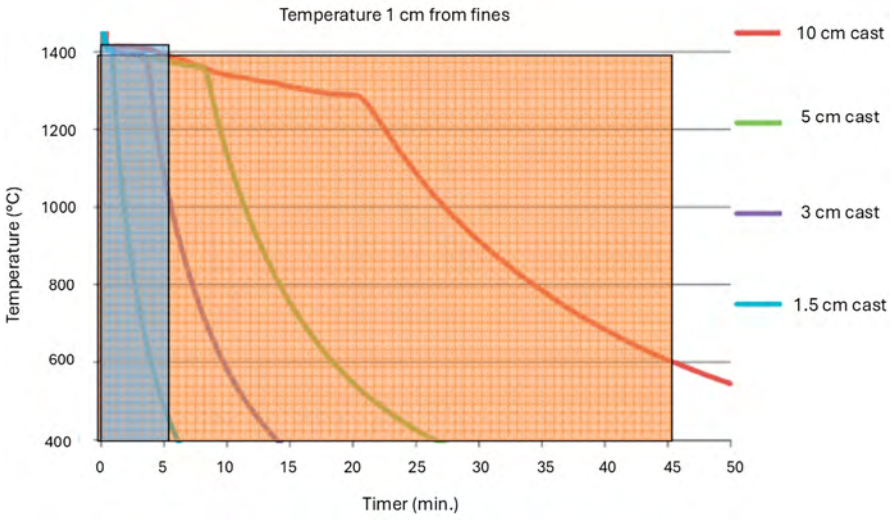


Figure 11.15 *Temperature 1 cm from the fines layer in 1.5, 3, 5 and 10 cm cast. Notice the large variation in the cooling rate within the blue rectangle length for the different casts (Møll, 2014). [Used with permission from Maria F. Møll].*

Transformation below the melting point of silicon

Heat treatments: effect on microstructure

Product homogeneity can be influenced by adjusting the cooling rate below the melting point of silicon, or by performing heat treatments once silicon has solidified, without affecting the grain size. The shape and number of intermetallic phases change when the cooling rate decreases after the solidification of primary silicon (Rong, 1992). Broggi and Tveit (2016) confirmed changes in microstructure after maintaining a desired temperature over time.

Heat treatments are effective when the temperature crosses the melting point of intermetallic phases. Figure 11.16 shows the cooling ranges for the most common intermetallic phases in MG–Si. These are the temperature ranges where the intermetallic phases can remelt during heating, or precipitate during cooling.

Common impurities in silicon include Al, Ca, Fe and Ti, as discussed in Chapter 10. These impurities form intermetallics at the grain boundaries of the silicon phase and affect the solidification temperature and structure. In an overview of literature on the topic, Møll (2014) concluded that there is a consensus on the typical intermetallic phases found in MG–Si, as listed in Figure 11.16. Calculations by Dons showed a solidification range of these intermetallic phases between 1100°C and 660°C. (Dons, 2009).

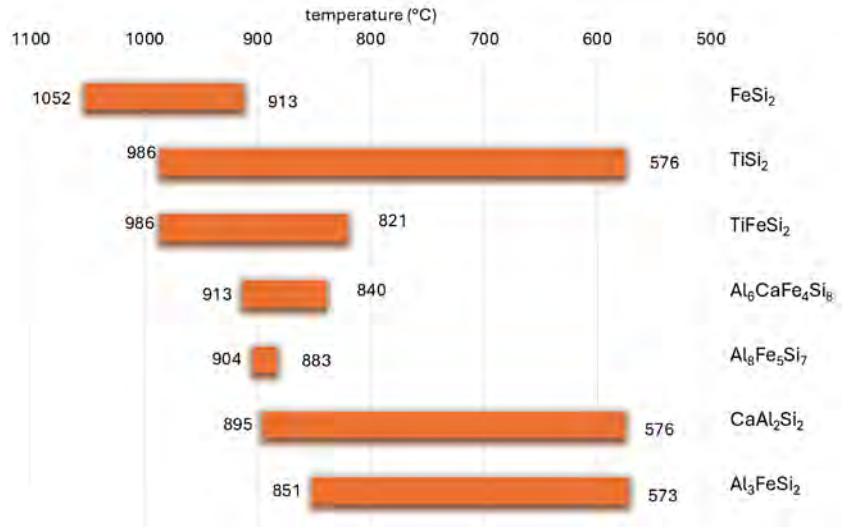


Figure 11.16 *Cooling ranges of intermetallic phases summarized by Dons (2009). The temperatures delimiting the melting range are written on the side of each bar. (Broggi and Tveit, 2016). [Used with permission from A. Broggi].*

It was found that the intermetallic phases change their microstructure after heat treatments at a temperature above 800°C. The intermetallic phases in the centre of the cast follow the grain-boundary profile. Their aspect ratio (a geometrical parameter, which decreases towards 1 as a shape is more circular) before the heat treatment can reach values between 5–13 (Broggi, 2015). After the treatment, the phases remelt, their aspect ratio decreases towards 2, and product homogeneity increases. There are radical changes in terms of average intermetallic particle size, aspect ratio and number of intermetallic phases per mm^2. The heat treatments are effective at above 900°C and durations exceeding 30 minutes.

The change in microstructure is attributed to a minimization of surface energy through splitting and coarsening (Broggi, 2015). At short holding times, the intermetallic phases will split. The number of intermetallic phases will increase through the cast, especially close to where the solidification fronts used to meet during solidification. At longer holding times, the intermetallic phases will coarsen and the particle number will decrease.

Cracking of intermetallic phases can affect product homogeneity. This phenomenon was also noticed by several authors (Møll, 2014; Broggi, 2015; Gueneau *et al.*, 1995; Ott, 2003). This effect might be meaningful in different downstream processes that are influenced by the intermetallic phase size distribution. During crushing and sieving, cracks would propagate; therefore, the intermetallic phases tend to end up in finer fractions. Møll (2014) found that in the + 0.3 mm fractions the trace elements were quite stable; however, in the –0.05 mm fraction, the level of trace elements was approximately doubled compared to the average value in the cast after crushing and sieving.

Margaria *et al.* (1992) found that the amount of four intermetallic phases $CaSi_2$, $FeSi_{2.4}$, $Al_6Fe_4CaSi_8$ and $CaAl_2Si_2$ respectively reaches an 'equilibrium point' after heat treatments at 925°C (Figure 11.17). This reaction is believed to increase the product purity in MG–Si and Fe–Si, as pure silicon is produced. The suggested phase equilibrium may be written:

$$3\ Al_2CaSi_2 + 4\ FeSi_2 \leftrightarrow Al_6CaFe_4Si_8 + 2\ CaSi_2 + Si$$

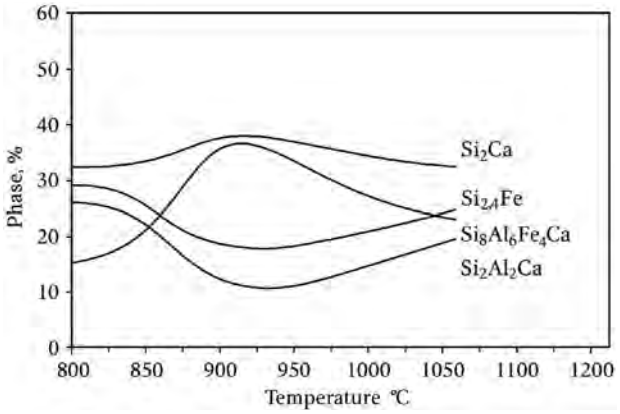


Figure 11.17 *Effect of annealing on the relative fractions of intermetallic compounds (Margaria et al., 1992).*

Another solid-state chemical reaction is the formation of tertiary silicon in Fe–Si alloys. The mechanism is suggested to be a two-step reaction (Boomgard, 1972):

1. Fe_3Si_7 transforms first into the phase $FeSi_{2r}$(Si) while cooling down. This phase has an excess of Si atoms and is therefore supersaturated.

$$Fe_3Si_7 \rightarrow FeSi_{2r}\left(Si\right)$$

2. Silicon precipitates out of the supersaturated phase.

$$FeSi_{2r}\left(Si\right) \rightarrow FeSi_2 + Si$$

This reaction creates a volume increase by 0.6% in the alloy (Holdhus, 1962). This volume change may also justify the disintegration of ferrosilicon and the formation of cracks. The difference in the expansion coefficient of Si and Fe_3Si_7 creates thermomechanical stress while the alloy cools. If the cast is thick and the volume expansion is limited by the surrounding solidified alloy, this reaction may practically lead to a self-crushing situation.

Tertiary silicon has a characteristic feather-like look, as seen in Figure 11.18 (Anisdahl, 1987). The reaction seems to nucleate at grain boundaries or matrix irregularities. The structure is finer than the typical grain structure found in 75% ferrosilicon. It was found that the kinetics of formation of tertiary silicon are too slow compared with the rapid solidification rates used in industry (de Huff, 1969). Figure 11.19 shows that the reaction starts if the metal is at 787 °C for 10–15 minutes. The optimum condition for completing the reaction (i.e. lowest temperature and shortest time) is approximately 718 °C with a holding time of 3 hours. The measured reaction heat is approximately 30 kJ/kg $FeSi_2$ (Tveit, 1988).

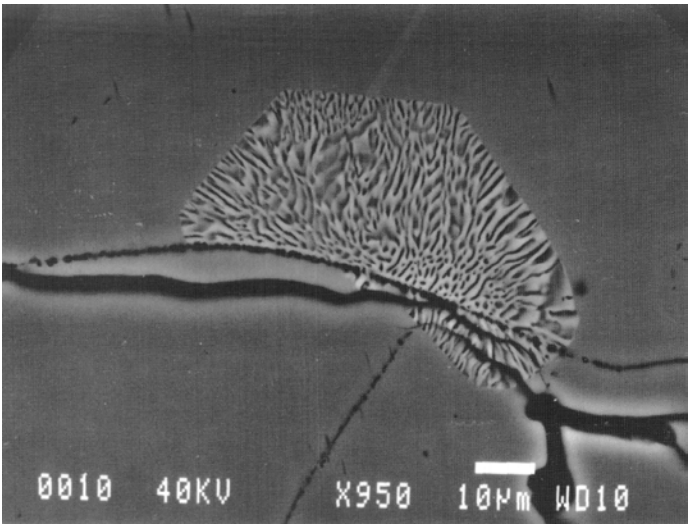


Figure 11.18 *Microscope image of tertiary silicon and $FeSi_2$ from solid-state reaction (Anisdahl, 1987).*

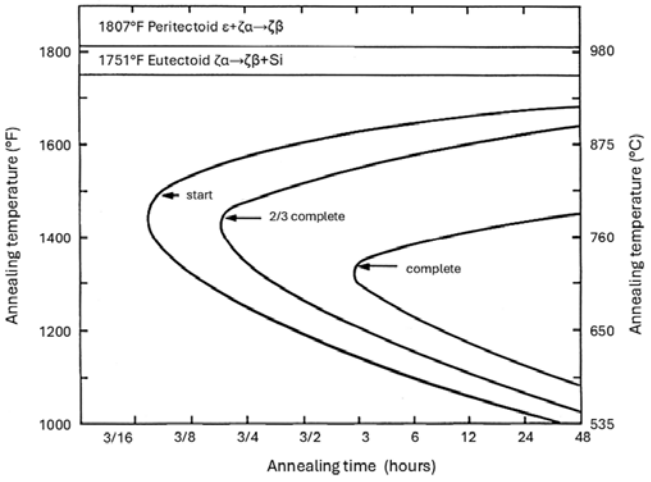


Figure 11.19 *Temperature-time diagram for the reaction ζ_a-phase $[Fe_3Si_7] \rightarrow FeSi_2 + Si$ (de Huff, 1969).*

References

Andresen, B. (2006) 'The silicon process', in *Proceedings of Silicon for the Chemical Industry VIII*. Trondheim, Norway, pp. 35–49.

Anisdahl, L. (1987) *Diffraction survey of 75% ferrosilicon*. SINTEF Report STF34 A87078. In Norwegian.

Baud, L. and Margaria, T. (1995) 'Silicon for silicones: A developing route for P.E.M.', in *Proceedings of INFACON VII*. Trondheim, Norway, pp. 655–664. Available at: https://www.pyrometallurgy.co.za/InfaconVII/655-Baud.pdf

Broggi, A. (2015) *Inclusion optimised silicon for the production of silicones*. MSc thesis. Norwegian University of Science and Technology (NTNU), Trondheim, Norway. Available at: https://hdl.handle.net/11250/2377287

Broggi, A. and Tveit, H. (2016) 'Growth of impurity phases below the melting point of silicon and consequences on fluidizied bed reactor efficiency', in *Silicon for the Chemical and Solar Industry XIII*. Kristiansand, Norway, 13 June, pp. 83–94.

Bullòn, J.C. and More, A. (2002) 'Experiences at Ferroàtlantica using the new casting machine', in *Silicon for the Chemical and Solar Industry VI*. Loen, Norway, pp. 47–54.

Bullòn, J.C., More, A. and Miguez, J.C. (2007) 'The improvements to copper casting machine for ferroalloys', in *Proceedings of INFACON XI*. New Dehli, India, pp. 539–547. Available at: https://www.pyrometallurgy.co.za/InfaconXI/539-Bullon.pdf

de Huff, J.A. (1969) 'The structure of ferrosilicon', paper presented at the 27th Electric Furnace Conference, *Electric Furnace Proceedings*.

Forwald, K.R. (1997) *Properties of some silicon rich alloys*. Doctoral thesis. Norwegian University of Science and Technology (NTNU).

Gueneau, C., Servant, C. and Manier, F. (1995) 'Relationships between the grinding behavior and the microstructure of ferro-silicon alloys with 65 wt% silicon', in *Proceedings of INFACON VII*. Trondheim, Norway. Available at: https://www.pyrometallurgy.co.za/InfaconVII/673-Gueneau.pdf

Hildal, K., Nelson, L.S., Bergstrøm, T. and Tuset, J.K. (2000) 'Interactions between molten silicon drops and water', in *Silicon for the Chemical and Solar Industry V*. Tromsø, Norway, pp. 171–181.

Holdhus, H. (1962) 'The transformation of the ζ-phase in iron-silicon alloys', *J. Iron and Steel Inst.*

HSC Chemistry (2023) *HSC Chemistry*. Version 9.0. Released.

Kattamis, T.Z., Coughlin, J.C. and Flemings, M.J. (1967) 'Influence of coarsening on dendrite arm spacing of aluminium copper alloys', *Trans. Met. Soc. AIME*, 239, pp. 1504–1511.

Kinoshita, M. and Champier, G. (1981) 'Recrystallization of cast polycrystalline silicon', *Materials Science and Engineering*, 47(1). Available at: https://doi.org/10.1016/0025-5416(81)90037-9

Leblanc, D., Boisvert, R. and Ksinsik, D. (2004) 'Production of silicon metal with controlled solidification rates – description of the various processes used at Bècancour Silicon Inc. and their potential benefits for conversion to methyl- and chlorosilanes', in *Silicon for the Chemical and Solar Industry VII*. Trondheim, Norway, pp. 33–44.

Margaria, T. (1994) 'Identification and control of the characteristics of silicon used in direct synthesis', in *Silicon for the Chemical and Solar Industry II*. Loen, Norway, pp. 21–31.

Margaria, T., Anglezio, T.J. and Servant, C. (1992) 'Intermetallic compounds in metallurgical grades silicon', in *Proceedings of INFACON VI*. Cape Town, South Africa. Available at: https://www.pyrometallurgy.co.za/InfaconVI/1209-Margaria.pdf

Møll, M.F. (2014) *Solidification of silicon: Macro- and microstructure as functions of thermal history and composition*. Doctoral thesis 2014:21. Norwegian University of Science and Technology (NTNU). Available at: https://hdl.handle.net/11250/249462

Nakajima, K. and Usami, N. (2009) *Crystal growth of Si for solar cells*. Springer.

Nygaard, L. (2006) 'Silicon solidification techniques for the chemical industry', in *Silicon for the Chemical and Solar Industry VIII*. Trondheim, Norway, 12 June, pp. 71–78.

Nygaard, L. and Brekken, H. (1994) 'Production of water granulated silicon', in *Silicon for the Chemical and Solar Industry II*. Trondheim, Norway, pp. 61–67.

Ott, E. (2003) *Solidification of two ferroalloys, FeSi 75 wt% Si and MC–FeMn: Formation of microstructure and cracks*. Norwegian University of Science and Technology (NTNU).

Pachaly, B. (1994) 'Process development in the MCS-production: For example water granulated silicon metal', in *Silicon for the Chemical and Solar Industry II*. Trondheim, Norway, pp. 55–60.

Rong, H. (1992) *Silicon for the direct process to methylchlorosilanes*. Doctoral thesis. Norges Tekniske Høgskole (NTH), now Norwegian University of Science and Technology (NTNU).

Tang, K. (2022) Private communication.

Tangstad, M., Ringdalen, E., Olsen, J.E., Einarsrud, K.E., Myrhaug, E. and Reynolds, Q. (2021) 'Conceptual model of tapping mechanisms in FeSi/Si furnaces', in *Proceedings of INFACON XVI*. Trondheim, Norway, 12 September. Available at: https://doi.org/10.2139/ssrn.3922189

Tveit, H. (1988) *Størkning av 75% ferrosilisium; forløp, struktur og styrke*. Doctoral thesis, in Norwegian. Norges Tekniske Høgskole (NTH), now Norwegian University of Science and Technology (NTNU). Available at: http://hdl.handle.net/11250/244559

van den Boomgard, J. (1972) 'Stability of the high-temperature phase FeSi2', *J. Iron and Steel Inst.*

Kero, I. and Tranell, G. (2026) 'Environmental aspects', in M. Tangstad, G. Tranell, H. Tveit and E. Ringdalen (Eds.), *Production of high silicon alloys* (2. ed.) (pp. 455–468). Fagbokforlaget. https://doi.org/10.55669/oa880812

12

Environmental aspects

Ida Kero and Gabriella Tranell

12.1 General

The use of metals and other materials has increased greatly in the last century, and this growth is expected to speed up further as the world transitions towards less fossil dependency. The technologies needed to combat climate change require vast amounts of base metals, but also many less common materials, such as lithium and rare earth elements.

Silicon is the raw material for many of the technologies enabling future sustainability and digitalization, such as semiconductors and electronics, batteries, and solar cells. Silicon-based alloys are also important additives in the production of iron and steel, aluminium, silicone rubbers, and many other chemical products. While the volume of silicon alloy production is minor compared to the base metals, the production of additives such as silicon must be included when assessing the total environmental impact of any base metal component or structure.

Nearly all aspects of the production and use of high-silicon alloys are energy-intensive, and most of the process steps in production emit pollutants of some sort, not least greenhouse gases (GHG) and dust. To minimize the environmental footprint, it is important to make use of the Best Available Technology (BAT) for every step of the production process. This chapter discusses some of the most important environmental parameters, with emphasis on the process-specific parameters of the primary production unit, i.e. the smelter.

This work is licensed under the Creative Commons Attribution 4.0 International License.
To view a copy of this license, visit https://creativecommons.org/licenses/by/4.0/

12.2 Occupational health

Workers in industrial settings may be exposed to various types of stress factors and pollutants, and the silicon industry is no exception. Generally acknowledged stress factors include heat exposure, noise, and night work, which are also common in this industry. More process-specific issues are typically related to personnel exposure to polluting substances from the different processes in the plant.

Fugitive or diffuse emissions are any type of emission that is not controlled or directed. However, these terms are often used only to designate airborne particulate matter. It is important to note, however, that any type of pollutant (gases or particles) can be diffuse or fugitive in nature. This means that they may affect the health of people not only working in a smelter, but also residents in the nearby area of the plant. Nevertheless, where occupational hygiene and local community air quality are concerned, dust (airborne particulate matter) is especially important.

Historically, the main visible effluent from silicon alloy smelters was dust consisting of amorphous silica particles. This dust was generated by the furnace process and emitted through chimney pipes. Unfortunately, fume could also leak into the furnace building and pollute the working atmosphere. This type of dust is still generated under the furnace hood, but today it is effectively collected in filters and often sold as a by-product ('silica fume'), which is used as a filler material, e.g. in concrete. However, furnace fume is just one example of the thermally generated dust commonly encountered in silicon smelters. Similar fumes are also produced by other hot processes, such as oxidative ladle refining, casting, and tapping; these also constitute potential sources of fugitive dust emission.

In many respects, exposure to dust and fume still constitutes the largest health risk and hygiene challenge for silicon smelters. Long-term inhalation of silica fume has been linked to cancer, pneumonia, chronic obstructive pulmonary disease (COPD), and other respiratory and cardiovascular syndromes (Hobbesland *et al.*, 1997a, 1997b; Johnsen, 2009; Johnsen *et al.*, 2008a, 2008b; Søyseth *et al.*, 2013, 2011a, 2011b).

12.3 Pollution control

Process emissions are often divided into three main categories: pollution to air, soil, and water. From the silicon process, air pollution is most significant. On the other hand, emissions to the air may later be converted into soil or water pollution.

As the fate of the various process streams becomes known, a mass balance for each element can be an efficient tool for describing the level of pollution. This method is commonly used for environmental reporting to authorities, for example emissions of heavy metals and sulphur. Sometimes generic emission factors have been established for a process or industrial branch, so that reporting can be simplified. Typically, most production emissions are calculated estimates based on the raw material mix, production tonnage, and emission factors. Control measurements are then carried out to verify the calculated numbers.

However, this approach is not always adequate. Some emissions are a result of the process itself and do not depend on the amount or mixture of elements fed to the process. One example is the NO_X emissions from the silicon process, where NO_X mainly forms from a reaction between the nitrogen and oxygen present in the cooling air drawn into the high-temperature zone of the furnace hood.

The main sources of pollution in the silicon process are:

- Electric energy delivered to the process. A variety of environmental problems may arise from the production of electricity.
- Reduction materials – coke, coal and woodchips. The carbon necessary for the reduction process will inevitably be converted to CO, CO_2 and, to a lesser extent, various hydrocarbon gases. Other elements in the reductants will be distributed between the off-gas, dust, slag, and alloy (as shown in Chapter 4).
- Quartzite minerals. The silica sources normally contain minor elements besides the SiO_2. These elements will be distributed between the off-gas, dust, slag, and alloy (as shown in Chapter 4).

There are clear dependencies between process parameters and certain types of pollution from the production processes. This means that, in some instances, changing the process parameters may reduce process emissions. The single most important process parameter is the silicon yield. An improved silicon yield will lower the amount of any input material or energy *per tonne product*, for example the *specific* energy consumption. This may lead to a reduction of many other specific parameters.

Emissions to soil and water

Whenever a solid waste or by-product is produced and disposed of, the risk of water or soil pollution must be considered. Before waste materials may go to any form of deposition, the risk of leakage must be assessed. For high silicon alloy smelters, the materials that may be deposited include slag, dust from the filters, spent refractories, and other minor by-products and waste materials. Skull formation in a ladle may also create an off-grade mixture of refractory, which must be disposed of.

Importantly, many airborne pollutants may be carried into soil or water systems by atmospheric deposition and rain.

Emissions to air

The issues of airborne emissions from high silicon alloy production are, in many ways, similar to the challenges of airborne emissions from other metallurgical industries, most notably the inherent energy intensity and the greenhouse gas emissions from both electricity production and the carbonaceous reducing agents. Certain challenges are, however, highly branch-specific, for example the dust types generated and the management of NO_X emissions by furnace design and operation.

Unwanted discharges to the air tend to be the most common environmental effect of silicon production. This type of pollution consists of both gases and airborne particulate matter (PM; dust). This chapter will focus on CO_2, NO_X, SO_2, PAH, PM, and trace elements, which are some of the most important and common types of airborne emissions from high silicon alloy production.

CO_2 and other greenhouse gas emissions

While CO_2 is by far the most important greenhouse gas (GHG) in high silicon alloy production, other GHGs may also be emitted. During combustion of the reductants and electrodes, volatile hydrocarbons may form and contribute to GHG emissions. The most important of these volatile organic compounds (VOC) is methane (CH_4). Since methane has a higher radiative forcing than CO_2, even relatively low concentrations may contribute significantly to the calculated CO_2 equivalents from a plant.

As described in previous chapters, the production of high silicon alloys requires the reduction of quartz using carbonaceous reductants like coal, coke, charcoal, and wood chips. In open or semi-closed furnaces, carbothermic reduction first generates CO gas, which then oxidizes to carbon dioxide (CO_2) at the furnace charge top. Additional CO_2 can also be generated inside the furnace charge, for example by the Boudouard reaction or by the reduction of iron oxides in FeSi production.

The reducing agents coke and coal are the main contributors to the GHG emissions, but other carbon-based materials, such as the electrodes and electrode paste, will also contribute. Hydrocarbon emissions are highly dependent on both alloy type and operation, which in turn leads to large variations and uncertainties in the reported data. Kero *et al.* (2017) found literature discrepancies of the order of a factor of 10.

Greenhouse gas emissions mainly depend on:

1. The type of alloy produced. Reduction of quartz requires more energy than most other oxides, e.g. iron oxides, which means higher consumption of both carbon and electricity. Thus, the higher the Si content, the higher the GHG emissions.
2. The carbon material mix. The levels of fixed carbon and volatile matter depend on the choice of reductants, which in turn affects GHG emissions. Note that emissions from biogenic carbon reductants are often exempt from GHG emission estimates.
3. The furnace operation and charging method strongly influence emissions, in particular of CH_4 and NO_X. More even charging will generally reduce emissions compared with batch-wise charging (Grådahl *et al.*, 2007; Kamfjord, 2012; Myrhaug *et al.*, 2012).

Lindstad *et al.* summarized official GHG emission factors for FeSi/Si products and reductants in the 2006 IPPC Greenhouse Gas Inventory Guidelines (Lindstad *et al.*, 2006).

Sulphur dioxide, SO_2

In the silicon alloy industry, SO_2 gas emissions are caused by the oxidation of sulphur contained in the raw materials, primarily the reducing agents. Reported emission levels are typically calculated based on material balances. Abatement methods for post-filter cleaning of SO_2, mainly limestone based, are available and are increasingly being installed in new silicon plants. While SO_2 is emitted continuously during combustion and reaction of the carbon materials, peaks of SO_2 and CO gas emissions have been shown to correlate with furnace events such as 'avalanches', i.e. the collapse of the charge burden near the electrodes (Grådahl *et al.*, 2007).

Nitrogen oxides, NO_x

Nitrogen oxides (NO and NO_2, the sum of which is referred to as NO_X) contribute to a number of environmental problems, including acid rain, ozone smog, eutrophication (stimulated growth of algae and bacteria), and bronchial suffering in animals and humans. NO_X may form by three different mechanisms, known respectively as prompt, fuel, and thermal generation. In silicon furnaces, the fuel and thermal formation mechanisms dominate. Fuel NO_X is formed by oxidation of the nitrogen components present in the solid raw materials. Thermal NO_X, on the other hand, is formed by direct oxidation of nitrogen from the air at temperatures above 1400°C. Such temperatures are frequently observed in the furnace hood (Kamfjord *et al.*, 2012; Ravary and Johansen, 1999; Solheim *et al.*, 2012).

Combustion of gaseous SiO above the charge surface and in the taphole may also locally increase the temperature. The amount of SiO(g) released from the charge will therefore influence NO_X formation, while measures that reduce SiO also seem to reduce NO_X emissions. NO_X production is therefore inversely proportional to the silicon yield (since low Si yield means high SiO losses), at least up to a certain level of silica fume formation. Furnace design and furnace operating procedures, such as stoking and charging, heavily influ-

ence NO_X emissions (Brede, 2013; Kamfjord *et al.*, 2012; Panjwani *et al.*, 2011; Ravary *et al.*, 2007; Ravary and Johansen, 1999; Solheim *et al.*, 2012; Solheim and Kamfjord, 2013). NO_X formation also correlates with the moisture content of the furnace gas and seems to decrease with increasing moisture content (Slizovskiy *et al.*, 2014).

The effect of the furnace hood design and the inlet of false air are key to understanding NO_X generation. The amount of air and its flow path throughout the hood determines when, where, and whether oxygen and nitrogen are mixed for a sufficiently long time in a sufficiently hot zone to produce thermal NO_X. Optimization of furnace hood designs can therefore decrease NO_X emissions but has proven to be a very complex task. As the trial-and-error approach is both time- and cost-consuming, modelling capabilities and tools for NO_X prediction are very desirable. It is possible to reduce NO_X emissions by means of furnace operation, process management, and/or by modifying the SAF system itself (Echterhof and Pfeifer, 2012, 2011; Kirschen *et al.*, 2005). For high silicon alloy production, this typically implies:

- Active cooling of the primary flame zone to control the combustion temperature (Tveit *et al.*, 2004).
- Avoid avalanches and other furnace events which may allow SiO-rich gas to 'blow' through the charge surface.
- Frequent stoking and continuous or semi-continuous charging. Grådahl *et al.* (2007) found that implementation of best practices could reduce NO_X emissions by 50%.
- Recycling the flue gas to reduce excess air above the charge.

Particulate matter (dust) emissions

Almost all processes involved in silicon alloy production produce particulate matter (PM; dust) in some form. In this chapter, the terms particulate matter and dust are used as synonyms and primarily describe airborne solid particles. The term fume relates to thermally generated particles. The largest source of dust is the furnace, where combustion of escaping SiO gas from the furnace hot zone results in the formation of SiO_2 particles, known as silica fume, above the charge surface. Modern ventilation and filter systems have enabled efficient collection of this type of furnace dust, which also constitutes

a profitable by-product, sometimes called microsilica. Furnace fume consists of agglomerates of amorphous SiO_2 spheres and includes both fine (FP) and ultrafine particles (UFP), i.e. particles with aerodynamic diameters of < 2.5 μm and < 0.1 μm, respectively (Dingsøyr *et al.*, 1992; Myrhaug and Tveit, 2000; Næss, 2013; Tveit and Myrhaug, 2000).

All the major sources of fugitive dust emissions, both dust remaining inside the plant and dust escaping out of the plant, involve the liquid alloy. Tapping, refining, casting, and other operations where high-temperature liquid alloy is in contact with air produce silica fume with many similarities to that produced during the oxidation of SiO originating from the reduction of quartz in the furnace (Kamfjord, 2012; Kero *et al.*, 2015, 2013; Næss, 2013). During oxidative ladle refining (OLR), the main mechanism for dust formation is the active oxidation of the liquid silicon alloy, while splashing (droplet expulsion) may contribute a smaller amount (<1%) of coarser particles (Næss *et al.*, 2012a). Active oxidation occurs in two steps: surface silicon first reacts with oxygen to form SiO gas, which then oxidizes further to SiO_2 (Næss *et al.*, 2013, 2012b, 2012a, 2011). The kinetics of this process are governed by oxygen access to the alloy surface and are therefore highly dependent on the dynamics and temperature of the alloy surface exposed to air (Olsen *et al.*, 2012, 2011).

Dust from the handling and transport of solid materials, such as the products and the raw materials, is fundamentally different from dust generated by active oxidation. Dust from handling solid materials is typically coarser, and its physical and chemical properties depend on the material from which it was generated. Raw material handling and transport can, for example, produce airborne crystalline alpha-quartz, which is a health hazard in its own right. Likewise, metallic dust (as opposed to oxide dust) can become explosive under certain circumstances, which constitutes a safety risk (see section on safety).

Particle-bound organic compounds including Polycyclic aromatic hydrocarbons

Polycyclic aromatic hydrocarbons (PAH) are organic compounds characterized by molecular structures with more than two aromatic (benzene) rings. Lighter compounds, with fewer aromatic rings, are gaseous at room temperature, whereas heavier compounds are liquid or solid. Hence, the larger molecules often follow the particulate matter in the off-gas system and are

collected in the filters. Particle-bound PAH may be either condensed PAH or PAH adsorbed onto particles (such as silica fume or soot).

From an occupational health point of view, PAH receive special attention among the organic emissions because some PAH compounds are linked to cancer. The term PAH is often used to denote only a particular subset of PAH compounds, more correctly known as the EPA-16. These 16 compounds have been identified by the United States Environmental Protection Agency (US EPA) due to their potential to induce adverse effects on the environment and health. Although the EPA-16 are the standard for emission reporting, determination of an extended list of PAH in the off-gas from silicon production has indicated that the EPA-16 account for only a fraction of those emitted (Arnesen *et al.*, 2024, 2023; Kero and Indresand, 2022).

Man-made PAHs are typically formed by incomplete combustion of organic materials. In silicon alloy production, the combustion of reductants in the furnace is the main source of PAH. Another important upstream source is the baking of electrodes. PAH formation is linked to soot formation, which in turn is influenced by furnace design and operation and varies throughout the charging cycle (Tveit *et al.*, 2004). As PAHs are destroyed at high temperatures, emissions can be significantly reduced by increasing off-gas temperatures. It is noteworthy, however, that increasing the off-gas temperature may have other unwanted side-effects, such as increased NO_X emissions (Grådahl *et al.*, 2007; Kero *et al.*, 2017).

There are several other types of complex, toxic, organic pollutants that may form in the furnace process. The single most important strategy to reduce emissions of complex organic compounds like dioxins, furans and PAH is to optimize furnace operation to ensure high enough temperatures and sufficient oxygen for complete combustion. Today's modern, semi-closed SAFs allow very efficient destruction of these types of compounds.

Particle-bound inorganic compounds: Trace elements and heavy metals

Trace elements, including heavy metals, enter the production process as low-concentration constituents in the raw materials and electrodes. In the process, the elements become redistributed to metal, slag, dust and gas. Emissions thus depend on the raw material mix, the alloy composition and the process

temperatures. At temperatures of 1600°C or higher, certain metals such as Zn, Pb, Cd, Na, Mn and Fe go into the gas phase and may escape as metal vapour. When the off-gas temperature drops, the metal vapours condense and may be collected with the dust. Myrhaug and Tveit (2000) showed that a boiling point model can be used to predict the redistribution of an element in the furnace, as discussed in Chapter 4. Næss *et al.* (2014) showed that the model is also applicable to the refining ladle, with some modifications due to the oxidation of elements.

Regulation of industrial emissions of heavy metals and other trace elements varies between countries and regions. The United Nations Environment Programme (UNEP) focuses on lead, cadmium and mercury, but many national authorities require emission control and reporting of many more elements, for example As, Cd, Co, Cr, Cu, Hg, Mo, Ni, Pb, Se and Zn. Reported emissions of trace elements are often based on material balances and may vary greatly between plants.

Among airborne heavy metal emissions, mercury is of particular environmental concern, and international legislation has long been stringent with respect to Hg emissions. In silicon alloy plants, particulate control devices (e.g. fabric filter or wet scrubber) capture particle-bound mercury. Elemental, more volatile mercury may, however, be emitted. Emission estimates to air through the filter systems should cover both gaseous and particle-bound heavy metals, but the low concentrations of these elements represent a major challenge with respect to analysis. The detection limit (DL) for Hg is often in units of parts per billion (ppb), whereas the other heavy metals typically have DLs of the order of magnitude of parts per million (ppm). Large uncertainties are also related to sampling and representativeness of samples. The total uncertainty for elements such as Co, Hg and Mo is usually around or above 100% (Næss *et al.*, 2014, 2013). The very significant measurement uncertainties often make it impossible to 'close' the material balance for individual elements.

References

Arnesen, K., Andersen, V., Jakovljevic, K., Enge, E.K., Gaertner, H., Aarhaug, T.A., Einarsrud, K.E. and Tranell, G. (2024) 'Analysis of nitro- and oxy-PAH emissions from a pilot scale silicon process with flue gas recirculation', *Environmental Science: Advances*, 3, pp. 239–248. Available at: https://doi.org/10.1039/D3VA00187C

Arnesen, K., Vachaparambil, K.J., Andersen, V., Panjwani, B., Jakovljevic, K., Enge, E.K., Gaertner, H., Aarhaug, T.A., Einarsrud, K.E. and Tranell, G. (2023) 'Analysis of polycyclic aromatic hydrocarbon emissions from a pilot scale silicon process with flue gas recirculation', *Industrial & Engineering Chemistry Research*, 62, pp. 7525–7538. Available at: https://doi.org/10.1021/acs.iecr.2c04578

Brede, I. (2013) Parameters contributing to the formation of NOx in the silicon furnace: The effect of the charging frequency and raw material composition on the formation of NO. MSc thesis, p. 125. Norwegian University of Science and Technology (NTNU), Trondheim, Norway. Available at: https://hdl.handle.net/11250/249366

Dingsøyr, E., Dåstøl, M. and Wedberg, W.C. (1992) 'Particle size and particle size distribution of Elkem Microsilica and its relevance to technical application', paper presented at *The 5th European Symposium on Particle Characterization*, Nuremberg, Germany.

Echterhof, T. and Pfeifer, H. (2011) 'Measurement and control of NOx emissions at two AC electric arc furnaces', *ISIJ International*, 51, pp. 1631–1636. Available at: https://doi.org/10.2355/isijinternational.51.1631

Echterhof, T. and Pfeifer, H. (2012) 'Nitrogen oxide formation in the electric arc furnace—measurement and modeling', *Metallurgical and Materials Transactions B*, 43, pp. 163–172. Available at: https://doi.org/10.1007/s11663-011-9564-8

Grådahl, S., Johansen, S.T., Ravary, B., Andresen, B. and Tveit, H. (2007) 'Reduction of emissions from ferroalloy furnaces', in *Proceedings of INFACON XI*. New Dehli, India, pp. 479–488. Available at: https://www.pyrometallurgy.co.za/InfaconXI/479-Gradahl.pdf

Hobbesland, Å., Kjuus, H. and Thelle, D.S. (1997a) 'Mortality from cardiovascular diseases and sudden death in ferroalloy plants', *Scandinavian Journal of Work, Environment & Health*, 23, pp. 334–341.

Hobbesland, Å., Kjuus, H. and Thelle, D.S. (1997b) 'Mortality from nonmalignant respiratory diseases among male workers in Norwegian ferroalloy plants', *Scandinavian Journal of Work, Environment & Health*, 23, pp. 342–350.

Johnsen, H.L. (2009) Lung function, respiratory symptoms, and occupational exposure: A five-year prospective study among employees in Norwegian smelters. Doctoral thesis. University of Oslo, Norway. Available at: https://hdl.handle.net/10852/28133

Johnsen, H.L., Hetland, S.M., Benth, J.S., Kongerud, J. and Søyseth, V. (2008a) 'Quantitative and qualitative assessment of exposure among employees in Norwegian smelters', *Annals of Occupational Hygiene*, 52, pp. 623–633. Available at: https://doi.org/10.1093/annhyg/men046

Johnsen, H.L., Søyseth, V., Hetland, S., Benth, J.S. and Kongerud, J. (2008b) 'Production of silicon alloys is associated with respiratory symptoms among employees in Norwegian smelters', *International Archives of Occupational and Environmental Health*, 81, pp. 451–459. Available at: https://doi.org/10.1007/s00420-007-0237-5

Kamfjord, N.E. (2012) *Mass and energy balances of the silicon process*. Doctoral thesis 2012:162. Norwegian University of Science and Technology (NTNU), Trondheim, Norway. Available at: https://hdl.handle.net/11250/249043

Kamfjord, N.E., Tveit, H. and Solheim, I. (2012) 'Pilot scale measurements of NO emissions from the silicon process', in *Proceedings of the 3rd International Symposium on High-Temperature Metallurgical Processing*. Orlando, Florida, USA. Available at: https://doi.org/10.1002/9781118364987.ch50

Kero, I., Grådahl, S. and Tranell, G. (2017) 'Airborne emissions from Si/FeSi production', *JOM*, 69, pp. 365–380. Available at: https://doi.org/10.1007/s11837-016-2149-x

Kero, I., Naess, M.K. and Tranell, G. (2015) 'Particle size distributions of particulate emissions from the ferroalloy industry evaluated by electrical low pressure impactor (ELPI)', *Journal of Occupational and Environmental Hygiene*, 12, pp. 37–44. Available at: https://doi.org/10.1080/15459624.2014.935783

Kero, I., Næss, M. and Tranell, G. (2013) 'Fume characterization in the ferroalloy industry', in *Proceedings of INFACON III*. Almaty, Kazakhstan.

Kero, I.T. and Indresand, H. (2022) Polycyclic aromatic hydrocarbons (PAH) in industrial emissions – challenges and strategies to measure, monitor, control and reduce PAH emissions. SINTEF Report No. 2022:00847. Trondheim, Norway.

Kirschen, M., Voj, L. and Pfeifer, H. (2005) 'NOx emission from electric arc furnace in steel industry: Contribution from electric arc and co-combustion reactions', *Clean Technologies and Environmental Policy*, 7, pp. 236–244. Available at: https://doi.org/10.1007/s10098-005-0010-y

Lindstad, T., Olsen, S., Tranell, G.M., Færden, T. and Lubetsky, J. (2006) 'Greenhouse gas emissions from ferroalloy production', in *Proceedings of INFACON XI*. New Dehli, India, pp. 457–466. Available at: https://www.pyrometallurgy.co.za/InfaconXI/457-Lindstad.pdf

Myrhaug, E.H. and Tveit, H. (2000) 'Material balances of trace elements in the ferrosllicon and silicon process', in *Proceedings of the 58th Electric Furnace Conference and 17th Process Technology Conference*. Orlando, Florida, USA: Iron and Steel Society.

Myrhaug, E.H., Tveit, H., Kamfjord, N.E., Andersen, J. and Grøvlen, Å. (2012) 'NOx emissions from silicon production', in *Proceedings of Silicon for the Chemical and Solar Industry XI*. Bergen–Ulvik, Norway.

Næss, M.K. (2013) *Mechanisms and kinetics of liquid silicon oxidation*. Doctoral thesis 2013:145. Norwegian University of Science and Technology (NTNU), Trondheim, Norway. Available at: https://hdl.handle.net/11250/249262

Næss, M.K., Kero, I. and Tranell, G. (2013) 'A new method for estimation of emissions and sources of measurements error in the silicon refining process', *JOM*, 65, pp. 997–1006. Available at: https://doi.org/10.1007/s11837-013-0661-9

Næss, M.K., Kero, I., Tranell, G., Tang, K. and Tveit, H. (2014) 'Element distribution in silicon refining: Thermodynamic model and industrial measurements', *JOM*, 66, pp. 2343–2354. Available at: https://doi.org/10.1007/s11837-013-0797-7

Næss, M.K., Tranell, G., Olsen, J.E., Kamfjord, N.E. and Tang, K. (2012a) 'Mechanisms and kinetics of liquid silicon oxidation during industrial refining', *Oxidation of Metals*, 78, pp. 239–251. Available at: https://doi.org/10.1007/s11085-012-9303-9

Næss, M.K., Tranell, G.M. and Kamfjord, N.E. (2011) 'Fugitive emissions related to oxidation of liquid silicon during ladle refining', in Hwang, J., Drelich, J., Downey, J., Jiang, T. and Cooksey, M. (eds) *2nd International Symposium on High-Temperature Metallurgical Processing*. Wiley, pp. 85–94. Available at: https://doi.org/10.1002/9781118062081.ch11

Næss, M.K., Young, D.J., Zhang, J., Olsen, J. and Tranell, G. (2012b) 'Active oxidation of liquid silicon: Experimental investigation of kinetics', *Oxidation of Metals*, 78, pp. 363–376. Available at: https://doi.org/10.1007/s11085-012-9312-8

Olsen, J., Næss, M. and Tranell, G. (2012) 'Understanding fuming during metal refining by CFD', *TMS Annual Meeting*, pp. 33–40.

Olsen, J.E., Næss, M. and Tranell, G. (2011) 'CFD modeling of silica fume formation during refining of silicon metal', paper presented at the *8th International Conference on CFD in Oil & Gas, Metallurgical and Process Industries*, SINTEF, Trondheim, Norway.

Panjwani, B., Andersson, S. and Midtdal, H. (2011) 'Effect of combustion on NOx emissions', in *Proceedings of the 8th International Conference on CFD in the Oil & Gas, Metallurgical and Process Industries*. Trondheim, Norway: SINTEF.

Ravary, B., Colomb, C. and Johansen, S.T. (2007) 'Modelling combustion and thermal NOx formation in electric arc furnaces for the production of ferrosilicon and silicon-metal', in *Proceedings of INFACON XI*. New Dehli, India, pp. 499–506. Available at: https://www.pyrometallurgy.co.za/InfaconXI/499-Ravary.pdf

Ravary, B. and Johansen, S.T. (1999) '2D modeling of the combustion and NOx formation in furnaces producing FeSi', in *Proceedings of the 2nd International Conference on CFD in the Oil & Gas, Metallurgical and Process Industries*. Melbourne, Australia: CSIRO, pp. 305–310.

Slizovskiy, D., Tveit, H., Brede, I., Tranell, G., Andersen, G.J., Kamfjord, N.E. and Wittgens, B. (2014) 'The industrial-scale study of the effect of charge frequency and H2O behaviour in the off-gases on NOx emissions in Si furnace', in *Proceedings of Silicon for the Chemical Industry XII*. Trondheim, Norway, pp. 207–218.

Solheim, I., Jensen, R. and Kamfjord, N.E. (2012) 'Equipment for pilot scale experiments of NOx emissions from the silicon process', in *Proceedings of the 3rd International Symposium on High-Temperature Metallurgical Processing*. Orlando, Florida, USA: Wiley, pp. 33–40. Available at: https://doi.org/10.1002/9781118364987.ch5

Solheim, I. and Kamfjord, N.E. (2013) 'NOx-emissions from the silicon process comparing wet and dry raw materials pilot scale experiment', in *Proceedings of INFACON XIII*. Almaty, Kazakhstan, pp. 1029–1035. Available at: https://www.pyrometallurgy.co.za/InfaconXIII/1029-Solheim.pdf

Søyseth, V., Johnsen, H.L., Bugge, M.D., Hetland, S.M. and Kongerud, J. (2011a) 'Prevalence of airflow limitation among employees in Norwegian smelters: A longitudinal study', *Occupational and Environmental Medicine*, 68, pp. 24–29. Available at: https://doi.org/10.1136/oem.2009.049452

Søyseth, V., Johnsen, H.L., Bugge, M.D., Hetland, S.M. and Kongerud, J. (2011b) 'Incidence of airflow limitation among employees in Norwegian smelters', *American Journal of Industrial Medicine*, 54, pp. 707–713. Available at: https://doi.org/10.1002/ajim.20946

Søyseth, V., Johnsen, H.L. and Kongerud, J. (2013) 'Respiratory hazards of metal smelting', *Current Opinion in Pulmonary Medicine*, 19, pp. 158–162. Available at: https://doi.org/10.1097/MCP.0b013e32835ceeae

Tveit, H. and Myrhaug, E. (2000) 'Important sub-processes in the silicon process. The behavior of trace elements', in *Proceedings of Silicon for the Chemical Industry V*. Tromsø, Norway, pp. 23–30.

Tveit, H., Storset, M. and Eikeland, I.J. (2004) 'The silicon process – improved environmental standards', in *Proceedings of Silicon for the Chemical Industry VII*. Bergen–Tromsø, Norway, pp. 55–66.

Tveit, H. (2026) 'Safety', in M. Tangstad, G. Tranell, H. Tveit and E. Ringdalen (Eds.), *Production of high silicon alloys* (2. ed.) (pp. 467–485). Fagbokforlaget. https://doi.org/10.55669/oa880813

13

Safety

Halvard Tveit

In general, all industrial development gives humans both an improved standard of living and increased wellbeing, but there is a darker side to this development, including accidents. The silicon industry has seen serious accidents in which operators or other employees have been harmed, and some have even died from work-related injuries. This chapter gives a short description of some of the specific safety challenges that are present in the production of silicon. It starts with a general presentation of safety and then mentions some examples from other industries.

13.1 General about industrial safety

Process safety is an integrated part of the Health, Safety & Environment (HSE) programmes in industrial production (the acronym EHS is a North American term with the same meaning). Every year there are a huge number of accidents in industry worldwide ('List of Historic Explosions,' n.d.). Fortunately, there has been an increased focus on avoiding injuries, and the safety standard has improved in many countries through systematic safety work. Safety work is a continuous process in which new learning from your own factory, as well as learning from others, improves the standard. Organized safety work is about 100 years old and started because of the huge number of accidents in the early days of industrialization. Injured workers and their families paid the highest price, but it also affected colleagues, the company and society.

This work is licensed under the Creative Commons Attribution 4.0 International License.
To view a copy of this license, visit https://creativecommons.org/licenses/by/4.0/

Improvement work seeks to minimize risk and remove hazards, unsafe conditions and unsafe behavior, thereby avoiding accidents through improved technical standards, better training, and more effective procedures. To measure injury rates, Norwegian industry uses standardized parameters defined by the Federation of Norwegian Industries (*Norsk Industri*)[1]:

- H-value (Frequency) shows the number of lost-time injuries (LTI) per 1 000 000 working hours.
- F-value (Absence)/ DISR (Disabling Injury Severity Rate) gives the number of days lost due to injuries per 1 000 000 working hours.
- A-value (Severity): provides a picture of how serious the accidents are (F-value divided by H-value).

The numbers often include injuries sustained by hired personnel or contractors performing work for the company.

There are several reasons to work on industrial safety, and the most important is to avoid employee harm or death in the workplace. However, there are also other important reasons to prioritize safety:

- Protection of the environment from damage from industrial accidents
- Protection of the business from serious financial loss from damage to plant and machinery
- Elimination of accidents causing work stoppage and production loss.
- Creating awareness of available good practices for the delivery of effective safety instrumented systems

Some claim that there can be a conflict between efficiency and the requirement for safe standards. One example is the understanding that simple ladders are not suited for elevated work. The standard requires the use of solid scaffolding, which is, of course, more time consuming to build than just grabbing a ladder. Here, safety concerns should prevail, as we know that fall injuries from more than 2 metres can easily result in serious injury or fatalities. It has been said that the most common start of an explanation for why short-cuts are made is: 'I was only going to …'

1 https://www.norskindustri.no/siteassets/dokumenter/annet/veileder-for-personskadestatistikk-i-norsk-industri.pdf

Work with better safety standards can improve efficiency at the same time as the working environment improves. One example is a part of safety work called '5S'. 5S stands for the 5 steps: Sort, Set in Order, Shine, Standardize, Sustain. These steps involve going through everything in a space, deciding what is necessary and what is not, putting things in order, cleaning, and setting up procedures for performing these tasks on a regular basis. This not only improves safety, but also efficiency and productivity.

In addition to physical harm to employees and the plant, serious accidents can also cause financial losses or legal consequences for workers, management and owners of the factory. Employees must be given adequate information about risks in their working environment, and the necessary training to do their work safely. Programmes that ensure documented safety training are mandatory for all employees. Special programmes and training for new employees are also necessary.

There are several different types of accidents:

- Near-miss: accidents with no damage or injury are called near-misses.
- Minor accident: accidents with damage that can be easily repaired, or injury with a short healing time.
- Serious accident: accidents with heavy damage and/or serious injury with a long healing time or permanent loss of function.
- Fatal accident: accidents with loss of life.

With serious or fatal accidents, Labour Inspection Authorities and police are often involved in the investigation to find the causes. Documentation showing risk understanding and safety training for all employees will be requested for their investigations.

13.2 General hazards for the silicon industry

The most common industrial accidents are:

- Pinching/crushing
- Fall from heights
- Falling objects
- Moving vehicles and equipment

This is also generally the case for the silicon industry and other metal-producing industries. However, there are other factors that may have a special influence on the silicon industry's safety:

- There are many simultaneous activities in a limited space. In addition, large numbers of workers who may not be familiar with normal factory activities are brought into the workplace for project work or major repair work.
- Many silicon factories are old and may not be well suited for large mobile equipment like payloaders and trucks.
- Work 7/24. Shift work, including nights, carries its own unique type of stress that may be dangerous. Studies have shown that changing sleep patterns can create stress with the potential to impact performance, decision-making skills, and safety.

The accident types listed above will normally have public or governmental safety standards. In the case of an accident, the labour inspection authority will refer to such standards. Penalties may be given if there is serious deviation from applicable safety standards.

There should be a comprehensive evaluation of the safety situation at the factory. This includes simple things like separating pedestrian walkways and vehicle roads.

13.3 Process specific hazards for the silicon industry – energy out of control

The introduction of electricity in the metallurgical process enabled industrial production of silicon and ferrosilicon. Electricity provided an effective means of reaching the very high process temperature needed for the SiO_2 reduction into silicon. Though important for the total process, different types of energy may also cause harm:

- Potential energy – fall from heights – converted to kinetic energy in an accident situation
- Kinetic energy – moving machinery, cars, trucks, tools

- Electrical energy – high and low voltage
- Thermal energy – warm charge, liquid silicon, warm off-gas
- Chemical energy – coal, coke, process gas before combustion, silicon

While all of these can cause serious harm and death, it is the huge amount of thermal and chemical energy that creates the process specific hazards, which can have catastrophic consequences. Another important factor is that the very high temperature may create extreme energy transfer into other forms of energy. In the following, four examples of extremely high energy hazards that are specific to the silicon industry (or, more generally, the metal producing industry) will be discussed.

Eruption of water vapour and process gas from the charge

The eruption of water vapour and process gas from the charge has been the big killer when looking at low-shaft furnaces like the silicon furnace on a global basis (Tveit and Breidenthal, 2020). The use of the word eruption reflects the relatively slow total reaction. A furnace eruption may happen without high pressure build up. However, if the furnace is closed, the large amount of gas during the eruption may create pressure build up inside the furnace hood.

There are several energy sources that may create an eruption:

- The main energy source is the extremely hot charge. If the charge is mixed with water, the heat transfer may be extreme.
- Inside the charge there is process gas that may burn quickly if exposed to air. Normally this is released in a controlled manner and evacuated safely through the off-gas system, but it may also escape uncontrolled together with the water vapour.
- Rapidly heated coal may defragment into very small pieces if rapidly heated (No and Syred, 1990). Fragmentation has been attributed to the pressure build-up within a particle when volatiles released internally cannot escape rapidly through pores in the coal. The defragmented coal may achieve a very high combustion rate. It was found that a 10 mm coal particle would use 100 s for the burn-out, while the 1 mm and 0.3 mm particles used about 1 s and 0.1 s respectively (Agarwal, 1986).

The energy transport out from the furnace may be enabled by either large volumes of water from leakages in the cooling systems or by fresh raw materials that are added too quickly. Figure 13.1 shows the principle of a water leakage out of control. The leakage may come from the furnace hood, the electrode clamps, or other water-cooled parts of the furnace. If the furnace is in full operation, it can tolerate a substantial leakage, as the water is evaporated and does not accumulate or move towards the furnace reaction zone. Evaporation does however have its limits, and if the furnace is stopped, the tolerance is much lower. Figure 13.2 and Figure 13.3 show how the accumulation of water can increase when power is cut and evaporation slows down.

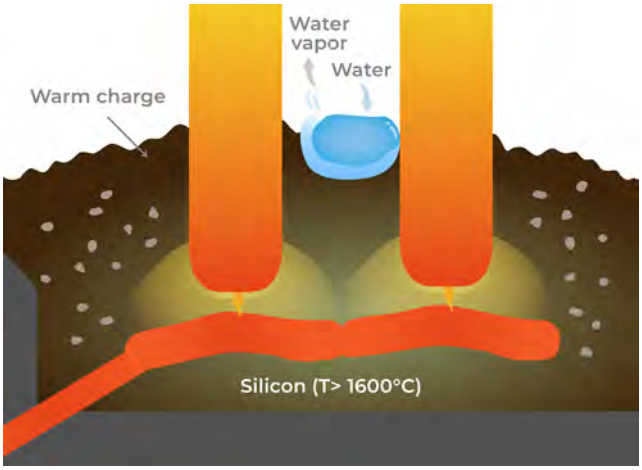


Figure 13.1 *shows a water leakage that accumulates in the upper part of the charge.*

The water may also mix with the charge, causing a violent boiling process. There are several reports of hearing an ominous rumbling noise.[2] People seem to never forget such an experience. Another possibility for too much water entering the furnace crater is through the charge itself. The charge will inherently always contain both moisture and volatiles, and levels of these may vary greatly depending on weather conditions, storage, and handling. If large amounts of fresh charge are added in an uncontrolled manner (too much – too

2 Private conversation with Ing. Peter Kallfelz, who is a private consultant in metallurgical processes.

quickly), the necessary evaporation will also suffer, allowing water to transit further down into the furnace.

When the main reaction takes place in these types of situations, the eruption of water vapour and process gas far exceeds the capacity of the off-gas system. The normal capacity of the off-gas system is in the order of 12–80 Nm^3/sec, dependent on furnace size and off-gas temperature. Calculations have indicated that the amount of water vapour and gas from the volatiles may reach several thousand m^3/sec during the eruption. As this overwhelms the off-gas system, it finds other ways out of the furnace through the gates and other openings. If the openings are too small, pressure will build up in the furnace, potentially destroying the furnace.

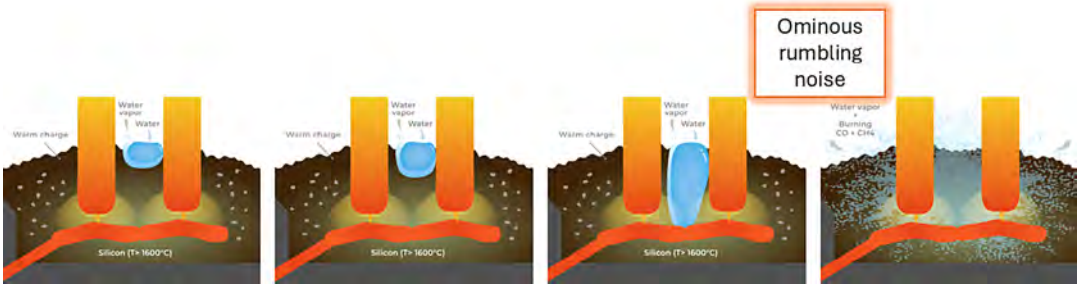


Figure 13.2 *shows steps from the start of a water leakage to an eruption.*



Figure 13.3 *shows the eruption. The mixed charge and water create an extreme energy transfer. A deadly mix of superheated water vapour and burning process gas and coal fines stream out from the furnace.*

The amount of off-gas from a 10 MW furnace is shown in Table 13.1. This table shows that more gas is needed to cool the off-gas to lower temperatures. Thus, it will totally be more gas when cooling it to 300 than 700°C. The amount of off-gas will vary somewhat with the composition of the charge, such as the amount of coal, coke, and woodchips.

Table 13.1 *The table shows the typical amount of off-gas from a 10 MW silicon furnace where it takes more gas to cool the off-gas to 300°C than 700°C.*

Off-gas temperature	Off-gas volume	Corresponding amount of water vapour at 400°C
300°C	32 Nm^3/sec	26 kg H_2O
500°C	18 Nm^3/sec	15 kg H_2O
700°C	12 Nm^3/sec	10 kg H_2O

Case 1 – the 2006 Elkem Thamshavn accident

On the 12th of April 2006, an eruption took place in Furnace #1. One operator was critically wounded and died four weeks later. The direct cause of the incident was a major water leakage in the electrode cooling system. A comprehensive investigation was carried out to find the root cause of the incident and measures to avoid similar accidents in the future. The investigation identified a continued inflow of water into the furnace after the power was turned off, enabling the accumulation of a high volume of water close to the reaction zone. In line with the Elkem ASA policy of being open with information that may help others avoid serious incidents and injuries, a presentation of the incident was published in 2008 (Tveit *et al.*, 2008). The investigation also included reviews of other similar incidents, showing that water vapour eruptions from silicon and ferro-alloy furnaces did happen occasionally and often resulted in multiple fatalities. The paper describes five known accidents with up to seven fatalities.

Case 2 – the 2010 Elkem Iceland accident

The tragic incident at Elkem Iceland on the 29th of June in 2010 was a reminder of the inherent risk involved with the production of high silicon-containing alloys. A severe eruption of gases from Furnace #1 ignited, killing one young operator. Again, an investigation had to be carried out to find the root causes and how to avoid similar incidents.

The first hypothesis suggested a major water leakage, as in the Thamshavn case, but no water leakages were found, and the furnace was in normal operation when the eruption took place. Video footage from CCTV cameras in the area provided valuable input to the investigation and the modelling of the incident. Figure 13.4 shows time-stamped pictures from the video, which allowed us to see how the eruption progressed. The investigation concluded that the incident was an eruption of process gases from the furnace that ignited on contact with oxygen outside of the furnace. The findings strongly indicate a major furnace cavity collapse, allowing fresh, newly fed charge to fall into the reaction zone before moisture and volatiles were evaporated, as seen in Figure 13.5.

The investigation, modelling and necessary calculations gave a frightening worst-case potential for fatal incidents when substantial amounts of fresh raw materials are mixed with very warm charge material and/or molten silicon. The literature suggests that high-volatile coal may defragment (or explode and be converted into small pieces) if it is heated too quickly. The resulting fragments of coal may release volatiles and have extremely fast combustion, with the release of huge amounts of energy. Several combustion and mixing scenarios were calculated. The worst-case scenario indicated an energy release in the order of 16 GW for 1 second – i.e. the total effect of Norwegian electricity production. This is not the most probable scenario, but all the calculated scenarios resulted in an overload of the off-gas system, according to the observations and measurements.

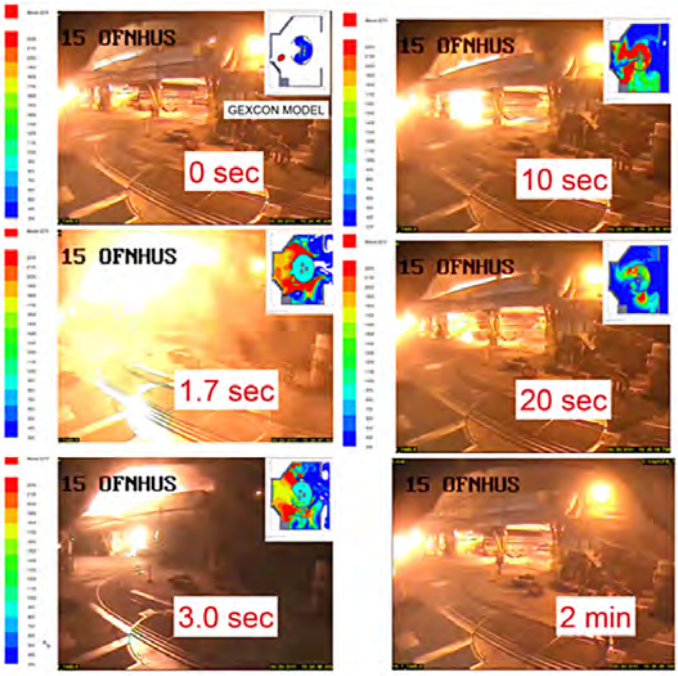


Figure 13.4 *The snap from a video shows the speed of the eruption at Elkem Iceland together with the model from Gexcon (2026). There were 2 maxima – after 0.7 and 1.7 sec. The major eruption time was about 1 sec – and after 2 minutes no trace of the accident could be seen on the video.*

Both cases mentioned above are extreme examples of what is typically called a furnace blow-out. Gases and materials are ejected with high force through furnace openings when an imbalance occurs in the off-gas evacuation system. Fans that normally create constant evacuation through the chimneys do not have sufficient capacity when the amount of process gas increases rapidly, replacing some of the cooling air and increasing the temperature in the furnace hood. Blow-outs on a smaller scale do happen frequently in silicon furnaces and can be anything from small amounts of smoke and particles exiting the furnace to burning flames and charge materials that can cause damage and fires in the area. This phenomenon will sometimes be heard as slamming of the furnace doors, due to the change of gas pressure and the reversal of the cooling air flow to the furnace.

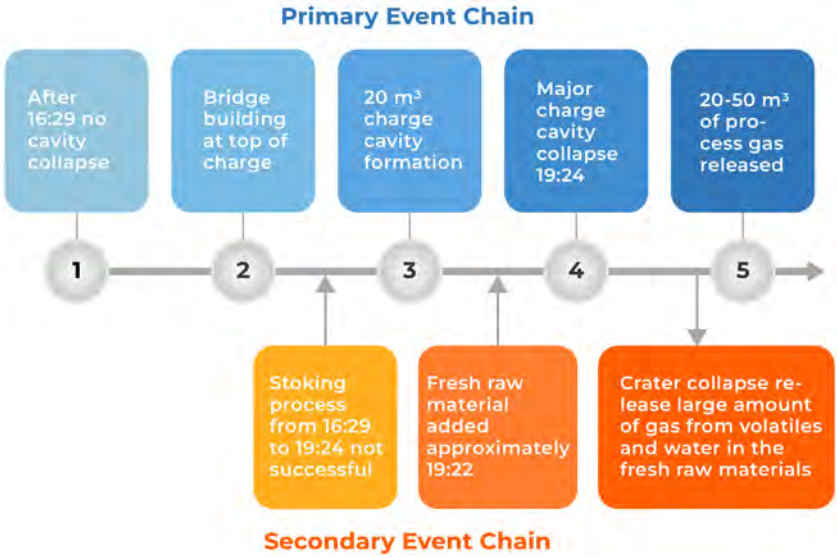


Figure 13.5 *shows the most likely chain of events for the Iceland example. The figure is included because a major cavity of 20 m³ was found at the top of the charge. The reason why the cavity did not collapse during the 3 hours of stoking is not fully understood.*

The main measures after the Elkem Iceland accident were changes to the charging process and limitations of access to the stoking floor area.



Figure 13.6 *shows the destruction of a closed CaSi furnace, where the author was participating in the investigation. The picture shows the extreme destruction when energy comes out of control.*

Explosion due to water encapsulated in molten or very hot metals and materials

Liquid water or moisture encapsulated in molten or very hot metal immediately evaporates, as shown in Figure 13.7. This generates sudden expansion and possible pressure build-up, enabling an explosion. The word explosion indicates a sudden pressure build-up with pressure release. The time for an explosion is less than 1 second. The molten substances that were around the water may be ejected with high force and velocity, causing harm to people and equipment in proximity, either by contact or by resulting fire, as illustrated in Figure 13.6.

There is practically no lower limit to the amount of water needed for this type of incident to occur. Any amount of water heating from 25°C to 1000°C will expand 1600 times as it becomes water vapour. This means that there is zero tolerance for water to be trapped in liquid silicon. Situations where this type of explosion can occur in silicon production are many: equipment leakages, rain, snow, or even residual moisture that has not been sufficiently dried in refractory materials or concrete floors have the potential to be encapsulated in liquid silicon or slag.

The phenomena of explosions caused by water enclosed in liquid metal have also been investigated in the steel and aluminium industry (Babaitsev and Kuznetsov, 2001). The explosive effect of 1000 kg of aluminium or steel is presented for different amounts of water entrapped in 2. To visualize the effect of this power, 1 kg of TNT will destroy all windows within a radius of 30 m, 80 kg TNT will destroy all windows within a radius of 250 m and destroy a normal roof at a 40 m distance and all walls at 23 m distance from the explosion.

Table 13.2 *The explosive effect of 1000 kgs of aluminium with amount of water trapped (Babaitsev and Kuznetsov, 2001).*

Amount of water	1 litre	10 litres	100 litres
Explosive power (kg TNT)	3	32	200

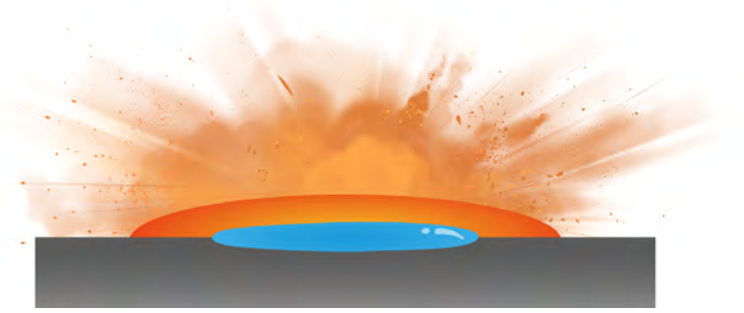


Figure 13.7 *shows the principle behind the start of a water explosion – i.e. water enclosed by liquid or hot silicon or slag.*

The enthalpy of silicon, both by volume and by mass, is much higher than that of aluminium and iron, so the explosion strength may be higher for silicon, as seen in Table 13.3. This type of explosion can harm people in multiple ways, through both pressure and temperature. A pressure wave can injure people directly, and indirectly by moving debris, particles, and equipment at high speeds. Temperature can injure people directly, through severe burns caused by contact, or through fumes caused by fires.

Table 13.3 *shows the enthalpy release through 100 ΔK and solidification ('HSC Chemistry', n.d.).*

	Temp in	Temp out	kWh/kmol	kWh/1000 kg	kWh/Nm3
Al	700	600	−4	−144	−389
Fe	1600	1500	−5	−91	−714
Si	1500	1400	−15	−524	−1221

Dust explosions – primary and secondary explosions or the formation of explosive gases or metal fines after a primary explosion

Most of the dust in primary silicon production facilities is SiO_2 and will not cause dust explosions, as it is inert. It may, however, cause serious health problems with exposure over time (potential to cause COPD) and must therefore be kept under close control. Dust from the further processing of silicon

alloys through crushing and sizing is a different story, as this type of dust is combustible. There will therefore almost always be the potential for combustible dust in a silicon facility, and the silicon industry has experienced dust explosions with fatal consequences (Abbasi and Abbasi, 2007; Eckhoff *et al.*, 1986). There are four conditions that must be in place for a dust explosion to happen, as illustrated in Figure 13.8 and Figure 13.9:

- The dust must be combustible
- Particles must be able to form a cloud exceeding min. explosion concentration
- Dust must be confined
- An ignition source must be present.

Most types of silicon alloy dust are difficult to ignite, but this varies strongly between different types of silicon alloys; the risk is higher with mixtures of ferrosilicon and magnesium or flammable solids. If they do ignite, however, the explosions can be extreme because of the stored energy. Over time, silicon dust will collect on walls and structures if it is not correctly contained and collected. This increases the potential for an explosive dust cloud forming after a primary water/metal explosion, if these processes are operated in the same area, as is often the case at a smelter. A primary metal/water explosion has more than sufficient energy to ignite the dust. In addition to silicon and ferrosilicon dust in the crushing and screening areas, fine carbon materials in the raw materials transportation systems are also candidates for dust explosions in the silicon industry.

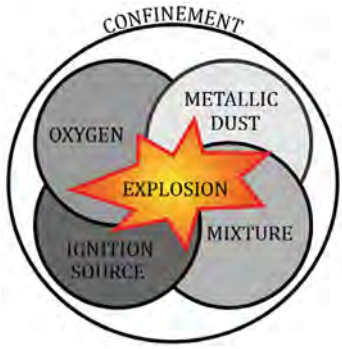


Figure 13.8 *shows the necessary conditions for a metallic dust explosion.*

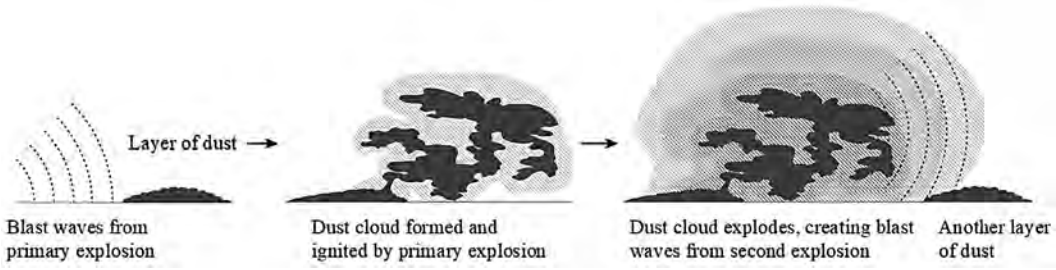


Figure 13.9 *shows the potential for a large secondary dust explosion following a smaller one.*

Burning of skin due to contact with warm gas or liquid or warm silicon

This type of injury is by far the most common when we experience blow-outs or explosions, and it may range from minor superficial burns to fatal burns. Breathing hot gases can also cause fatal burn injuries, as it may affect a person's throat and lungs. Most of the minor to medium-severity burns in silicon production happen in the tapping and post-taphole areas, where there is close contact between molten silicon and operators. High-pressure process gas ejection from the taphole, or loss of confinement of molten silicon from ladles or casting molds, are the main causes of this type of incident. Fatal burn injuries are more connected to major explosions, like the ones described in case 1 and 2 above.

13.4 Active and passive measures for increased safety

The work for increased safety may be divided into active and passive measures. Active measures are taken to avoid accidents. Eruption-type incidents can be mitigated with instrumented control of cooling water flow, to detect leakages easily before they become critical. Examples of passive measures are preventing access to high hazard areas like the stoking floor, and either making control room windows stronger or removing them completely, and

using camera surveillance instead of direct view through a window. For the type 2 explosions, the main active measure is preventing water from coming close to liquid silicon.

13.5 Conclusion

Production of silicon alloys has an inherent risk of explosion and serious injury because of very high temperatures and very high amounts of energy. Fully understanding the mechanisms behind this risk is of the utmost importance to operate the process safely and prevent harm from happening. Controlling this risk involves fully understanding the process, implementing equipment, automation, and methods to remove operators from dangerous work, and using better personal protective equipment. The more general type of accidents is more frequent. It is important to have a continuous safety focus, with participation of all employees at the silicon plant.

A personal comment from the author of this chapter

I have been working in the metal producing industry all my life. It has been a good and interesting time. Most of the work has been on the positive side – working with good colleagues to improve the process and the environment. Unfortunately, the industry may also show a darker side! Out of 'people I knew', friends and colleagues I have lost 8 in work accidents. And I have participated in the investigation of 4 fatal accidents in different countries.

To come to a plant that has suffered a loss of a colleague is to come to a sad plant. It is not easy to describe the feelings when you talk to his working companions. The plant that gave wellbeing to them and their family has suddenly shown a grimmer face. Whole families have suddenly got a sad and uncertain situation. To investigate is to try to find out the root cause of the accident. In that process, you need to study the last hours of the deceased. You get to know a person you will never meet.

This is my background for writing this chapter. If the learning here will contribute to avoiding one single accident with serious harm or death, I will be grateful.

Halvard Tveit

References

Abbasi, T. and Abbasi, S.A. (2007) 'Dust explosions–cases, causes, consequences, and control', *Journal of Hazardous Materials*, 140, pp. 7–44. Available at: https://doi.org/10.1016/j.jhazmat.2006.11.007

Agarwal, P.K. (1986) 'A single particle model for the evolution and combustion of coal volatiles', *Fuel*, 65, pp. 803–810. Available at: https://doi.org/10.1016/0016-2361(86)90073-6

Babaitsev, I.V. and Kuznetsov, O.V. (2001) 'Energy of explosions occurring when water falls onto a layer of molten metal', *Metallurgist*, 45, pp. 185–188. Available at: https://doi.org/10.1023/A:1012398700677

Eckhoff, R.K., Parker, S.J., Gruvin, B., Hatcher, M. and Johansson, T. (1986) 'Ignitability and explosibility of silicon dust clouds: Influence of dust fineness', *J. Electrochem. Soc.*, 133, p. 2631. Available at: https://doi.org/10.1149/1.2108493

Gexcon (2026) *Gexcon | World leading fire & explosion safety consultants*. Available at: https://www.gexcon.com/ (Accessed: 14 May 2026).

Explosion Hazards (n.d.) *List of historic explosions*. Available at: https://www.explosionhazards.co.uk/list-of-historic-explosions/ (Accessed: 14 May 2026).

Metso (n.d.) *HSC Chemistry*. Available at: https://www.metso.com/portfolio/hsc-chemistry/ (Accessed: 14 May 2026).

No, S.Y. and Syred, N. (1990) 'Thermal stress and pressure effects on coal particle fragmentation and burning behaviour in a cyclone combustor', *J. Energy Institute*, 63, pp. 151–159.

Tveit, H. and Breidenthal, M. (2020) 'The EHS Achilles heel of the silicon furnace – the potential for energy out of control', in *Proceedings of Silicon for the Chemical and Solar Industry XIV*. Svolvær, Norway.

Tveit, H., Garcia, M., Delbeck, H., Haug, A.T., Saugestad, B. and Eikeland, I.J. (2008) 'Water leakages in ferroalloy and silicon reduction furnaces – experience gained from a severe accident in 2006', in *Proceedings of Silicon for the Chemical and Solar Industry IX*. Oslo, Norway, pp. 11–24.

Appendix A

Equilibrium calculations

The interpretation of the carbothermic silicon process is, to a large degree, based on chemical equilibria, and a sound understanding of these equilibria is essential. This appendix presents the most important equilibrium calculations, reviews the available data sources, and warns against some common errors in the use of equilibrium calculations in the Si–O–C system.

Reactions in the submerged arc furnace

There are several approaches to the equilibrium evaluation of a system, and we will describe in detail one method that we think is both illustrative and convenient for the silicon process. In brief, we study the equilibria between the gas and the possible combinations of condensed phases. We write down a complete set of independent reactions for the possible phase combinations and derive the equilibrium relations from the mass action law. This procedure should provide a broad understanding of the equilibria of the furnace reactions in the silicon process.

Brief description of the system

The Si–O–C system has a gas phase and four condensed phases, SiO_2, C, SiC and Si, in the temperature range 1400–2500°C where the main reactions take place. Species SiO_2 and Si have melting points within the temperature range of the reactions, and SiO_2 has several modifications. However, phase transformations within the species have no significant influence on the equilibria of the silicon process and will not be considered further. Any mutual solubility between the condensed phases is ignored. In the gas phase, the main species are CO and SiO, while several species occur in low concentrations: CO_2, Si,

This work is licensed under the Creative Commons Attribution 4.0 International License.
To view a copy of this license, visit https://creativecommons.org/licenses/by/4.0/

Si_2C, SiC_2, etc. It has also been claimed that SiO can occur as a condensed species. It is disregarded in the calculations, but its existence will be discussed in connection with the data sources in Section A.2.

Calculation of equilibria

Motzfeldt gave one of the first interpretations of the silicon process based on equilibrium calculations (Motzfeldt, 1961). He calculated the vapour pressures for the possible combinations of condensed phases around the temperature of silicon formation and set up a crude process model based on the results. The numerical values of his pressure calculations are misleading because the thermochemical data then available were incorrect, but his general approach to the problem will be used here with more recent data (Chase *et al.*, 1985). He used a graphical treatment that gives a very good sense of the chemistry of the system, but numerical calculation on a computer is much faster and gives better accuracy than measurements on a graph. Here, the problem will be approached, and the results will be presented, as in a graphical method, but all the calculations have been carried out on a computer.

In a two-dimensional diagram, it is possible to represent system properties as a function of one independent variable. The conditions for unambiguous specification are given by the phase rule for the system. Generally, a system may consist of a number *C* of components and have a number *Ph* of phases. At equilibrium, it has a restricted number *F* of free variables, or 'degrees of freedom'. According to Gibbs' phase rule, we then have

$$Ph + F = C + 2 \qquad [A.1]$$

Determining the correct number of components, *C*, sometimes causes difficulties, but in high-temperature systems with reduction/oxidation reactions it is safe to take *C* as the number of elements. Thus, in the present case $C = 3$ (Si, O, C), and we have

$$Ph + F = 5 \qquad [A.2]$$

In systems without reduction/oxidation reactions, *C* may be lower than the number of elements. An example is the slag system SiO_2–CaO, which has only

two components even if there are three elements. Rigid rules for determining the number of components can be found in standard texts of thermodynamics.

When we present an equilibrium as a two-dimensional graph, we need one degree of freedom for the independent variable. The sum of phases and fixed variables must therefore be four to determine the dependent variables unambiguously for a given value of the independent variable. The thermodynamic variables considered are temperature, pressure and chemical composition of the phases. The chemical composition of the gas phase is given as the partial pressure. In equilibrium calculations, all reactions are equally correct if they are balanced and the system is completely determined according to the phase rule. It does not matter whether a reaction really occurs. The selection of reactions for the calculation is therefore mainly a matter of convenience. The result is the same for all correct combinations of reactions in the calculation.

The calculations are based upon the constant K in the mass action law. This constant for a Reaction [x] can be calculated by the equation

$$lnK_x = \frac{-\Delta G_x^0}{RT} \qquad [A.3]$$

where ΔG_x^0 is the difference in standard Gibbs energy between the right- and left-hand sides of the Reaction [x], R is the gas constant 8.314 $J/K^{-1}mol^{-1}$, and T is the temperature in K. The K_X values are, as a rule, calculated from (Chase *et al.*, 1985). We assume that the gases in all systems are ideal and use the partial pressures directly in the mass action law. The partial pressure p in equilibrium calculations is a relative pressure, defined as the ratio between the actual pressure and the pressure in the standard state of the thermochemical data. It is therefore really a dimensionless number, but the unit (bar) is normally added to indicate that the standard state is 1 bar.

The calculation will be shown in several examples later. Generally, it starts with a system that is completely determined according to the phase rule. Then, as a first approximation, it is assumed that CO and SiO are the only gas species in the system. The mass action law equations are correct even if there are other gas species present, and the approximation is introduced in the equation that relates the partial pressures to the ambient pressure P_{amb}.

$$p_{SiO} + p_{CO} = p_s = P_{amb} - p_X \qquad [A.4]$$

where p_s is defined by the equation, P_{amb} is the pressure of the surroundings (normally 1 bar for a silicon furnace), and p_X is the sum of the partial pressures of all other gases in the system. The first approximation $p_s = P_{amb} = 1$ bar gives approximate SiO and CO pressures. To introduce other gas species, an additional mass action equation with the new species must be added. The calculation of the partial pressure of CO_2 will be shown as an example. The additional mass action equation can be based on any reaction between CO_2 and the other species, and we select one that is convenient for the calculation, such as

$$SiO_2 + CO = SiO + CO_2 \qquad [A.5]$$

with the mass action equation

$$\frac{p_{SiO} \cdot p_{CO_2}}{p_{CO}} = K_{A.5} \text{ that is } p_{CO_2} = K_{A.5} \cdot \frac{p_{CO}}{p_{SiO}} \qquad [A.6]$$

The approximate partial pressures of SiO and CO are known from the first approximation. The CO_2 partial pressure can provide an improved p_s by Equation [A.4], and then new partial pressures of SiO and CO, which in turn can give an improved partial pressure of CO_2. This iteration can be repeated until the sum of the partial pressures is equal to the ambient pressure with sufficient accuracy. Other gas species such as Si, Si_2, SiC_2, Si_2C, etc. can be included in the calculation simultaneously by analogous reactions. Calculations for the conditions in silicon furnaces show that, for most purposes, it is sufficient to assume that SiO and CO are the only gas species.

Equilibria with two condensed phases

A gas phase is always present in the furnace reactions. For two condensed phases, the phase rule then gives two degrees of freedom. One is used for the free variable; one additional property then has to be fixed to determine the dependent variable completely. The equilibrium can therefore be determined at *constant temperature* or *constant pressure*.

The system has a total of four condensed phases in the interesting temperature range: SiO_2, C, SiC and Si. There are six combinations of two condensed phases, and these combinations can be expressed as chemical reactions:

SiO_2, C $\quad SiO_2(s,l) + C(s) = SiO(g) + CO(g)$ [A.7]

SiO_2, SiC $\quad 2\ SiO_2(s,l) + SiC(s) = 3\ SiO(g) + CO(g)$ [A.8]

SiO_2, Si $\quad SiO_2(s,l) + Si(s,l) = 2\ SiO(g)$ [A.9]

C, SiC $\quad SiO(g) + 2\ C(s) = SiC(s) + CO(g)$ [A.10]

C, Si $\quad SiO(g) + C(s) = Si(s,l) + CO(g)$ (Metastable) [A.11]

SiC, Si $\quad SiO(g) + SiC(s) = 2\ Si(s,l) + CO(g)$ [A.12]

Reaction [A.11] is metastable because Si will react with C at all relevant temperatures until either Si or C is consumed:

$Si(s,l) + C(s) = SiC(s)$ [A.13]

The condensed phases are then either C–SiC or Si–SiC, and the corresponding reactions are Reactions [A.10] and [A.12], respectively.

Constant temperature

At constant temperature, two condensed phases and one partial pressure specify the system completely according to the phase rule. We choose the CO pressure as the independent variable and show the SiO pressure as the dependent variable. The equilibrium Reactions [A.7]–[A.12] give mass action laws, written here in logarithmic form for reasons that will be explained later:

$$lgp_{CO} + lgp_{SiO} = lgK_{A.7} \quad [A.14]$$

$$lgp_{CO} + 3lgp_{SiO} = lgK_{A.8} \quad [A.15]$$

$$2\ lgp_{SiO} = lgK_{A.9} \quad [A.16]$$

$$lgp_{CO} - lgp_{SiO} = lgK_{A.10} \quad [A.17]$$

$$lgp_{CO} - lgp_{SiO} = lgK_{A.11} \quad [A.18]$$

$$lgp_{CO} - lgp_{SiO} = lgK_{A.12} \quad [A.19]$$

When T is constant, Equations [A.14]–[A.19] give straight lines in a graph of lg p_{SiO} as a function of lg p_{CO}. This linear relation is why the mass action equations are written in logarithmic form. An example of equilibrium is shown in Figure A.1, and changes with temperature are indicated in Figure A.2. The directions of the lines are determined by the stoichiometry of the equations; temperature affects only the magnitude of the equilibrium constant K_x. When temperature changes, a line is displaced parallel to the original line. With increasing temperature, the stability ranges for C and SiC come closer. Figure A.2 can be interpreted as the projection of a three-dimensional graph of the SiO pressure as a function of the CO pressure and the temperature.

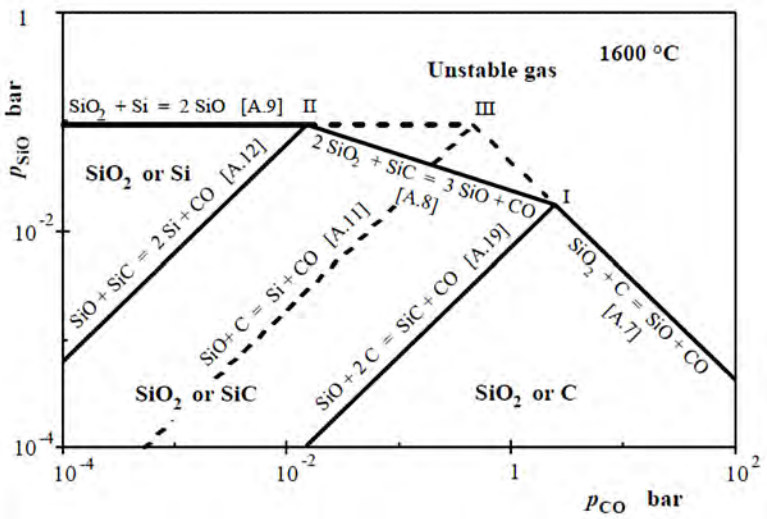


Figure A.1 *Vapour pressures at constant temperature 1600°C of reactions with two condensed phases in the system Si–O–C. The broken lines represent metastable equilibria.*

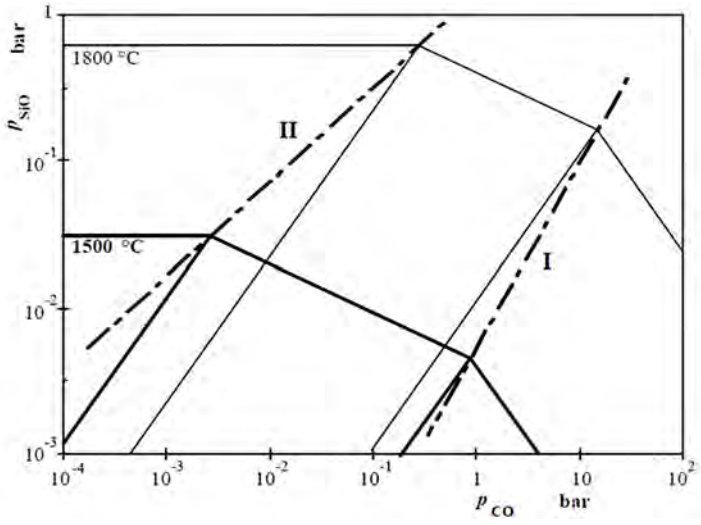


Figure A.2 *The displacement with temperature of the vapour pressure graphs shown in Figure A.1.*

The graphs split the area of Figure A.1 into stability zones. As an example, we consider the reaction

$$SiO_2 + C = SiO + CO \qquad [A.7]$$

For gas compositions corresponding to points above the graph, the product $p_{SiO} \cdot p_{CO}$ is larger than the equilibrium value in the mass action law. If SiO and CO are removed in the ratio given by the stoichiometry of the reaction, the product $p_{SiO} \cdot p_{CO}$ moves towards the equilibrium value. Therefore, in Reaction [A.7] the gas is unstable. Analogous arguments apply to Reactions [A.8] and [A.9], and the three reactions together define the zone Unstable gas in Figure A.1. Gas mixtures corresponding to points in this area cannot exist at equilibrium.

In the area between the graphs, one condensed phase is allowed. The phase SiO_2 is stable for all stable gas compositions, since there are no reactions between it and the gas species SiO and CO that can form the other condensed species. Therefore, the stable condensed phase in an area will be SiO_2 *or* one of the phases C, SiC and Si. The condensed phases other than SiO_2 have stability areas that can be found by discussing the chemical reactions.

As an example, we discuss the stability range of Si. Si is stable for SiO pressures higher than the equilibrium value of

$$SiO + SiC = 2\ Si + CO \qquad [A.12]$$

In the diagram, Si is stable above the graph of Reaction [A.12]; below the graph it becomes unstable relative to SiC. However, above the graph of

$$SiO_2 + Si = 2\ SiO \qquad [A.9]$$

the gas is unstable. Therefore, Si is stable only between the graphs of Reactions [A.9] and [A.12], to the left of the intersection. The stability ranges of SiC and C can be discussed similarly. The complete stability distribution is indicated in Figure A.1. The metastable system shown by broken lines is ignored in the stability discussion.

Constant pressure

At constant pressure, two condensed phases and the temperature specify the system completely according to Equation [A.1]. Therefore, the SiO pressure can be presented in a graph as a function of temperature. Such graphs will be calculated for equilibria of Reactions [A.7]–[A.12]. The partial pressures must obey the mass action equations of the reactions, and their sum must equal the ambient pressure.

For Reaction [A.7] we have the mass action reaction

$$p_{SiO} \cdot p_{CO} = K_{A.7} \qquad [A.20]$$

together with

$$p_{SiO} + p_{CO} = P_{amb} - p_x = p_s \qquad [A.4]$$

where p_X symbolizes the sum of the other gas species in the system (CO_2, Si, Si_2, SiC_2, Si_2C, …), and p_S is the sum $p_{SiO} + p_{CO}$ corrected for the other gas species. The pressures of these gas species can be calculated as indicated above in connection with Equation [A.4]. Equations [A.20] and [A.4] combine to

$$p_{SiO}^2 - p_s \cdot p_{SiO} + K_{A.7} = 0 \quad [A.21]$$

The solution of this equation can be taken as the intersection between the curves

$$y_1 = p_{SiO}^2 - p_S \cdot p_{SiO} + K_{A.7} \text{ and} \quad [A.22]$$

$$y_2 = 0 \quad [A.23]$$

Equation [A.22] gives

$$\frac{dy_1}{dp_{SiO}} = 2 \cdot p_{SiO} - p_S$$

$$\frac{d^2 y_1}{dp_{SiO}^2} = 2$$

The variable y_1 has a minimum for $p_{SiO} = 0.5\, p_S$. The graphs for y_1 and y_2 have two intersections if

$$y_{1,min} = 0.25 p_S^2 - 0.5 p_S^2 + K_{A.7} = K_{A1.7} - 0.25 p_{SiO}^2 < 0$$

and one intersection with $p_{SiO} = 0.5\, p_S$ if $y_{1,min} = 0$. If $y_{1,min}$ is higher, the graphs do not intersect, which means that Equation [A.22] has no real solutions. In the range with two solutions, one is larger and one is smaller than 0.5. The condition for a solution is

$$p_S \geq 2 \cdot \sqrt{K_{A.7}} \quad (p_s \text{ and } K_{A.7} \text{ are always positive}) \quad [A.24]$$

Equation [A.22] can be solved analytically:

$$p_{SiO} = 0.5 p_s \pm \sqrt{0.25 p_S^2 - K_{A.7}} \quad [A.25]$$

The solution is shown in Figure A.3. The stoichiometry of the reaction

$$SiO_2 + C = SiO + CO \quad [A.5]$$

does not allow solutions with $p_{SiO} > 0.5$ from the reactants SiO_2 and C, and establishing this equilibrium will require an external source of SiO. As can be seen from Figure A.3, the high SiO pressures are unstable relative to

$$SiO_2 + Si = 2\ SiO \qquad [A.9]$$

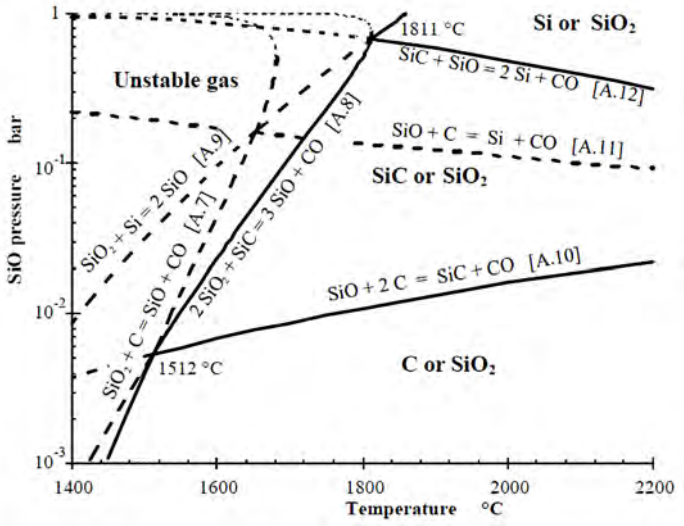


Figure A.3 *Equilibrium SiO pressures above the condensed phase combinations C–SiC, C–Si, SiO_2–C, SiO_2–SiC, SiC–Si and SiO_2–Si calculated with data from the JANAF Thermochemical Tables (Chase, 1985). The broken lines indicate metastable equilibria.*

Similarly, Reaction [A.8] gives an equation

$$p_{SiO}^4 - p_S p_{SiO}^3 + K_{A.8} = 0 \qquad [A.26]$$

A discussion similar to that for Reaction [A.7] shows that the equation has two solutions for

$$y_{1.min} = K_{A.8} - 0.1055 p_S^4 < 0 \qquad [A.27]$$

and one solution for $y_{1,min} = 0$. The equation has real solutions if

$$p_S \geq 1.755 \cdot \sqrt[4]{K_{A.8}} \qquad [A.28]$$

It can be solved by 'trial and error' or by a systematic iteration method, e.g. by Newton iteration. The graph is included in Figure A.3. The stoichiometry does not allow solutions with $p_{SiO} > 0.75$ from the reactants SiO_2 and SiC.

The SiO pressure of Reaction [A.9] is independent of the presence of other gases:

$$p_{SiO} = \sqrt{K_{A.9}} \qquad [A.29]$$

Reactions [A.10], [A.11] and [A.12] have similar mass action equations; only the value of the equilibrium constant K_x is different.

$$\frac{p_{CO}}{p_{SiO}} = K_x \qquad [A.30]$$

$$p_{SiO} + p_{CO} = p_S \qquad [A.20]$$

The solution is

$$p_{SiO} = \frac{p_S}{K_S + 1} \qquad [A.31]$$

The areas between the graphs in Figure A.3 do not uniquely define which condensed phase is stable. Gas compositions to the left of one of Reactions [A.7], [A.8] and [A.9] are unstable with respect to condensation, and the reactions together define the area Unstable gas as in Figure A.1. The stability of condensed phases between the graphs can be discussed analogously to Figure A.1, and the resulting stable phases are shown in the figure. The stability zones are not important, since the graphs will be used mainly in discussing situations where two or three condensed phases are present.

Equilibria with three condensed phases

Figure A.1 shows which condensed phases can coexist in equilibrium. At the intersection of the lines in Figure A.1, there are three condensed species, and the gas composition is fixed for the given temperature. There are three intersections:

I Condensed phases: SiO_2, C, SiC

II Condensed phases: SiO_2, SiC, Si

III Condensed phases: SiO_2, C, Si metastable

In addition, there is a fourth combination of three phases:

IV Condensed phases: C, SiC, Si metastable

Combination IV does not appear in a CO–SiO diagram. It is metastable and uninteresting for a production process because it does not include the silicon source SiO_2. It will not be discussed further.

The pressures of CO and SiO can be calculated directly by combining the reactions that give the intersections. Figure A.1 gives three reactions for each intersection, and the most convenient reactions for calculation are chosen.

Point of intersection I: Combining Reactions [A.7] and [A.10]:

$$p_{SiO} = \sqrt{K_{4.7} / K_{A.10}} \qquad [A.32]$$

$$p_{CO} = \sqrt{K_{4.7} \cdot K_{A.10}} \qquad [A.33]$$

Point of intersection II: Combining Reactions [A.9] and [A.12]:

$$p_{SiO} = \sqrt{K_{A.9}} \qquad [A.29]$$

$$p_{CO} = \sqrt{K_{A.9}} \cdot K_{A.12} \qquad [A.34]$$

Point of intersection III: Combining Reactions [A.9] and [A.11]:

$$p_{SiO} = \sqrt{K_{A.9}} \qquad [A.29]$$

$$p_{CO} = \sqrt{K_{A.9}} \cdot K_{A.11} \qquad [A.35]$$

This combination is metastable and will not be discussed further.

The gas pressure in phase combination I (SiO_2–C–SiC) is shown in Figure 2.7, and the pressure in phase combination II (SiO_2–SiC–Si) in Figure 2.8.

Equilibrium with four condensed phases

SiO_2, C, SiC and Si can, in principle, coexist and give a completely determined system. In an extension of Figure A.2, the system can be found as the intersection of graphs I and II. With increasing temperature, the graphs move closer and closer together. Numerical calculation shows that they are still apart at 2700°C. At approximately this temperature, SiC dissociates to C and a Si phase with a high content of carbon. The assumptions for the calculation of a four-phase equilibrium then break down. It can be concluded that equilibrium among the four condensed phases SiO_2, C, SiC and Si corresponds to very high temperature and pressure. Most likely, it cannot be realized because SiC dissociates at a lower temperature. In any case, it lies outside the interesting temperature range of the silicon process.

The data sources

Thermochemical data for the Si–O–C system are available in FactSage and HSC Chemistry. In the first version of this book (1998), they were taken from JANAF Thermochemical Tables (Bahrin, 1995; Bahrin *et al.*, 1977; Bahrin and Knacke, 1973; Chase *et al.*, 1985; Knacke and Kubaschewski, 1991; Kubaschewski *et al.*, 1993). Differences between the sources account for temperature differences of about 20 K. The data were compiled from measurements with scatter and were sometimes extrapolated outside the experimental range. Therefore, they always have a rather large uncertainty, and the results should be interpreted with care. When reaction temperatures are calculated, the result is not reliable to the nearest °C. Still, there is no reason to expect that improved accuracy of the data will give a qualitative change in process understanding.

Most printed data sources give tables with values for each 100 K, as well as additional values for transition points such as melting, vaporization and transformations of the crystalline structure. For computer calculations, it would be more convenient to store the data in a form where the value for any given temperature could be retrieved directly. With the present availability of fairly high-powered personal computers, there is really no need for tables. Kubaschewski *et al.* have a formula system for tabulation of thermochemical data in formula form, but calculation of $\Delta G°$ data from these tables is still rather time-consuming (Kubaschewski *et al.*, 1993). Programmes for thermochemical

calculations (e.g. HSC Chemistry) contain extensive data compilations with information about the data sources. Without access to suitable programmes, one can use tables and obtain fairly high accuracy by interpolating linearly between the given temperatures.

Thermochemical calculations from about 1965 and earlier are based on incorrect data. The reason was an erroneous measurement of the heat of formation for SiO_2. These data gave inconsistent results in thermodynamic analysis. Chipman showed that the inconsistencies disappeared if the heat of formation of SiO_2 was changed (Chipman, 1961). Later, new measurements showed that Chipman's indications were correct, and revised data were included in the thermochemical tables. The consequence of the correction for the Si–O–C system is discussed in (Schei, 1967; Schei and Sandberg, 1966).

In the data sources used here, SiO is not included as a stable condensed material, most likely because the compilers found no convincing experimental demonstration of its existence. Kubaschewski *et al.* (1993, reprinted from earlier editions of the book) give an example where the thermochemical properties of condensed (amorphous) SiO are assessed tentatively, but they do not include it in their compilation of data. Still, Nagamori *et al.* used these tentative data as background for a new interpretation of the silicon process (Nagamori *et al.*, 1986). They calculated the equilibrium for the reaction when [SiO_2 + x SiC] is heated, and found that the reactants will gasify without Si formation according to

$$2\ SiO_2 + SiC = 3\ SiO + CO \qquad [A.8]$$

Therefore, they concluded that Si cannot be produced in an isothermal reaction in this system. When they introduced condensed SiO into the calculation with the tentative data of Kubaschewski, the SiO(cond)–SiC–Si system at 1 bar gave Si. Therefore, in their opinion, condensed SiO is an essential intermediate in the reaction between SiO_2 and C or SiC. Rosenquist and Tuset pointed out that there is no reliable evidence for the existence of SiO(l) and claimed that existing metallurgical theory explains the silicon process satisfactorily (Rosenqvist and Tuset, 1987). However, Nagamori *et al.* (1987) repeated their claims that Si production would be impossible without condensed SiO.

The reasoning of Nagamori *et al.* (1986) was based on a calculation indicating vaporization without Si formation when mixtures [SiO_2 + x SiC] are

heated. This result differs from the calculation in Chapter 2 and several similar published calculations. The reason for the difference is that Nagamori *et al.* (1986) used the approximate data of Turkdogan instead of Turkdogan's source, which is an earlier edition of the JANAF Thermochemical Tables (this edition gives essentially the same data as the later edition for the relevant species) (Chase *et al.*, 1985; Turkdogan, 1980). In the paper of Nagamori *et al.* (1986), the calculated temperature in the inner zone of the furnace increases when condensed SiO is introduced, because a higher temperature becomes necessary to obtain an overall pressure of 1 bar. This higher temperature gives a more favorable ratio p_{CO}/p_{SiO} for silicon formation. However, direct measurements of the SiO_2–SiC–Si system give a total vapour pressure fairly close to the values calculated from the JANAF data (Gjerstad, 1968). If condensed SiO really is formed in the furnace, it should also have been present in the measurements; these measurements must then be valid for the SiO(cond)–SiC–Si system. Therefore, the temperatures and SiO content calculated in Chapter 2 should be qualitatively correct, whether condensed SiO is stable or not. The existence of condensed SiO is not relevant for estimation of the temperature in the furnace, and the paper of Nagamori *et al.* does not corroborate its existence (Nagamori *et al.*, 1987).

Common errors in equilibrium calculations

The literature shows some errors in equilibrium calculations for the silicon process. In this Section, we present some examples of common errors as a warning. However, apparently erroneous calculations are not always mistakes. In some cases, one can simulate kinetics by applying equilibrium calculations in systems that are only semistable. For example, in the cooling of the gas mixture SiO and CO, we know from experience that the product is SiO_2(s,l) and Si(l), while equilibrium results in Figure A.3 indicate SiO_2(s,l) and SiC(s) or C(s). This experience shows that the equilibrium reactions are slow, and we can simulate the real situation by calculating the semistable reaction.

$$2\ SiO(g) = SiO_2(s,l) + Si(l) \qquad [A.9]$$

Loss of accuracy by data treatment

High-temperature thermochemical data always have rather high error limits, but uncertainty should not be increased by mathematical treatment. Personal computers and calculation programmes with data are now widely available, and there is no reason to use strong simplifications, such as the one proposed by Turkdogan (1980). In this simplification, the Gibbs energy of formation is expressed as

$$\Delta_f G^\circ = A + B\,T \qquad [A.36]$$

where A and B are constants over a given temperature range. This approach will cause problems with phase transitions. An example of a mistake caused by this error is the above-mentioned new interpretation of the silicon process by Nagamori *et al.* (1986, 1987).

Combination of species that cannot coexist

If we write the reaction

$$SiO_2 + 2\,C = Si + 2\,CO(g) \qquad [A.37]$$

we can calculate values of $K_{A.37}$ for the requested temperatures. However, the result is not meaningful, because the species C and Si cannot coexist. This impossibility can be seen from the Gibbs energy of the reaction

$$Si + C = SiC \qquad [A.13]$$

which is negative over the interesting temperature range (Table A.1). This error can be avoided if we set up a phase stability diagram (also called a predominance diagram). The diagrams in Figures A.1–A.3 are examples of phase stability diagrams that show which phases can coexist. Si cannot be formed in a reaction between SiO_2 and C before all the C is consumed, and the real equilibrium reaction will be a combination of the following reactions:

$$SiO_2 + 3\,C = SiC + 2\,CO(g) \qquad [A.38]$$

$$SiO_2 + C = SiO(g) + CO(g) \qquad [A.7]$$

However, the SiO content in the resulting gas will be low, and Reaction [A.38] is a good approximation of the real reaction.

Table A.1 *The standard Gibbs energy of Reaction [A.13] calculated by HSC Chemistry.*

Temperature	°C	0	500	1000	1500	2000
$\Delta G°$ [A.13]	kJ	−71.05	−67.24	−63.80	−57.66	−39.36

Ignoring important species

Another interpretation of the error of equilibrium calculations based on Reaction [A.37] is that we have ignored the important species SiC and SiO. Ignoring important species is especially dangerous if we carry out equilibrium calculations by minimization of the free energy. In that case, the programme varies the contents of the species that are included and reports the combination that gives the lowest free energy. This result may, however, be misleading, since the ignored species could have given a lower free energy.

Inattention to the phase rule

The reaction system of Reaction [A.37] has three condensed phases, and at fixed ambient pressure it has no degrees of freedom according to the phase rule. We can calculate the equilibrium constant for any temperature by ordinary methods and derive an equation for the partial pressure of CO as a function of temperature. However, since the system has no degrees of freedom, the temperature is determined by the system, and the calculated partial pressure is correct only at this temperature. We can use the equation together with another equation to determine the equilibrium temperature, but not to find the partial pressure of CO at an arbitrary temperature.

Unsuitable interpretation of the reaction conditions

If we want to find the partial pressure over SiO_2 and SiC at constant ambient pressure 1 bar, we can use the reaction

$$2\ SiO_2 + SiC = 3\ SiO(g) + CO(g) \qquad [A.8]$$

combined with a relation between partial and total pressure. The condition must be

$$p_{SiO} + p_{CO} = 1 \qquad [A.39]$$

and not

$$p_{SiO} = 3\, p_{CO} \qquad [A.40]$$

The condition [A.40] is correct if the total pressure is not specified and the resulting gas combination is stable.

Another example may be the estimation of the equilibrium when a mixture [SiO_2 + 2 C] is heated at 1 bar to a temperature slightly above the triple point at 1811°C (Figure A.3). We assume that the sample is placed in a crucible with a small opening and heated. The criterion for reaction is then

$$p_{total} \approx p_{SiO} + p_{CO} = P_{amb} = 1 \text{ bar}$$

This criterion, which is really based on kinetic reasoning, is discussed in detail in Chapter 2. It gives a reaction sequence:

- Slow reaction to the triple point at 1512°C
- Formation of SiC until the C is consumed slightly above 1512°C, gas CO–SiO with a small content of SiO given off
- Slow reaction between SiO_2 and SiC to the triple point at 1811°C
- Formation of Si slightly above 1811°C until the SiO_2 is consumed, gas CO–SiO with a high content of SiO given off.

This reaction sequence gives a certain overall reaction. If we calculate the equilibrium for the mixture [SiO_2 + x C] directly at temperature 1811°C, by means such as the minimization of the free energy, we will get a different overall reaction. The reason is that the open crucible gives off CO to the surroundings slightly above 1512°C, and this CO is not present in the reaction at 1811°C in the reaction sequence. As a result, the reaction at 1811°C will have a higher SiO content in the sequential reaction than in the direct reaction, and the more favorable ratio p_{CO}/p_{SiO} gives a higher Si yield.

Erroneous use of 'The reaction goes to the right for $\Delta G^\circ < 0$'

The rule is always correct for phase combinations where no phase is a mixture. The reaction

$$Si + C = SiC \qquad [A.13]$$

is a good example. If $\Delta G°$ is negative, the reaction will go to the right until at least one of the phases Si or C is consumed. However, when at least one of the phases is a mixture, $\Delta G° = 0$ only means that K has the value 1. For a gas producing reaction, the rule is true if the gas is a pure species and the ambient pressure is 1 bar. This condition is approximately fulfilled for the reaction

$$SiO_2 + 3\ C = SiC + 2\ CO(g) \qquad [A.38]$$

and the rule is a good approximation. For a more complex reaction, such as

$$SiO(g) + SiC = 2\ Si + CO(g) \qquad [A.12]$$

$\Delta G^O_{A.12}$ gives

$$\frac{a_{Si}^2 \cdot p_{Co}}{p_{SiO}} = 1$$

When the product is pure silicon, the direction of the reaction depends on the gas pressure ratio. If the silicon phase is an alloy, a low Si activity can contribute strongly to drive the reaction to the right.

References

Bahrin, I. (1995) *Thermochemical data of pure substances*. 3rd edn. Wiley-VCH. Available at: https://doi.org/10.1002/9783527619825

Bahrin, I. and Knacke, O. (1973) *Thermochemical properties of inorganic substances*. 1st edn. Springer-Verlag Stahleisen.

Bahrin, I., Knacke, O. and Kubaschewski, O. (1977) *Thermochemical properties of inorganic substances: Supplement*. 1st edn. Springer-Verlag Stahleisen.

Chase, M.V. Jr., Davies, C.A., Downey, J.R. Jr., Frurip, D.J., MacDonald, R.A. and Syverud, A. (1985) *NIST-JANAF Thermochemical Tables*. Available at: https://janaf.nist.gov/janbanr.html (Accessed: 22 May 2025).

Chipman, J. (1961) 'The free energy og silica', *J. Am. Chem. Soc.*, 83, pp. 1762–1763.

Gjerstad, S. (1968) *Chemical metallurgical investigations concerning carbothermic reduction of alumina and silica*. Doctoral thesis. Norges Tekniske Høgskole (NTH), now Norwegian University of Science and Technology (NTNU).

Knacke, O. and Kubaschewski, O. (1991) *Thermochemical properties of inorganic substances*. 2nd edn. Springer-Verlag Stahleisen.

Kubaschewski, O., Alcock, C.B. and Spencer, P.J. (1993) *Materials thermochemistry*. 6th edn. Pergamon Press.

Motzfeldt, K. (1961) *An evaluation of the chemistry of the ferrosilicon process, with the special aim of increasing the silicon recovery*. Report for Elkem, in Norwegian. Institute of Silicate Science at Norges Tekniske Høgskole (NTH), now Norwegian University of Science and Technology (NTNU), Trondheim, Norway.

Nagamori, M., Malinsky, I. and Claveau, A. (1986) 'Thermodynamics of the Si–C–O system for the production of silicon carbide and metallic silicon', *Metallurgical Transactions B*, 17, pp. 503–514. Available at: https://doi.org/10.1007/BF02670216

Nagamori, M., Malinsky, I. and Claveau, A. (1987) 'The role of SiO(l) in the production of metallic silicon. Authors' reply to a discussion contribution by Rosenqvist and Tuset (1987)', *Metallurgical Transactions B*, 18, pp. 472–477.

Roine, A. (1997) *HSC Chemistry for Windows v. 9*. Outotec Research, Pori, Finland.

Rosenqvist, T. and Tuset, J.K. (1987) 'Discusiion of "Thermodynamics of the Si–O–C system for the production of silicon carbide and metallic silicon" (see Nagamori *et al.*, 1986)', *Metallurgical Transactions B*, 18B, pp. 471–472; authors' reply pp. 472–477.

Schei, A. (1967) 'On the chemistry of ferrosilicon production', *Kjemi Bergvesen*, 27, pp. 152–158.

Schei, A. and Sandberg, O. (1966) 'Back reactions during production of silicon metal in a submerged arc electric furnace', in *Scandinavian University Books*. Oslo: Universitetsforlaget, pp. 141–150.

Turkdogan, E.T. (1980) *Physical chemistry of high temperature technology*. New York: Academic Press.

Appendix B

Pilot scale excavations

Further information about the state of the furnace is available from careful excavations after the run. Schei and Sandberg smelted silicon and ferrosilicon in a 50 kW one-phase furnace with one electrode and bottom contact (Schei, 1967; Schei and Sandberg, 1966). A summary of several excavations is given in Figure B.1. The intention was to operate the furnace in the same way as an industrial furnace, but owing to the small size, some modifications were necessary. The following cycle is typical: the furnace was filled with charge; the charge was heated for some time; produced metal was tapped; the upper layer of the charge was stoked down by wooden stokers; the furnace was charged again; etc. Most of the time, the gas rose smoothly from the surface. It contained some white fumes, which became increasingly apparent with time from charging.

This work is licensed under the Creative Commons Attribution 4.0 International License.
To view a copy of this license, visit https://creativecommons.org/licenses/by/4.0/

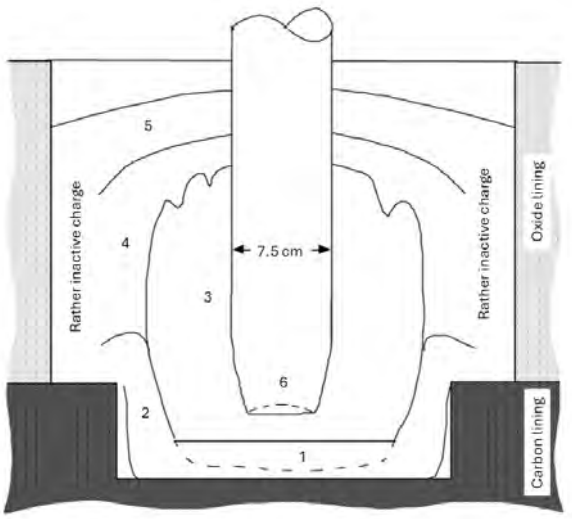


Figure B.1 *Excavation after smelting of ferrosilicon in a 40 kW one-phase furnace with a graphite electrode 75 mm diameter (Schei, 1967). The furnace was planned for convenient excavation. It was flanged so it could be split to make the contents open for observation. The drawing is based on several experiments. The current was shut down with the electrode in working position, and the furnace was allowed to cool. The charge was quartz, gas coke, and sintered iron ore pellets to give 75 per cent silicon.*

1. *Ferrosilicon.*
2. *Coarse crystals of silicon carbide, the pores between the crystals partly filled with ferrosilicon.*
3. *Cavity.*
4. *Greenish layer consisting of quartz pieces partly turned glassy, green porous lumps, and ferrosilicon drops glued together with a slightly porous, brownish glassy substance. The green lumps contain SiC, some free C and some SiO_2. Towards the cavity, the walls are partly covered by a 2–3 mm thick brownish glaze substance, mainly SiO_2.*
5. *Mainly charge materials in original form with deposits of a brown substance consisting of SiO_2 + Si. This substance is especially abundant on and near the electrode.*
6. *Graphite electrode somewhat tapered towards the lower end. The lower end is concave.*

The particles in the upper charge layer were glued together by a dense, brown substance that was especially abundant on and near the electrode. In the optical microscope, the brown substance consisted of small white droplets in a dark matrix. In the electron microprobe, the droplets were identified as Si and the matrix as SiO_2. A greenish dense substance was also found; it consisted of SiC in a matrix of SiO_2. This mass often appeared as a thin layer on the brown substance. The crater wall was partly covered with a brownish glaze that resembled the brown substance, but in the microscope it proved to contain only a few small drops of silicon.

The small-scale operation described above, together with an equilibrium discussion, has suggested that the two reactions

$$SiO + 2C = SiC + CO \qquad [2.6]$$

and

$$2\ SiO = SiO_2 + Si \qquad [\text{reversed } 2.5]$$

are very important. Two experiments were run in a modified small-scale furnace to elucidate these reactions further (Schei, 1967). The furnace pot was as before, but the electrode was hollow, and pellets [SiO_2 + C] were fed through the hole. According to the stoichiometry, these pellets should give a gas mixture [SiO + CO]; however, since the vapourization is not an equilibrium reaction, the composition of the gas will vary somewhat.

In the first of the mechanism experiments, the furnace was charged with only coke. This charge gave stable electric resistance and a gas that burnt, giving negligible amounts of white smoke. The coke layer gradually became red-hot up to the top. The excavation showed an irregular cavity at the electrode tip. Above and around the cavity, several consecutive layers were found, in the direction from the hottest zone: coarse crystalline SiC; light green transformed coke particles rich in SiC; a thin layer of black coke covered with a thin layer of the above-mentioned brown substance of SiO_2 and Si; and, at the top, black coke. The layer of green particles ended rather abruptly at a distance below the top. The reason is probably that the kinetics of SiC formation requires a high temperature, and that the strongly heat-producing condensation to brown substance is necessary to heat the carbon to a sufficiently high temperature.

Reaction [3.3] was studied with the set-up of the previous experiment, except that the furnace was filled with Al_2O_3-pellets. This experiment is a larger-scale variant of a study of the condensation of [SiO + x CO] by Poch and Dietzel (1962). These pellets were thought to be as inert as possible in the condensing gas. The electric resistance was fairly stable, and the furnace produced a gas that burnt with negligible amounts of white smoke. The charge gradually became hot at the top. The charge slid down, and some refilling was necessary. The result of the excavation is shown in Figure B.2. At the bottom there was a layer of alumina-containing slag and a considerable amount of silicon with a high aluminium content. Above a small cavity there was a roof of sintered substance, and further up there were pellets with the surface covered by a thick deposit. The deposit on the pellets changed with the height from the bottom. At the lowest level it was greenish throughout; then brown with an outer greenish layer; and towards the top brown throughout. The experiment demonstrates that evaporation and condensation of SiO may be an important reaction mechanism in the process. At first, the condensate consists of the brown substance, with very small drops of Si in a matrix of SiO_2. The Si and the SiO_2 may separate at higher temperatures, or the Si may pick up carbon from CO in the gas and give a greenish substance of SiC in a silica matrix.

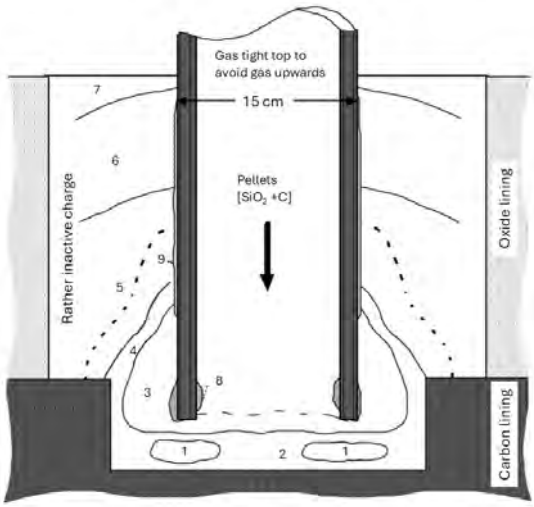


Figure B.2 *Excavation after an experiment with cooling of a gas mixture SiO + CO on a layer of alumina pellets.*

1. *Alloy (about 85% Si, 9% Al, 4% Fe, 0.2% C).*
2. *Slag (88% Al_2O_3, 6% SiO_2, 0.7% C).*
3. *Cavity.*
4. *Sintered oxidic material with metal drops.*
5. *Pellets with a green outer layer. In the inner part of this zone, the green shell lies directly on the oxidic core, and in the outer part there was a brown layer between the oxidic core and green shell.*
6. *Pellets covered with a brown substance, which was up to 3 mm thick.*
7. *White pellets partly blackened.*
8. *Deposits on the electrode (oxide, metal, silicon carbide).*
9. *Thick layer of brown substance deposited on the electrode.*

Small furnaces are well suited for excavation, and new ideas for operation can be tested. Still, it is always a question whether the results obtained are typical for large-scale and extended-time industrial operation. Large furnaces are occasionally dug out for repair in industrial operation. Even with rapid removal of the furnace content, interesting observations can be made. Metre-sized blocks of silicon-containing silicon carbide are taken out, showing that the deposit at the furnace bottom may be very thick in a large furnace. Kurosawa *et al.* dug out a 6500 kVA three-phase rotating furnace that had produced silicon metal (Kurosawa *et al.*, 1972). The furnace charging was stopped immediately before the electric shut down. In their sketch of the furnace, the cavity was very small, but they did not comment on it. The electrode tip had a position about 50 cm above the bottom carbon lining at excavation. They took out samples in a grid at several depths and sectional positions, and investigated them by chemical analysis, X-ray diffraction, and microscopy. In the charge areas close to the wall and in the centre, they found a considerable amount of SiC high up in the furnace. In the electrode path in the rotating furnace, the upper layers contained less SiC and more Si and SiO_2. These facts indicated that the charge had been consumed mainly in and close to the electrode path in the rotating furnace. Below the electrodes, the deposit consisted of Si-containing SiC and some SiO_2.

References

Kurosawa, T., Yagihashi, T., Ochiai, S. and Nakamura, T. (1972) 'Several aspects on the products of silicon-making electric furnace', *Journal of the Mining Institute of Japan*, 88, pp. 489–494. Available at: https://doi.org/10.2473/shigentosozai1953.88.1014_489

Poch, W. and Dietzel, A. (1962) 'Formation of silicon carbide from silicon dioxide and carbon', *Ber. Dtsch. Keram. Ges.*, 39, pp. 413–426.

Schei, A. (1967) 'On the chemistry of ferrosilicon production', *Kjemi Bergvesen*, 27, pp. 152–158.

Schei, A. and Sandberg, O. (1966) 'Back reactions during production of silicon metal in a submerged arc electric furnace', in *Scandinavian University Books*. Oslo: Universitets-forlaget, pp. 141–150.

Table C–1 *Literature review list for slag refining with crude silicon. Adapted from Zhu (2021).*

Author	Furnace type	Crucible type	Temperature (°C)	Si Source/ Initial B	Metal system	Slag system	Gas phase	Slag/ metal mass ratio	Holding time (h)	L_B
(Suzuki and Sano, 1991)	Resistance	Graphite	1450–1550	MG–Si B: 30–90 ppmw	Si	$CaO–SiO_2$	Ar, CO, Ar + CO_2	1	2	0.31–1.15
(Weiss and Schwerdtfeger, 1994)	Resistance	Quartz	1500	MG–Si	Si	$CaO–SiO_2$	Ar	2.5	4, 6.5	5.5
(Fujiwara *et al.*, 2005)	Induction + mechanical stirring	Alumina	1600	B: 7.6 ppmw	Si	$CaO–SiO_2$	Ar	-	-	-
(Teixeira *et al.*, 2009)	Resistance	Graphite	1550	B: 150 ppmw	Si	$CaO–SiO_2$	Ar	2.2	18	2–5.5
(Luo *et al.*, 2011)	Induction 200 kW–3000 Hz	Quartz	1550–1600	B: 15 ppmw	Si	$CaO–SiO_2$	Ar	0.1	0.5–2	2.2
(Ding *et al.*, 2012)	Induction	Graphite	1550	MG–Si B: 22 ppmw	Si	$CaO–SiO_2$	Ar	-	-	1.02
(Nishimoto *et al.*, 2012)	Resistance	Graphite	1550	B: c.a. 300 ppmw	Si	$CaO–SiO_2$	Ar	1.25–2.5	3	2.16
(White and Sichen, 2014)	Resistance + mechanical stirring	Graphite	1550	EG–Si	Si	$CaO–SiO_2$	-	1	0.17	1.98, 2.45

Author	Furnace type	Crucible type	Temperature (°C)	Si Source/ Initial B	Metal system	Slag system	Gas phase	Slag/ metal mass ratio	Holding time (h)	L_B
(Wei *et al.*, 2015)	Induction	Graphite	1550	B: 22 ppmw	Si	$CaO–SiO_2$	Ar	-	0.5–3	0.7–1.6
(Jakobsson and Tangstad, 2015)	Resistance	Graphite	1600	-	Si	$CaO–SiO_2$	Ar	1	0.6–18	2.13–2.52
(Jakobsson and Tangstad, 2015)	Resistance	Graphite	1600	-	Si	$MgO–SiO_2$	Ar	1	0.6–18	1.92–2.41
(Safarian, 2019)	Induction	Graphite	1500–1600	Si–B alloy, B: 500 ppmw	Si	$BaO–SiO_2$	Ar	-	2	0.9–1.35
(Suzuki and Sano, 1991)	Resistance	Graphite	1450	MG–Si B: 30–90 ppmw	Si	$CaO–MgO–SiO_2$	CO	1	2	1–1.6
(White *et al.*, 2013a)	Resistance	Graphite	1600	EG–Si	Si	$CaO–MgO–SiO_2$	CO (0.6, 0.8, 1 atm)	3.3	48	2.3–3.45
(White *et al.*, 2013b)	Resistance	Graphite	1600	EG–Si	Si	$CaO–MgO–SiO_2$	Ar + CO, $CO + N_2$	3.3	48	1.3–3.4
(Jakobsson and Tangstad, 2015)	Resistance	Graphite	1600	-	Si	$CaO–MgO–SiO_2$	Ar	1	0.6–18	1.84–2.52
(Suzuki and Sano, 1991)	Resistance	Graphite	1450	MG–Si B: 30–90 ppmw	Si	$CaO–BaO–SiO_2$	CO	1	2	1.5–2
(Safarian, 2019)	Induction	Graphite	1500–1600	Si–B alloy B: 500 ppmw	Si	$CaO–BaO–SiO_2$	Ar	-	2	1.9–2.2

Author	Furnace type	Crucible type	Temperature (°C)	Si Source/ Initial B	Metal system	Slag system	Gas phase	Slag/ metal mass ratio	Holding time (h)	L_B
(Suzuki and Sano, 1991)	Resistance	Graphite	1450	MG–Si B: 30–90 ppmw	Si	CaO–SiO_2–CaF_2	CO	1	2	1–1.7
(Teixeira and Morita, 2009)	Resistance	Graphite	1550	-	Si	CaO–SiO_2–CaF_2	Ar	2.2	18	1–2.4
(Cai *et al.*, 2011)	Induction	Graphite	1600, 1500–1700	B: 6–9 ppmw	Si	CaO–SiO_2–CaF_2	Ar	3	1	2.86–4.61
(Cheng *et al.*, 2018)	Induction	Graphite	1550	-	Si	CaO–SiO_2–CaF_2	Ambient air	2.2	2	-
(Cheng *et al.*, 2019)	Induction	Graphite	1600	-	Si	CaO–SiO_2–CaF_2	Ambient air	1–3	0.25–0.5	1.2–1.8
(Suzuki and Sano, 1991)	Resistance	Graphite	1450	MG–Si B: 30–90 ppmw	Si	CaO–MgO–SiO_2–CaF_2	CO	1	2	1–1.4
(Suzuki and Sano, 1991)	Resistance	Graphite	1450	MG–Si B: 30–90 ppmw	Si	CaO–BaO–SiO_2–CaF_2	CO	1	2	1.2–6
(Ding *et al.*, 2012)	Induction	Graphite	1550	MG–Si B: 22 ppmw	Si	CaO–SiO_2–LiF	Ar	0.5–5		1.0–2.77
(Y. Li *et al.*, 2014)	Induction	Graphite	1550	-	Si	CaO–SiO_2–LiF	Ar	1	0.25–3	1.8
(Wang *et al.*, 2016)	Induction	Graphite	1550	B: 13 ppmw	Si	CaO–ZnO–SiO_2	Ar	1	1	1.8–3.04

Author	Furnace type	Crucible type	Temperature (°C)	Si Source/ Initial B	Metal system	Slag system	Gas phase	Slag/ metal mass ratio	Holding time (h)	L_B
(Lai *et al.*, 2016)	Induction	Graphite	1700	-	Si	$Li_2O–SiO_2$	Ambient air	0.5–3	0.17–0.5	-
(Y. Li *et al.*, 2014)	Induction	Graphite	1550	-	Si	$Li_2O–CaO–SiO_2$	Ar	1	0.25–3	1.4
(Lai *et al.*, 2016)	Induction	Graphite	1700	-	Si	$Li_2O–SiO_2–CaF_2$	Ambient air	1	0.17–1	
(Ding *et al.*, 2012)	Induction	Graphite	1550	MG–Si B: 22 ppmw	Si	$Li_2O–CaO–SiO_2$	Ar	0.5–5	0.5–4	1.0–2.0
(Wu *et al.*, 2012)	Induction	Graphite	1600	-	Si	$Li_2O–CaO–SiO_2$	Ar	0.5–4	2	0.82–1.56
(Safarian *et al.*, 2013)	Induction	Graphite	1500, 1550	-	Si	$Na_2O–SiO_2$	Ar	2	0.25–0.75	0.3–1
(Fang *et al.*, 2014)	Induction	Graphite	1550–1750	-	Si	$Na_2O–SiO_2$	Ambient air	0.5–2.5	0.5	-
(Li *et al.*, 2018)	Induction	Graphite	1600	-	Si	$Na_2O–SiO_2$	-	0.5–1.5	0.17–1	-
(Teixeira and Morita, 2009)	Resistance	Graphite	1550	-	Si	$Na_2O–CaO–SiO_2$	Ar	2.2	1	1.6–2.3
(Zhang *et al.*, 2013)	Induction	Graphite, Quartz	1500	-	Si	$Na_2O–CaO–SiO_2$	Ar	0.2	1	2.12–5.81
(Safarian *et al.*, 2015)	Induction	Graphite	1600	-	Si	$Na_2O–CaO–SiO_2$	Ar	1–3	0.17–2	2.4, 2.6
(Y. Li *et al.*, 2014)	Induction	Graphite	1550	-	Si	$K_2CO_3–CaO–SiO_2$	Ar	1	0.25–3	1.9

Author	Furnace type	Crucible type	Temperature (°C)	Si Source/ Initial B	Metal system	Slag system	Gas phase	Slag/ metal mass ratio	Holding time (h)	L_B
(Wu *et al.*, 2016)	Induction	Graphite	1550	-	Si	K_2CO_3–CaO–SiO_2	Ar	1	0.5–5	1.17–2.08
(Jakobsson and Tangstad, 2018)	Resistance	Graphite	1600	-	Si	CaO–Al_2O_3-SiO_2	Ar	1	6–9	1.33–2.08
(J. Li *et al.*, 2014)	Induction	Graphite	1800	-	Si	CaO–Al_2O_3–SiO_2–CaF_2	Ambient air	0.4–1	0.5–2	1.0–2.2
(Johnston and Barati, 2010)	Resistance	Alumina	1500	B: 0.19–0.26wt%	Si	BaO–Al_2O_3–SiO_2	Ar	1.4	2	0.1–0.5
(Jakobsson and Tangstad, 2018)	Resistance	Graphite	1600	-	Si	MgO–Al_2O_3–SiO_2	Ar	1	6–9	1.8
(Johnston and Barati, 2010)	Resistance	Alumina, MgO	1500	B: 0.19–0.26wt%	Si	CaO–MgO–Al_2O_3–SiO_2	Ar	1.4	2	0.9–1.8 1–2
(Yin *et al.*, 2011)	Induction	Graphite	1600–1750	-	Si	Na_2O–CaO–Al_2O_3–SiO_2	-	0.1–0.5	0–4	-
(Wang *et al.*, 2014)	Resistance	Graphite	1450	-	Si	CaO–SiO_2–$CaCl_2$	Ar	2	12	0.23–2.4

References C–1

Cai, J., Li, J., Chen, W., Chen, C., Luo, X. (2011) Boron removal from metallurgical silicon using CaO–SiO_2–CaF2 slags. *Transactions of Nonferrous Metals Society of China 21*, 1402–1406. https://doi.org/10.1016/S1003-6326(11)60873-X

Cheng, H., Zheng, S., Chen, C. (2019) Evaluation of Factors on Removing Boron from Silicon by Slag Refining Under Atmospheric Conditions. *JOM 71*, 2120–2127. https://doi.org/10.1007/s11837-019-03450-7

Cheng, H., Zheng, S., Chen, C. (2018) The behavior of Ca and its compounds in Si during the slag refining with CaO–SiO_2–CaF_2 system under air atmosphere. *Separation and Purification Technology 201*, 60–70. https://doi.org/10.1016/j.seppur.2018.02.052

Ding, Z., Ma, W., Wei, K., Wu, J., Zhou, Y., Xie, K. (2012) Boron removal from metallurgical-grade silicon using lithium containing slag. *Journal of Non-Crystalline Solids 358*, 2708–2712. https://doi.org/10.1016/j.jnoncrysol.2012.06.031

Fang, M., Lu, C., Huang, L., Lai, H., Chen, J., Yang, X., Li, J., Ma, W., Xing, P., Luo, X. (2014) Multiple Slag Operation on Boron Removal from Metallurgical-Grade Silicon Using Na_2O–SiO_2 Slags. *Ind. Eng. Chem. Res. 53*, 12054–12062. https://doi.org/10.1021/ie404427c

Fujiwara, H., Otsuka, R., Wada, K., Fukuyama, T. (2005) *Silicon purifying method, slag for purifying silicon and purified silicon*.

Jakobsson, L.K., Tangstad, M. (2018) Thermodynamics of Boron Removal from Silicon Using CaO–MgO–Al_2O_3–SiO_2 Slags. *Metallurgical and Materials Transactions B 49*, 1699–1708. https://doi.org/10.1007/s11663-018-1250-7

Jakobsson, L.K., Tangstad, M. (2015) Thermodynamic Activities and Distributions of Calcium and Magnesium Between Silicon and CaO–MgO–SiO_2 Slags at 1873 K (1600°C). *Metallurgical and Materials Transactions B 46*, 595–605. https://doi.org/10.1007/s11663-014-0268-8

Johnston, M.D., Barati, M. (2010) Distribution of impurity elements in slag–silicon equilibria for oxidative refining of metallurgical silicon for solar cell applications. *Solar Energy Materials and Solar Cells 94*, 2085–2090. https://doi.org/10.1016/j.solmat.2010.06.025

Lai, H., Huang, L., Lu, C., Fang, M., Ma, W., Xing, P., Li, J., Luo, X. (2016) Reaction Mechanism and Kinetics of Boron Removal from Metallurgical-Grade Silicon Based on Li_2O–SiO_2 Slags. *JOM 68*, 2371–2380. https://doi.org/10.1007/s11837-015-1656-5

Li, J., Zhang, L., Tan, Y., Jiang, D., Wang, D., Li, Y. (2014) Research of boron removal from polysilicon using CaO–Al_2O_3–SiO_2–CaF_2 slags. *Vacuum 103*, 33–37. https://doi.org/10.1016/j.vacuum.2013.12.002

Li, P., Wang, K., Fang, M., Zhang, L., Jiang, D., Li, J., Tan, Y. (2018) Boron removal from silicon by slag refining using Na_2O–SiO_2 in industrial applications. *Separation Science and Technology 53*, 2144–2149. https://doi.org/10.1080/01496395.2017.1405035

Li, Y., Wu, J., Ma, W. (2014) Kinetics of Boron Removal from Metallurgical Grade Silicon using a Slag Refining Technique Based on CaO–SiO_2 Binary System. *Separation Science and Technology 49*, 1946–1952. https://doi.org/10.1080/01496395.2014.904877

Luo, D., Liu, N., Lu, Y., Zhang, G., Li, T. (2011) Removal of boron from metallurgical grade silicon by electromagnetic induction slag melting. *Transactions of Nonferrous Metals Society of China 21*, 1178–1184. https://doi.org/10.1016/S1003-6326(11)60840-6

Nishimoto, H., Kang, Y., Yoshikawa, T., Morita, K. (2012) The Rate of Boron Removal from Molten Silicon by $CaO–SiO_2$ Slag and Cl_2 Treatment. *High Temperature Materials and Processes 31*, 471–477. https://doi.org/10.1515/htmp-2012-0083

Safarian, J. (2019) Thermochemical Aspects of Boron and Phosphorus Distribution Between Silicon and $BaO–SiO_2$ and $CaO–BaO–SiO_2$ lags. *Silicon 11*, 437–451. https://doi.org/10.1007/s12633-018-9919-8

Safarian, J., Tranell, G., Tangstad, M. (2015) Boron Removal from Silicon by $CaO–Na_2O–SiO_2$ Ternary Slag. *Metallurgical and Materials Transactions E 2*, 109–118. https://doi.org/10.1007/s40553-015-0048-7

Safarian, J., Tranell, G., Tangstad, M. (2013) Thermodynamic and Kinetic Behavior of B and Na Through the Contact of B-Doped Silicon with $Na_2O–SiO_2$ Slags. *Metall and Materi Trans B 44*, 571–583. https://doi.org/10.1007/s11663-013-9823-y

Suzuki, K., Sano, N. (1991) Thermodynamics for Removal of Boron from Metallurgical Silicon by Flux Treatment, in: Luque, A., Sala, G., Palz, W., Santos, G., Helm, P. (ed.), *Tenth E.C. Photovoltaic Solar Energy Conference*. Springer Netherlands, Dordrecht, pp. 273–275. https://doi.org/10.1007/978-94-011-3622-8_68

Teixeira, L.A.V., Morita, K. (2009) Removal of Boron from Molten Silicon Using $CaO–SiO_2$ Based Slags. *ISIJ Int. 49*, 783–787. https://doi.org/10.2355/isijinternational.49.783

Teixeira, L.A.V., Tokuda, Y., Yoko, T., Morita, K. (2009) Behavior and State of Boron in $CaO–SiO_2$ Slags during Refining of Solar Grade Silicon. *ISIJ Int. 49*, 777–782. https://doi.org/10.2355/isijinternational.49.777

Wang, F., Wu, J., Ma, W., Xu, M., Lei, Y., Yang, B. (2016) Removal of impurities from metallurgical grade silicon by addition of ZnO to calcium silicate slag. *Separation and Purification Technology 170*, 248–255. https://doi.org/10.1016/j.seppur.2016.06.060

Wang, Y., Ma, X., Morita, K. (2014) Evaporation Removal of Boron from Metallurgical-Grade Silicon Using $CaO–CaCl_2–SiO_2$ Slag. *Metall Mater Trans B 45*, 334–337. https://doi.org/10.1007/s11663-014-0031-1

Wei, K.-X., Lu, H.-F., Ma, W.-H., Li, Y.-L., Ding, Z., Wu, J.-J., Dai, Y.-N. (2015) Boron removal from metallurgical-grade silicon by $CaO–SiO_2$ slag refining. *Rare Met. 34*, 522–526. https://doi.org/10.1007/s12598-015-0496-3

Weiss, T., Schwerdtfeger, K. (1994) Chemical equilibria between silicon and slag melts. *Metall Mater Trans B 25*, 497–504. https://doi.org/10.1007/BF02650071

White, J.F., Allertz, C., Sichen, D. (2013a) The thermodynamics of boron extraction from liquid silicon using $SiO_2–CaO–MgO$ slag treatment. *International Journal of Materials Research 104*, 229–234. https://doi.org/10.3139/146.110867

White, J.F., Allertz, C., Sichen, D. (2013b) Boron partitioning between $SiO_2–CaO–MgO$ slags and liquid silicon at controlled nitrogen potential. *International Journal of Materials Research 104*, 650–656. https://doi.org/10.3139/146.110913

White, J.F., Sichen, D. (2014) Mass Transfer in Slag Refining of Silicon with Mechanical Stirring: Transient Interfacial Phenomena. *Metall Mater Trans B 45*, 96–105. https://doi.org/10.1007/s11663-013-0010-y

Wu, J., Ma, W., Jia, B., Yang, B., Liu, D., Dai, Y. (2012) Boron removal from metallurgical grade silicon using a $CaO–Li_2O–SiO_2$ molten slag refining technique. *Journal of Non-Crystalline Solids 358*, 3079–3083. https://doi.org/10.1016/j.jnoncrysol.2012.09.004

Wu, J., Wang, F., Ma, W., Lei, Y., Yang, B. (2016) Thermodynamics and Kinetics of Boron Removal from Metallurgical Grade Silicon by Addition of High Basic Potassium Carbonate to Calcium Silicate Slag. *Metall Mater Trans B 47*, 1796–1803. https://doi.org/10.1007/s11663-016-0615-z

Yin, C., Hu, B., Huang, X. (2011) Boron removal from molten silicon using sodium-based slags. *J. Semicond. 32*, 092003. https://doi.org/10.1088/1674-4926/32/9/092003

Zhang, L., Tan, Y., Xu, F.M., Li, J.Y., Wang, H.Y., Gu, Z., 2013. Removal of Boron from Molten Silicon using $Na_2O–CaO–SiO_2$ Slags. *Separation Science and Technology 48*, 1140–1144. https://doi.org/10.1080/01496395.2012.714438

Zhu, M. (2021) *Silicon purification by acid leaching and slag refining techniques* (Doctoral Thesis, 2021:117). Norwegian University of Science and Technology (NTNU), Trondheim, Norway. https://doi.org/https://hdl.handle.net/11250/2738488

Table C-2 *Review list of literature on gas refining of Si for boron removal with H_2–x% H_2O gases. Adapted from Hoseinpur (2021).*

Author	Furnace type	Crucible	Temperature(°C)	Si- Material	Gas composition	Gas flow rate (NL/min)	Holding time (h)	k_t(μm/s)
(Altenberend *et al.*, 2017)	Inductively coupled plasma torch	a. Cold crucible (copper) b. Silica plates c. Graphite crucible	a. 1410 b. 1500 c. 1500–1700	a. UMG–Si with 30 ppmw B b. UMG–Si with 30 ppmw B c. EG–Si with 30 ppmw B	Ar, H_2 and O_2	a. 7.2–7.6 (Nm^3/h) b. 7.7 (Nm^3/h) c. 7.6 (Nm^3/h)	a. 6 b. - c. -	
(Hoseinpur *et al.*, 2020)	Vacuum induction	Graphite	1500	Mixture of commercial-grade silicon HQ-Silgrain, purity 99.76%, and FBR silicon, with 11.76 ppmw B	H_2–3%H_2O	3 NL/min	1.67	17.33
(Hoseinpur *et al.*, 2022)	Vacuum induction	Graphite Alumina	1450, 1500, 1600	213 g Si, mixture of 50 wt% FBR polysilicon, 8N purity, and 50 wt% Silgrain HQ micron cut; initial B about 15–20 ppmw	H_2 or H_2–3%H_2O; with Ar, He, or vacuum	3 NL/min	0.83–2	0.9–23.3

Author	Furnace type	Crucible	Temperature(°C)	Si- Material	Gas composition	Gas flow rate (NL/min)	Holding time (h)	k_t(µm/s)
(Nakamura *et al.*, 2004)	Steam added plasma	Silica Graphite	1600–1700 1550–1600	UMG–Si with 5–10 ppmw B HP-Si with 0.7–30 ppmw B	Ar, Ar + He, Ar + H_2, with H_2O + H_2	$2.5*10^{-4}$ – $7.1*10^{-2}$ (Nm^3/s)	8.33	-
(Nordstrand and Tangstad, 2012)	Vacuum induction	Graphite	1450, 1500, 1550, 1600	EG–Si with 50/130/150 ppmw B	H_2O, H_2 and Ar	3	2, 4.5	1.2–13
(Safarian *et al.*, 2016)	Induction	Graphite, high-purity quartz, alumina	1460, 1500, 1530	EG–Si with 10–25 ppmw B	H_2 and H_2O	0.5, 1, 1.5, 3, 6, 9	1, 3.25	1.5–25
(Sortland and Tangstad, 2014)	Induction Resistance	Graphite	1500	EG–Si with 36 to 128 ppmw B	H_2O, H_2 and Ar	0.5–16	0.6–2.5	0.1–51.1

References C-2

Altenberend, J., Chichignoud, G. and Delannoy, Y. (2017) 'Study of mass transfer in gas blowing processes for silicon purification', *Metallurgical and Materials Transactions E*, 4, pp. 41–50. Available at: https://doi.org/10.1007/s40553-016-0105-x

Hoseinpur, A. (2021) *Vacuum and gas refining of silicon for solar cell applications*. Doctoral thesis 2021:244. Norwegian University of Science and Technology (NTNU). Available at: https://hdl.handle.net/11250/2760867

Hoseinpur, A., Andersson, S., Müller, M., Tang, K. and Safarian, J. (2022) 'Boron removal from silicon melt by gas blowing technique', *High Temperature Materials and Processes*, 41, pp. 69–91. Available at: https://doi.org/10.1515/htmp-2022-0011

Hoseinpur, A., Tranell, G. and Safarian, J. (2020) 'Phosphorus and boron removal from Si by vacuum and gas refining processes', in *Proceedings of Silicon for the Chemical and Solar Industry XV*. Trondheim, Norway.

Nakamura, N., Baba, H., Sakaguchi, Y. and Kato, Y. (2004) 'Boron removal in molten silicon by a steam-added plasma melting method', *Materials Transactions*, 45, pp. 858–864. Available at: https://doi.org/10.2320/matertrans.45.858

Nordstrand, E.F. and Tangstad, M. (2012) 'Removal of boron from silicon by moist hydrogen gas', *Metallurgical and Materials Transactions B*, 43, pp. 814–822. Available at: https://doi.org/10.1007/s11663-012-9671-1

Safarian, J., Tang, K., Olsen, J.E., Andersson, S., Tranell, G. and Hildal, K. (2016) 'Mechanisms and kinetics of boron removal from silicon by humidified hydrogen', *Metallurgical and Materials Transactions B*, 47, pp. 1063–1079. Available at: https://doi.org/10.1007/s11663-015-0566-9

Sortland, Ø.S. and Tangstad, M. (2014) 'Boron removal from silicon melts by H2O/H2 gas blowing: Mass transfer in gas and melt', *Metallurgical and Materials Transactions E*, 1, pp. 211–225. Available at: https://doi.org/10.1007/s40553-014-0021-x

Table C-3 *Review list of literature on slag refining with silicon alloy. Adapted from Zhu (2021).*

Author	Furnace type	Crucible	Temperature (°C)	Metal system	Alloy composition	Slag system	Gas phase	Slag / Metal mass ratio	Holding time (h)	L_B
(Ma *et al.*, 2013)	Induction	Graphite	1400	Si–Sn	0–82.4 mol% Sn	$CaO–SiO_2–CaF_2$	Ar	3	18	2.3–200
(Li *et al.*, 2016)	Resistance	Graphite	1450	Si–Sn	0–50 mol% Sn	$Na_2SiO_2–CaO–SiO_2$	Ar	1–2	0.5–3	-
(Al-Khazraji *et al.*, 2018)	Resistance	Graphite	1500	Si–Sn	25 wt% Sn	$CaCl_2$, CaO/SiO_2 = 0.5–2	Ar	1, 2	0–1	-
(Li *et al.*, 2014)	Resistance	Alumina	1500	Si–Cu	70 wt% Cu	$Na_2O–CaO–Al_2O_3–SiO_2$	Ar	10	0.17	0.7–46.8
(Huang *et al.*, 2016)	Induction	Graphite	1550	Si–Cu	30–70 wt% Cu	$CaO–SiO_2–CaCl_2$	Ambient air	1	0.5	-
(Jakobsson, 2013)	Resistance	Graphite	1600	Si–Fe	0–50 wt% Fe	$CaO–SiO_2$	Ar	1	6	2.6–3.0
(Krystad *et al.*, 2017)	Resistance	Graphite	1600	Si–Fe	0–85 wt% Fe	$CaO–SiO_2$	Ar	0.57	0–3	2.4–6.0
(Hosseinpour and Tafaghodi Khajavi, 2018)	Resistance	Alumina	1600	Si–Fe	20 wt% Fe	$CaO–Al_2O_3–SiO_2$	Ar	1	0–8	0.8–11.4
(Zhu *et al.*, 2021)	Induction	Graphite	1600±20	Si–Sn	10 wt% Sn	$CaO–SiO_2$ $CaO–La_2O_3–SiO_2$	Ar	1	1	2.93, 3.33, 3.65

References C-3

Al-khazraji, R., Li, Y. and Zhang, L. (2018) 'Boron separation from Si–Sn alloy by slag treatment', *International Journal of Minerals, Metallurgy and Materials*, 25, pp. 1439–1446. Available at: https://doi.org/10.1007/s12613-018-1698-0

Hosseinpour, A. and Tafaghodi Khajavi, L. (2018) 'Thermodynamics of boron removal in slag refining of Fe–Si alloy', *Journal of Alloys and Compounds*, 768, pp. 545–552. Available at: https://doi.org/10.1016/j.jallcom.2018.07.246

Huang, L., Lai, H., Gan, C., Xiong, H., Xing, P. and Luo, X. (2016) 'Separation of boron and phosphorus from Cu-alloyed metallurgical grade silicon by CaO–SiO2–CaCl2 slag treatment', *Separation and Purification Technology*, 170, pp. 408–416. Available at: https://doi.org/10.1016/j.seppur.2016.07.004

Jakobsson, L.K. (2013) Distribution of boron between silicon and CaO–SiO2, MgO–SiO2, CaO–MgO–SiO2 and CaO–Al2O3–SiO2 slags at 1600°C. Doctoral thesis. Norwegian University of Science and Technology (NTNU).

Krystad, E., Jakobsson, L.K., Tang, K. and Tranell, G. (2017) 'Thermodynamic behavior and mass transfer kinetics of boron between ferrosilicon and CaO–SiO2 slag', *Metallurgical and Materials Transactions B*, 48, pp. 2574–2582. Available at: https://doi.org/10.1007/s11663-017-1015-8

Li, J., Cao, P., Ni, P., Li, Y. and Tan, Y. (2016) 'Enhanced boron removal from metallurgical grade silicon by the slag refining method with the addition of tin', *Separation Science and Technology*, pp. 1–6. Available at: https://doi.org/10.1080/01496395.2016.1165702

Li, M., Utigard, T. and Barati, M. (2014) 'Removal of boron and phosphorus from silicon using CaO–SiO2–Na2O–Al2O3 flux', *Metallurgical and Materials Transactions B*, 45, pp. 221–228. Available at: https://doi.org/10.1007/s11663-013-0011-x

Ma, X., Yoshikawa, T. and Morita, K. (2013) 'Removal of boron from silicon-tin solvent by slag treatment', *Metallurgical and Materials Transactions B*, 44, pp. 528–533. Available at: https://doi.org/10.1007/s11663-013-9812-1

Zhu, M. (2021) *Silicon purification by acid leaching and slag refining techniques*. Doctoral thesis 2021:117. Norwegian University of Science and Technology (NTNU), Trondheim, Norway. Available at: https://hdl.handle.net/11250/2738488

Zhu, M., Wu, G., Azarov, A., Monakhov, E., Tang, K., Müller, M. and Safarian, J. (2021) 'Effects of La2O3 addition into CaO–SiO2 slag: Structural evolution and impurity separation from Si–Sn alloy', *Metallurgical and Materials Transactions B*, 52, pp. 3045–3063. Available at: https://doi.org/10.1007/s11663-021-02232-4

About the authors

Merete Tangstad is a Professor of Process Metallurgy at NTNU and a recognized expert in the production of silicon, ferrosilicon, and manganese alloys. She has previously worked in the metallurgical industry. Her research encompasses raw materials, reduction processes, furnace operation, slag chemistry, and sustainable metal production. Over several decades, she has contributed to the advancement of metallurgical research and education and has worked closely with the Norwegian and international process industries to improve metallurgical processes and resource utilization.

Gabriella Tranell is Professor of process metallurgy at NTNU. She holds an MSc in Metallurgy from Luleå University of Technology and a PhD in Materials Engineering from the University of New South Wales. Her research focuses on the production of silicon and ferroalloys, metal recycling, emission reduction, and sustainable metal production. Over many years, she has contributed significantly to strengthening collaboration between industry, research, and higher education in the field of metallurgy.

Halvard Tveit holds a degree in process metallurgy from NTH (the Norwegian Institute of Technology). He has worked at AS Norsk Jernverk, Bjølvefossen, and Orkla Metall, and most recently served as a Corporate Specialist at Elkem. For 25 years, he combined his position at Elkem with an appointment as Adjunct Professor at NTNU. His areas of interest include the production of silicon and ferrosilicon, furnace operation, process control, energy utilization, and environmental improvements in the smelting industry. He has authored several publications on safety and the working environment.

Eli Ringdalen is a Senior Research Scientist at SINTEF Industry, holding an MSc in Geology and a PhD in Metallurgy. She also has experience in both research and operations at various mines and smelters. Her work is particularly related to raw materials, silicon and ferroalloy production, reaction mechanisms in high-temperature processes, and the development of more sustainable metallurgical processes. Throughout her long research career, she has contributed to both fundamental and applied knowledge for the Norwegian and international ferroalloy industry.

Index

A

AC furnace 328
activity coefficient 111–113, 143, 148–151, 153, 395, 405, 409, 414–415
additional elements 19, 109, 141, 154
agglomerate reaction 204–205
agglomerated charge 213, 342, 344–346
agglomerates 26, 70, 205–206, 340, 344–346, 462
air pollution 457
alkali metal oxides 119, 140
alkalis 177
alloying elements 154, 376, 417–418
alternating current 79, 83, 231, 331–332
alternating current electric arc 243, 251
aluminium 15, 21–22, 117, 119, 130, 144–145, 283, 302, 363–364, 366–368, 381, 384, 388, 391–392, 394, 397, 455, 480–481, 510
aluminothermic 327, 363–364
amorphous SiO_2 19, 177, 462
Andreae's rule 235, 238, 242
anode 86, 263–264, 365–368
arc 62, 81, 85–87, 92, 95, 170, 198, 223, 230, 232–235, 239–244, 249–253, 256, 263, 265, 302, 304, 309–310, 331, 347–350
arc chamber 85, 263–265
arc current 263
arc furnace 16–19, 78, 250, 252, 347
arc resistance 231, 234, 241

B

baking of the electrode 258, 463
beds of fines 434–435
binary phase diagram 31, 122–123, 305
biocarbon 169, 180, 183, 185, 327, 360, 368
blast furnace 77, 189, 347, 351
boiler 287, 289–290
boiling point model 138, 174, 464
boron refining 411
briquettes 344–345
brown condensate 55, 96–97, 172, 193
brown mass 55, 97
brownish glaze 508–509
burn injuries 483
bus bar 190

C

C_1 236
C_3 236–237, 243, 261–262
calcium silicides 154–155
carbon 30, 181–184
carbon capture and storage (CCS) 334, 354
carbon capture and use (CCU) 334–335
carbon capture (CC) 334
carbon content of the charge 86, 208, 210, 212, 214, 220, 265, 321
carbon loss 183, 279, 283
carbon materials 25, 30, 41, 43, 45–46, 68, 84–85, 139, 171, 181–185, 187–188, 192, 196, 205–206, 211, 246, 248, 250, 281–283, 285, 287, 290, 294, 303–304, 460, 482

carbon reaction 204
carbon reactivity index, CRI 185
carbon solubility 56, 159, 304
carbon sources 173, 183–184, 188, 281–282
carbon materials 184
carbothermic 70, 77, 105, 117, 302, 326–327, 334, 358, 368, 399, 459, 487
casting equipment 440
cast-to-shape 436
cathode 86, 263–264, 348, 366–367
cathode voltage drop 263
cavity collapse 477
CCS 331, 334, 336, 354
char 25, 45, 152, 157, 180, 187, 246–247, 303
characteristic of the arc 251–252
charcoal 180, 187
charge collapse 346
charge current 232, 234, 240–241
charge top 38, 62, 82, 88, 138, 152, 170–171, 175, 177, 191–193, 327–328, 459
chemical equilibria 487
chemical industry 21–22
chlorination 375–376, 394–395, 397
chlorine 22, 368, 375, 394, 397
chopping disc 86
clay minerals 119
clogging of the taphole 320
closed furnace 152, 327–330, 333, 336
closed loop control 196
CO2 reactivity test 185
coal 180, 182, 184
coke 180, 182, 184
cold strength 181
combustible dust 482
composite agglomerates 26, 70, 340, 345
computer control 196
condensates 56, 58, 60, 92, 172, 298, 311
condensation reactions 54, 60, 62, 94, 96, 104, 200, 310–311
conductivity 187, 243, 246
contact angle 134, 136–137
continuous feed mode 216, 218, 223
continuous tapping 83, 94, 312
cooling rate 403, 418, 440–441, 444–448
cooling water leakage 474–477
counter-current 155, 200, 210, 310, 349, 406
crater pressure 94, 314, 320
cristobalite 32, 50, 66, 177
critical rate of rotation 83
crusts 310–311
crusty silica 393
current paths 238–239, 244, 248, 254, 298, 300, 311, 316, 319
current through the charge 244
current through the electric arc 250
current through the furnace 87, 243

D

data sources 487–488, 499–500
DC furnace 328
decarbonization 326, 354
decarburization 399–400
deficit of carbon 209
deposits in the furnace 297–298
deviation from equilibrium 100, 215–216
direct current 264, 331–332
direct current arcs 251
directional solidification 366, 398, 400–403
distribution equilibria 141, 378
dust explosion 481–483
dynamic model 199, 214, 216–218, 221–223

E

electric conductivity 250
electric operation 191, 229–231, 235, 237, 258, 260
electricity 19, 24, 27, 279–280, 287, 289–290, 292, 327, 354, 457–459, 472, 477
electricity supply 279
electrode consumption 85, 220, 234, 241, 258, 263–265, 303, 310, 331
electrode slip control 258

electrolysis 354, 363–368
electrolyte 365–367
electron beam 399
electronic devices 15, 23
Ellingham diagram 139, 141, 353–354
emulsification 134
energy balance 195, 199, 269, 271, 275–276, 279, 284, 286–288, 336, 388, 391
energy control of the silicon furnace 258
energy efficiency 280–281
energy losses 279–280, 326–327
energy out of control 472
energy recovery 16, 167–168, 190–191, 194, 289–291, 294, 326–327, 432
energy sources 358, 473
energy supply system 191, 326
energy yield factor 281
enthalpy balance 160, 293
enthalpy change 271–272
environmental aspects 327, 455
equilibrium calculations 30, 34, 41, 62, 85, 158, 355, 382, 487–489, 501, 503
equilibrium pressure of SiO 60
equivalent circuit 243–244, 255, 259
errors in equilibrium calculations 501
excavation of furnaces 88

F

ferrosilicon 155–156, 284–286
FFC Cambridge process 366
FGR 338
filtration 399
fines generation 175, 177, 179, 183
fire 480–481
Fix C 188, 303
fixed C 30, 157, 159, 161
fixed C balance 155
floating slags 384
flow of charge 353
flue gas recycling (FGR) 336–337, 339
formation of cracks 451
formation of deposits 79, 297
four condensed phases 36, 38, 487, 491, 499
furnace blow-out 478
furnace body 191, 279, 287, 302, 329, 332, 346
furnace eruption 473
furnace hood 191–192, 280, 333–334, 456–457, 460–461, 473–474, 478
furnace resistance 145, 231, 240, 243, 248
furnace transformers 258–259

G

gas blowing 411
gas cleaning 80, 168, 190–191, 335
gas velocity 66, 171, 283
Gibbs phase rule 154
Gibbs-Duhem equation 113
glass melts 121
grain growth 442
grain size 177, 433, 436, 442–445, 447–448
granulation 436, 438–441, 445
graphite 30
greenhouse gas (GHG) 326–327, 361, 455, 458–459

H

Hall-Heroult process 364–366
handling raw materials 192
heat balance 157, 160, 206, 341, 377, 388
heat distribution 232–234
heat of mixing 110, 112, 159
heat production 81, 229, 231, 234, 242, 263, 332, 346, 349
Henry's law 113
HES 311
hot zone 138, 142, 461
HSE 469
hydrogen plasma 354, 358, 360

I

ideal solution 111
inactive slag zone 169

industrial process 278–279, 285, 290, 294, 358, 433
inert anode 364–366
inert electrode 350
inner lining 191
inner structure 79, 83–85, 91, 155, 169, 214, 232, 239, 297, 311, 321
inner zone 95, 97–98
interfacial properties 130, 137
interfacial tensions 132, 134–135
interfacial turbulence 134
intermetallic phases 363, 393, 434, 436, 441–442, 447–450
iron 155–157, 189
iron addition 284
iron ore 155, 157, 160, 189, 508
iron oxide 34, 155–157, 169, 173, 189, 243–245, 284–286, 459
iron oxide reduction 157, 159, 284
iron sources 26, 173, 189, 284–286

K
kinetic parameters 216
Knapsack 244, 254
Kroll process 361

L
Life Cycle Assessment (LCA) 26
limestone 169, 377, 387, 460
lining 82, 92, 172, 190–191, 193–194, 314–315, 317, 320, 331, 333, 512
liquidus isotherms 124
Lissajous figures 251
long-term dynamics 218, 223

M
magnesiothermia 361
mass action law 487, 489, 491, 493
material balance 202, 273, 275–276, 287, 344, 390, 460, 464
metal bath 84, 92, 169–171, 231, 314
metallothermia 360
metallurgical control 258
methane 26, 70, 354, 360, 459
microsilica 16, 19, 194, 209, 462
mill scales 155
model of Elkem 198–199, 215, 222
molten oxide electrolysis (MOE) 367
molten silicon 18, 84, 86, 94, 131–132, 320, 350, 401, 477, 483

N
non-atmospheric pressure 351
non-carbothermic processes 353
non-transferred arc 348–349

O
off-gas temperature 171, 191, 278–279, 290, 293, 334–335, 463–464, 475–476
operational problems 194, 297
optimum carbon content 209–210, 218
origin of the silicon furnace 77
outer steel shell 191
outer zone 98–99
oxidative refining 384, 404
oxide activities 141
oxide inclusions 393
oxygen in silicon 393
oxygen lance 82–83, 193
oxygen potential 141, 378

P
PAH 330, 458, 462–463
particulate matter 378, 456, 458, 461–462
partition 215
permeability 26, 170–171, 181, 321
personal protective equipment 484
phase rule 35, 154, 201, 355, 488–491, 503
phase separation 135, 393
photovoltaic cells 24
plasma burner 348–349
plasma reactor 347, 349
pollution 48, 53, 320, 365, 457–458
polycyclic aromatic hydrocarbons 462
polymorphs 50, 177
porosity 43–45, 185, 188
pre-reaction zone 169–172, 175
pressure build-up 473, 480
probes in the furnace 83

process emissions 327, 457–458
process safety 469
programmes for thermochemical calculations 499

Q

qualitative models 198
quartz 176–179
quartzite 25, 119–120, 176, 269, 347, 457
quenching 350

R

Raoult's law 111, 113
raw material 173–175, 192
reacting materials zone 170, 172
reaction mechanism 41, 66–68, 70, 176, 355, 510
reaction path 381, 387–388
reaction zones 169
reactivities 157, 175, 184, 188
reactivity number 205–206, 211
real furnace 99, 220, 262, 287
real solutions 111, 495–496
recovering reactions for SiO 16, 96
reduction furnaces 167
reduction material 25, 144, 152, 180, 269, 457
refractory oxides 141, 143
removal of deposits 310
removal of phosphorus 411
resistance 231, 233–234
resistivity of the charge 81, 235, 246, 349
root cause analysis 476–477, 484
rotating furnace 240, 310, 512

S

SAF 167, 229, 253, 327, 338, 345, 360, 368, 375, 377, 385, 461, 463
Scheil equation 403, 420
scrap 109, 139, 189, 284, 363
scrap iron 155, 159–160
secondary dust explosion 483
segregation 175, 211, 248, 398, 406–407, 416–418, 420, 433, 435, 438, 446
segregation coefficient 401–402, 407, 417
selectivity 23, 393
self-crushing 438, 451
semi-closed furnaces 191, 459
sessile drop 131–132, 134, 137, 179
settling 399
short-term dynamics 220
Si sources 514
Si_2C 32, 37, 488, 490, 494
Si–C system 30, 350
SiC_2 32, 37, 488, 490, 494
SiH_2 process 359
silane 363
silica activity 155
silica as solvent 117
silica films 392
silica reduction 154, 156, 161
silicate melt 131, 136
silicochromium 236
silicomanganese 154–155, 236, 304
silicon activity 154, 158, 161, 284
silicon applications 21
silicon as solvent 109
silicon halides 367
silicon metal 16, 31, 79, 84, 113, 154, 236, 326, 333–334, 345, 445, 512
silicon smelting 141, 143, 155
Silicon Valley 15
silicon yield 17, 80, 161, 170, 172, 195, 199, 229, 272, 274, 278–279, 286, 289, 326, 458, 460
silicones 22–23, 27
simulations 137, 198, 200, 222, 253, 337, 347, 350, 363
SINTEF SiO reactivity test 188
sintered charge materials 297
SiO loss 68, 96, 184, 222, 284, 333, 342, 346, 460
Si-O system 32
SiO_2-SiC–C 37
SiO_2–SiC–Si 37–38, 352–353, 498, 501
SiO_2 + x C reaction 208–209
SiO_2 + x SiC reaction 51, 500
Si–O–C system 29, 41, 109, 276, 487, 499–500

SisAl technology 363
sizing 48, 68, 175, 436–437, 482
slag formation 140, 155, 173, 378–379, 384
slag systems 129, 381, 405–406, 408, 488, 514
slagging 375–376
slag/metal separation 135
softening 61, 176, 178, 247, 313
solid solubility 400–401, 416
solidification time 437, 443
solubility of carbon 158, 304
solubility of oxygen 393
sources of pollution 457
specific energy 159, 161, 189, 195, 274, 277, 281, 283, 458
split charge 347, 353
split furnace 302, 329, 332, 346
spreading coefficient 134–135
stability of oxides 109, 139
stationary furnace 240, 310
steam 19, 194, 287, 289–290, 440, 523
steel and cast iron 21
steel scrap 189
stoichiometric analysis 97, 269
stoichiometric model 199–201, 207–208, 210, 212–214, 217–218, 222–223, 302–303
stoking cycles mode 216
storage 167, 192, 437, 474
sulphur dioxide 460
surface burning 283
surface energy 59, 130, 135–136, 450
surface properties 134–135, 380
surface tension 130–133, 135, 442
surplus of carbon 70, 209
Søderberg 258, 263

T

tapping channels 191, 194, 320
tapping electrode 82–83
tar 328–330
theoretical energy consumption 365
thermal shock 177, 179, 192, 434, 436
thermal strength 177, 181, 183
thermal strength index, TSI 177, 179
thermodynamic variables 35–36, 489
three condensed phases 36, 154, 497, 503
tie-lines 127
tramp elements 183, 189
transferred arc 348–349
transition metal 121, 123, 143
transport ladle 194, 434
turbine 290
two condensed phases 38, 490–492, 494

U

uneven gas distribution 200, 209, 211
unidirectional solidification 399
universal model 223

V

vacuum 51, 65, 250, 352, 376, 399, 409, 411–412, 415, 522
vacuum refining 411
visual probe 84–87
volatile compounds 281
volatile impurities 152
volatiles 152, 157, 171, 181, 184, 193, 195, 246–247, 281–282, 284–286, 288–290, 328, 473–475, 477

W

warm strength 177, 179
water leakage 474–477
weighing system 192
Westly's rule 236, 242
wetting angle 134, 136
white condensate 172
white smoke 80, 82, 87, 96, 509–510
wind sieving 283
woodchips 26, 152, 169, 171, 180, 188–189, 281–282, 288, 457, 476
world production 19

Z

ζ_α-phase 430, 452
ζ_β-phase 430
zone refining 366